Amiril Sahab Abdul Sani ·
Muhammed Nafis Osman Zahid ·
Mohamad Rusydi Mohamad Yasin ·
Siti Zubaidah Ismail · Mohd Zairulnizam Mohd Zawawi ·
Ahmad Rosli Abdul Manaf · Siti Nadiah Mohd Saffe ·
Radhiyah Abd Aziz · Faiz Mohd Turan   *Editors*

Enabling Industry 4.0 through Advances in Manufacturing and Materials

Selected Articles from iM3F 2021, Malaysia

Springer

Lecture Notes in Mechanical Engineering

Amiril Sahab Abdul Sani ·
Muhammed Nafis Osman Zahid ·
Mohamad Rusydi Mohamad Yasin ·
Siti Zubaidah Ismail ·
Mohd Zairulnizam Mohd Zawawi ·
Ahmad Rosli Abdul Manaf ·
Siti Nadiah Mohd Saffe · Radhiyah Abd Aziz ·
Faiz Mohd Turan
Editors

Enabling Industry 4.0 through Advances in Manufacturing and Materials

Selected Articles from iM3F 2021, Malaysia

iM3F

🦔 Springer

Editors
Amiril Sahab Abdul Sani
Faculty of Manufacturing and Mechatronic
Engineering Technology
Universiti Malaysia Pahang
Pekan, Pahang, Malaysia

Muhammed Nafis Osman Zahid
Faculty of Manufacturing and Mechatronic
Engineering Technology
Universiti Malaysia Pahang
Pekan, Pahang, Malaysia

Mohamad Rusydi Mohamad Yasin
Faculty of Manufacturing and Mechatronic
Engineering Technology
Universiti Malaysia Pahang
Pekan, Pahang, Malaysia

Siti Zubaidah Ismail
Faculty of Manufacturing and Mechatronic
Engineering Technology
Universiti Malaysia Pahang
Pekan, Pahang, Malaysia

Mohd Zairulnizam Mohd Zawawi
Faculty of Manufacturing and Mechatronic
Engineering Technology
Universiti Malaysia Pahang
Pekan, Pahang, Malaysia

Ahmad Rosli Abdul Manaf
Faculty of Manufacturing and Mechatronic
Engineering Technology
Universiti Malaysia Pahang
Pekan, Malaysia

Siti Nadiah Mohd Saffe
Faculty of Manufacturing and Mechatronic
Engineering Technology
Universiti Malaysia Pahang
Pekan, Pahang, Malaysia

Radhiyah Abd Aziz
Faculty of Manufacturing and Mechatronic
Engineering Technology
Universiti Malaysia Pahang
Pekan, Pahang, Malaysia

Faiz Mohd Turan
Faculty of Manufacturing and Mechatronic
Engineering Technology
Universiti Malaysia Pahang
Pekan, Pahang, Malaysia

Preface

The second edition forum of The Innovative Manufacturing, Mechatronics and Materials Forum 2021 (iM3F 2021) organized by Universiti Malaysia Pahang through its Faculty of Manufacturing and Mechatronic Engineering Technology was held on 20 September 2021. The main field focuses on manufacturing, mechatronics as well as materials.

More than 132 submissions were received during iM3F 2021 and were reviewed in a single-blind manner, and 60 papers were advocated by the reviewers to be published in the Lecture Notes in Mechanical Engineering. The editors would like to express their gratitude to all the authors who submitted their papers. The papers published in this proceeding have been thoroughly reviewed by the appointed technical review committee consisting of various experts in the field of mechanical, manufacturing and material engineering sciences.

The conference had brought a new outlook on cutting-edge issues shared through keynote speeches by Prof. Ir. Dr. Jamaluddin Mahmud and Prof. Dr. Mohammad Osman Tokhi.

Finally, the editors hope that readers find this volume informative as we thank LNME for undertaking this volume publication. We also would like to thank the conference organization staff and the International Program Committees' members for their hard work.

Pekan, Pahang, Malaysia
November 2021

Amiril Sahab Abdul Sani
Muhammed Nafis Osman Zahid
Mohamad Rusydi Mohamad Yasin
Siti Zubaidah Ismail
Mohd Zairulnizam Mohd Zawawi
Ahmad Rosli Abdul Manaf
Siti Nadiah Mohd Saffe
Radhiyah Abd Aziz
Faiz Mohd Turan

Contents

Contents

Cutting Force in Dry Slot-Milling of Hastelloy X

Nor Aznan Mohd Nor, B. T. Hang Tuah Baharudin, Zulkiflle Leman, and Mohd Khairol Anuar Mohd Ariffin

Abstract Increasing spindle speed accompanied with decreasing feed per tooth during slot-milling of nickel-based superalloys, is a common approach in aircraft manufacturing industry for achieving low cutting force. This is due to nickel-based superalloys is difficult-to-machine materials, thus increase in spindle speed will lead to thermal softening that may reduce cutting force, while decrease in feed per tooth will decrease the amount to shear unwanted material at the tool edge and may avoid excessive cutting force. By considering this approach, an effective validation is vital. This manuscript elucidates the influence of spindle speed and feed per tooth during dry slot-milling of Hastelloy X on cutting force. Conventional-milling and climb-milling are performed experimentally using Kennametal KYS40 solid ceramic end-mill. Experimental results indicate that cutting force firstly decrease and then increase with increase in spindle speed, whereas cutting force increases with increase in feed per tooth. Feed per tooth has significant effect on cutting force. In contrast, spindle speed, and the interaction between spindle speed and feed per tooth have effect on cutting force but not significant. The lowest cutting force can be obtained using medium spindle speed (24,100 rev/min) accompanied with lowest feed per tooth (0.013 mm/tooth), instead of using highest spindle speed (26,800 rev/min) accompanied with lowest feed per tooth (0.013 mm/tooth).

Keywords Dry slot-milling · ASME SB435 Hastelloy X · Cutting force

N. A. Mohd Nor (✉)
Technology and Technical Accreditation Secretariat, Malaysia Board of Technologists, 62000 Putrajaya, Malaysia
e-mail: noraznan.namn@gmail.com

B. T. H. T. Baharudin · Z. Leman · M. K. A. Mohd Ariffin
Faculty of Engineering, Universiti Putra Malaysia, 43400 Serdang, Malaysia

1   Introduction

Hastelloy X is increasingly applied in the aircraft manufacturing industry [1, 2], especially in the manufacture of combustion chambers [1]. This is due to the characteristics of nickel-based superalloys that are high resistance to elevated temperature, high resistance to corrosion and oxidation, high feasibility for manufacturing, high resistance to thermal fatigue, low cost, low thermal expansion, low density and low elastic modulus [1], which perfectly suit the working principle of combustion chambers. In the aspect of machinability, Hastelloy X can be categorized as difficult-to-machine material [3]. Due to this, high cutting force will be generated from the use of conventional machining methods.

Machining Hastelloy X using conventional machining methods is very challenging. Which is why increasing spindle speed accompanied with decreasing feed per tooth during milling process becomes a common approach by aircraft manufacturing industry for achieving low cutting force. In addition, this approach can be related to the findings indicated by Masmiati et al. [4], where they claimed that increase in cutting speed and decrease in feed rate, reduces the cutting force. Increasing spindle speed during milling process leads to greater thermal softening of machined material at the tool-chip interface, thus energy requirement is decreased and subsequently reduce cutting force [4, 5]. On the other hand, decreasing in feed per tooth will decrease the amount of unwanted material to be removed during the end-mill slides and bites the machined material [4, 6]. Low cutting force in milling process may restrain vibrations then leads to improve the quality of machinability [7]. Thus. validating the effectiveness of increasing spindle speed accompanied with decreasing feed per tooth during milling of Hastelloy X for achieving low cutting force is vital.

Slot-milling is a versatile form of milling process, which capable of machining slot. In slot-milling, the direction of end-mill rotation is normally constant, while the direction of feed is changing. Therefore, slot-milling can be divided into two distinct processes of removing an unwanted material as depicted in Fig. 1; conventional-milling and climb-milling. Conventional-milling refers to the direction of feed opposed to direction of end-mill rotation, while climb-milling refers to the direction of feed same as direction of end-mill rotation.

In this manuscript, dry slot-milling in conventional-milling and climb-milling are experimentally carried out on Hastelloy X. Apart of this, the influence of spindle speed and feed per tooth on cutting force is elucidated, for the purpose to validate the effectiveness of increasing spindle speed accompanied with decreasing feed per tooth for achieving low cutting force. In addition, dry condition is chosen as this research intends to encourage sustainable manufacturing of nickel-based superalloys. Thus, solid ceramic end-mill is applied due this type of end-mill has excellent thermal resistance which can avoid from the damaging effect of heat. Cutting force behaviour induced by spindle speed and feed per tooth is explicated systematically, subsequently the optimal spindle speed accompanied with feed per tooth for achieving the lowest cutting force is simultaneously proposed.
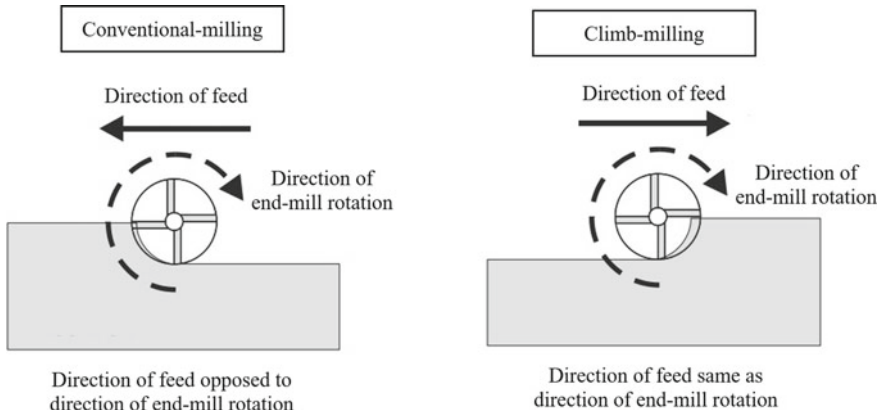
Fig. 1 Schematic illustration of conventional-milling and climb-milling

2 Experimental Setup

Dry slot-milling was carried out on ASME SB435 Hastelloy X 90 × 40 × 10 mm using Mori Seiki NV 4000 DCG vertical machining centre. Conventional-milling and climb-milling were performed with Kennametal KYS40 solid ceramic end-mill diameter of 6 mm. The cutting parameters used in the experimental test are shown in Table 1. In addition, the cutting parameters set in the experimental test were selected by taking into consideration ISO 3002/4 standard as recommended by solid ceramic end-mill manufacturer.

Cutting force components; feed force (F_x), normal force (F_y), and axial force (F_z) at each run were measured simultaneously using Kistler 9129AA dynamometer. The measurements were performed three times at each run to obtain the average value, thus the total sample for 9 runs are 27 samples. The average value was then inserted into the equation below [8] to calculate the cutting force or resultant force (F_r).

$$F_r = \sqrt{F_x^2 + F_y^2 + F_z^2} \tag{1}$$

Further, the calculated cutting force was elucidated via main effects plot and Pareto chart of the standardized effects in Minitab software.

Table 1 Cutting parameters used in the experimental test

Cutting parameter	Level
Spindle speed (rev/min)	21,400, 24,100 and 26,800
Feed per tooth (mm/tooth)	0.013, 0.016 and 0.019
Axial depth of cut (mm)	0.2

3   Results and Discussion

Figure 2 depicts the overall experimental results of dry slot-milling on Hastelloy X during conventional-milling and climb-milling. X-axis and Y-axis represent spindle speed and cutting force respectively, while orange trend-line, lavender trend-line

(a)

(b)
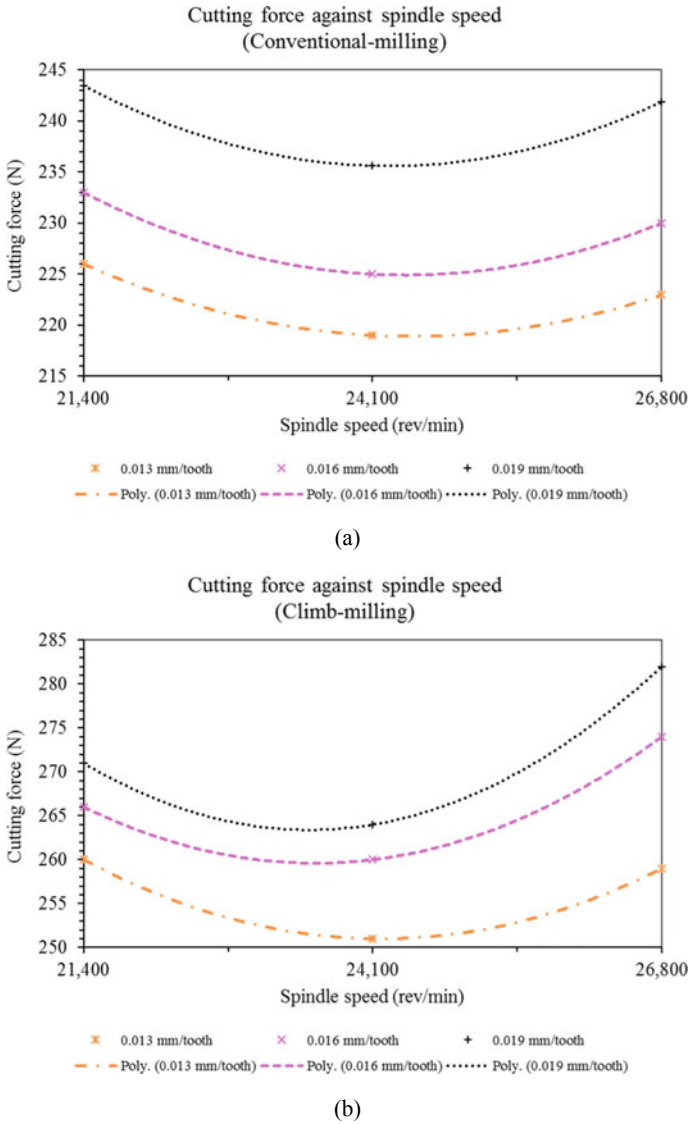
Fig. 2   Overall experimental results: **a** conventional-milling and **b** climb-milling
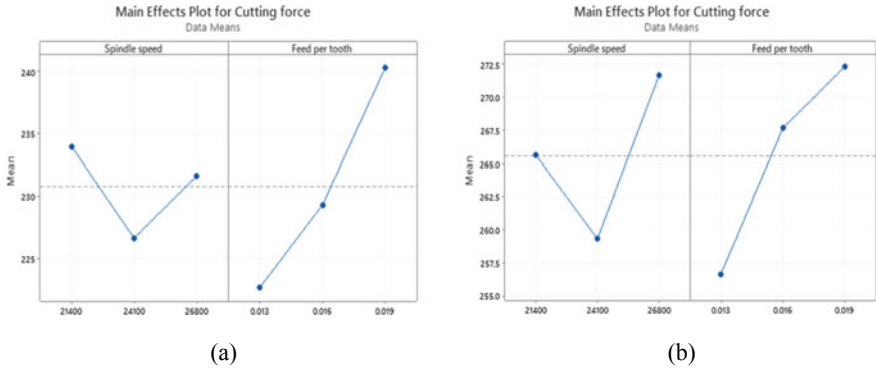
Fig. 3 Main effects plot: **a** conventional-milling and **b** climb-milling

and black trend-line represent feed per tooth 0.013 mm/tooth, 0.016 mm/tooth and 0.019 mm/tooth, respectively.

As presented in Fig. 3, main effects plot is used to quantitatively assess the influence of spindle speed and feed per tooth on cutting force. The dotted line represents the overall mean cutting force.

In both conventional-milling and climb-milling, cutting force firstly decreased when spindle speed was increased from 21,400 to 24,100 rev/min, and then increased with increase in spindle speed higher than 24,100 rev/min. This cutting force behavior is contradictory to the cutting force behaviour observed by Masmiati et al. [4] where cutting force decreases with increased in spindle speed. The behavior of cutting force firstly decreases and then increases after reaching a specific spindle speed is in line with the research conducted by Mohd Nor et al. [9], where it can be associated with ductile-to-brittle transition, in which Hastelloy X undergoes brittle cutting mode at spindle speed 24,100 rev/min and subsequently leads to fluctuation in cutting force. As expected, cutting force increased when feed per tooth was increased from 0.013 to 0.019 mm/tooth. This can be associated with the increase amount of unwanted Hastelloy X to be sheared during dry slot-milling [4, 6]. Another factor that can be associated is due to the increase in feed per tooth which causes the strain hardening effect, and consequently increases cutting force [10]. Therefore, the higher the feed per tooth, the higher the cutting force. Figures 2 and 3 confirm that using spindle speed 26,800 rev/min accompanied with feed per tooth 0.013 mm/tooth will not achieve low cutting force. Therefore, the approach of increasing spindle speed accompanied with decreasing feed per tooth for achieving low cutting force is non-effective. The good rule of thumb for achieving the lowest cutting force during dry slot-milling of Hastelloy X is to use spindle speed 24,100 rev/min accompanied with feed per tooth 0.013 mm/tooth, instead of the maximum spindle speed (26,800 rev/min) accompanied with the minimum feed per tooth (0.013 mm/tooth).

In search of determining the magnitude and the importance of the effects, Pareto chart of the standardized effects is used as depicted in Fig. 4. Factor that crosses the dotted line is statistically significant.
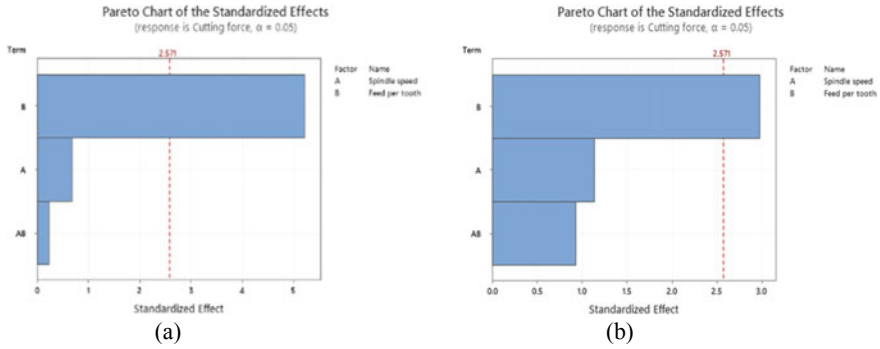
Fig. 4 Pareto chart of the standardized effects: **a** conventional-milling and **b** climb-milling

From Fig. 4, feed per tooth was the dominant factor affecting cutting force in both conventional-milling and climb-milling, followed by spindle speed and the interaction between spindle speed and feed per tooth. Since feed per tooth extended past the dotted line, thus it can be considered that feed per tooth had significant effect on cutting force at 0.05 significance level. Whereas, spindle speed and the interaction between spindle speed and feed per tooth both had effect on cutting force but not statistically significant. It can be claimed that the variation of cutting force behavior during dry-slot milling of Hastelloy X is closely related to the increasing and decreasing feed per tooth, when compared to the increasing and decreasing spindle speed. Therefore, a precise selection of feed per tooth value is crucial in order to prevent cutting force catastrophe.

4   Conclusion

Dry slot-milling of Hastelloy X was performed by conventional-milling and climb-milling using Kennametal KYS40 solid ceramic end-mill. The following conclusions can be drawn from this experimental test:

- Cutting force firstly decreased as spindle speed was increased from 21,400 to 24,100 rev/min, then cutting force increased as spindle speed increased higher than 24,100 rev/min.
- Cutting force increased with the rise of feed per tooth from 0.013 to 0.019 mm/tooth.
- Increasing spindle speed accompanied with decreasing feed per tooth for achieving low cutting force is non-effective approach.
- Spindle speed 24,100 rev/min (medium spindle speed) accompanied with feed per tooth at 0.013 mm/tooth (lowest feed per tooth) were found to achieve the lowest cutting force, instead of spindle speed 26,800 rev/min (highest spindle speed) accompanied with feed per tooth 0.013 mm/tooth (lowest feed per tooth).

- Feed per tooth is the most influential cutting parameters for the cutting force generated during dry slot-milling, while spindle speed and the interaction between spindle speed and feed per tooth have effect but not significant.
- Future research should be focused on surface integrity of Hastelloy X and tool wear of KYS40 solid ceramic end-mill.

References

1. Romero-Jabalquinto A, Velasco-Téllez A, Zambrano-Robledo P, Bermúdez-Reyes B (2016) Feasibility of manufacturing combustion chambers for aeronautical use in Mexico. J Appl Res Technol 14(3):167–172
2. Han Q, Gu Y, Huang J, Wang L, Low KWQ, Feng Q, Yin Y, Setchi R (2020) Selective laser melting of Hastelloy X nanocomposite: effects of TiC reinforcement on crack elimination and strength improvement. Compos B Eng 202:108442
3. Şirin E, Kıvak T, Yıldırım ÇV (2021) Effects of mono/hybrid nanofluid strategies and surfactants on machining performance in the drilling of Hastelloy X. Tribol Int 157:106894
4. Masmiati N, Sarhan AAD, Hassan MAN, Hamdi M (2016) Optimization of cutting conditions for minimum residual stress, cutting force and surface roughness in end milling of S50C medium carbon steel. Measurement 86:253–265
5. Bhirud NL, Gawande RR (2017) Measurement and prediction of cutting temperatures during dry milling: review and discussions. J Braz Soc Mech Sci Eng 39(12):5135–5158
6. Grzesik W (2017) Chapter fifteen—Advanced machining processes, 2nd edn. Elsevier
7. Ducroux E, Fromentin G, Viprey F, Prat D, D'Acunto A (2021) New mechanistic cutting force model for milling additive manufactured Inconel 718 considering effects of tool wear evolution and actual tool geometry. J Manuf Process 64:67–80
8. Shixiong W, Wei M, Bin L, Chengyong W (2016) Trochoidal machining for the high-speed milling of pockets. J Mater Process Technol 233:29–43
9. Mohd Nor NA, Baharudin BTHT, Ghani JA, Leman Z, Mohd Ariffin MKA (2020) Effect of chip load and spindle speed on cutting force of Hastelloy X. J Mech Eng Sci 14(1):6497–6503
10. Danish M, Yasir M, Mia M, Nazir K, Ahmed T, Rani AMA (2020) Chapter 10—High speed machining of magnesium and its alloys. Academic

Compressive Failure Behaviour of Kevlar Epoxy and Glass Epoxy Composite Laminates Due to the Effects of Cutout Size and Variation in Fibre Orientations

Zeno Michael, Jamaluddin Mahmud, Syed Mahathir Al-Attas, Tri Hartutuk Ningsih, and Ayoub Guerrah

Abstract At present, rigorous research are carried out to produce the finest possible properties of composite materials. This phenomenon has made it possible to expand the application of composite laminates, which originally meant for only defence and aeronautical industries towards more public and general applications. To avoid catastrophic failure of composite structures, its failure behaviour should be established. Nevertheless, composite laminates may deform in various modes and thus, these modes of failure should be well understood before designing a composite structure, especially with the cutouts. This paper aims to study the effect of the circular cutout on the failure behaviour of Kevlar Epoxy and Glass Epoxy composite laminates with various fibre orientations. The work was conducted in two stages. The preliminary work involved mesh convergence analysis and numerical validation. The laminate modelling and failure analysis was performed using a finite element software (ANSYS). The model with stacking sequence is $[\theta_4/0_4/-\theta_4]s$ and various fibre orientation, θ from 0° to 90° were investigated. Failure was determined using Maximum Stress Theory. The results show substantial strength reduction between composite laminates with and without circular cutout. Comparing Kevlar Epoxy and Glass Epoxy at 0° fibre angle, the results show that the circular cutout has more influence on Kevlar Epoxy (10 times weakened) than the Glass Epoxy (3 times weakened).

Z. Michael
College of Engineering (Mechanical), Universiti Teknologi MARA, Kampus Pasir Gudang, 81750 Masai, Johor, Malaysia

J. Mahmud (✉)
School of Mechanical Engineering, College of Engineering, Universiti Teknologi MARA, 40450 Shah Alam, Selangor, Malaysia
e-mail: jm@uitm.edu.my

S. M. Al-Attas
Quadrant 2 Technologies Sdn Bhd, Taman TTDI Jaya, 40150 Shah Alam, Selangor, Malaysia

T. H. Ningsih
Department of Mechanical Engineering, Universitas Negeri Surabaya, Ketintang Campus, Surabaya, Indonesia

A. Guerrah
Mechanical Engineering Department, University of El Qued, P.O. Box 789, El-Qued, Algeria

However, when the fibre angle varied, both composites exhibit the similar trend of failure. Therefore, it is proven that the current study is essential in understanding the failure behaviour of composite plates with circular cutout.

Keywords Failure analysis · Glass Epoxy · Kevlar Epoxy · Circular cutout · ANSYS · Maximum Stress Theory

1 Introduction

The utilisation of composite laminates has expanded from only for defence and aeronautical industries to civil and consumer use, such as construction, sports equipment, and automotive parts [1]. This is due to the advantage of its mechanical properties along with the materials and research development. It has been marked as the new generation material because of the demand for both the industry's rapid growth and change in technology [2]. Since material strength is an essential property in selecting material for design of any structure [3], this material becomes popular because of its tailorable properties and high strength to weight ratio [4]. The strength of a material is the capability of the material to hold the load. Nahas et al. [3] has claimed that a material failed when the applied load reaches the limit of its load carrying capacity. The laminate failure led to permanent loss of integrity within the laminate and degradation of stiffness and strength of the material [5].

The ideal approach to analyse the failure of material is from the physical test. The data obtained from this approach is acceptable due to its accuracy and validity. However, physical tests are tedious and time. Latterly, along with computer software development, researchers use more favourable numerical methods to conduct the failure analysis [1]. In a numerical approach, the idea of failure theory is implemented to estimate the strength of laminated composite through advanced computational methods using finite element analysis, much preferred by researchers in predicting laminate failure [6, 7]. Rahimi et al. [8] have analysed analytical and finite elements on woven Kevlar Epoxy laminate to identify failures on the material. The results of predicting the strength of laminates were determined and compared between the two methods. Mali et al. [9] also conducted a study on the effects of the V-notch and the variation of fibre orientation angle to the strength of Glass Epoxy composite laminates. The failure behaviour of the plain plate and V-notch plate laminate was analysed under bending load. Içten et al. [10] has conducted failure analysis of both numerically and experimentally on woven Kevlar Epoxy pin joints under tensile load. Failure mode and failure load of composite plates were determined using Hashin, Hoffman and Maximum Stress criteria. For laminated composite of a flat plate with a circular cutout under a compression state, Mali et al. [11] studied the effects of the angle of fibre orientation to woven Kevlar Epoxy laminates.

To fully understand the property of composite laminates, the failure behaviour of this material should be well analysed, considering this composite laminate was widely used in marine, aerospace and automobile structure [12]. Since it plays a

crucial role in engineering application, there is a need for a different type of holes and size in the composites for specific structure accommodating bolts, nuts, rivet and others. The presence of cuts is inevitable and their existence is surely to reduce load carrying capacity and hence strength [13]. Therefore, it must be tested to determine its limit of strength to prevent any failure. Even though, many studies have been carried out on the failure analysis of cutouts Kevlar fibre [14]. However, there are still not many studies on the effect of various square cutout shapes related to Kevlar Epoxy and Glass Epoxy, respectively. Thus, the behaviour of these structures is not fully understood.

The present paper aims to study the effect of the circular cutout on the failure behaviour of Kevlar Epoxy and Glass Epoxy composite laminates with various fibre orientations. A numerical method analysis was conducted to analyse failure using Maximum stress theory as the failure criteria. This study helps to recommend a proper selection of Kevlar Epoxy and Glass Epoxy with a suitable cutout to prevent future problems such as delamination and cracking of laminate.

2   Methodology

Generally, this study uses a mechanical finite element analysis software (ANSYS r16.0 2014 SAS IP, Inc.) to model the Kevlar Epoxy and Glass Epoxy composite laminates with a circular cutout under uniaxial compression. The failure load is predicted using the available built-in failure criteria function, Maximum stress theory. For better organization and clarity, the methodology adapted in the study was conducted based on the steps as described followed: (1) Mesh Convergence Analysis, (2) Numerical validation and (3) Failure Analysis on the effect of the circular cutout on both Kevlar Epoxy and Glass Epoxy composite laminates with various fibre orientation.

2.1   Stage 1: Mesh Convergence Analysis

Mesh size is crucial in conducting a numerical analysis. It is also primarily influenced by numerical accuracy, computing time and cost [2]. Therefore, a small meshing size could lead to the higher accuracy of simulated results. Since convergence analysis is essential, the study initially performing the convergence analysis before any other investigations. The various mapped meshing of (2×2, 3×3, 4×4, 6×6, 8×8, 12×12 and 16×16) with quadrilateral elements under constant uniaxial tension for Kevlar Epoxy and Glass Epoxy were analysed. Analysis results show that the optimum size of 6×6 was the best mesh size for accurate results. The plate was meshed using 8-noded shell element (Shell281).

Table 1 Mechanical properties of Kevlar Epoxy and Glass Epoxy

(a) Kevlar Epoxy				(b) Glass Epoxy			
Elastic parameter		Strength data		Elastic parameter		Strength data	
E_1	76.0 GPa	X_T	1380 MPa	E_1	54.0 GPa	X_T	1035 MPa
$E_2 = E_3$	5.50 GPa	X_C	276 MPa	$E_2 = E_3$	18.0 GPa	X_C	1035 MPa
$v_{12} = v_{23} = v_{13}$	0.34	Y_T	28 MPa	$v_{12} = v_{23} = v_{13}$	0.25	Y_T	28 MPa
$G_{12} = G_{23} = G_{13}$	2.10 GPa	Y_C	138 MPa	$G_{12} = G_{23} = G_{13}$	9.0 GPa	Y_C	138 MPa
		S	44 MPa			S	41 MPa

Fig. 1 The model under uniaxial load
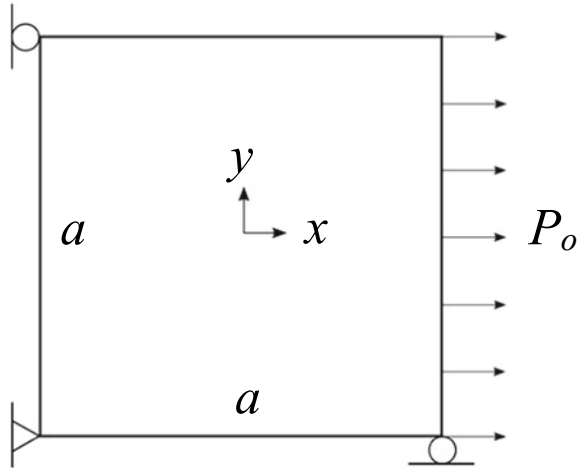
2.2 Stage 2: Numerical Validation

A numerical analysis approach was used to predict the maximum displacement for x-direction and y-direction under uniaxial tension load, respectively. The model with stacking sequence is $[\theta_4/0_4/-\theta_4]s$ and the angle of fibre orientation, θ from 0° to 90° were simulated for the analysis. Table 1 shows the elasticity and strength value of Kevlar Epoxy and Fig. 1 shows the uniaxial model. Comparative results between analytical and MATLAB are presented in Table 2.

2.3 Stage 3: Failure Analysis

The properties of both (a) Kevlar Epoxy and (b) Glass Epoxy of each lamina are presented in Table 1, respectively. The shape of the model with cutout are shown in

Table 2 Analytical and simulation (FEA) results for composite laminates under uniaxial load

Angle, θ (°)		0	30	45	90
Simulation (ANSYS)	Max. x (mm)	9.87E−05	1.75E−04	2.43E−04	2.57E−04
	Max. y (mm)	1.68E−05	1.07E−04	9.38E−05	4.58E−06
Analytical	Max. x (mm)	9.869E−05	1.746E−04	2.434E−04	2.571E−04
	Max. y (mm)	1.678E−05	1.075E−04	9.385E−05	4.578E−06
Error %	Max. x (mm)	0.0162	0.2109	0.1466	0.0182
	Max. y (mm)	0.1414	0.4290	0.0481	0.0461

Fig. 2. The length of the plate is equal to the width of the plate. The length of the plate, a, is 0.279 m, having an aspect ratio (S = a/h) of 150. Therefore, the thickness of the plate, h, is 1.86×10^{-3} m and the cross-sectional area (A = ah) is 5.189×10^{-4} m^2. The 24 layers of laminates in this study having the layup of ($\theta_4/0_4/-\theta_4$)s. The laminates to analyse are with and without a central cutout of a circular shape with several cutout sizes. The cutout sizes of areas designated as (A1, A2 and A3) and their detailed dimensions are presented in Table 3. Under uniaxial compressive loading, this area used to observe the effect of cutout shape on the failure behaviour of the laminate. The area used to observe the effect of cutout shape on the failure

Fig. 2 Uniaxial compression model with cutout
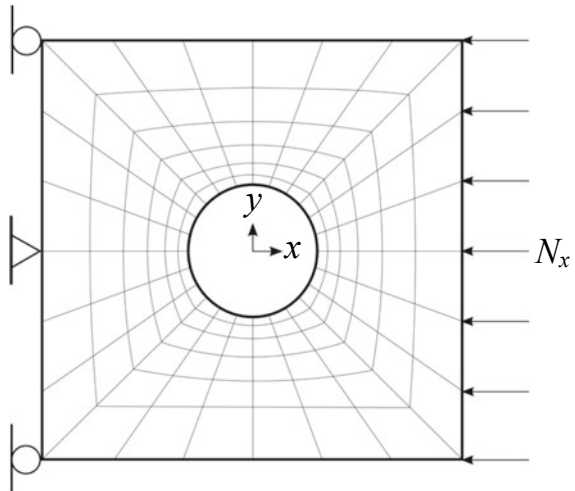
Table 3 Details of cutout shapes and their dimension

Cutout shape	Cutout size	A₁	A₂	A₃
Circular	Ratio, d/b	0.158	0.316	0.474
	Diameter, d (m)	0.022	0.044	0.066

Note d is diameter and b is width of the square laminate

behaviour of the laminate under uniaxial compressive loading. The aspect ratio of d/b represents the circular cutout shape area.

3   Results and Discussion

Maximum displacement and failure results for each models are recorded and tabulated in Fig. 3 (Glass Epoxy) and Fig. 4 (Kevlar Epoxy) respectively. Although the displacement results for the Glass Epoxy plate with no cutout show a small increment on the displacement, the flat curves prove that they are not much affected by fibre orientation change. However, the Kevlar Epoxy plate with no cutout shows otherwise in Fig. 4. The increment shows in maximum x-displacement and fluctuated trend in maximum y-displacement. This result has been found similar to the previous study
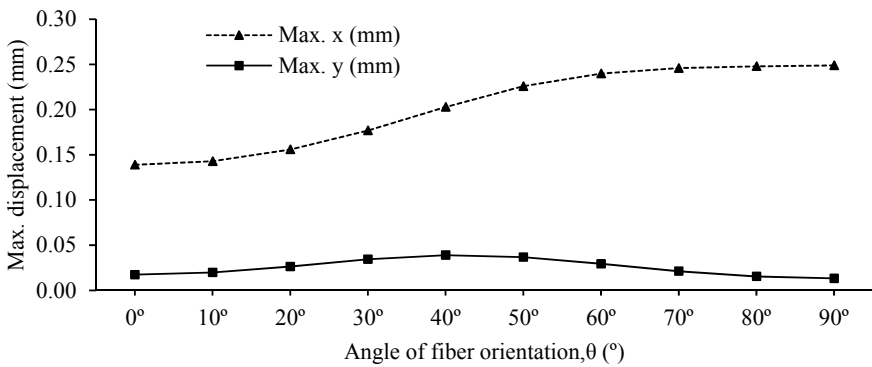
Fig. 3 The displacement curves in x-direction and y-direction for Glass Epoxy
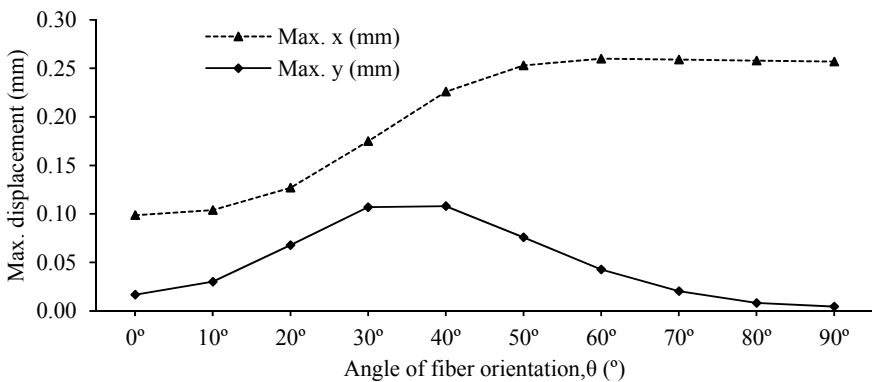
Fig. 4 Displacement curves in x-direction and y-direction for Kevlar Epoxy

of using different types of composite material [15]. All in all, out of the displacement curves, the changes of fibre orientation would affect the plate displacement for Kevlar Epoxy.

Moreover, the failure curves for Glass Epoxy and Kevlar Epoxy with and without cutout are presented in Figs. 5 and 6. A match failure curves pattern developed from the results of Glass Epoxy with and without cutout in Fig. 5. In term of strength, especially in Glass Epoxy with cutout, it does not affect much with the change of the angle in fibre orientation. Both figures also show the failure curves for all cutout with the change of strength in the material by the size of its cutout. The gap in between no cutout and A1 cutout is tremendous at 0-degree fibre orientation. The gap is then reduced with the increase of fibre orientation. There are few differences between all cutouts (A1, A2 and A3), with a slight fluctuated trend towards increasing fibre orientation. This trend proved that the strength of the material is affected by the size
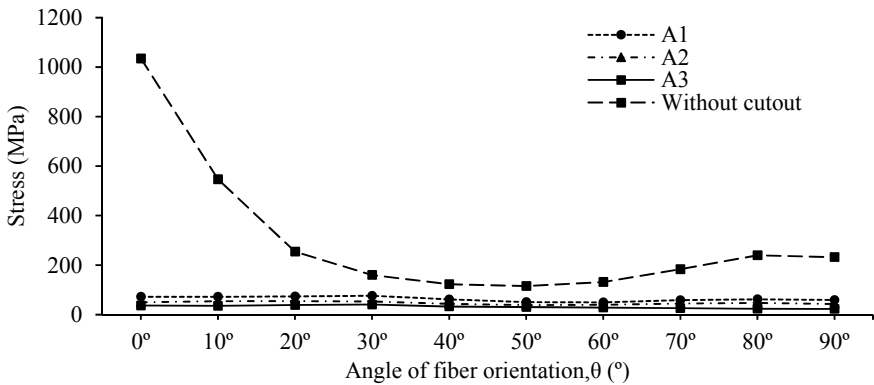
Fig. 5 Failure curves for glass epoxy composite laminate
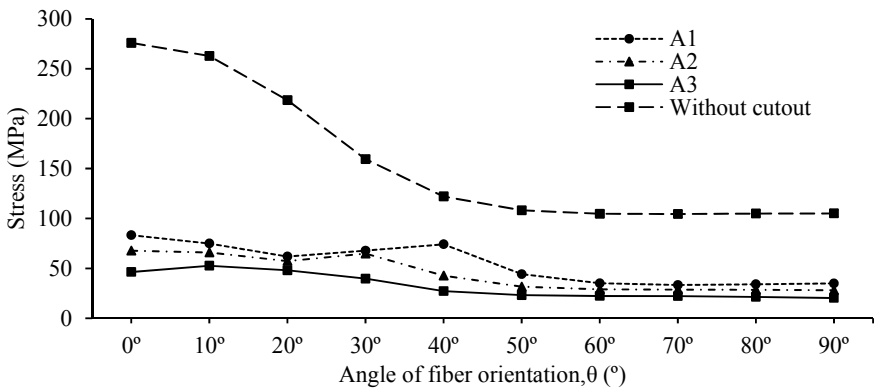
Fig. 6 Failure curves for Kevlar Epoxy composite laminate

of cutout. This finding parallels past studies on the influences of open holes shape on the failure fracture of composite laminates under compressive loading [16].

Figure 6 shows the strength of Kevlar Epoxy composite laminate. It is found that Kevlar Epoxy's strength affects the fibre orientation but did not much affect the model with cutout. The strength values of Kevlar Epoxy without cutout decreasing from 0º to 60º of fibre orientation and then show a constant value until it reaches at 90º. However, all three types of cutout (A1, A2 and A3) show a constant value and are almost equal. Consistency is found in results gaps for all three cutout sizes on all fibre orientation are slightly different by only 2%. Although it is not much, all the failure curves for cutout are gradually maintained by increasing fibre orientation. This flat-trend pattern is similar to past results on the composite plates with circular cutout [17]. The results also show that a noticeable difference value of stress with no cutout results. For the laminate with 0º fibre angle, 276 MPa was needed to induce the failure of the laminate without cutout but only 83.3 MPa was needed for the laminate with a circular cutout. Therefore, the circular cutout has weakened the laminate substantially, by about 3–4 times.

Results for failure comparison in between Kevlar Epoxy and Glass Epoxy are presented in Fig. 7 for no cutout. In this figure, the stress curve for the Glass Epoxy shows a decreasing trend with a sudden drop from 0º to 20º. The stress curve pattern for Kevlar Epoxy shows a moderate decrease in strength when increasing the fibre orientation. This shows that the alteration of angle could effect on Glass Epoxy than Kevlar Epoxy.

Figures 8 and 9 show the stress curve in different cutout sizes for both Glass Epoxy and Kevlar Epoxy, respectively. Both figures show the same trends with decreasing in strength when increasing the cutout size. This shows that the plates with a smaller cutout size show better strength. This can be concluded that plate with cutout would decrease the material strength with different fibre orientation. In addition, a large cutout size could reduce the material strength. Comparing the Kevlar Epoxy and Glass Epoxy, the results show that the circular cutout has more influence on Kevlar
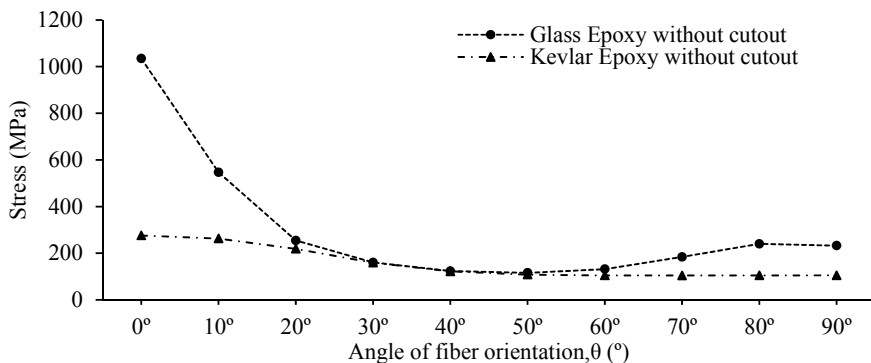
Fig. 7 Failure curves for Kevlar Epoxy and Glass Epoxy with no cutout
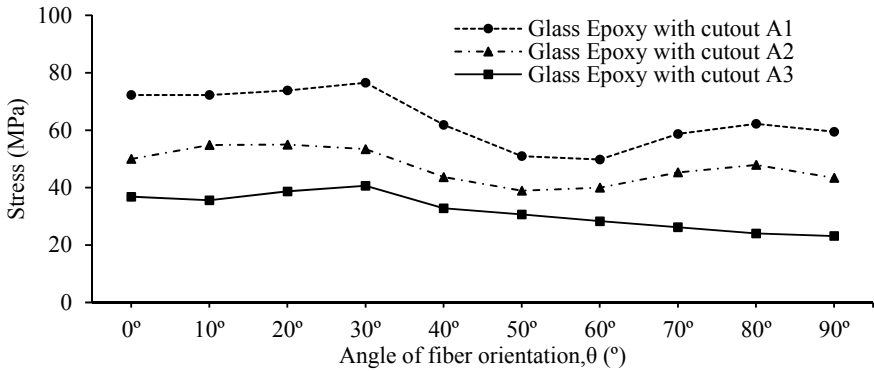
Fig. 8 Failure curves for Glass Epoxy with various cutout size
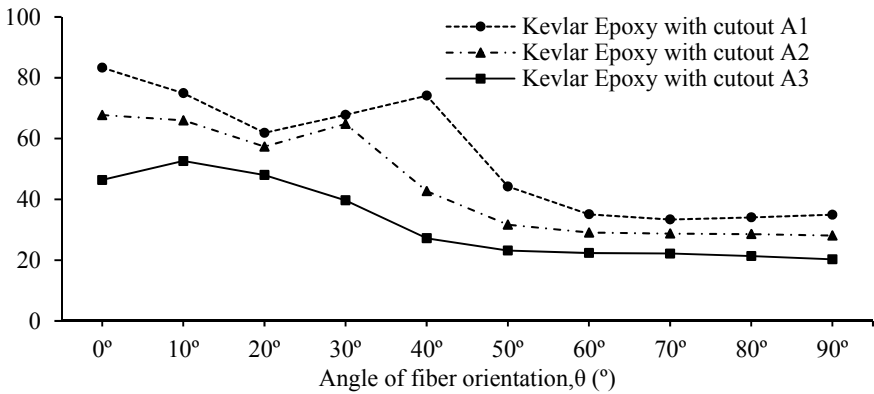
Fig. 9 Failure curves for Kevlar Epoxy with various cutout size

Epoxy 10 times than the Glass Epoxy with 3 times to the composite laminates without cutout.

4   Conclusion

This paper presents the effects of circular cutout sizes and fibre angles arrangement to Kevlar Epoxy and Glass Epoxy composite laminates. The results show substantial strength reduction between composite laminates with and without circular cutout. Comparing Kevlar Epoxy and Glass Epoxy at 0° fibre angle, the results show that the circular cutout has more influence on Kevlar Epoxy (10 times weakened) than the Glass Epoxy (3 times weakened). However, when the cutout size and fibre angle varied, both composites exhibit the similar trend of failure. The main finding that

can be deduced from the study is that the material removal due to cutout reduced the strength composite laminates substantially. Although the direction of fibre orientation does affect the material with no cutout, it does not affect so much the failure behaviour of both Kevlar Epoxy and Glass Epoxy composite laminates with circular cutouts. From the results, it is proven that the current study is essential in understanding the failure behaviour of the composite plates in which can help contribute the knowledge for further research.

References

1. Mali M, Samsudin AH, Mahmud J, Hussain AK, Alansary MD (2017) Failure analysis of composite laminates under biaxial tensile load due to variations in lamination scheme. J Mech Eng SI 4(5):167–182
2. Ahmed MN, Kumar PV, Shivanand HK, Muzammil SB (2013) A study on effect of variation of thickness on tensile properties of hybrid polymer composites (Glass fibre-carbon fibre-graphite) and GFRP composites. Int J Eng Res Appl 3(4):2015–2024
3. Nahas MN (1986) Survey of failure and post-failure theories of laminated fiber-reinforced composites. J Compos Technol Res 8(4):138–153
4. Noh NN, Samsudin AH, Mahmud J (2017) Failure analysis of Glass/Epoxy and Graphite/Epoxy laminates due to the effect of variation in lamination scheme and angle of fibre orientation. Mater Sci Forum 889:36–44
5. Samsudin AH, Hussain AK, Mahmud J (2015) Deformation and failure analysis due to variations in fiber orientations. ARPN J Eng Appl Sci 10(17):7336–7344
6. Rahimi N, Hussain AK, Meon MS, Mahmud J (2012) Capability assessment of finite element software in predicting the Last Ply Failure of composite laminates. Procedia Eng 41:1647–1653
7. Rahim MA, Rahimi N, Hussain AK, Mahmud J, Musa M (2012) Parametric study on failure analysis of composite laminate under uniaxial tensile loading. In: 2012 IEEE colloquium on humanities, science and engineering (CHUSER), pp 805–809
8. Rahimi N, Hussain AK, Dawood MSIS, Alias AZM, Yusoff MHAM, Mahmud J (2018) Failure analysis of Woven Kevlar/Epoxy under uniaxial tension. Int J Eng Technol 7(4):235–239
9. Mali M, Hussain AK, Zahrullaili MZ, Alias MF, Mahmud J (2019) Failure analysis on woven glass/epoxy composite laminates due to the effect of V-Notch and angle of fiber orientation. J Mech Eng 8(1):192–199
10. Içten BM, Karakuzu R, Toygar ME (2006) Failure analysis of woven Kevlar fiber reinforced epoxy composites pinned joints. Compos Struct
11. Mali M, Hussain AK, Muzafar MA, Zainol AFM, Mahmud J (2019) Failure analysis of woven Kevlar/epoxy composite laminates under compression due to variations in fiber orientation. J Phys Conf Ser 1349(1):0–7
12. Lakshminarayana A, Vijayakumar R, Rao GK (2016) Progressive failure analysis of laminated composite plates with elliptical or circular cutout using finite element method. IOP Conf Ser Mater Sci Eng 149(1)
13. Anand A, Babu M, Kumar MK (2016) Stress concentration study of laminated composite with multiple holes by finite element analysis. Am J Eng Res 5(10):238–243
14. Abu Talib AR, Ramadhan AA, Mohd Rafie AS, Zahari R (2013) Influence of cut-out hole on multi-layer Kevlar-29/epoxy composite laminated plates. Mater Des 43:89–98

15. Michael Z, Mahisham I, Mahadi MF, Mohd Amin AN, Syed Ahmad SIH, Mahmud J (2020) Deformation and failure behavior of hybrid composite laminates made of Glass Epoxy and woven Kevlar Epoxy. Mater Today Proc 46:1618–1625
16. Feng ZY, Yang Q, Yin XY, Chen ZC, Zou TC (2011) Failure factor research of composite laminates containing holes based on MSC.Nastran. Adv Mater Res 160–162:71–75
17. Khechai A, Tati A, Belarbi MO, Guettala A (2015) Finite element analysis of stress concentrations in isotropic and composite plates with elliptical holes. Design and modeling of mechanical systems—II. Lecture notes in mechanical engineering, pp 427–436

Material Failure Assessment of Leakage in a Low Alloy Steel Choke Body

J. Alias and N. A. Alang

Abstract This paper highlighted the material failure of the low nickel–chromium-molybdenum steel choke body by visual observation, microstructure characterization, chemical composition, and hardness analysis. A choke body failed due to leakage at the choke body after 11 years in service. A combination of fluid flow condition and electrochemical reaction of the choke body in the non-associated gas (NAG) containing CO_2 environment induces localised corrosion such as erosion and preferential weld corrosion (PWC). The severe corrosion penetration along the weld bead adjacent to the eroded region was observed as the primary cause of choke body leakage. The evidence of less chromium composition at the weldment region due to carbide coarsening could contribute to the decrease in corrosion resistance and induce localized corrosion of the weldment leading to PWC. To prevent the recurrence of failure, it is recommended that the material of the weldment should be of high corrosion resistance, which can be achieved by microstructure modification and avoidance of galvanic reaction between the weldment and other regions. Careful consideration of the fluid flow condition is also required as it may exacerbate the PWC.

Keywords Choke valve · Low alloy steel · Erosion corrosion · Preferential weld corrosion · Microstructure

1 Introduction

Diverse grades of steel and stainless steels are used for the majority of process devices, for example, pipe, tube, fitting devices, valves and chokes used in the oil

J. Alias (✉)

Department of Mechanical Engineering, College of Engineering, Universiti Malaysia Pahang, 26300 Gambang, Kuantan, Pahang, Malaysia
e-mail: juliawati@ump.edu.my

N. A. Alang

Faculty of Mechanical and Automotive Engineering Technology, Universiti Malaysia Pahang, 26600 Pekan, Pahang, Malaysia

and gas sector due to economic and good characteristics reasons [1–3]. Plain carbon steels such as API 5L, ASTM A106 are the most commonly used alloys for these applications. However, they are unable to meet the needs of the modern oil industry for greater wear and corrosion resistant. The use of low alloy steel, which containing up to 1 wt.% of Cr, is a type of steel developed specifically for the use in CO_2 environments for high strength and good hardenability [4, 5].

A choke valve is a mechanical device that induces restriction in a flow line, causing either a pressure drops or a reduction in the rate of flow. In the oil and gas industry, choke valves are normally located on top of each well, as depicted in Fig. 1 [6]. The choke valves are used to control the pressure on several wells into a common manifold. Chokes used in oil and gas wells are classified into two types depending upon the operation mode, either be adjustable or positive. Adjustable chokes are flexible in that they allow the fluid flow and pressure to be adjusted in accordance with production requirements. Positive chokes do not provide that flexibility; however, they are more resistant to damage by abrasion or erosion.

A mixture of the fluids, inhibitors and output hydrocarbons, including oil, gas, water, sand, H_2S and even CO_2, is regulated by choking valves. During operation, chokes are vulnerable to a variety of types of damage and localised corrosion, including erosion, wear, cavitation, weld corrosion, stress corrosion cracking, and corrosion fatigue [6–9].

Carbon dioxide, CO_2-corrosion is the most prominent failure cause on the steel equipment due to material's synergistic impact during operation in CO_2-containing medium. As a result, it is important to conduct a thorough investigation to determine

Fig. 1 Flow line consists of wellhead and choke valve
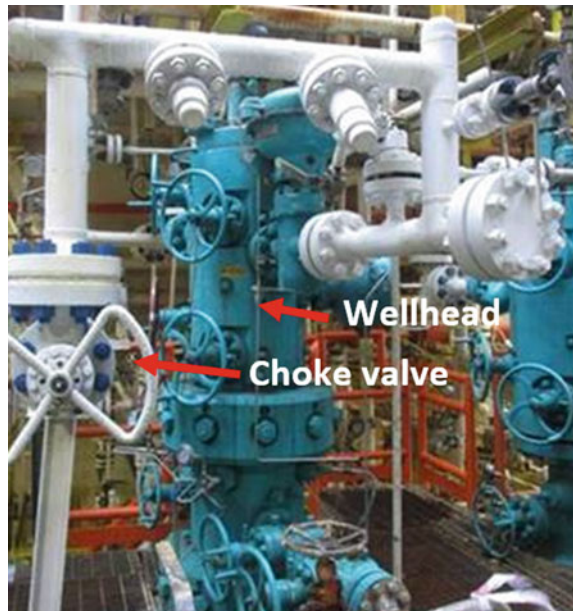
the root cause of the failure in order to avoid it in the future. The influence of dissolved carbon dioxide on the increase of the carbon steel corrosion rate has been studied by [10]. Carbon dioxide (CO_2) is generally non-corrosive in the gaseous state. However, hydration has taken place and a more reactionary chemical species, carbonic acid (H_2CO_3), has been produced in the presence of water and hydrogen. The reaction is then accompanied by a dissociation reaction, which leads to acidic, corrosive solution [11–13] in order to form bicarbonate (HCO^{3-}), carbonate (CO_3^{2-}), and hydrogen (H^+) ions. The formation and chemical inhibition of iron carbonate, $FeCO_3$ and iron sulphide and FeS help minimise carbon steel corrosion rates. However, the iron carbonate/sulphide scale or protective inhibitor layer may be affected by the small amount of sand or debris and therefore create a synergistic erosion-corrosion effect.

As a result, internal corrosion risk assessment and corrosion inhibition must be considered to ensure technical integrity over the equipment's lifetime. In the last two decades, however, the results have questioned the explicitly labeled concepts regarding these process mechanisms [14–19].

This paper focuses on the damage analysis involved in the leaked steel choke body in order to determine the mechanisms and cause of the corrosion.

2   Method and Materials

According to the documentation and inspection histories, the choke body was constructed of two different sections and joined by a fusion welding process. The first section consists of the valve body until the choke seat, while another section is from the downstream of the choke seat until the outlet. The design life was 25 years. The inlet and outlet diameters of the valve were 3″ and 4″ outer diameter (OD), respectively. The operating temperature and pressure of the steam water were in the range of 6.6–120 °C and 800 psi, respectively. The working flow rate was measured at 14 mmscfd. The medium of the choke body consisted of non-associated gas (NAG) with 15% CO_2 and less than 2 ppm H_2S content. Water content was measured approximately 1110 bbl per day.

The first leakage was started at the weldment after about 11 years in service. It was then repaired by insulating with Belzona metal repair. After 7 months, the leakage was leaked at the choke body that caused well shut. Accordingly, the choke was replaced by a second choke of the same design and material of construction from another flowline, which then failed again after less than 12 months service. Schematic diagram of leakage locations at the weldment and the surrounding environment of the choke valve is provided in Fig. 2. The choke body was cut carefully and split to half to observe the internal condition. An oxy-acetylene torch was used to separate both the flange units and followed by a milling process to cut the choke body. Manual cutting machine was then used to prepare small samples for microstructure characterization and hardness measurement.

Sample for microstructure characterization was mounted, mechanical ground from 240 grit abrasive paper to 1200 grit, and polished with diamond slurry. The
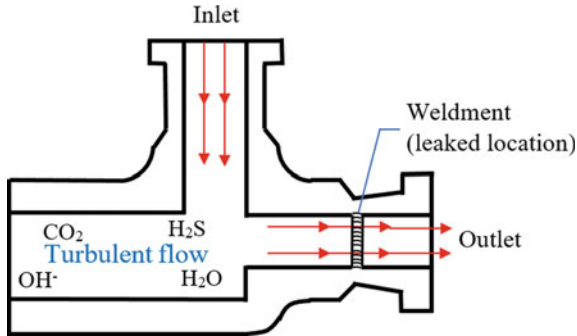
Fig. 2 Schematic diagram of leaked locations at weldment and the surrounding environment of the choke body

sample was finally etched with 2% Nital solution for 3 s. The microstructure of the outlet, inlet and weldment regions was observed using optical microscopy. A similar sample was applied for Vickers microhardness for 15 indentations at three measurement regions for accuracy and reproducibility. The Vickers method was performed in compliance with ASTM E384-17. The applied load for the hardness test was 100 gf.

Positive material identification (PMI) was conducted to the body material of three regions; inlet, outlet and weldment, by using optical emission spectroscopy (OES). The leaked region was observed further by using a low magnification stereo macroscope. The analysis of the corrosion product was performed by FEI scanning electron microscope (SEM) and Bruker D8 Advance X-Ray Diffractometer (XRD). The pattern was recorded from 7° to 100° 2 theta using cobalt Kα radiation for phase identification.

3 Results and Discussion

3.1 Visual Observation

Figure 3 depicts the as-received split halve of the leaked choke body. The sample obtained by sectioning around the weldment adjacent to the leaked region and then metallographic preparation is shown in the inset image. The unit's exterior surface is in excellent condition, with no visible signs of mechanical damage, dent, or gauging. There are no signs of rust, and the coating is in good condition. The inner surface revealed significant metal loss, especially downstream of the choke seat, severe corrosion penetration at the weldment, an erosion pattern, and a few cavitation downstream of the outlet.
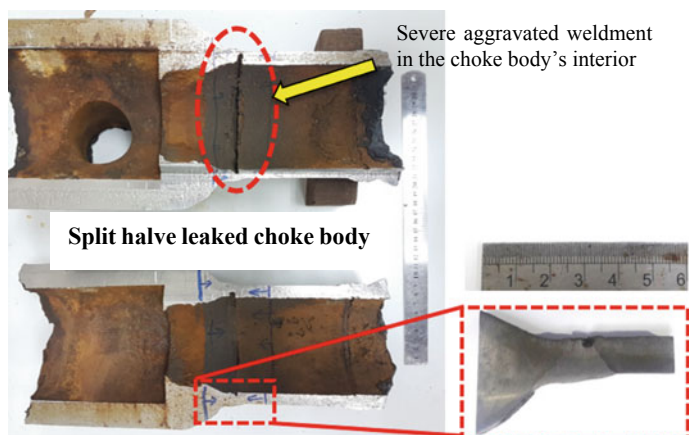
Fig. 3 Overview of split halve of the choke valve. The inset image displays the sample obtained by sectioning around the weldment adjacent to the leaked region and further proceeded for metallographic preparation

3.2 Chemical Composition

The chemical composition of the choke body material is listed in Table 1. The composition was conformed to the specified ASTM standard, A487 Grade 4 and 9 for standard specification for steel castings suitable for pressure service [20]. The compositions of ASTM A487 Grade 4 and 9 were included in Table 2. Both materials' alloying content is nearly in the nominal range for the referred composition, but lower Cr content was measured at the weldment area. The body material is cast steel that has been quenched and tempered as part of the heat treatment for product fabrication, according to the ASTM A487 standard specification for steel castings suitable for pressure operation. Both alloys have tempering temperatures ranging from 595 to 675 °C.

The inlet compositions are referred to the composition of ASTM A487 Grade 4, while the outlet compositions are referred to ASTM A487 Grade 9 [20].

Table 1 Measured chemical composition of choke valve's material including inlet, outlet and weldment region

Area	Element composition (wt.%)								
	C	Si	Mn	P	Mo	S	Cr	Ni	Fe
Inlet	0.157	0.228	0.777	0.004	0.183	0.007	0.50	0.504	Bal
Outlet	0.295	0.241	0.556	0.007	0.235	0.004	1.11	0.182	Bal
Weldment	0.107	0.293	1.920	0.009	0.377	0.004	0.093	0.395	Bal

Table 2 Nominal referred composition of ASTM A487 Grade 4 and ASTM A487 Grade 9

Limits	Nominal composition (wt.%)								
	C	Si	Mn	P	Mo	S	Cr	Ni	Fe
ASTM A487 Grade 4 (inlet)	0.30 max	0.80 max	1.00 max	0.04 max	0.15–0.30	0.045 max	0.40–0.80	0.40–0.80	Bal
ASTM A487 Grade 9 (outlet)	0.05–0.33	0.80 max	0.60–1.00	0.04 max	0.15–0.30	0.045 max	0.75–1.10	N/A	Bal

3.3 Microstructural Characterization

Figure 4a shows the overview of the sectioned sample for microstructure observation at outlet (A), inlet (C) and weldment (B) regions. Figure 4b and d shows the microstructures of both inlet and outlet consist of a fully tempered martensite structure. Finer size of tempered martensite at the outlet was observed than the inlet region, as the outlet is made of grade 4 steel casting, while the inlet is Grade 9 steel casting, which conformed by the composition analysis. The welded region consisted of a variation of microstructure (Fig. 4c), including grain boundary ferrite (GBF) and also evident of coarse martensite. The transformation of microstructures and properties during tempering is generally dependent on the primary microstructure. Precipitation of cementite, Fe_3C, occurred during tempering from the martensitic process due to the reaction of iron with carbon in the solid state, accompanied by the formation of rich-carbide-(Mo,Cr) precipitates and carbide coarsening [21, 22]. As a result, the composition of C and Cr at the weldment, as shown in Table 1, is reduced due to carbon segregation to form Cr-carbide precipitates.
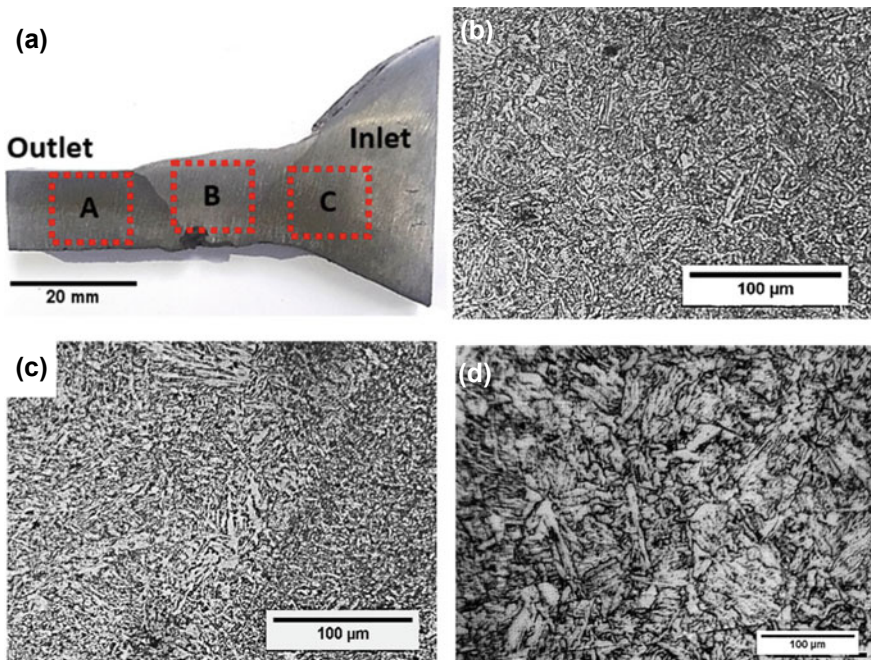
Fig. 4 **a** Overview of sectioned sample for microstructure observation at outlet (A), inlet (C) and weldment (B) regions; **b** tempered martensite microstructure observed at outlet (A); **c** tempered martensite and GBF microstructure at weldment (B); and **d** tempered martensite microstructure at inlet (C). Take note that the micrograph of inlet region (C) has been enlarged with magnification of $20\times$

3.4 Hardness Profile

Hardness test was conducted for the choke body near to the welded region by using Vickers microhardness. The hardness value is influenced by the heat input level, chemical composition and microstructure development during welding. The profile of hardness is aimed to reveal any effect of hardness and microstructural dependence on PWC. Three (3) measurements of 25 indentation points were plotted across the region of the weldment, with a distance of 0.5 mm between an indentation. Figure 5 displays the hardness profile across the distance. The average hardness value as shown in Table 3, indicated the hardness value at weldment-fusion boundary of
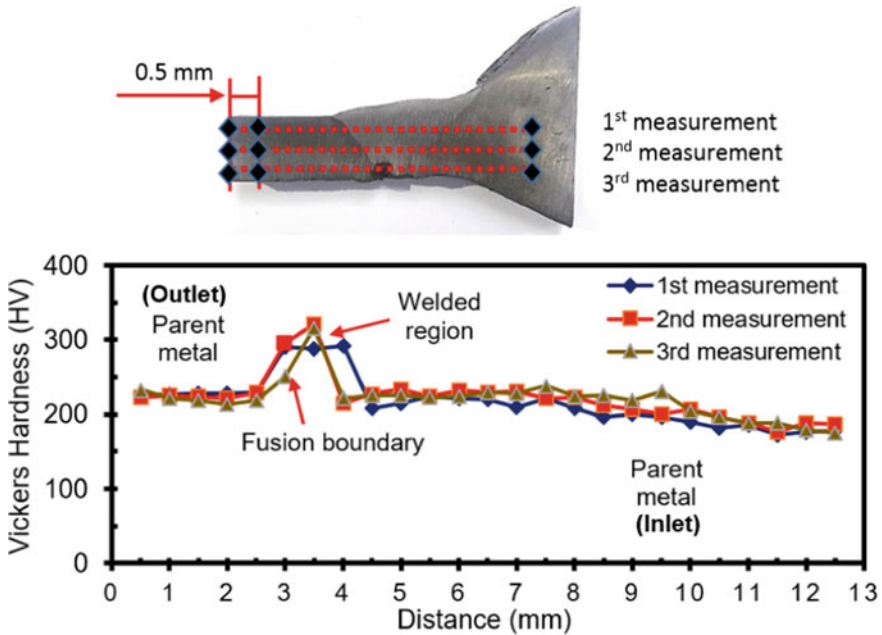
Fig. 5 Indentation points during hardness test and hardness profile across the distance (mm) of parent metal (outlet and inlet) and welded region

Table 3 Average Vickers microhardness (HV) of the welded region and parent metal

Measurement	Fusion boundary-welded region (HV)	Outlet parent metal (HV)	Inlet parent metal (HV)
1	290	228	200
2	309	224	211
3	283	221	213
Average	294	224	208
Standard Dev.	13.5	3.5	7

294 HV based on the three hardness measurements. Both outlet and inlet materials indicated a hardness value of 224 HV and 208 HV, respectively. The hardness level of weldment and the other region is considered more than those recommended based on NACE standard practice, SP0472 in H2S-containing environment which ruled out the maximum allowable weld deposit hardness of 210 HV and 248 HV for heat-affected zone (HAZ) to prevent environmental crack occurrence [23]. By taking into account on the structure of body-centered tetragonal (BCT) of the alloy, the carbon trapping in the alloy following the carbide precipitation, induced strain field in the cell and restricted the dislocation movement. The precipitation of carbide in (Cr, Mo) will then begin, and thus, the precipitation strengthening becomes effective [24–26]. Furthermore, as the weldment having a mixture of martensite and GBF, the carbide coarsening became inevitable and increases the strength and hardness. Coarser carbide determines the increase of hardness value. The use of Hollomon-Jaffe parameter is usually referred to dictate the changes in the hardness of steel during tempering [27, 28].

3.5 *Damage Analysis*

The inspection of point of leakage is applied by using dye penetrant test to the choke body. A pin-hole was identified as marked by yellow arrows shown in Fig. 6a. From the inspection, two pinholes in the size of less than 10 mm were detected at the weldment region. Observing to the internal body (Fig. 6b), pink colorant of dye penetrant marked the exact location of pinhole, depicted by yellow arrow. The pinhole
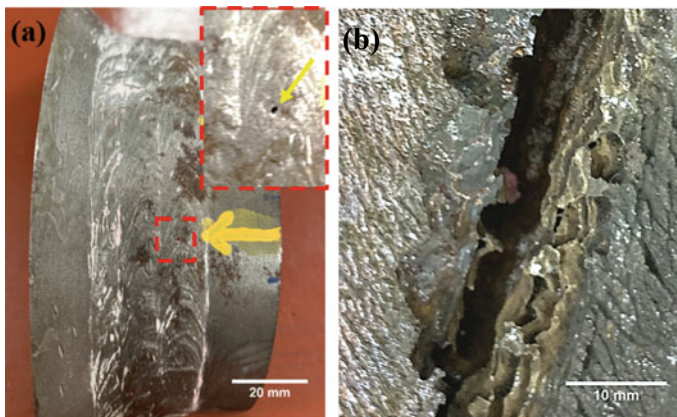
Fig. 6 Image of pinhole located at weldment **a** observing from the outer choke body. The inset image displays the enlarged image of the pinhole in red dash box, and **b** pink colorant from dye penetrant test indicated the location of pinhole, observed from inner choke body

is located at the corroded region which was deeply aggravated than the surrounding regions.

3.6   Localized Damage by Erosion Corrosion

Figure 7 displays the micrograph of the corroded choke body adjacent to the severely degraded weldment. Erosion corrosion is obviously figured based on the flow pattern direction. In this case, the flow pattern has obviously followed the direction to the outlet suggesting the occurrence of vortices of flow. Under the operational temperature (6.6–120 °C) and pressure of about 800 psi, at the corroded area, the flow-accelerated corrosion or erosion corrosion is possible.

According to Barker et al. [16], corrosion failures occur in regions where the steady-state flow patterns are disrupted, such as over the internal weld beads on the pipe body. In this case, the erosion or flow pattern near the region revealed the phenomenon of vortices flow, which primarily contributed to erosion corrosion and led to PWC of the weld bead at the same time. Impingement on the weld bead occurred as a result of fluid ejection due to the formation of flow vortices. Previously, Nøkleberg and Søntvedt [6] stated that cavitation occurs in chokes for multiphase flow if the local pressure is lower than the water vapour pressure. Due to moisture and gas flow, the hydrocarbon gas bubbles produced in the choke inlet collapse, resulting in cavitation formation. The presence of a high flow rate could also lead to high shear stress that could reduce the stability of the film of the inhibitor. According to [29], the existence of an inhibitor improved the galvanic impact of a weld and other regions. Serious localised corrosion of the welded metal can easily occur, in particular erosion
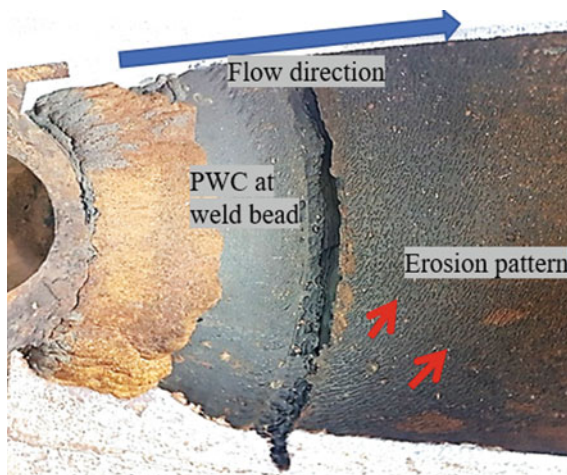
Fig. 7 Localized damage including erosion corrosion and preferential weld corrosion (PWC)

and galvanic corrosion at high flow rates and with a reducing of the efficiency of the inhibitor. Thus, even under inhibited conditions, the presence of fine debris from the corrosion product in the internal choke, especially at the weldment area, induces erosion and preferential weld corrosion. The instability of the inhibitor film at the weldment, especially near the eroded area, and its electrochemical negativity cause the weldment to be selectively disrupted compared to the other region.

3.7   Preferential Weld Corrosion (PWC)

Also displayed in Fig. 7 is the preferential weldment corrosion which contributed to the leakage. It is demonstrated that the leak of the pipeline should be attributed to the galvanic corrosion or preferential weld corrosion induced by less corrosion resistance and electronegativity of weldment compared to the inlet and outlet region [15, 19]. In this operation, nickel filler type ER7018 was employed for the welding of choke body. According to [19], a variation of regions of weldment possesses a different electrochemical potential value that contributed to a variation of susceptibility to corrosion. The weldment is anodic to the parent metal, then the localized metal loss can be easier to take place in this region.

The composition of the region, as tabulated in Table 1, confirmed that the chromium weight percent at weldment is 0.0926 wt.%, which is less than 5 and 12 times the composition of the chromium at the inlet and outlet regions, respectively. As a result of the lower chromium content, the weldment has lower corrosion resistance than regions with higher chromium content Any high chromium content region is expected to have galvanic resistance due to the significant effect of chromium content. Furthermore, the formation of Cr-rich compounds in the corrosion product, i.e. $FeCO_3$, also offers corrosion resistance. The more chromium in the alloy, the greater the amount of chromium compounds that form the protective layer [30]. However, in this situation, the impact of flow vortices aggravates corrosion at the weldment. This effect is exacerbated further by the limited surface areas of the weldment (anode) in comparison to the large surface area of the parent content (cathode). The increased hardenability of alloyed steel caused by coarsening of Cr-rich carbide precipitates often increases localised corrosion caused by microstructure transformation [19].

3.8   A Synergy of Erosion-Preferential Weld Corrosion (PWC) Effect

From the damage analysis, it can be found that the extensive metal loss was located right beside the choke seat location that possibly where the initiation of the gas vortex. This position also exhibited a reduction in wall geometry, which contributed
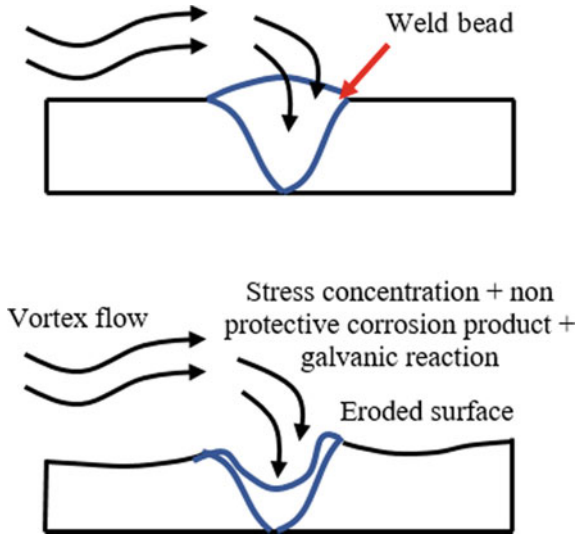
Fig. 8 The impact of stress concentration, non-protective corrosion product and galvanic reaction on the PWC

to the gas vortex. The droplets and particles in the vortices flow leading to alloy's film thinning that can weaken the corrosion resistance at the weldment. The geometric inhomogeneity near the welded joint can also lead to stress concentration at the weld bead [31]. High stress can affect corrosion by changing the properties of the corrosion product film and disrupts over the weld bead. Because of the action of the stresses, localised corrosion tends to occur at the weld bead, and the corrosion product film integrity and adhesion is lost. The corrosion product completely detached and offered no protection, as well as no resistance due to the lower chromium content. The impact of stress concentration, non-protective corrosion product and galvanic reaction on the PWC is illustrated in Fig. 8.

3.9 Analysis of Corrosion Product

The corrosion product is viewed in the brownish color, the common iron carbonate, $FeCO_3$ composition. The SEM micrograph of the corroded choke body with the accumulation of corrosion product is depicted in Fig. 9. As exhibited in the figure, the surface appeared to have tiny pits and loose corrosion products. Cracks can also be seen that were caused by surface dehydration.

A few EDX analysis was carried out to reveal the chemical compositions of the corrosion product. Figure 9 showed one of the SEM–EDX spectrum 1 result. The corrosion product mainly contained the elements of C, Al, Si, S, Cr, Mn, Fe and Ni. The elements of Si, Cr, Mn, Fe and Ni were from the metal-based elements.

Element	Weight %
C K	19.82
O K	13.01
Si K	0.33
S K	1.09
Cr K	0.52
Mn K	1.69
Fe K	54.85
Ni K	8.69
Total	100.00
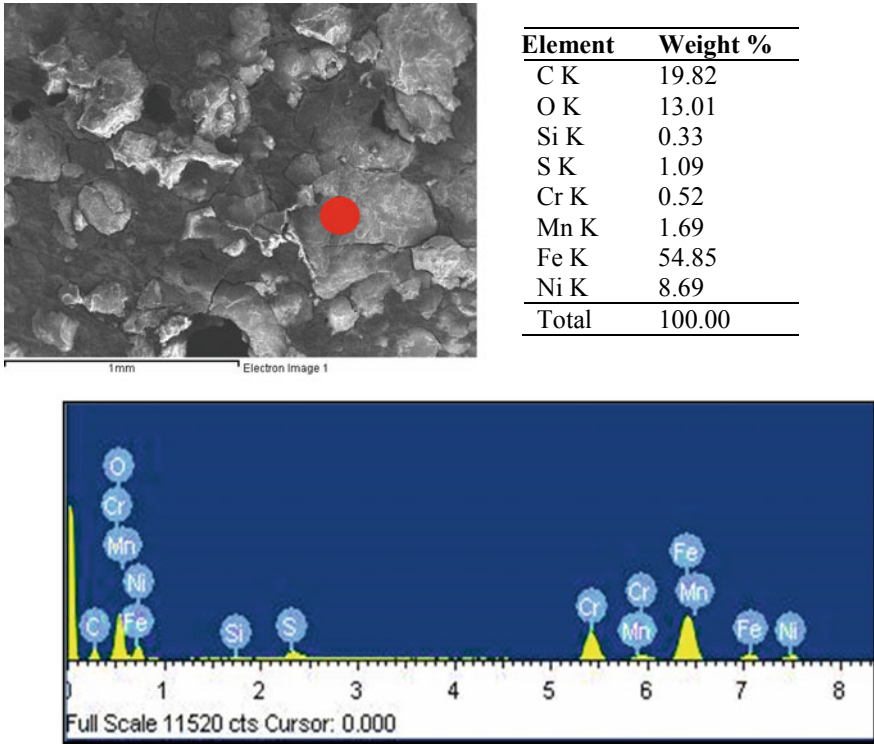
Fig. 9 SEM micrograph and EDX spectrum of the corroded choke body with accumulation of corrosion product consists of iron carbonate, $FeCO_3$

Carbon, C and oxide, O elements were also considered as the corrosive elements, with the high composition (%) was found. The corrosion product on the alloy was also analyzed with XRD spectra as provided in Fig. 10. The peak was found match with the composition of $FeCO_3$. Detection of some compounds such as FeS seems limited, probably due to less presence of H_2S. Also, there must be some compounds, such as Fe_2O_3 compounds, which were undetected by XRD.

Two phase chemical reactions that involve in the formation of corrosion product are provided in the reaction (1)–(6) [3]. The iron carbonate, $FeCO_3$ are the main corrosion products of carbon steel typically formed in the reaction involved with CO_2 corrosion. The medium in operation is also containing wet gas of H_2S that reacted with CO_2. CO_2 then is dissolved in the medium and formed weak H_2CO_3 acid resulting in an acidic and corrosive solution that ingresses damage of carbon steel. The reaction scheme is shown in the following (1)–(4) reactions.

$$Fe \rightleftharpoons Fe^{2+} + 2e^- \tag{1}$$

$$CO_{2(g)} \rightleftharpoons CO_{2(aq)} \tag{2}$$
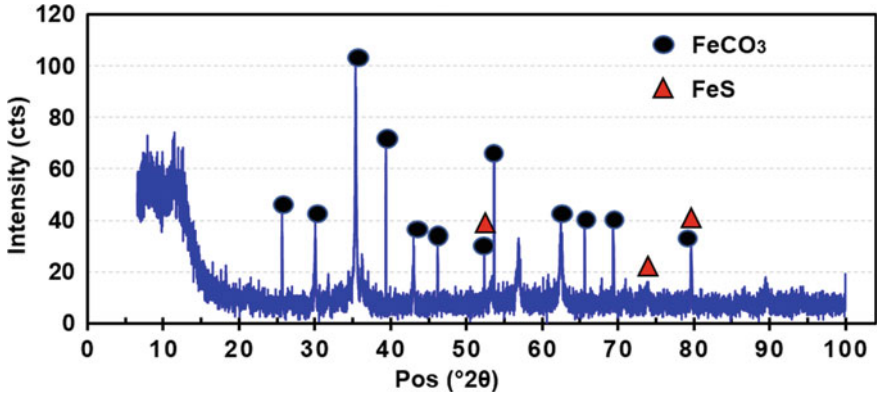
Fig. 10 XRD analysis indicating $FeCO_3$ as the main corrosion product. Low peak intensities dedicated to FeS, due to the presence of H_2S

$$CO_{2(aq)} + H_2O_{(l)} \rightleftharpoons H_2CO_{3(aq)} \tag{3}$$

$$Fe + 2H_2CO_{3(aq)} \rightleftharpoons 2FeCO_3 + 2H_2O_{(l)} \tag{4}$$

$$H_2S_{(g)} \rightleftharpoons H_2S_{(aq)} \tag{5}$$

$$Fe + 2H_2S_{(aq)} \rightleftharpoons FeS + 2H_2O_{(l)} \tag{6}$$
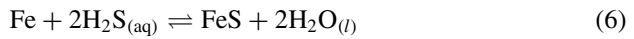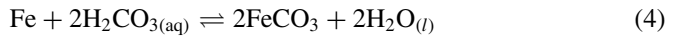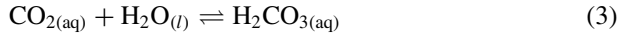
Besides, FeS is also formed as a corrosion product from the second phase reaction of carbon steel with the H_2S from the following chemical reactions (5) and (6). However, less intensity of FeS peak is presented in XRD analysis, due to the little percentage of H_2S composition in the medium. Corrosion products are generally protective or corrosive depending on pH and ambient temperature. The morphology and composition of the corrosion product decide whether an attack manifests itself as worst-case corrosion, low corrosion with protective films, or mesa corrosion. The corrosion layer also affects the efficiency and availability of the corrosion inhibitor at the surface and thus play an important role for the inhibitor. When the $FeCO_3$ product is formed at a high temperature, normally greater than 60 °C, the formation rate is rapid and the supersaturation is low. Dense crystalline films that offer good protection often are created. While, with the low temperature of the medium, the relative supersaturation of $FeCO_3$ product formation is high. The corrosion product exhibited low crystallinity, porous, loosely adherent, and much less protective than those formed at higher temperatures [32].

4 Conclusions

Throughout this analysis, the following points could be drawn:

(1)   The dominant cause of leakage in the choke valve is preferential weld corrosion (PWC) at the weld bead in the CO_2 medium.

(2)   PWC is exacerbated by the action of the stresses and the formation of non-protective corrosion product film. The flow pattern associated with the erosion corrosion was evidenced due to the turbulence/vortex flow that induces stress within the weldment.

(3)   The coarsening of chromium carbide precipitates increases the hardness value at weldment.

(4)   The driving force for the PWC is less chromium composition of the weldment region that decreases the corrosion resistance of the weldment. It is also associated with the galvanic effect from the difference between the areas of the weldment and the inlet and outlet. The weldment region acts as the anode with the small area as compared to the large area of the parent material that served as the cathode.

References

 1. Dawson JL, John G, Oliver K (2010) Management of corrosion in the oil and gas industry. Shreir's Corros 3230–3269
 2. Moiseeva LS (2005) Carbon dioxide corrosion of oil and gas field equipment. Prot Met
 3. Kahyarian A, Achour M, Nesic S (2017) CO_2 corrosion of mild steel. Elsevier Ltd
 4. Di Schino A (2019) Environmental impact of steel industry. Handbook of environmental materials management, pp 2463–2483
 5. Pyshmintsev YI, Veselov IN, Maltseva AN, Uskov DP (2018) Specific effects of microalloying elements on the development of the strength properties of low-alloyed chromium-molybdenum pipe steels. AIP Conf Proc 2053
 6. Nøkleberg L, Søntvedt T (1995) Erosion in choke valves-oil and gas industry applications. Wear 186–187:401–412
 7. Oil AFOR (2019) Method and apparatus for oil and gas operations, p 1
 8. Liu W, Shi T, Li S, Lu Q, Zhang Z, Feng S, Ming C, Wu K (2019) Failure analysis of a fracture tubing used in the formate annulus protection fluid. Eng Fail Anal 95:248–262
 9. Rintamäki K, Kuusela P (2010) Stress corrosion cracking of carbon steel in amine units. Key Eng Mater 2177–2184
10. Tawancy HM, Alhems LM (2016) Damage analysis of choke bean used in an oil–gas well. Case Stud Eng Fail Anal 7:56–64
11. Liu Z, Gao X, Du L, Li J, Li P, Yu C, Misra RDK, Wang Y (2017) Comparison of corrosion behaviour of low-alloy pipeline steel exposed to H_2S/CO_2-saturated brine and vapour-saturated H_2S/CO_2 environments. Electrochim Acta 232:528–541

12. das Chagas Almeida T, Bandeira MCE, Moreira RM, Mattos OR (2017) New insights on the role of CO_2 in the mechanism of carbon steel corrosion. Corros Sci 120:239–250
13. Song FM (2010) A comprehensive model for predicting CO_2 corrosion rate in oil and gas production and transportation systems. Electrochim Acta 55:689–700
14. Darihaki F, Hajidavalloo E, Ghasemzadeh A, Safian GA (2017) Erosion prediction for slurry flow in choke geometry. Wear 372–373
15. Adegbite MA, Robinson MJ, Impey SA (2016) Evaluation of flow enhanced preferential weld corrosion of X65 pipeline steel using a novel submerged impingement jet, pp 1–12
16. Barker R, Hu X, Neville A (2013) The influence of high shear and sand impingement on preferential weld corrosion of carbon steel pipework in CO_2-saturated environments. Tribol Int 68:17–25
17. Zhu J, Xu L, Feng Z, Frankel GS, Lu M, Chang W (2016) Galvanic corrosion of a welded joint in 3Cr low alloy pipeline steel. Corros Sci 111:391–403
18. Bland LG, Troconis BCR, Santucci RJ, Fitz-Gerald JM, Scully JR (2016) Metallurgical and electrochemical characterization of the corrosion of a Mg-Al-Zn alloy AZ31B-H24 tungsten inert gas weld: galvanic corrosion between weld zones. Corrosion 72:1226–1242
19. Pantelis DI, Tsiourva TE (2017) Corrosion of weldments. Elsevier Ltd
20. ASTM International (2015) Standard specification for steel castings suitable for pressure service
21. Bignozzi MC, Calcinelli L, Carati M, Ceschini L, Chiavari C, Masi G, Morri A (2019) Effect of heat treatment conditions on retained austenite and corrosion resistance of the X190CrVMo20-4-1 stainless steel. Met Mater Int
22. Hao L, Ji X, Zhang G, Zhao W, Sun M, Peng Y (2020) Carbide precipitation behavior and mechanical properties of micro-alloyed medium Mn steel. J Mater Sci Technol 47:122–130
23. International N (2015) Methods and controls to prevent in-service environmental cracking of carbon steel weldments in corrosive petroleum refining environments, p 36
24. Escrivà-Cerdán C, Ooi SW, Joshi GR, Morana R, Bhadeshia HKDH, Akid R (2019) Effect of tempering heat treatment on the CO_2 corrosion resistance of quench-hardened Cr-Mo low-alloy steels for oil and gas applications. Corros Sci
25. Ju Y, Goodall A, Strangwood M, Davis C (2018) Characterisation of precipitation and carbide coarsening in low carbon low alloy Q&T steels during the early stages of tempering. Mater Sci Eng A
26. Miller MK (1998) Carbide precipitation in martensite during the early stages of tempering Cr- and Mo-containing low alloy steels. Acta Mater
27. Dai T, Lippold JC (2018) Tempering effect on the fusion boundary region of alloy 625 weld overlay on 8630 steel. Weld World
28. Saha DC, Nayak SS, Biro E, Gerlich AP, Zhou Y (2014) Mechanism of secondary hardening in rapid tempering of dual-phase steel. Metall Mater Trans A 45:6153–6162
29. Alawadhi K, Robinson MJ (2011) Preferential weld corrosion of X65 pipeline steel in flowing brines containing carbon dioxide. Corros Eng Sci Technol 46:318–329
30. Sun J, Sun C, Lin X, Cheng X, Liu H (2016) Effect of chromium on corrosion behavior of P110 steels in CO_2-H_2S environment with high pressure and high temperature. Materials 9:1–14
31. Qiao Q, Cheng G, Wu W, Li Y, Huang H, Wei Z (2016) Failure analysis of corrosion at an inhomogeneous welded joint in a natural gas gathering pipeline considering the combined action of multiple factors. Eng Fail Anal 126–143
32. Dugstad A (2006) Fundamental aspects of CO_2 metal loss corrosion. Part I: Mechanism. In: Corrosion Nace expo 2006, pp 1–18

Investigation of Tool Wear Mechanisms in Face Milling of Inconel 718 with Different Cutting Fluids

Tiyamike Banda, Man Shen Song, Ali Akhavan Farid, and Chin Seong Lim

Abstract Inconel 718 is a hard-to-machine nickel-based alloy used for aerospace component manufacturing. The machining of Inconel 718 causes severe tool failure due to the heat generated by high friction forces. Therefore, cutting tool performance can be optimized by using a suitable cutting fluid. This paper compares the effects of synthetic and oil-based cutting fluids on wear mechanisms and failure modes of the PVD-TiAlN/NbN coated inserts during face milling of Inconel 718. Face milling was conducted by varying cutting speed at constant feed rate, axial and radial depth of cut. Flank wear (V_B) was measured before the inserts were examined in SEM and EDX for tool wear mechanisms characterisation. Chipping, built-up edge (BUE) and severe notching were the most dominant failure modes observed in all cutting conditions. Pitting, galling and coat delamination associated with chipping and minor BUE were observed at low cutting speed. At high speed, progressive nose notching was the main cause of tool failure. At low cutting speed, dry cutting produced the longest tool life followed by oil-based and synthetic cutting fluids. At higher cutting speed, synthetic fluid had the longest tool life followed by oil-based cutting fluid and dry cutting. This research provides an insight on the influence of cutting speed to the choice of cutting fluids during machining so that tool wear can be minimized.

Keywords Cutting fluids · Wear mechanisms · Tool life · Inconel 718

1 Introduction

Inconel 718 is widely used in the aerospace industry due to their superior mechanical, thermal and corrosive properties. It has exceptional application in jet engines and turbine, which are exposed to high thermal and fatigue stresses. However, it is hard to machine due to high mechanical strength and hardness, formation of highly

T. Banda · M. S. Song · A. Akhavan Farid · C. S. Lim (✉)

Department of Mechanical, Materials and Manufacturing Engineering, University of Nottingham Malaysia, 43500 Semenyih, Malaysia

e-mail: chinseong.lim@nottingham.edu.my

abrasive carbide particles in the microstructure, high work hardening, low thermal conductivity and strong tendency to weld and form BUE during machining [1].

The main modes of tool failure during milling of Inconel 718 are flank wear chipping, BUE, notching and abrasion. However, most researches seldom considered unprecedented tool failure caused by galling, pitting, flaking and coating delamination. Galling is induced by adhesion and particle diffusion, which often occurs while metal surfaces are in contact or slide against each other, thus, it is a common issue in metal sheet forming industries [2]. Whereas flaking is caused by the high temperature generated at the chip-tool interface [3]. Pitting corrosion leads to small cavities induced by the chemical reaction of the medium environment or workpiece especially those materials that contain aggressive chemical chloride [4]. These tool wear mechanisms and failure modes can be minimised by reducing the heat and friction forces by applying the cutting fluids during the machining process.

The cutting fluid is always considered an important machining element, which helps to improve tool life when cutting hard-to-machine metals. Cutting fluids are applied to minimise heat at relatively high cutting speed and reduce friction at relatively low speed [5]. Cutting fluids can be classified as water-based or oil-based which represent the cooling capability and lubrication properties, respectively [6]. Normally, the water-based fluids are applied for both cooling and lubrication while the oil-based fluids are specifically applied for lubrication. The water-based cutting fluids are more apt to be used in high speed regime while oil-based cutting fluids are more apt to be used in low speed regime [5, 6]. Pereira et al. [7] found out that ECO-350 recycled oil and oleic sunflower oil improved tool life by 30% and 15% respectively compared to commercial canola oil. It was also observed that oil–water emulsion can reduce tool wear more than ethanol [8] because of good combination of cooling and lubrication properties. Sterle et al. [9] discovered that the addition of solid lubricant molybdenum di-sulphide (MoS_2) in oil-based coolant enhanced cooling property which gives a better surface finish than normal oil-based coolant.

In recent years, cryogenic cooling method had been used as an alternative cooling technique during machining of Inconel 718. Chaaban et al. [10] observed a higher work hardening on Inconel 718 surface during CO_2 cryogenic cooling which increases the friction due to low lubrication. The internal CO_2 CryoMQL (minimum quantity lubrication) and external CryoMQL has less cooling property which reduces tool life as compared to conventional oil-based flood coolant [11]. It was observed that cryogenic CO_2 cooling reduced the cutting force by 23% which minimised notching, flaking and abrasion wear and improved the surface roughness by 88% compared to dry cutting [12]. An alternative to CO_2 in cryogenic is LN_2. Halim et al. [13] found out that cryogenic CO_2 has better cooling property which improves tool life more than cryogenic LN_2 cooling. Zhang et al. [14] discovered that addition of micro-droplets of vegetable oil to cryogenic compressed air increased lubrication and improved tool life by 1.57 times as compared dry cutting.

Beside cryogenic cooling, there are new discoveries of nano-particles which improve the lubrication properties of cutting fluids. The addition of nano-particles improved the cutting fluids by reducing circularity errors, burr heights and thrust force which are common problems experienced in oil-based flood cooling and MQL

conditions [15]. Bertolini et al. [16] observed that graphene nano-platelets improved surface roughness and cutting force by 38% and 59%, respectively as compared to oil-based fluids. Marques et al. [17] discovered that the MoS_2 solid lubricants in LB 2000 oil minimised notching, abrasion, diffusion and chipping wear which increased the tool life by 12% and 46% as compared to dry cutting and pure LB 2000 fluid, respectively.

Although advanced techniques such as nanofluid have shown substantial improvement in lubrication properties, the conventional water-based synthetic and oil-based fluids still offers the best cooling and lubricating properties. Most of the researches focused much on the effect of various cutting fluids on tool wear evolution, cutting forces, and surface roughness. However, the characterisation and identification of wear mechanisms, which influence unprecedented failure modes of tools are equally important in the optimisation of tool life. This research presents the study of the tool wear mechanisms, failure modes and tool life of PVD TiAlN-NbN coated cemented carbide insert under the application of synthetic and oil-based cutting fluids during face milling of Inconel 718. The effect of different cutting speeds on the selection of cutting fluid for CNC milling of Inconel 718 will also be discussed in this research.

2 Methodology

2.1 Materials and Methods

The experiment was carried out on a 14 kW model of DMC 835V-DECKEL MAHO CNC milling machine. Figure 1 shows the CNC milling environment and the equipment used for the experiment. TiAlN-NbN coated cemented carbide inserts with 32 mm diameter face milling cutter were used in this research. The cutter was placed at the centerline of the workpiece and symmetric face milling was chosen as the milling method. The symmetric milling method was more apt to tool wear phenomenon which was dominant of end of tool life instead of tool breakage. The cutting insert had an approach angle of 45°; rake angle of 18°; radial rake angle of 8°. The synthetic cutting fluid consists of 50% water, 20% corrosion Inhibitors, 29% Bio-stable Agents and 1% Biocides. The oil-based cutting fluid consists of 85% mineral oil-15% additives to water ratio of 1–18 to prevent fire risk or creating smoke that will result in an unsafe work environment because pure oil has poor heat dissipating properties which are not suitable for high-speed milling process. The cutting process was performed on $100 \times 50 \times 25$ mm Inconel 718 block. Rough milling was done by removing 1 mm axial depth in all surfaces before commencing the main experiment. The chemical composition of the Inconel 718 and tool properties are shown in Tables 1 and 2. The PVD coated tools were tested at 3 cutting speeds which were 50, 75, 100 m/min. Dry cutting was performed for comparison purpose. The constant feed rate (f) was 0.08 mm/tooth and axial depth of cut (ADOC) was 1 mm.
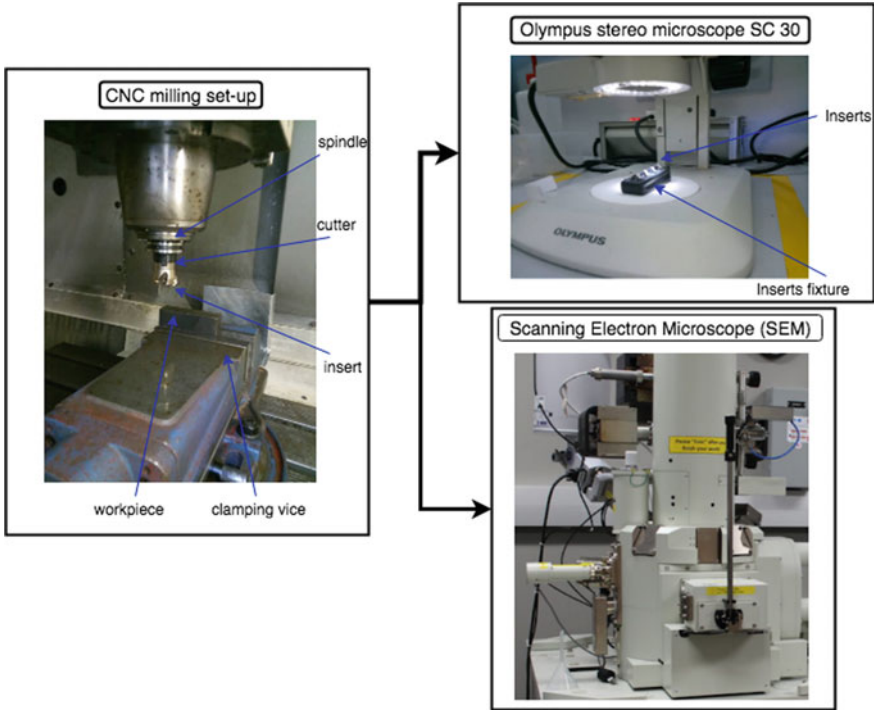
Fig. 1 CNC milling set-up and the characterization equipment

Table 1 Chemical composition of Inconel 718

Element	C	Cr	Mo	Ti	Ni	Nb	Al	Cu	Si	Fe
Weight	0.08	21	3.3	1.15	55	5.5	0.8	0.3	0.1	12.8

Table 2 TiAlN-NbN coating properties

Vickers hardness	Oxidation temperature (°C)	Friction coefficient	Thickness	Surface roughness
2800	800	70	2–4 µm	40

The coated cutting tool inserts were tested at 3 cutting speeds under synthetic, oil-based cutting fluids and dry cutting conditions. The experiments were interrupted at least 5 times during the machining trial to measure the flank wear, chipping and examine other failure modes under stereo microscope.

The worn inserts were collected and characterized thoroughly by an EDX analysis under a scanning electron microscope (SEM). The SEM EDX analysis was performed to study the coating delamination and diffusion of chip material on the cutting edge of the tool. The experiments were terminated when the tool inserts reached the end

of tool life. The end of tool life was determined based on the following tool wear criteria [18]: Average flank wear (V_B) of any insert reached 0.7 mm (4 cutting inserts per test) or chipping and flaking larger than 0.4 mm occur or maximum flank wear depth reached 1.2 mm and fracture.

3 Results and Discussion

3.1 Effects of Cutting Speed on Tool Wear and Tool Life

The tool wear measurement and dominant wear mechanisms under various cutting speed were observed and measured under the stereo-microscope. The tool life was observed to decrease with an increase in the cutting speed for all the cutting conditions, as shown in Table 3. This was because the temperature increased with cutting speed, which weakens the bonding strength and hardness of the tool coating, eventually facilitating the abrasion and TiAlN-NbN coating delamination. The second reason was due to an increase in dynamic forces and vibration, which facilitate the heavy shock and fatigue to cause severe chipping and notching.

Figure 2 shows the average flank wear measurement taken on 4 inserts of the cutter. The tool life for the dry cutting condition was 47 min, outperforming all cutting fluids at a low cutting speed of 50 m/min. The average flank wear formed slowly in dry cutting (Fig. 2a) than in cutting fluids condition at low speed because of moderate heat, which minimised wear mechanisms like abrasion, oxidation and diffusion. However, dry cutting enhanced thermos-softening of Inconel 718, which significantly reduced the impact of the cutting force and friction to minimise mechanical wear. On the other hand, cyclic thermal shock or rapid variation of cutting temperature caused by cutting fluids hardened the workpiece surface by heat treatment, which increased the friction force, thereby accelerating mechanical failure on the tool's cutting edge [19]. Thus, the precipitation hardening of Inconel 718, which increased the cutting

Table 3 Tool life for all cutting conditions at $f = 0.08$ mm/tooth; ADOC = 1 mm

V (m/min)	Cutting condition	Tool life (min)
50	Synthetic cutting fluid	29
	Oil-based cutting fluid	33
	Dry cutting	47
75	Synthetic cutting fluid	21
	Oil-based cutting fluid	19.5
	Dry cutting	16
100	Synthetic cutting fluid	18.5
	Oil-based cutting fluid	16
	Dry cutting	9.5
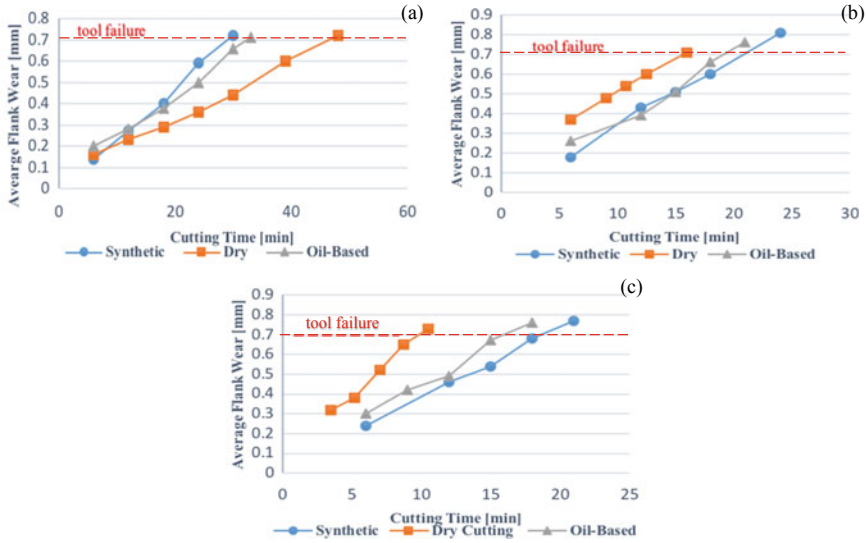
Fig. 2 Average flank wear at cutting condition at **a** $V = 50$ m/min; **b** $V = 75$ m/min, and **c** $V = 100$ m/min

force accelerated coating delamination, galling, chipping, and flaking. The tool life with oil-based cutting fluids was slightly longer (33 min) than the synthetic cutting fluids (29 min) at a low cutting speed of 50 m/min. This was attributed by lubricating effects of oil-based fluid, which reduced some friction forces to minimise abrasion wear [20]. Therefore, dry cutting was preferable when face milling Inconel 718 at low speed, followed by oil-based and synthetic cutting fluids.

At moderate and high cutting speed, the rate of tool wear with dry cutting tremendously decreased (Fig. 2b and c), yielding the shortest tool life at 100 m/min, as shown in Fig. 2c. During dry cutting, the cutting zone experienced high temperature, which caused thermally induced wear mechanisms, such as diffusion, oxidation, plastic deformation, and adhesion wear [21, 22], which significantly increase the unprecedented failure modes like abrasion, chipping, and other stress-related failure modes. It was noted that at high speed regime, heat accumulated at the chip-tool interface region. Under such condition, high cutting forces caused by hardened Inconel 718 surface accelerated some mechanical failure mechanisms like galling wear due to cyclic adhesion. However, the synthetic cutting fluid gave a better performance than oil-based cutting fluid, in terms of minimising flank wear to improve tool life at 75 m/min and 100 m/min, as shown in Table 3. This was attributed to a low penetration rate of oil-based coolant to provide sufficient cooling due to limited wettability, inhibiting heat reduction on the tool-workpiece contact zone. On the other hand, the flood cooling of water-diluted synthetic fluids offered the best wettability, which improves the heat dissipation capability on the shear zone [23], providing better cooling and lubrication effect than oil-based fluids at the highest temperature region [24], while preventing chemical wear using anti-oxidants. Thus, the cooling effect

of synthetic fluid reduced the thermally induced failure mechanisms at moderate and high cutting speed [22], thereby minimising progressive chipping, pitting, galling, and coat delamination to improve tool life. Therefore, the tool life at moderate and high cutting speed was more dependent on cooling than lubrication effect of the cutting fluid. Hence, a cutting fluid with a better cooling effect (synthetic) is more suitable for cutting Inconel 718 at a high cutting speed more than 75 m/min.

3.2 Failure Modes and Wear Mechanism Under SEM

To comprehend the development of tool wear mechanism, which influenced the tool life, the rake face and edges of worn tool inserts were examined under the SEM. The wear modes and mechanisms observed include galling, pitting, flaking, coating delamination, progressive and severe chipping. The dominant wear modes/mechanism at various cutting speed under different cutting fluids/dry cutting conditions are shown in Table 4. The dominant wear modes evolved from micro-chipping to severe chipping at highest cutting speed.

At the low cutting speed, the dominant failure modes for all cutting conditions were galling, flaking and coating delamination. Based on Fig. 3a and b, it was observed that the galling and flaking on rake face and cutting edge occurred at low cutting speed. The occurrence of galling failure signified diffusion mechanisms of TiAlN particles to Inconel 718 surface due to high friction at the chip-tool interface region. The localized heat zone at chip-tool interface increased during machining which induces the plasticity of TiAlN coating properties and caused the diffusion of tool material resulting in galling after subsequent cuts [2]. Flaking is caused by the interaction of high thermal and mechanical stress at the chip-tool interface [3]. The sudden impact when the tool penetrated the workpiece removes large fragments of tool material as shown in Fig. 3a.

Table 4 Dominant tool wear mechanisms observed on the worn inserts

V (m/min)	Cutting condition	g	p	fl	cd	pc	sc
50	Synthetic fluid	✓		✓	✓		
	Oil-based fluid	✓		✓	✓		
	Dry cutting	✓		✓	✓		
75	Synthetic fluid	✓	✓	✓	✓		
	Oil-based fluid	✓	✓	✓	✓		
	Dry cutting	✓		✓		✓	
100	Synthetic fluid	✓		✓		✓	
	Oil-based fluid	✓		✓			✓
	Dry cutting	✓		✓			✓

g: galling, p: pitting, fl: flaking, cd: coating delamination; pc: progressive chipping; sc: severe chipping
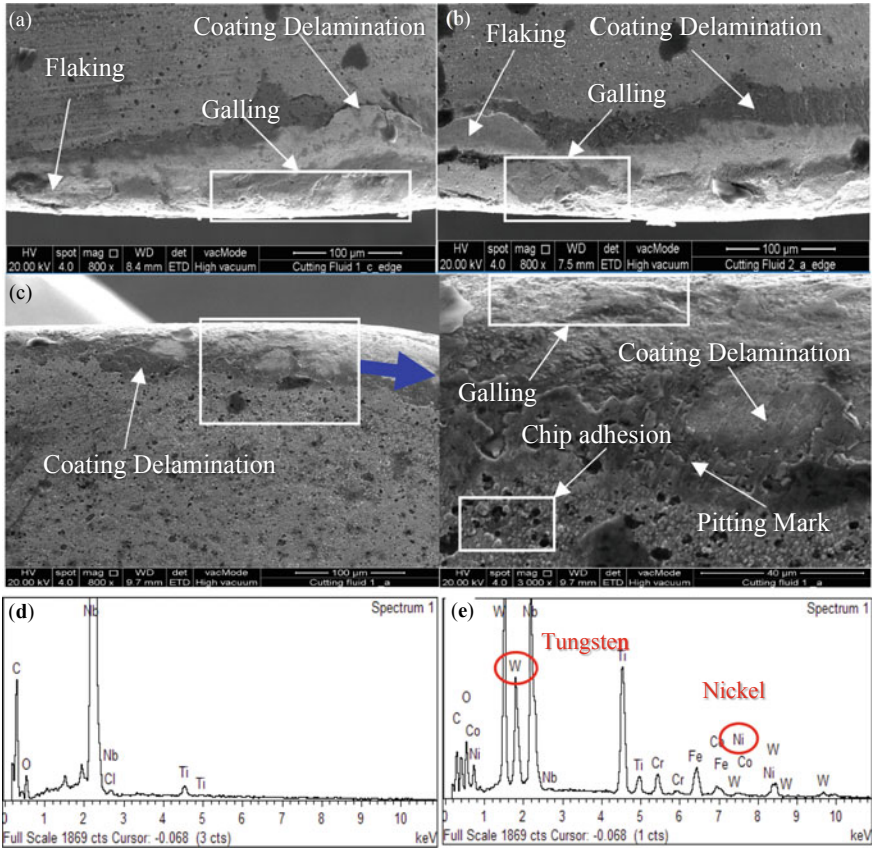
Fig. 3 SEM micrograph of tool wear mechanisms under **a** synthetic fluid at V = 50 m/min; **b** oil-based fluid at V = 75 m/min; **c** synthetic fluid at V = 75 m/min; **d** EDS of a new insert and **e** EDS of used insert for synthetic fluid V = 75 m/min

The EDX analysis in Fig. 3d and e extracted the chip-tool interface region to determine the coating delamination and chip adhesion phenomenon. Based on the comparison between Fig. 3d and e, a large amount of tungsten (W) was detected which initially settled under the TiAlN coating layer. This implied that the coating layer was peeled off to expose W from the substrate. The TiAlN-NbN coating gets peeled together with the welded chips as they get removed when the tool insert re-enters or exits the workpiece. Besides, the EDX analysis, Fig. 3e also showed that the presence of Nickel (Ni) was found in the rake face of the coated tool. This suggested that the chip adhesion phenomenon happened at the rake face which is caused by the diffusion of chip material at high temperature and friction in the contact zone.

Pitting corrosion existed in oil-based and synthetic cutting fluids at 75 m/min as shown in Table 4. The pitting mark under synthetic fluid at 75 m/min is shown in Fig. 3c. The occurrence of pitting was due to the chemical reaction between the
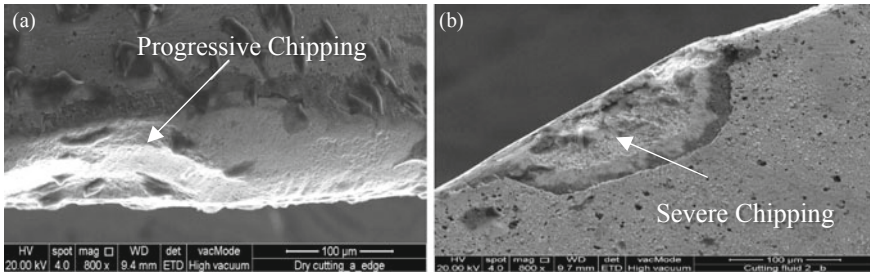
Fig. 4 SEM images of progressive chipping and severe chipping under **a** dry cutting condition at V = 75 m/min and **b** oil-based fluid at V = 100 m/min, respectively

environment and tool material. As the presence of chemical composition in both cutting fluids, it damaged the passive film at the high-temperature chip-tool interface during machining which eventually led to the pitting wear mode [4].

As the cutting speed increased, the wear region grows from microscale tool wear to progressive chipping which evolved to severe chipping and resulted in tool breakage as shown in Fig. 4a and b. At the high cutting speed of 100 m/min, severe chipping occurred in oil-based cutting fluids and dry cutting condition which progressed to tool fracture by nose notching. This was attributed to high thermal and mechanical stresses caused by high temperature due to poor cooling capability of oil-based cutting fluid and dry cutting condition. Therefore, the cutting at higher speed makes the tool inserts disposed to chipping and plastic deformation. As the chipping progresses, the original edge-sharpness is altered by increasing the nose radius, thus, resulting in high-stress concentration region at the sharp section which leads to high deformation, crack initiation and propagation, and accelerated fracture [19].

4 Conclusions

The effect of cutting speed and performance of synthetic, oil-based cutting fluids, and dry cutting condition on wear characteristics of a TiAlN coated cemented carbide insert was investigated when face milling Inconel 718. The tool life reduced with increase in cutting speed for all cutting fluids/dry cutting tested. The dry cutting gave a better tool life, followed by the oil-based and synthetic cutting fluids at a low cutting speed of 50 m/min. The synthetic cutting fluid gave a better tool life as the cutting speed was raised, followed by the oil-based fluid and dry cutting. This was due to the high-speed machining prone to better cooling capabilities than lubrication properties. The coated tool in dry cutting gave tool life less than 10 min at a high cutting speed of 100 m/min. The dominant wear modes included galling, pitting, flaking, coating delamination, progressive and severe chipping under the SEM micrographs. The dominant wear modes were growing at higher cutting speed from micro-chipping to severe chipping which resulted in tool breakage by severe

nose notching. The research can also be used to optimise the tool life by selecting the best speed and cutting fluids which minimises the failure modes and tool wear mechanisms of TiAlN coated inserts during machining of Inconel 718.

References

1. Jahanbakhsh M, Akhavan Farid A, Lotfi M (2018) Optimal flank wear in turning of Inconel 625 super-alloy using ceramic tool. Proc Inst Mech Eng Part B J Eng Manuf 232(2):208–216
2. Gåård A, Krakhmalev PV, Bergström J, Hallbäck N (2007) Galling resistance and wear mechanisms—cold work tool materials sliding against carbon steel sheets. Tribol Lett 26(1):67–72
3. Ibrahim GA, Che Haron CH, Ghani JA (2016) Tool wear mechanism in continuous cutting of difficult-to-cut material under dry machining. Adv Mater Res 2010(126–128):195–201
4. Houchuan Y, Zhitong C, ZiTong Z (2015) Influence of cutting speed and tool wear on the surface integrity of the titanium alloy Ti-1023 during milling. Int J Adv Manuf Technol 78(5–8):1113–1126
5. Milton SC (2005) Metal cutting principles, 2nd edn. Oxford University Press
6. Sharif MN, Pervaiz S, Deiab I (2017) Potential of alternative lubrication strategies for metal cutting processes: a review. Int J Adv Manuf Technol 89:2447–2479
7. Pereira O, Martín-Alfonso JE, Rodríguez A, Calleja A, Fernández-Valdivielso A, López de Lacalle LN (2017) Sustainability analysis of lubricant oils for minimum quantity lubrication based on their tribo-rheological performance. J Clean Prod 164:1419–1429
8. Aslantas K, Çiçek A (2018) The effects of cooling/lubrication techniques on cutting performance in micro-milling of Inconel 718 superalloy. Procedia CIRP [Internet] 77(Hpc):70–73. Available from: https://doi.org/10.1016/j.procir.2018.08.219
9. Sterle L, Mallipeddi D, Krajnik P, Pušavec F (2020) The influence of single-channel liquid CO_2 and MQL delivery on surface integrity in machining of Inconel 718. Procedia CIRP [Internet] 87:164–169. Available from: https://doi.org/10.1016/j.procir.2020.02.032
10. Chaabani S, Arrazola PJ, Ayed Y, Madariaga A, Tidu A, Germain G (2020) Surface integrity when machining Inconel 718 using conventional lubrication and carbon dioxide coolant. Procedia Manuf [Internet] 47:530–534. Available from: https://doi.org/10.1016/j.promfg.2020.04.150
11. Pereira O, Urbikain G, Rodríguez A, Fernández-Valdivielso A, Calleja A, Ayesta I et al (2017) Internal cryolubrication approach for Inconel 718 milling. Procedia Manuf [Internet] 13:89–93. Available from: https://doi.org/10.1016/j.promfg.2017.09.013
12. Musfirah AH, Ghani JA, Haron CHC (2017) Tool wear and surface integrity of Inconel 718 in dry and cryogenic coolant at high cutting speed. Wear 376–377:125–133
13. Halim NHA, Haron CHC, Ghani JA, Azhar MF (2019) Prediction of cutting force for milling of Inconel 718 under cryogenic condition by response surface methodology. J Mech Eng 16(1):1–16
14. Zhang S, Li JF, Wang YW (2012) Tool life and cutting forces in end milling Inconel 718 under dry and minimum quantity cooling lubrication cutting conditions. J Clean Prod 32:81–87
15. Khanafer K, Eltaggaz A, Deiab I, Agarwal H, Abdul-latif A (2020) Toward sustainable micro-drilling of Inconel 718 superalloy using MQL-nanofluid. Int J Adv Manuf Technol 107(7–8):3459–3469
16. Bertolini R, Gong L, Ghiotti A, Bruschi S (2020) Graphene nanoplatelets-assisted minimum quantity lubrication in turning to enhance Inconel 718 surface integrity. Procedia CIRP [Internet] 87:71–76. Available from: https://doi.org/10.1016/j.procir.2020.02.021
17. Marques A, Paipa Suarez M, Falco Sales W, Rocha Machado Á (2019) Turning of Inconel 718 with whisker-reinforced ceramic tools applying vegetable-based cutting fluid mixed with solid

lubricants by MQL. J Mater Process Technol [Internet] 266:530–543. Available from: https://doi.org/10.1016/j.jmatprotec.2018.11.032

18. Caldeirani Filho J, Diniz AE (2002) Influence of cutting conditions on tool life, tool wear and surface finish in the face milling process. J Braz Soc Mech Sci [Internet] 24(1):10–14. Available from: http://www.scielo.br/scielo.php?script=sci_arttext&pid=S0100-73862002000100002&lng=en&tlng=en. Cited 19 May 2021

19. Chetan, Ghosh S, Venkateswara Rao P (2015) Application of sustainable techniques in metal cutting for enhanced machinability: a review. J Clean Prod [Internet] 100:17–34. Available from: https://doi.org/10.1016/j.jclepro.2015.03.039

20. Nandy AK, Gowrishankar MC, Paul S (2009) Some studies on high-pressure cooling in turning of Ti-6Al-4V. Int J Mach Tools Manuf 49(2):182–198

21. Zhao H, Barber GC, Zou Q (2002) A study of flank wear in orthogonal cutting with internal cooling. Wear 253(9–10):957–962

22. Sharma VS, Dogra M, Suri NM (2009) Cooling techniques for improved productivity in turning. Int J Mach Tools Manuf 49:435–453

23. Sales WF, Diniz AE, Machado ÁR (2001) Application of cutting fluids in machining processes. J Braz Soc Mech Sci [Internet] 23(2):227–240. Available from: http://www.scielo.br/j/jbsms/a/DfB8pRH7pM6LNHtYn8nVxmJ/?lang=en. Cited 19 Aug 2021

24. Diniz AE, Micaroni R (2007) Influence of the direction and flow rate of the cutting fluid on tool life in turning process of AISI 1045 steel. Int J Mach Tools Manuf 47(2):247–254

Assessing Integrated TOPSIS Model with Exponential Intuitionistic Entropy Measure: A Case Study

Omar Ayasrah and **Faiz Mohd Turan**

Abstract Solving multi-criteria decision-making (MCDM) problems requires assigning weights to the problem's criteria, the determination of criteria weights could be subjectively or objectively. Many studies emphasized the effectiveness of using objective techniques to derive criteria weights, like using entropy as a measure of fuzziness of the fuzzy sets to detect criteria weights. Despite that, still this subject under study and debate between researchers. This is due to the importance and effect of the criteria weights on the final results. The proposed MCDM method integrates the TOPSIS approach with the intuitionistic fuzzy entropy measure in exponential form, aiming to have an MCDM method that is simple to be implemented and compensate the need to determining the criteria weights. In this paper, the process of the new MCDM method is introduced, with two practical examples to demonstrate the simplicity of the proposed method, and to prove its effectiveness without the need to determine the attribute weights. At the end of each example, a comparison table is provided to benchmark the generated result from the new method with the results from other comparable methods.

Keywords Intuitionistic fuzzy entropy · Exponential intuitionistic fuzzy entropy · Intuitionistic fuzzy TOPSIS · MCDM

1 Introduction

In recent complicated life, selecting the best decisions turns out to be a tough part of the management job in both private and government enterprises. Recently, decision-makers have become unwilling to take gut feeling-based decisions, and instead look to adapt quantitative techniques to take and analyze their decisions [1].

Multi-criteria decision-making (MCDM) methods support decision-makers to confront problems with multiple criteria to provide a solution. Usually, a single

O. Ayasrah · F. Mohd Turan (✉)
Faculty of Manufacturing and Mechatronic Engineering Technology, Universiti Malaysia Pahang, 26600 Pekan, Pahang, Malaysia
e-mail: faizmt@ump.edu.my

optimal solution for such problems does not exist. So, preferences from decision-makers differentiate between solutions (alternatives). In other words, MCDM aims to aid decision-makers to shortlist alternatives or choose a single alternative that fulfills the attributes and is aligned with their preferences [2].

The solution of the MCDM problem is derived from the preferences of a group of decision-makers and, due to the vagueness and imprecision in the available information, DMs use intuitionistic fuzzy numbers (IFNs) to give their preferences and build a decision matrix [3, 4].

Criteria weights having a significant effect on the final rank of the alternatives [5]. The used techniques to detecting weights for attributes could be grouped into two categories: subjective, based on decision-makers evaluation (like using AHP), and objective, that derived from given decision-makers preferences (like using the Entropy method) [6]. Hatefi [7] claimed that using objective methods would be more robust and rational than using subjective methods.

Entropy measure is used to evaluate the fuzziness and vagueness of the fuzzy sets [8]. Zadeh [9] presented the fuzzy entropy first. Then Deluca and Termini [10] explored the definition of fuzzy entropy. Then, many fuzzy entropy measures were introduced, and the IF entropy measure was introduced by Burillo and Bustince [11].

2 The Intuitionistic Fuzzy MCDM Method Based on the New IF Entropy

The proposed method aims to integrate a new intuitionistic fuzzy entropy measure in an exponential with TOPSIS approach. The process of the new method is presented in Fig. 1.
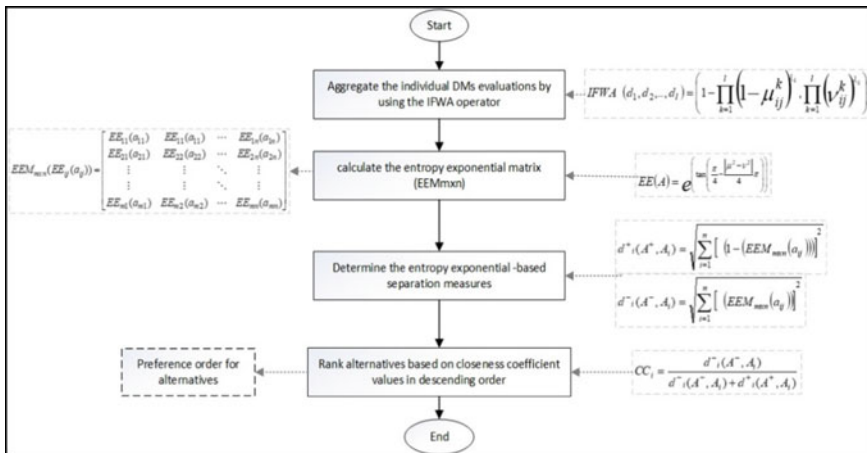
Fig. 1 The process of the new method

The rationale of using the IF-Entropy measure in exponential form is to simplify the implementation of the new MCDM method, without the need to assign weights for criteria. Moreover, engaging the TOPSIS approach would add more simplicity to the developed MCDM method.

3 Illustrative Examples

Example 1 This example is adapted from Chen et al. [12] and Aikhuele and Turan [13], and used by Liu et al. [14]:

An investment corporation intends to invest a sum of money in the best firm. There are three alternatives firm A_1 (a car firm), A_2 (a TV firm), and A_3 (a food firm) to be evaluated based on three criteria U_1 (risk), U_2 (growth), and U_3 (environmental impact) by three DMs, i.e., the director (D_1), the manager (D_2) and the assistant manager (D_3). Suppose that the weights λ_1, λ_2, and λ_3 of the DMs d_1, d_2, and d_3 are 0.36, 0.32, and 0.32, respectively (Table 1).

- Aggregating the individual assessment matrices by using the IFWA operator to have the group assessment matrix (Table 2).

Table 1 The individual decision matrix for Example 1

DMs	Alternatives	Attributes		
		U_1	U_2	U_3
D_1	A_1	(0.8, 0)	(0.5, 0.3)	(0.5, 0.2)
	A_2	(0.85, 0.01)	(0.85, 0.15)	(0.8, 0.1)
	A_3	(0.99, 0.01)	(0.9, 0.05)	(0.85, 0.05)
D_2	A_1	(0.1, 0.9)	(0.15, 0.7)	(0.2, 0.6)
	A_2	(0.2, 0.65)	(0.35, 0.6)	(0.3, 0.5)
	A_3	(0.25, 0.01)	(0.5, 0.4)	(0.4, 0.4)
D_3	A_1	(0.05, 0.95)	(0.2, 0.75)	(0.15, 0.65)
	A_2	(0.15, 0.8)	(0.4, 0.6)	(0.3, 0.6)
	A_3	(0.35, 0.6)	(0.5, 0.4)	(0.35, 0.5)

Table 2 The aggregated assessment matrix for Example 1

Alternatives	Attributes		
	U_1	U_2	U_3
A_1	(0.467, 0)	(0.311, 0.527)	(0.311, 0.414)
A_2	(0.554, 0.155)	(0.626, 0.364)	(0.554, 0.297)
A_3	(0.849, 0.037)	(0.72, 0.189)	(0.626, 0.203)

Table 3 The entropy exponential matrix for Example 1

Alternatives	Attributes		
	U_1	U_2	U_3
A_1	2.024	2.115	2.432
A_2	1.881	1.930	2.022
A_3	1.252	1.538	1.749

- Calculating the entropy exponential matrix (Table 3).

- Determining the separation measures, closeness coefficient for each alternative, and ranking alternative (Table 4).

Table 5 shows the alternatives' preference order of the proposed method with a comparison with results from other methods. Where the preference order for Zeng and Su [15], and Chen et al. [12] coincide with the proposed method results. And most of the methods considered alternative A3 as the best one among the three alternatives.

Example 2 Chen et al. [12]: A decision-maker wants to invest money in a company. There are six alternatives to be assessed, as follows:

Table 4 The preference order of the alternatives for Example 1

Alternatives	Attributes			$d_i^-(A^-, A_i)$	$d_i^+(A^+, A_i)$	Closeness coefficient	Rank
	U_1	U_2	U_3				
A1	2.024	2.115	2.432	2.083891	3.805867	0.64618	3
A_2	1.881	1.930	2.022	1.63876	3.3692	0.67276	2
A_3	1.252	1.538	1.749	0.955957	2.644133	0.73446	1

Table 5 A comparison of the preference order of the alternatives for different methods for Example 1

Method		Preference order
Xu [16]		A3 > A1 > A2
Yue [17]		A1 > A3 > A2
Zeng and Su [15]		A3 > A2 > A1
Chen et al. [12]		A3 > A2 > A1
Liu [14]	$\Upsilon = -4$	A3 > A1 > A2
	$\Upsilon = 0$	A3 > A1 > A2
	$\Upsilon = 4$	A1 > A3 > A2
The proposed method		A3 > A2 > A1

(1) A_1: a chemical company,
(2) A_2: a food company,
(3) A_3: a computer company,
(4) A_4: a car company,
(5) A_5: a furniture company,
(6) A_6: a pharmaceutical company.

Considering the following attributes:

(1) U_1: benefits in the short term,
(2) U_2: benefits in the midterm,
(3) U_3: benefits in the long term,
(4) U_4: risk of the investment,
(5) U_5: the difficulty to invest,
(6) U_6: other factors.

Three experts D_1, D_2, and D_3 evaluated the alternatives with DM's weights of 0.3, 0.3, and 0.4 respectively (Table 6).

- The group assessment matrix (Table 7).

Table 6 The individual decision matrix for Example 2

DM	Alternatives	Attributes					
		U_1	U_2	U_3	U_4	U_5	U_6
D_1	A_1	(0.5, 0.4)	(0.5, 0.3)	(0.2, 0.6)	(0.4, 0.4)	(0.5, 0.4)	(0.3, 0.5)
	A_2	(0.7, 0.3)	(0.7, 0.3)	(0.6, 0.2)	(0.6, 0.2)	(0.7, 0.2)	(0.4, 0.5)
	A_3	(0.5, 0.4)	(0.6, 0.4)	(0.6, 0.2)	(0.5, 0.3)	(0.6, 0.3)	(0.4, 0.4)
	A_4	(0.7, 0.2)	(0.7, 0.2)	(0.4, 0.2)	(0.5, 0.2)	(0.4, 0.4)	(0.6, 0.3)
	A_5	(0.4, 0.3)	(0.5, 0.2)	(0.4, 0.5)	(0.4, 0.6)	(0.3, 0.4)	(0.7, 0.2)
	A_6	(0.6, 0.2)	(0.4, 0.3)	(0.7, 0.3)	(0.6, 0.3)	(0.5, 0.4)	(0.6, 0.2)
D_2	A_1	(0.5, 0.5)	(0.8, 0.2)	(0.6, 0.2)	(0.7, 0.2)	(0.6, 0.3)	(0.5, 0.4)
	A_2	(0.4, 0.5)	(0.6, 0.2)	(0.7, 0.3)	(0.3, 0.4)	(0.7, 0.1)	(0.8, 0.2)
	A_3	(0.5, 0.2)	(0.7, 0.2)	(0.8, 0.1)	(0.7, 0.1)	(0.3, 0.4)	(0.6, 0.3)
	A_4	(0.6, 0.2)	(0.3, 0.4)	(0.5, 0.5)	(0.6, 0.2)	(0.4, 0.5)	(0.5, 0.2)
	A_5	(0.7, 0.1)	(0.5, 0.1)	(0.3, 0.2)	(0.4, 0.3)	(0.7, 0.2)	(0.4, 0.3)
	A_6	(0.7, 0.3)	(0.8, 0.2)	(0.6, 0.3)	(0.6, 0.2)	(0.5, 0.3)	(0.7, 0.2)
D_3	A_1	(0.5, 0.3)	(0.7, 0.2)	(0.5, 0.3)	(0.5, 0.4)	(0.7, 0.3)	(0.4, 0.3)
	A_2	(0.6, 0.3)	(0.6, 0.2)	(0.6, 0.2)	(0.8, 0.1)	(0.5, 0.4)	(0.6, 0.2)
	A_3	(0.7, 0.3)	(0.4, 0.4)	(0.7, 0.3)	(0.4, 0.2)	(0.6, 0.3)	(0.4, 0.4)
	A_4	(0.4, 0.4)	(0.6, 0.2)	(0.4, 0.2)	(0.7, 0.2)	(0.6, 0.2)	(0.5, 0.3)
	A_5	(0.7, 0.2)	(0.7, 0.3)	(0.6, 0.1)	(0.7, 0.3)	(0.5, 0.3)	(0.3, 0.4)
	A_6	(0.5, 0.2)	(0.5, 0.3)	(0.8, 0.2)	(0.6, 0.1)	(0.6, 0.2)	(0.6, 0.2)

Table 7 The aggregated assessment matrix for Example 2

Alternatives	Attributes					
	U_1	U_2	U_3	U_4	U_5	U_6
A_1	(0.5, 0.381)	(0.69, 0.226)	(0.462, 0.327)	(0.547, 0.325)	(0.619, 0.327)	(0.405, 0.381)
A_2	(0.586, 0.35)	(0.633, 0.226)	(0.633, 0.226)	(0.641, 0.187)	(0.632, 0.214)	(0.633, 0.263)
A_3	(0.592, 0.29)	(0.568, 0.325)	(0.71, 0.191)	(0.539, 0.183)	(0.527, 0.327)	(0.469, 0.367)
A_4	(0.568, 0.264)	(0.566, 0.246)	(0.432, 0.263)	(0.619, 0.2)	(0.49, 0.324)	(0.532, 0.266)
A_5	(0.631, 0.183)	(0.592, 0.191)	(0.466, 0.2)	(0.545, 0.369)	(0.525, 0.29)	(0.482, 0.298)
A_6	(0.599, 0.226)	(0.599, 0.266)	(0.722, 0.255)	(0.6, 0.171)	(0.543, 0.278)	(0.633, 0.2)

- Entropy exponential values, separation measures, closeness coefficient for each alternative, and rank of alternatives (Table 8).

Table 9 presents a comparison of alternative orders for different methods, where the proposed method gave the same results as Xu [16], Yue [17], and Cheng [12] methods (i.e. A2 > A6 > A3 > A4 > A5 > A1), and for most cases of Zeng and Su's method the best alternative is A2 which is matching with the proposed method's one.

4 Conclusion

The results from the presented examples show the validity of the new method to solve MCDM problems simply. The IF-entropy measure has been used in many types of research to calculate the criteria weights while solving MCDM. In this paper, we proofed by two examples that combining the TOPSIS approach with the new proposed intuitionistic fuzzy entropy in exponential form could solve MCDM problems. This new method is performed without the need to know or calculate attribute weights. In the future, we will study extending this new method to determine DM's weights objectively under an intuitionistic fuzzy environment.

Table 8 The preference order of the alternatives for Example 2

Alternatives	Attributes						$d_i^-(A^-, A_i)$	$d_i^+(A^+, A_i)$	Closeness coefficient	Rank
	U_1	U_2	U_3	U_4	U_5	U_6				
A_1	2.334	1.623	2.330	2.084	1.895	2.641	2.9334	5.3309	0.6451	6
A_2	2.018	1.751	1.751	1.704	1.744	1.785	1.9570	4.3973	0.6920	1
A_3	1.914	2.025	1.559	1.937	2.143	2.398	2.5171	4.9281	0.6619	3
A_4	1.943	1.929	2.295	1.764	2.243	2.036	2.5755	5.0055	0.6603	5
A_5	1.726	1.817	2.126	2.170	2.087	2.219	2.5494	4.9789	0.6614	4
A_6	1.831	1.870	1.576	1.786	2.026	1.731	1.9962	4.4302	0.6894	2

Table 9 A comparison of alternatives preference order of Example 2 for different methods

Method	Parameter	Preference order
Xu [16]		A2 > A6 > A3 > A4 > A5 > A1
Yue [17]		A2 > A6 > A3 > A4 > A5 > A1
Zeng and Su [15]	Use the Max operator	A2 > A6 > A3 > A5 > A4 > A1
	Use the Min operator	A5 > A6 > A1 > A2 > A4 > A3
	Use the IFWHD operator	A2 > A6 > A3 > A5 > A4 > A1
	Use the IFWED operator	A2 > A6 > A3 > A5 > A4 > A1
	Use the IFOWHD operator	A6 > A2 > A5 > A4 > A3 > A1
	Use the IFOWED operator	A2 > A6 > A5 > A4 > A3 > A1
	Use the IFOWGD operator	A2 > A6 > A5 > A4 > A3 > A1
Cheng [12]		A2 > A6 > A3 > A4 > A5 > A1
The proposed method		A2 > A6 > A3 > A4 > A5 > A1

References

1. Brunelli M (2015) Introduction to the analytic hierarchy process. Springer
2. Khan BM, Bilal R, Young R (2018) Fuzzy-TOPSIS based Cluster Head selection in mobile wireless sensor networks. J Electr Syst Inf Technol 5(3)
3. Eslaminasab Z, Hamzehee A (2019) Determining appropriate weight for criteria in multi criteria group decision making problems using an LP model and similarity measure
4. Aikhuele DO, Turan FBM (2016) Intuitionistic fuzzy-based model for failure detection. Springerplus 5(1):1–15
5. Garg H (2017) Generalized intuitionistic fuzzy entropy-based approach for solving multi-attribute decision-making problems with unknown attribute weights
6. Arian H, Ashkan H, Huchang L, Francisco H (2019) An overview of MULTIMOORA for multi-criteria decision-making: theory, developments, applications, and challenges
7. Hatefi M (2019) Indifference threshold-based attribute ratio analysis: a method for assigning the weights to the attributes in multiple attribute decision making
8. Liu M, Ren H (2014) A new intuitionistic fuzzy entropy and application in multi-attribute decision making. Information 5(4):587–601
9. Zadeh LA (1968) Probability measures of fuzzy events. J Math Anal Appl 23:421–427
10. De Luca A, Termini S (1972) A definition of non-probabilistic entropy in the setting of fuzzy set theory. Inf Control 20:301–312
11. Burillo P, Bustince H (2001) Entropy on intuitionistic fuzzy sets and on interval-valued fuzzy sets. Fuzzy Sets Syst 118:305–316
12. Chen S-M, Cheng S-H, Chiou C-H (2016) Fuzzy multiattribute group decision making based on intuitionistic fuzzy sets and evidential reasoning methodology. Inf Fusion 27(2):215–227
13. Aikhuele D, Turan F (2017) An intuitionistic fuzzy multi-criteria decision-making method based on an exponential-related function. Int J Fuzzy Syst Appl 6(4):33–46

14. Liu S, Yu W, Liu L, Hu Y (2019) Variable weights theory and its application to multi-attribute group decision making with intuitionistic fuzzy numbers on determining decision maker's weights
15. Zeng S, Su W (2011) Intuitionistic fuzzy ordered weighted distance operator. Knowl-Based Syst 24(8):1224–1232
16. Xu Z (2010) A deviation-based approach to intuitionistic fuzzy multiple attribute group decision making. Group Decis Negot 19(1):57–76
17. Yue Z (2014) TOPSIS-based group decision-making methodology in intuitionistic fuzzy setting. Inf Sci 277:141–153

Performance of Assessment Model for Injection Moulding Parameters

Nur Qurratul Ain Adanan, Faiz Mohd Turan , **Kartina Johan,**
Anis Izzati Md Yusoff, and Yuen Weng Yee

Abstract In order to manufacture a better quality of plastic product, the best injection moulding parameters have to be identified. Therefore, this research studies the performance of assessment model for injection moulding parameters using Taguchi and ANOVA method. The objective of this research is to identify the best injection moulding parameters in producing plastic pallets in term of compressive strength when subjected to a constant load. Melting temperature, charging speed and holding pressure and polypropylene material were chosen as the parameters to study their effect on compressive strength. According to the results obtained, the melting temperature of 230 °C, charging speed of 93 rpm and holding pressure of 25 MPa were found to be the best combination of injection moulding parameters to fabricate the better performance of plastic pallet which give the maximum ultimate load with 6376.7 kg. Based on the statistical ANOVA analysis results, the most significant parameter affecting the compressive strength of plastic pallet is melting temperature, which is indicated by the percentage contribution of $P = 63.67\%$, followed by holding pressure with 21.79%. Charging speed is the least significant parameter with 2.96%. To conclude that, Taguchi and ANOVA method show that melting temperature is the most significant parameter in order to get the best compressive strength.

Keywords Injection moulding · Compressive strength · Taguchi · ANOVA

1   Introduction

Nowadays, injection moulding is one of the most common process to manufactured various plastic products from the smallest bottles to entire body of cars. Injection moulding is a simple manufacturing process where the material is fed into the barrel, and injected into the mold and the parts will be produced [1]. Besides that, the product design in plastic injection molding had become more complicated and the quality

N. Q. A. Adanan · F. Mohd Turan (✉) · K. Johan · A. I. Md Yusoff · Y. W. Yee
Faculty of Manufacturing and Mechatronic Engineering Technology, Universiti Malaysia Pahang,
26600 Pekan, Pahang, Malaysia
e-mail: faizmt@ump.edu.my

59

requirements also become more stringent. The quality of the products is depending on material properties, mold design, part design and selection of molding parameters [2, 3]. However, the part design and mold design are done at initial stage of product development, it cannot be change easily [4]. So, the proper selection of injection parameters is the only method to decrease defects and increase quality [5]. Even in this high-tech era, proper selection of injection molding parameters is depending on the experience technician and trial and error process [6]. In order to solve this problem, optimization of injection molding parameters is a must.

This study was focused to optimize the injection molding parameters of plastic pallet in term of compressive strength which is reflected by the compressive deflection when subjected to a constant load. Polypropylene will be used in this study. Therefore, design of experiment in Taguchi method will be used to optimize the injection molding parameters of plastic pallet in term of compressive strength. Lastly, ANOVA is used to analyses the results and identify the most influence factor among the injection molding parameters.

2   Methodology

In this study, the injection moulding process parameters which influence product mechanical properties are based on the research of literature review. Polypropylene is choosing as a raw material are used to produce plastic pallet with the help of JU2400, Haitian injection molding machine. Polypropylene plastic pallet is processed by using different set of process parameters like melting temperature, holding pressure and changing speed. Each parameter has three levels which are low, medium and high. After the parameters was chosen, an appropriate orthogonal array will be selected to conduct the experiments. The flow chart of this study is shown in Fig. 1.

In Fig. 2, L9 orthogonal array is chosen which have 3 injection moulding parameters with 3 level of factors. Next, using the Minitab software, it will generate the experiment condition and run the injection moulding. After the plastic pallet is produced, the quality test of compressive strength on the pallet will be conducted. The compressive strength results obtained is used to calculate the S/N ratio to identify the best combination of the injection moulding parameters. Furthermore, a statistical analysis of variance (ANOVA) is performed to analyses and identify which injection moulding parameters have the most significant effect on compressive strength of the pallet when subjected to a constant load by calculating the F-value and percentage of contribution. With the S/N and ANOVA analyses, the optimal combination of the process parameters can be predicted.

Fig. 1 Research flow chart

Fig. 2 Orthogonal array selection
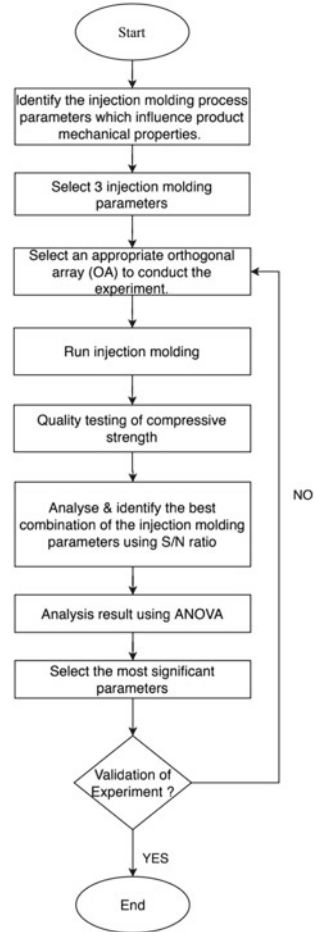
	Number of Parameters (P)																													
	2	3	4	5	6	7	8	9	10	11	12	13	14	15	16	17	18	19	20	21	22	23	24	25	26	27	28	29	30	31
2	L4	L4	L8	L8	L8	L8	L12	L12	L12	L12	L16	L16	L16	L16	L32	L32	L32	L32	L32	L32	L32	L32	L32	L32	L32	L32	L32	L32	L32	L32
3	L9	L9	L9	L18	L18	L18	L18	L27	L27	L27	L27	L36	L36	L36	L36	L36	L36	L36	L36	L36										
4	L'16	L'16	L'16	L'16	L'32	L'32	L'32	L'32	L'32																					
5	L25	L25	L25	L25	L25	L50	L50	L50	L50	L50	L50																			

Number of Levels

2.1 Selection of Injection Moulding Parameters

There are 3 injection molding parameters namely melting temperature, holding pressure and charging speed are used to investigate the effect on the performance of a plastic pallet in term of compressive strength when subjected to a constant load. The parameters in this study have three level, the melting temperature is select in the

Table 1 The selected parameters in 3 level

Symbol	Process parameters	Level 1	Level 2	Level 3
A	Melting temperature (°C)	210	220	230
B	Charging speed (rpm)	88	93	98
C	Holding pressure (MPa)	25	35	45

range at 210–230 °C. The range of Charging speed is choosing at 88–98 rpm and holding pressure is select in the range at 25–45 MPa. The selected injection molding process parameters along with their levels are shown in Table 1.

3   Results and Discussions

In this study, the experimental results obtained are analyzed using statistical analysis. The analysis will conclude the optimum parameter that will be implemented in the compressive strength testing process to achieve the project's objective which is to identify the best combination of injection molding parameters that give the best performance of a plastic pallet in term of compressive strength when subjected to a constant load. Therefore, the optimum parameters obtained from the Taguchi method will be analyzed using Minitab software. As the final step, the data collected from the experiments will be analyzed and discussed.

All the process parameter was set accordingly based on the Taguchi experimental design. Each specimen came together with specimen for tensile test and specimen for flexural testing. The tests were carried out according to ASTM D638 using a Type 1 tensile bar on a tensile test machine with a 5 kN load cell and flexural assessed in accordance with ASTM D790.

3.1   Signal to Noise (S/N) Ratio

This study is focuses on the effect of three process parameters of the mechanical performance of the polypropylene plastic pallet. All the results obtained from the testing determine the compressive strength when subjected to a constant load and analyzed and discussed statistically based on the Taguchi method. This study uses the S/N ratio to convert the experimental results as single response instead of using the average value to analyzed the compressive strength. The S/N ratio is the statistical quantity representing the power of a response signal divided by the power of the variation in the signal due to noise. Using the S/N ratio data (in dB) in Table 2, the average performance or main effects for each factor are computed. As show in Table 2, since S/N ratios have not changed significantly, no abnormal were introduced in the calculations or measurements. According to the ultimate load test data shown in

Table 2 Summary of results of tests and S/N ratio values

Experimental number	Process parameter			Ultimate load test ($\times 10^3$ kg)	S/N ratio (dB)
	Melting temperature (°C)	Charging speed (rpm)	Holding pressure (MPa)		
1	230	98	45	5.1602	74.2533
2	230	93	35	6.3767	76.0919
3	230	88	25	6.0911	75.6939
4	220	98	35	4.4078	72.8844
5	220	93	25	4.9000	73.8039
6	220	88	45	4.4549	72.9768
7	210	98	25	5.6267	75.0051
8	210	93	45	4.7161	73.4717
9	210	88	35	4.8104	73.6436

Table 2, it seems that higher melting temperature might have increase the ultimate load in some of the experiment runs.

By using the Minitab19 software, the main effect graph in Fig. 3 shows the changes in compressive strength due to variations of injection moulding parameters and the sets of process parameters can be estimated further. There are three types of S/N ratio used to predict the optimal sets namely the smaller the better, the nominal the best, and the larger is better. In this framework, the larger is better quality characteristic is chosen to improve the mechanical properties of the part produced through the optimal
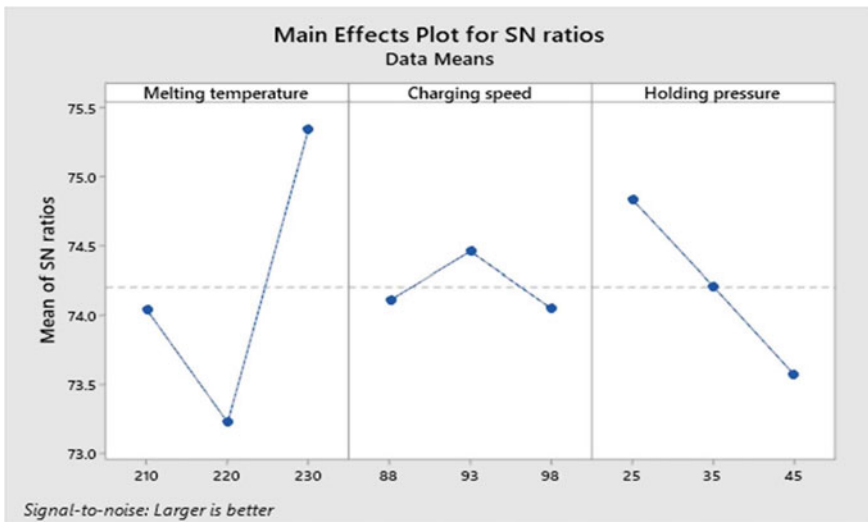
Fig. 3 Main effects plot of S/N ratios for compressive strength

levels of processing parameters. The best combination injection moulding parameters in order to get better compressive strength of product when subjected to a constant load is based on the graph of main effects plot for S/N ratios in Fig. 3. From Fig. 3, the main effects plot for S/N ratios show that the higher melting temperature, the higher the S/N ratio while the lower the holding pressure, the higher the S/N ratios. From the result, the higher melting temperature with lower holding pressure are the most significant parameters and it will give best result of compressive strength. The best combination of the injection moulding parameters is 230 °C melting temperature, 93 rpm charging speed and 25 MPa holding pressure as shown in Fig. 3.

3.2   Analysis of Variance (ANOVA)

From the F-distribution statistic table, the $F_{(0.05,2,8)} = 4.46$ for a level of significant factor equals to 0.05 (or 95% confidence level). Melting temperature (A) [F-statistic $= 5.50 > 4.46$] is thus identified as significant factor. The ANOVA result of the experiment shows the melting temperature have a greatest influence on compressive strength when subjected to a constant load. For charging speed (B) [F-statistic $= 0.26 < 4.46$] and holding pressure (C) [F-statistic $= 1.88 < 4.46$] show that both factors are not significant to the compressive strength. From this, it indicates the significant and insignificant factors to compressive strength. Referring to Table 3, there are 2 out of 3 processing parameters selected in the experiment show P values greater than 5%. As a level of confidence of 95% is used in this study, melting temperature and holding pressure are significantly affect the quality characteristics while charging speed is least significantly affected. In Table3, the most significant factor for the compressive strength of the plastic pallet is melting temperature, which is about 63.67%. Holding pressure is the second most influential factor, which is about 21.79% and lastly the charging speed contribute the least to the compressive strength with 2.96%.

Table 3 ANOVA summary for the compressive strength

Source	DOE	SS	V	F	P(%)
Melting temperature	2	2,555,408	1,277,704	5.50	63.67
Charging speed	2	118,679	59,340	0.26	2.96
Holding pressure	2	874,645	437,322	1.88	21.79
Error	2	465,022	232,511		
Total	8	4,013,754			100

4   Conclusion

In conclusion, the injection moulding parameters which influence product mechanical properties is identified which are melting temperature, charging speed and holding pressure. In this framework, the optimization of injection moulding parameters has been successfully developed through the design of experiments by Taguchi method. The melting temperature of 230 °C, charging speed of 93 rpm and holding pressure of 25 MPa are found to be the best combination of injection moulding parameters to fabricate the better performance of plastic pallet which give the maximum ultimate load with 6376.7 kg. Based on the statistical ANOVA analysis results, the most significant parameter affecting the compressive strength of plastic pallet is melting temperature, which is indicated by the percentage contribution of $P = 63.67\%$, followed by holding pressure with 21.79%. Charging speed is the least significant parameter with 2.96%. To conclude that, Taguchi and ANOVA method show that melting temperature is the most significant parameter in order to get the best compressive strength.

References

1. Mengistu N, Koneru S, Indra Reddy A, Koteswararao B (2019) Design and development of hand operated injection moulding machine for manufacturing recycled plastic articles. Int J Recent Technol Eng 8:2544–2554
2. Panneerselvam V, Turan FM (2019) Optimization of process parameters of injection moldings for plastic pallets manufacturing industry. J Manuf Syst Technol 02:75–83
3. Panneerselvam V, Turan FM (2020) Multi response optimisation of injection moulding process parameter using Taguchi and desirability function. J Manuf Syst Technol. SympoSIMM 2019, LNME 252–264
4. Kumar D, Kapoor A (2019) Optimization of process parameters in injection-molding by recent methods for optimization—literature review. In: National conference on sustainable and emerging trends in mechanical engineering "NCSETME 2018" at: Poornima Group of Institutions, Jaipur
5. Shi H, Xie S, Wang X (2013) A warpage optimization method for injection molding using artificial neural network with parametric sampling evaluation strategy. Int J Adv Manuf Technol 65:343–353
6. Singh G, Pradhan MK, Verma A (2018) Multi response optimization of injection moulding process parameters to reduce cycle time and warpage. Mater Today Proc 5:8398–8405

Optimising Casting Film Parameters for LPDE Material Assessment

Nur Qurratul Ain Adanan, Faiz Mohd Turan (ORCID)**, Kartina Johan, Anis Izzati Md Yusoff, and Wong Hui Xin**

Abstract The growing demand for disposable gloves, especially from the healthcare industry amidst the ongoing Covid-19 pandemic and rising awareness about Healthcare-Associated Infections (HAIs). One of the ways to produce disposable gloves is using cast LDPE film machine. The quality of the products depends on material resin used, machine casting film design, part design and the selection of process parameters. However, the part design and casting film design are done at the initial stage of product development, it cannot be change easily. To manufacture a better quality of cast LDPE gloves, the best LDPE casting film parameters have to be identified. This research aims to identify the best LDPE casting film parameters in producing disposable gloves in terms of strong sealed but edges failed defect rate in production line. The three LDPE casting film parameters such as tensile strength, melt flow index (MFI) and load weight of resin were chosen to study their effect on the defect rate. In this research, the Taguchi method is used to optimize the best process parameters. On the other hand, an orthogonal array (OA), signal-to-noise (S/N) ratio, and ANOVA were employed to investigate the strong sealed but edges failed defect rate. According to the results obtained, the tensile strength of 34 MPa, melt flow index of 3 g/10 min and load weight of 2 kg were found to be the best combination of LDPE casting film parameters to fabricate the better performance of LDPE disposable gloves which give the lowest strong sealed but edges failed defect rate with 2%. Based on the statistical ANOVA analysis results, the most significant parameter affecting the strong sealed but edges failed defect rate of LDPE disposable gloves is tensile strength, which is indicated by the percentage contribution of $P = 55.56\%$, followed by melt flow index with 38.89%. The load weight of LDPE resin is the least significant parameter with 5.55%. To conclude, Taguchi and ANOVA method show that tensile strength is the most significant parameter to get the least strong sealed but edges failed defect rate.

N. Q. A. Adanan · F. Mohd Turan (✉) · K. Johan · A. I. Md Yusoff · W. H. Xin
Faculty of Manufacturing and Mechatronic Engineering Technology, Universiti Malaysia Pahang, 26600 Pekan, Pahang, Malaysia
e-mail: faizmt@ump.edu.my

Keywords Low-density polyethylene · Orthogonal array · Melt flow index · Load weight

1 Introduction

Polymer mechanical characteristics, particularly as a function of temperature and strain rate, are critical for the use of these polymers in design. The response of low-density polyethylene (LDPE) was examined in this research over a wide range of strain rates and temperatures. The mechanical reaction is considered to be temperature and strain rate dependent, with stress increasing with rising strain rate or reducing with temperature.

The key substance of the CPE gloves is all LDPE, LLDPE and some MLLDPE, much the same but different manufacture. CPE gloves are fitted with a casting film. The casting film device can output as thin as 18 microns, and the thickness and consistency can be very stable, even better than the blowing machine, and the machines are therefore much larger than the blowing film machines. Since different film projects trigger a very different kind of results. CPE gloves are much better than PE gloves, but they're more costly than PE gloves, and they cannot be that thinner.

Quality requirements of Low-Density Polyethylene (LDPE) glove products have become more stringent. The relationship of tensile strength, melt flow index and load weight of casting LDPE is the crucial on in this project. According to Lyondell-Basell, melt flow index and its tensile strength are tightly co-related to each other as mentioned in titled research paper named A Guide Polyolefin Film Extrusion [1]. The paper concluded that when the melt flow index (MFI) higher, the tensile strength of its LDPE resin will be reduced.

Nevertheless, both the design of the component and the design of the cast are mostly carried out at the initial stage of product creation, which cannot be modified quickly and directly. Therefore, the correct selection of process parameters is the best way to minimize errors and boost efficiency [2, 3]. Taguchi's approach is one of the versatile methods for developing the right quality framework. Taguchi concepts are committed to a simple, effective and comprehensive approach to optimization, cost and quality. In comparison, the research conceptual model allows the study of more than ten parameters without a considerable amount of testing, making it possible to implement much of the technical challenges [4]. The Taguchi approach is generally used worldwide for product design and process optimization. The lower number of experiments required by this approach resulted in a substantial reduction in costs and time [5].

This study was focused to investigate the optimum cast LDPE glove parameters in disposable film glove processing machine. Taguchi and ANOVA method will be used to optimize identified LDPE casting process parameters. In addition, this research will determine the significant process parameters of cast LDPE glove' resin material between Lotte and Muntajat.

2 Methodology

In this study, the cast LDPE film process parameters which influence product mechanical properties are based on the review of the literature. Low-density polypropylene is choosing as a raw material are used to produce LDPE disposable gloves with the help of XND-65/100/80x2350, cast LDPE film machine. Low-density polyethylene disposable gloves are processed by using different set of process parameters that is tensile strength, melt flow index and load weight. Each parameter has three levels which are low, medium and high. In Fig. 1, after the parameters was selected, L9 orthogonal array is chosen to conduct the experiments will be selected based on the condition that have 3 cast LDPE film process parameters with 3 level of factors. Next, Minitab software will be used to generate the experiment condition and run

Fig. 1 Research flowchart
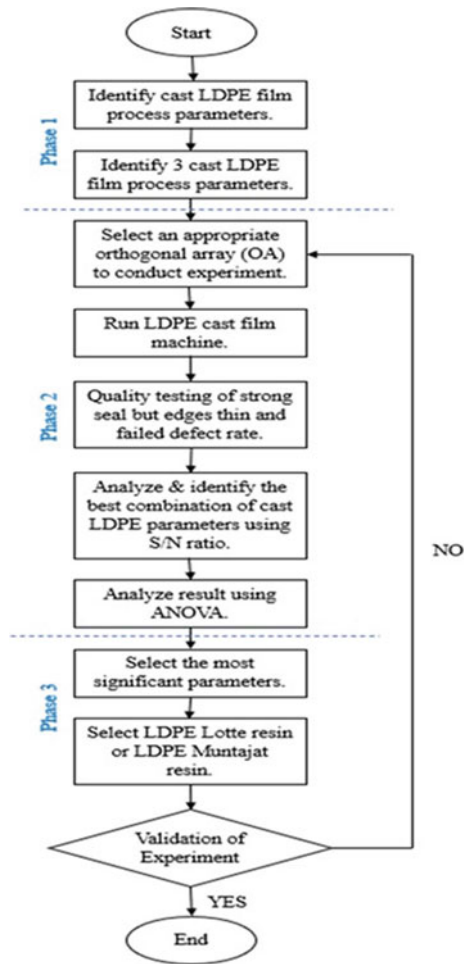
the LDPE cast film. After the LDPE disposable glove is produced, the quality test of strong seal but edges thin and failed defect on the gloves will be conducted. The defect rate results obtained is used to calculate the S/N ratio to identify the best combination of the cast LDPE film parameters. Furthermore, a statistical analysis of variance (ANOVA) is performed to analyses and identify which cast LDPE film process parameters have the most significant effect on strong seal but edges thin and failed of the LDPE disposable gloves by calculating the F-value and percentage of contribution. With the S/N and ANOVA analyses, the optimal combination of the process parameters and best LDPE resin can be predicted.

3 Results

In this study, the experimental results obtained are analyzed using statistical analysis. The analysis will conclude the optimum parameter that will be implemented in collecting strong seal but edges thin and failed defect rate to achieve the project's objective which is to identify the best combination of cast LDPE film parameters that give the best performance of LDPE disposable gloves in term of lowest defect rate. Therefore, the optimum parameters obtained from the Taguchi method will be analyzed using Minitab software. As the final step, the data collected from the experiments will be analyzed and discussed.

3.1 Selection of Cast LDPE Film Parameters

There are 3 cast LDPE film parameters namely melting temperature, holding pressure and charging speed are used to investigate the effect on the performance of a plastic pallet in term of compressive strength when subjected to a constant load. The parameters in this study have three level, the tensile strength is select in the range at 20–34 MPa. The range of melt flow index is choosing at 1–3 g/10 min and load weight is select in the range at 1–3 kg. The selected cast LDPE film process parameters along with their levels are shown in Table 1.

Table 1 The selected parameters in 3 level

Predictor symbol	Process parameters	Level 1	Level 2	Level 3
A	Tensile strength (MPa)	20	25	34
B	Melt flow index (g/10 min)	1	2	3
C	Load weight (kg)	1	2	3

3.2 Signal to Noise (S/N) Ratio

This study is focuses on the effect of three process parameters of the mechanical performance of the low-density polyethylene disposable gloves. All the results obtained from the testing determine the strong seal but edges thin and failed, and analyzed and discussed statistically based on the Taguchi method. This study uses the S/N ratio to convert the experimental results as single response instead of using the average value to analyzed the defect rate. The S/N ratio is the statistical quantity representing the power of a response signal divided by the power of the variation in the signal due to noise. Using the S/N ratio data (in dB) in Table 2, the average performance or main effects for each factor are computed. As show in Table 2, since S/N ratios have not changed significantly, no abnormal were introduced in the calculations or measurements. According to the ultimate load test data shown in Table 2, it seems that higher tensile strength might have less defect rate in some of the experiment runs, melt flow index increase, the ultimate load decrease. According to the S/N ratio response as shown in Table 2, the highest difference value from each factor can be chosen as the best combination of parameters. The rank shows which factor affects the strong sealed but edges thin and failed the most starting with tensile strength in the first rank followed by melt flow index and the least affecting factor that is the load weight.

By using the Minitab19 software, the main effect graph in Fig. 2 shows the changes in strong sealed but edges failed due to variations of LDPE casting parameters and the sets of process parameters can be estimated further. In this framework, the smaller is better to get better quality characteristic is selected to get less defects of LDPE gloves produced through the optimal levels of processing parameters. The best combination LDPE casting parameters in order to get smaller defect rate is based on the graph of main effects plot for S/N ratios in Fig. 2. From Fig. 2, the main effects plot

Table 2 Summary of results of tests and S/N ratio values

Experiment number	Process parameter			Defect rate (%)	S/N ratio (dB)
	Tensile strength (MPa)	Melt flow index (g/10 min)	Load weight (kg)		
1	20	1	1	8	−18.0618
2	20	2	2	7	−16.9020
3	20	3	3	6	−15.5630
4	25	1	2	7	−16.9020
5	25	2	3	6	−15.5630
6	25	3	1	5	−13.9794
7	34	1	3	5	−13.9794
8	34	2	1	4	−12.0412
9	34	3	2	2	−6.0206
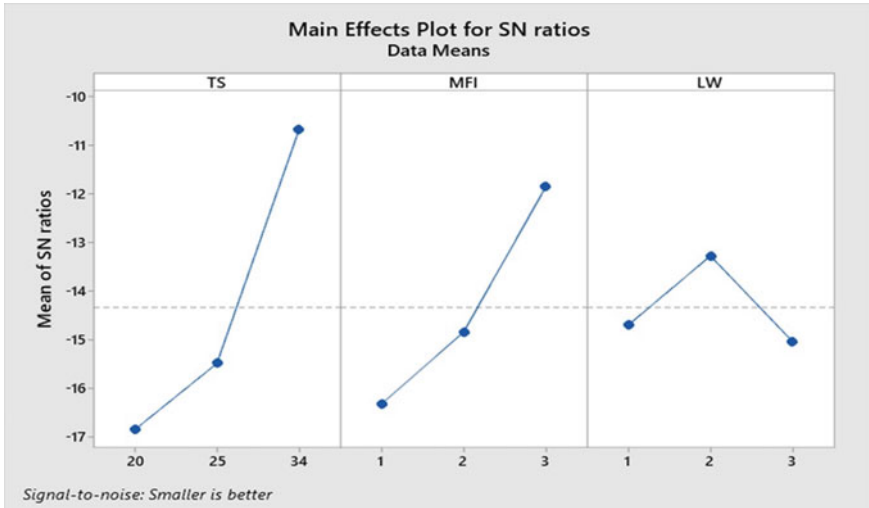
Fig. 2 Main effects plot of S/N ratios for strong seal but edges thin and failed defect rate

for S/N ratios show that the higher tensile strength, the higher the melt flow index while the medium or moderate the load weight, the higher the S/N ratios. From the result, the higher tensile strength with higher melt flow index are the most significant parameters and it will give lowest strong sealed but edges failed defect rate. The best combination of the LDPE casting parameters are 34 MPa tensile strength, 3 g/10 min melt flow index and 2 kg load weight in Fig. 2.

3.3 Analysis of Variance (ANOVA)

This study is to determine whether any of the differences between the means are statistically significant, compare the p-value to your significance level to assess the null hypothesis. From Table 3 shows p-value is 0.000, which is less than the significance level of 0.05. Reject the null hypothesis and conclude that one of the LDPE casting resins have different means and it is statistically significant.

Use the interval plot to display the mean and confidence interval for each group. The interval plots show the following: Each dot represents a sample mean. Each

Table 3 Outcome for analysis of variance (ANOVA)

Source	DF	Adj SS	Adj MS	F-value	p-value
Factor	1	96.10	96.10	61.37	0.000
Error	38	59.50	1.57		
Total	39	155.60			

interval is a 95% confidence interval for the mean of a group. From Fig. 3, LDPE Lotte has the lower defect rate and LDPE Muntajat has the lower defect rate. It cannot be determined from Fig. 3 whether any differences are practically significant. To determine practically significance, assess the confidence intervals for the differences of means.

From Table 4, LDPE Lotte and LDPE Muntajat has a confidence interval for its mean strong sealed but edges failed defect rate. The multiple comparison results for these data show that defect rate of Lotte is significantly lower than Muntajat. That LDPE Lotte is better than LDPE Muntajat does not show that LDPE Lotte is good enough for the requirement of quality of LDPE gloves. The confidence interval for the group mean is better for judging whether LDPE Lotte is less defect and good enough.
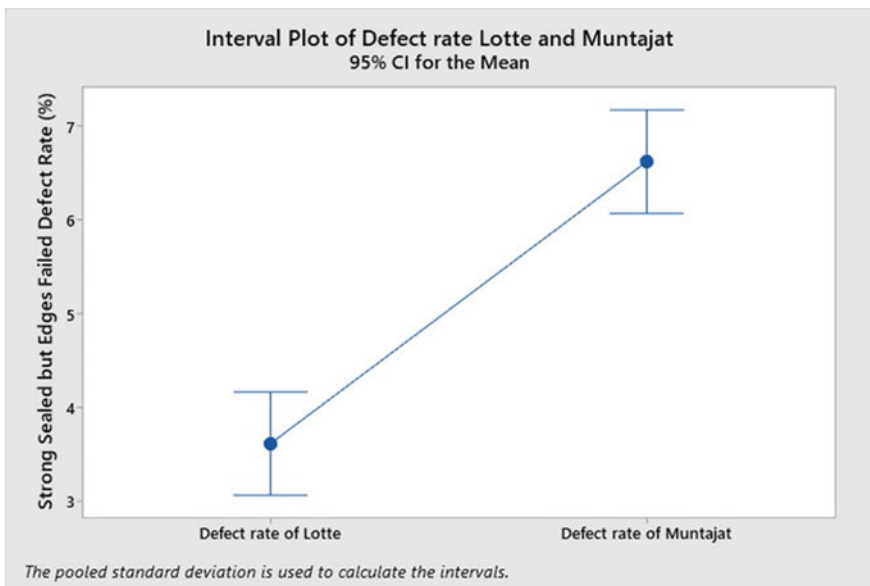
Fig.3 Interval plot of defect rate LDPE Lotte and LDPE Muntajat

Table 4 Means of LDPE Lotte and LDPE Muntajat in Minitab

Factor	N	Mean	StDev	95% Cl
Defect rate of Lotte	20	3.550	1.234	(2.984, 4.116)
Defect rate of Muntajat	20	6.650	1.268	(6.084, 7.216)
LDPE Muntajat–LDPE Lotte				(2.984, 7.216)

4 Conclusion

This paper reports the attempt to find best combination of process parameters and analysis to select LDPE Lotte or LDPE Muntajat resin for good quality gloves. In addition, strong seal but edges thin and failed defect rate is also integrated in the proposed method. Once the least defect rate condition is met, the best combination of process parameters is selected and thus best resin is chosen. In this framework, the optimization of LDPE casting parameters has been successfully developed through the design of experiments by Taguchi method. The tensile strength of 34 MPa, melt flow index of 3 g/10 min and load weight of 2 kg are found to be the best combination of LDPE casting parameters to fabricate the better performance of LDPE gloves which give the minimum defect rate with 2%. Based on results, the most significant parameter affecting the strong sealed but edges failed defect is tensile strength, which is indicated by the percentage contribution of P = 55.56%, followed by melt flow index with 38.89%. Load weight is the least significant parameter with 5.55%.

To conclude that, Taguchi and ANOVA method show that tensile strength is the most significant parameter in order to get the lower defect rate. LDPE Lotte is more suitable selection to produce LDPE disposable gloves than LDPE Muntajat. The research can be extended to use combining between Taguchi method with another method such as Neural Network, Response Surface Methodology (RSM) and Regression model through Tensile strength and Charpy impact test to get the better results.

References

1. LyondellBasell: a guide to polyolefin film extrusion (2015). Retrieved from: https://www.lyondellbasell.com/globalassets/documents/polymers-technical-literature/A_Guide_to_Polyolefin_Film_Extrusion.pdf
2. Panneerselvam V, Turan FM (2019) Optimization of process parameters of injection moldings for plastic pallets manufacturing industry. J Manuf Syst Technol 02:75–83
3. Panneerselvam V, Turan FM (2020) Multi response optimisation of injection moulding process parameter using Taguchi and desirability function. J Manuf Syst Technol. SympoSIMM 2019, LNME 252–264
4. Mitra AC, Jawarkar M, Soni T, Kiranchand GR (2016) Implementation of Taguchi method for robust suspension design. Procedia Eng 144:77–84
5. Kamaruddin S, Khan ZA, Wan KS (2004) The use of the Taguchi method in determining the optimum plastic injection moulding parameters for the production of a consumer product. J Mek 18:98–110

The Effect of Printing Orientation on the Mechanical Properties of FDM 3D Printed Parts

Mohd Aidil Nashruffi bin Mohd Khairul Nizam,
Khairul Izwan bin Ismail , and Tze Chuen Yap

Abstract Addictive manufacturing (AM) or 3D printing has a huge potential in building products especially in a fabrication process. Fused deposition modelling is one of AM technologies that rapidly growing due to its ability to fabricate complex geometric parts with lower cost. However, this technique requires further improvement and further investigation due to the shortcomings such as poor surface finish and low mechanical strength. This work is to determine the best printing orientation to print a model for different mechanical properties, namely the tensile strength, impact strength, and hardness. ABS specimens are printed out according to the ASTM D638, ASTM D785, and ASTM D256 standard for each mechanical property. Experiments were conducted to investigate the mechanical properties. Samples printed in YZ (on edge) direction showed better tensile and impact behaviors than samples printed in XY and ZX directions. However, XY-axis (flat) is the best orientation if maximum hardness is the requirement.

Keywords Additive manufacturing · Fused deposition modeling · Fused filament fabrication · Tensile strength · Impact strength · Hardness

1 Introduction

Additive Manufacturing (AM), also known as Layered Manufacturing or 3D Printing is a group of technologies that can produce a product with a physical prototype without any additional tooling and basically just rely on the Computer Aided Design (CAD) model. This is an invaluable characteristic because there is a need of quick manufacturing of the physical product of a designed part [1]. In recent years, the use of the 3D printing technology has been rapidly increasing and this phenomenon is

M. A. N. Mohd Khairul Nizam
Sapura Energy Berhad, 43300 Seri Kembangan, Selangor, Malaysia

M. A. N. Mohd Khairul Nizam · K. I. Ismail · T. C. Yap (✉)
School of Engineering and Physical Sciences, Heriot-Watt University Malaysia, No. 1, Jalan Venna P5/2, Precinct 5, 62200 Putrajaya, Malaysia
e-mail: t.yap@hw.ac.uk

Fig. 1 Schematic of extrusion-based system [3]
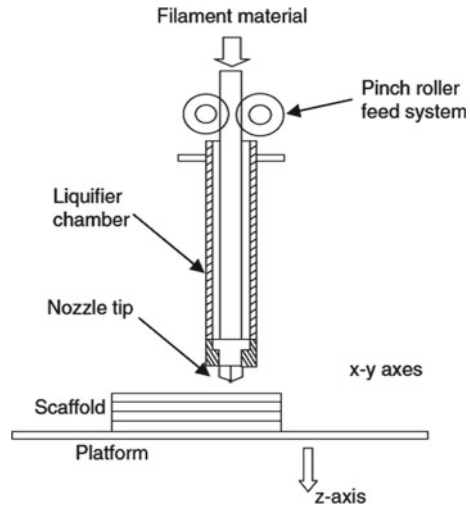
foreseen. There are several technologies of 3D printing which are stereolithography, powder bed fusion/selective laser sintering, direct printing, binder printing, laminated object manufacturing and last but not least fused deposition modelling (FDM) or fused filament fabrication (FFF), each of the technologies has its own advantages and disadvantages [2].

Fused deposition modeling (FDM) or Fused filament fabrication (FFF) is one of the most popular technologies due to the relative low cost of the FDM printers. FDM is a process of layered deposition of plasticized build and support material supplied in form of a solid wire by an extrusion head as shown in Fig. 1. The common materials for FDM products are Acrylonitrile Butadiene Styrene (ABS), Polylactide (PLA), Polyethylene terephthalate (PET) etc.

During the last decades, additive manufacturing technology has been tested and used in various fields and industries such as automotive industry, aeronautical/aviation industry, medical applications and many more. The advantages that can be obtained from this technology are the flexibility of the manufacturing, and ability of mass customization. However, existing techniques have some weaknesses such as weak material combination, lower accuracy, limited choice of materials for certain techniques, and limited choice of bio-compatible materials (for medical application). Some of these shortcomings such as lower mechanical properties and accuracy can be avoided by knowing the proper selection of techniques and materials which affect the mechanical properties and dimensional accuracies of the printed object [4–9].

There are many investigations that investigated how printing parameters affects mechanical properties. In order to determine the impacts of build orientation on mechanical reliability on ABS 3D printed products, 47 tests were conducted based on ASTM D638 [6]. The experiment used Weibull analysis to analyze the fracture strength of the printed specimen in different orientation XY, XZ and C + 45 axis with a hole and without a hole. The orientation of the specimens printed is shown

in Fig. 2. Scanning electron microscope was also used to scan the fracture surface of the specimen individually. They found that, sample printed at XZ-axis orientation has the highest fracture strength for both specimens with hole and without hole while C + 45 has the lowest fracture strength. Similar investigations were conducted by Tanoto et al. [7]. They reported strength, dimensional accuracy and printing speed of 3D printed ABS at three different printing orientations. The printing orientations were XY (flat), YX (on-edge) and ZX-axis (upright), as shown in Fig. 3. The tensile specimens were printed based on the ASTM D638 standard tensile test. YX-axis (on-edge) has the highest tensile strength which was 7.77 MPa compared to the other two which were 6.8 MPa for XY-axis and 3.31 MPa for ZX-axis. The fastest printing speed is ZX- axis followed by XY and YX-axis. For the dimensional accuracy, thickness, length, and width have been measured for all the test specimens. The closest specimen printed according to the standard is ZX-axis which the difference was 0.2 mm followed by XY-axis and lastly YX-axis. Tensile behavior for PLA sample printed at three printing orientations, 0°, 45°, 90° on horizontal plane was also investigated [8] and 45° was found to be the weakness in term of tensile behavior among all three printing orientations. Although most of the previous investigations were experimental based, theoretical model was successfully developed to understand and predict the ultimate tensile strength of FDM 3D printed PLA parts [10].

Impact properties of 3D printed ABS samples at four different printing orientation were investigated by Roberson et al. [11]. The four orientations are provided in Fig. 4 and the tests were conducted according to ASTM standard D256. Scanning electron microscopy (SEM) was used to perform and explore the fracture surfaces of the

Fig. 2 Specimens printing orientation [6]

XY-Axis　　　　　　　YX-axis　　　　　　　ZX-axis
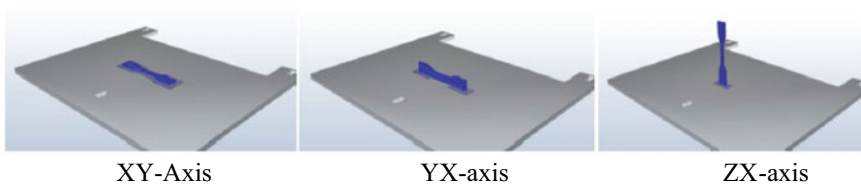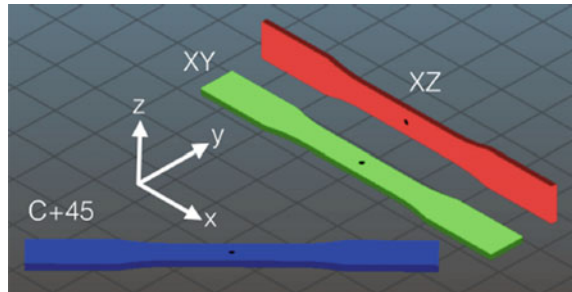
Fig. 3 Printing orientation from research [7]
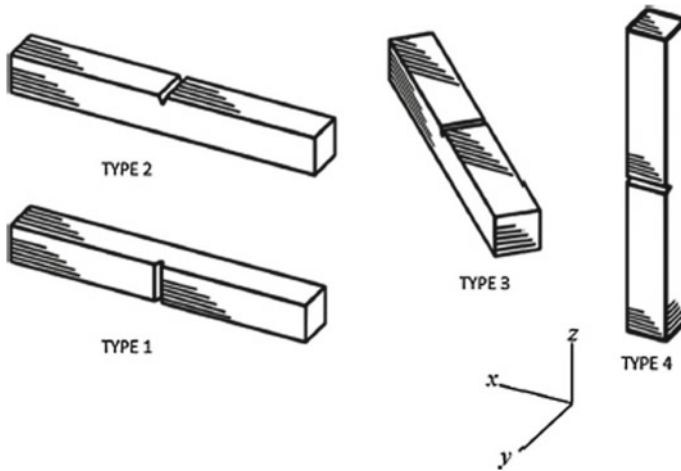
Fig. 4 Printing orientation for research [11]

specimens. Impact resistance and impact strength data were collected and analysed from the experimental. From the observation and results, Type 2 printing orientation has the best impact resistance compared to the rest while Type 4 is the worst. The result same goes for impact strength where Type 2 is the best and Type 4 is the lowest among all.

In other research work, Chacón et al. [12] investigate the effect of build orientation, layer thickness and feed rate on the mechanical behavior of 3D printed PLA samples. Result shows flat and on-edge orientation have highest strength and stiffness while upright orientation shows the lowest mechanical performance. Based on their observations, there are two main failure modes, which are (i) inter-layer failure and (ii) trans-layer failure, which also relates to layer-to-layer bonding and direction of filament deposition.

Previous works reported that printing orientations has effect on mechanical properties. However, most of the previous works focused on the effect of printing orientations on only one mechanical property. Furthermore, different machines and different materials were used in separated work, and this caused direct comparison of results from different works is challenging. Therefore, the objective of this study is to investigate the effects of printing orientation on tensile strength, hardness, and impact strength of FDM printed samples from a same machine and same material. Current work is aimed to determine the best printing orientation (XY, YZ, ZX-axis) for three different mechanical properties.

2 Methodology

2.1 Printer and Filament

The 3D printer model used was 3D Printer Ultimaker 2+ and the filament chosen for this experimental was Acrylonitrile Butadiene Styrene (ABS) filament of diameter 2.85 mm.

2.2 Sample Preparations

3D printed samples for tensile, hardness, and impact were prepared according to the standard ASTM D638, ASTM D256 and ASTM D785, as shown in Fig. 5. The cross-sectional area of hardness sample is 40×40 mm^2 with height of 6.4 mm. The Creo CAD was used to create the models according to the dimension required before the file was being transferred to a slicing software, Ultimaker Cura. Ultimaker Cura was used in slicing the model file that has been designed into layers and generating the g-code. Printing parameters for all samples were remain constant such as layer height of 0.15 mm, the nozzle size of 0.4 mm in size and infill of 100%. Besides, build plate adhesion was activated to enable easy removal of printed parts. Heated bed was set at 90 °C and nozzle temperature was 260 °C. The parameter investigated in this work was printing orientation. Three different printing orientations XY-(flat), YZ-(on edge) and ZX-axis (upright) were studied and printing orientations for tensile samples are illustrated in Fig. 6. No post-processing was applied on printed samples before mechanical test.

(a)   (b)   (c)
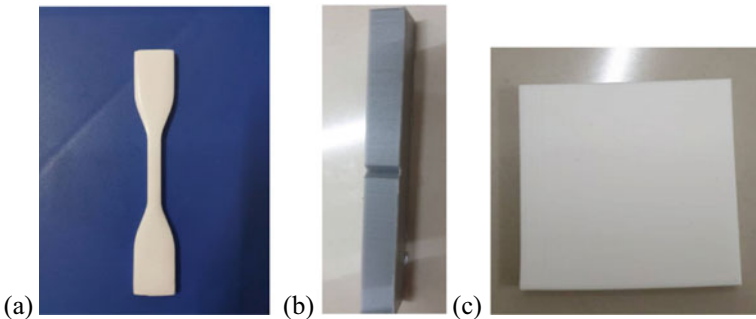
Fig. 5 FDM 3D printed samples for **a** tensile, **b** impact, **c** hardness
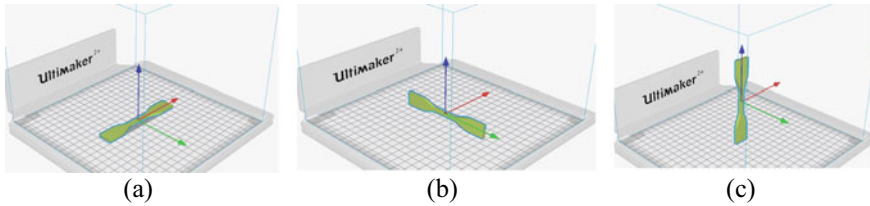
Fig. 6 Printing orientations of tensile samples **a** XY-axis **b** YZ-axis **c** ZX-axis

3 Experimental Testing

3D printed samples were tested by using three different tests, tensile strength, impact strength and hardness test.

3.1 Tensile Strength Experiment

Universal Testing Machine Quasar 25 was used to perform tensile test for total 18 samples at three different printing orientation (6 tests are done for each orientation). The machine's software GraphWork 5 was used to collect data. The data of each testing was then tabulated and averaged.

3.2 Impact Strength Experiment

For impact strength, Impact Tester CH/IMP-300TL was used. The specimen was placed on the designated area and the impact hammer was controlled by a remote. A total of 18 different tests was conducted with 6 tests per orientation. The results were obtained from the computer connected to machine, and the average value for each orientation was used for discussion.

3.3 Hardness Experiment

The hardness tests were conducted on a Sinowon hardness tester. A Rockwell test procedure was used to measure the hardness of the 3D printed samples. Time for the indentation depth is fixed for 5 s for all the experiments. The results were obtained digitally from the screen of the machine and 18 tests were carried out for the experiment. Six tests per orientation were conducted and the hardness values were averaged and plotted in a graph for the comparison and shown in the discussion section.

4 Results and Discussion

4.1 Tensile Strength

Tensile results, including yield strength, ultimate tensile strength (UTS) and breaking point at three different printing orientations are shown in Fig. 7. Sample printed at YZ-axis shows the best ultimate tensile strength with the average reading of 15.45 MPa and followed by printed at XY-axis with 11.79 MPa and lastly printed at ZX-axis with 10.29 MPa. However, XY-axis is slightly higher in yield strength and followed by YZ-axis and lastly ZX-axis. Thus, specimen printed at YZ-axis is the best printing orientation for tensile strength followed by XY-axis and ZX-axis. ZX-axis is the weakest because ABS layer patterns produced under this orientation were perpendicular to the direction of tensile force, hence, bonds between layers can be separated easily than the other two orientations. Similar results for were reported for ULTEM® 9085 material [9], ABS [13], and PLA-Sugarcane bagasse fibre composite [14]. Liu et al. reported that 'vertical' printed sample has lower tensile strength than the 'parallel' printed sample, and it was caused by poor bonding between line and line [14]. YZ-axis has the highest tensile strength, and this is because it has more layers than XY-axis even they are parallel to the tensile force (Fig. 8), as suggested by Tanoto et al. [7]. Current work confirms that printing orientation has significant effect to the tensile force of the specimen. If the specimen has more layers during printing, and the orientation is parallel to the tensile force, it can hold much better. This finding can be used to optimize tensile behavior of model which required tension force.
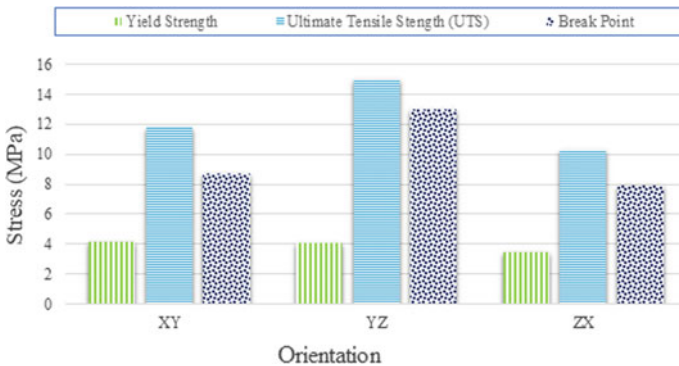
Fig. 7 Tensile strength for orientations XY-, YZ- and ZX-axis
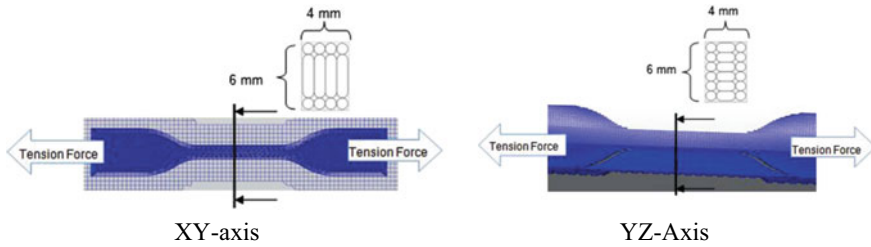
Fig. 8 Comparison tension force of XY-axis and YZ-axis [7]

4.2 Impact Strength

As shown in Fig. 9, YZ-axis has the highest average impact toughness which is 1.55 J/cm^2 followed by XY-axis at 1.07 J/cm^2 and ZX-axis which is the lowest at 0.27 J/cm^2. ZX-axis is the lowest because ZX-orientation produced layer patterns that were perpendicular to the impact force, therefore, this caused the bonds between layers were easily separated than the other XY and YZ orientations. YZ-axis has the highest impact toughness because it had more layers than XY- axis that were parallel to the impact force. Sample printed at YZ- axis has more layers due to the specimen height during printing under this printing orientation. Additional layers acted as additional resistance to impact force. The best printing orientation for impact strength is also the best printing orientation for tensile strength, as reported in previous section, and similar to previous works [13]. Figure 10 shows the printing point and the height of the specimen that makes the specimen stronger in terms of break energy. Higher height means more layer during printing because layer thickness for all specimens is fixed. Therefore, that is why YZ-axis shows a higher result compared to XY-axis. The more layers used during the printing, the stronger it is to break while the printing orientation must be parallel to the impact force. Hence, YZ-axis shows the best result
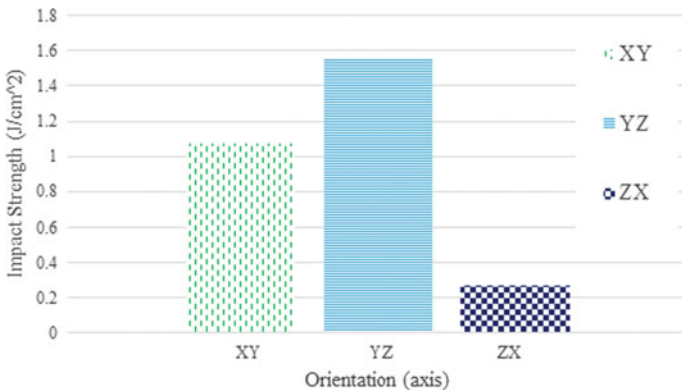
Fig. 9 Impact toughness against orientation of XY, YZ and ZX-axis
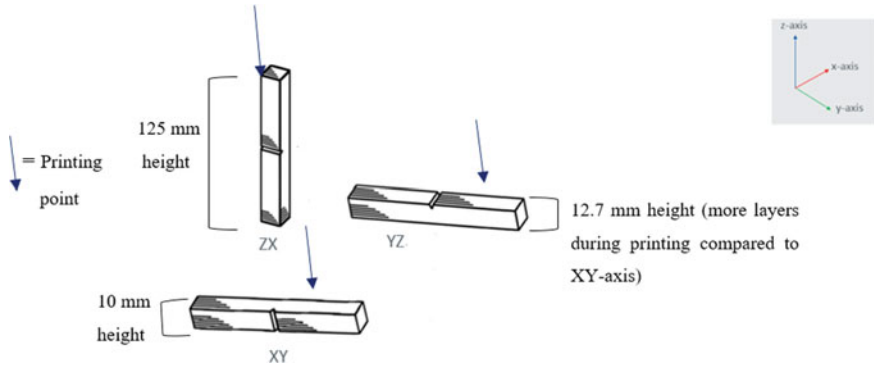
Fig. 10 Printing orientations and height of the specimen during printing

and is consistent with previous study [11]. Hence, they orientation of printing plays a big part because different orientation will give different layers of the specimen. The specimen dimension is 125 mm × 12.7 mm × 10 mm. Different orientation will give different printing height with the same dimension for each specimen. Increasing in height means increasing of layers during printing.

4.3 Hardness

Figure 11 shows that XY-axis has the highest hardness which is 87.73 HRB followed by YZ-axis which is 73.5 HRB and lastly is ZX axis which is the lowest at 65.9 HRB. The printing orientation for hardness sample is shown in Fig. 12. XY-axis orientation is the strongest because it has the strongest foundation during printing due to larger cross-sectional area of 40×40 mm^2 compared to the rest. Outer layer from another end to another end during layer printing is much closer and make it stronger in term
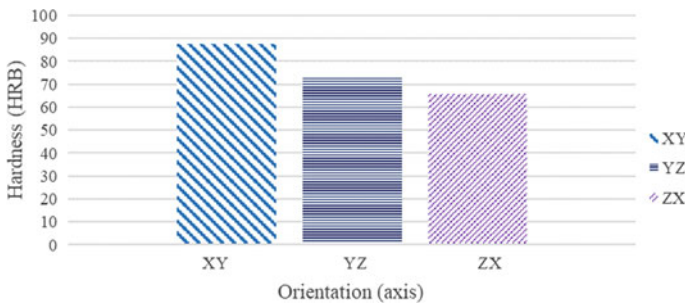
Fig. 11 Hardness against orientation of XY, YZ and ZX-axis
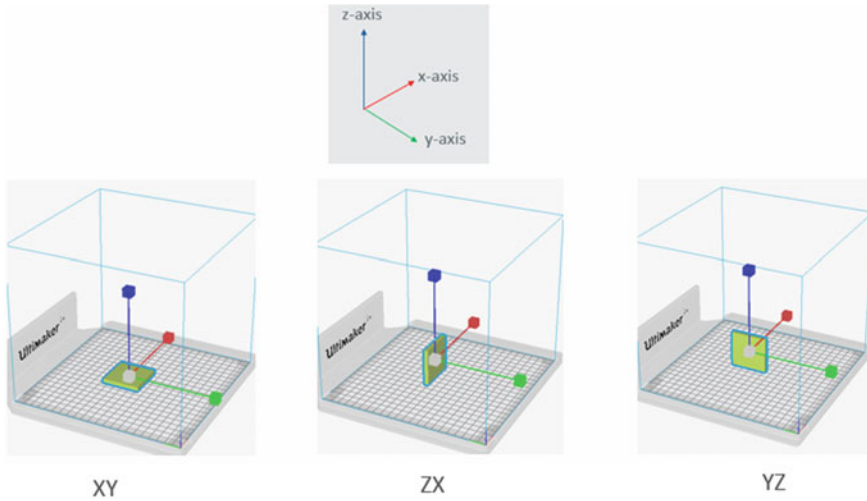
Fig. 12 Printing orientation of XY, ZX and YZ axis

of hardness compared to the rest which has small printing cross-sectional area and result to a weaker foundation of the model.

ZX-axis orientation is the weakest as it was printed vertically which is weaker in foundation and has many layers to be printed in a small area and result to a weaker bond between the print layers compared to XY-axis orientation. Therefore, bigger cross-sectional area in printing orientation produces a greater hardness for the model. This result is in different pattern compared to the tensile and impact strength as it depends on how big the cross-sectional area of the printed object is.

5   Conclusion

Current works have successfully identified the best printing orientation for ABS to optimize tensile strength, impact strength, and hardness. The best printing orientation for tensile strength and impact strength is YZ-axis which achieved 15.45 MPa, and 1.55 J/cm^2 respectively, while the best printing orientation for hardness is XY-axis at 87.73 HRB. The findings also suggests that the higher the tensile strength of the model, the stronger the impact strength of the model. With the results obtained, it proves that printing orientation affects the mechanical properties and qualities of the models. Hence, a best model in terms of mechanical property can be printed by using the optimised printing orientation if the purpose of model is known. Additional investigations such as more orientations and reinforcement can be tested to improve the strength of 3D printed samples.

References

1. Ahn SH, Baek C, Lee S, Ahn IS (2003) Int J Mod Phys B 17:1510
2. Štefanić I, Raos P, Samardžić I, Tintor B, Musser E (2012) Teh Vjesn 19:459
3. Gibson I, Rosen DW, Stucker B (2010) Additive manufacturing technologies rapid prototyping to direct digital manufacturing. Springer, Boston, MA
4. Giri J, Chiwande A, Gupta Y, Mahatme C, Giri P (2021) Mater Today Proc
5. Cherkia H, Kar S, Singh SS, Satpathy A (2020) Lect Notes Mech Eng 1
6. Keleş Ö, Blevins CW, Bowman KJ (2017) Rapid Prototyp J 23:320
7. Tanoto YY, Anggono J, Siahaan IH, Budiman W (2017) AIP Conf Proc 1788:1
8. Vălean C, Marşavina L, Mărghitaşl M, Linul E, Razavi J, Berto F (2020) Procedia Struct Integr 26:313
9. Zaldivar RJ, Witkin DB, McLouth T, Patel DN, Schmitt K, Nokes JP (2017) Addit Manuf 13:71
10. Yao T, Deng Z, Zhang K, Li S (2019) Compos Part B Eng 163:393
11. Roberson DA, Torrado Perez AR, Shemelya CM, Rivera A, MacDonald E, Wicker RB (2015) Addit Manuf 7:1
12. Caminero MÁ, Chacón JM, García-Plaza E, Núñez PJ, Reverte JM, Becar JP (2019) Polymers (Basel) 11
13. Patadiya NH, Dave HK, Rajpurohit SR (2020) In: Shunmugam M, Kanthababu M (eds) Advances in additive manufacturing and joining. Lecture notes on multidisciplinary industrial engineering. Springer, Singapore, pp 301–307
14. Liu H, He H, Peng X, Huang B, Li J (2019) Polym Adv Technol 30:910

Aerodynamic Investigation on Geometrical Features of a Drone

Z. H. Lim, K.-C. Wong, Linus Lau, K. C. Law, S. H. Tan, and C. S. Lim

Abstract Among the classifications of unmanned aerial vehicle (UAV), vertical take-off and landing (VTOL) has high operational flexibility and controllability. However, it has limited endurance due to high energy demand and limited onboard energy. Improvement on geometrical design is able to improve its aerodynamic performance and enhance endurance. This study aims to numerically investigate the geometrical effect on aerodynamic performance of a drone designed by RF Station (RFS). The geometrical parameters are the edge radius of drone's arm and the top surface curvature of a body cover added to the RFS drone. The numerical results of these modified designs are validated with wind tunnel experimental results, showing good agreement. The aerodynamic performances are compared with the original drone of RFS and another commercial drone, called DJI Phantom 4. The results showed that the introduction of edge radius at the arm of drone reduces drag coefficient C_D and lift coefficient C_L by a maximum of 7% and 3.4%, respectively. Over the range investigated, the body cover with the highest surface radius improves by 4.6% in C_D and 39.7% in C_L, as compared to the lowest one. The modified RFS drone incorporating both the edge radius and body cover is capable of achieving drag reduction and lift improvement of about 17.4% and 33.3%, respectively as compared to original RFS drone at flow velocity of 8 m/s.

Keywords Aerodynamic performance · Drone · Arm · Body cover

Z. H. Lim · K.-C. Wong (✉) · C. S. Lim
Department of Mechanical, Materials and Manufacturing Engineering, University of Nottingham Malaysia, 43500 Semenyih, Malaysia
e-mail: Kok-Cheong.Wong@nottingham.edu.my

L. Lau · K. C. Law · S. H. Tan
RF Station Sdn. Bhd., A-2-7, Glomac Damansara No. 699, Jalan Damansara, Taman Tun Dr Ismail, 60000 Kuala Lumpur, Malaysia

1   Introduction

Unmanned aerial vehicle, which commonly known as drone, is a type of vehicle that can fly without pilot present onboard. It can be controlled remotely by control equipment from the ground or by onboard electronics equipment with a reliable wireless connection. A systematic review by Watts et al. [1] discussed UAV classifications for civil usage depending on their characteristics such as size, capabilities and flight endurance. Among these classifications, VTOL is able to operate in a compact and cluttered space, hover at fixed position and does not requires long runway take-off and hence increases its operational flexibility [2]. They can be equipped with sensors and camera for various purposes, such as rescue mission, environmental protection, photography and delivery. However, it has limited endurance due to high energy demand and limited storage capacity. Researchers were looking into ways in enhancing power management through battery optimisation, implementing solar panel, reducing airframe drag and optimising propellers [3, 4] to improve endurance and efficiency.

Several studies [5–7] had been conducted using CFD to analyse the aerodynamic behaviour of UAV. However, there is a lack of studies for the aerodynamic performance of VTOL and its design optimisation. Felismina et al. [5] performed a CFD analysis on an agricultural seeder UAV to obtain a suitable flight plan that prolong the endurance by varying the pitch angles. Lowest drag was observed when cruising at 0° pitch angle when cruising and at 30° pitch angle during take-off. However, there was no validation mechanism mentioned. Israr and Dahalan [6] performed an aerodynamic performance analysis of UTM Elang-1 UAV by using CFD simulation and DATCOM analytical method. Both showed good agreement on lift coefficient, especially at low angle of attack with simulation having a higher drag coefficient estimation. Petterson [7] performed a computational study into the effect of turbulence model on the flow field characteristics of an unmanned combat aerial vehicle (UCAV) and compared with experiment. All turbulence models showed over-prediction of drag at low angle of attack. Complex vortical structures are not able to resolve successfully at higher angle of attack.

Kontogiannis and Ekaterinaris [8] designed a light UAV reconnaissance plane and performed optimisation on wing planform, twist and application of winglets using CFD to improve endurance and reduce power requirements. The implementation of fairings provided a beneficial impact on performance by eliminating vortex and diminishing pressure gradient caused by flow separation. Flight tests showed good agreement with CFD simulation in terms of longitudinal stability. Similar study was conducted by Boschetti et al. [9] to evaluate the aerodynamic performance and optimised the Unmanned Aircraft for Ecological Conservation (ANCE) through theoretical analysis and wind tunnel experiment. Modifications were performed on landing gear and twist of the wing tip. Both theoretical method and experimental results showed reduction in drag coefficient and increase in efficiency. Bagul et al. [10] performed CFD analysis on MQ-1 predator unmanned combat aerial vehicle to study the effects of external geometrical modifications on aerodynamic performance

at various flight conditions. Addition of features including antennas and projectiles increased drag and reduce lift. However, drag can be reduced by up to 96% locally and 0.5% globally by modify the location of the placement and take advantages of the wake region produced. These indicates that the aerodynamic performance can be affected drastically through external geometrical modification, especially for small UAV where the effects are significant. Modifications to fuselage design, aerofoil shape, wing aspect ratio and application of wingtip device are also effective in reducing drag generated by the wing [4]. However, these modifications are only suitable for fixed-wing UAV or UCAV. There are also flow control techniques without major external modifications such as riblet coating, vortex generator and dielectric barrier discharge plasma actuator [11]. Although these techniques show the effectiveness in flow control, extra cost and weight are not desire on a civilian VTOL.

Russell et al. [12] conducted a wind tunnel test on 5 commercially available multicopter UAV to analyse their performance with three configurations, including full vehicle, bare airframe and isolated rotor. The curved surface at the top of the larger DAx8 generated higher lift than DJI Phantom 3 but produced significantly larger drag. The lift generated able to reduce energy demand for the propeller to generate thrust. It is also found that the effect of rotor-airframe and rotor-rotor interactions can be estimated through full vehicle, bare airframe and isolated rotor results. High level of vibration was observed during the full vehicle and isolated rotor testings. Corrections were applied and uncertainties due to hysteresis, repeatability were included in the results. Kim and Chung [13] performed CFD simulation and wind tunnel experiment on the TR-E2S1 tilt-rotor UAV to investigate its aerodynamic characteristics. 12% scale model was used during wind tunnel experiment. Hence only the trends for aerodynamic characteristics and stability were focused on as the qualitative data was assumed to be small and not accurate. Identical trends were shown in both CFD and wind tunnel results. It is shown that CFD simulation is an excellent alternative for analysing and providing accurate trends on the aerodynamic characteristics and stabilities.

The present study aims to improve the aerodynamics performance of the RFS drone by looking into the design of its arm and body. The original RFS drone is a quadcopter drone developed by RF Station Sdn. Bhd. with a mission of goods delivery as illustrated in Fig. 1a. Comparison of the aerodynamic performances will be conducted between the original RFS drone, the RFS drone with body cover (Fig. 1b), and a commercial drone called DJI Phantom 4 (Fig. 1c).

Based on the bare airframe of RFS drone shown in Fig. 1a, all four arms' edge radius R (Fig. 2) along the blue edges are varied for investigation as rounded edges are expected to reduce the drag. For the body of the drone, an additional cover is added to the drone (Fig. 1c) and the internal radius of the cover is varied for investigation. The cover with curvature over the body is expected to produce positive lift effectively [12] and smoothen the flow over the drone. Figure 3a shows the body cover and Fig. 3b shows the axisymmetric cross section of the body cover. The curvature is defined by a radius r which the centre is along the axisymmetric axis. These designs with different edge radius or with added cover are called modified RFS drone hereafter.
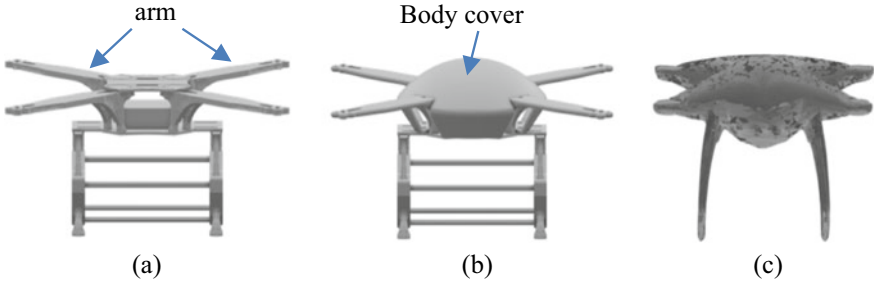
Fig. 1 CAD models of **a** RFS drone, **b** RFS drone with cover and **c** DJI drone
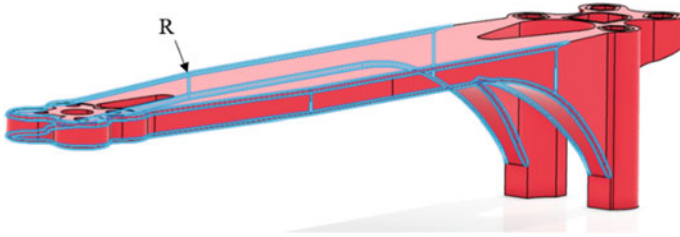
Fig. 2 Edge radius R on the arm along the blue edges

Fig. 3 **a** Body cover and **b** axisymmetric section of the body cover with thickness 3 mm

2 Methodology

In the study, numerical simulations were carried out on the 3 models presented in Fig. 1a and b. For RFS Drone shown in Fig. 1a, simulations are conducted for different edge radius, $R = 0, 0.7, 1.4, 2.1, 2.8$ mm. For RFS drone with body cover shown in Fig. 1b, simulations are conducted for different surface curvature of the body cover, $r = 133, 143, 153, 163, 173$ mm and the edge radius of arms is fixed at $R = 2.8$ mm. All simulations were conducted under same conditions for comparison. Wind tunnel experiments were conducted to validate the results of the numerical model of the DJI drone and RFS drone. Original Prusa i3 MK3S+ fused deposition modelling (FDM) 3D printer was used to produce the models for wind tunnel experiment using Polylactic acid (PLA) material.

2.1 Numerical Methods

3DEXPERIENCE Fluid Dynamics Engineer (FMK) were used for the simulations. As shown in Fig. 4, the dimensions of the computational domain conform to the dimensions of the wind tunnel setup, which is 1 m × 1 m × 1.5 m. The center of the drone is located at 0.5 m away from velocity inlet and 1 m away from pressure outlet. All the models are positioned with an 8° pitch angle towards the flow to represent the cruising motion at 8 m/s [14].

Mesh convergence study was conducted to ensure the mesh refinement does not affect the simulation result. It was found that a difference of 0.136% and 0.1% in drag and lift value, respectively, between 2.26 million and 2.82 million elements. It indicated a good convergence, hence mesh settings for 2.26 million elements was selected. Similar method was used for other models. Hex dominant mesh was created, with finer mesh created near the drone model to capture the flow separation.

Realizable k-ε turbulence model was used as it shows good prediction in drag and lift value in various cases [15, 16]. AMG-CG linear solver was selected for pressure equation while ILU-FGMRES linear solver was selected for momentum and turbulence equation. The boundary conditions applied to the computational domain are shown in Fig. 4. Velocity inlet is set to the inlet with velocity of 8 m/s to represent the cruising speed of the drone. Pressure outlet is set at the outlet. Slip wall condition is assigned to the walls to ignore the viscous effect of the fluid at the walls. The surface of the drone model is treated as non-slip wall. Air with density of 1.225 kg/m^3 and viscosity of 1.85×10^{-5} Pa s is applied. Frontal area of the drone body was determined from digital image by masking out the pixels for the drone using Adobe Photoshop and open-source raster graphics editor GIMP as proposed by [17]. A predetermined reference area (A_R) was placed beside the drone to correlate this area with number of images pixels (n_{pR}) to determine area units per pixel (p_A).
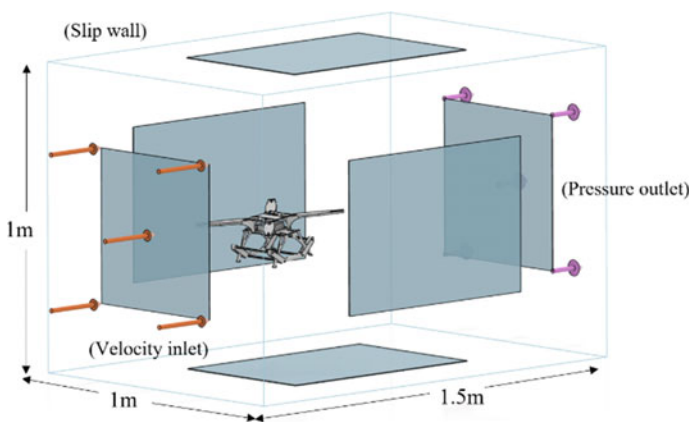
Fig. 4 Computational domain dimensions and boundary conditions

$$p_A = \frac{A_R}{n_{pR}} \qquad (1)$$

Frontal area of the drone A_D projected along the velocity vector was determined by multiplying the number of image pixels of drone (n_{pd}) with the area units per pixel obtained previously. The value of frontal area was used to obtain drag and lift coefficient.

$$A_D = n_{pd} \cdot p_A \qquad (2)$$

The objective of the study is to reduce drag coefficient (C_D) and increasing lift coefficient (C_L). Drag and lift coefficient are obtained through Eqs. 3 and 4.

$$C_D = \frac{2D}{\rho u^2 A_D} \qquad (3)$$

$$C_L = \frac{2L}{\rho u^2 A_D} \qquad (4)$$

where D is drag force, L is lift force, ρ is air density, u is flow velocity.

2.2 Experimental Procedures

The 3D printed models of RFS drone, modified RFS drone and DJI phantom 4 were tested in an open loop wind tunnel at Universiti Putra Malaysia. The wind tunnel has a test section of $1 \times 1 \times 2.5$ m and equipped with a 10-blade fan with a maximum speed of 50 m/s. During the tests, the atmospheric conditions were measured. A pitot tube connected to a digital manometer was placed at upstream to measure the flow velocity. The velocity was set to 3, 5 and 8 m/s to obtain the drag and lift force of the models at these conditions using six-component balance at an 8° pitch angle at all conditions. Data acquisition, reduction and control system (DARCS) was used to gather information from the six-component balance. The capacity of the six-component balance in x- and y-direction is 500 N while 1000 N in z-direction. The largest projected frontal area among the experimental models was 0.0216 m², which corresponds to 2.16% of the wind tunnel test section area. Blockage effect can be neglected as the blockage ratio is less than 5% [18]. Figure 5 shows the modified RFS drone with a model mounting is mounted on the sting. The directions of the flow and forces measured by the six-component balance is shown as well.
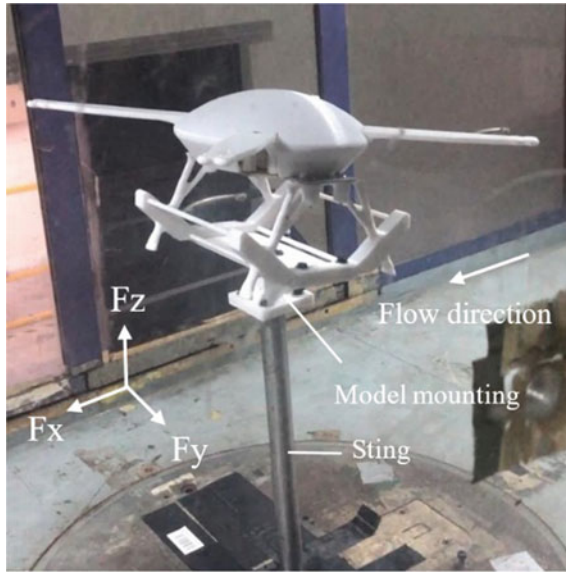
Fig. 5 Modified RFS drone with body cover mounted on sting in wind tunnel

3 Results and Discussion

As shown in Fig. 6a, the simulation results of the drag coefficient C_D and lift coefficient C_L for different edge radius R are presented. The results show that higher edge radius results in lower C_D. The case of with $R = 2.8$ gives a 7% of reduction in C_D as compared to the case of $R = 0$ (the original RFS drone). However, the drag difference between $R = 2.1$ and $R = 2.8$ is not significant, with only 0.1% difference in C_D. The value of C_L increases to the peak at edge radius of $R = 1.4$ but reduces slightly for higher edge radius $R = 2.1$ and $R = 2.8$. The maximum improvement in C_L is 3.35% for $R = 1.4$ as compared to the case without radius. This is obvious that adding radius at the edges on the arms enhance aerodynamic performance.
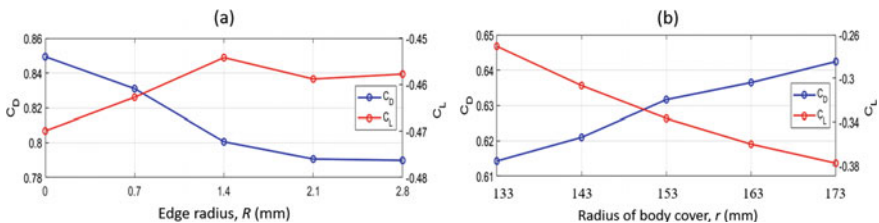
Fig. 6 Lift and drag coefficients for modified RFS drone with **a** different arm edge radius, R without body cover, and **b** body cover of different surface radius r with fixed $R = 2.8$ mm

Considering the overall aerodynamic performance of lift and drag coefficient in Fig. 6a, the performance for edge radii $R = 1.4$, $R = 2.1$ and $R = 2.8$ are comparable. Detailed analysis on the flow patterns over the drone reveals that when the edges are blunt without radius, certain area on the arm is form to cause flow separation. This explains why lower drag generated when edges are made rounded.

Subsequently for the simulations of RFS drone with body cover, the edge radius is fixed with one of the values, i.e. $R = 2.8$, and the results obtained are presented in Fig. 6b. From the results of modified RFS drone with body cover shown in Fig. 6b, it can be seen that the increase in radius of body cover r is detrimental to the aerodynamic performance with obvious increase in C_D and decrease in C_L. Comparing the cases of lowest and highest cover radius i.e., $r = 133$ mm and $r = 173$ mm, the difference is C_D and C_L are 4.6% and 39.7%, respectively. The flow over the drone's body are illustrated in Fig. 7a and b.

The flow over the RFS drones with minimum and maximum value of r (i.e. $r = 133, 173$ mm) at the centre plane are shown in Fig. 7a and b, respectively, for analysis. The velocities contour show that the former has a larger velocity difference between the top surface and the base of the cover and hence giving larger pressure difference, which results in higher lift as compared to the latter. Observation at the wake region reveals that, eddies are formed at the wake region for $r = 173$ mm whereas for $r = 133$ mm, eddies are not formed. The wake region with eddies increase the pressure and therefore results in higher pressure drag.

Numerical results for 3 different models for 3 different velocities are presented in Fig. 8. The 3 models of drones are the original RFS model, Modified RFS model with body cover of $R = 2.8$ mm, and DJI model. Figure 8a shows that the drag increases as the flow velocity increases. The results also show that the Modified RFS drone is effective in drag reduction as compared to the original RFS model. In Fig. 8b, the modified RFS drone also demonstrated higher lift as compared to original RFS model. This shows that implementing edge radius on the arm and addition of body cover enhances the aerodynamic performances. As for the performance of the DJI model, it presents slightly higher drag, but far higher lift as compared to the other two models. Further analysis was carried out to understand how the physical geometries affect the aerodynamic performances, and the velocity profiles with streamlines are presented for the 3 models in Fig. 9.

Observation on the streamlines and velocities in Fig. 9 show that, there exist high velocity difference between the upper surface and base of the drone for the DJI Model but the least for the original RFS drone. This would also mean the DJI model generates
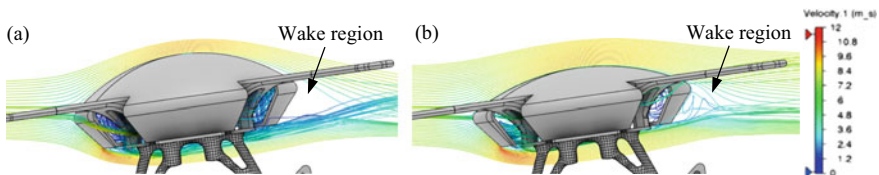
Fig. 7 Streamlines around body cover with **a** $r = 133$ mm and **b** $r = 173$ mm at centre plane
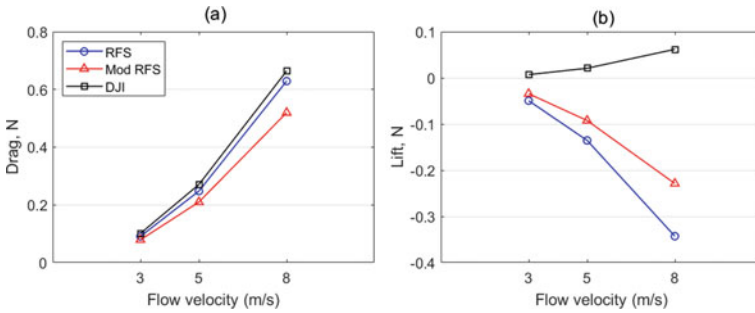
Fig. 8 Numerical results of **a** drag and **b** lift for original RFS model, modified RFS model (with cover and R = 2.8 mm) and DJI model at different flow velocity

Fig. 9 Streamlines around **a** original RFS drone **b** modified RFS drone **c** DJI Phantom 4

highest pressure difference between the upper surface and the base and therefore the highest lift. Likewise, as shown in Fig. 9a, the original RFS drone generate the lowest difference in terms of the velocities and pressure between the upper surface and the base of the body, and hence the lowest lift. On the other hand, the modified RFS drone in Fig. 9b shows continuous flow without flow separation and the flow from the upper surface and the base of body meets at the wake smoother. This leads to lowest drag among the 3 models as the pressure difference between the wake and the upstream is low. Whereas, for the DJI model in Fig. 9c, it is evident that the flow separation is most severe and contributed to large pressure drag. These observations imply that, the body cover added to the RFS drone prevents flow separation by having the flow through the upper surface remain attached to the surface.

For the validation of the numerical models, experiments have been conducted for each type of model for 3 different flow velocities. The results of drag obtained numerically and experimentally are presented in Fig. 10. Figure 10 shows a good agreement between the numerical and experimental results for the drag, with maximum discrepancies for original RFS drone, modified RFS drone with cover body and DJI drone at 5.53%, 8.11% and 18.6%, respectively.
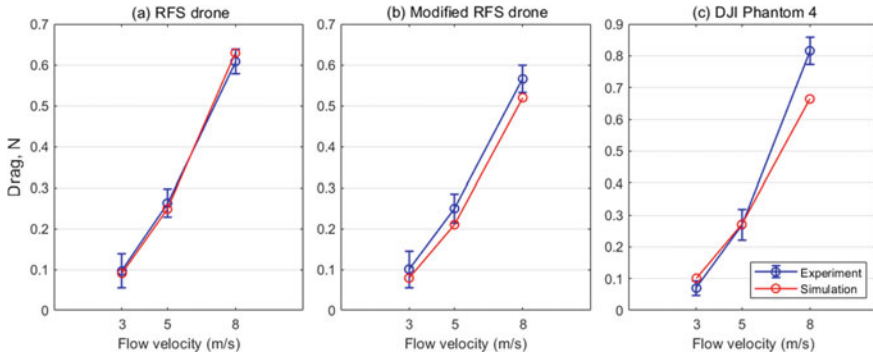
Fig. 10 Comparison of drag at different flow velocity

4 Conclusion

The numerical model is validated with the experimental results where both results are in good agreement. In order to study aerodynamic performance enhancement of RFS drone based on drag and lift, numerical investigation through geometrical studies were conducted. Two parameters namely edge radius of drone's arms and body cover curvature were studied. The study concluded that,

- The introduction of arm edge radius on RFS drone reduces drag and enhances lift by reducing flow separation, and this align with most flow phenomena that enhancement in lift and drag can be achieved if flow separation is not occurring.
- Body cover with the larger curvature or smaller radius results in lower drag and higher lift as it alters the flow to give higher pressure difference over the body and smoother flow without flow separation.
- The modified RFS drone is capable of achieving drag reduction and lift improvement of about 17.4% and 33.3%, respectively as compared to original RFS drone at flow velocity of 8 m/s.

References

1. Watts AC, Ambrosia VG, Hinkley EA (2012) Unmanned aircraft systems in remote sensing and scientific research: classification and considerations of use. Remote Sens 4(6):1671–1692
2. Czyba R, Lemanowicz M, Gorol Z, Kudala T (2018) Construction prototyping, flight dynamics modeling, and aerodynamic analysis of hybrid VTOL unmanned aircraft. J Adv Transp 2018:13–16

3. Amoiralis EI, Tsili MA, Spathopoulos V, Hatziefremidis A (2014) Energy efficiency optimization in UAVs: a review. Mater Sci Forum 792:281–286
4. Jin W, Lee YG (2015) Drag reduction design for a long-endurance electric powered UAV. Int J Aeronaut Space Sci 16(2):311–324
5. Felismina R, Silva M, Mateus A, Malça C (2017) Study on the aerodynamic behavior of a UAV with an applied seeder for agricultural practices. AIP Conf Proc 1836
6. Israr HA, Dahalan MN (2008) Estimation of lift and drag characteristics of UTM Elang-1 UAV. In: 2nd regional conference on vehicle engineering and technology, Oct 2008, pp 0–6
7. Petterson K (2006) CFD analysis of the low-speed aerodynamic characteristics of a UCAV. In: Collection of technical papers—44th AIAA aerospace sciences meeting and exhibit, vol 20, pp 15258–15270
8. Kontogiannis SG, Ekaterinaris JA (2013) Design, performance evaluation and optimization of a UAV. Aerosp Sci Technol 29(1):339–350
9. Boschetti PJ, Cárdenas EM, Amerio A (2005) Aerodynamic optimization of an UAV design. In: Collection of technical papers—AIAA 5th ATIO and the AIAA 16th lighter-than-air systems technology conference and balloon systems conference, vol 2, pp 916–932
10. Bagul P, Rana ZA, Jenkins KW, Könözsy L (2020) Computational engineering analysis of external geometrical modifications on MQ-1 unmanned combat aerial vehicle. Chin J Aeronaut 33(4):1154–1165
11. Panagiotou P, Yakinthos K (2019) Aerodynamic efficiency and performance enhancement of fixed-wing UAVs. Aerosp Sci Technol 99:105575
12. Russell C, Jung J, Willink G, Glasner B (2016) Wind tunnel and hover performance test results for multicopter UAS vehicles. Annu Forum Proc AHS Int 4:3448–3467
13. Kim C, Chung J (2006) Aerodynamic analysis of tilt-rotor Unmanned Aerial Vehicle with computational fluid dynamics. J Mech Sci Technol 20(4):561–568
14. Theys B, De Schutter J (2020) Forward flight tests of a quadcopter unmanned aerial vehicle with various spherical body diameters. Int J Micro Air Veh 12
15. Sadikin A et al (2018) A comparative study of turbulence models on aerodynamics characteristics of a NACA0012 airfoil. Int J Integr Eng 10(1):134–137
16. Zhang C, Bounds CP, Foster L, Uddin M (2019) Turbulence modeling effects on the CFD predictions of flow over a detailed full-scale sedan vehicle. Fluids 4(3):1–28
17. Ainegren M, Jonsson P (2018) Drag area, frontal area and drag coefficient in cross-country skiing techniques. Proceedings 2(6):313
18. Choi CK, Kwon DK (1998) Wind tunnel blockage effects on aerodynamic behavior of bluff body. Wind Struct Int J 1(4):351–364

Design and Development of a Flexible Test Rig for Biomedical Engineering PIV Experiment

**Mohamad Fairul Hubakri, Mohd Amirul Syafiq Zamri,
Mohd Noor Akmal Hamzah, Rabiatul Adawiyah Roslan,
Wan Naimah Wan Ab Naim, and Mohd Jamil Mohamed Mokhtarudin**

Abstract Particle image velocimetry (PIV) is applied in biomedical engineering to visualize fluid flow in artificial blood vessel. However, this requires a test rig to place the artificial blood vessel, which is usually built for specific application and lack flexibility. Thus, this study aims to design and develop a flexible test rig that suits a wide range of applications. Firstly, three designs have been proposed and the suitable design has been chosen for further development. Then, the strength of the inlet and outlet of the chosen test rig design are evaluated using finite element analysis (FEA). From the analysis, Design 3 has been chosen for further development. For this design, the artificial blood vessel of any size and position could be fitted into the test rig by using the adjusted wing nut and hose pipe clamp. In addition, the calculated factor of safety from the FEA implies that the wing nut and clamp can withstand the fluid pressure applied during the PIV experiment. This test rig is suitable to be used for any diameter and numbers of inlet and outlet of the artificial blood vessels for biomedical engineering experiments.

Keywords Particle image velocimetry · Test rig · Artificial blood vessel

1 Introduction

Particle image velocimetry (PIV) is a method to allow for qualitative flow visualization and quantitative analysis of the flow velocity distribution and other fluid related properties, which is suitable to be used in education and research [1–4]. With PIV, the fluid under investigation is first seeded with sufficiently small tracer particles that are assumed to follow the flow dynamics of that fluid [2, 3, 5, 6]. Then, the

M. F. Hubakri · M. A. S. Zamri · M. N. A. Hamzah · R. A. Roslan ·
M. J. Mohamed Mokhtarudin (✉)
College of Engineering, Universiti Malaysia Pahang, Gambang, 26300 Pahang, Malaysia
e-mail: mohdjamil@ump.edu.my

W. N. Wan Ab Naim
Faculty of Mechanical and Automotive Engineering Technology, Universiti Malaysia Pahang, Pekan, 26600 Pahang, Malaysia

fluid is illuminated with a thin sheet of laser to visualize the particle [1, 3]. The motion of the particles is then calculated to determine the velocity field of the fluid being studied using a built-in software [1, 3]. Typically, a PIV equipment consists of cameras, a laser that normally has been converged to become a line of light beam, the seeding particles mixed with the fluid under investigation, and a specialized test rig for the investigation of the fluid flow [3]. PIV is usually used to study the flow in aerodynamics such as in the wind tunnel [7] and liquid in a complex structure such as in the biomedical application [8–11].

In the biomedical engineering application, PIV is widely used to visualize flow in the artificial blood vessels and organs, both in the normal and disease conditions [8, 9, 12]. Apart from the education purposes, the aim of blood flow visualization is to predict and plan for the treatment outcome, for example in planning the suitable treatment for congenital heart disease [12] and to test the functionality of the heart valve [13]. The human blood vessel and organ has complex anatomical structures where each individual present with different size and shape. Hence, the currently used test rigs are built based on its specific application and lack of flexibility. It is only suitable to be used once with the limited size and position of the phantom. Phantom here refers to the transparent material that mimics the blood vessels or organs.

Thus, this study aims to design and develop a flexible that suits a wide range of phantom size and position. This test rig is hopefully can be used multiple times with different types of phantoms, thus avoiding the need to design a new test rig. This new proposed product could be used by undergraduate and postgraduate university students, both local and international.

2 Methodology

This section will briefly describe the designing and fabrication process for the PIV test rig used for blood vessel application. This section is organized as follows: firstly, the various designs of the PIV test rig, followed by the equipment and material selection, then the calculation of the factor of safety (FOS) using the finite element analysis (FEA), and lastly the fabrication process.

2.1 PIV Test Rig Design

Initially, three test rig designs have been proposed (Fig. 1). After evaluating the advantages and disadvantages of each design and the estimation cost, Design 3 has been selected. The detailed comparisons between the designs are further discuss in the "Results and Discussion" section.

Final design of the test rig (Design 3) is then drawn using SolidWorks software. Each component of the design is created separately before assembly (Fig. 2). Test
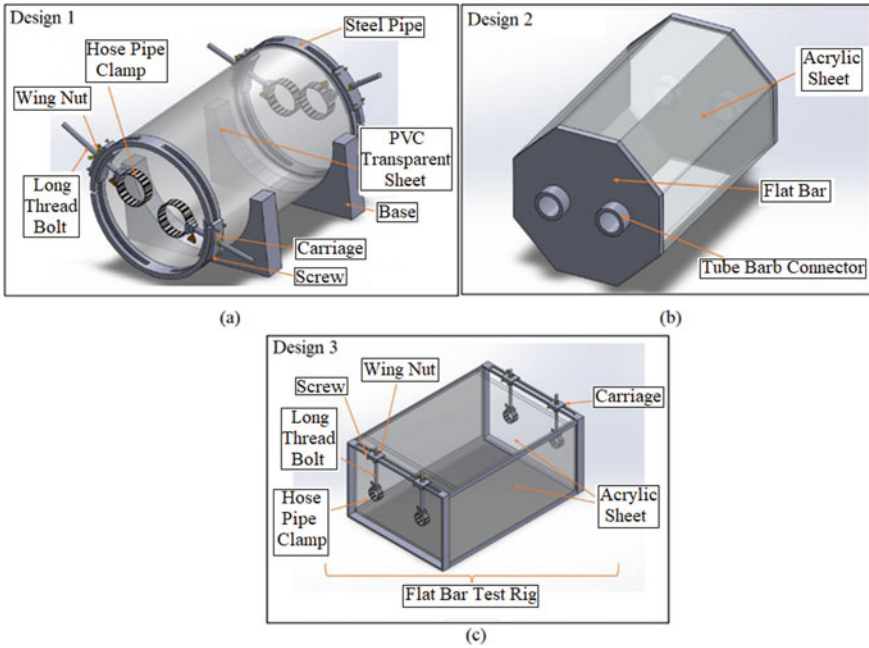
Fig. 1 Three proposed test rig designs; **a** Design 1; **b** Design 2; and **c** Design 3
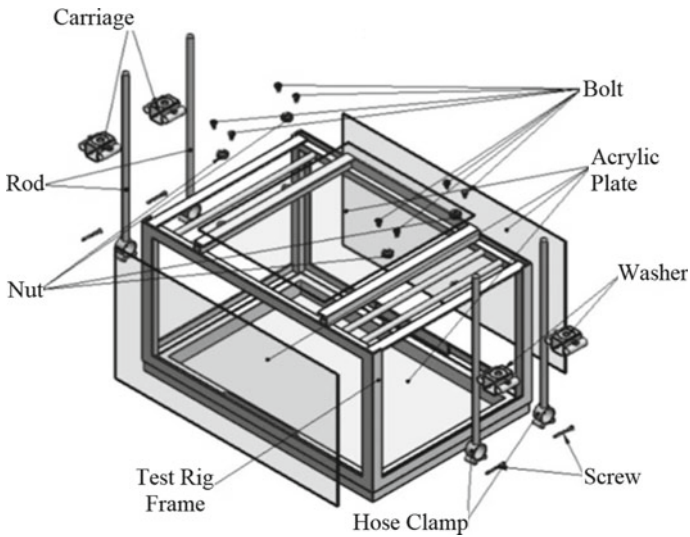
Fig. 2 Technical drawing of Design 3 in exploded view

Table 1 Material with functional specification

No.	Material	Function
1	Acrylic sheet	To ensure optical access for both camera and laser
2	Hose pipe clip	To tighten the PVC pipe so that it would stay in place and not sliding down its position
3	Mild steel flat bar	To hold the acrylic sheet
4	Long thread bolt	To adjust the movement of the valve
5	Wing nut	To adjust the movement of the long thread bolt
6	Screw	To tighten the carriage
7	Stainless steel	To fabricate hose pipe clamp and carriage

rig is designed using a simple rectangular shape. Complex design of the test rig will not give any advantage as it will only act as a place to hold the phantom.

2.2 Material Selection

Table 1 shows the material used with its functional specification.

2.3 FOS Analysis Using Finite Element

The load-carrying capacity of a system beyond what the system supports is known as the FOS. The FOS can be calculated by taking the ratio of the absolute strength of a structure (yield stress) to the actual applied load on the design (allowable stress) as shown in Eq. 1.

$$FOS = \frac{Yield\ stress}{Allowable\ stress} \tag{1}$$

FOS is required to determine the overload the system might have to endure and to avoid any occurrence of design damages. Based on the test rig design, the possible part that a damage can occur during the experiment is hose pipe clamp. Thus, this part will be further analyzed for FOS using FEA. FOS analysis will be evaluated under three conditions, i.e. at the upper, lower and all regions inside the clamp (Fig. 3). The FEA simulation will be run using the COMSOL Multiphysics.

Geometry and Meshing. After creating the geometry of the hose pipe clamp as in the design section, the geometry it will be meshed using finer mesh. The number of mesh produced is approximately 1,000,000.
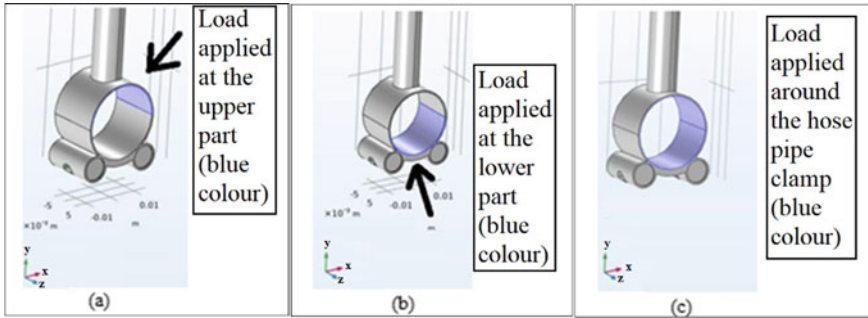
Fig. 3 FOS analysis at **a** upper; **b** lower and **c** all regions inside the hose clamp

Simulation Setting. In this work, the load will be applied under three conditions, i.e. the upper, the lower and all regions inside the clamp (Fig. 3). The load applied is similar to the maximum blood pressure, which is 15,998.7 Pa.

2.4 PIV Test Rig Fabrication

The test rig design is divided into four main components, which are the frame, hose pipe clamp, carriage, and the wall. Below is the fabrication process for each component.

Frame. The material used for the frame is a mild steel flat bar. It is used because it has high impact, high tensile strength, good ductility, and good weldability. The fabrication of the frame consists of cutting, grinding and welding using Metal Inert Gas (MIG) welding Machine. Firstly, all of the dimensions of the mild steel flat bar are measured following the test rig design. Then, the mild steel is cut based on the dimension using the cutting and grinding machine. All of the mild steel is later joined together to form the frame by using the MIG welding machine.

Hose pipe clamp. The material used for hose pipe clamps is stainless steel or galvanized iron. It is used because it has a high tensile strength, is easy to fabricate and has a low-maintenance and long lasting. The hose pipe clamp is joined with a long thread using the Tungsten Inert Gas (TIG) welding machine. TIG welding is a suitable process in joining the materials because they are made of stainless steel.

Carriage. The material used for carriage is stainless steel which consists of stainless-steel hollow, shaft and stainless-steel bolt nut. The joining process for the carriage also uses the TIG welding machine.

Wall. The material used for the wall is acrylic sheet since the wall must be transparent and thin to allow for the laser to pass through. The acrylic is assembled to the frame bar using screws.

3 Results and Discussion

Human blood vessels such as aorta and coronary arteries, and the organs are complex anatomically, where their size and shape are varied among different persons. Thus, the test rig designed in this work aims to suit a wide range of phantom size and position of blood vessels or organs that allow for the test rig to be used multiple times. In this work, three test rig designs have been proposed (Fig. 1).

For Design 1, a cylindrical shape has been proposed. The size and position of the inlet and outlet can be adjusted. However, this design needs an additional part, which is the base to prevent the test rig from rolling over. Besides, the cylindrical shape is also difficult to fabricate.

Meanwhile, Design 2 uses octagonal shape. Even though this design can enclose space more efficiently compared to the other designs, this design is quite difficult to be fabricated due to its octagonal shape. This is because there will be more acrylic sheets to be cut before assembling it into octagonal form. Besides that, this design is also not balanced because the surface area of the base is small. This design also has fixed inlet and outlet size and position that does not meet with our aim.

On the other hand, Design 3 has a rectangular shape. This design has a higher stability because the base is flat and it also has adjustable size and position for the inlet and outlet. Because of its advantages compared to the other designs, Design 3 has been chosen. Table 2 shows the detailed advantages and disadvantages for each design and Table 3 shows the screening process for each design.

Figure 4 shows the final product of the test rig based on Design 3. The position of the phantom can be adjusted as the wing nut could be moved left, right, up, or down. Besides, the hose pipe clamp allows for any size of phantom to be fitted. This product also has higher stability because the base is flat, thus it is easier to move the carriage without causing much disturbances to the system. However, further modification on

Table 2 Advantages and disadvantages of Designs 1, 2 and 3

Design	Advantages	Disadvantages
1	• Adjustable size of inlet and outlet • Adjustable position of inlet and outlet	• Low stability and requires base for support • Difficult to fabricate (cylindrical form) • Inlet and outlet only can be adjusted in one direction (up and down), cannot be moved forward and backward
2	• Encloses space more efficiently	• Low stability because the base surface area is small • Difficult to fabricate (octagonal shape) • Fixed size and position of inlet and outlet
3	• Adjustable size of inlet and outlet • Adjustable position of inlet and outlet • Higher stability (rectangular base) • Easy to fabricate	• Inlet and outlet only can be adjusted in one direction (up and down), cannot be moved forward and backward

Table 3 Design screening

No.	Design 1	Design 2	Design 3
Easy to manufacture	−	−	+
Strength	−	−	0
Adjustability	+	−	+
Durability	+	+	+
Safety	+	0	+
Multifunction	+	−	+
Sum "+"	4	1	5
Sum "−"	2	4	0
Sum "0"	0	1	1
Net score	2	−3	5
Rank	2	3	1
Continue	No	No	Yes

The adjustable wing nut that can be moved left and right and up and down that suits phantom position

Test rig frame

Wall made from acrylic sheet

The adjustable hose pipe clamp that suits the phantom size
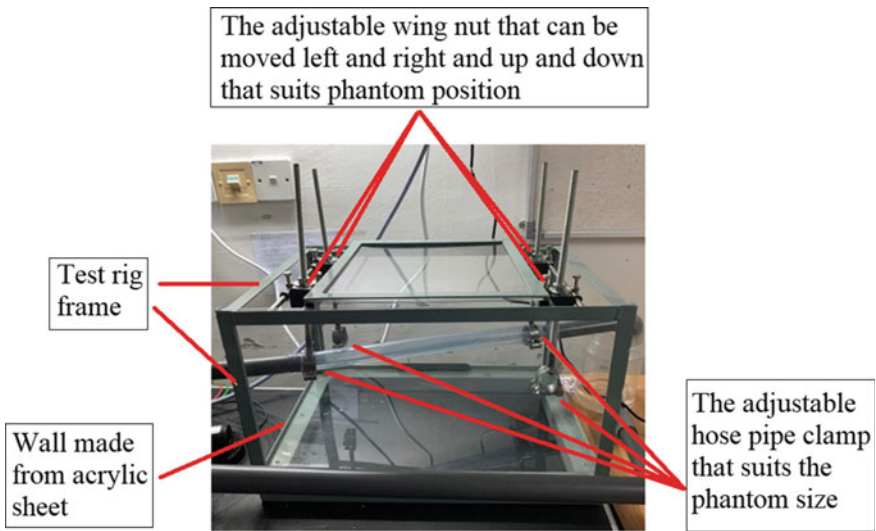
Fig. 4 Final product of the test rig

this product should be made in the future as at the moment the length of the carriage is fixed and cannot be adjusted. Since this is an initial work that aims to design and fabricate the flexible test rig, further experiment using PIV equipment is not included in this work.

Meanwhile, the FEA results are as shown in Fig. 5. These results are later used to calculate the FOS using Eq. (1) and results are tabulated in Table 4. Since all the FOS values are more than one, this implies that only a small force is imposed on the host clamp by the maximum blood pressure as compared to the maximum yield
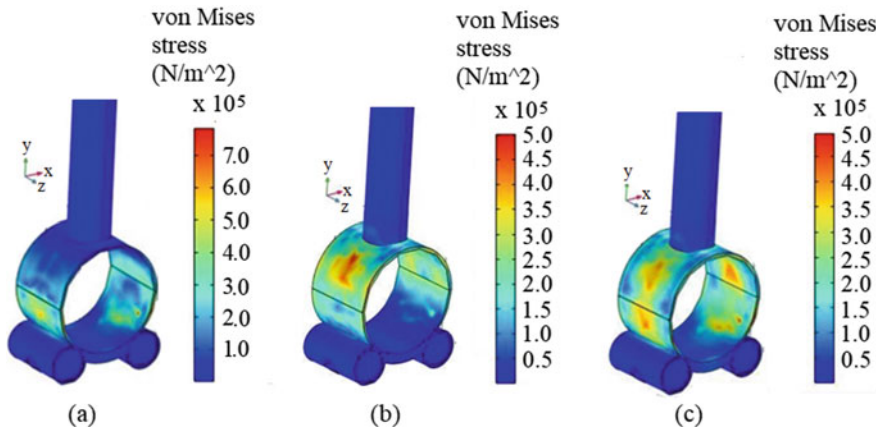
Fig. 5 Von Mises stress distribution when 15,998.7 Pa is applied at; **a** lower; **b** upper and **c** all regions inside the hose pipe clamp

Table 4 FOS values at the lower, upper and all region inside the hose pipe clamp

No.	Applied load location	FOS values
1	Lower region of the hose pipe clamp	256.25
2	Upper region of the hose pipe clamp	410.00
3	All region inside the hose pipe clamp	410.00

stress value the clamp can withstand. Hence, the probability that the hose pipe clamp will break is very small.

4 Conclusions

This study aims to design and develop a flexible test rig that suits a wide range of phantom size and position of blood vessel and organ. To achieve this, three test rig designs have been proposed. Based on the evaluation of advantages and disadvantages of each design, Design 3 has been chosen because it has a higher stability, is easy to fabricate, and the inlet and outlet have flexible size and position. The final product based on Design 3 has been developed where its position and size of the inlet and outlet could be adjusted using the wing nut and hose pipe clamp. In addition, the FEA analysis has been done and shows that only the hose clamp can withstand the maximum blood pressure applied during a PIV experiment. Further improvement is needed to enable the length of the test rig to be adjusted.

References

1. Minichiello A, Armijo D, Mukherjee S, Caldwell L, Kulyukin V, Truscott T, Elliott J, Bhouraskar A (2020) Developing a mobile application-based particle image velocimetry tool for enhanced teaching and learning in fluid mechanics: a design-based research approach. Comput Appl Eng Educ

2. Dabiri D (2006) Cross-correlation digital particle image velocimetry—a review. Turbul ABCM Curitiba 155–199

3. Abdulwahab MR, Ali YH, Habeeb FJ, Borhana AA, Abdelrhman AM, Al-Obaidi SMA (2020) A review in particle image velocimetry techniques (developments and applications). J Adv Res Fluid Mech Therm Sci 65(2):213–229

4. Roloff C, Stucht D, Beuing O, Berg P (2019) Comparison of intracranial aneurysm flow quantification techniques: standard PIV vs stereoscopic PIV vs tomographic PIV vs phase-contrast MRI vs CFD. J Neurointervent Surg 11(3):275–282

5. Melling A (1997) Tracer particles and seeding for particle image velocimetry. Meas Sci Technol 8(12):1406

6. Steinmann T, Casas J, Braud P, David L (2021) Coupled measurements of interface topography and three-dimensional velocity field of a free surface flow. Exp Fluids 62(1):1–16

7. Kompenhans J, Raffel M, Dieterle L, Dewhirst T, Vollmers H, Ehrenfried K, Willert C, Pengel K, Kähler C, Schröder A (2000) Particle image velocimetry in aerodynamics: Technology and applications in wind tunnels. J Visualization 2(3, 4):229–244

8. Zhu G, Wei Y, Yuan Q, Yang J, Yeo JH (2019) PIV investigation of the flow fields in subject-specific vertebro-basilar (VA-BA) junction. Biomed Eng Online 18(1):1–19

9. Mokhtar NH, Abas A, Teong SL, Razak N (2016) Particle image velocimetry experiment of blood flow through stent in artery bifurcation aneurysm problem. AIP Conf Proc

10. Yu P, Durgesh V, Xing T, Budwig R (2021) Application of proper orthogonal decomposition to study coherent flow structures in a saccular aneurysm. J Biomech Eng 143(6):061008

11. Brindise MC, Rothenberger S, Dickerhoff B, Schnell S, Markl M, Saloner D, Rayz VL, Vlachos PP (2019) Multi-modality cerebral aneurysm haemodynamic analysis: in vivo 4D flow MRI, in vitro volumetric particle velocimetry and in silico computational fluid dynamics. J R Soc Interface 16(158):20190465

12. Kitajima HD, Sundareswaran KS, Teisseyre TZ, Astary GW, Parks WJ, Skrinjar O, Oshinski JN, Yoganathan AP (2008) Comparison of particle image velocimetry and phase contrast MRI in a patient-specific extracardiac total cavopulmonary connection. J Biomech Eng 130(4)

13. Knapp Y, Bertrand E (2005) Particle imaging velocimetry measurements in a heart simulator. J Visualization 8(3):217–224

Possible Health Risk of Cellulose-Based Materials

Haziqatulhanis Ibrahim, Norazlianie Sazali, Wan Norharyati Wan Salleh, and Rishen Nair Krishnan

Abstract Cellulose-based products are currently receiving tremendous attention from researchers all over the world. It can be used in wide variety of applications including water treatment industry. However, there are scarce publications that touch on the possible risk that evolved from the usage of cellulose-based materials. This mini review aims to cover the respiratory risk possibility of nanocellulose by summarizing the findings by various researchers of their in vivo test. It was concluded that cautions need to be taken when handling the materials to prevent the exposure to higher risk.

Keywords Cellulose · Green technology · Risk evaluation · Adsorbent

1 Introduction

Over the last decades, development of green products for replacement of current conventional adsorbent has garnered tremendous attention from global researchers. Biosorbent is an eco-friendly type of adsorbent, usually made up from waste using safe chemicals and manufactured for sorption application. Bio-based materials were reported to dominate the market for sustainable materials due to its comparable performance at a lower manufacturing cost. Natural polymer that can be found abundantly in the world, cellulose, is currently in the list of sustainable materials of high interest by the academician and people from the industries. The term 'nanotechnology' was first employed by Eric Dexler Kim, which defines as the study of materials having dimensions between 1 and 100 nm [1, 2]. Unique properties of nano-sized cellulose (NC) have made them the emerging potential candidate for biosorbent and

H. Ibrahim · N. Sazali (✉) · R. N. Krishnan
College of Engineering, Universiti Malaysia Pahang, 26300 Gambang, Pahang, Malaysia
e-mail: azlianie@ump.edu.my

W. N. Wan Salleh
Advanced Membrane Technology Research Centre (AMTEC), School of Chemical and Energy, Faculty of Engineering, Universiti Teknologi Malaysia, 81310 Skudai, Johor Darul Takzim, Malaysia

in other wide range of applications. To name a few, NC are largely studied for applications in water treatment application to remove various types of pollutants, whilst it is also employed in medical sector as drug delivery carrier and for wound dressings. However, the utilization of NC as adsorbent has raised few concerns on its possible risk [3]. Owing to its nanoscale size, it might be able to permeate through the skin and cell membranes [4]. Thus, it is very important to critically evaluate the toxicity of NC as well as the health hazards that may occur.

Two types of cellulose-based biosorbent that being evaluated in this chapter are nanocrystal cellulose (NCC) and nanofibre cellulose (NCF). Generally, toxicology studies for NC are very challenging due to the complexity of the mechanism. There are many toxicological inducers that could affect the toxicity of the NC such as the material size, shapes, surface reactivity and many more. Differences in techniques applied for synthesising the NC could also alter its psychochemical properties and produce adverse effect to the health. Concerns about the health implications of the synthesised NC for biosorption application has been raised as the long-term effects of the exposure are still unknown. There is also a raised concern on the possibility of substance inhalation during material handling. To date, the literature discussing on NC toxicity is still scarce. Nevertheless, the number of in vitro and in vivo study of NC materials keep increasing over the years due to increasing interest among researchers and the government [5]. In order to assess the risk possesses by the nanomaterial, which in this case is NC, variety of risk analysis tools and assessment technique has been proposed [6–9]. Nonetheless, according to Grieger et al. [10], the advantages and drawbacks of the framework and assessment method cannot be outline as there are only a few that utilized the approaches while the rest reported only the initial screening.

2 Risk Assessment

Risk can be defined as possible harm that may pose to the users. In other word, it can be defined as product of hazard and exposure as explained by Shatkin and Kim [11]. All chemicals and utilization of any substance should have a thorough safety assessment to be done first in order to classify whether it is safe for usage or the other way round. Generally, the parent of NC, bulk cellulose is deemed as not toxic and safe to use but safety of NC as biosorbents is still a challenge due to complex system and uncertainties. Even though it has the same chemical structure as the parent derivatives, NC possess different physicochemical properties. Varying size, shape, surface reactivity and charge are some of the factors that contributes to the different toxicity of NC. It was resulted from different treatments done to the bulk cellulose.

NCC has higher crystallinity compared to NCF due to removal of amorphous region in one of the many steps in producing NCC. Dimension of NCC usually in the range of 50–500 nm in length and 3–5 nm width while NCF was reported to have length of 500–2000 nm with width of 4–20 nm [12]. Other than that, other

Risk governance

Includes social aspect in its assessment, suitable for policy makers and government agencies.

Example: International Risk Governance Center (IRGC) Risk Governance Framework, Comprehensive Environmental Assessment (CEA)

Screening level

Evaluation of risk through life cycle analysis of the materials or identification of potential risk through criteria listed in matrix table.

Example: Precautionary Matrix, Nano Life Cycle Risk Assessment Framework (LCRA)

Framework to assess nanomaterials risk

Risk assessment and management

Characterisation and description of the potential risk and mainly used for industries or manufacturers.

Example: Nano Risk Framework, Certifiable Nanospecific Risk Management and Monitoring System (CENARIOS®)

Adaptable risk assessment tools

Score-based analysis, established rank system for the potential risk.

Example: Multi-Criteria Decision Analysis (MCDA), XL Insurance Database Protocol

Fig. 1 Frameworks to assess nanomaterials risk

factors that could influence the toxicity are from biochemical mechanism such as necrosis, necroptosis, oxidative stress, DNA damage and many more [13]. Despite of material size affecting its toxicity, it is also dependant on the type of NC-based biosorbent studied. Large specific surface of NC provides higher affinity in absorbing biomolecules and thus producing toxicity via biochemical reaction. Other than that, NC biosorbent are usually tailored for its application for environmental remediation. If the target pollutant is negatively charged, the biosorbent used would be cationic for them to bind with each other. A researcher stated that the charges of NC significantly affect the cellular uptake, meaning that NC could possibly attached on living cell membranes and accumulates [10]. Figure 1 shows the summary of the nanomaterials risk assessment framework.

3 Toxicity of Nanocellulose

Increasing study in utilization of NC in various applications makes the evaluation of toxicology effect became vital for public health regulators. Cellulose is grouped in Generally Regarded As Safe (GRAS) substance by the Food and Drug Administration (FDA), but it is extremely important to declare whether NC based materials are regarded as safe too. Limited literature published on the toxicological effect of NC does not help to close the knowledge gaps and instead, raises public concern due

to some contradicted findings between researchers. Some classified the NC as non-toxic while some found out that NCC possess more health risk compared to NCF [14, 15]. Exposures to NC can occur in many ways, primarily from inhalation. Thus, more studies were directed towards pulmonary toxicity, which is the medical term for foreign materials that entered the respiratory system and have adverse health impact. The word 'in vivo' refers to a study that is conducted in a living organism, whether animal model or by human clinical trials. Rats and rabbit are two of common animals that were tested for in vivo studies in the laboratory. To conduct these studies, certain regulations must be followed and permission need to be obtained before commencing the animal testing. The effect of NC varies according to parameters tested and time of exposure. It can be as early as 1 h or even progressing for months to thoroughly assess the risk when continuously exposed to the substance. Toxicity assessment was divided according to human organ systems.

There are three division in the respiratory system which are nasal-pharyngeal-laryngeal, tracheobronchial and alveolar division where the exchange of gas occurs. Yanamala et al. [16] did pharyngeal aspiration test on a female mice C57BL/6 exposed to NCC. Two types of NCC were used which were freeze-dried product and 10 wt% suspension of NCC. The NCC was manufactured in Forest Products Laboratory via typical 64 wt% sulfuric acid hydrolysis method. Pharyngeal test is done by placing the NC under the animal's tongue at its base and extending the tongue so that the aspiration of substance would happen due to the rat reflexes.

Outcome from the tests indicates that the respiratory system damaged the tissue and gave inflammatory effect, with oxidative stress depends on the dosage of NCC. It should be noted that different effect was demonstrated when different types of NC and different mean of delivery was employed. For instance, a group of researchers explored the same parameter that was conducted to several rats but using NCF instead of NCC [17]. Also, the method of delivery was by exposure to aerosol. Inflammatory response was detected after 1 day of exposure, proving the effect of NC exposure to the respiratory system. Table 1 addressed some of respiratory system studies done by past researchers. Generally, all foreign particles that goes into the lung are considered as potential hazard, unless it is proven otherwise.

4   Conclusion

It is hard to conclude on one conclusion since there are many variables that need to be taken into account. Even with only single dosage, the animal needs longer time for recovery and these could worsen if it were exposed continuously in a long time. For studies that were conducted less than one month, it is hard to observe the histopathological changes that occur in the lungs. However, from the tests done by researchers, it was proved that NC does affect the respiratory system and therefore, precaution are needed when handling the materials.

Table 1 In-vivo test done by various researchers

NC type	Animal strain	Maximum Dose (mg/kg)	Dose frequency	Experimental details	References
NCF	Mouse (C57BL/6)	0.9	Single	• Spotted lung recovery in 4 weeks • Increasing neutrophil amount in bronchoalveolar lavage fluid (BALF) • Carboxymethylated NCF gave lower inflammation reaction compared to NCF	[18]
NCF	Mouse (BALB/c)	4	Single	• Lung recovery in 2 weeks • Increasing cytokines	[19]
NCF	Mouse (C57BL/6)	2	Single	• Lung recovery was observed within 4 weeks • NCF were administered in 4 different forms • Agglomeration was observed	[20]
TEMPO-NCF			Single	• Dosage of either 10, 40, 80 or 200 µg per mouse • Higher dose produce higher cellulosic accumulation in bronchi and alveoli	[21]
NCC	Mouse (C57BL/6)	10	Single	• Rcovery in 1 day • NCC were administered in 2 forms • Inflammatory cells and damaged tissue were observed • NCC suspension gave higher oxidative stress compared to powdery NCC	[16]

Table 1 (continued)

NC type	Animal strain	Maximum Dose (mg/kg)	Dose frequency	Experimental details	References
NCC	Mouse (C57BL/6)	2	Twice per week	• Test was done for 3 consecutive weeks • Recovery took 3 months • Chronic inflammation was observed	[22]

References

1. Service RF (2004) Nanotoxicology: nanotechnology grows up. Science 304:1732–1734. https://doi.org/10.1126/science.304.5678.1732

2. Toumey CP (2008) Reading Feynman into nanotechnology. Techné Res Philos Technol 12:133–168. https://doi.org/10.5840/techne20081231

3. Shvedova AA, Yanamala N, Kisin ER, Tkach AV, Murray AR, Hubbs A, Chirila MM, Keohavong P, Sycheva LP, Kagan VE, Castranova V (2014) Long-term effects of carbon containing engineered nanomaterials and asbestos in the lung: one year postexposure comparisons. Am J Physiol Cell Mol Physiol 306:L170–L182. https://doi.org/10.1152/ajplung.00167.2013

4. Chen X, Schluesener HJ (2008) Nanosilver: A nanoproduct in medical application. Toxicol Lett 176:1–12. https://doi.org/10.1016/j.toxlet.2007.10.004

5. Perkel JM (2012) Life science technologies: animal-free toxicology: sometimes, in vitro is better. Science 335:1122–1125. https://doi.org/10.1126/science.335.6072.1122

6. Linkov I, Satterstrom FK, Steevens J, Ferguson E, Pleus RC (2007) Multi-criteria decision analysis and environmental risk assessment for nanomaterials. J Nanoparticle Res 9:543–554. https://doi.org/10.1007/s11051-007-9211-0

7. Hansen SF (2009) Regulation and risk assessment of nanomaterials: too little, too late? http://www2.er.dtu.dk/publications/fulltext/2009/ENV2009-069.pdf

8. Metcalfe C, Bennett E, Chappell M, Steevens J, Depledge M, Goss G, Goudey S, Kaczmar S, O'Brien N, Picado A, Ramadan AB (2009) Smarten. In: Nanomaterials: risks and benefits. Springer Netherlands, Dordrecht, pp 95–109. https://doi.org/10.1007/978-1-4020-9491-0_7.

9. Tervonen T, Linkov I, Figueira JR, Steevens J, Chappell M, Merad M (2009) Risk-based classification system of nanomaterials. J Nanoparticle Res 11:757–766. https://doi.org/10.1007/s11051-008-9546-1

10. Grieger KD, Linkov I, Hansen SF, Baun A (2012) Environmental risk analysis for nanomaterials: review and evaluation of frameworks. Nanotoxicology 6:196–212. https://doi.org/10.3109/17435390.2011.569095

11. Shatkin JA, Kim B (2017) Environmental health and safety of cellulose nanomaterials and composites. In: Handbook of nanocellulose and cellulose nanocomposites. Wiley-VCH Verlag GmbH & Co. KGaA, Weinheim, Germany, pp 683–729. https://doi.org/10.1002/9783527689972.ch21

12. Moon RJ, Martini A, Nairn J, Simonsen J, Youngblood J (2011) Cellulose nanomaterials review: structure, properties and nanocomposites. Chem Soc Rev 40:3941

13. Li Y, Wang S, Ju D (2020) Toxicity of polymeric nanomaterials. In: Nanotoxicity. Elsevier, pp 167–191. https://doi.org/10.1016/B978-0-12-819943-5.00008-7

14. Roman M (2015) Toxicity of cellulose nanocrystals: a review. Ind Biotechnol 11:25–33. https://doi.org/10.1089/ind.2014.0024

15. Camarero-Espinosa S, Endes C, Mueller S, Petri-Fink A, Rothen-Rutishauser B, Weder C, Clift M, Foster E (2016) Elucidating the potential biological impact of cellulose nanocrystals. Fibers 4:21. https://doi.org/10.3390/fib4030021
16. Yanamala N, Farcas MT, Hatfield MK, Kisin ER, Kagan VE, Geraci CL, Shvedova AA (2014) In vivo evaluation of the pulmonary toxicity of cellulose nanocrystals: a renewable and sustainable nanomaterial of the future. ACS Sustain Chem Eng 2:1691–1698. https://doi.org/10.1021/sc500153k
17. Cullen RT, Searl A, Miller BG, Davis JMG, Jones AD (2000) Pulmonary and intraperitoneal inflammation induced by cellulose fibres. J Appl Toxicol 20:49–60
18. Hadrup N, Knudsen KB, Berthing T, Wolff H, Bengtson S, Kofoed C, Espersen R, Højgaard C, Winther JR, Willemoës M, Wedin I, Nuopponen M, Alenius H, Norppa H, Wallin H, Vogel U (2019) Pulmonary effects of nanofibrillated celluloses in mice suggest that carboxylation lowers the inflammatory and acute phase responses. Environ Toxicol Pharmacol 66:116–125. https://doi.org/10.1016/j.etap.2019.01.003
19. Park E-J, Khaliullin TO, Shurin MR, Kisin ER, Yanamala N, Fadeel B, Chang J, Shvedova AA (2018) Fibrous nanocellulose, crystalline nanocellulose, carbon nanotubes, and crocidolite asbestos elicit disparate immune responses upon pharyngeal aspiration in mice. J Immunotoxicol 15:12–23. https://doi.org/10.1080/1547691X.2017.1414339
20. Ilves M, Vilske S, Aimonen K, Lindberg HK, Pesonen S, Wedin I, Nuopponen M, Vanhala E, Højgaard C, Winther JR, Willemoës M, Vogel U, Wolff H, Norppa H, Savolainen K, Alenius H (2018) Nanofibrillated cellulose causes acute pulmonary inflammation that subsides within a month. Nanotoxicology 12:729–746. https://doi.org/10.1080/17435390.2018.1472312
21. Catalán J, Rydman E, Aimonen, K., Hannukainen K.-S., Suhonen S, Vanhala E, Moreno C, Meyer V, da Perez DS, Sneck A, Forsström U, Højgaard C, Willemoes M, Winther JR, Vogel U, Wolff H, Alenius H, Savolainen KM, Norppa H (2017) Genotoxic and inflammatory effects of nanofibrillated cellulose in murine lungs. Mutagenesis 32:23–31. https://doi.org/10.1093/mutage/gew035
22. Shvedova AA, Kisin ER, Yanamala N, Farcas MT, Menas AL, Williams A, Fournier PM, Reynolds JS, Gutkin DW, Star A, Reiner RS, Halappanavar S, Kagan VE (2015) Gender differences in murine pulmonary responses elicited by cellulose nanocrystals. Part Fibre Toxicol 13:28. https://doi.org/10.1186/s12989-016-0140-x

Effect of Masked Abrasive Waterjet Texturing on Surface Roughness Using Taguchi Method

Hafiz Husin, Norman Zaidi, M. A. Gebremariam, and Azmir Azhari

Abstract High pressure waterjet technology has received a wider acceptance for various applications involving machining, cleaning, surface treatment and material cutting. Surface texturing is a popular method to improve the wear resistance of a surface. The present study applied a masked abrasive waterjet texturing process to produce a circular crater on a surface of stainless steel 304. The effect of machining parameters namely traverse rate, water pressure, standoff distance and number of passes on the roughness of the crater surface was analysed. Taguchi method of experimental design was employed by utilizing the L_9 orthogonal array. The result shows that the water pressure is the most significant parameter in determining the roughness of the crater surface. Also, based on at the optimum parameters has shown an improvement of surface roughness as compared the initial optimal setting. The optimum parameters to deliver an improved R_a are u at 100 mm/s, p at 100 MPa, s at 5 mm and n at 1. This shows that the Taguchi method can be conveniently used to analyse the surface roughness during the AWJ texturing process of stainless steel 304.

Keywords Masked abrasive waterjet texturing · Surface roughness · Circular crater · Taguchi method

H. Husin (✉) · N. Zaidi · A. Azhari
Faculty of Manufacturing Engineering and Mechatronics Engineering Technology, Universiti Malaysia Pahang, 26600 Pekan, Malaysia
e-mail: hafidzuka@yahoo.com

H. Husin
Centre for Foundation Studies, International Islamic University Malaysia, 26300 Gambang, Malaysia

M. A. Gebremariam
College of Engineering, Universiti Malaysia Pahang, 26300 Gambang, Pahang, Malaysia

1 Introduction

The abrasive waterjet (AWJ) machining process has been used widely in many industrial applications. This technology is versatile to the material workpiece and flexible to machining since it has minimal chatter, no heat effect, and imposes minimal stress on the workpiece [1]. Compared with other processes, AWJ machining can machine almost any material since there is no heat damage, minimal force, and environmentally friendly [2]. The fundamental of the AWJ machining mechanism is by jetting a high pressure of water stream combined with abrasive particle force through a nozzle thus removing the surface material [3]. This high-velocity mixture with high kinetic energy jetted from the nozzle impinges the target material, causing the surface material to be eroded. Surface texturing is a technique widely used in industries to improve the surface wear resistance and its friction characteristics [4]. Surface texturing can be defined as purposely producing specific forms and shapes on material surfaces [5]. The surface texturing produces certain design features on surface structure for specific desirable purposes and functions [6]. This purpose includes producing specific surface geometry which affect its tactile friction as well as the look and feel for the sensation to the touch [7].

It is a challenge for AWJ machining process to generate small textures on the surface normally because the crater or channel width has a larger dimension than its waterjet stream diameter approximately greater than 0.5 mm [8]. Micro nozzle is recently available as tiny as 130 µm, nevertheless, reducing the size of nozzle remarkably may cause its blockage and inconsistency in abrasive flow [9]. A potential method to generate a smaller crater size during AWJ surface texturing is using a mask placed on the workpiece surface. Hence, the present study examines the effect of parameters during masked AWJ surface texturing in generating circular craters on the surface of stainless steel.

2 Main Experiment

2.1 Material

The material used in the present study is a commercially available tainless Steel SS304 having dimension of 25 mm (length) × 25 mm (width) × 4 mm (height).

2.2 Equipment

A commercial waterjet cutting machine was used for the entire experiment. It uses a pneumatic-driven water pump with water pressure capacity of up to 200 MPa. A computer numerically controlled (CNC) system manages the movement of the

nozzle in 3-dimensional directions. A ruby orifice having a diameter of 0.127 mm and a tungsten carbide focusing tube with diameters and lengths of 0.76 mm and 76.2 mm, respectively, were used for all experiments.

2.3 Experimental Design

The experiment was conducted using Taguchi method. Overall, four machining parameters were selected namely traverse rate (u), water pressure (p), standoff distance (s) and number of passes (n). Additionally, the type of material is also selected as another control factor in the Taguchi's design of experiments. With a total of five control factors, consequently, a L_9 orthogonal array with 9 rows which corresponds to the number of experiments was chosen. Table 1 shows the experimental layout using the L_9 orthogonal array and their measured surface roughness (R_a) values.

In all experiments, orifice diameter and impact angle were kept constant at 0.127 mm and 90°, respectively. During the experiment, a mask made of stainless steel 304 having a similar dimension and thickness of 2 mm was clamped together with the workpiece. The mask consists of many through holes with a diameter of 1 mm. The jet hits the workpiece by passing through the hole on the mask thus creating a crater over the surface as illustrated in Fig. 1a. The machining parameters were set to the intended levels based on the L_9 orthogonal array for each experimental run. Once all the parameters were set to their respective levels, then the workpiece were textured according to the row. Each row represents different experimental run as shown in Fig. 1b. The surface roughness measurement was determined by using a 3D measurement laser microscope (Olympus Lext OLS5000). The average roughness profile of three craters was assessed using the average arithmetic roughness parameters (R_a).

Table 1 Experimental design using L_9 orthogonal array

Experiment No.	u (mm/s)	p (MPa)	s (mm)	n	R_a (μm)
1	50	50	5	1	5.346
2	50	75	10	2	6.677
3	50	100	15	3	5.631
4	100	50	10	3	5.186
5	100	75	15	1	4.336
6	100	100	5	2	3.809
7	150	50	15	2	6.208
8	150	75	5	3	4.701
9	150	100	10	1	3.022
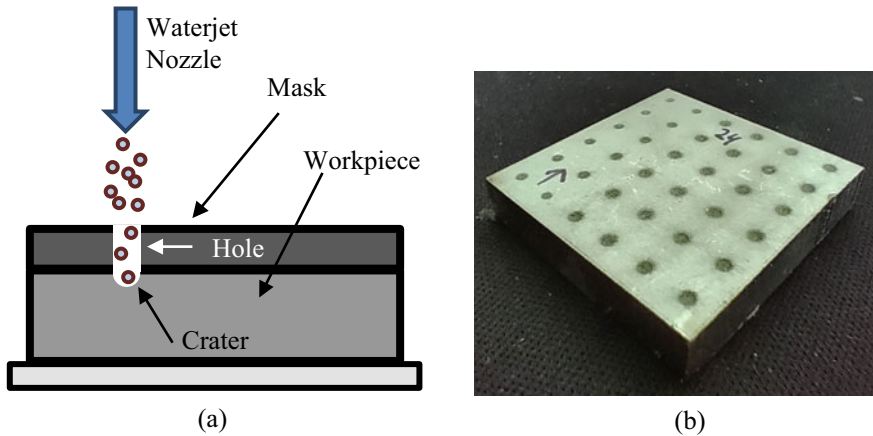
Fig. 1 **a** illustration of masked abrasive waterjet texturing process, **b** textured surface (arrow indicates the nozzle traverse movement)

3 Result and Discussion

3.1 *Effect of Process Factors on Surface Roughness*

An example of 3D surface structure of the crater is shown in Fig. 2a. Its roughness profile is shown in Fig. 2b. The values of R_a for the L_9 orthogonal array were determined to be between 3.022 and 6.677 µm as shown in Table 1.

The effect of parameters was analysed based on Taguchi's signal to noise (S/N) ratio. Based on the information of sample variances, it defines the relationship between the magnitude of the control factor effects and the magnitude of the experimental error [1]. The results of S/N ratio for each parameter in determining the crater surface roughness are shown in Table 2. It is ranked according to the criteria of having a smaller R_a is better (i.e., smaller the better). It can be observed that the pressure has the most significant effect on the surface roughness of the crater surface. It is then followed by the traverse speed and the number of passes. The standoff distance has the least significant effect on the surface roughness.

Figure 3 shows the main effect plot for S/N ratios. The mean S/N ratio shows the relative effects of various parameters on R_a during the AWJ surface texturing process, where a higher value of the mean S/N ratio is considered as a better quality characteristic [1]. According to Fig. 3, the optimum parameters for resulting in a smoother surface of the crater are given by the combination of traverse speed at 100 mm/s, pressure at 100 MPa, standoff distance at 5 mm and the number of passes at 1. A confirmation test was later conducted at the optimum combination of parameters. This test is used to verify the improvement of R_a against the initial parameter setting at middle levels for all parameters (i.e., u at 100 mm/s, p at 75 MPa, s at 10 mm and n at 2). It was found that the R_a at the optimum parameters has improved to

(a)

(b)
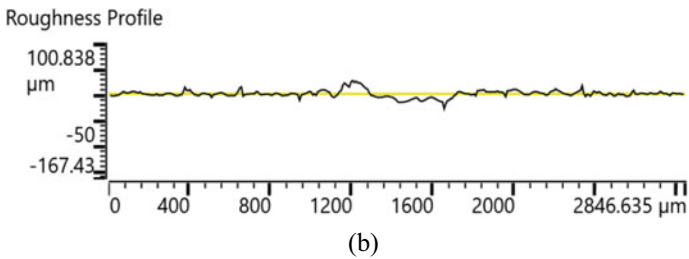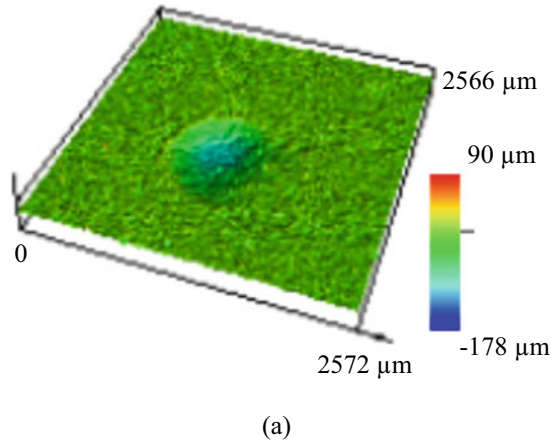
Fig. 2 **a** 3D structure of crater surface for experimental run no. 1, **b** roughness profile of crater surface for experimental run no. 1

Table 2 Response table surface roughness

Level	Traverse speed	Water pressure	Standoff distance	Multi passes
1	−15.35	−14.91	−13.21	−12.30
2	−12.88	−14.23	−13.46	−14.66
3	−12.97	−12.08	−14.54	−14.25
Delta	2.47	2.83	1.33	2.35
Rank	2	1	4	3

3.12 μm from the initial optimal setting with R_a of 3.5698 μm. 3D structure of the crater surface at optimum parameters is shown in Fig. 4a. Its roughness profile is shown in Fig. 4b. Although, the R_a at the optimum parameters is slightly higher than experiment number 9 with R_a of 3.022 μm, the difference is almost negligible. Therefore, this shows that Taguchi's S/N ratios can be conveniently used to optimize the surface roughness during the AWJ texturing process of stainless steel 304.
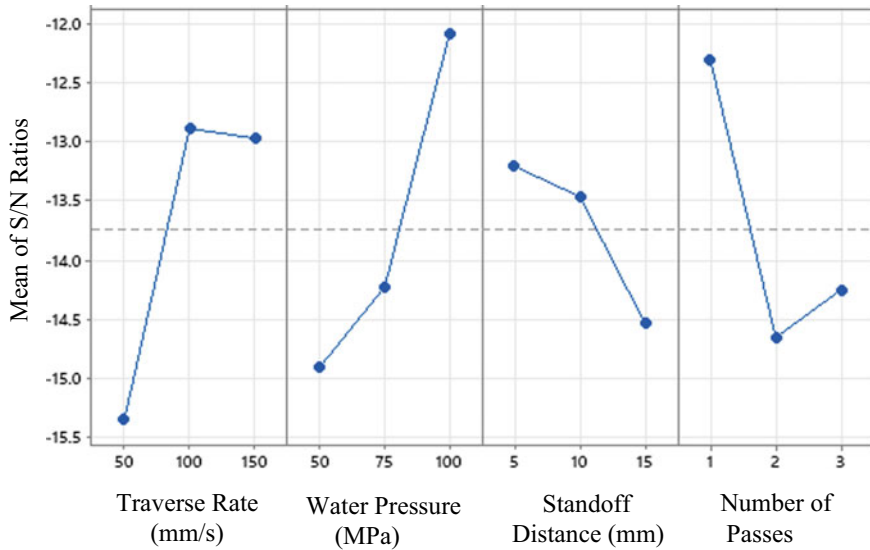
Fig. 3 Main effects plot for S/N ratios

3.2 Modeling

In the present study, the predictive model based on linear regression analysis for R_a as a function of traverse speed, pressure, standoff distance, and the number of passes was developed using Minitab software tools. The predictive model is shown in Eq. 1.

$$R_a(\mu m) = 6.66 - 0.01241u - 0.0285p + 0.0773s + 0.469n \qquad (1)$$

The residual plot was used to check the significance of the predicted model. The capability of the model was determined by the value of R^2, which was found about 0.71. This value is closer to 1 thus indicating that the model is capable to sufficiently predict the surface roughness of the crater within the limit of the present study [10]. The residual plot for the study is shown in Fig. 5. The plot shows that the residual falls nearly straight line thus suggesting the significance of the model produced.

4 Conclusion

The optimization of the parameters in producing a smoother circular crater during AWJ texturing process of stainless steel 304 was successfully conducted using the Taguchi method. The optimum parameters to deliver an improved R_a are u at 100 mm/s, p at 100 MPa, s at 5 mm and n at 1. The optimum parameters have shown an improvement of surface roughness as compared the initial optimal setting.

2565 μm

88 μm

0

-101 μm

2572 μm

(a)

Roughness Profile

88 μm

-101 μm

0   400   800   1200   1600   2000   2846.635 μm

(b)
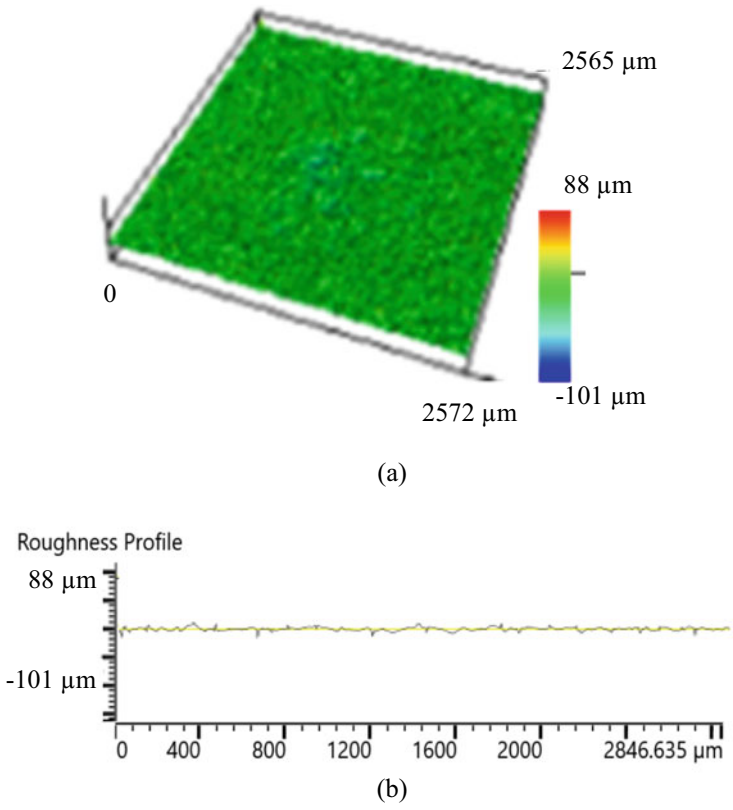
Fig. 4 **a** 3D structure of crater surface for optimize parameter, **b** roughness profile of crater surface for optimize parameter

This shows that the Taguchi method can be conveniently used to analyse the surface roughness during the AWJ texturing process of stainless steel 304.
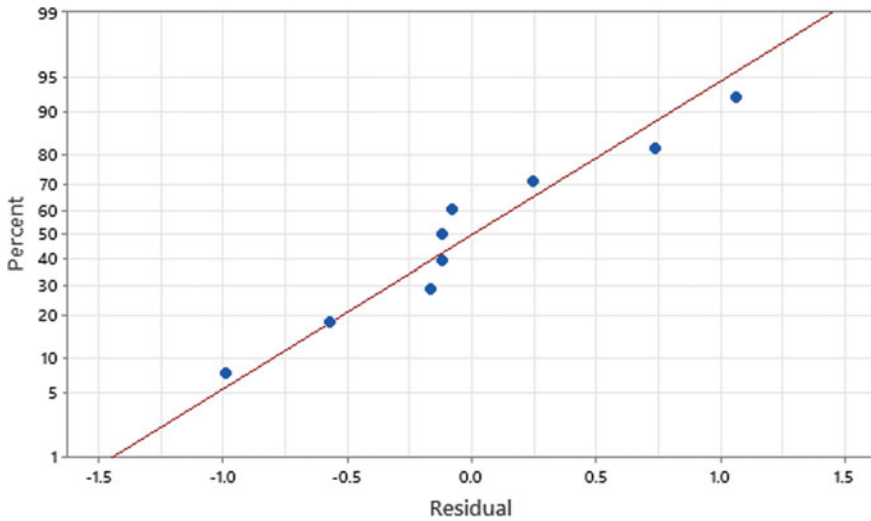
Fig. 5 Normal probability plot of the residual for surface roughness

References

1. Azmir MA, Ahsan AK (2008) Investigation on glass/epoxy composite surfaces machined by abrasive water jet machining. J Mater Process Technol 198(1–3):122–128
2. Folkes J (2009) Waterjet—an innovative tool for manufacturing. J Mater Process Technol 209(20):6181–6189
3. Supriya SB, Srinivas S (2018) Machinability studies on stainless steel by abrasive water jet—review. Mater Today Proc 5(1):2871–2876
4. Won SJ, Kim HS (2019) Effects of laser parameters on morphological change and surface properties of aluminum alloy in masked laser surface texturing. J Manuf Process 48(May):260–269
5. Gropper D, Wang L, Harvey TJ (2016) Hydrodynamic lubrication of textured surfaces: a review of modeling techniques and key findings. Tribol Int 94:509–529
6. Stout KJ, Blunt L (2001) A contribution to the debate on surface classifications—random, systematic, unstructured, structured and engineered. Int J Mach Tools Manuf 41(13–14):2039–2044
7. Van Kuilenburg J, Masen MA, Groenendijk MNW, Bana V, Van Der Heide E (2012) An experimental study on the relation between surface texture and tactile friction. Tribol Int 48:15–21
8. Husin H, Nawi MNM, Gebremariam MA, Azhari A (2021) Investigation on the use of mask in waterjet surface texturing of stainless steel BT—recent trends in manufacturing and materials towards Industry 4.0, pp 519–525.

9. Melentiev R, Fang F (2018) Recent advances and challenges of abrasive jet machining. CIRP J Manuf Sci Technol 22:1–20
10. Sivaiah P, Chakradhar D (2019) Modeling and optimization of sustainable manufacturing process in machining of 17–4 PH stainless steel. Meas J Int Meas Confed 134:142–152

Heat Conduction Modelling of Battery Thermal Management System for Electric Vehicle

W. I. H. W. Mohamad, F. R. M. Romlay, M. A. H. Rasid, I. Ishak, and A. Ghazali

Abstract A battery thermal management system is crucial for electric-vehicle (EV) and hybrid-vehicle (HV) battery packs to operate effectively in all climates. Battery packs are critical components of electric vehicles. The system is designed for higher life cycles utilization. However, temperature affects the performance and life span of the batteries. Keep the temperatures distribution low within the operating temperature range among all modules and battery cells is the main factor to increase the life of the battery system. This paper studied the effects of having the ventilation system by positioning the air inlets and outlets with and without heat sink as greater heat dissipates among battery packs. The heat dissipation and temperature distribution determine the battery life span. A computational fluid dynamics model was created for the purpose to analyze the temperature distribution and airflow profile. The battery pack was designed to keep the compartment smaller but with better cooling efficiency. The results show that the locations and shapes of inlets and outlets have a significant impact on battery heat dissipation. A strategy was proposed to minimize the temperature variation of the battery cells compartment. The temperature changes between the highest and lowest ones for the evaluated event are reduced from 26.04 to 23.67 °C and the heat dissipation rate is improved by 9.10%.

Keywords Electric vehicle · Computational Fluid Dynamic and Battery Thermal Management System

W. I. H. W. Mohamad · F. R. M. Romlay (✉) · M. A. H. Rasid · I. Ishak
Machine Manufacturing Union in Mechatronics Laboratory, Manufacturing Focus Group, Universiti Malaysia Pahang, 26600 Pekan Pahang, Malaysia
e-mail: fadhlur@ump.edu.my

A. Ghazali
Sapura Technical Centre, No 11, Jalan P/1, Section13, Kawasan Perindustrian Bangi, 43650 Bandar Baru Bangi, Selangor, Malaysia

1 Introduction on Electric Vehicle

People have paid great attention to global warming, which is recognized mainly because of greenhouse gas emissions from fossil fuel combustion. Electric vehicles (EVs) are the mainstream of future transport vehicles to help ease global warming and the depletion of crude oil. A battery pack as the main power source of EV is required to meet high energy and power density, long life cycle, long lifetime, and so on. Lithium-ion batteries are one of the common energy storage systems for electric vehicles. Generally, the battery pack has several battery modules or cells in series and/or in parallel to achieve the required voltage and capacity. In the case of long-distance travel, the vehicle would be equipped with a larger battery pack and therefore a large amount of heat. Single-cell overheating and failure can occur and degrade the performance of the entire pack; therefore, a favorable ventilation system design can quickly remove the enormous heat generated by high power demand (hard acceleration, climbing, etc.) and maintain the performance of the battery pack. The common ventilation systems are air-cooling, liquid-cooling, phase change cooling, or any combination. Air cooling system has the advantages of simple structure, lightweight, low cost, easy maintenance and repair, and no liquid leakage problems. It is suitable for electric vehicles. Temperature affects the battery's performance and lifespan. Well distributed temperatures within the operating temperature range amongst all modules and battery cells are one of the key factors to prolong battery life.

High temperatures degrade the life of the Li-ion batteries, while cold temperatures reduce the power and energy performance of the EVs, thus limiting the driving range and performance of the EVs[1]. Li-ion batteries using olivine-type lithium-iron-phosphate (LiFePO4) cathode have attracted a great deal of attention as a power source for EVs and HVs due to their low material cost and non-toxicity. Their weakness, however, is the temperature that affects their performance, safety, and life. Both [2] and [3] reported that, although the capacity increases as the operating temperature are raised, the degree of capacity fade also increases. Both reported poor performance at low operating temperatures.

The battery design optimization is used to maintain the batteries operating at a desirable temperature range, thus preventing them from exceeding the high-temperature limit that can damage the batteries or reduce their life. Moreover, the uneven temperature distribution in the battery pack leads to unbalanced battery cells and reduced performance. Several battery optimizations, use mainly air cooling [3], liquid cooling [4] or phase-change materials (PCMs) [5].

2 Electric Vehicle Technology Review

Battery Electric Vehicles (BEVs) have an internal energy source an electric motor powered by electrical batteries located in the vehicle. The powertrain gives BEV

the possibility to utilize with zero emissions at the place of use. Many of the engineered solutions embraced for the construction of BEVs also make use of the "energy recovery" technologies that allow the electric motor to be used both as a source of propulsion and as a generator when braking or when the vehicle moves freely under gravitational action. The advantages of using BEV in traffic are the high torque of the electric motor that is distributed to the wheels and the simpler air resistance (and deceleration) compared to the internal combustion engine (ICE) vehicles. BEVs also do not emit noise while using an electric motor and do not generate environmental pollution [6]. The aspects make BEVs the ideal vehicles to be used in cities and urban areas.

On the other hand, the actual terminal voltage of the battery E_{emf} detracts from the electromotive balance force (electrode potential) due to the electrochemical polarization of the battery. This method yields Q_p heat, which is a loss of energy during the polarization of the battery charge and discharge. $Q_p = I2R_p$, where R_p is the polarization resistance that is associated with the polarization process. Finally, the Joule heat Q_j is generated due to the internal ohm resistance of the battery the heat generated during the charging/discharge process is $Q_j = I2R_i$, where R_i is the internal ohm resistance of the Li-ion cell.

Xu et. al. conducted a CFD and observational heat transfer performance study of the symmetrical fractal silicon thin-film network under-stimulation [7]. The results showed that the heat transfer rate at pulsation frequency (2–10 and 30–40 Hz) increased by 25–40 percent and was significantly greater than that at (10–20 Hz) when the Re number remained constant. By raising the Re number, the enhancement factors dropped significantly from 40 to 5% for the above frequency range, as opposed to steady-state cases. Doubling the frequency of Re caused a drop in the wall temperature and an increase in the number of Nu. There was no big variation in the pressure drop between steady and pulsed flow cases [7].

Yu et. al. have studied numerically the effect of agitator plates inserted within the HS channels to enhance the heat transfer by antagonism [8]. Periodic motion in the radial direction generated by the agitator plate increased the thermal efficiency. Maximum heat transfer results and insights were approximately 61% by agitation. They tracked a sharp enhancement in heat transfer on the base surface as the size of the tip gap between the agitator plate and the channel was reduced. On the other hand, there was no effect of the size of the tip gap observed on the heat transfer on the side walls. Higher thermal conductivity rate from the channel wall was measured when the amplitude or frequency of the agitator plate risen. It can be seen that there was very limited research in this area of research the cooling mechanism used to remove heat from heat sinks is one way of categorizing heat sinks. It can be divided into two categories [9]. Passive heat sinks are used either in natural convection implementations or in applications where heat dissipation does not rely on a demarcated airflow supply. Typical height at heat inlet: 10 mm to large. Standard load limit 5–50 W. Semi-Active Heat Sinks leverage existing fans in the system. Typical height at heat inlet: -10 mm. Load limit 15–25 W. Active Heat Sinks use designated fans for their use, such as ventilator heat sinks in either impingement or vertical streams. This type of heat sink usually involves mechanically moving components, and its

reliability depends heavily on the reliability of the moving parts [10]. The heat sink is the most critical part of the proposed. It must have a large size to have a small thermal resistance value and a volume and weight that can be tolerated for EV applications. The heat sink absorbs the power pumped from battery cold surfaces and the heat generated by itself. Heat sink performance affects the system's highest possible temperature range and excellent thermal stability [2]. The heat sink selected should be capable of dissipating the power generated by the Lead-acid cell (Qc = 6 W).

CFD can provide insight into flow patterns that are difficult, expensive, or impossible to study using methodological approaches. Experiments can provide a quantitative description of flow phenomena using observations for one quantity at a time, at a limited set of characteristics and times. If a full-scale model is not obtainable or is not practical, scale models or dummy models may be used. Experiments may have a limited range of problems and operating conditions. Simulations can predict flow profiles by applying computer-aided CFD software for all desired parameters, with a function of space and time, and virtually any problem and realistic operating conditions. For confirmation, the results may need to be validated. To maintain the reliability of the mesh size, the length of the fluid may need to be affirmed. We used CFD post-processing software, SOLIDWORK, in this study. The mesh size of 5 mm is chosen for the whole pack.

3 Methodology of Electrical Vehicle Battery Pack Simulation

3.1 Heat Transfer Analysis

An analysis on battery thermal management was conducted through computational fluid dynamic (CFD) flow simulation to obtain the heat flow, making the study of the thermal analysis overall. The heat sink performance considered the material thermal conductivity, compartment geometry, fin-type, heat transfer coefficient, airflow rate, and ducting components arrangement. A conceptual approach can be made to evaluate the surface performance of the heat sink (Fig. 1).

Alternatively, thermal performance may be measured experimentally by the temperature sensing approach. This chapter will discuss the mentioned methods for the determination of the thermal effect to the battery compartment of the electric vehicle system. Aluminum alloys are the most common and effective heat sink materials which are in this study specifically choose aluminum alloys 6061 grade (Table 1).

The fin shape of a heat sink can significantly impact its ability to distribute thermal energy into the environment. The quantity and size of the fin determine the efficiency of the heat transfer components as a medium to release the heat faster. For a better concept design, the fins are not in any cover but attach to a flat solid aluminum plate. This is a way to increase the opening surface area to the air.
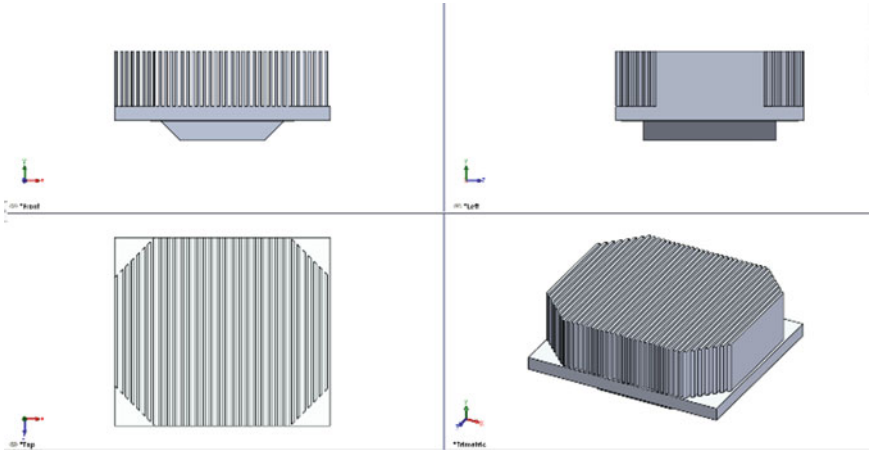
Fig. 1 Flat straight fin heat sink

Table 1 Heat properties

Properties	Description
Thermal load (heat power)	6.0 W
Power	576 W
Convection coefficient	28 W/(m^2 K)
Temperature	303 K
Material	Aluminum Grade 6061

3.2 Computational Fluid Dynamic (CFD) Analysis

To obtain the airflow simulation on the battery pack thermal management, a simulation is performed by using SOLIDWORK flow simulation 2020. The input data and mesh generate should be recognized for the software to perform simulation. In SOLIDWORKS flow simulation a wizard study is created, and the properties for the material involved is being set as shown in Table 2.

The heat sink was selected as the component which the material is aluminum 6061 while the battery pack casing was made up of alloy substance. The heat generation mode of CFD was selected which aligns with the airflow investigation study and the

Table 2 CFD basis assumption

Properties	Description
Model type	Linear elastic isotropic
Default failure criterion	Maximum Von Mises stress
Specific heat	900 J/(kg K)
Mass density	2700 kg/m^3

Table 3 CFD properties and setup

Parameter	Description
Mode	Heat generation rate
Coordinate system	Global coordinate system
Heat generation rate	6.0 W
Flow parameters	Inlet flow vector direction: normal to face
Thermodynamic parameters	Environment pressure: 101,325.00 Pa
Turbulence parameters	Turbulence intensity and length Intensity: 0.10% Length: 0.003 m

fluid condition was set up as an air parameter. In CFD analysis, two types of goals were set which were the global goal and surface goals, both goals were selected in an average type of goal to be calculated. Global goal mainly focused on the fluid temperature, overall compartment temperature, and wall temperature. Detailed of the setup are tabulated in Table 3 while the mesh properties are specified in Table 4.

Before the CFD simulation being run, all opening sections of the geometry must be closed as a defined boundary condition. The feature was constructed by inserting a lid feature and the size of the computational domain need to be greater than the battery pack compartment

Table 4 CFD mesh properties and setup
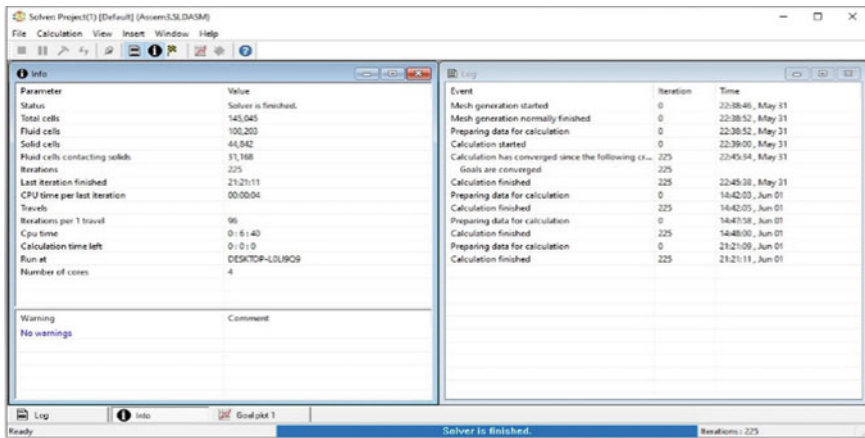
4 Battery Pack with Heat Sink

Figure 2 shows the installation of PID fan controller assembly with heat sink being placed on top of the battery component, this section shows how the arrangement of the battery thermal management is set up. Mainly two cases were focused and highlighted. The first one has simulated the inlet air intake without the heat sink meanwhile for the second case study was the heatsink that was placed on top of the battery compartment.

The idea is to maintain a constant temperature by controlling the speed of a fan by changing its supply voltage. It uses a PID (Proportional-Integral-Derivative) control algorithm to calculate the adequate power % to apply to the fan, through a PWM controlled MOSFET. The goal design builds a system to maintain the right temperature at the battery pack. It can be used in any forced ventilation application though.

Figure 3 shows the geometrical configuration of a plate-fin sink with a horizontal inlet cooling flow. Both the base size and the width are 50 mm. The total heat dissipation of 6 W is uniformly applied over the base plate of the heat sink with a base thickness of 20 mm. The thermal conductivity of the heat sink is 200 W/m K. The ambient air temperature is 25 °C. The conductivity of the air is 0.0267 W/m K and the air density is 1.177 kg/m. The task is to determine the maximum temperature on the heat sink to operate at the optimum range. This material Aluminium alloys 6061 with thermal conductivity values of 201 W/m K is operated with a thermal load (heat power) of 6 W which we get by using the online micro calculator in determining the thermal load.
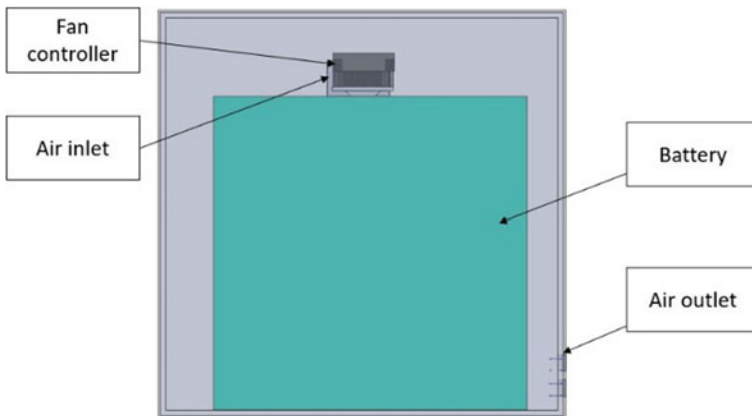
Fig. 2 Components arrangement of the EV battery pack

Name	Type	Min	Max
Thermal1	TEMP: Temperature	6.785e+01Celsius Node: 1657	8.328e+01Celsius Node: 2602
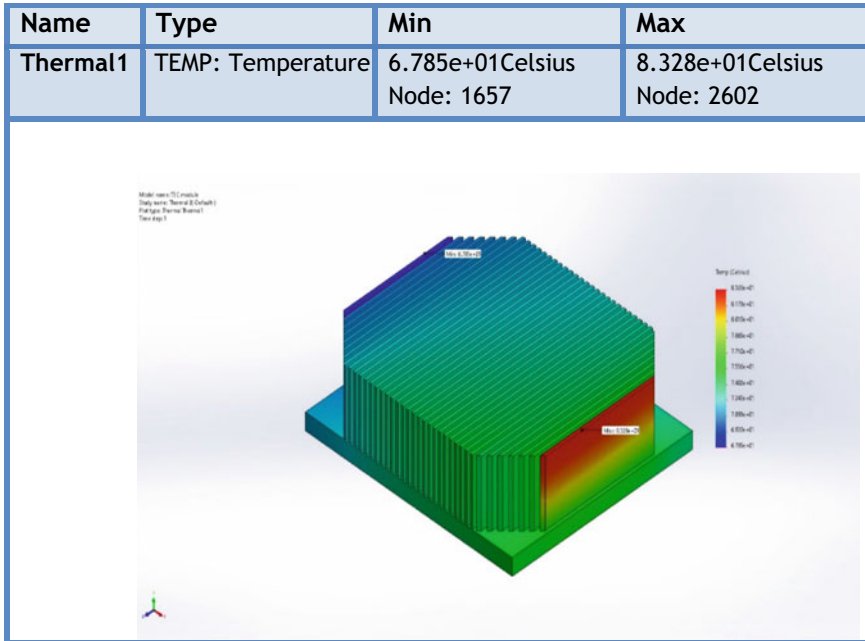
Fig. 3 Heat sink thermal temperature distribution

5 Flow Trajectories

Figure 4 shows the streamline arrow of the first case study whereas the fan blower only without heatsink is being placed up at the inlet of air intake. As can be seen in the figure the streamline is in a cool state, but the air streamlines are not uniformly from the air inlet through the fan and exit through the outer lid. The streamline of the airflow at 6.0 W is illustrated below.

Figure 5 shows the streamline arrow of the second case study whereas the fan blower and heatsink were being placed on top of the battery compartment. As can be seen in the figure, the streamline is in a cool state where the heat is dissipating uniformly from the air inlet through the fan and exits through the outer lid. The streamline of the airflow at 6.0 W.

From the parametric analysis on the power rate, the fan speed, and the location of the heatsink on the thermal performance, it is found that the temperature distribution among the battery cells is not even within the battery module for the first case study. It was found that even the authors change the three key parameters in a large range, the temperatures on the rear battery cells are still larger than those on the front battery cells.

However, the temperature uniformity distribution for the second case study which shows a greater airflow distribution and the heat dissipation flow has a great impact on the capacity and battery cycle life. Extensive studies have shown that a high

Fig. 4 First case of the CFD simulation without heat sink
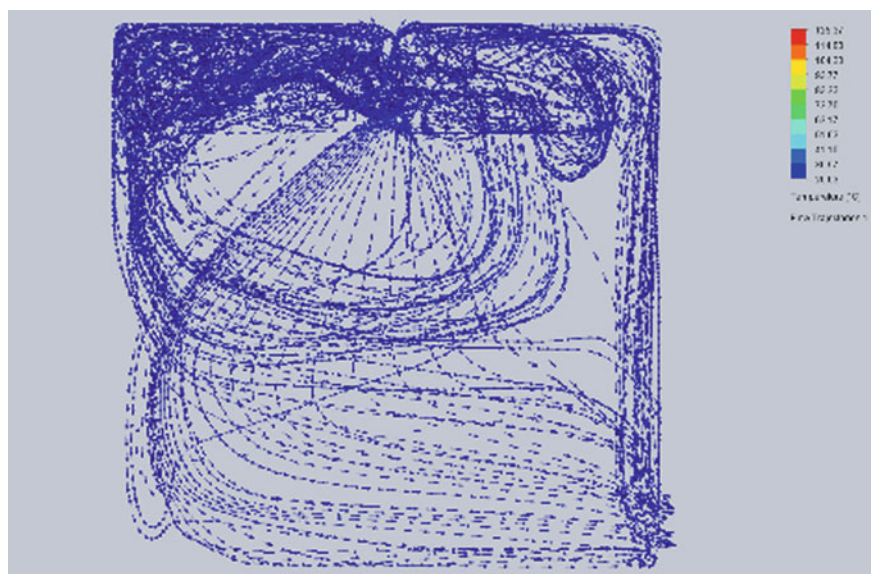
Fig. 5 Second case of the CFD simulation with heat sink

temperature will accelerate the degradation of the capacity and shorten the life cycle (Fig. 6).

The temperature uniformity of a single battery cell is affected by its intrinsic properties, such as electrode and electrolyte materials, thermal conductivity, battery dimensions, and extrinsic factors like convection heat transfer coefficient and media. The temperature uniformity of a battery module is affected by the passage spacing size, cooling air, manifold configuration, and others.

Based on Fig. 7, due to the heat taken away by the cooling air, the cooling air temperature plays an important role in the temperature on the battery cell. The figure shows the specific heat and thermal conductivity of the heatsink that is being placed in the battery pack.
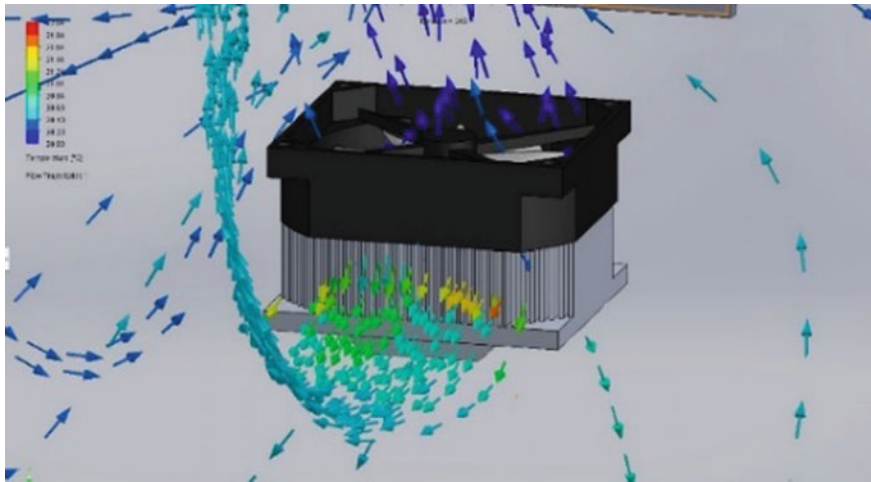
Fig. 6 Second case CFD simulation focused on heat sink
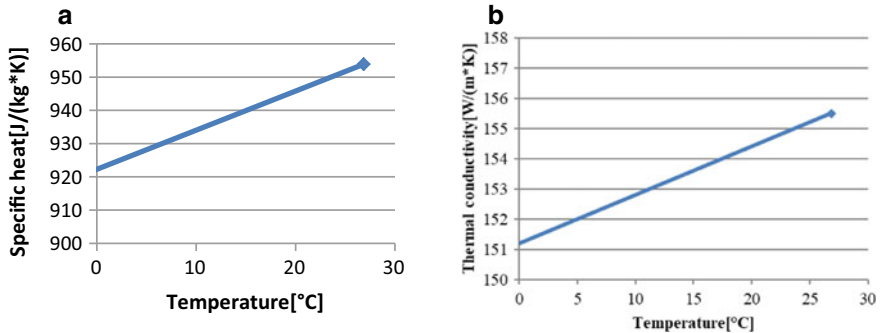
Fig. 7 **a** Specific heat of heat sink, **b** thermal conductivity heat sink
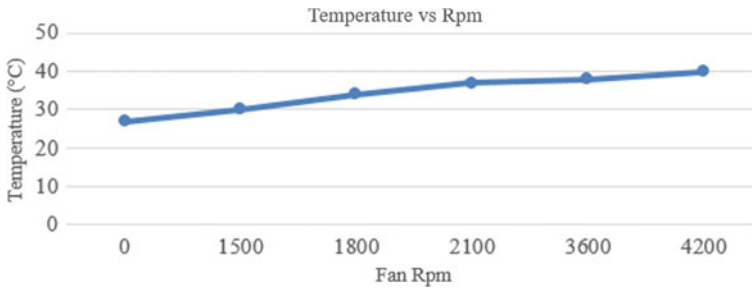
Fig. 8 Temperature versus RPM graph

During the study on the 1 case it shows, due to the pressure drop in the manifold, it is challenging to eliminate the pressure difference when the inlet is being placed as the fan blower for the battery pack. This causes the flow area of each passage to be another factor that largely affects the distribution of the passage heat flow. Thus, the heatsink fan blower is placed on top of the battery because it shows a greater uniform of airflow streamlines, causing the temperature to drop greater.

Figure 8 shows the temperature of the surrounding in the battery pack, when the temperature sensor detects an increase of heat, the fan speed or Rpm will increase radiantly with temperature. The Figure shows the increases in the temperature that triggers the fan speed.

The thermal efficiency of the optimized battery pack based on the maximum and minimum temperature is gain from the heat sink dissipation. The heat-sink can reduce 2.37 °C or 9.10% more dissipation performed around the battery compartment.

6 Conclusions

This study presents a heat sink and PID fan as a type of air-cooling ventilation system for an electric scooter battery pack that differs from the typical ventilation system by relocating cooling air inlets and outlets, modifying inlet forms, and combining with a PID fan system to the battery pack. According to simulation results, the design of battery ventilation can effectively reduce the maximum temperature and the maximum temperature difference in the pack, the temperature difference between the highest and lowest ones for the evaluated event is reduced from 26.04 to 23.67 °C and the heat dissipation rate is improved with 9.10%. The uniformity of the temperature distribution has an improvement of 9.10%. which eventually extends the service cycles of the battery cells and enhances the reliability of the battery pack. As to the conceptual design stage, with the help of the CFD simulation technology, one can quickly predict the result of the ventilation system design which shortens the development process to achieve the purpose of cost-saving.

References

1. Shkarah AJ et al (2013). A 3D numerical study of heat transfer in a single-phase micro-channel heat sink using graphene, aluminum and silicon as substrates. Int Commun Heat Mass Transf 108–115
2. Fan YZ (2021) Optimization of cooling strategies for an electric vehicle in high-temperature environment. Appl Thermal Eng
3. Li H-Y, Chen K-Y (2007) Thermal performance of plate-fin heat sinks under confined impinging jet conditions. Int J Heat Mass Transf 50:1963–1970
4. Li H-Y, Chao S-M (2009) Measurement of performance of plate-fin heat sinks with cross flow cooling. Int J Heat Mass Transf 52:2949–2955
5. Lee C, Chen R (2015) Optimal self-tuning PID controller based on low power consumption for a server fan cooling system. Sensors
6. Lee DW (2014) Development of BLDC motor and multi-blade fan for HEV battery cooling system. Int J Autom Technol
7. Liu M et al (2011) Experimental study on liquid flow and heat transfer in micro square pin fin heat sink. Int J Heat Mass Transf 54:5602–5611
8. Pesaran AA (2001) Battery thermal management in EV and HEVs: issues and solutions. Battery Man 43(5):34–49
9. Qu Z et al (2012) Passive thermal management using metal foam saturated with phase change material in a heat sink. Int Commun Heat Mass Transf 39:1546–1549
10. Pesaran A, Keyser M, Burch S (1999) An approach for designing thermal management systems for electric and hybrid vehicle battery packs. National Renewable Energy Laboratory, Golden

Development of Mg-Graphene Composites and Effect on Microstructure and Mechanical Properties—A Review

J. Alias, N. F. A. Bakar, M. A. F. Romzi, M. I. M. Ramli, and N. A. Alang

Abstract The role of GNPs in magnesium matrix composites and their influence on the development of microstructure and mechanical properties are reviewed thoroughly. Magnesium (Mg) is a well-known light metal that is used in a variety of engineering applications, particularly as biodegradable implant materials and automotive engine parts. However, the potential of Mg in a wide range of applications is limited by its low strength and high activity in most environments. More research is needed to improve its strength and ductility, either through the development of alloys or composite materials. Because of their low density and superior specific properties, Mg metal matrix composites (Mg-MMCs) are appealing materials. Two-dimensional GNPs with distinct electrical, mechanical, and thermal conductivity properties are being considered as intriguing reinforcement. The use of GNPs as reinforcement in Mg-MMCs effectively serves as a strengthening potential for the development of new lightweight, high-strength, and high-performance Mg matrix nanocomposites. This paper discusses the effect of GNPs on the mechanical characteristics and microstructure of magnesium as a guide to the development of more promising Mg material.

Keywords Graphene · Magnesium · Grain refinement · Strengthening mechanism

J. Alias (✉) · N. F. A. Bakar · M. A. F. Romzi
Department of Mechanical Engineering, College of Engineering, Universiti Malaysia Pahang, 26300 Gambang, Kuantan, Pahang, Malaysia
e-mail: juliawati@ump.edu.my

Present Address:
M. I. M. Ramli
Automotive Excellence Centre, Faculty of Mechanical and Automotive Engineering Technology, Universiti Malaysia Pahang, 26600 Pekan, Pahang, Malaysia

N. A. Alang
Faculty of Mechanical and Automotive Engineering Technology, Universiti Malaysia Pahang, 26600 Pekan, Pahang, Malaysia

1   Introduction

Magnesium, with a solid-state density of 1.74 g/cm^3, has piqued the interest of the aerospace and automotive industries as the lightest conventional structural metal state [1–4]. It facilitates weight reduction in the transportation industry, which improves fuel efficiency [5, 6]. When compared to other metals, magnesium is weak, ductile, and corrosion resistant. Many alloys and composite materials have been developed to help alleviate the problem [7–11].

Composite materials have the ability to integrate reinforcing phase qualities with matrix phase properties, resulting in composite materials that surpass their monolithic counterparts in terms of characteristics [12–14]. Their properties can be tailored to the end user by carefully choosing the reinforcement phase, matrix phase, and production technique. Magnesium-matrix composites (MMCs) can be made by dispersing reinforcing particles in the metal magnesium using either solid- or liquid-phase processes.

Carbon nanotubes (CNTs) have received a lot of attention in recent years as a reinforcement to boost the strength of magnesium and its alloys. However, the limitation of CNTs are its negative impact on ductility, and the application using CNTs as an industrial reinforcement for composites leads to poor dispersion in the matrix caused by agglomeration due to van der Waals forces between carbon atoms [7, 15–17]. Graphene has also been employed in various applications, such as metal-graphene composites, electronics material and polymer reinforcement. In the realm of thermal interface materials, graphene (a thermally conductive nanomaterial) was exploited as an outstanding filler (TIMs). The strong graphene bonding (a single atomic layer of sp2 hybridised carbon) to the metal matrix particles increased the heat conductivity of the resultant composite by up to 2300%. Nonetheless, there have been few research on the application of graphene for metal reinforcement [18–23]. As a result of its unique features, graphene is gaining extensive interest for usage as a reinforcing material.

The effect of graphene on the microstructure and mechanical properties of magnesium is reviewed in this article. The potential of graphene as a magnesium reinforcement material can be significant in the exploration of magnesium's wide range of applications.

2   Microstructure Development of Graphene-Mg Composites

GNPs have received a great deal of attention in recent years as a two-dimensional material. GNPs and their derivatives have been demonstrated in several studies to have the potential to be utilised as reinforcement to improve the performance of metals and composites. Various study reports have identified better mechanical, microstructural and interface properties of GNPs/Mg composites [19, 24–27], GNPs/Al [28–31]

and GNPs/Ti [32–36]. However, an excessive number of carbon layers may degrade graphene's good characteristics [37].

Reference [38] investigated the microstructure of AZ80 magnesium alloy with incorporation of GNPs produced by rheo casting and hot extrusion process. The microstructure characterization was performed by field emission scanning electron microscopy (FESEM). The FESEM micrograph of GNPs is shown in Fig. 1. The GNPs is characterized by 4–12 μm in internal length, and thickness of 2–18 nm. The microstructure having significant carbon accumulation (Fig. 2), and the element map indicated the carbon element that can be found in the matrix of both composites. They concluded that the accumulation of carbon increases with the increase in GNPs. The Van der Waals interaction between carbon layers and the huge GNP surface area was implicated for the accumulation of carbon [37].

According to Parizi et al. [38], GNPs were also found to be embedded within the Mg matrix and segregated at the eutectic particle distribution (Fig. 3). GNPs may be present in α-Mg grains as a result of α-Mg grains nucleating on GNP surfaces and engulfing GNPs within the solidification front. As depicted in Fig. 4, the grain structure of as-cast AZ80 alloy composed a typical semi-coarse dendrites structure. Addition of GNPs revealed a transition of much coarser and globular dendritic structure. The change in grain morphology is attributed to the increase molten slurry friction caused by the presence of GNPs during the stirring process.

Earlier, by using a semi powder metallurgy method followed by hot extrusion, Rashad [39] produced a magnesium-10 wt% titanium alloy with the addition of 0.18 wt% GNPs. The surface of pure magnesium is smooth and free of macrostructural defects, indicating good bonding between magnesium particles and reinforcement. The grain boundaries are visible from the micrograph and also presence of small pores. However, the presence of Ti-GNPs nanoparticles in the Mg matrix is

Fig. 1 FESEM micrograph of as received GNPs [38]
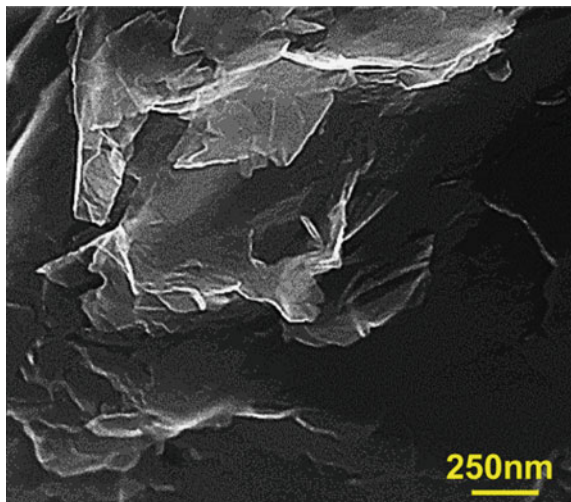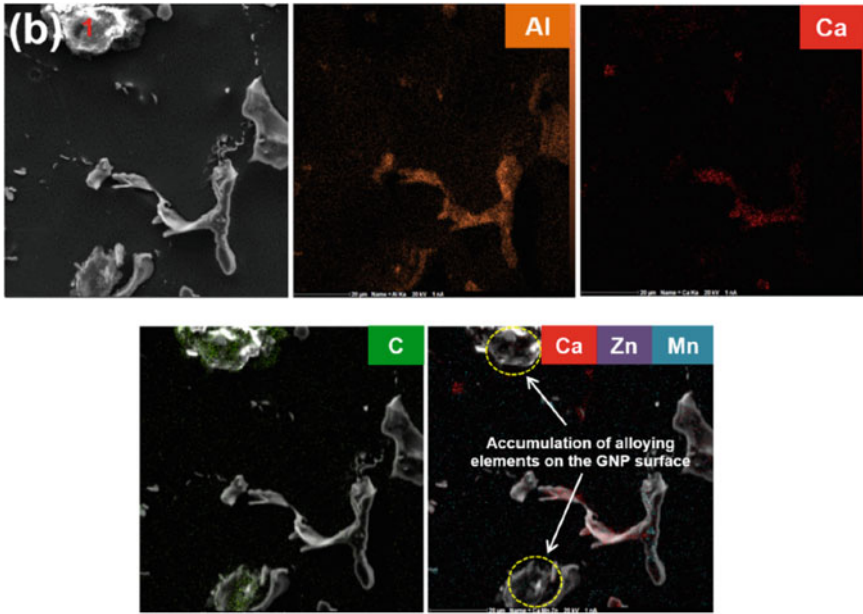
Fig. 2 FESEM images and element maps of AZ80 with 0.1 GNPs composite [38]
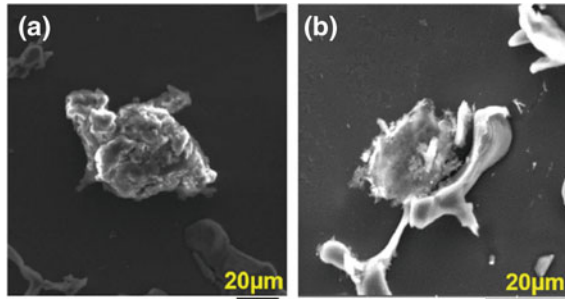
Fig. 3 FESEM images indicated the distribution of GNPs **a** within the α-Mg matrix grain, **b** in close vicinity to the eutectic phase [38]
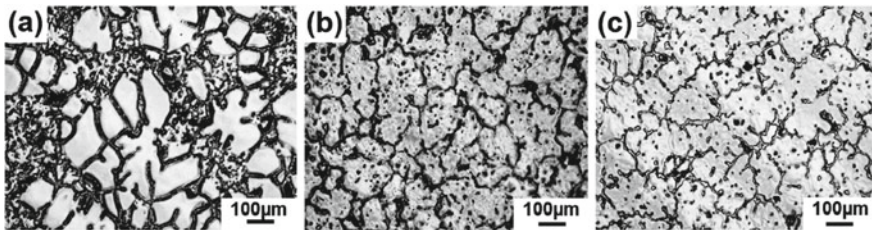
Fig. 4 Optical micrograph of as cast **a** AZ80 alloy, **b** AZ80 with addition of 0.1GNPs and **c** AZ80 with addition of 0.6GNPs composites [38]
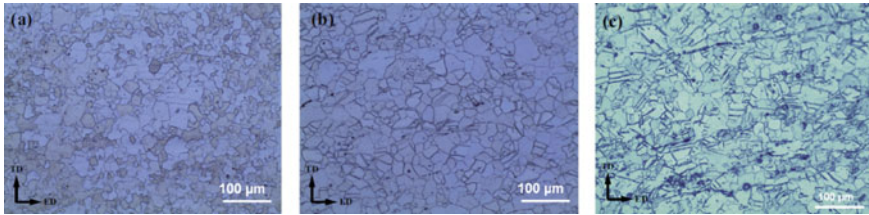
Fig. 5 Micrographs of **a** pure Mg, Mg matrix composites with **b** 0.10 wt% GNPs and **c** 0.25 wt % GNPs [40]

rather difficult to detect, due to the very low content of Ti-GNPs nanoparticles in the composite.

Rashad et al. [18] produced GNPs reinforced AZ91D composites by thixomolding process. They investigated the homogeneous distribution of GNPs reinforcement act as obstacles in the magnesium matrix with high dislocation density, and thus, increases the strength of composites.

Xiang et al. [40] investigated the addition of 0.25 wt% GNP to Mg using disintegrated melt deposition technique, and revealed the correlation of microstructure with inhomogeneous deformation pattern. The micrographs of the Mg and composites are shown in Fig. 5a–c. Uniform grain refinement of Mg matrix occurred followed by induced twin lamellae in the composites.

A study was conducted by [41] to study the microstructure, mechanical, tribological properties of GNPs assimilated AZ31 magnesium through friction stir processing (FSP). The composites exhibit a grain refined microstructure with presence of GNPs. The base modal has a typical bimodal microstructure with fine grains about ~10.2 μm.

Chen et al. [42] studied the addition of GNPs to Mg composites reduces defects of thixomolded products. The composites have grain refinement, reduction in porosity, and improvement in fluidity. However, it is also observed that, with addition of GNPs more than 0.6 wt%, can resulted to poor grain refinement (Fig. 6).

Kavimani et al. [5] revealed a uniform dispersion of carbonaceous particles in the Mg matrix located at the vicinity of micro-crack, which formed as a consequence of weaker bonding between the matrix and its reinforcement particles. The increase in r-GO addition emphasizes the enormous distribution of porosity, which jeopardized the mechanical strength of magnesium matrix.

Turan et al. [43] investigated the effects of GNPs contents (0.1, 0.25 and 0.5 wt%) on pure magnesium. Figure 7 shows a segregation of the GNPs along the grain boundaries. This occurrence was because of the properties of graphene with high surface area and Van der Waals bonding between the carbon atoms. Sun et al. [20] confirmed that GNPs can act as effective nucleation substrates for Mg heterogeneous nucleation. The heterogeneous nucleation requires less energy and, the GNPs preferably nucleate at the Mg grains by heterogeneous nucleation and causing grain refinement.
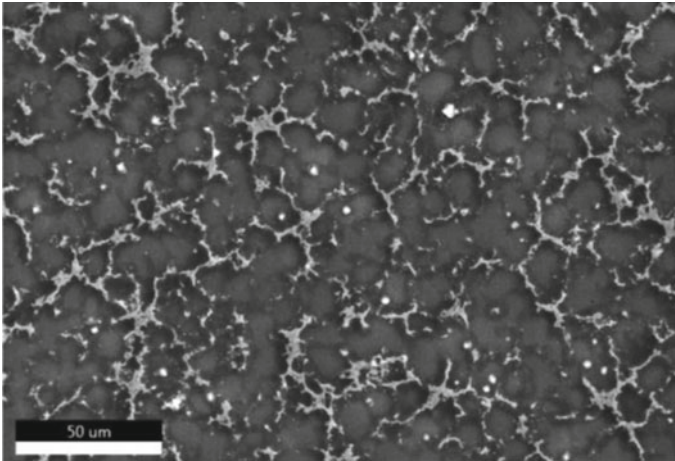
Fig. 6 SEM image of AZ91D with 0.6 wt% GNPs [42]
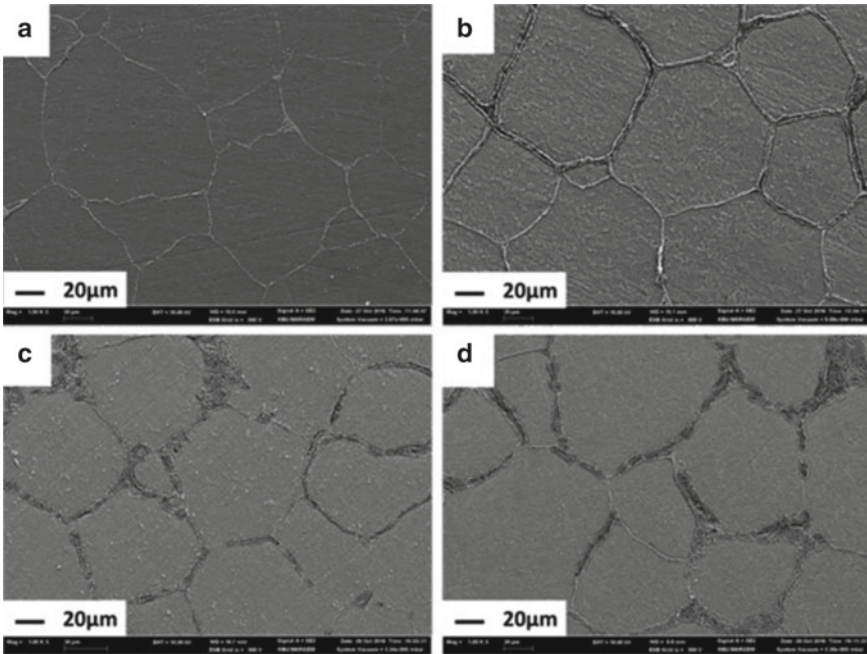
Fig. 7 SEM micrographs of samples: **a** Pure Mg, **b** Mg with 0.1 wt% GNP, **c** Mg-0.25 wt% GNP, and **d** Mg-0.5 wt% GNP [43]

3 Effect of Graphene on the Mechanical Properties of Mg

Parizi et al. [44] produced AZ80 magnesium alloy by two stages process including semi-solid powder metallurgy and rheocasting method. Existence of GNPs was found segregated at the eutectic phase by solidification front, which is also at the vicinity of micro crack. They obtained an improvement in microhardness, tensile yield strength (TYS) and compressive yield strength (CYS) with increasing GNP content as observed in Fig. 8. The dispersion of GNPs decreases the slip distance of dislocations and suppress the dislocation activities. However, as cracks are located at the GNPs accumulation, it is also lead to decrease mechanical properties. The arrangement of GNPs also responsible for the performance of mechanical strength.

Das and Harimkar [45] conducted an experiment to study the effect of GNPs reinforcement on the mechanical behaviour of magnesium matrix composites by using spark plasma sintering method. It was observed that the hardness was relatively increasing with increasing GNP content until 2-vol.% GNPs as tabulated in Table 1 together with its compressive strength and as shown in Fig. 9.

Rashad et al. [15] studied the synergetic effect on mechanical properties of pure magnesium of GNPs and multi-wall carbon nanotubes (MW-CNTs), with correlation to texture. The results, listed in Table 2, showed that the addition of GNPs improved elongation, ultimate tensile stress, and Vickers hardness when compared to pure
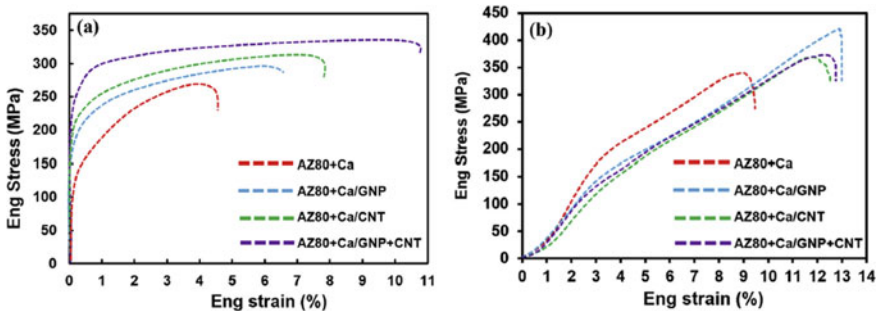
Fig. 8 Stress–strain graph for AZ80 alloy and its composites [38]

Table 1 Hardness and compressive strength of Mg and Mg-GNP composites

Materials	GNP content (wt%)	Hardness (HV)	Compressive strength (MPa)
Magnesium	0	46	220
Mg-GNP	1	54	159
Mg-GNP	2	63	201
Mg-GNP	5	50	123
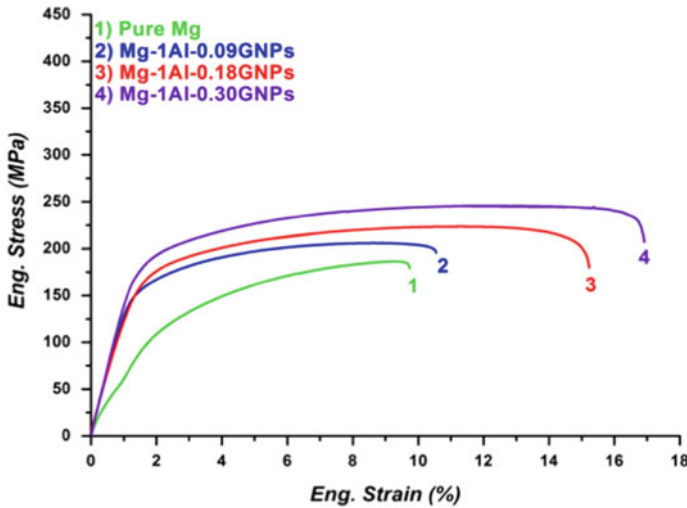
Fig. 9 Tensile stress–strain curves for magnesium and its composites [46]

Table 2 Mechanical properties of Mg and its composites with addition of GNP [15]

Material (wt%)	Vickers hardness (HV)	0.2% YS (MPa)	UTS (MPa)	Failure strain (%)
Mg	41 ± 3.5	5.98	186 ± 6	9.7 ± 3
Mg-1Al-0.09GNP	48 ± 2.9	13.40	206 ± 4	10.5 ± 3.4
Mg-1Al-0.18GNP	51 ± 3	12.18	223 ± 5	15.2 ± 2
Mg-1Al-0.30GNP	55 ± 4	13.84	246 ± 3.5	16.9 ± 3

magnesium. The mismatch in the coefficient of thermal expansion of magnesium-GNPs leads to the strengthening of composites. The change in texture was also revealed with the presence of GNPs.

Grain refinement, load transfer, thermal mismatch, and Orowan loops are among the strengthening mechanism in composite material. According to Xiao et al. [47], shear stress generated at the AZ31B-GNPs interface can transmit load from the matrix to the reinforcement in GNPs-reinforced composites. It limited dislocation movement, leading in an increase in yield stress.

Munir et al. [48] investigated the improvements in mechanical properties with addition of GNPs that caused by the strengthening efficiencies. A lower GNP content resulted in fewer defects in their graphitic structure and uniform dispersion within the Mg matrix, contributing to the grain refinement of the Mg composite. The strengthening factors including thermal mismatch and grain refinement in the Mg matrix with the reinforced GNPs are responsible to the improvement in mechanical strength.

4 Conclusions

This review expands on the potential of GNPs as a reinforcement in magnesium matrix composites. Their properties can be tailored to the end-user by carefully selecting the reinforcement phase, matrix phase, and processing technique. Overall, GNPs presence in magnesium, led to grain refinement and thus, increases strengthening and improve mechanical properties of magnesium-based composite.

References

1. Chalisgaonkar R (2019) Insight in applications, manufacturing and corrosion behaviour of magnesium and its alloys—a review. Mater Today Proc 26:1060–1071
2. Saboori A, Dadkhah M, Fino P, Pavese M (2018) An overview of metal matrix nanocomposites reinforced with graphene nanoplatelets. Mechanical, electrical and thermophysical properties. Metals (Basel) 8:423
3. Alias J (2020) Role of aluminium on the microstructure and corrosion behaviour of magnesium prepared by powder metallurgy method. Int J Autom Mech Eng 17(3):8206–8213
4. Alias J, Harun WSW, Ayu HM (2019) A review on the preparation of magnesium-based alloys prepared by powder metallurgy and the evolution of microstructure and mechanical properties. Key Eng Mater 796:3–10
5. Kavimani V, Soorya Prakash K, Thankachan T (2019) Investigation of graphene-reinforced magnesium metal matrix composites processed through a solvent-based powder metallurgy route. Bull Mater Sci 42:39
6. Neelameggham R (2013) Primary production of magnesium. In: Fundamentals of magnesium alloy metallurgy. Elsevier, Amsterdam, pp 1–32. https://doi.org/10.1533/9780857097293.1
7. Rashad M, Pan F, Asif M, Tang A (2014) Powder metallurgy of Mg-1%Al-1%Sn alloy reinforced with low content of graphene nanoplatelets (GNPs). J Ind Eng Chem 20:4250–4255
8. Rashad M, Pan F, Lin D, Asif M (2016) High temperature mechanical behavior of AZ61 magnesium alloy reinforced with graphene nanoplatelets. Mater Des 89:1242–1250
9. Wu L, Wu R, Zhang J, Hou L, Zhang M (2018) Synergistic effect of carbon nanotube and graphene nanoplatelet addition on microstructure and mechanical properties of AZ31 prepared using hot-pressing sintering. J Mater Res 33:4261–4269
10. Suneesh E, Sivapragash M (2018) Comprehensive studies on processing and characterization of hybrid magnesium composites. Mater Manuf Process 33:1324–1345
11. Ma G, Xiao H, Ye J, He Y (2020) Research status and development of magnesium matrix composites. Mater Sci Technol 36:645–653
12. Purohit R, Dewang Y, Rana RS, Koli D, Dwivedi S (2018) Fabrication of magnesium matrix composites using powder metallurgy process and testing of properties. Mater Today Proc 5:6009–6017
13. Bhat Panemangalore D, Shabadi R, Tingaud D, Touzin M, Ji G (2019) Biocompatible silica-based magnesium composites. J Alloys Compd 772:49–57
14. Meng L et al (2018) Graphene nanoplatelets reinforced Mg matrix composite with enhanced mechanical properties by structure construction. Mater Sci Eng A 733:414–418

15. Rashad M, Pan F, Asif M (2015) Magnesium matrix composites reinforced with graphene nanoplatelets. Graphene materials. Wiley, New York, pp 151–189. https://doi.org/10.1002/9781119131816.ch5
16. Ding Y et al (2020) High performance carbon nanotube-reinforced magnesium nanocomposite. Mater Sci Eng A 771:138575
17. Tanaka K, Iijima S (2014) Carbon nanotubes and grapheme, 2nd edn. https://doi.org/10.1016/C2011-0-07380-5
18. Rashad M et al (2015) Development of magnesium-graphene nanoplatelets composite. J Compos Mater 49:285–293
19. Shahin M, Munir K, Wen C, Li Y (2020) Magnesium-based composites reinforced with graphene nanoplatelets as biodegradable implant materials. J Alloys Compd 828:154461
20. Sun X et al (2020) Microstructures and properties of graphene-nanoplatelet-reinforced magnesium-matrix composites fabricated by an in situ reaction process. J Alloys Compd 835:1–20
21. Rashad M, Pan F, Asif M, Chen X (2017) Corrosion behavior of magnesium-graphene composites in sodium chloride solutions. J Magnes Alloy 5:271–276
22. Ramezanzade S, Ebrahimi GR, Torabi Parizi M, Ezatpour H (2019) R: Synergetic effect of GNPs and MgOs on the mechanical properties of Mg–Sr–Ca alloy. Mater Sci Eng A 761:138025
23. Kumar R, Pandey KK, Islam A, Keshri AK (2019) Graphene nanoplatelets: a promising corrosion inhibitor and toughening inclusion in plasma sprayed cerium oxide coating. J Alloys Compd 809:151819
24. Zhang D, Peng F, Liu X (2021) Protection of magnesium alloys: from physical barrier coating to smart self-healing coating. J Alloys Compd 853
25. Abazari S, Shamsipur A, Bakhsheshi-Rad HR, Ramakrishna S, Berto F (2020) Graphene family nanomaterial reinforced magnesium-based matrix composites for biomedical application: a comprehensive review. Metals (Basel) 10:1002
26. Wu L, Wu R, Hou L, Zhang J, Zhang M (2018) Microstructure, mechanical properties and wear performance of AZ31 matrix composites reinforced by graphene nanoplatelets(GNPs). J Alloys Compd 750:530–536
27. Du X, Du W, Wang Z, Liu K, Li S (2018) Ultra-high strengthening efficiency of graphene nanoplatelets reinforced magnesium matrix composites. Mater Sci Eng A 711:633–642
28. Brodova IG et al (2021) Mechanical properties of submicrocrystalline aluminium matrix composites reinforced by "in situ" graphene through severe plastic deformation processes. J Alloys Compd 859:158387
29. Rashad M et al (2015) Investigation on microstructural, mechanical and electrochemical properties of aluminum composites reinforced with graphene nanoplatelets. Prog Nat Sci Mater Int 25:460–470
30. Su J, Teng J (2021) Recent progress in graphene-reinforced aluminum matrix composites. Front Mater Sci 15:79–97
31. Zhang L et al (2018) Aluminum/graphene composites with enhanced heat-dissipation properties by in-situ reduction of graphene oxide on aluminum particles. J Alloys Compd 748:854–860
32. Rashad M et al (2013) Effect of graphene nanoplatelets (GNPs) addition on strength and ductility of magnesium-titanium alloys. J Magnes Alloy 1:242–248
33. Gürbüz M, Mutuk T, Uyan P (2021) Mechanical, wear and thermal behaviors of graphene reinforced titanium composites. Met Mater Int 27:744–752
34. Cao H, Liang Y (2020) The microstructures and mechanical properties of graphene-reinforced titanium matrix composites. J Alloys Compd 812:152057
35. Tang W et al (2020) Mechanical properties and enhancement mechanisms of titanium-graphene nanocomposites. Acta Mech Sin 36:855–865
36. Gürbüz M, Mutuk T (2018) Effect of process parameters on hardness and microstructure of graphene reinforced titanium composites. J Compos Mater 52:543–551
37. Zhou X, Liu X (2020) Mechanical properties and strengthening mechanism of graphene nanoplatelets reinforced magnesium matrix composites. Jinshu Xuebao/Acta Metall Sin 56

38. Torabi Parizi M, Ebrahimi GR, Ezatpour HR (2019) Effect of graphene nanoplatelets content on the microstructural and mechanical properties of AZ80 magnesium alloy. Mater Sci Eng A 742:373–389
39. Rashad M et al (2013) Effect of graphene nanoplatelets (GNPs) addition on strength and ductility of magnesium-titanium alloys. J Magnes Alloy
40. Xiang SL et al (2017) Enhanced overall strength and ductility of magnesium matrix composites by low content of graphene nanoplatelets. Compos Part A Appl Sci Manuf 100:183–193
41. Arab M, Marashi SPH (2019) Effect of graphene nanoplatelets (GNPs) content on improvement of mechanical and tribological properties of AZ31 Mg matrix nanocomposite. Tribol Int 1–10
42. Chen L et al (2019) Development of AZ91D magnesium alloy-graphene nanoplatelets composites using thixomolding process. J Alloys Compd 778:359–374
43. Turan ME, Sun Y, Akgul Y, Turen Y, Ahlatci H (2017) The effect of GNPs on wear and corrosion behaviors of pure magnesium. J Alloys Compd 724:14–23
44. Parizi MT, Ebrahimi GR, Ezatpour HR, Paidar M (2019) The structure effect of carbonaceous reinforcement on the microstructural characterization and mechanical behavior of AZ80 magnesium alloy. J Alloys Compd 809:151682
45. Das A, Harimkar SP (2014) Effect of graphene nanoplate and silicon carbide nanoparticle reinforcement on mechanical and tribological properties of spark plasma sintered magnesium matrix composites. J Mater Sci Technol 30:1059–1070
46. Rashad M et al (2015) Enhanced tensile properties of magnesium composites reinforced with graphene nanoplatelets. Mater Sci Eng A 630:36–44
47. Xiao H, Ma G, Ye J, He Y (2021) Preparation of graphene reinforced AZ31B magnesium-based composites by stirring casting. Vacuum 191:110281
48. Munir K, Wen C, Li Y (2020) Graphene nanoplatelets-reinforced magnesium metal matrix nanocomposites with superior mechanical and corrosion performance for biomedical applications. J Magnes Alloy 8:269–290

Experimental Study of Lubricant Oil Film Behavior on Al6061 Under MQL Milling Process

Nur Elya Haniza Zamiruddin, Nurrina Rosli, and Amiril Sahab Abdul Sani

Abstract Minumum Quantity Lubrication (MQL) technology has proven to give better surface roughness and tool life performance compared to conventional lubricating method despite its very little usage of lubricant oil. Therefore, it is crucial to deeply understand the lubricating mechanism of MQL to explain this phenomenon. However, most experimental studies conducted in the past was focused to investigate the relationship between effects of machining parameter to the machining performance. Here, the behavior of lubricant oil from MQL generator during the milling process was investigated in this study by using Laser-Induced Fluorescence method to measure the lubricant oil film thickness. Experiments were conducted during the milling process under different oil viscosity and cutting speed. The average surface roughness of workpiece was also measured to relate the lubricant oil behavior and the machining performance. Overall, lubricant oil film thickness fluctuation was found to dramatically change with decreasing oil viscosity. The oil film thickness was also found to increase with increasing cutting speed up until 24.514 m/min. Moreover, the lubricant oil was found to accumulate on the beginning of the milled area. The lubricant oil film thickness drastically dropped at the position of cutting tool. The average lubricant oil film thickness was found at approximately 2.0 mm for the lowest viscous oil and 0.02 mm for the largest viscous oil. The average surface roughness was found to decrease with increasing cutting speed, which has confirmed the results of lubricant oil film thickness that shows more lubricant supplied on the workpiece gives better surface finishing for the workpiece.

Keywords Minimum quantity lubrication · Liquid film thickness · Oil viscosity · Laser-induced fluorescence · Surface roughness

N. E. H. Zamiruddin · N. Rosli (✉) · A. S. Abdul Sani
Faculty of Manufacturing and Mechatronic Engineering Technology, Universiti Malaysia Pahang, 26600 Pekan, Pahang, Malaysia
e-mail: nurrinarosli@ump.edu.my

1 Introduction

Machining process performance is significantly affected by metal workings fluid such as coolant or lubricant that is used to minimize the heat of high temperature appeared during the operation. The capability in lubricating the cutting zone, cooling down the cutting tool and simultaneously flushing away the chips during the cutting process have made the metal workings to be essentially needed for the machining industry [1]. Minimum Quantity Lubrication (MQL) technology is among the alternative approach in replacing the conventional flood coolant or wet machining lubricating method. MQL technology uses a mixture of air pressure and lubricant oil to produce an aerosol form of oil mist from MQL nozzle. During lubricating process, the oil mist could form an extremely thin film of lubricant oil on the cutting zone to reduce friction between tool-workpiece interface, even with very minimal amount at oil flow rate being used [2]. In addition, oil consumption can also be reduced and in turn lessen the excessive lubricant disposal. Thus, MQL is well-known as an environmental-friendly lubricating method [3]. Furthermore, natural biodegradable oil is also commonly being used as base oil for MQL technology. Hence, occupational health hazards among industrial workers can also be reduced [4].

As for the performance, MQL technology has proven to give better surface roughness and tool life performance compared to conventional lubricating method [5]. Moreover, degradation of built-up-edge on the workpiece contributed by lower cutting force has also been attained by applying MQL technology [6]. Hence, depletion in cutting temperature throughout the machining process due to the low friction conditions appeared on the tool-workpiece interface has also been reported [7]. Finally, the overall manufacturing cost has been reported to reduce significantly due to the reduction of oil usage during the machining process [8].

Since the performance of MQL was better compared to conventional lubricating method despite its very little usage of lubricant oil, it is crucial to deeply understand the lubricating mechanism of MQL to explain this phenomenon. Specifically, it is important to clarify the ability of oil mist to penetrate the cutting zone which can give a smoother workpiece or longer tool life as the machining outcome. However, most of the experimental study of MQL application conducted in the past have been solely applied to investigate the relationship between effects of machining parameter to the machining performance. This issue might be due to the complexity of experimental setup when the machining process is on-going and the fact that natural flow of lubricant oil cannot be interrupted to maintain the outcome of machining process [9].

To cater this issue, the behavior of lubricant oil from MQL generator during the milling process is investigated in this study by using a non-intrusive method known as Laser-Induced Fluorescence method to measure the lubricant oil film thickness. Experiments are conducted during the milling process under different oil viscosity and cutting speed. Moreover, the average surface roughness of workpiece is also measured to relate the lubricant oil behavior and the machining performance.

2   Experimental Method

In this study, a 2001 MAKINO KE55 CNC Vertical Mill machine was employed to run the milling process. An MQL generator was equipped beside the milling machine to disperse lubricant oil precisely into the cutting area. A 10 mm-diameter uncoated carbide end mill was used as the cutting tool to mill an Al6061 with dimension of about 100 mm × 100 mm × 100 mm. Four different types of lubricant oil, i.e., mixed esters oil, sunflower oil, olive oil and calophyllum inophyllum oil were utilized as the working oil. The oil properties are listed in Table 1. Meanwhile, a summary of experimental conditions and parameters being applied throughout this study are given in Table 2.

To measure the thickness profile of lubricant oil, a non-intrusive optical approach called as Laser-Induced Fluorescence (LIF) was conducted, which has been done in the previous study [10]. To apply this approach, a calibration procedure was carried out beforehand to obtain the relationship between fluorescence light intensity and oil film thickness. Theoretically, the lubricant oil film thickness increases with increasing of fluorescence light intensity. The results of calibration for all types of oil being used are summarized in Table 3. From the equations, the thickness profile on the workpiece can be calculated by substituting the obtained value of fluorescence light intensity. Moreover, the average surface roughness was measured by taking three average values from sampling length at the distance of 20, 60 and 80 mm on the milled workpiece.

Table 1   Working oil characteristics

Oil types	Kinematic viscosity, ν [mm^2/s]	Dynamic viscosity, η [mPa·s]	Density, ρ [g/cm^3]
Mixed esters	11.954	11.075	0.9265
Sunflower	33.383	30.224	0.9054
Olive	39.216	35.260	0.8991
Calophyllum inophyllum	67.871	63.223	0.9315

Table 2   Experimental conditions and parameters

Properties	Value
Feed per tooth, f_z	0.0893 mm/tooth
Axial depth of cut, a_p	0.50 mm
Cutting speed, V_c	14.514, 19.514, 24.514, 29.514 m/min
Table feed, V_f	315 mm/min
MQL flow rate	116.667 mL/h
MQL nozzle distance	3 mm
MQL lubricant oil	Mixed esters, sunflower, olive, calophyllum inophyllum oil

Table 3 Calibration linear
equations

Oil types	Linear equations
Mixed esters	$I = 2.4713\delta + 4.7994$
Sunflower	$I = 0.3234\delta + 2.166$
Olive	$I = 3.4190\delta + 1.3071$
Calophyllum inophyllum	$I = 0.1922\delta + 0.7667$

3 Results and Discussion

3.1 Effects of Cutting Speed to Average Lubricant Oil Film Thickness Under Different Oil Viscosity

Average lubricant oil film thickness was analyzed when cutter position located at 45–55 mm during the milling process. At this point, a further analysis of lubricant oil behavior related to oil viscosity was clarified. Figure 1 presents the results of average lubricant oil film thickness, δ against distance from milling starting point, x.

The oil flow rate of MQL were consistent at 116.667 mL/h throughout the investigation to disperse oil uniformly onto the milling zone. Overall, it was found that the lubricant oil film thickness fluctuation dramatically changed with decreasing oil viscosity. The oil film thickness was also found to increase with increasing cutting speed up until 24.514 m/min before reduced back to lower thickness upon cutting speed of 29.514 m/min. For all conditions, the lubricant oil was also found to accumulate on the beginning of the milled area. This happened due to the position of nozzle during the milling process.

For oil viscosity at 11.075 cSt i.e., the mixed esters oil, the thickest lubricant oil accumulated on the milled area was found at approximately 2.0 mm. This occurrence probably happened due to properties of low viscous oil that tends to produce greater amount of oil approached onto the workpiece as it is easier injected from the outlet of MQL nozzle [10, 11]. However, the lubricant oil film thickness drastically dropped at the position between 45 and 55 mm for all machining cutting speeds. The position of milling cutter located at 50 mm has obstructed the lubricant oil to properly penetrate the cutting zone. These findings were similarly reported by the past study which has claimed that the lubricant oil film thickness was found lower near to the edge of cutting tool [12].

For oil viscosity of 30.224 cSt i.e., the sunflower oil, the lubricant oil film decreased with increasing of cutting speed before the distance of 45 mm from machining starting point. The range of lubricant oil film thickness was measured from 0.50 mm to 1.50 mm, 0.40 mm to 1.45 mm, 0.45 mm to 1.40 mm and 0.30 to 1.40 mm for cutting speeds of 14.514 m/min, 19.514 m/min, 24.514 m/min and 29.514 m/min, respectively. However, a slightly thicker amount of oil was observed accumulated on the beginning of milling distance. The broad spraying effects of lubricant oil from the MQL nozzle was probably caused by the deeper penetration of
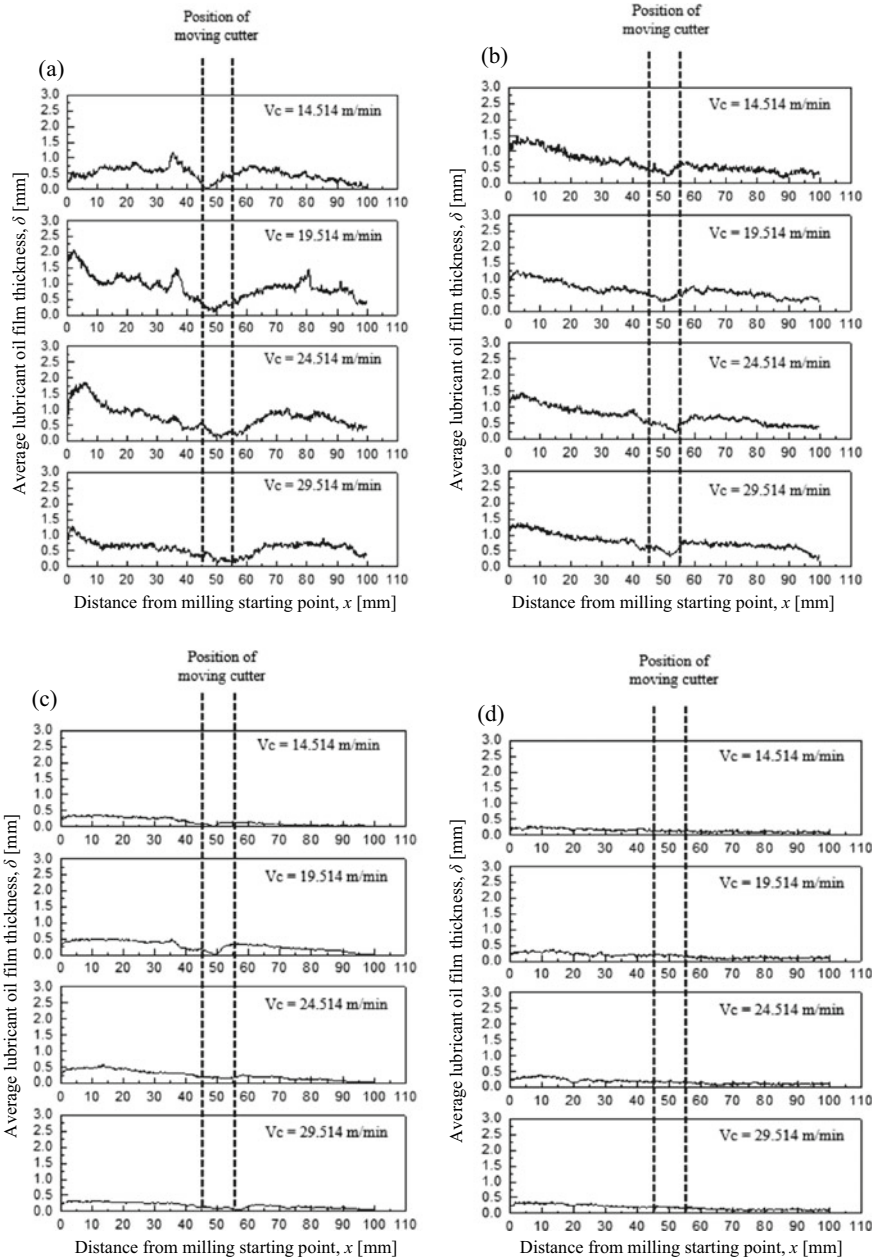
Fig. 1 Average lubricant oil film thickness, δ against distance from milling starting point, x for oil viscosity of **a** 11.075 cSt, **b** 30.224 cSt, **c** 35.260 cSt and **d** 63.223 cSt

sunflower oil that tends to supply more amount of lubricant oil onto the workpiece [13].

Furthermore, it was observed that the lubricant oil film thickness at oil viscosity of 35.260 cSt i.e., the olive oil increased with increasing cutting speed by ranging from 0.02 to 0.20 mm, 0.05 to 0.50 mm and 0.10 to 0.55 mm before depicting a spectacular decrease approximately at distance from 45 to 55 mm. However, approaching to cutting speed of 29.514 m/min, the lubricant oil film thickness was found to decrease compared to previous conditions. This implies that the lubricant oil tends to spatter away from entering milled surface due to vigorous movement and rotation of cutting tool. Hence, the accumulation of lubricant out from the milling zone has reduced the proper lubrication properties onto the workpiece.

Other than that, at oil viscosity of 63.223 cSt, i.e., the calophyllum inophyllum oil, lower lubricant oil film thickness accumulated on the workpiece was measured for all condition of cutting speeds. This could be explained by the poor penetration properties of high viscous calophyllum inophyllum oil itself. Moreover, the bigger particle sizes as compared to lower viscous oil has made it harder to disperse out from the outlet of MQL nozzle [10]. For this reason, fewer oil droplets were produced and eventually reduced the lubricant oil film thickness. Nevertheless, there was a decreasing pattern of lubricant oil film thickness after the position of 55 mm from starting point for all conditions. This phenomenon is probably because lubricant oil tends to adhere onto the cutting tool instead of the workpiece. Consequently, lubricant mists did not fall onto the milling path.

3.2   Average Surface Roughness of Workpiece After MQL Milling Process

Figure 2 presents the results of average surface roughness, R_a and R_z against distance from milling starting point, x. Overall, the average surface roughness was found to decrease with increasing cutting speed. This finding has confirmed the results lubricant oil film thickness that was found to increase under the same conditions, indicating that more lubricant supplied on the workpiece gives better surface finishing for the workpiece.

A detail observation suggests that the average surface roughness at 20 mm for oil viscosity 30.224 cSt increased from 3.892, 4.116 and 4.358 µm for cutting speeds of 14.514, 19.514 and 24.514 m/min. This occurrence might be happened due to insufficient lubricant oil being supplied at the milling path, which can be clarified by the results of Fig. 1 that shows the decreasing trends of lubricant oil film thickness. Again, this has confirmed that limited supply of lubricant oil leads to poor surface finishing of workpiece.

Other than that, the average surface roughness of workpiece at oil viscosity of 35.260 cSt, i.e., the olive oil was found to decrease with increasing cutting speed. Besides, the lowest average surface roughness value was recorded in olive oil. The
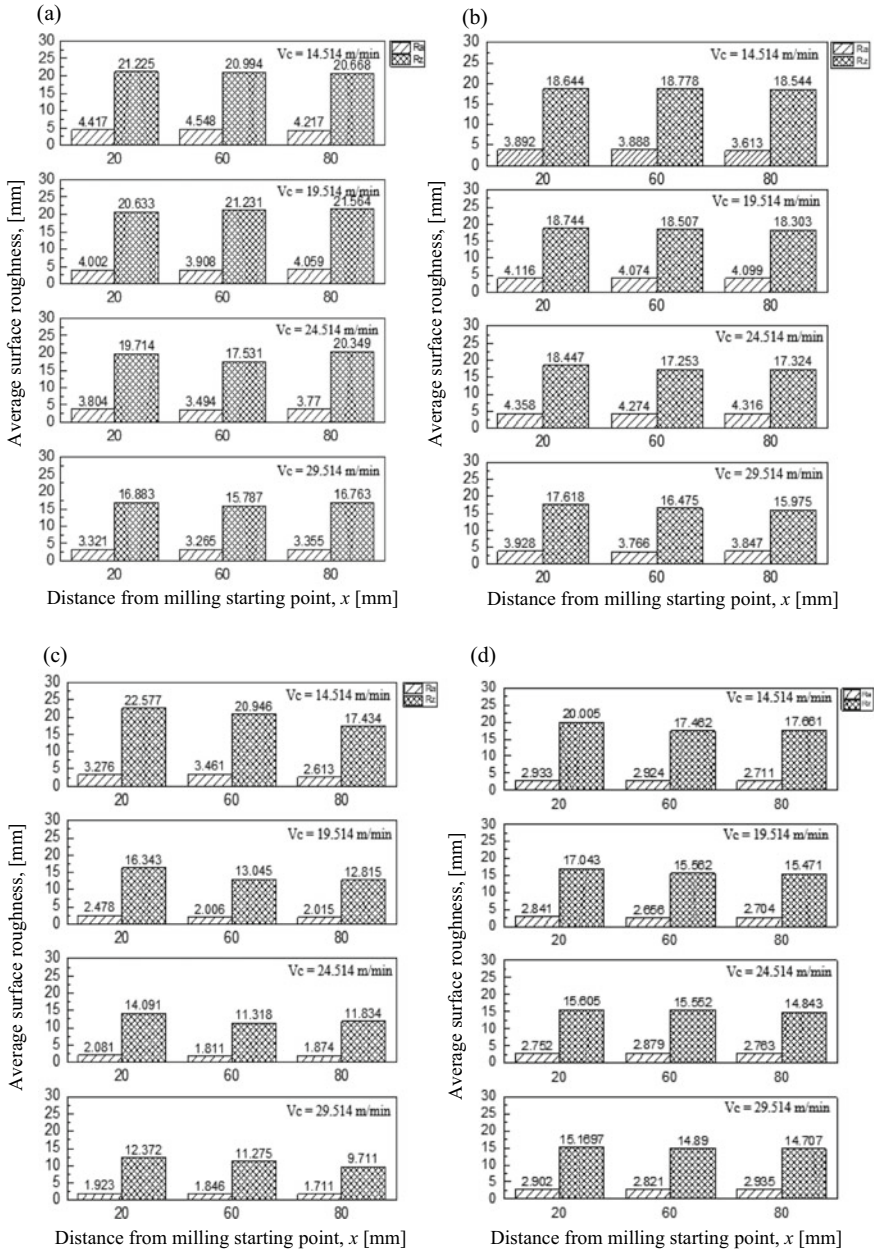
Fig. 2 Average surface roughness of workpiece after MQL milling process for oil viscosity of **a** 11.075 cSt, **b** 30.224 cSt, **c** 35.260 cSt and **d** 63.223 cSt

smaller oil particles of olive oil give a greater capability effects to a deeply penetrate the cutting zone [14]. Thus, cutting friction can be lessen and hence provide a greater lubricating effect on the workpiece. Eventually, surface roughness value can be decreased.

Meanwhile, lower surface roughness was obtained throughout the milling process for oil viscosity of 63.223 cSt, i.e., the calophyllum inophyllum oil. The average surface roughness was found to decrease with increasing cutting speed. However, the average surface roughness at cutting speed of 29.514 m/min slightly increased. These results support the previous discussion, which explained that the lubricant oil spattering away from entering the cutting zone has reduced the lubricant oil film thickness. Concurrently, it minimized the lubrication properties and thus increased the average surface roughness value.

4 Conclusion

The behavior of lubricant oil from MQL technology during the milling process was investigated in this study by using a non-intrusive method known as Laser-Induced Fluorescence method to measure the lubricant oil film thickness. Experiments were conducted during the milling process under different oil viscosity and cutting speed. Moreover, the average surface roughness of workpiece was also measured to relate the lubricant oil behavior and the machining performance. Few conclusions were drawn as follows:

- The lubricant oil film thickness fluctuation dramatically changed with decreasing oil viscosity. The oil film thickness was also found to increase with increasing cutting speed up until 24.514 m/min. However, at cutting speed of 29.514 m/min, the lubricant oil film thickness was found to decrease.
- For all conditions, the lubricant oil was found to accumulate on the beginning of the milled area. The lubricant oil film thickness drastically dropped at the position between 45 and 55 mm from milling starting point as it was obstructed by the cutting tool located exactly at that location.
- The average lubricant oil film thickness was found at approximately 2.0 mm for the lowest viscous-mixed esters oil and 0.02 mm for the largest viscous-calophyllum inophyllum oil.
- Overall, the average surface roughness was found to decrease with increasing cutting speed. This finding has confirmed the results of lubricant oil film thickness that was found to increase under the same conditions, indicating that more lubricant supplied on the workpiece gives better surface finishing for the workpiece.

References

1. Kouam J, Songmene V, Balazinski M, Hendrick P (2015) Effects of minimum quantity lubricating (MQL) conditions on machining of 7075–T6 aluminum alloy. Int J Adv Manuf Technol 79(5–8):1325–1334
2. Sharma VS, Singh G, Sørby K (2015) A review on minimum quantity lubrication for machining processes. Mach Processes 6914
3. Hood R, Morris J, Soo SL (2016) Workpiece surface integrity when milling Udimet 720 superalloy. Procedia CIRP 45:283–286
4. Vazquez E, Gomar J, Ciurana J, Rodríguez CA (2015) Analyzing effects of cooling and lubrication conditions in micromilling of Ti6Al4V. J Clean Prod 87:906–913
5. Li K, Chou S (2010) Experimental evaluation of minimum quantity lubrication in near micromilling. J Mater Process Tech 210(15):2163–2170
6. Al M, Mozammel B, Nikhil M, Dhar R (2018) Investigations on surface milling of hardened AISI 4140 steel with pulse jet MQL applicator. J. Inst. Eng. Ser. C 99(3):301–314
7. Chatha SS, Pal A, Singh T (2016) Performance evaluation of aluminium 6063 drilling under the influence of nanofluid minimum quantity lubrication. J Clean Prod 137:537–545
8. Khan WA, Hoang NM, Tai B, Hung WNP (2018) Through-tool minimum quantity lubrication and effect on machinability. J Manuf Process 34(March):750–757
9. Zamiruddin NEH, Sani ASA, Rosli N (2021) Oil viscosity effects on lubricant oil film behaviour under minimum quantity lubrication. IOP Conf Ser Mater Sci Eng 1092(1):012029
10. Cabanettes F, Faverjon P, Sova A, Dumont F, Rech J (2017) MQL machining: from mist generation to tribological behavior of different oils. Int J Adv Manuf Technol 90(1–4):1119–1130
11. Muaz M, Choudhury SK (2019) Experimental investigations and multi-objective optimization of MQL-assisted milling process for finishing of AISI 4340 steel
12. Huang CY, Murthy TG, Chandrasekar S (2014) Simultaneous measurements of thickness and temperature profile of the lubricant film at chip-tool interface during machining process using luminescent sensors. Procedia Eng 79:9–16
13. Anand KN, Mathew J (2020) Evaluation of size effect and improvement in surface characteristics using sunflower oil-based MQL for sustainable micro-endmilling of Inconel 718. J Braz Soc Mech Sci Eng 42(3):156
14. Babu MN, Anandan V, Muthukrishnan N, Santhanakumar M (2019) End milling of AISI 304 steel using minimum quantity lubrication. Measurement 138:681–689

Multi-objectives Optimization of Volumetric Shrinkage and Warpage for Disposable Mouth Mirrors Using Taguchi Method, ANOVA and Grey Relational Analysis (GRA)

J. B. Saedon, M. Z. Azlan, M. S. Adenan, and M. Azuddin

Abstract Volumetric shrinkage and warpage are the most two common defects in plastic injection moulding process that affects the overall quality characteristics of the plastics part. The use of the Taguchi optimization technique to assess and minimized volumetric shrinkage and warpage concerns that impact processing parameters during the production of disposable mouth mirrors made of Polypropylene (PP) plastic is described in this article. The process parameters that have been selected includes melting temperature, flow rate, cooling time and mold temperature during the injection moulding process simulation based on three levels and four factors in L_9 orthogonal array. The Taguchi Method was used to further analyze the simulated responses, followed by Grey Relational Analysis (GRA). The signal-to-noise (S/N) ratio graphs are examined to determine the influence of process parameters. Furthered, the Analysis of Variance (ANOVA) has been used to verify the accuracy of the optimization findings. Finally, an optimal combination of operating parameters has been proposed: melting temperature at 180 °C, flow rate at 243.6 cm^3/s, cooling time at 12 s and mold temperature at 30 °C was suggest for best optimum combination.

Keywords Parameter optimization · Taguchi method · ANOVA · Grey relational analysis (GRA) · Disposable mouth mirrors

1 Introduction

Plastic injection moulding is another key procedure for high quality goods, and it is divided into three stages: filling, packing, and cooling (together with additional

J. B. Saedon (✉) · M. Z. Azlan · M. S. Adenan
School of Mechanical Engineering, Universiti Teknologi MARA, 40450 Shah Alam, Selangor, Malaysia
e-mail: jurisaedon41@uitm.edu.my

M. Azuddin
Department of Mechanical Engineering, Faculty of Engineering, University of Malaya, Kuala Lumpur, Malaysia

mechanical actions such as mould opening, component ejection, mould closure, and molten material into the injection unit) [1]. Plastic injection moulding has several advantages as well, such as short cycle time, high quality component surfaces, excellent mechanical characteristics, low cost, and light weight. Therefore, it is becoming increasingly important in today's plastic injection industries [2]. However, like with any manufacturing process, defects might develop in the parts, causing them to be rejected during the quality control process. Weld lines, shrinkage, sink mark, and part deformation (warpage) are all regarded undesirable defects in conventional injection. Defects in goods can arise at any stage of the process. Today, several industry professionals and researchers have attempted to reduce these flaws by optimizing any of the process's features such as controlling parameter, modifying mold or material selection [3]. To manage these defects, it is important to understand the impact on injection parameters on the quality of the plastic part [1].

There are numerous existing parameter optimization techniques that are already in use. Taguchi method is one of the most well-known approaches between researchers. The Taguchi techniques were developed by Taguchi and Konishi [2]. The Taguchi technique is a comprehensive quality strategy that uses an orthogonal array to run a small number of trials and incorporates resilience into a process at the design stage [4]. Taguchi is a technique that uses a series of tests to predict the significant and insignificant factors, as well as the optimal level of the design variables. Taguchi is divided into three stages: system design, parameter design, and tolerance design. The goal of system design is to develop parts using scientific and engineering information [4].

According to current study, multi-objective optimization of process parameters has emerged as new trend in the injection moulding process [5]. Many academics have focused their energy and resources to optimizing process parameters. Researchers frequently depend on their experience and a trial-and-error technique to determine the best process parameter settings for the plastics part based on plastic injection moulding process by utilizing the Taguchi approach [6]. Li et al. [5] studies the multi-objective optimization of the fiber reinforced composite using Taguchi, RSM and NSGA-II. Sreedhan et al. [7] integrated the Taguchi, ANOVA and Grey Relational Analysis (GRA) method to identify the effect of molding parameters on sink mark and weld line for ABS product. Kitayama et al. [8] examine the cooling performance, short cycle time and warpage reduction using conformal cooling channel and the multi-objective optimization using ANOVA and neural network. Oliaei et al. [9] investigates the influences of five significant process parameters in minimizing the warpage and shrinkage on polylactic acid (PLA) of biodegradable plastic spoon part. The study coupled the Taguchi approach with ANOVA and ANN by collecting the data from computer aided engineering (CAE) software tools Autodesk Moldflow™ Plastics. From the previous research, it can be concluded that parameter optimization and finite element analysis software works well in minimizing the product defects for plastic injection moulding process. In addition, the Design of Experiment (DOE) can also aid in determining the responses of change in factor values. This method works very well for injection molding product and process design in terms of selecting the

optimal combination of levels of the elements that impact the process, and quality of the product.

This article addresses the use of computer aided engineering (CAE) technology for the injection moulding of a disposable mouth mirror made of Polypropylene (PP) utilizing the Moldflow Plastic Insight Package. Design of experiment (DOE)—L9 Orthogonal array was utilized to plan outline of the simulation. Four controlling parameters were chosen: melting temperature, flow rate, cooling time and mold temperature which each of the parameters having three levels. The Taguchi Method was used to further analyze the simulated responses, followed by Grey Relational Analysis (GRA). The signal-to-noise (S/N) ratio graphs are examined to determine the influence of process parameters. Furthered, the Analysis of Variance (ANOVA) has been used to verify the accuracy of the optimization findings using Minitab 19 software.

2 Experimental and Test Details

This study's aims to discover the optimum operating parameter that impacts the disposable mouth mirror on the plastic injection moulding process by utilizing the combined Taguchi technique, ANOVA and Grey Relational Analysis. Disposable mouth mirror is an essential dental tool that must be used by all dental practitioners for a variety of reasons, including allowing indirect vision of the inspected area of any part of the oral cavity, reflecting the light onto desired surfaces where direct light does not reach, retracting the lips, cheek and tongue and viewing tartar problems behind the last tooth [10]. In this study, a multi-cavities of disposable mouth mirror have been developed by using Moldflow™ Plastics Insight (MPI) software packages. Figure 1 display disposable mouth mirror settings together with feeding system. This chosen component weights 8 g, has a mirror diameter of 24 mm, a length of 160 mm, a density of 1.004 kg/m^3 and a volume of 5.03×10^{-6} m^3. This part has a 45° angle

Fig. 1 Disposable mouth mirror model analysis
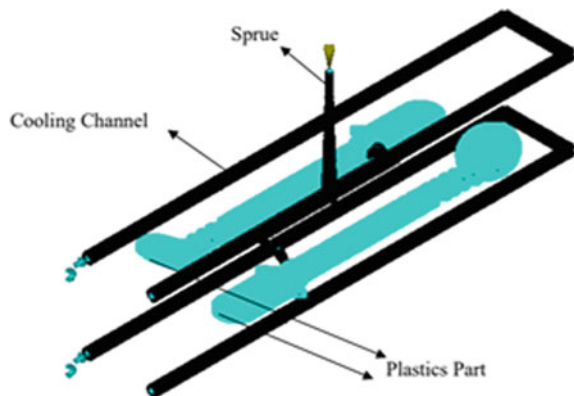
between the shank and the working area (mirror), it was developed with a 40 mm long gripping area on a handle and a 7 mm thick handle with overall length of the part 160 mm. The 3D part of disposable mouth mirror undergoes the meshing process Moldflow™ Plastics Insight (MPI). This section has a 3D mesh of 127,286 triangle elements, 63,671 nodes, and 50 sprue, runner, and gate elements. The sprue diameter is 3 mm with a length of 60 mm, and the runners have a diameter of 3 mm. Based on the simulation, this part total volume including sprue, runner and gate are 11.95 cm^3. Meanwhile, total volume for two parts (multi-cavity) of disposable mouth mirror is 10.0233 cm^3.

2.1 Parameter Optimization Method

To identify the optimal operating parameter, designs of experiment (DOE) rely mostly on one of the Taguchi techniques. This method was utilized to enhance the designs of disposable mouth mirror. A set of orthogonal arrays then was integrated into the Moldflow™ packages on the disposable mouth mirror. Then, data generated from the simulation results has been analyzed in signal to noise ratio to determine the best operating parameter for the selected output. ANOVA was used to identify the most significant effect affects the products defect i.e., volumetric shrinkage and warpage. Grey relational analysis was integrated to identify the multi-objective optimization of volumetric shrinkage and warpage on the disposable mouth mirror. To validate the findings obtained from the optimization technique, a confirmation test was performed. If there is no improvement in the proportion of defects on the product, the procedure will be repeated to discover the best operating parameter. Parameter optimization process has been done using Minitab 19 software.

In this study, four injection moulding parameters will be investigated: melting temperature, flow rate, cooling time, and mold temperature, along with three levels, to decrease part shrinkage and warpage. Based on literature and the current best practice, the range of the selected parameter has been specified as in Table 1. The parameters used were determined using a simulated analysis procedure utilizing results generated by Autodesk Moldflow™ Plastics Insight.

Table 1 Controlling Parameters and Their Levels

Symbol	Parameters	Unit	Level 1	Level 2	Level 3
A	Melting temperature	°C	180	200	220
B	Flow rate	cm^3/s	162.4	203	243.6
C	Cooling time	s	8	10	12
D	Mold temperature	°C	30	50	70

Parameter	Value
Melt temperature (°C)	191–263
Injection mould temp. (°C)	27–66
Tensile strength (MPa)	55.2
Shrink rate (%)	0.1–0.3
Density (kg/m^3)	728.28
Melt flow index (g/min)	0.2

Table 2 Mechanical properties of polypropylene

2.2 Material Selection

The material selection and characteristics are specified by computing polypropylene with 20% glass fiber filler by weight into the software material selection data. This material settings on the Moldflow™ software is based on manufacturer Avient with serial number Trilliant™ HC HC5210-0020 RS Natural based on the manufacturer's technical data sheet. Polypropylene (PP) was selected as the molten material for disposable mouth mirrors because of the low melt viscosity, the plastics flow very smoothly, especially in small spaces like the grip region on the handle. The shrinkage rate of polypropylene is around 0.1–0.3%, although the numbers vary depending on the number of variables and the governing factors. Table 2 illustrates the mechanical characteristics of the polypropylene utilized in this investigation based on the scientific data sheet.

3 Results and Discussion

3.1 Signal to Noise (S/N) Ratio

The Taguchi approach suggests a signal to noise (S/N) ratio to identify the quality characteristics to be considered for any engineering design challenge. The S/N ratio has three phases: the smaller the better, nominal is the best and the bigger the better [4]. In this study, the smaller the better-quality characteristics is chosen to minimize volumetric shrinkage and warpage by controlling each process parameter to the optimal level. The S/N ratios for the nine trials were computed and results are shown in Table 3. The computed results of S/N ratio for both volumetric shrinkage and warpage were ranges between 9.923 and 11.57% for volumetric shrinkage and 3.09–3.414 mm for warpage, respectively. It can be concluded that experiment number 8 yields the highest value of volumetric shrinkage, meanwhile experiment number 4 gave a highest value for warpage.

Table 4 shows, the S/N ratio response table for volumetric shrinkage and warpage. The results show that the following are the best process parameter combinations for

Table 3 S/N ratio for volumetric shrinkage and warpage as response parameter

Orthogonal array					Output			
Run No.	A	B	C	D	Volumetric shrinkage (%)	Volumetric Shrinkage, S/N ratio	Warpage (mm)	Warpage, S/N ratio
1	180	162.4	8	30	9.923	−19.932	3.188	−10.070
2	180	203	10	50	10.36	−20.307	3.173	−10.029
3	180	243.6	12	70	10.45	−20.382	3.090	−9.7991
4	200	162.4	10	70	10.73	−20.611	3.414	−10.665
5	200	203	12	30	10.77	−20.644	3.180	−10.048
6	200	243.6	8	50	11.15	−20.945	3.175	−10.034
7	220	162.4	12	50	11.48	−21.198	3.374	−10.562
8	220	203	8	70	11.57	−21.266	3.369	−10.550
9	220	243.6	10	30	11.56	−21.259	3.170	−10.021

Table 4 Response table of S/N ratio for volumetric shrinkage and warpage

Level	Factors				Level	Factors			
	Volumetric shrinkage					Warpage			
	A	B	C	D		A	B	C	D
1	−20.21	−20.58	−20.72	−20.61	1	−9.97	−10.43	−10.22	−10.05
2	−20.73	−20.74	−20.73	−20.82	2	−10.25	−10.21	−10.24	−10.21
3	−21.24	−20.86	−20.74	−20.75	3	−10.38	−9.95	−10.14	−10.34
Delta	1.03	0.28	0.03	0.21	Delta	0.412	0.481	0.102	0.291
Rank	1	2	4	3	Rank	2	1	4	3

volumetric shrinkage: $A_1 B_1 C_1 D_1$ these variations correspond to a melting temperature of 180 °C, a flow rate of 162.4 cm³/s, a cooling time of 8 s, and a mold temperature of 30 °C. Indicating the response value for volumetric shrinkage of disposable mouth mirror on multiple cavities at A_1 (−20.21), B_3 (−20.58), C_3 (−20.72), D_1 (−20.61). Based on the table, the rank indicating the most influential parameters to the shrinkage contribution. It revealed that the order of significance of each parameter on volumetric shrinkage is A > B > D > C. Figure 2 shows, the main effects plot for volumetric shrinkage, it is clearly showing that melting temperature parameter gives the most influential parameter to the occurrence of volumetric shrinkage follows by flow rate, mold temperature and cooling time. Meanwhile Fig. 3 shows, the main effects plot for warpage.

Meanwhile, the most optimal parameter combination for warpage is $A_1 B_3 C_3 D_1$. These variations correspond to a melting temperature of 180 °C, a flow rate of 243.6 cm³/s, a cooling time of 12 s, and a mould temperature of 30 °C, indicating the response value for warpage for disposable mouth mirror on multiple cavities at A1 (−9.966), B3 (−9.952), C3 (−10.137), and D1 (−10.047). The importance of each
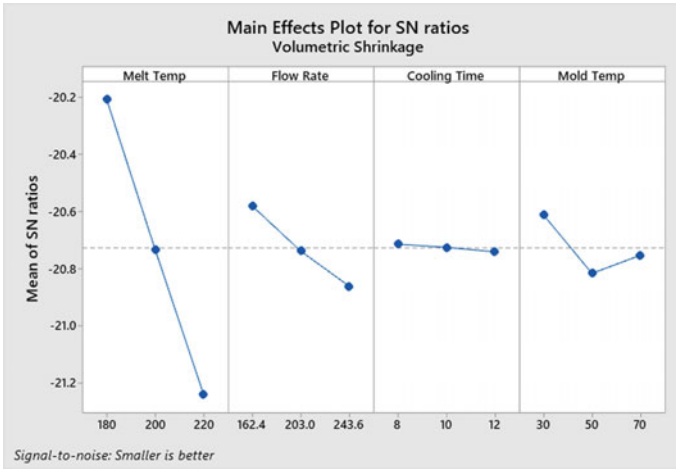
Fig. 2 Main effects plot for S/N ratios of volumetric shrinkage

design parameter for warpage is evaluated and found to be B > A > D > C. According to results, flow rate is the most significant element in reducing warpage. This might be because the flow rate of the disposable mouth mirror changes constantly throughout the filling stage.

Fig. 3 Main effects plot for S/N ratios of warpage

3.2   Analysis of Variance (ANOVA)

The goal of ANOVA is to identify the statistically significant parameters impacting quality characteristics in a specific experimental study [5]. Table 5 shows, the ANOVA table for volumetric shrinkage defect. It shows melting temperature parameter gave the highest percentage contribution of (90.26%), furthermore, the F value for melting temperature recorded is 10.3517 proved that this parameter gave the most significant im- pact on the part. Meanwhile, flow rate (6.44%), cooling time (0.02%) and mold temperature (3.28%). From the table, it shows that the most influence parameter meets the results from S/N response table. This results match those observed in earlier studies that found that melting temperature gave the highest contribution to volumetric shrinkage as found in [11].

Table 6 shows, the ANOVA statistical results for warpage. It is apparent from this table that each parameter gave a significant value of contribution for warpage on disposable mouth mirror. The most significant parameter is flow rate with 45.56% and F value of 135.97613. Follows with melting temperature (34.75%), mold temperature (17.50%) and lastly cooling time (2.19%). However, the F value for each parameter results in higher than $F > 4$, meaning that all controlling parameters gave an impact on the occurrence of warpage. From this observation, it clearly shows, cooling time resulted in the lowest value of contribution for both volumetric shrinkage and warpage. The present findings seem to be consistent with other research which found

Table 5 ANOVA table for volumetric shrinkage

Symbol	Parameters/factors	DOF	SS_T	SS_m	F	ρ (%)
A	Melting temp	2	2.51829	1.25914	10.3517	90.26
B	Flow rate	2	0.17975	0.08987	0.73890	6.44
C	Cooling time	2	0.00057	0.00028	0.00234	0.02
D	Mold temp	2	0.09148	0.04574	0.37605	3.28
	All other/error	0		0.12163		
	Total	8	2.79010	0.34876		100.00

Table 6 ANOVA table for warpage

Symbol	Parameters/factors	DOF	SS_T	SS_m	F	ρ (%)
A	Melting temp	2	0.0372	0.01862	103.72390	34.75
B	Flow rate	2	0.0488	0.02442	135.97613	45.56
C	Cooling time	2	0.0023	0.00117	6.53791	2.19
D	Mold temp	2	0.0187	0.00938	52.24278	17.50
	All other/error	0		0.00017		
	Total	8	0.1072	0.01340		

that melt and mold temperatures, packing pressure, and cooling time are all proved to be significant factors in presence of warpage for injection-molded part.

3.3 Grey Relational Analysis (GRA)

The grey relation analysis is primarily a quantitative investigation of the hierarchical operation. It calculates the degree of vicinity based on similarities or differences between variables after normalized. The optimum set of values for the parameters will be determined in GRA analysis.

Table 7 shows, the grey relation coefficient and grey relational grade for all 9 experiments after normalization has been calculated for all experiments. The values of grey relational grade, which is the weighted sum of the grey relational coefficient, were rated for the whole run, from higher to lower values. The greater the value of grey relation- ship grade, the better the various performance characteristics. As a result, the multi- objective optimization issue has been reduced to a single-objective optimization problem. In Table 7 shows the greatest relationship grade values of 0.85 in experiment number 1. It can thus be inferred from all nine trials that experiment number 1 offers the finest multi-response characteristics.

Grey relational influence parameters were highlighted by bold type where the higher values were given for all three levels, as the most affected parameters as in Table 8. From the table, the results shows that the best combination is $A_1B_3C_3D_1$ indicating melting temperature—180 °C, flow rate—243.6 cm³/s, cooling time—12 s and mold temperature—30 °C.

The analysis of the variance (ANOVA) is used for the overall mean of the Gray Relational Grade to get the most significant process parameters. The ANOVA performance criterion results with computed F value of each component are shown in Table 9. From the results, melting temperature shows the greatest contribution to the

Table 7 Grey relation coefficient and grey relational grade values

Orthogonal array					GRC		GRG	Order
Run No.	A	B	C	D	Shrinkage	Warpage		
1	1	1	1	1	1	0.6975	0.85	1
2	1	2	2	2	0.7347	0.7438	0.74	3
3	1	3	3	3	0.6800	1	0.84	2
4	2	1	2	3	0.5100	0	0.25	7
5	2	2	3	1	0.4857	0.7222	0.60	4
6	2	3	1	2	0.2550	0.7377	0.50	5
7	3	1	3	2	0.0546	0.1234	0.09	8
8	3	2	1	3	0	0.1389	0.07	9
9	3	3	2	1	0.0060	0.7531	0.38	6

Table 8 Influence parameters on grey relational grade

Symbol	Parameters/Factors	Unit	Level 1	Level 2	Level 3
A	Melting temperature	°C	**0.81**	0.45	0.18
B	Flow rate	cm³/s	0.39	0.47	**0.57**
C	Cooling time	sec	0.47	0.45	**0.51**
D	Mold temperature	°C	**0.61**	0.44	0.38

Table 9 ANOVA table on volumetric shrinkage and warpage

Symbol	Parameter/factors	DOF	SS_T	SS_m	F	ρ (%)
A	Melting temp	2	0.5994	0.2997	35.10288	81.09
B	Flow rate	2	0.0488	0.0244	2.857892	6.60
C	Cooling time	2	0.0056	0.0028	0.327955	0.76
D	Mold temp	2	0.0854	0.0427	5.001312	11.55
	All other /Error	0		0.0085		
	Total	8	0.7392	0.0924		100.00

process control with 81.09% contribution in the existence of volumetric shrinkage and warpage on the disposable mouth mirror. Followed by mold temperature with 11.55% and flow rate 6.60%. In contrast to earlier findings, however, no evidence of cooling time gave a significant impact on the product defects. This may be due to the parameters controlled on the simulation software does not meet the actual phenomenon of the cooling time. Meanwhile the F value for melting temperature recorded the higher value with 35.1028 and higher than $F > 4$ and follows with mold temperature which is 5.0013. This prove that melt temperature and mold temperature are two most significant parameter in product defects performance. This finding supports previous research into the correlation of product defect between melt and mold temperature.

3.4 Validation and Confirmation Test

In this section, a validation and confirmation test has been run in the Moldflow simulation software package based on the best combination of parameters that has been discovered in Grey relational analysis. Table 10 shows, the confirmation test using the optimal simulated parameters. The optimum process parameters combination for achieving minimum volumetric shrinkage and warpage are; melt temperature 180 °C, flow rate 243.6 cm³/s, cooling time 12 s, and mold temperature 30 °C. As presents in Table 10, the volumetric shrinkage has been minimized from 11.57% to 9.928% which showing 14.19% improvement, while warpage also shows an improvement

Table 10 Confirmation test for volumetric shrinkage and warpage

	Initial simulation parameter	Optimal parameter		% Improvement
	Orthogonal Array	Prediction by GRA	Confirmation Experiment	
Setting level	$A_3 B_2 C_1 D_3$	$A_1 B_3 C_3 D_1$	$A_1 B_3 C_3 D_1$	
Shrinkage	11.57		9.928	14.19
Warpage	3.369		1.265	62.45
Grey relational grade	0.07		0.99	
Improvement of the Grey Relational Grade = 0.92				

at 62.45% which the value has been decrease from 3.369 to 1.265 mm. This validates the efficiency of Taguchi DOE and Grey relational analysis in identifying the multi-objective optimization to find the best combination of parameter.

4 Conclusion

The CAD/CAE/DOE has been presented, to optimize parameters of the injection molding process with the multiple performance characteristics. Using Taguchi experimental design, the volumetric shrinkage and warpage of an injection molding process have been independently optimized by four control variables particularly melting temperature, flow rate, cooling time and mold temperature for the purposes of a disposable mouth mirror analysis. The application of gray relational analyzes the volumetric shrinkage and warpage can turn multi-performance optimization into the optimization of one performance feature known as the gray relational grade. This technique can therefore considerably simplify the optimization of the complex multiple performance criteria. For this investigation, the best injection-molding process parameter; melting temperature, level 1: 180 °C, flow rate, level 3: 243.6 cm³/s, cooling time, level 1: 12 s and mold temperature, level 1: 30 °C.

References

1. López A, Aisa J, Martinez A, Mercado D (2016) Injection moulding parameters influence on weight quality of complex parts by means of DOE application: case study. Meas J Int Meas Confed 90:349–356
2. Oktem H, Erzurumlu T, Uzman I (2007) Application of Taguchi optimization technique in determining plastic injection molding process parameters for a thin-shell part. Mater Des 28(4):1271–1278
3. Khan RM, Acharya G (2016) Plastic injection molding process and its aspects for quality: a review. Eur J Adv Eng Technol 3(4):66–70
4. Moayyedian M, Abhary K, Marian R (2016) Gate design and filling process analysis of the cavity in injection molding process. Adv Manuf 4(2):123–133
5. Li K, Yan S, Zhong Y, Pan W, Zhao G (2018) Multi-objective optimization of the fiber-reinforced composite injection molding process using Taguchi method, RSM, and NSGA-II. Simul Model Pract Theory 91:69–82
6. Kuram E, Tasci E, Altan AI, Medar MM, Yilmaz F, Ozcelik B (2013) Investigating the effects of recycling number and injection parameters on the mechanical properties of glass-fibre reinforced nylon 6 using Taguchi method. Mater Des 49:139–150
7. Sreedharan J, Jeevanantham AK (2018) Optimization of injection molding process to minimize weld-line and sink-mark defects using Taguchi based grey relational analysis. Mater. Today Proc. 5(5):12615–12622
8. Kitayama S, Miyakawa H, Takano M, Aiba S (2017) Multi-objective optimization of injection molding process parameters for short cycle time and warpage reduction using conformal cooling channel, pp 1735–1736
9. Oliaei E et al (2016) Warpage and shrinkage optimization of injection-molded plastic spoon parts for biodegradable polymers using Taguchi, ANOVA and artificial neural network methods. J Mater Sci Technol 32(8)
10. Chetan D (2011) Mouth mirror (dental mirror)—parts, types and functions. [Online]. Available: https://www.drchetan.com/mouth-mirror.html
11. Ramakrishnan R, Mao K (2017) Minimization of shrinkage in injection molding process of acetal polymer gear using Taguchi DOE optimization and ANOVA method. Int J Mech Ind Technol 4(2):72–79

Quasi-static Axial Crushing of E-Glass Fiber Reinforced Epoxy Composite by Different Number of Plies

K. Ganesh Kumar, Saijod T. W. Lau, Chockalingam Palanisamy, M. M. H. Megat Ahmad, and M. Y. Yuhazri

Abstract The purpose of this study is to analyze the effect of the crushing mechanism on e-glass under various loading. To do so, cylindrical composites tubes are required to be fabricated as the specimen. To test the various variable that might affect the energy absorption of the specimen, the hand's lay-up process had been selected. Glass fiber reinforced composites tubes were fabricated with a fiber content of 1 to 3 layers. To evaluate the effect of the crushing mechanism of the fabricated composite tubes, a compression test was conducted. The effect of fabrication method and thickness of specimen were studied. In addition, the response of crush load–displacement, peak load, total energy absorption, specific energy absorption, and crush force efficiency were determined. Furthermore, the microstructure of all the specimens was analyzed using the digital microscope. As a result, it indicates that energy absorption capabilities are highly dominated by a higher reinforcement layers. H3 has the highest specific energy absorption which is 9.3 kJ/kg.

Keywords Manufacturing process · Composite material · Mechanical properties

1 Introduction

Nowadays, structural crashworthiness is a crucial requirement in the design of the automobiles field. The crash-worthy structure is designed to absorb energy impact in a controlled manner in the event of a crash [1–3]. For instance, the side beams

K. Ganesh Kumar (✉) · S. T. W. Lau · C. Palanisamy
Faculty of Engineering and Technology (FET), Multimedia University, Jalan Ayer keroh Lama, 75450 Melaka, Malaysia
e-mail: ganesh.krishnan@mmu.edu.my

K. Ganesh Kumar · M. M. H. Megat Ahmad
Department of Mechanical Engineering, Faculty of Engineering, National Defence University of Malaysia, Sungai Besi Camp, 57000 Kuala Lumpur, Malaysia

M. Y. Yuhazri
Faculty of Mechanical and Manufacturing Engineering Technology, Universiti Teknikal Malaysia Melaka, Hang Tuah Jaya, Durian Tunggal, 76100 Melaka, Malaysia

on the engine for an automobile had been well designed to absorb impact energy in a controlled condition. Generally, metals are the preferred material used in crashworthy structural applications. But with the success story in the aerospace industry, it is proven that through plastic deformation the impact energy can be absorbed and polymer composites are the materials that stand out in this case [4–6].

Polymer composite materials had been accepted as it provides significant technical advantages over metals [7, 8]. However, there is a major challenge to use polymer composites as a controlled energy absorber. The reason that polymer composites behave better than metals is because of the characteristics of the polymer composites as it consists of plastic deformation which is helpful in energy absorption [9]. Besides that, several variables could affect the characteristics of the energy absorption of polymer composite materials that can be concluded to the main 4 part. The first is microstructural variables, followed by conditions of manufacture, the geometry of the tube, and conditions of testing [10]. Epoxy are one of the most regularly used polymer in structural applications.

Fibers occupy a largest volume fraction of composites and able to withstand a huge external load. Glass fiber is one of the most common fibers in the composites industry. The main reason is because of its relatively low costs and lightweight. However, glass fibers are weak in compressive strength. This raises the concern of the study on how to improve the compressive strength of glass fiber. A previous study showed that glass fiber can be successfully replaced metal as a car bumper [11]. Hence it is proved that glass fiber is eligible to serve as a crashworthy application.

Generally, manufacturing using composites involves the processing of two main ingredient materials to make a final product. The ingredients involve the matrix and fiber materials. There is various type of manufacturing process. The most common and simple one is the hand lay-up method. To cope with the problem mentioned above, the motivation of this study is to enhance the energy absorption capabilities of an e-glass fiber under various conditions.

2 Materials and Methods

2.1 Materials Preparation

The materials that had been selected to fabricate cylindrical composite tubes are epoxy and E-glass fiber supplied by Chemi-Bond from Selangor, Malaysia. The resin used in this project was Auto-Fix 1345 B hardener and Auto-Fix 1710 A epoxy. The epoxy and hardener are mixed by the ratio of 1:1 by weight as recommended by the supplier. Electric stirring was used in the mixing to reduced bubble formation. For E-glass fiber, it was cut in 200 mm in width and the length of the perimeter for the 50 mm inner diameter tube depending on the number of layers used. For the current study, composite with 1, 2, and 3 plies were investigated. The reason the plies or

(a)	(b)	(c)
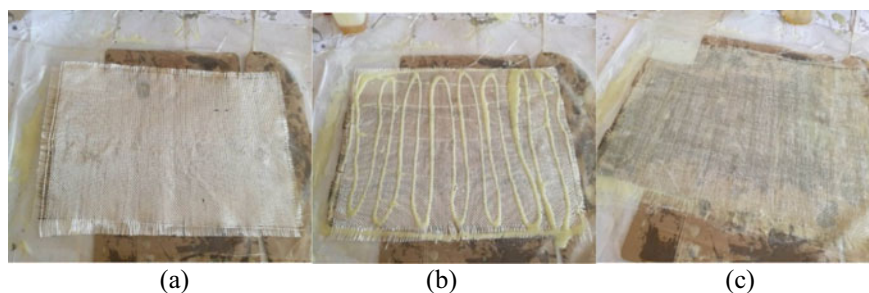
Fig. 1 E-glass fiber **a** before pouring resin **b** after pouring resin **c** the finished prepreg

stopped at 3 plies as, when it goes to 4 plies the fiber starts to undulating thus will result some gaps between the plies [12].

In the hand lay-up process, a 50 mm diameter steel mandrel was used. The mandrel was wrapped with PTFE plastic film and a release agent was applied. On the other hand, epoxy was applied to the E-glass fiber surface. The wetting of the glass fiber was rolled on the mandrel. At the same time, a steel roller was used to compress the fiber and it also helps to release bubbles form in between layers. After the fiber rolled on the mandrel, PTFE film again rolled on the mandrel against the fiber to produce a small compression force to hold the fiber in place. The composite was left to cure for 24 h at room temperature. After curing, the composite was separated from the mandrel and cut to 100 mm in length as testing specimens (Fig. 1).

2.2 Experiment Procedure

For the testing, quasi-static axial crushing was carried out. The test used Shimadzu AG-I Universal Testing Machine with a 100 kN load cell. It was carried out based on ASTM D7336M-16 standard with stroke length set to 50 mm. In the test, crushing of 10 mm/min was used [13]. The specimen was placed under the moving platen during crushing. During crushing, the static photograph was taken utilizing a camera with 48-megapixel resolution. The crushing pics were taken with every 2 mm moving platen to observed its deformation. From the test, the data history of force versus displacement was recorded automatically. For post-crushing, the crushed specimens were under a microscope to observe their crushing effect.

3 Results and Discussion

From the crushing history curve, it can be seen that the crushing peak load for all the specimens reaches their peak at about 5–6 mm after the moving platen as shown
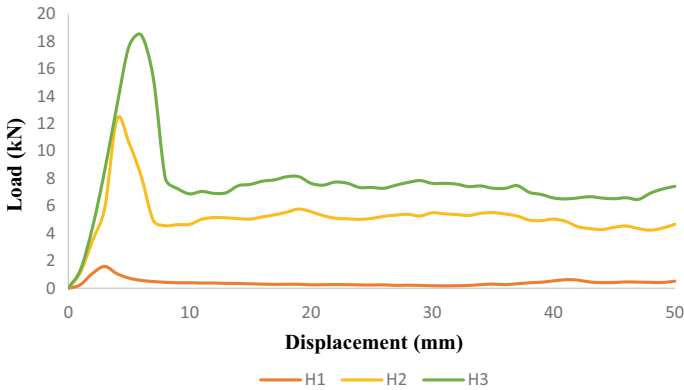
Fig. 2 Graph for Hand lay-up method with different layers of reinforcement; H1-1 layer, H2-2 layers, and H3-3 layers

in Fig. 2. Moreover, the crushing for the specimen was crushed progressively at the duration of 50 mm crushing length. However, from the test, the peak load was varied due to differences in the number of fiber plies used. As the plies number increases, the peak load increase. This is due to the more materials able to support a more compressive load. In a one-ply composite tube, the peak load of 1.6 kN was attained at a displacement of about 5 mm of moving platen. At that time, the structure began to have local buckling [14]. Subsequently, the top of the structure started to crack. The failure of the top part leads to progressive crushing in the test. This also happened to the test for structure with two plies. In the test, the two-ply structure reaches its peak load at 12.3 kN with a platen displacement of 5.3 mm. Moreover, the 3-ply cylindrical structure also behaves in the same manner. For the 3-ply structure, it achieved its peak load at 18.5 kN where the platen displacement at 6.9 mm. From the test, all the structures were having the same characteristic which is local buckling and cracks begin at the top part of the structures. Then, the structure's wall started to bend outwards till the end of the test. The results of the tests are listed in Table 1.

From the test, all specimen behaved in the same manner which crushed progressively. From the post-crushing, all the specimen begins to crack by bending outwards. During this moment, the wall began to splay which simulate the tension stress at the wall which is usually denoted as mode I failure [15–17] as shown in Fig. 3. Apart from that, the structures also experience bending at the wall. At this point, mode II

Table 1 Data was recorded for specimens made of 3 different reinforcement layers

Sample	Peak load (kN)	Mean load (kN)	Total Energy absorption (J)	Specific energy absorption (kJ/kg)
1	1.6	0.4	20.7	1.6
2	12.3	5.4	261.5	7.5
3	18.5	7.7	389.1	9.3
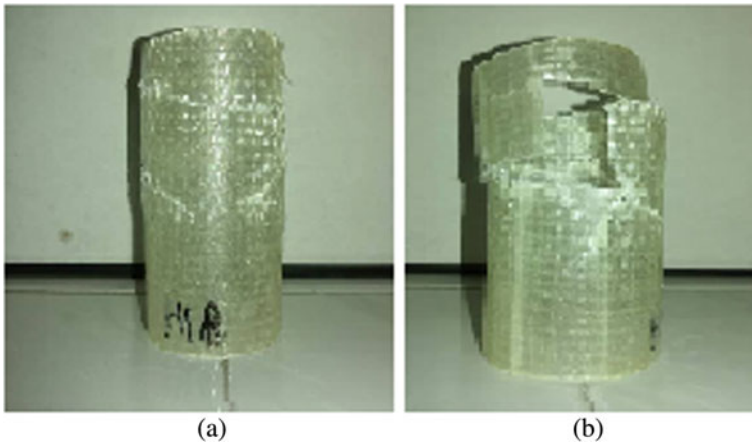
Fig. 3 **a** mode I failure and **b** mode II failure

can be observed. Mode II is referred to as interlaminar shear between the walls [18, 19]. From the failure mentioned, these have been contributed to energy absorption by the structures [20].

4 Conclusion

From this work, it can be concluded that the higher the number of plies used in the structures, the better its performance. It was observed the number of plies does not influence the crushing characteristics. Moreover, it increases the crushing performance of the tubes. Apart from that, specific energy absorption also does not affect the number of plies used. For the crushing characteristics, Mode I and Mode II are the main dominant in contributing the energy absorption for all the structures.

References

1. Lau STW, Yuhazri MY, Amirhafizan MH, Sihombing H (2020) Performance comparison on using metal and Kenaf FRP composite hollow structure in oblique crushing. Technol Rep Kansai Univ 62:5581–5585
2. Babazadeh J, Rahmani K, Hashemi SJ, Sadooghi A (2021) Effect of glass, carbon, and kevlar fibers on mechanical properties for polymeric composite tubes produced by a unidirectional winding method. Mater Res Express 8:45301
3. Guan W, Yu Y, Gao G (2021) Crashworthiness performance and multiobjective optimization of a combined splitting circular tube energy absorber under eccentric impact for subway vehicles. Int J Impact Eng 158:104006

4. Hertzberg RW, Vinci RP, Hertzberg JL (2012) Deformation and fracture mechanics of engineering materials, 5th edn. Wiley, New York
5. Praveen Kumar A, Pradeep C, Sai Rahul Gupta S, Vamshi Krishna G, Harshavardhan G (2021) Impact loading behavior of woven glass fabric polymer composite bi-tubular square sections. Mater Today Proc
6. Huang S, Fu Q, Yan L, Kasal B (2021) Characterization of interfacial properties between fibre and polymer matrix in composite materials—a critical review. J Mater Res Technol 13:1441–1484
7. Teng JG, Yu T, Fernando D (2012) Strengthening of steel structures with fiber-reinforced polymer composites. J Constr Steel Res 78
8. Al Rashid A, Khan SA, G. Al-Ghamdi S, Koç M (2021) Additive manufacturing of polymer nanocomposites: needs and challenges in materials, processes, and applications. J Mater Res Technol 14:910–941
9. Mahdi E, Hamouda ASM, Sen AC (2004) Quasi-static crushing behaviour of hybrid and non-hybrid natural fibre composite solid cones. Compos Struct 66:647–663
10. Ma Y, Sugahara T, Yang Y, Hamada H (2015) A study on the energy absorption properties of carbon/aramid fiber filament winding composite tube. Compos Struct 123:301–311
11. Prabhakaran S, Chinnarasu K, Kumar MS (2012) Design and fabrication of composite bumper for light passenger vehicles. Int J Mod Eng Res 2:2552–2556
12. Nourmohammadi N, O'Dowd NP, Weaver PM (2020) Effective bending modulus of thin ply fibre composites with uniform fibre spacing. Int J Solids Struct 196–197:26–40
13. Zang M, Hu Y, Zhang J, Ye W, Zhao M (2020) Crashworthiness of CFRP/aluminum alloy hybrid tubes under quasi-static axial crushing. J Mater Res Technol 9:7740–7753
14. Pavan Kumar Reddy R, Prabhu M, Ashraff Ali KS (2021) A review on investigation of compressive load and buckling load on composite pipe for windmill application. Mater Today Proc
15. Sivagurunathan R, Way SLT, Sivagurunathan L, Yaakob MY (2018) The effects of triggering mechanisms on the energy absorption capability of circular jute/epoxy composite tubes under quasi-static axial loading. Appl Compos Mater 6:1401–1417
16. Mahdi E, Ochoa D, Vaziri A, Eltai E (2019) Energy absorption capability of date palm leaf fiber reinforced epoxy composites rectangular tubes. Compos Struct 224
17. Daneshjoo Z, Shokrieh MM, Fakoor M, Alderliesten RC (2018) A new mixed mode I/II failure criterion for laminated composites considering fracture process zone. Theor Appl Fract Mech 98:48–58
18. Zeinedini A, Moradi MH, Taghibeigi H, Jamali J (2020) On the mixed mode I/II/III translaminar fracture toughness of cotton/epoxy laminated composites. Theor Appl Fract Mech 109:102760
19. Torabi AR, Pirhadi E (2019) Failure analysis of round-tip V-notched laminated composite plates under mixed mode I/II loading. Theor Appl Fract Mech 1040:102342
20. Zimmermann N, Wang PH (2020) A review of failure modes and fracture analysis of aircraft composite materials. Eng Fail Anal 115:104692

Optimising MIG Weld Bead Geometry of Hot Rolled Carbon Steel Using Response Surface Method

Junita Mohd Said and Faiz Mohd Turan

Abstract This paper presents the optimisation of weld bead geometry, through Metal Inert Gas butt-welding. Many failures occur in joints due to the bad quality of welding, influenced by a range of parameters across the welding process. With the rapid advancement of computer and automated technologies, new statistical methods for modelling and optimising have been developed. These have eliminated the need for performing experiments on the basis of conventional trial and error, for performance and quality. Experimental methods were set by selecting process parameters, which include the welding current, arc voltage and welding speed and employing a central composite design of Response Surface Methodology method. These methods were adopted as the statistical design of experimental techniques to analyse the performance of the weld bead geometry, i.e. bead height, bead width and penetration, in order to expound the numerical expression between the welding process parameters and the output variable. The results obtained from developing these models indicate that the model predicts weld bead geometry adequately. The effectiveness of process parameters can be estimated by applying the developed mathematical models to a given bead geometry, indicating the change of parameters influences the bead height and width more significantly than penetration alone.

Keywords Failure · Weld bead geometry · RSM · Optimisation

J. Mohd Said · F. Mohd Turan (✉)
Faculty of Manufacturing and Mechatronic Engineering Technology, Universiti Malaysia Pahang, 26600 Pekan, Pahang, Malaysia
e-mail: faizmt@ump.edu.my

J. Mohd Said
University Kuala Lumpur Malaysia France Institute (UniKL MFI), 43650 Bandar Baru Bangi, Selangor, Malaysia

1 Introduction

Welding is known as a fabrication process to joining parts. It is a complex process with successful outcomes dependent on a range of input parameters. However, it is very difficult to obtain relationship between welding quality and process parameters due to the high nonlinearity [1]. Fatigue failures in engineering structures occur predominately at component connections especially welding, due to variable stresses in the material. It is become the largest parts of failure on metallic components and leads to a major threat to many structures [2–4]. The result from various discontinuities influence by many factors, hence will affect the quality of welding joint, these characteristics include a lack of penetration at the weld root, undercutting at weld toes, and slag inclusion or gas pores. The rate of energy input will also affect the weldment characteristic, which reduces the welding quality and productivity, whilst increasing the cost of the welding joint [5–8].

Metal Inert Gas (MIG) is one of the arc welding process types and the most widely used in today's world. It became an important, easiest and strongest welding techniques used in manufacturing industries, oil and gas industries, and in building construction [9–11]. During MIG welding process, the transient heat source is supplied between filler metal and parent metal in a localized fusion zone. This heating melts and solidifies the filler metal and parent metal. The process involves critical parameters or criteria, such as welding speed, current, voltage, nozzle-plate distance, torch angle and the electrode diameter [12].

Rapid development in the advancement of computer and technologies in the manufacturing-based optimisation procedure, i.e. Design of Experiments (DoE), optimisation technique has been significantly exploited to represent and optimise the manufacturing processes to enhance performance, quality and lower costs [13]. Numerous weldment characteristic methods have been studied, leading to research in theoretical developments, statistical analysis and numerous experiments by various researchers [14–17], with the aim of enhancing productivity, the optimisation of welding parameters must be considered in order to achieve optimal welding quality to predicting weld bead geometry, mechanical properties, and Heat Affected Zones (HAZ) and others [18, 19].

Conventionally, it is time consuming to define suitable weld input parameters when producing a new welded joint, with required specifications, through trial and error. Fortunately, one of the best-known optimisation techniques of experimental design is the Response Surface Methods (RSM) technique, which aids analysis of experiments with the least experimental effort [20, 21]. RSM is an accepted study method for the collection of mathematical and statistical techniques to facilitate the developing, improving and optimisation of this process. The response of interest is influenced by several variables and the objective is to optimise the variables [22]. At the same time, it is also possible to estimate linear, interaction and quadratic effects of the factors and to develop a prediction model for the response. With these vigorous methods, it is possible to not only cover prediction of the system responses, but also to assist in conducting the analysis of experiments in order to define the

optimum quality process of parameter settings with minimised experimental effort [23].

Based on the above overview, the effects of welding parameters through experimental investigations have been discussed in this article, focusing on a weld bead of 3 mm thick hot rolled carbon steel plates JIS G3131. According to the relevant scope of work, the experiments were performed based on the Central Composite Design (CCD) matrix that led to the main objective of this study, i.e. to optimise the process parameters by maximising the aspect ratio of the weld bead under the premise of acceptable weld bead dimensions. Therefore, the limits of welding parameters will also be obtained. RSM was then used to develop mathematical models to predict the relationship between the processing parameters and the weld bead profile. Based on regression models, the optimal welding conditions can be identified, providing valuable guidance for production.

2 Methodology

The welding experimental procedure was designed based on RSM as the statistical DoE technique. The overall experimental methodology process flow of the research work is planned to be carried out as shown in Fig. 1. It was chosen as an effective way to model a quadratic relationship and would reveal good results for identifying the optimal welding conditions. RSM has widely been used to predict the weld-bead properties and to find the optimum responses of interest in many welding processes [24–26].

The ultimate objective of the RSM method is to establish the optimal operating conditions of experimental requirement. For the analysis, the relevant statistical-based software was then used to create the design matrix and analyse the experimental data.

2.1 Process Selection for RSM Procedure

All the regression model building methods and tools are significant to ensure the adequacy of the model, and therefore it is appropriate in RSM [27]. In order to define limitations of the selected process input welding parameter, three-factor and three levels (33) independent variables of the welding process parameter were identified and evaluated in random design. A pilot experimental test setting, based on the welding standards recommended by the American Welding Society (AWS), and the manuals for MIG welding equipment were consulted. In MIG welding, the variable parameter affecting the weldment quality are welding current (C), welding speed (S) and welding voltage (V) and were run according to CCD. The values of the independent process variable and experimental design levels, with their limits and notations are given in Table 1.

Fig. 1 The experimental
process flow for the research
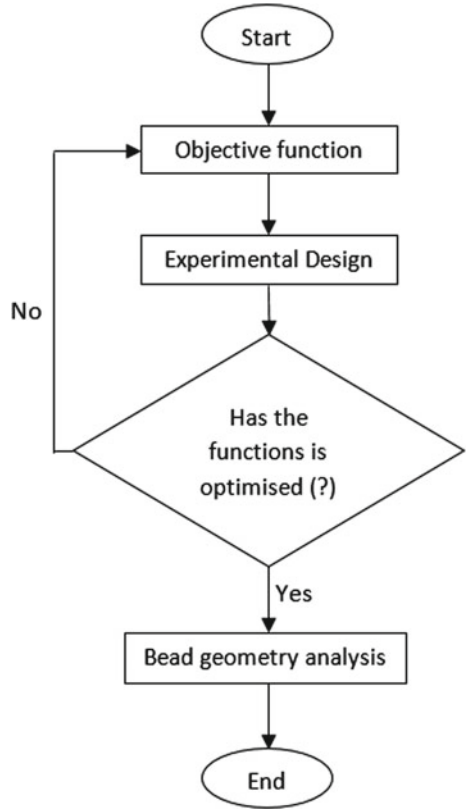
Table 1 Independent process variables and experimental design levels

Variable	Code			
	Unit	Low	Medium	High
		−1	0	+1
Welding current (C)	Amps	100	110	120
Welding speed (S)	Cm min^{-1}	20	25	30
Arc voltage (V)	Volts	17	18	19

The experimental measured responses are defined as heat input and weld bead geometry, contained weld width, penetration, and weld height. Figure 2 illustrates the criterion of weld bead geometry which normally occurs during the welding process. The welding quality criteria was defined and set as a goal to establish the optimal setting of welding parameters.

The aim of the experiment is to measure the possible reaction and then to generate a design matrix, as shown in Tables 2 and 3, respectively. The total generated design by software can also be defined by a matrix form as Eqs. 1 and 2.

Fig. 2 Experimental weld bead geometry and illustration of measured responses
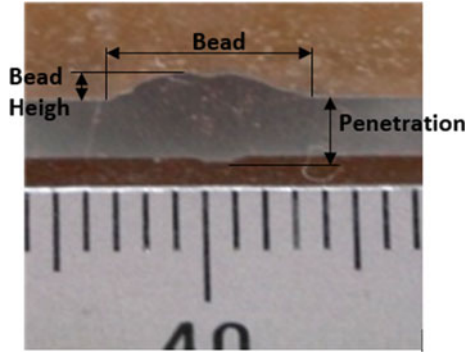
Table 2 Goals of experimental measured responses

Responses	Unit	Goal
Heat input (HI)	J/mm	Minimum
Weld penetration (WP)	mm	Minimum
Weld width (WW)	mm	Minimum
Weld height (WH)	mm	Minimum

$$y = X\beta + \varepsilon \tag{1}$$

$$y = \begin{bmatrix} y_1 \\ y_2 \\ \cdots \\ y_n \end{bmatrix}, \quad X = \begin{bmatrix} 1 & x_{11} & \cdots & x_{1k} \\ 1 & 1 & \cdots & x_{2k} \\ \cdots & \cdots & \cdots & \cdots \\ 1 & & \cdots & x_{nk} \end{bmatrix},$$

$$\beta = \begin{bmatrix} \beta_0 \\ \beta_1 \\ \cdots \\ \beta_k \end{bmatrix}, \quad \text{and} \quad \varepsilon = \begin{bmatrix} \varepsilon_1 \\ \varepsilon_2 \\ \cdots \\ \varepsilon_n \end{bmatrix} \tag{2}$$

where y is the monitored value of response function, depending upon the levels $x_1, x_2, \ldots, x_k$ of some k quantitative factors of design variable, β is the regression coefficient vector and ε is the noise of error in term of monitoring the response. The quadratic response model consists of all the linear terms, square terms and linear interactions.

Table 3 Design matrix with actual independent process variables

Std	Run	Value		
		C (Amp)	S (cm/min)	V (volts)
1	16	100	20	17
2	7	120	20	17
3	12	100	30	17
4	10	120	30	17
5	1	100	20	19
6	2	120	20	19
7	3	100	30	19
8	17	120	30	19
9	6	100	25	18
10	19	120	25	18
11	18	110	20	18
12	11	110	30	18
13	9	110	25	17
14	4	110	25	19
15	5	110	25	18
16	14	110	25	18
17	15	110	25	18
18	8	110	25	18
19	13	110	25	18
20	20	110	25	18

2.2 Materials and Experimental Work

The material used in this experiment was hot rolled carbon steel plates with the standard serial number of JIS G3131 SPH270C. The inert gas used was carbon dioxide (CO_2) and the electrode wire ER70S-6 was selected based on the properties and characteristic of the base material, weld dimension and existing filler wire inventory. The material composition and filler metal are tabulated in Table 4.

Welding assemblies were prepared by the MIG butt joint welding process of a 3 mm thick sheet and was conducted on the two plates with dimensions of 200 × 80 widths respectively. Basic geometry of the specimens was prepared according to the AWS D1.1 standard [28], as illustrated in Fig. 3. The experimental work was carried out using the MIG robot welding procedure and according to the total 20 conditions of design matrix as tabulated in Table 3. These design matrixes were generated by statistical software in a random order. To minimise any systematic error in the experiment, the welded plates were cleaned in order to make sure all solidified molten drops were removed from the intended test surface. To obtain and record an average value of the measured responses of weld bead geometry, at least two

Table 4 Nominal composition of carbon steel G3131 and filler wire Er70s-6 (weight in %)

Elements	Nominal carbon steel G3131	ER70S-6
C	0.13	0.06–0.15
Si	0.05	0.80–1.15
Mn	0.5	1.40–1.85
P	0.035	0.025 max
S	0.035	0.025 max
Cu	…	0.50
Alt	0.010	…

Fig. 3 The geometry of the tested specimen
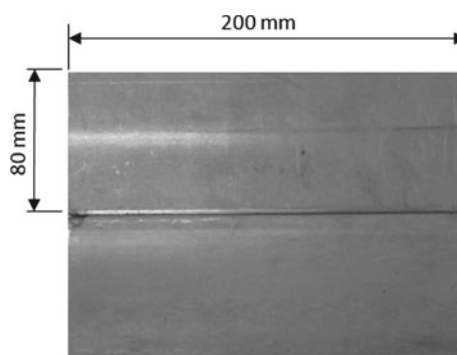
transverse sections of the specimen were cut from each respective welded specimen, according to AWS D1.1 standard [28].

The specimen was then grinded to remove the cold work, and cut and polished as per standard metallographic procedures to obtain better edge flatness by silicon carbide abrasive paper of grades 100, 240, 400, 800 and 1200 grit, on a rotating polishing wheel machine. The resulting weld bead geometry profile was attained through the measurement process described in Fig. 2, after cutting and polishing according to the welded specimen perpendicular to the direction of welding process.

3   Preliminary Result

The measures responses result of experiments from every test material are tabulated in Table 5. The RSM was used on the experimental data to obtain the impact of the regression models on the individual model, and to determine the mathematical models with best fits. The associated p-value of less than 0.05, (i.e., α is Equal to 0.05 or 95% confident level) indicates that the model terms can be considered as statistically significant. The coefficients and their lack-of-fit through the step wise regression method were used, which Eliminated the irrelevant model term. The indicated variance Value and the significance of each model terms respectively. The

Table 5 The measures responses results of experiments

STD	Responses			
	HI (J/mm)	Weld bead geometry		
		WP (mm)	WW (mm)	WH (mm)
1	5100	3.320	8.820	1.960
2	6120	3.220	9.210	1.750
3	3400	2.930	7.040	1.470
4	4080	3.500	7.810	1.680
5	5700	3.230	8.820	1.960
6	6840	3.730	9.120	1.040
7	3800	2.930	7.560	2.010
8	4560	4.250	8.480	1.220
9	4320	3.280	8.100	1.740
10	5184	4.150	7.570	1.770
11	5940	4.200	9.260	1.910
12	3960	3.420	8.590	2.560
13	4488	3.550	7.500	1.850
14	5016	4.470	8.600	0.820
15	4752	3.460	8.560	1.510
16	4752	3.330	8.230	1.950
17	4752	3.200	8.230	1.660
18	4752	2.750	8.810	2.200
19	4752	3.810	8.050	1.780
20	4752	3.670	7.920	1.750

complete model was checked through the verification coefficient (R^2) where its value was always in a range of 0–1. This value was defined as the indicator to calculate an optimal choice of the responses. The nearer its value is to 1, the more accurate the developed model is [29].

4 Conclusion

The detailed methodology of the RSM optimisation technique for MIG butt welding of hot rolled carbon steel plates JIS G3131 SPH270C was studied and statistically will be analysed. The purpose of this was to evaluate a combination of optimal parameters with acceptance responses of penetration and weld bead of HAZ. This has important criteria for welded joints through reducing the weld metal consumption by providing deeper penetration and lower bead height and width, where the mechanical metallurgical characteristics of the weld joint is influenced by HAZ sizes. This is

therefore expected to minimise HAZ width and depth, which is necessary to avoid drastic micro-structure changes between HAZ and the parent metal.

References

1. Gao Z, Shao X, Jiang P, Cao L, Zhou Q, Yue C, Liu Y, Wang C (2016) Parameter optimization of hybrid fiber laser-arc butt welding on 316L stainless steel using Kriging model and GA. Opt Laser Technol 83:153–162
2. Atzori B, Lazzarin P, Meneghetti G, Ricotta M (2009) Fatigue design of complex welded structures. Int J Fatigue 31:59–69
3. Lazić V, Aleksandrović S, Nikolić R, Prokić-Cvetković R, Popović O, Milosavljević D, Čukić R (2012) Estimates of weldability and selection of the optimal procedure and technology for welding of high strength steels. Procedia Eng 40:310–315
4. Ramos-Jaime D, Juárez IL, Perez P (2013) Effect of process parameters on robotic gmaw bead area estimation. Procedia Technol 7:398–405
5. Balasubramanian M (2016) Prediction of optimum weld pool geometry of PCTIG welded titanium alloy using statistical design. Eng Sci Technol Int J 19:15–21
6. Sharma C, Dwivedi DK, Kumar P (2012) Effect of welding parameters on microstructure and mechanical properties of friction stir welded joints of AA7039 aluminum alloy. Mater Des 36:379–390
7. Ganjigatti JP, Pratihar DK, Roy Choudhury A (2007) Global versus cluster-wise regression analyses for prediction of bead geometry in MIG welding process. J Mater Process Technol 189:352–366
8. Ibrahim IA, Mohamat SA, Amir A, Ghalib A (2010) Effect of arc voltage, welding current and welding speed on fatigue life, impact energy and bead penetration of AA6061 joints produced by robotic MIG welding. Indian J Sci Technol 3(2)
9. Palani PK, Murugan N (2006) Review selection of parameter of pulsed current gas metal arc welding. J Mater Process Technol 172:1–10
10. Kolahan F, Heidari M (2009) A new approach for predicting and optimizing weld bead geometry in GMAW, vol 59. World Academy of Science, Engineering and Technology
11. Pal A, Handuja S (2014) The analysis of MIG welding parameters for multi response optimization using Taguchi's Orthogonal array and Grey relational approach. Int J Adv Res Eng Sci Technol
12. Asibeluo IS, Emifoniye E (2015) Effect of arc welding current on the mechanical properties of a36 carbon steel weld joints. SSRG Int J Mech Eng 2
13. Ai Y, Jiang P, Shao X, Wang C, Li P, Mi G, Liu Y, Liu W (2016) A defect-responsive optimization method for the fiber laser butt welding of dissimilar materials. Mater Des 90:669–681
14. Eltawahni HA, Olabi AG, Benyounis KY (2010) Effect of process parameters and optimization of CO_2 laser cutting of ultra high-performance polyethylene. Mater Des 31:4029–4038
15. Elatharasana G, Kumar VSS (2013) An experimental analysis and optimization of process parameter on friction stir welding of AA 6061-T6 aluminum alloy using RSM. Procedia Eng 64:1227–1234
16. Khan MMA, Romoli L, Fiaschi M, Dini G, Sarri F (2011) Experimental design approach to the process parameter optimization for laser welding of martensitic stainless steels in a constrained overlap configuration. Opt Laser Technol 43:158–172

17. Bidi L, Le Masson P, Cicala E, Primault C (2017) Experimental design method to the weld bead geometry optimization for hybrid laser-MAG welding in a narrow chamfer configuration. Opt Laser Technol 89:114–125
18. Umanath K, Palanikumar K (2015) Influence of process parameter on microstructural characteristics and tensile properties of friction welded ASS304L alloy. Appl Mech Mater 766–767
19. Palani PK, Murugan N (2007) Optimization of weld bead geometry for stainless steel claddings deposited by FCAW. J Mater Process Technol 190:291–299
20. Elatharasan G, Kumar VSS (2012) Modelling and optimization of friction stir welding parameters for dissimilar aluminium alloys using RSM. Procedia Eng 38:3477–3481
21. Ruggiero A, Tricarico L, Olabi AG, Benyounis KY (2011) Weld-bead profile and costs optimisation of the CO_2 dissimilar laser welding process of low carbon steel and austenitic steel AISI316. Opt Laser Technol 43:82–90
22. Acherjee B, Misra D, Bose D, Venkadeshwaran K (2009) Prediction of weld strength and seam width for laser transmission welding of thermoplastic using response surface methodology. Opt Laser Technol 41:956–967
23. Khataee AR, Fathinia M, Aber S, Zarei M (2010) Optimization of photocatalytic treatment of dye solution on supported TiO_2 nanoparticles by central composite design: Intermediate's identification. J Hazard Mater 181:886–897
24. Benyounis KY, Olabi AG, Hashmi MSJ (2005) Optimizing the laser-welded butt joints of medium carbon steel using RSM. J Mater Process Technol 164–165:986–989
25. Panneerselvam K, Lenin K (2015) Parameter's optimization in FSW of polypropylene based on RSM. Multidiscip Model Mater Struct 11:32–42
26. Lakshminarayanan AK, Balasubramanian V (2009) Comparison of RSM with ANN in predicting tensile strength of friction stir welded AA7039 aluminium alloy joints. Trans Nonferrous Metals Soc China 19:9–18
27. Reisgen U, Schleser M, Mokrov O, Ahmed E (2012) Statistical modeling of laser welding of DP/TRIP steel sheets. Opt Laser Technol 44:92–101
28. Jenney CL, O'Brien A (2001) Welding handbook, 9th edn., vol 1. Welding Science and Technology, American Welding Society (AWS)
29. Zhao Y, Zhang Y, Hu W, Lai X (2012) Optimization of laser welding thin-gage galvanized steel via response surface methodology. Opt Lasers Eng 50:1267–1273

The Concepts and Determinants of Manufacturing Flexibility

Mohd Ghazali bin Maarof, Gusman bin Nawanir, and Muhammad Fakhrul

Abstract Manufacturing companies nowadays are facing intense global challenges to sustain in this competitive market. As the global market are becoming more globalized and many new technologies being introduce, it has changed the demand preference for new products. The new market demand requires that the manufacturing firms to deliver customize products that can meet the individual customer's needs. This has created high level of market uncertainty and add complexity to the manufacturing processes set-up in many manufacturing companies. Manufacturing flexibilities provide a better way for manufacturers to overcome this uncertainty. This article will examine the contributing factors that can assist manufacturing firms to implement effective manufacturing flexibility in their manufacturing processes. Method used in conducting this review analysis is based on analysing the literature review done by the past researchers. This study reveals that the contributing factors can be simplified into three categories, namely advance manufacturing technology (AMT), organizational and environment. Findings from this study is expected to expand the knowledge on manufacturing flexibility requirements. In addition, this study can help industrial practitioners to implement manufacturing flexibility in a much better way.

Keywords Manufacturing flexibility · Technology · Review analysis

1 Introduction

1.1 *A Subsection Sample*

Manufacturing companies nowadays are facing intense global challenges characterized by fierce competition, shift towards customized products and unprecedented

M. G. Maarof (✉)
Universiti Malaysia Pahang, 26600 Pekan, Malaysia
e-mail: mohdghazali@ump.edu.my

G. Nawanir · M. Fakhrul
Universiti Malaysia Pahang, 26300 Gambang, Malaysia

changes [26]. The shift towards customized products has brings a lot of uncertainty to the market, requiring some form of flexibility capabilities in today's businesses environment [5, 33]. In the past, manufacturing activities were predominantly focus on the effort to reduce the operation cost and to improve quality as a way to sustain in the business [50, 51]. Mass production system was the common means to manufacture high volume of similar products with the assumptions that demand is always stable, predictable, less variety and long product life cycles [6]. However, as the market are becoming more globalized and many new technologies being introduced, it has changed the customers preference for new products.

The current market requires that the manufacturing firms to deliver customize products that can meet the individual customer's needs at a much lower price [9] and at a much faster rate [4, 55]. Such requirements post new challenges such as the need to ensure shorter product life-cycle, shorter delivery lead time, and increase product variety with a higher quality products [1, 7, 12]. Fulfilling those customer needs are crucial for the sustainability of firms in the market [11, 21, 23]. However, these new requirement has increased the complexity of the manufacturing processes set-up and create a high level of uncertainty [9, 37, 48, 53, 54].

Production system design should be able to cater for various demand by the customers with minimum operation costs, and flexibility [26]. The production design should respond appropriately to uncertainty posted by volatile market environment [30]. Therefore, the urge to tackle different uncertainties quickly and effectively has driven many manufacturing firms to adopt manufacturing flexibility in their manufacturing process [24, 38].

Gothwal and Raj [15] states that companies that adopted a flexible manufacturing system have the advantage to address issues pertaining to market changes better than those that use the mass production system. Through manufacturing flexibility capability, manufacturers can deal with the volatile customer demand, such as new and rapid technological development and frequent product changeover [27] and smaller lot sizes [12].

Unfortunately, very few research really deals with elements that influence the implementation of flexible manufacturing system in a firm [28]. Most works on manufacturing flexibility are still in disordered and unregulated despite consensus that believe manufacturing flexibility can benefit firms in coping with uncertainty [31]. Poor understanding on the concepts of manufacturing flexibility has influence the firm's attainments to the real benefits of manufacturing flexibility [28, 44]. As a result, many manufacturing firms have lose the synergistic benefits of flexible manufacturing system in improving business performance [34, 43].

This paper aims to examine the contributing factors that can enhance effective implementation of manufacturing flexibility by answering two research questions:

RQ1: What is manufacturing flexibility?
RQ2: What are the critical determinants to implement manufacturing flexibility in the manufacturing industry.

Findings from this study is expected to expand the knowledge on manufacturing flexibility requirements. Furthermore, this study can also help industrial practitioners to implement manufacturing flexibility in a much better way. Result from this research can assist the government agencies involved in developing the manufacturing industry to devise or review current policies to improve manufacturing industry practices in Malaysia.

2 Literature Review

2.1 Definition of Manufacturing Flexibility

Past researchers were not able to derive to a consensus on defining manufacturing flexibility [14, 35]. This is because every company has its own perspectives in defining manufacturing flexibility [29], making it hard for researchers to come up with the

Table 1 Manufacturing flexibility definition

References	Manufacturing flexibility
[42]	The ability of a manufacturing system to manage volume or product variation changes without affecting to the firm's performance
[17]	The manufacturing system ability to keep up with the changes exerted by the environment conditions
[46]	Flexibility defines the ability of a firm to react to changes with minimum impacts to business performance
[45]	The system ability to quickly adapt to any changes happened with the product, process, workload, or machine failure
[49]	The firm's capability to react to anticipate and unanticipated changes resulting from competitive pressures
[32]	The ability to consume the existing resources effectively in response to the impact exerted by the environmental factors
[55]	Ability to produce wide variation of products to satisfy the customers demand while maintaining high business performance
[4]	The ability of a manufacturing company to deal with the uncertain situation within or outside of the organization
[10]	Organization adaptability capabilities to deal with changing environmental condition
[19]	System ability to react to the environmental uncertainties (internal and external) effectively and efficiently to produce high quality customized product at a competitive price
[52]	The manufacturing system ability to withstand variations in part combination without affecting to the assembly line progress

most appropriate definition for manufacturing flexibility [15]. Table 1 summarized the definition of manufacturing flexibility given by past researchers.

Based on the definition given by the authors' above, manufacturing flexibility is defined as the firm's ability to manage and adapt to changes in the internal and external environments effectively without incurring additional cost or interruptions to the operation.

2.2   The Manufacturing Flexibility Concept

In managing demand uncertainty, a flexible manufacturing system can help to find the right fit between supply and demand in the turbulent market [34]. The ability for firms to make such adjustment without affecting its average costs is crucial to maintain firm's competitiveness in the dynamic market environment [18]. The concept of manufacturing flexibility was highly been discussed during the early 1980s as the businesses were experiencing a major shift in the global market demand [28]. David Williamson has introduced the idea on flexibility in England during the 1960s, in which he introduced a flexible computer controlled machine tools that can work automatically 24 h a day [8]. His work has been developed to a much broader applications known as the flexible manufacturing system. This flexible manufacturing system was later referred as manufacturing flexibility.

Past studies has categorized manufacturing flexibility into three major groups: inbound, in-house and outbound [41]. Inbound flexibility includes the supplier flexibility and sourcing flexibility dimensions to address the unstable nature of the raw materials or components sourcing due to change in demand. In-house flexibility refers to the organization's capability to absorb changes in the internal production process in converting the inputs into complete products. Example of the in-house flexibility dimensions are the product, machine, labor, routing, processing times, volume, process, operation, material handling, and postponement [41]. Outbound flexibility refers to the logistic activities to transfer the completed products to the marketplace. The outbound logistics dimensions include transshipment flexibility, access flexibility, and delivery flexibility.

However, different levels of uncertainties and variations will require different type of manufacturing flexibility adoption [16, 29] and it depends on a specific situation [20]. Thus, flexibility constitute making responses to various problems under a particular condition.

2.3 Critical Determinants of Manufacturing Flexibility

At the plant level, flexibility is a mixture of several supporting factors such as hardware, software, procedure, organizations, techniques, and manufacturing infrastructure [42]. In term of value chain factors, manufacturing flexibility implementation is affected by the infrastructure, human resource, technology, procurement, inbound and outbound logistics, operations, marketing and sales, and services [22]. Another researcher revealed eight different factors that affect manufacturing flexibility achievement, namely, operational improvement practices (OIPs), technology, human resource practices, supplier flexibility, supplier integration, customer integration, product/process technology integration, and marketing and manufacturing integration [28].

Other approach taken by firms to enhance their manufacturing flexibility include applying flexible product design and postponement to develop product mix flexibility [36]. Cross-training can prepare firms with the ability to develop both product mix as well as volume flexibility capability [3]. The use of temporary or contract staffs were used by electronics manufacturers to build volume flexibility in their production process [40]. Furthermore, original equipment manufacturers (OEM) services can support firms to develop volume flexibility during peak demand [39].

Additive manufacturing (AM) has been used to build process flexibility in the new products development to speed up time to market [2]. The use of autonomous mobile robots (AMR) helps firms to increase their material handling responsiveness to changes in the discrete manufacturing system [13]. The use of Industry 4.0 technologies can help manufacturers to develop the smart factory concept into their production lines [50, 51]. For instance, augmented reality (AR) can serve as a unified platform for aiding operators in the training procedures which is flexible enough to be adapted into various manufacturing sectors [25].

Table 2 summarized the discussion on the three categories that contribute to manufacturing flexibility implementation.

Table 2 Summary of the manufacturing flexibility contributing factors

References	AMT	Organizational	Environmental
[42]	X	X	X
[3]		X	
[22]	X	X	X
[40]		X	
[36]	X		
[39]		X	
[25]	X		
[2]	X		
[50, 51]	X		
[13]	X		

3 Discussion and Conclusion

This conceptual paper presents the discussion on the definition of manufacturing flexibility. Furthermore, it summarizes the elements that can enhance the implementation of manufacturing flexibility in a company that can be summarized into three main categories: advance manufacturing technology (AMT) factors, organizational factors, and environmental factors. This discussion is important due to the changes happened around the business environment that bring about the need to overcome market uncertainty.

Although this article clearly has not resolved all the issues about factors contributing to manufacturing flexibility implementation, hopefully it can provide some useful suggestions to researchers or industry practitioners before implementing manufacturing flexibility. Future study should work on developing empirical investigation to identify factors that can contribute to the effective implementation of manufacturing flexibility in a company.

References

1. Abdelilah B, El Korchi A, Balambo MA (2018) Flexibility and agility: evolution and relationship. J Manuf Technol Manag 29(7):1138–1162. https://doi.org/10.1108/JMTM-03-2018-0090
2. Achillas C, Aidonis D, Iakovou E, Thymianidis M, Tzetzis D (2015) A methodological framework for the inclusion of modern additive manufacturing into the production portfolio of a focused factory. J Manuf Syst 37:328–339. https://doi.org/10.1016/j.jmsy.2014.07.014
3. Adler PS (1988) Managing flexible automation. Calif Manage Rev 30(3):34–56. https://doi.org/10.2307/41166513
4. Agus A (2011) Supply chain management, supply chain flexibility and business performance. J Glob Strat Manag 9:134–145
5. Ariss SS, Zhang Q (2002) The impact of flexible process capability on the product-process matrix: An empirical examination. Int J Prod Econ 76(2):135–145. https://doi.org/10.1016/S0925-5273(01)00146-3
6. Beach R, Muhlemann AP, Price DHR, Paterson A, Sharp JA (2000) Review of manufacturing flexibility. Eur J Oper Res 122(1):41–57. https://doi.org/10.1016/S0377-2217(99)00062-4
7. Brettel M, Klein M, Friederichsen N (2016) The relevance of manufacturing flexibility in the context of industrie 4.0. Procedia CIRP 41:105–110. https://doi.org/10.1016/j.procir.2015.12.047
8. Buzacott JA, Yao DD (1986) Flexible manufacturing systems: a review of analytical models. Manage Sci 32(7):890–905. https://doi.org/10.1287/mnsc.32.7.890
9. Chavez R, Fynes B, Gimenez C, Wiengarten F (2012) Assessing the effect of industry clockspeed on the supply chain management practice-performance relationship. Supply Chain Manage Int J 17(3):235–248. https://doi.org/10.1108/13598541211227081
10. Chryssolouris G, Efthymiou K, Papakostas N, Mourtzis D, Pagoropoulos A (2013) Flexibility and complexity: Is it a trade-off? Int J Prod Res 51(23–24):6788–6802. https://doi.org/10.1080/00207543.2012.761362

11. Dey S, Sharma RRK, Pandey BK (2019) Relationship of manufacturing flexibility with organizational strategy. Glob J Flex Syst Manag 20(3):237–256. https://doi.org/10.1007/s40171-019-00212-x
12. ElMaraghy H, ElMaraghy W (2016) Smart adaptable assembly systems. Procedia CIRP 44:4–13. https://doi.org/10.1016/j.procir.2016.04.107
13. Fragapane G, Ivanov D, Peron M, Sgarbossa F, Strandhagen JO (2020) Increasing flexibility and productivity in Industry 4.0 production networks with autonomous mobile robots and smart intralogistics. Ann Oper Res. https://doi.org/10.1007/s10479-020-03526-7
14. Gerwin D (1993) Manufacturing flexibility. A strategic perspective. Manage Sci 39(4):395–410. https://doi.org/10.1287/mnsc.39.4.395
15. Gothwal S, Raj T (2017) Analyzing the factors affecting the flexibility in FMS using weighted interpretive structural modeling (WISM) approach. Int J Syst Assur Eng Manag 8(2):408–422. https://doi.org/10.1007/s13198-016-0443-1
16. Gupta D, Buzacott JA (1996) A "goodness test" for operational measures of manufacturing flexibility. Int J Flex Manuf Syst 8(3):233–245. https://doi.org/10.1007/BF00403126
17. Gupta YP, Goyal S (1989) Flexibility of manufacturing systems: concepts and measurements. Eur J Oper Res 43(2):119–135. https://doi.org/10.1016/0377-2217(89)90206-3
18. Hirsch S, Mishra A, Möhring N, Finger R (2019) Revisiting firm flexibility and efficiency: evidence from the EU dairy processing industry. Eur Rev Agric Econ 1–38. https://doi.org/10.1093/erae/jbz003
19. Jain A, Jain PK, Chan FTS, Singh S (2013) A review on manufacturing flexibility. Int J Prod Res 51(19):5946–5970. https://doi.org/10.1080/00207543.2013.824627
20. Kara S, Kayis B (2004) Manufacturing flexibility and variability: an overview. J Manuf Technol Manag 15(6):466–478. https://doi.org/10.1108/17410380410547870
21. Kaur SP, Kumar J, Kumar R (2016) Impact of flexibility of manufacturing system components on competitiveness of SMEs in Northern India. J Eng Project Prod Manage 6(1):63–76. https://doi.org/10.32738/jeppm.201601.0006
22. Kim C (1991) Issues on manufacturing flexibility. Integr Manuf Syst 2(2):4–7. https://doi.org/10.1108/09576069110006181
23. Koste LL, Malhotra MK (1999) A theoretical framework for analyzing the dimensions of manufacturing flexibility. J Oper Manag 18:75–93
24. Lafou M, Mathieu L, Pois S, Alochet M (2016) Manufacturing system flexibility: product flexibility assessment. Procedia CIRP 41:99–104. https://doi.org/10.1016/j.procir.2015.12.046
25. Martínez H, Laukkanen S, Mattila J (2014) A new flexible augmented reality platform for development of maintenance and educational applications. Int J Virtual Worlds Human Computer Inter 2:18–27. https://doi.org/10.11159/vwhci.2014.003
26. Mishra D, Sharma RRK, Gunasekaran A, Papadopoulos T, Dubey R (2019) Role of decoupling point in examining manufacturing flexibility: an empirical study for different business strategies. Total Qual Manag Bus Excell 30(9–10):1126–1150. https://doi.org/10.1080/14783363.2017.1359527
27. Mishra R, Pundir AK, Ganapathy L (2014) Assessment of manufacturing flexibility: a review of research and conceptual framework. Manag Res Rev 37(8):750–776. https://doi.org/10.1108/MRR-03-2013-0055
28. Mishra R, Pundir AK, Ganapathy L (2018) Empirical assessment of factors influencing potential of manufacturing flexibility in organization. Bus Process Manag J 24(1):158–182. https://doi.org/10.1108/BPMJ-07-2016-0157
29. Ojstersek R, Buchmeister B (2020) The impact of manufacturing flexibility and multi-criteria optimization on the sustainability of manufacturing systems. Symmetry 12(1):157. https://doi.org/10.3390/sym12010157
30. Palominos P, Quezada L, Donoso J, Gonzalez M (2019) A model of economic evaluation for the acquisition of flexible manufacturing technologies. Procedia Manuf 39:565–573. https://doi.org/10.1016/j.promfg.2020.01.420
31. Pérez-Pérez M, Serrano-Bedia AM, López-Fernández MC, García-Piqueres G (2018) Research opportunities on manufacturing flexibility domain: a review and theory-based research agenda. J Manuf Syst 48:9–20. https://doi.org/10.1016/j.jmsy.2018.05.009

32. Petroni A, Bevilacqua M (2002) Identifying manufacturing flexibility best practices in small and medium enterprises. Int J Oper Prod Manag 22(7–8):929–947. https://doi.org/10.1108/01443570210436217

33. Rajesh R (2020) Flexible business strategies to enhance resilience in manufacturing supply chains: an empirical study. J Manuf Syst. https://doi.org/10.1016/j.jmsy.2020.10.010

34. Rogers PP, Ojha D, White RE (2011) Conceptualising complementarities in manufacturing flexibility: a comprehensive view. Int J Prod Res 49(12):3767–3793. https://doi.org/10.1080/00207543.2010.499116

35. Saleh JH, Mark G, Jordan NC (2009) Flexibility: a multi-disciplinary literature review and a research agenda for designing flexible engineering systems. J Eng Des 20(3):307–323. https://doi.org/10.1080/09544820701870813

36. Salvador F, Forza C, Rungtusanatham M (2002) Modularity, product variety, production volume, and component sourcing: theorizing beyond generic prescriptions. J Oper Manag 20(5):549–575. https://doi.org/10.1016/S0272-6963(02)00027-X

37. Salvador F, Rungtusanatham MJ, Madiedo Montanez JP (2015) Antecedents of mass customization capability: direct and interaction effects. IEEE Trans Eng Manage 62(4):618–630. https://doi.org/10.1109/TEM.2015.2477276

38. Seebacher G, Winkler H (2014) Evaluating flexibility in discrete manufacturing based on performance and efficiency. Int J Prod Econ 153:340–351. https://doi.org/10.1016/j.ijpe.2014.03.018

39. Stevenson M, Spring M (2007) Flexibility from a supply chain perspective: definition and review. Int J Oper Prod Manag 27(7):685–713. https://doi.org/10.1108/01443570710756956

40. Suarez FF, Cusumano MA, Fine CH (1996) An empirical study of manufacturing flexibility in printed circuit board assembly. Oper Res 44(1):223–240. https://doi.org/10.1287/opre.44.1.223

41. Sushil (2018) Interpretive multi-criteria valuation of flexibility initiatives on direct value chain. Benchmarking 25(9):3720–3742. https://doi.org/10.1108/BIJ-03-2018-0057

42. Swamidass PM, Newell WT (1987) Manufacturing strategy, environmental uncertainty and performance: a path analytic model. Manage Sci 33(4):509–524. https://doi.org/10.1287/mnsc.33.4.509

43. Tan KW (2016). Impact of manufacturing flexibility on manufacturing performance and business performance among Malaysian manufacturing firms. Doctor of Philosophy, Universiti Utara Malaysia

44. Tan KW, Lim KT (2019) Impact of manufacturing flexibility on business performance: Malaysian's perspective. Gadjah Mada Int J Bus 21(3):308–329. https://doi.org/10.22146/gamaijb.27402

45. Tsubone H, Horikawa M (1999) Comparison between machine flexibility and routing flexibility. Int J Flex Manuf Syst 11(1):83–101. https://doi.org/10.1023/A:1008096724273

46. Upton DM (1994) The management of manufacturing flexibility. Calif Manage Rev 36(2):72–89. https://doi.org/10.2307/41165745

47. Upton DM (1997) Process range in manufacturing: an empirical study of flexibility. Manage Sci 43(8):1079–1092. https://doi.org/10.1287/mnsc.43.8.1079

48. Veile JW, Kiel D, Muller JM, Voigt K-I (2019) Lessons learned from Industry 4.0 implementation in the German manufacturing industry. J Manuf Technol Manage 31(5):977–997. https://doi.org/10.1108/JMTM-08-2018-0270

49. Vokurka RJ, O'Leary-Kelly SW (2000) Review of empirical research on manufacturing flexibility. J Oper Manag 18(4):485–501. https://doi.org/10.1016/S0272-6963(00)00031-0

50. Wang S, Wan J, Zhang D, Li D, Zhang C (2016) Towards smart factory for industry 4.0: A self-organized multi-agent system with big data based feedback and coordination. Comput Netw 101:158–168. https://doi.org/10.1016/j.comnet.2015.12.017

51. Wang Z, Zhang M, Sun H, Zhu G (2016) Effects of standardization and innovation on mass customization: an empirical investigation. Technovation 48–49:79–86. https://doi.org/10.1016/j.technovation.2016.01.003

52. Yadav A, Jayswal SC (2018) Modelling of flexible manufacturing system: a review. Int J Prod Res 56(7):2464–2487. https://doi.org/10.1080/00207543.2017.1387302
53. Zeltzer L, Aghezzaf EH, Limère V (2017) Workload balancing and manufacturing complexity levelling in mixed-model assembly lines. Int J Prod Res 55(10):2829–2844. https://doi.org/10.1080/00207543.2016.1213452
54. Zhang M, Qi Y, Zhao X, Duray R (2015) Mass customisation systems: complementarities and performance consequences. Int J Log Res Appl 18(6):459–475. https://doi.org/10.1080/13675567.2015.1015507
55. Zhang Q, Vonderembse MA, Lim JS (2003) Manufacturing flexibility: defining and analyzing relationships among competence, capability, and customer satisfaction. J Oper Manag 21:173–191

The Experimental Investigation on Surface Roughness of Aluminium 6061 Using Carbide Tools in Dry End Milling

Nurul Hidayah Razak and **Ng Chun Hao**

Abstract This paper presents an experimental investigation on surface roughness of Alumunium 6061 using carbide tools in dry milling. Process parameters include the cutting speed, feed rate and depth of cut. There were two types of cutting inserts used in the experiment which were TiAlN coated and uncoated carbide. Response surface method (RSM) with analysis of variance (ANOVA) analysis has been used to determine factors that influence the surface roughness. Based on the ANOVA analysis, it is shown that the most influential parameter affects the surface roughness for coated and uncoated insert are cutting speed followed by feed rate, and depth of cut. Furthermore, the TiAlN coated insert resulted in lower surface roughness value compare to the uncoated carbide insert.

Keywords Surface roughness · Alumunium 6061 · RSM method · ANOVA

1 Introduction

Aluminum alloy 6061 is classified as one of the most popular metals in the manufacturing industries for the automotive, aerospace, food packaging and sports equipment. This is due to its outstanding mechanical properties such as great strength to light weight ratio, corrosion resistant, hardness and able to weld [1]. One of the challenges in machining this material is the high temperature generated during machining operation that finally reducing the tool life, increasing the cutting force thus resulting in low quality of machined surface [2, 3]. According to Adhip et al. [2], a good machinability particularly in producing a good surface roughness of Aluminium reducing a significant impact to the manufacturing cost in the industry.

With regards to the issue addressing above, this study was conducted with the purpose of investigating on the surface roughness of Aluminium 6061 using TiAlN

N. H. Razak (✉) · N. Chun Hao
Faculty of Manufacturing and Mechatronic Engineering, Universiti Malaysia Pahang, 26600 Pahang, Malaysia
e-mail: hidayahrazak@ump.edu.my

coated and uncoated carbide inserts in dry end milling. Response surface methodology (RSM) integrated with ANOVA analysis was used to correlate the machining input parameters to the response surface roughness of Aluminium 6061.

2 Experiment Setup

2.1 Milling Machine and Fixtures

In this study, milling operations were carried on a MAKINO KE55 milling machine as shown in Fig. 1a and the experiments setup is shown in Fig. 1b. The milling

(a) CNC milling machine
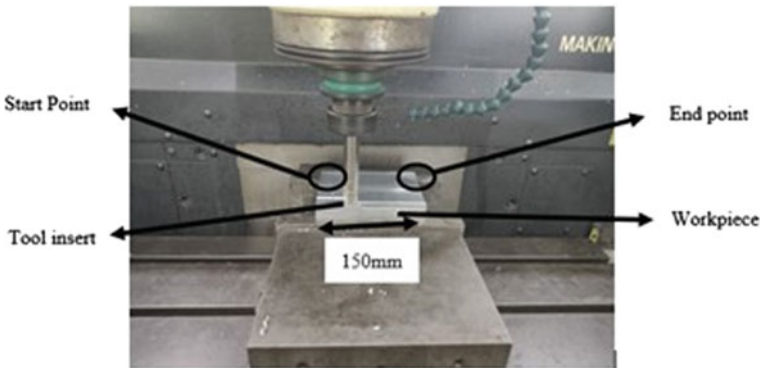
(b) The milling set up

Fig. 1 **a** shows CNC milling machine with a clamped workpiece where in Fig. 1 **b** shows the milling set up with a workpiece of 150 mm in length where the start and end points of the cutting insert were marked

Table 1 Mechanical properties of aluminum alloy 6061

Properties	Values
Density	2.7 g/cm^3
Elongation at break	12–25%
Poisson's ratio	0.33
Tensile strength	124–290 MPa
Young's modulus	68.9 GPa

Table 2 Machining parameters

Level of factors	Low	High
Cutting speed, m/min	29	86
Feed rate, mm/min	165	365
Depth of cut, mm	0.4	0.8

operation started from the 'Start point' and finished after completing one pass at the end point of the workpiece. The milling distance was 1500 mm per one milling pass.

2.2 Workpiece Materials and Cutting Tools

Aluminum alloy 6061 was selected as the material used in this experiment with dimension of 150 mm × 150 mm × 35 mm. Table 1 shows the mechanical properties of Aluminum alloy 6061. Meanwhile, Table 2 indicates the selected cutting parameters and theirs corresponding level values.

2.3 Machining Parameters

Response Surface Methodology (RSM) was used to determine the factor that influence the surface roughness of Alumunium 6061. Design of experiment (DOE) was adapted in designing the set of machining parameters where the cutting speed (*CS*), feed rate (*FR*) and depth of cut (*DoC*) were the cutting parameters of the experiments and shown in Table 3.

3 Results and Discussion

The analysis of variance is presented in Table 4 for TiAlN coated carbide insert and Table 5 for uncoated carbide respectively. At a level of confidence of 95% the model is checked for its adequacy. Based on Tables 4 and 5, both models are adequate due

Table 3 Machining parameters

Standard order	Run order	Spindle speed (rpm)	Cutting speed (m/min)	Feed rate (mm/tooth)	Depth of cut (mm)
1	9	520	29	165	0.6
2	15	2520	143	165	0.6
3	7	520	29	365	0.6
4	6	2520	143	365	0.6
5	1	520	29	265	0.4
6	2	2520	143	265	0.4
7	5	520	29	265	0.8
8	3	2520	143	265	0.8
9	11	1520	86	165	0.4
10	12	1520	86	365	0.4
11	10	1520	86	165	0.8
12	4	1520	86	365	0.8
13	13	1520	86	265	0.6
14	8	1520	86	265	0.6
15	14	1520	86	265	0.6

Table 4 Analysis of variance for TiAlN coated carbide insert

Source of variation	Degree of freedom	Sum of squares	Means of square	F ratio	P value
Regression	9	1.46412	0.16280	67.80	0.000
Linear	3	1.07662	0.358875	149.56	0.000
square	3	0.22487	0.074958	31.24	0.001
Interaction	3	0.16263	0.054209	22.59	0.002
Residual error	5	0.001200	0.002400		
Lack of fit	3	0.01003	0.003344	3.40	0.235
Pure error	2	0.00196	0.000982		
Total	14	1.47612			

Table 5 Analysis of variance for uncoated carbide insert

Source of variation	Degree of freedom	Sum of squares	Means of square	F ratio	P value
Regression	9	3.19323	0.35480	118.77	0.000
Linear	3	2.42671	0.80890	270.78	0.000
Square	3	0.55956	0.18652	186.66	0.000
Interaction	3	0.20696	0.06899	23.09	0.002
Residual error	5	0.01494	0.00299		
Lack of fit	3	0.01029	0.00343	1.47	0.429
Pure error	2	0.00465	0.00233		
Total	14	3.20817			

to the *P*-values of lack-of-fit are not significant as the *P*-value exceeds 0.05. Thus, the model could fit and acceptable.

Equations 1 and 2 show the second order regression co-efficient for TiAlN coated carbide and uncoated carbide inserts, where *Ra* is the corresponding response, *CS*, *FR* and *DoC* are cutting speed (m/min), feed rate (mm/tooth) and depth of cut (mm) respectively. Based on the models, it can be seen that cutting speed has the most influential factor in determining surface roughness value, followed by feed rate and depth of cut.

$$
\begin{aligned}
a = {} & 0.533 - 0.01330CS + 0.00571FR - 1.302DOC \\
& + 0.000075CS*CS - 0.000002FR*FR + 0.786DOC*DOC \\
& - 0.000033CS*FR + 0.00557CS*DOC - 0.00078FR*DOC
\end{aligned}
\tag{1}
$$

$$
\begin{aligned}
Ra = {} & 0.091 - 0.01560CS + 0.00381FR + 1.404DOC \\
& + 0.000120CS*CS + 0.000005FR*FR \\
& + 0.349DOC*DOC - 0.000036CS*FR \\
& - 0.00717CS*DOC - 0.00236FR*DOC
\end{aligned}
\tag{2}
$$

Figure 2 shows the effect of surface roughness opposed to feed rate and cutting speed. It can be seen that as the decrease value of feed rate and an increase in cutting speed has resulted in the lower value of surface roughness. Meanwhile in Fig. 2b reveals that the value of surface roughness decreases as the cutting speed value increases at any value for feed rate. It can be observed that the surface roughness reaches the highest value when the cutting speed is at the low value while the feed rate is at the high value. This observation is similar with uncoated carbide inserts as shown in Fig. 3a, b.

Furthermore, Fig. 4 shows the comparison value of surface roughness when the TiAlN coating is applied. It is observed that the TiAlN coating resulted in lower value in surface roughness compared to the uncoated carbide insert. The similar observation is also found in Masooth et al. [4] and Nalbant et al. [5] where they concluded the lower value in surface roughness in coating is due to reduction in friction value of TiAlN coating compared to the uncoated insert.

4   Conclusion

Based on the RSM analysis, it can be concluded that cutting speed has the most dominant factor that affects the surface roughness, followed by feed rate and depth of cut. Besides that, TiAlN coating has shown a significant effect in reducing surface roughness value of Aluminium 6061 compared to the uncoated insert.
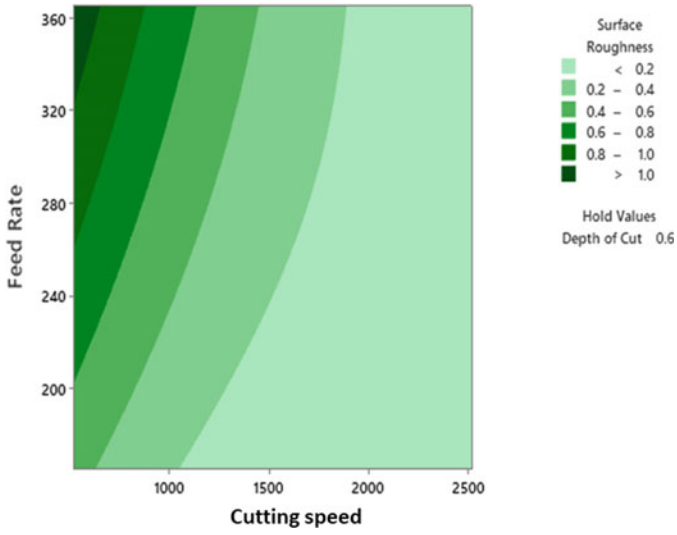
(a) Contour plot 2D
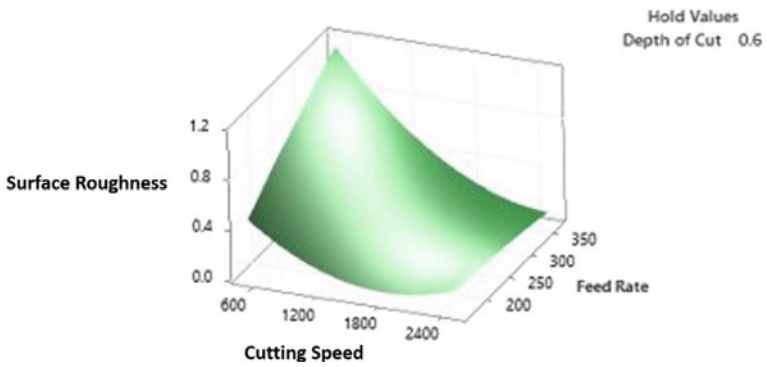
(b) Surface plot 3 D

Fig. 2 Variation of surface roughness against cutting speed and feed rate **a** contour plot 2D and **b** surface plot 3D for TiAlN coated carbide insert
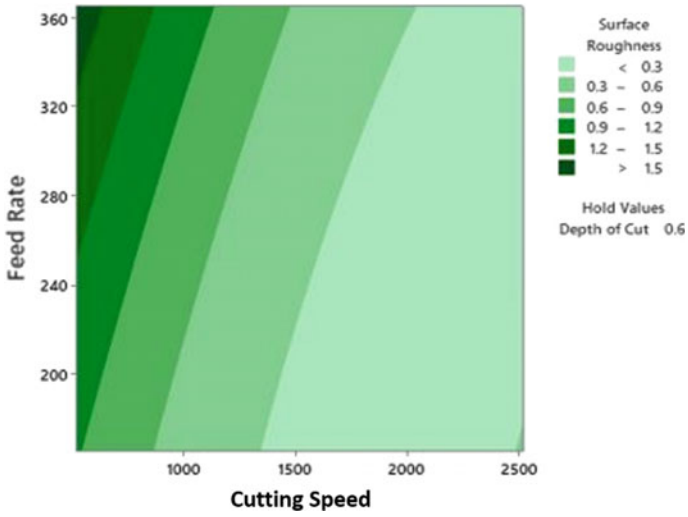
(a) Contour plot 2D
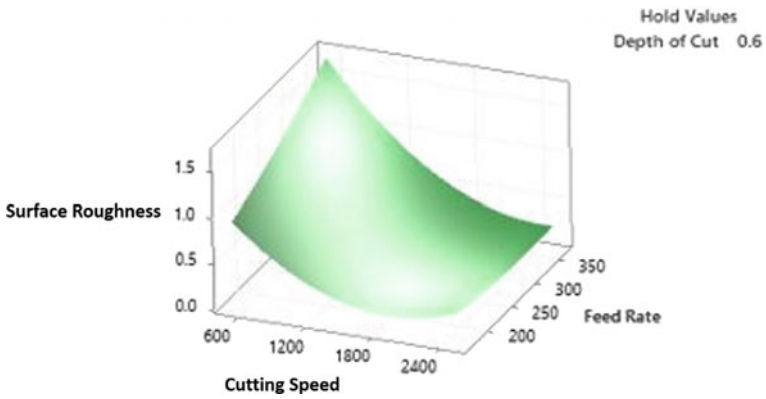
(b) Surface plot 3 D

Fig. 3 Variation of surface roughness against cutting speed and feed rate **a** contour plot 2D and **b** surface plot 3D for uncoated carbide insert
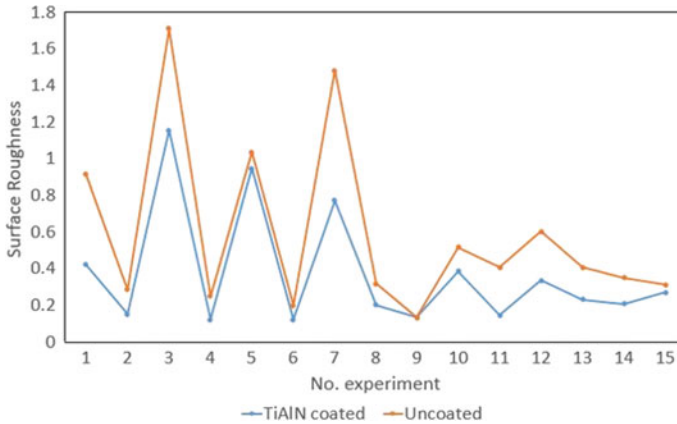
Fig. 4 Comparison of TiAlN coated insert and uncoated insert

References

1. Ojolo SJ, Money O, David, Ismail OS (2015) Experimental investigation of cutting parameters on surface roughness prediction during end milling of Aluminium 6061 under MQL (minimum quantity lubricant). J Mech Eng Autom 1–13
2. Adhip S, Aman K, Deepak RU (2020) Performance comparison of dry, flood and vegetable oil based minimum quantity lubrication environments during CNC milling of Aluminium 6061. Mater Today Proc 21:1483–1488
3. Çakīr O et al (2007) Selection of cutting fluids in machining processes. J Achiev Mater Manuf Eng 25(2):99–102
4. Masooth PHS, Jayakumar V, Bharathiraja G (2020) Experimental investigation on surface roughness in CNC end milling process by uncoated and TiAlN coated carbide end mill under dry conditions. Mater Today Proc 726–736
5. Nalbant M, Gokkaya H, Gokhansur IT (2009) The experimental investigation of the effects of uncoated, PVD and CVD coated cemented carbide inserts and cutting parameters on surface roughness in CNC turning and its prediction using artificial neural networks. Robot Comput Integr Manuf 25(1):211–223

Development of Nanoindentation Simulation Technique for Y-TZP Ceramic Material Characterization

J. B. Saedon, M. F. Othman, M. S. Meon, N. H. M. Nor, H. Husain, S. Shawal, and S. K. H. Baharudin

Abstract Nanoindentation is a technique broadly established and practiced for material characterization, however, the experimental nanoindentation is very complex and is highly susceptible to several factors. If issues such as initial penetration, thermal drift, instrument compliance, etc. have not been correctly handled, the result could be incorrect. The purpose of this study is to employ the nanoindentation technique for measuring the material characteristics such as the elastic and plastic deformation of zirconia ceramic material using the simulation method. The nanoindentation simulation model is developed based on Berkovich indenter using ABAQUS 6.14 software. The study starts with the modelling of the sample and the indenter. Four materials are considered for the sample, copper, iron, ceramic similar to glass and ceramic similar to metal films and finally Y-TZP ceramic. Total indenter displacement of 200 nm, 550 nm or 1000 nm was imposed, and then unloaded and taken back to the initial position. The result on the deformation response of the sample and the load–displacement curve is obtained from the nanoindentation simulated model. Furthermore, the results were compared with published journals for validation purposes. The model successfully obtained the same load–displacement curve as obtained by the researchers. As the sample models are successfully varified, the result obtained for Y-TZP ceramic is valid as well. In conclusion, this study managed to develop the nanoindentation simulation technique using Berkovich indenter to measure and study in-depth the material characterization of Y-TZP ceramic which are used for prosthetic restorations.

Keywords FEM · Nanoindentation · ABAQUS · Y-TZP ceramic

J. B. Saedon (✉) · M. F. Othman · M. S. Meon · N. H. M. Nor · H. Husain · S. Shawal · S. K. H. Baharudin
School of Mechanical Engineering, College of Engineering, Universiti Teknologi MARA, Selangor, Malaysia
e-mail: jurisaedon41@uitm.edu.my

1 Introduction

Nanoindentation is a non-destructive technique that produces nano-size indents which are less than 200 nm, as prescribed based on ISO 14577-1. As the sample model has a thickness of micron, it is not suitable to use the experiment indentation method to obtain the mechanical and tribological properties because its initial penetration or instrument's compliance has not been correctly handled, thus nanoindentation technique is used [1]. As experimental nanoindentation shows limitations, the simulation of the nanoindentation technique is introduced. The test is carried out by using an indenter that has a tip of a diamond shape loaded into the tested material with a certain depth before being withdrawn. Then, the depth and load applied are recorded, later depicted as a load versus displacement graph. A Berkovich indenter is used, in which the tip has a geometry of a three-sided pyramid [2].

The obtained load–displacement relationship from the test can be used to derive material characteristics of any kind that possess elastic and plastic behaviour [3]. The data of the load–displacement (P–h) obtained from the indentation test can be applied to extract a full elastic–plastic stress–strain relationship when combined with the power-law (n) of the work-hardening behaviour [4]. With an increase of demands to incorporate more materials and indenter settings, solution algorithms have become even more sophisticated in recent years. Many researchers have opted for finite element (FE) techniques with a variety of modifications in the indentation method to address this difficulty [5].

One of the commonly used materials in prosthetic restorations, Yttria-stabilized tetragonal zirconia polycrystals (Y-TZP) is strongly preferred due to their good mechanical strength, chemical properties and dimensional stability as well as great biological compatibility with the human body [6]. In a scenario of small-scale contact, a zirconia fixed dental prosthesis may need a final modification by grinding once it is returned from the laboratory. A small-scale contact also may expose it to repeated occlusions, which could cause local contact damages and result in a loss of physical qualities. Thus, establishing contact damage resistance is very crucial for zirconia dental ceramics in clinical applications. As a result, determining its material properties like Young's modulus and hardness using FEM has been utilized in modelling its material characterization using the nanoindentation procedures [7].

The purpose of this study is to employ the nanoindentation technique for measuring the material characterization of ceramic materials, to develop the simulation of nanoindentation model by Berkovich indenter with ABAQUS 6.14 software and lastly, to validate the nanoindentation simulation with the published journals.

2   Methodology

2.1   Setting up the Model

The model is built up in ABAQUS 6.14 using a 2-D axisymmetric rectangle with a side length larger than the depth of indentation and a rigid Berkovich indenter. The model is made axisymmetrically around the indenter central axis (Y-axis). The ceramic samples and the metal samples (copper and iron) use two different dimensions to follow their respective reference journals [8, 9] as shown in Fig. 1a. As the size of the zirconia sample was not stated by Shao [10], and since zirconia is a ceramic material, the dimension of the zirconia sample is assumed to have the same dimension as the ceramic samples. The indenter is built up as a rigid surface with an angle of 70.3° and a reference point at the tip. The indenter tip is set to touch the edge of the sample, however, for sample copper and iron, the indenter is set to be 2 μm away from the sample. This is to follow the exact procedure as their respective reference journal to achieve the same results. The elastic and plastic properties of copper, iron, ceramics similar to glass and ceramics similar to the metal film are shown in Table 1.

   To generate the meshes, a 4-mode bilinear axisymmetric quadrilateral integration element type with hourglass control (CAX4R in ABAQUS) is adopted. The indentation region is very small when compared to the specimen size and the indenter size.
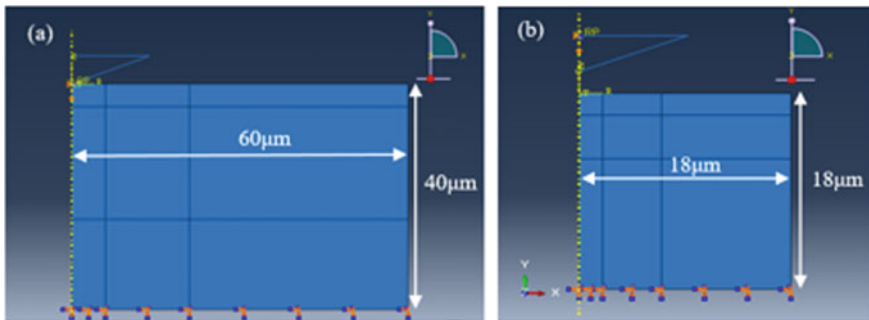
Fig. 1   FEM model system for material: **a** copper and iron, **b** all-ceramic

Table 1   Materials and mechanical properties [7–9]

Material	Young's modulus, E (GPa)	Poisson's ratio, υ	Yield stress (MPa)	Hardening law
Copper	120	0.25	33	Yes
Iron	215	0.25	200	Yes
Ceramic (glass)	72	0.20	3000	No
Ceramic (metal film)	72	0.30	600	No

Table 2 Mesh and elements data for each material

Material	Mesh size	Number of element
Copper	100 nm × 100 nm	1482
Iron	100 nm × 100 nm	1482
Ceramic (glass)	100 nm × 100 nm	12,384
Ceramic (metal film)	500 nm × 500 nm	5184

Table 3 Mesh convergence test for the sample Y-TZP ceramic

Mesh size	Number of element	Converge	Time taken (s)	Maximum von Mises stress
50 nm × 50 nm	25,704	Yes	1080	1.800×10^{-2}
100 nm × 100 nm	12,384	Yes	360	1.800×10^{-2}
500 nm × 500 nm	5184	Yes	65	1.195×10^{-2}
1000 nm × 1000 nm	2400	Yes	45	1.141×10^{-2}

To accurately simulate the deformation of the region, a higher density of meshes with very fine mesh is needed under the indenter contact area. The size of the elements is progressively increased toward the other end of the sample model by making a few partitions onto the sample and selecting the mesh size individually using seed edge, which resulted as shown in Fig. 1b. The mesh element type used for this system are CAX4R, the meshing size and the number of elements of each material are shown in Table 2.

The mesh size of a sample is determined by using the mesh convergence test. This test compares the difference in maximum stress value obtained by each mesh size and the time needed to complete the simulation of the nanoindentation. Table 3 shows the mesh convergence test for the sample Y-TZP ceramic. As there is no difference of the Von Mises stress between the mesh size of 50 nm × 50 nm and the 100 nm × 100 nm, the later mesh size (100 nm × 100 nm) is chosen as the sample since the time needed to complete the nanoindentation simulation is shorter. However, for ceramic similar to metal film, a coarser mesh size of 500 nm × 500 nm is chosen instead because the sample does not converge when adopting a finer mesh size.

2.2 Boundary Condition and Material Parameter

The loading and unloading steps of the indenter are simulated by imposing the downward and upward displacement at the reference point, which gradually increases from 0 to h_{max} and then returned to the original position, this is performed by assigning an amplitude to the system. The h_{max} values of 200 nm, 550 nm and 1000 are imposed for copper, iron and ceramics respectively. The friction coefficient of the contact is

assumed to be zero due to negligible effect on the result [11], however, in the case of material copper and iron, the friction coefficient is set to be 0.1. To enforce contact between the indenter and the specimen, the indenter surface is defined as the "*master*" surface while the specimen surface is defined as the "*slave*" surface.

The nodes at the bottom edges of the rectangle are restrained not to move in their normal direction (ENCASTRE; U1 = U2 = U3 = UR1 = UR2 = UR3 = 0). For the indenter, it is constrained to move horizontally at the reference point. The sample model is considered homogenous and isotropic and behaves like plastic. The material parameters for the simulation are selected to be matched with the mechanical properties measured in the published journals' nanoindentation.

2.3   Inverse Analysis

The Young's modulus and the yield stress of zirconia are determined by an inverse analysis by Shao et al. [10]. The inverse analysis makes use of bilinear assumption or kinematic of hardening plastic properties and obtains the load–displacement curve similar to that obtained from the nanoindentation experiment [1]. This analysis also has been widely applied by many researchers [12–14]. The unloading part of the load–displacement curve is commonly deemed as a pure elastic rebound of the material which is related to the elastic property of the material. If the area in contact remains constant during initial unloading, the elastic behaviour can be described as a blunt punch indenting an elastic solid. Pharr and Oliver [15] proposed Eq. (1) that can be applied to any indenter that can be described as a revolution body of a smooth function for determining Young's modulus.

$$E = \frac{1 - \upsilon^2}{2} \sqrt{\frac{\pi}{A}} \frac{dP}{dh_s} \tag{1}$$

The Young's modulus of the simulated nanoindentation is characterized by using Eq. (1) while the simulated hardness is defined by Eq. (2):

$$H = \frac{P_{\text{max}}}{A} \tag{2}$$

where P is the indentation load and A is the projected contact area. The hardness value is determined directly from the load–displacement curves by using the Olive-Pharr method [15].

3 Result and Discussion

The comparison of numerically simulated results and the result obtained by Bressan et al. [8] for the indentation of copper is presented in Fig. 2. This sample uses a mesh size of 100 nm × 100 nm with an indentation depth of 550 nm. The maximum load of indenter is expected to be higher for a Berkovich when compared to conical indenter and this is shown in Fig. 3. The Young's modulus obtained from the result by using Eq. (1) is 84.76 GPa.

Figure 3 shows the comparison between the simulation results and the same journal for the material iron that has a mesh size of 100 nm × 100 nm with an indentation depth of 200 nm. The maximum load is slightly more than the journal (5.06 mN) and the unloading curve is different from the journal. The modulus of elasticity obtained by simulation is calculated to be 146.19 GPa, this gives a percentage difference of 32%. This error is possible due to the hardening law. According to research
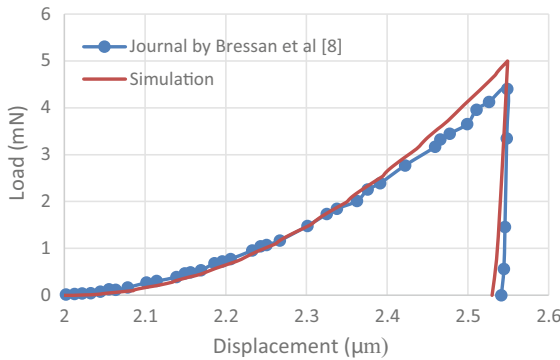
Fig. 2 The comparison of indentation load versus penetration depth for copper between the simulation and published journal [8]
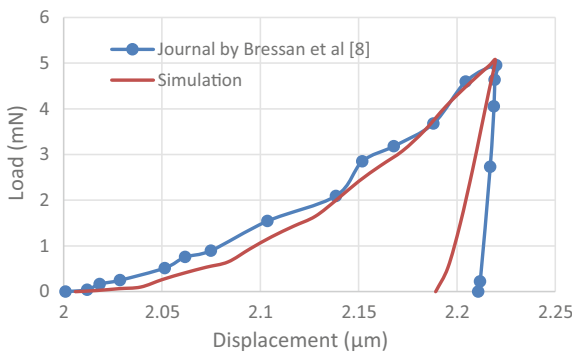
Fig. 3 The comparison of indentation load versus penetration depth for iron between the simulation and published journal [8]
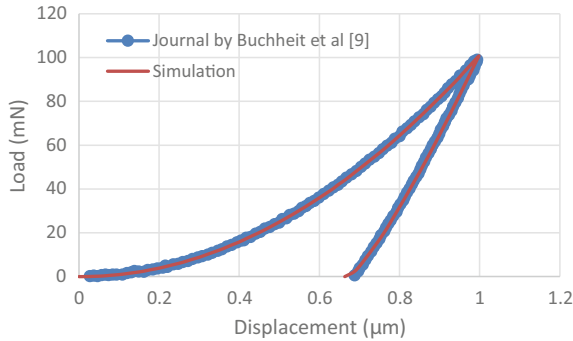
Fig. 4 The comparison of indentation load versus penetration depth for ceramic similar to the glass between the simulation and published journal [9]

done by Yao et al. [16], the value of the power-law strain-hardening coefficient, n, will affect the maximum load and the unloading curve of a material.

In Fig. 4, the comparison of simulation results for ceramic is similar to glass with a mesh size of 100 nm × 100 nm, with an indentation depth of 1000 nm. The maximum load by simulation (100.79 mN) is higher (99.11 mN) compared to Buchheit and Tandon [9] which has a percentage difference of 1.70%. The Young's modulus obtains from the simulation's loading–unloading curve is 71.32 GPa with a percentage difference of 0.94%.

By using best-fit values of the loading curve, Fig. 5 shows, the comparison of simulation results for ceramic similar to the metal film which has a mesh size of 500 nm × 500 nm with an indentation depth of 1000 nm and the result obtained by Buchheit and Tandon [9]. The unloading curve is similar to the reference journal however, the maximum load by the simulation is 47.95 mN which is higher compared to the published journal (43.98 mN). The Young's modulus value obtained from the extrapolation of the simulation curve is $E = 67.00$ GPa which has a percentage
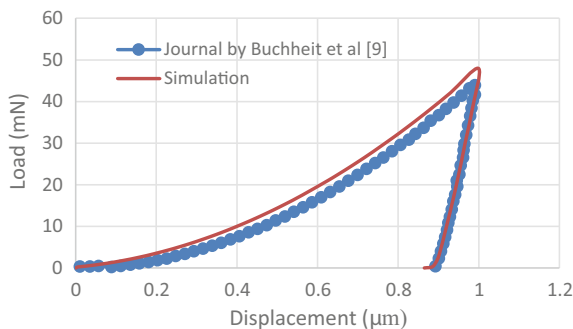
Fig. 5 The comparison of indentation load versus penetration depth for ceramic similar to metal film between the simulation and published journal [9]

difference of 7.46% compared to the theoretical value. This may be due to the coarse mesh size used for the simulation which resulted in the less accurate result.

Figure 6 shows the comparison between the P/P_{max} versus h/h_{max} curve obtains by the simulated result and the journal by Shao et al. [10] of the zirconia sample. The actual maximum load obtained by the simulation is higher than the load obtained by the experiment result of the journal which is 493 mN and 481 mN respectively. The distribution of the von Mises stress under the tip of the indenter is also shown in Fig. 6, which also indicated a small plastic zone under the area of the tip.
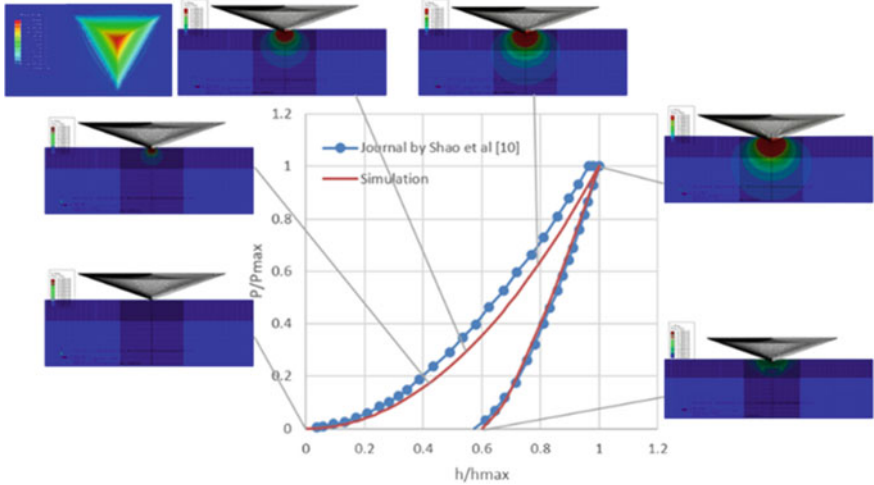
Fig. 6 The comparison of nanoindentation test results for indentation load versus penetration depth for zirconia ceramic between the simulation and published journal [10], and the distribution during indentation of the equivalent von Mises stress

Table 4 Young's modulus and hardness difference

Material	Young's Modulus, E (GPa)	Simulated Young's modulus, E (GPa)	Error (%)	Journal hardness (GPa)	Simulated hardness (GPa)	Percentage error (%)
Copper	120	84.76	29.37	0.596	0.71	19.46
Iron	215	146.19	32.00	4.18	5.29	26.77
Ceramic (glass)	72	71.32	0.94	6.48	7.17	10.65
Ceramic (metal film)	72	67.00	7.46	2.19	2.40	9.59
Ceramic (Y-TZP)	319.29	329.54	3.21	42.85	44.45	3.73

To find the accuracy of the proposed method, Table 4 summarizes the comparison between the hardness and Young's modulus values obtained from the simulation and the reference journal. The result shows that materials such as copper and iron that were defined with hardening law have a very high percentage error (max 32%) of Young's modulus, however, all-ceramic materials which were defined as perfect plasticity which no hardening law used have low percentage errors (7.5%) when compared to their respective journals. However, for hardness values, all the samples material has a low percentage error for the hardness values.

4 Conclusion

This study employed the nanoindentation technique to measure the material characteristics properties such as the elastic and plastic deformation of ceramic materials, developed the simulation of nanoindentation model by using Berkovich indenter with ABAQUS 6.14 and lastly, validated the nanoindentation simulation with published journals. The nanoindentation simulation results of the load–displacement curves of ceramic materials obtained in this study are similar to the result obtained by the researchers of the journals. The simulation of the nanoindentation model by using Berkovich indenter showed that the maximum load was higher than the conical indenter which is similar to the journals as well. The simulation results also show that they were strongly relied on the indenter tip radius, mesh size and hardening law imposed on the model. All the nanoindentation of ceramic samples has a percentage error of 0–11% compared to the journals' result and the medical ceramic has a percentage error of less than 5%. Thus, it is best to consider that this study has managed to develop the nanoindentation technique for analyzing the material properties of zirconia ceramic materials and can be applied for material characterization of Y-TZP ceramic as well. For future work, since Y-TZP ceramic is widely used for dental prostheses, the outcome of this study will be applied to investigate further its mechanical characteristics for preventive measures in avoiding failure and injury to its users.

References

1. Alaboodi S, Hussain Z (2019) Finite element modeling of nano-indentation technique to characterize thin film coatings. J King Saud Univ Eng Sci 31(1):61–69
2. Moore SW, Manzari MT, Shen YL (2010) Nanoindentation in elastoplastic materials: insights from numerical simulations. Int J Smart Nano Mater 1(2):95–114

3. Bull SJ (2005) Nanoindentation of coatings. J Phys D: Appl Phys 38(24)
4. Lee H, Huen WY, Vimonsatit V, Mendis P (2019) An investigation of nanomechanical properties of materials using nanoindentation and artificial neural network. Sci Rep 9(1)
5. Bolshakov, Oliver WC, Pharr GM (1996) Influences of stress on the measurement of mechanical properties using nanoindentation: part II. Finite element simulations. J Mater Res 11(3)
6. Chevalier J (2006) What future for zirconia as a biomaterial? Biomaterials 27(4):535–543
7. Pelletier H, Krier J, Cornet A, Mille P (2000) Limits of using bilinear stress-strain curve for finite element modeling of nanoindentation response on bulk materials. Thin Solid Films 379(1–2):147–155
8. Bressan JD, Tramontin A, Rosa C (2005) Modeling of nanoindentation of bulk and thin film by finite element method. Wear 258:115–122
9. Buchheit TE, Tandon R (2007) Measuring residual stress in glasses and ceramics using instrumented indentation. J Mater Res 22(10):2875–2887
10. Shao L, Jiang D, Gong J (2013) Nanoindentation characterization of the hardness of zirconia dental ceramics. Adv Eng Mater 15(8):704–707
11. Bhattacharya K, Nix WD (1988) Finite element simulation of indentation experiments. Int J Solids Struct 24(9):881–891
12. Clausner A, Richter F (2015) Determination of yield stress from nanoindentation experiments. Eur J Mech A/Solids 51
13. Ghaednia H, Mifflin G, Lunia P, O'Neill EO, Brake MRW (2020) Strain hardening from elastic-perfectly plastic to perfectly elastic indentation single asperity contact. Front Mech Eng 6
14. Chang C, Garrido MA, Ruiz-Hervias J, Zhang Z, Zhang L-L (2018) Representative stress-strain curve by spherical indentation on elastic-plastic materials. Adv Mater Sci Eng 1
15. Pharr GM, Oliver WC (1991) On the generality of the relationship among contact stiffness, contact area and elastic modulus during indentation. J Mater Res 7(3)
16. Yao Z, Kang B, Ever Barbero CJ, Xingbo Liu C-C, Davalos JF, Creese RC (2005) Development of an indentation method for material surface mechanical properties measurement

A Novel Calophyllum-Inophyllum Oil from Pahang Malaysia as a Green Metalworking Fluid

Amiril Sahab Abdul Sani [iD] **, Puteri Humairah Megat Ahmad Radzi,**
Ummu Izzati Abd Rahman, and Norfazillah Talib [iD]

Abstract Crude Calophyllum-Inophyllum or Tamanu oil (CTO) is considered one of the non-edible vegetable-based lubricant that have high viscosity value compared to other non-edible plant-based oil such as Jatropha and synthetic ester. In the pursuit of finding sustainable metalworking fluids (MWFs) that pose low environmental and health risks, this vegetable oil is a viable contender to replace mineral-based oil. Following on from this huge potential, this study aims to investigate the oil yield of CTO extracted raw from Pahang, Malaysia. There are two mechanical extraction methods that determine the difference of oil yield. The mechanical extraction has found that Method B had 3% higher oil yield than Method A. The oil yield percentage from these mechanical extractions, Method A (49%) and Method B (52%) is found to be higher than the soxhlet extraction method (46%). The CTO are then analyzed for their physicochemical properties, e.g. dynamic viscosity, kinematic viscosity, density, thermal conductivity, flash point, free fatty acid and total acid number. A four-ball wear test was carried out to test their tribological properties in accordance to ASTM D4172 standard. CTO that possesses high viscosity value and low viscosity index is proposed for physicochemical modification to improve its lubrication and thermal degradation effect for better machining performances during the metalwork.

Keywords Crude Tamanu oil · Callophylum-Inophyllum · Four ball wear test · Mechanical extraction · Physicochemical properties · Tribofilm

A. S. Abdul Sani (✉) · P. H. Megat Ahmad Radzi · U. I. Abd Rahman
Faculty of Manufacturing and Mechatronic Engineering Technology, Universiti Malaysia Pahang, 26600 Pekan , Pahang, Malaysia
e-mail: amiril@ump.edu.my

N. Talib
Faculty of Mechanical and Manufacturing Engineering, Universiti Tun Hussein Onn Malaysia, 86400 Parit Raja, Batu Pahat, Johor, Malaysia

1   Introduction

In the manufacturing industry, metalworking fluid is extensively used and plays an important role in the machining shop floor. Machining is defined as the process of removing material whether through the modification of size, shape, or surfaces of the workpiece. However, the evolvement of high-cutting speed and new engineering materials makes the metalworking fluids ever required as before [1]. Metalworking fluid is applied for example on the machining zone to reduce cutting temperature, diminishes the existing friction between the workpiece and cutting tool, increases tool life, and enhances the efficiency of machining and the quality of the surfaces. Furthermore, it acts as an agent in machining such as cleaning, cooling, lubrication, and reducing corrosion by creating a protective layer [1, 2]. Since metalworking fluid was introduced, mineral-based oils are the main sources for lubricant production, and they are being widely employed by the manufacturer in many aspects of the production lines. Based on the data released by BP statistical review of Global Energy, it shows that the consumption of fossil fuel-based on different fuel type is getting an increase each year since 1965 until now [3, 4].

To find an alternative for replacing the depleting resources of fossil fuel, people need to extract oils from different sources, such as from animal or plant. Extracting the oil from the plant requires specific tools and devices like mechanical apparatus or chemical solvents. Designing the mechanical extractor are important whereas, the different mechanisms applied will affect the oil yield [5]. It is reported that, engine driven screw press extracted oil from 68% up to 80% yield, whereas ram press achieved from 60 to 65% yield of the available oil. However, Bhargavi et al. [6] stated that, the ram press extraction efficiency is from 57 to 62%. It is also noted from Table 1 that, oil extracted from mechanical press needs further treatment like filtration and degumming process. Furthermore, some mechanical press designs are not suited for some seeds [7]. Table 1 shows the percentage of oil yield that can be obtained using the mechanical extraction methods.

The benefits of mechanical extraction are to avoid the use of chemicals, and production of crude oil could be instantly consumable. It also contributes to low electrical power requirement, non-expensive equipment, and the use of manual skills compared to other extraction methods. However, the limitation of mechanical extraction devices could be the high oil content that resides in the waste, which leads to lower yield and less profitable [6].

Table 1 Oil yield percentage from mechanical extraction methods [7]

Press	Oil yield (%)	Oil treatment
Engine driven screw press	68.0	
	80.0	
	79.0	Filtering and degumming
Ram press	62.5	
	62.5	

The main objective of this research is to investigate the effect of two different approaches of drying the fresh Calophyllum Inophyllum (CTO) fruits before one can extract the plant-based oil from the seeds using a mechanical extraction method. The yield results will be compared with the yield from a soxhlet extraction method in literature. The physicochemical properties of the oil yields in terms of dynamic viscosity, kinematic viscosity, density, viscosity index, flash point, thermal conductivity, acid values, and the tribological properties in terms of coefficient of friction, wear scar diameter and surface roughness will be investigated systematically.

2 Methodology

2.1 Drying and Mechanical Extraction of CTO

The mechanical extraction for the oil yield of the Callophyllum Inophyllym fruits are divided into two approaches. In Method A, two drying processes were introduced, whereby the fresh fruits are dried first for 24 h at about 60 °C before the seeds were peeled off from the endocarp. Then the seeds are dried for another 48 h also at about 60 °C prior the mechanical grinding process. In Method B, the seeds are taken out raw from the endocarp of the fresh fruits before being subjected to drying for 48 h at the same drying temperature. However, Method B is more challenging since the fresh fruit is difficult to be cracked open before taking out the seeds. For both approaches, 5 kg of Calophyllum Inophyllum fruits are required. Both methods are repeated twice for data comparison.

An electric screw press machine is used to extract the raw Calophyllum Inophyllum oil from the seeds. The dried and sliced seeds are fed into the machine feeder and compressed to extract the crude oil, as shown in Fig. 1. The raw plant-based oils obtained are then filtered, to separate the oil from dirt, using Whatman
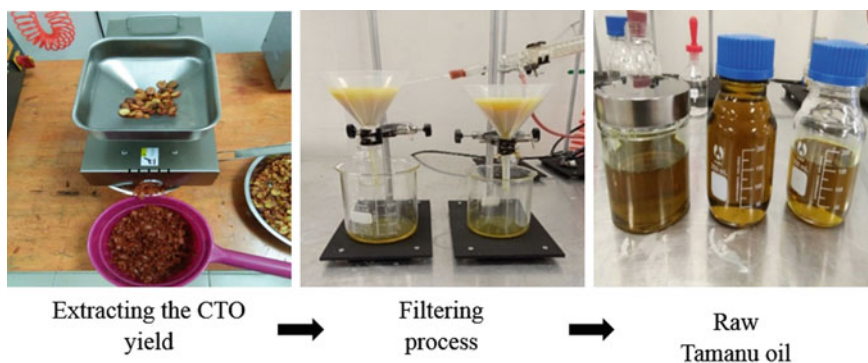
Fig. 1 The mechanical extraction process for raw Tamanu oil yield
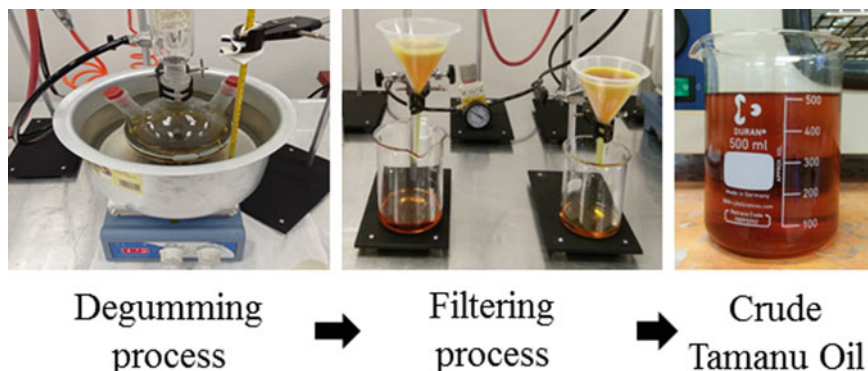
Fig. 2 Degumming process set up

filter paper at Grade 4 (20–25 μm). A dark greenish oil is produced which indicates a raw plant-based oil extracted from the seeds, that contains resin, water, and other water-insoluble extractives [8, 9].

Degumming process for the raw Calophyllum Inophyllum oil is necessary to separate the oils from resin, and to improve the oxidization stability of the oil. In this process, 1 wt% of phosphoric acid (3%) is dripped into the CTO, which was initially heated in a three-necked flask inside a hot bath and stirred at a constant temperature of 60 °C. The total time taken to complete the degumming process is 1 h. After that, the oil was dried in an oven for 16 h at 110 °C, to ensure the water inside the oil are fully removed. Then, the oil is filtered to separate the resin from the crude oil, as shown in Fig. 2. A reddish yellow-colored oil is produced and the physical as well as the chemical properties of the CTO are measured for further validation of the oil yield [9].

2.2 Physicochemical Properties Tests

The density, kinematic viscosity, dynamic viscosity, and viscosity index were measured automatically using a Portable Viscometer (Anton Paar SVM 3001). The ASTM standards for measuring these physical properties are density (ASTM D4052, EN ISO 12185), dynamic viscosity (ASTM D7042), kinematic viscosity (ASTM D7024, EN 16896) and Viscosity Index (ASTM D2270). The data was taken at temperature of 40 and 100 °C each. The flash point test using a closed cup Pensky Martens PMA-4 machine was conducted following the ASTM D93 method. Thermal conductivity is measured at temperature 27 °C until 70 °C (300–343 K). Crude Jatropha oil as purchased is also tested for data comparison.

In the FFA test (AOCS Ca 5a-40), 1 g of oils are placed inside a conical flask, and heated to 60 °C. Next, 50 ml of methanol and 6 drops of phenolphthalein are added in the conical flask. Then, sodium hydroxide solution is titrated slowly into

the flask, while gently shaking the mixture, until the solution changes color to pink and last for 30 s. After that, the amount of sodium hydroxide used were recorded to calculate the percentage of FFA by using the formula expressed as in Eq. (1).

$$FFA\% = 28.2 \times N \times V \times m^{-1} \tag{1}$$

where V is a volume of sodium hydroxide (NaOH) used in milliliter, N is the concentration of sodium hydroxide (NaOH, 0.25 M) and m is the weight of the CTO in gram.

2.3 Tribological Properties Test

Four-ball wear test is a lubrication testing, which is to investigate the efficiency of lubricant in reducing wear and friction of the sliding surfaces. This test was done using a four-ball test rig (Ducom TR-30L) as depicted in Fig. 3. According to the ASTM D4172 method, four chrome steel balls (AISI 52100) with a diameter of 12.7 mm were used. Three ball bearings were put in the ball pot together with the oil sample (approximately 10 ml). The other one ball will be clamped at the top as the rotating ball. The top ball is pressed against the three stationary balls using a 392 N force and rotates at 1200 rpm for 60 min. The testing temperature is set at 75 °C throughout the experiment.

Wear scar diameter was observed to investigate the average scar on the three steel balls, to determine the efficiency of the plant-based oil to reduce wear. Wear scar diameter (WSD) is measured by using an optical microscope (Olympus BX51M Metallurgical Microscope). Besides that, Scanning Electron Microscope machine (FEI, Quanta 450) was also used to identify the topological surfaces of the worn area after the four-ball wear test. Surface roughness measurement on the worn scar area on the ball bearing surface was conducted using an Accretech—Surfcom Touch 50

Fig. 3 Ducom TR-30L (left) and ball pot (right)

Table 2 Comparison of the crude Calophyllum Inophyllum yield

Items	Method A	Method B
Initial mass, %	100	100
Mass yield of dry fruits, %	68.63	–
Mass yield of dry seeds, %	53.47	68.86
Mass yield of raw Tamanu oil, %	48.81	51.78

machine. The cut off length, λ_c is set at 0.08 mm with an evaluation length (L_c) of 0.56 mm. The tip radius used for this test was 2 μm.

3 Results and Discussion

3.1 Oil Yield

In this study, the raw Calophyllum Inophyllum oil was produced in-house through a mechanical extraction method, with two different fruit-seed drying approaches. For Method A, there are two steps of drying processes (first dry the fruits then dry the seeds). In Method B, the seeds are taken out from the fresh fruits and directly goes into the drying process (seeds drying). The initial texture of the seeds is soft and will change to a hardened peanut after being dried. As shown in Table 2, the seed mass for Method B is more than the seed mass obtained in Method A. Surprisingly, the output of raw oil for Method B is found to be higher than Method A. It is noted that the mass of seeds contributes to the raw oil yield, with higher seed mass produces higher oil yield. This is also contributed by the high initial content of water and oil in the fresh seeds compared to the seeds taken from the fruits that were dried first. The initial drying process of the fruits in Method A could have dried the water and oil contained in the seeds, thus lowering the oil yield [10].

The percentage of the CTO yield result by using the mechanical extraction methods are compared with the result from a Soxhlet solvent extraction process, which a type of a chemical extraction method. From the study by [3], it is shown that the percentage of CTO by using the mechanical extraction methods (Method A—48.8% and Method B—51.8%) are higher than the yield obtained from the Soxhlet extraction method (46.2%).

3.2 Physicochemical and Tribological Properties

The CTO is measured for dynamic viscosity, kinematic viscosity as well as the density values at two temperatures of 40 and 100 °C. The average density of CTO at temperature 40 °C and 100 °C are 0.931 g/ml and 0.891 g/ml, respectively. The
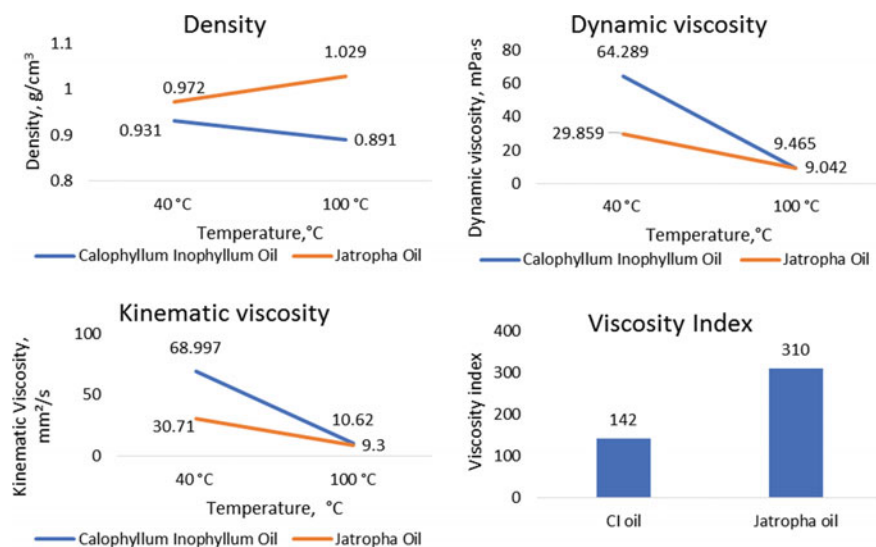
Fig. 4 Physical properties of the crude Tamanu oil

average dynamic viscosity value of CTO measured also at the same temperature of 40 °C and 100 °C are found to be 64.3 mPa.s and 9.5 mPa.s. Figure 4 summarizes the findings of the physical properties of the CTO compared with the crude Jatropha oil (CJO). From the diagrams, the dynamic and kinematic viscosity values of CTO is notably higher than the CJO. However, CJO is found denser than the CTO.

The viscosity index for CTO is measured at 142, while CJO possess higher value at 310. This leads to the result of which the viscosity of the CTO is highly affected by the temperature changes compared to the CJO. Flash point result for CTO is reported at 220 °C and CJO is at 240 °C. The flash point test is to find out in what temperature the plant-based oil will ignite when it being exposed to the flame. So, the higher the temperature of flash point, the safer the output of oil to be used. The thermal conductivity test carried out on CTO are measured at temperature 27 °C until 70 °C (300–343 K). The average value of thermal conductivity of CTO is 0.124 W/mK, while for CJO it is found to be 0.174 W/mK [11]. The low thermal conductivity of the CTO may be contributed by the thicker oil property of the crude plant-based oil, thus lower the quantity of heat that could be transmitted through the oil [12].

The physical properties such as the density, dynamic viscosity and kinematic viscosity of the CTO is found to be comparable to the CJO at high working temperature and thus in terms of oil fluidity with the changes of temperatures, it could perform in the engineering and manufacturing processes, where lubricants that could sustain high temperature working condition and with cooling effect are demanded. The free fatty acid (FFA) for CTO is 32%, while CJO is 20%. The total acid number for CTO is calculated at 22.44 and 16.21% for CJO. CTO possesses higher acidity than CJO. This finding increases the necessity for the reduction of the FFA percentage of the

plant-based oils according to the ASTM D6751 (FFA $\leq$ 1%) [13]. Further structural modification process e.g. chemical modification (transesterification processes) is required, to improve its current physical and chemical properties prior its use as industrial lubricants.

The wear scar diameter (WSD) from the four ball wear tests is measured for each ball bearings. Average coefficient of friction (COF) as well as the surface roughness of the worn scars are observed. Table 3 presents the results of average coefficient of friction, WSD as well as the surface roughness value for CTO and CJO as comparison. CTO has lower COF value than CJO, which is directly contributed by the high viscosity value of the oil. However, higher viscosity oil does not produce smoother surface as compared to CJO. CJO produces better lubrication effect on the metal sliding surfaces thus reduces friction and wear altogether. Figure 5 portrays the worn scar surfaces on the ball bearing after being lubricated by CTO and CJO. SEM–EDX images are presented to identify the presence of elements on the wear scar surfaces after being lubricated by the plant-base oils.

Figure 6 shows the elements that are scanned on the middle of the worn scar surfaces after being lubricated by CTO. From Fig. 5, both scar surfaces illustrate the present of abrasive wear lines, whereby surfaces lubricated by CJO shows a lesser scarring lines compared to the surface lubricated by CTO. This could explain on the smoother surface roughness resulted from the good lubrication effect by CJO [13]. In addition, the element that was found on the wear scar surface were mostly C (Carbon), Cr (Chromium) and Fe (Iron), which represents the material of the AISI

Table 3 Four ball wear test results

Type of lubricant	Average COF	Average WSD	Surface roughness, *Ra* in μm
Crude Jatropha Oil	0.065	0.555	0.125
Crude Tamanu Oil	0.055	0.562	0.245
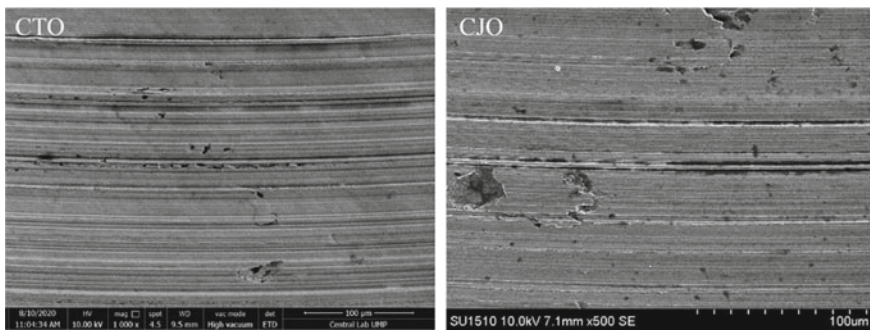
Fig. 5 SEM images of the worn scars
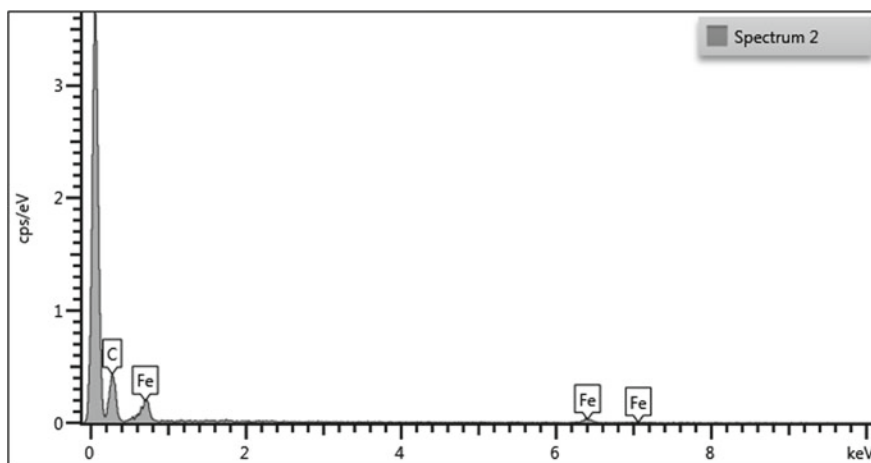
Fig. 6 EDX spectra of the worn surface lubricated by CTO

52100 ball bearings [14]. No adhered material on the scanned spot is detected, thus supporting the lubrication behavior of both plant-based oil that reduces friction and wear by protecting the sliding surfaces with a sacrificial layer thin enough to prevent direct contact between the sliding metals [14, 15].

4 Conclusion

This study highlights the two drying approaches in mechanical extraction methods used for producing the crude Tamanu oil (CTO). The second approach (Method B) produces yield result of 2.97% higher than the first (Method A). Furthermore, this study also reveals that the mechanical extraction method produces higher oil yield compared to the solvent extraction method (soxhlet extraction).

Next highlights are the physicochemical properties of CTO and CJO, where the latter was shown to be more significant than the former in terms of higher viscosity index value as well as lower total acid number. However, this work has also shown that CTO possesses good physicochemical properties and a great potential as a feedstock for plant-based lubricants as good as CJO. The tribological properties for CTO also revealed that the high viscosity value of the oil could reduce the friction coefficient of the metal sliding surfaces better than CJO. Nevertheless, a sufficient thick lubrication layer is only required to reduce wear and friction during the tribological tests.

Thus, the physicochemical properties of CTO is found to be best if it would be modified and altered for a specific manufacturing application such as machining in order to reduce its viscosity value and total acid number, improve its antifriction and antiwear properties as well as improving its thermal and oxidative stabilities for

this notable engineering applications. CTO could become another potential as green lubricant feedstock that supports the sustainable manufacturing growth in Malaysia.

References

1. Pei Y, Yiming R, Gang W (2015) The effect of cutting fluids applied in metal cutting process. Proc Inst Mech Eng, Part B: J Eng Manuf 230(1):19–37
2. Sani ASA, Nor Athira J, Ahmad Shahir J, Norfazillah T (2021) Calophyllum-Inophyllum from Pahang Malaysia as biolubricant feedstock for industrial application. In: Recent trends in manufacturing and materials towards industry 4.0. Lecture notes in mechanical engineering. Springer
3. Nur Atiqah MS, Suzana Y, Wan Asma I, Awais B, Lai FC (2015) Oil extraction from Calophyllum inophyllum L. via soxhlet extraction optimization using response surface methodology (RSM). In: 10th Asian control conference (ASCC), pp 1–6
4. Sani ASA, Erween AR, Safian S, Hiroyuki S (2019) Machining performance of vegetable oil with phosphonium- and ammonium-based ionic liquids via MQL technique. J Clean Prod 209:947–964
5. Bhuiya MMK, Rasul MG, Khan MMK, Ashwath N, Azad AK, Mofijur M (2015) Optimisation of oil extraction process from Australian native beauty leaf seed (Calophyllum Inophyllum). Energy Procedia 75:56–61
6. Bhargavi G, Nageswara Rao P, Renganathan S (2018) Review on the extraction methods of crude oil from all generation biofuels in last few decades. IOP Conf Ser: Mater Sci Eng 330(1)
7. Atabani AE, Silitonga AS, Badruddin IA, Mahlia TMI, Masjuki HH, Mekhilef S (2012) A comprehensive review on biodiesel as an alternative energy resource and its characteristics. Renew Sustain Energy Rev 16(4):2070–2093
8. Kartika IA, Cerny M, Vandenbossche V, Rigal L, Sablayrolles C, Vialle C, Suparnoa O, Ariono D, Evon P (2018) Direct Calophyllum oil extraction and resin separation with a binary solvent of n-hexane and methanol mixture. Fuel 221:159–164 (2018)
9. Nisa N (2021) The effect of use microwave irradiation in produce biodiesel nyamplung oil (calophyllum inophyllum linn) using KOH catalyst. J Phys: Conf Ser 1845(2021):012064
10. Ángel CS, Leontina L, Marina CL, Abdolreza K, Klaudia M, Ángel ACB, Adam F (2020) Comparison of traditional and novel drying techniques and its effect on quality of fruits, vegetables and aromatic herbs. Foods 9(9):1261
11. Rajaganapathy C, Vasudevan D (2020) Tribological and thermo-physical properties of jatropha oil containing TiO_2 nanoparticles. Trans Can Soc Mech Eng 45(2):262–272
12. Sundar LS, Irurueta GO, Venkata RE, Manoj KS, Sousa ACM (2016) Thermal conductivity and viscosity of hybrid nanofluids prepared with magnetic nanodiamond-cobalt oxide (ND-Co_3O_4) nanocomposite. Case Stud Therm Eng 7(2016):66–77
13. Amiril SAS, Rahim EA, Embong Z, Syahrullail S (2018) Tribological investigations on the application of oil-miscible ionic liquids additives in modified Jatropha-based metalworking fluid. Tribol Int 120:520–534
14. Norfazillah T, Erween R (2015) Performance evaluation of chemically modified crude jatropha oil as a bio-based metalworking fluids for machining process. Procedia CIRP 26(2015):346–350
15. Rahim EA, Talib N, Amiril Sahab AS, Syahrullail S, Mohid Z (2017) Tribological evaluation on various formulation of modified RBD palm olein as sustainable metalworking fluids for machining process. Mater Sci Forum 882:13–17

Effect of Adding Fillet to Protruded Rectangular Rib in a Microchannel Heat Sink Subject to Jet Impingement Cooling

W. J. Chen, K.-C. Wong, and K. C. Ng

Abstract Microchannel heat sinks (MCHS) subjected to jet impinging have been proven to be very efficient in dissipating heat energy. Many researchers have introduced surface augmentation on the heat sink for improving the cooling efficiency. The present research explores the effects of height and fillet radius of protruded rib on the thermal performance of a microchannel heat sink subjected to slot-jet impingement. A 3D conjugate heat transfer model coupled with the k-ω Shear Stress Transport turbulence closure is developed to investigate the geometrical effects of protruded ribs on the heat transfer capabilities of the hybrid cooling module. The model is validated. The MCHS with protruded rib added with fillet radius show significant increase in the average Nusselt number and better temperature uniformity as compared to the case without fillet radius. In addition, the pressure drop decreases when shorter protruded rib is used in combination with the fillet.

Keywords Jet impingement · Microchannel heat sink · Protrusion · Thermal performance · Fillet

1 Introduction

As modern technology advances, many electronic devices generate very high heat energy due to high power densities over a small area. Therefore, innovative designs that provides efficient thermal dissipation are crucial. In the early years of microchannel heat sink (MCHS) development, Tuckerman and Pease [1] studied the heat dissipating capabilities of a compact water-cooled MCHS experimentally. The MCHS made of silicon has a maximum thermal resistance of 0.09 °C/W over an area of 1 cm^2. MCHS subject to jet impingement are proven to provide high heat dissipation rate for cooling applications. Glynn et al. [2] found that having a submerged, confined circular jet impingement condition is capable in achieving much higher

W. J. Chen · K.-C. Wong (✉) · K. C. Ng
Department of Mechanical, Materials and Manufacturing Engineering, University of Nottingham Malaysia, 43500 Semenyih, Malaysia
e-mail: Kok-Cheong.Wong@nottingham.edu.my

heat transfer rates when compared to a free-surface jet impingement. Jang et al. [3] discovered that the thermal resistance of a MCHS subjected to an impinging jet is 6.1 °C/W while the MCHS with parallel air flow along the channel is 11.85 °C/W. It is almost half the thermal resistance of the standard MCHS with parallel flow. Sung and Mudawar [4] discussed the merits of combining an array of jets impinging into a MCHS in achieving a more uniform surface temperature even when high heat flux is being supplied. Based on their research, the temperature profile is more uniform when low Reynolds number is applied at the inlet. At high Reynolds number or when the jets are too close to each other, there will be strong interaction between the jets where the upstream jets will cause disturbance to the downstream jets. Sung and Mudawar [5] concluded that an array of circular jets resulted in a much larger pressure drop when compared to the slot jets just to achieve a slightly higher heat flux. The hybrid cooling module was able to maintain a good degree of temperature uniformity along the surface of the channel with a maximum difference of 2 °C. From their research, it is also concluded that decreasing the width of the jet would result in the decrease in maximum temperature but adversely affecting the temperature gradient along the channel of the heat sink. Sexton et al. [6] studied the effect of varying the slot jet's aspect ratio, L_{jet}/W_{jet}, on thermal and hydrodynamic behaviours. The results showed that the Nusselt number profile stays almost the same within the length of the jet and less vortices induced.

There are also many studies associated with the enhancement of heat transfer with addition of protruded profiles in a MCHS. Protrusions can take up many shapes and sizes, such shapes include, V-shaped ribs, rectangular ribs, hemispherical protrusions [7–9]. Shen et al. [7] introduced the idea of a single circular jet impingement into a MCHS with hemispherical protrusions and dimples. Their research shows that having the coolant impinging onto the protrusion located on the channel of the heat sink exhibits better thermal performance compared to a flat surface or a dimple. Further research was conducted by Ming et al. [8, 9] to study the effects hemispherical protrusion on the channel of the MCHS with jet impingement by varying the radius of the hemispherical protrusion [8] and by varying the height and the arrangement of the protrusion [9]. The studies concluded that an optimum cooling performance can be obtained with larger and higher hemispherical protrusions. However, the thermal performance would deteriorate if the arrangement of the protrusion is not aligned beneath the jets.

Based on the literature review, various protrusion shapes have been considered, i.e. rib, dimple, etc. There are still unexplored geometrical features of protrusion in MCHS under jet impingement cooling. The gaps that the present study will be working is on the how fillet radius and height of a protruded rib placed in the middle of channel extended from inlet to outlet of MCHS affects the thermal and hydraulic performance.

2 Methodology

Figure 1 shows the schematic diagram of the hybrid MHSJI module with reference to the model used by Kim et al. [10]. The fluid impinges into the microchannel through the slot jet with $L_{jet} = 1384\,\mu m$, $w_{jet} = 84\,\mu m$. The hybrid module has overall dimensions of $L_x(0.792\,\text{mm}) \times L_y(10\,\text{mm}) \times L_z(10\,\text{mm})$.

A 3D fluid–solid conjugate heat transfer model is considered. Figure 2a shows the repeated section of the microchannel viewed from the direction of the flow. The computational domain shown in Fig. 2b is a quarter symmetry of the repeated section shown in Fig. 2a. Note that there is protruded rectangular rib along each channel with rib height h_p, width w_p and fillet radius r_p at the 4 corners of the rib as illustrated in Fig. 2a. Two parameters are varied for investigation. First, dimensionless radius R at the corners of rectangular protrusion is varied i.e. R = 0, R = 0.25 and R = 0.5 as can be seen from Fig. 3a–c, respectively. Second, the dimensionless height of the rectangular protrusion is varied, i.e. H = 0.1, H = 0.05, H = 0.025 as can be seen from Fig. 3a, d, e, respectively. The dimensionless height and fillet radius are defined as follows:

$$H = h_p/h_{ch} \tag{1}$$

$$R = r_p/w_p \tag{2}$$

The substrate of the MCHS is silicon with a thermal conductivity of $k_s = 148\ \text{Wm}^{-1}\text{K}^{-1}$. The coolant used is water with thermal conductivity $k_f =$
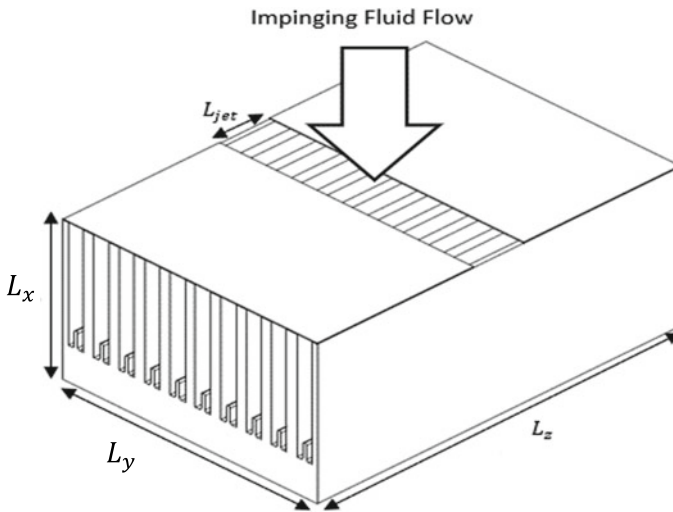
Fig. 1 Schematic diagram of the MCHS subjected to jet impingement with protruded ribs
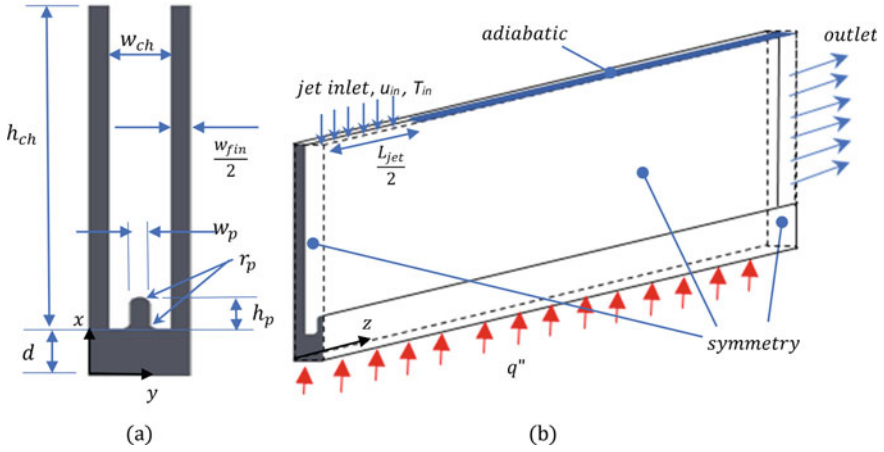
Fig. 2 Illustration of **a** single channel (section view) with $d = 100$ μm, $h_{ch} = 692$ μm, $w_{ch} = w_{jet} = 84$ μm, $w_{fin} = 56$ μm, $w_p = 42$ μm and **b** the computational domain based on quarter symmetric of the single microchannel
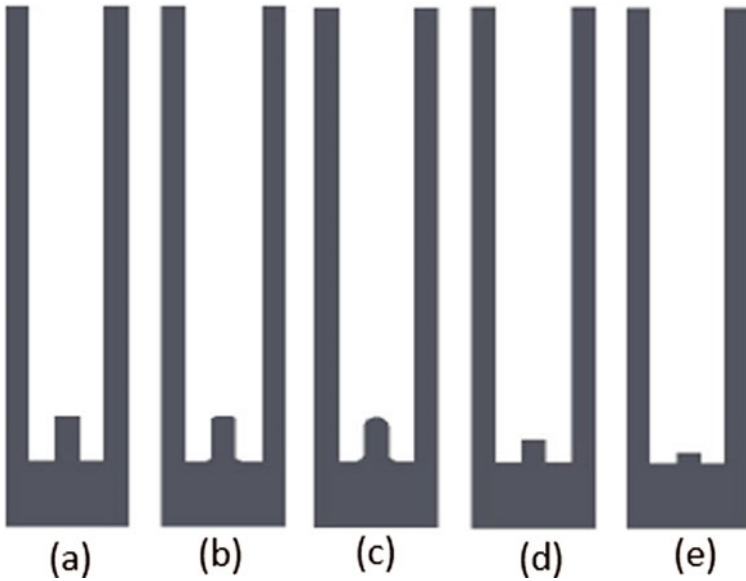
Fig. 3 Illustration of the geometry of protruded rib for different configurations **a** H = 0.1, R = 0, **b** H = 0.1, R = 0.25, **c** H = 0.1, R = 0.5, **d** H = 0.05, R = 0, **e** H = 0.025, R = 0

0.613 $Wm^{-1}K^{-1}$, dynamic viscosity $\mu = 0.000855$ $kgm^{-1}s^{-1}$, density $\rho = 997$ kgm^{-3} and heat capacity $c_p = 4179$ $Jkg^{-1}K^{-1}$. The inlet temperature, T_{in}, is 290 K. A uniform heat flux, $q'' = 100$ W/cm^2 is applied to the bottom wall.

The k-ω Shear Strain Transport (SST) turbulence model is adopted in the present study as several studies demonstrated that the results are in good agreement with experiment and suitable for complex flow features such as high pressure gradient, flow separation and recirculation. The Reynolds number employed in the present study ranges from 150 to 900. It is expected that the transition of flow happens earlier when the hydraulic diameter is reduced, the present study applied a turbulence model as the formation of eddies are expected.

The assumptions made in this study are: (1) steady-state incompressible flow; (2) single phase fluid domain; (3) constant fluid and solid properties; (4) gravitational forces, heat transfer due to radiation, contact resistance between the interfaces of the MCHS are negligible. The continuity, momentum and energy equations for fluid are expressed in the Cartesian tensor form as follows:

$$\frac{\partial u_i}{\partial x_i} = 0 \tag{3}$$

$$\rho u_j \frac{\partial u_i}{\partial x_j} = -\frac{\partial p}{\partial x_i} + \frac{\partial}{\partial x_j}\left((\mu + \mu_t)\frac{\partial u_i}{\partial x_j}\right) \tag{4}$$

$$\rho c_p u_j \frac{\partial T}{\partial x_j} = \frac{\partial}{\partial x_j}\left(\left(k_f + \frac{c_p \mu_t}{Pr_t}\right)\frac{\partial T_i}{\partial x_j}\right) \tag{5}$$

where

$$\mu_t = \rho \frac{k}{\omega}, \quad Pr_t = 0.85 \tag{6}$$

The energy equation for solid domain is:

$$\frac{\partial}{\partial x_j}\left(k_s \frac{\partial T_s}{\partial x_j}\right) = 0 \tag{7}$$

The k-ω SST model transport equations are:

$$\rho u_j \frac{\partial k}{\partial x_j} = P - \beta^* \rho \omega k + \frac{\partial}{\partial x_j}\left((\mu + \sigma_k \mu_t)\frac{\partial k}{\partial x_j}\right) \tag{8}$$

$$\rho u_j \frac{\partial \omega}{\partial x_j} = \frac{\rho \gamma}{\mu_t} P - \beta \rho \omega^2 + \frac{\partial}{\partial x_j}\left((\mu + \sigma_\omega \mu_t)\frac{\partial \omega}{\partial x_j}\right)$$
$$+ 2(1 - F_1)\rho \sigma_{\omega 2}\frac{1}{\omega}\frac{\partial k}{\partial x_j}\frac{\partial \omega}{\partial x_j} \tag{9}$$

The conditions set for the k-ω Shear Strain Transport (SST) in the present study is identical to those used by Barrau et al. [11]. The boundary conditions set at the following boundaries are:

- Bottom wall: Uniform heat flux q''
- Jet inlet: inlet velocity u_{in}, inlet temperature T_{in}
- Outlet: Pressure outlet with gauge pressure, $p_{out} = 0$.
- Fluid–solid interfaces: $u = 0, v = 0, w = 0, T_f = T_s, k_s \frac{\partial T_s}{\partial n} = k_f \frac{\partial T}{\partial n}$.
- Symmetrical faces: symmetric conditions
- Other solid walls: adiabatic wall.

The second order upwind scheme is applied for solving the convective terms in momentum and energy equations while the SIMPLE algorithm is used for pressure–velocity coupling. A convergence criterion of 1×10^{-5} is set in the present study.

A grid independence test is conducted. The grid sizes of 25,596, 121,500, 232,991, 340,452 and 464,340 were tested and the results of average outlet temperature were compared. As compared to the highest grid size, the results show the variation becomes negligibly small at grid size 340,452. Hence, the mesh corresponding to the number of grids of 340,452 is used hereafter. The numerical model is validated by comparing the results obtained by Kim et al. [10] as shown in Fig. 4. A maximum discrepancy of 2.6% is observed showing good agreement.

In the presents study, the thermal and hydraulic performances are evaluated for MCHS with different geometry of protruded ribs i.e. with different height (H = 0.1, H = 0.05, H = 0.025) and radius R at the corners of rectangular protrusion is varied (R = 0, R = 0.25 and R = 0.5), as illustrated in Fig. 3. The thermal performance are evaluated with $\overline{\text{Nu}}$ while the hydraulic performance are evaluated with pressure drop defined as follows:
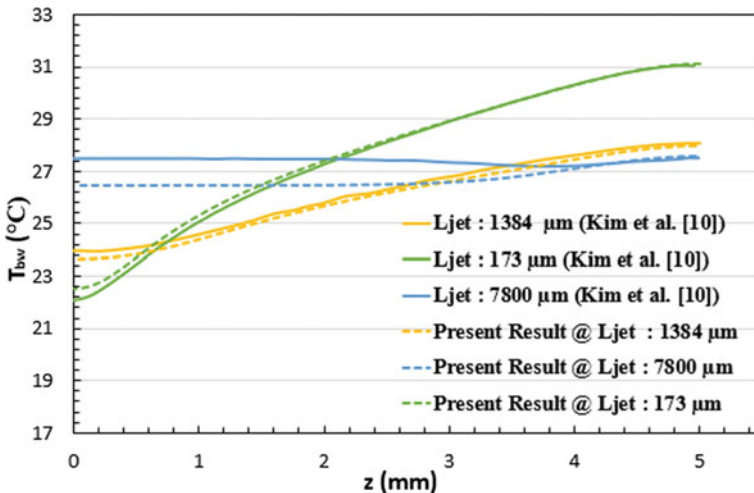
Fig. 4 Axial wall temperature at the base of heated surface along middle of flat microchannel

$$\overline{\text{Nu}} = \frac{\overline{h} D_{jet}}{k_f} \qquad (10)$$

$$\Delta P = P_{in} - P_{out} \qquad (11)$$

in which, P_{in} and P_{out} are the pressures at inlet and outlet, respectively, and $\overline{h}$ and D_{jet} are expressed respectively as follows:

$$\overline{h} = \frac{q''}{(T_b - T_{in})} \qquad (12)$$

$$D_{jet} = \frac{2L_{jet} W_{jet}}{(L_{jet} + W_{jet})} \qquad (13)$$

3 Results and Discussion

The results of $\overline{\text{Nu}}$ against R for different Reynolds number are obtained and shown in Fig. 5 at a constant rib height of H = 0.025. The Reynolds number is expressed as follows:

$$\text{Re} = \frac{\rho u_{in} D_{jet}}{\mu} \qquad (14)$$
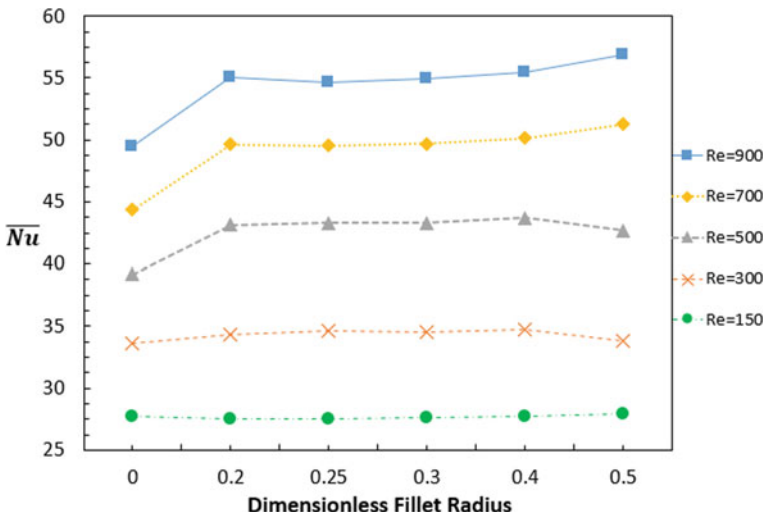
Fig. 5 Results of $\overline{\text{Nu}}$ with varying dimensionless fillet radius R and Re at H = 0.025
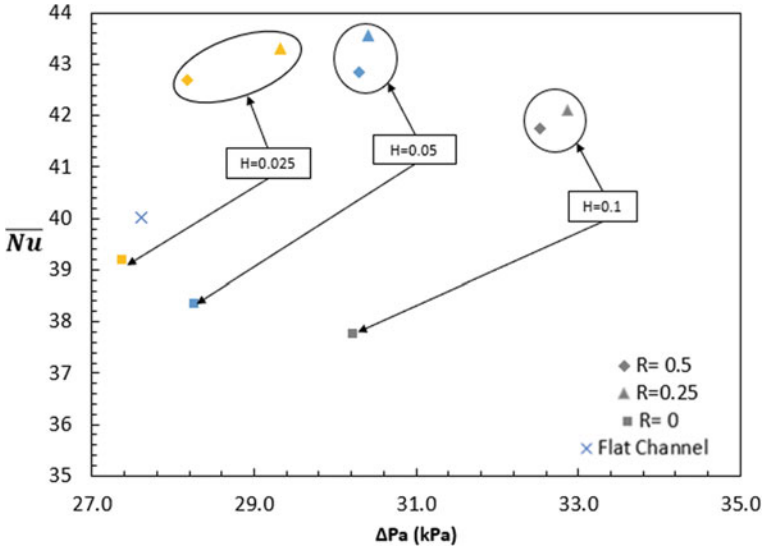
Fig. 6 $\overline{Nu}$ against pressure drop for MCSH with ribs of various fillet radius and height at Re $= 500$

The results show that the effect of fillet radius on $\overline{Nu}$ is not significant at Re $\leq$ 300. For Re $\geq$ 500, the variation $\overline{Nu}$ for $R \geq 0.2$ remain small. However, it can be observed in Fig. 5 that, the value of $\overline{Nu}$ for $R \geq 0.2$ is significant higher as compared to the case of $R = 0$ (case without fillet). This means, as long as rib is added fillet radius or the corners of rib is rounded, the value of $\overline{Nu}$ is higher than the case without fillet. This implies that sharp corners on the protruded rib are detrimental to heat transfer.

The effect of fillet radius and rib heights on $\overline{Nu}$ and pressure drop are examined at fixed Re $= 500$. The results are presented in Fig. 6. Note that the cross mark "$\times$" in Fig. 6 represent the case of MCHS with flat channel (without protruded rib). The results show that, the lower the rib height, the lower the pressure drop. Normally, the thermal performance is enhanced at the expense of pressure drop, but the results in Fig. 6 particularly the case of $H = 0.025$ suggest that, smaller rib height do not result in lower $\overline{Nu}$ if fillet radius is added at the corners of protruded rib. Relative to the flat channel, for small fillet radius i.e., R $= 0.25$, $\overline{Nu}$ increase significantly with only minor increase in pressure drop.

To study the temperature uniformity along of the MCHS, the results of $\overline{T_{bw}}$ is presented in Fig. 7 for various values of R and H. Generally, the results show that geometry of protruded rib with R $= 0$ (without fillet radius) has large temperature difference across the base of MCHS, regardless of the value of H. $\overline{T_{bw}}$ along the axial direction remain low near the stagnation area within the jet span, but increases sharply towards the flow exit. This is consistent with the observations from various studies associated with jet impingement cooling in microchannel subject to heat source at the base [4, 6, 10] which show low temperature (or high local Nusselt
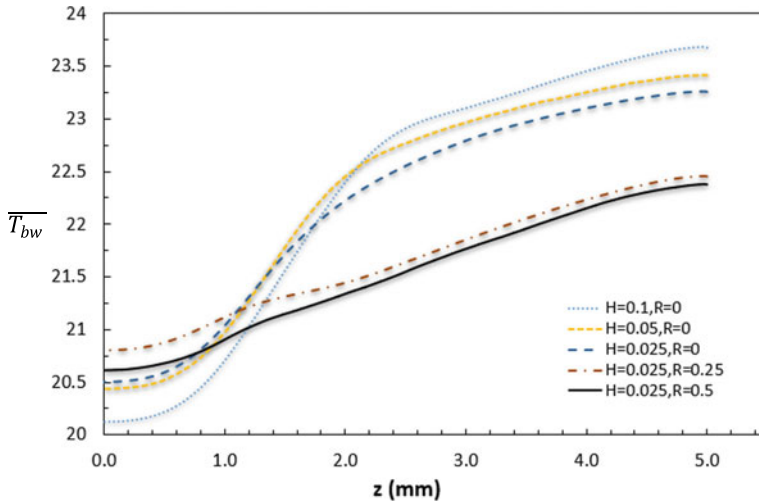
Fig. 7 Average axial wall temperature $\overline{T_{bw}}$ at the base of heated surface at Re $= 900$

number) within the distance of jet span from the stagnation, and with drastic increase in temperature (or decrease in local Nusselt number) towards the outlet. This is the issue of low temperature uniformity which might induce thermal stresses and failure to the electronic devices. For the case with fillet radius either R $= 0.25$ or R $= 0.5$ as shown in Fig. 7, the temperature difference across the base of MCHS is significantly lower. This suggest that, the fillet radius is able to improve the temperature uniformity or reduce the temperature difference across the MCHS.

4 Conclusion

The effects of varying the fillet radius and the height of the protruded rib on the thermal performance of the hybrid cooling module have been investigated. The numerical model has been validated with the literature with good agreement.

The presence of fillet radius on the protruded rib enhances the heat transfer as compared to the case without fillet and it is understood that sharp corners are detrimental to heat transfer. The merit of adding fillet radius to the protruded rib is further enhanced when shorter protruded rib is used as it results in lower pressure drop. The study also reveals that the addition of fillet radius to the edges of the protruded rib improves the temperature uniformity as compared to the protruded rib without fillet radius.

References

1. Tuckerman DB, Pease RFW (1981) High-performance heat sinking for VLSI. IEEE Electron Dev Lett EDL-2(5):126–129
2. Glynn C, O'Donovan T, Murray D (2005) Jet impingement cooling. In: Proceedings of 9th UK national heat transfer conference, Jan 2005
3. Jang SP, Kim SJ, Paik KW (2003) Experimental investigation of thermal characteristics for a microchannel heat sink subject to an impinging jet, using a micro-thermal sensor array. Sens Actuators A Phys 105(2):211–224
4. Sung M, Mudawar I (2006) Experimental and numerical investigation of single-phase heat transfer using a hybrid jet-impingement/micro-channel cooling scheme. Int J Heat Mass Transf 49:682–694
5. Sung MK, Mudawar I (2009) Single-phase and two-phase hybrid cooling schemes for high-heat-flux thermal management of defense electronics. J Electron Packag 131(2)
6. Sexton A, Punch J, Stafford J, Jeffers N (2018) The thermal and hydrodynamic behaviour of confined, normally impinging laminar slot jets. Int J Heat Mass Transf 123:40–53
7. Shen Z, Jing Q, Xie Y, Zhang D (2017) Thermal performance of miniscale heat sink with jet impingement and dimple/protrusion structure. J Heat Transfer 139(5)
8. Ming T, Cai C, Yang W, Shen W, Gan T (2018) Optimization of dimples in microchannel heat sink with impinging jets—Part A: mathematical model and the influence of dimple radius. J Therm Sci 27(3):195–202
9. Ming T, Cai C, Yang W, Shen W, Feng W, Zhou N (2018) Optimization of dimples in microchannel heat sink with impinging jets—Part B: the influences of dimple height and arrangement. J Therm Sci 27:1–10
10. Kim C-B, Leng C, Wang X-D, Wang T-H, Yan W-M (2015) Effects of slot-jet length on the cooling performance of hybrid microchannel/slot-jet module. Int J Heat Mass Transf 89:838–845
11. Barrau J, Omri M, Chemisana D, Rosell J, Ibañez M, Tadrist L (2012) Numerical study of a hybrid jet impingement/micro-channel cooling scheme. Appl Therm Eng 33–34:237–245

Design, Fabrication and Performance Evaluation of Charcoal Barbecue with Air Ventilation System

N. M. Mokhtar, M. A. Bappu, W. N. A. S. W. M. Fazli, L. W. S. Wilson, J. Thorairajoo, N. F. M. Yunus, R. M. Ramli, and M. S. Hadi

Abstract Domestic barbecues are an integral part of outdoor social activity in many countries where consumers are able to choose from a various type of charcoal grills. However, most commercial barbecues are installed in manual mode where the hand fan is needed to distribute heat and smoke. In this work, a charcoal barbecue equipped with air ventilation system was developed. The prototype was designed with a 3D drawing using NX10 modelling. The prototype was then fabricated based on the proposed design, including the fabrication of major components such as the body, charcoal port, hot rack and blower. Subsequently, an electrical part was commissioned to control the speed of the blower. Apart from the improvisation of ventilation, a comparison between coconut shell charcoal and mangrove wood charcoal was carried out to determine the best fuel. It can be observed that the maximum blower speed of approximately 21.9 knots was reached when the voltage was set at 7.3 V. In terms of charcoal performance, coconut charcoal was chosen as the best fuel with up to 33% more heat transfer than mangrove wood charcoal. In addition, the coconut shell charcoal is selected as the most effective fuel as it is capable of generating a maximum hot air temperature of about 74.57 °C with a smokeless fire.

Keywords Barbecue · Charcoal · Air ventilation · Grill · Heat transfer

N. M. Mokhtar (✉) · M. A. Bappu · W. N. A. S. W. M. Fazli · L. W. S. Wilson · J. Thorairajoo · N. F. M. Yunus
Faculty of Civil Engineering Technology, Universiti Malaysia Pahang, Lebuhraya Tun Razak, 26300 Kuantan, , Pahang, Malaysia
e-mail: nadzirah@ump.edu.my

R. M. Ramli
Faculty of Electrical and Electronics Engineering Technology, Universiti Malaysia Pahang, 26600 Pekan, , Pahang, Malaysia

M. S. Hadi
School of Mechanical Engineering, Universiti Teknologi MARA, 40450 Shah Alam, Selangor, Malaysia

1   Introduction

Barbecuing is normally a social occasion and is a safe activity. In Malaysia, Environmental Quality Act 1974 [Act 127] Environmental Quality (Prescribed Activities) (Open Burning) Order 2000 stated that open burning from outdoor grills, barbecues or fireplaces for the preparation of food which is not carried out at any peat soil area is allowed [1]. The most conventional way to make a barbecue is to put the firewood into a metal container and the meat on a grill over the embers once the embers are ready. With the era of modernization, there are various types of barbecue machines that are used worldwide. These include electric barbecue machines, charcoal barbecue machine, and gas barbecue machine [2]. As expected, electric grills are not convenient to use outdoors because of the need for electrical power.

Compared to gas, charcoal remains the principal fuel for grilling food in many countries due to the authentic flavor of charcoals. In addition, charcoal is readily available and inexpensive to use with a moderate level of combustion favored by consumers. For this purpose, consumers may choose from various types of charcoal grills of all shapes and sizes [3]. The choice usually depends on the building quality, size, cooking area, temperature and stability control, ease of use and cleaning, durability and additional accessories. Up to now, grill manufacturers are continually striving to develop barbecue grill that will safely and efficiently cook meat or other foods while retaining the natural flavor of the food being cooked. Despite the product design, it is also important to consider the aspect of the heat transfer mechanism such as convection heating system created from the circular shape of the charcoal grill, the air supplied to the fuel and etc. In view of this, an efficient ventilation system on the barbecue set is also important to ensure healthy, comfortable and productive cooking process [4].

Other issues related to the barbecue is the charcoal type. Currently, the traditional charcoal used for barbecue still has low energy efficiency and generates high smoke emissions. More time is required to produce heat and the burning of charcoal affects the quality of the surrounding air. It usually takes about 30 min to light up charcoal with a manual fanning. This wastes time and affects the dining experience. Furthermore, the grease that releases polycyclic aromatic hydrocarbons (PAHs) from food is detrimental to consumers' health [5]. PAHs are carcinogenic chemicals that are released in a high temperature environment. According to literature, barbecue cooking style is the main contributor to PAHs and suspended particulate emissions [6]. PAHs are reported to be generated by incomplete burning and pyrolysis of thermal agents, food nutrients, and food oil and fat content during the barbecue process [7]. In addition, the grease drippings will come into direct contact with the heat source and create an unequal distribution of heat to food.

The objective of this work is to develop a prototype charcoal barbecue with an air ventilation system. A performance evaluation will be performed to determine the impact of the ventilation process on the grilling process. Throughout the development of the prototype, all major aspects were considered such as the compatibility of the design with semi-auto portable concept, the air ventilation system at which the device
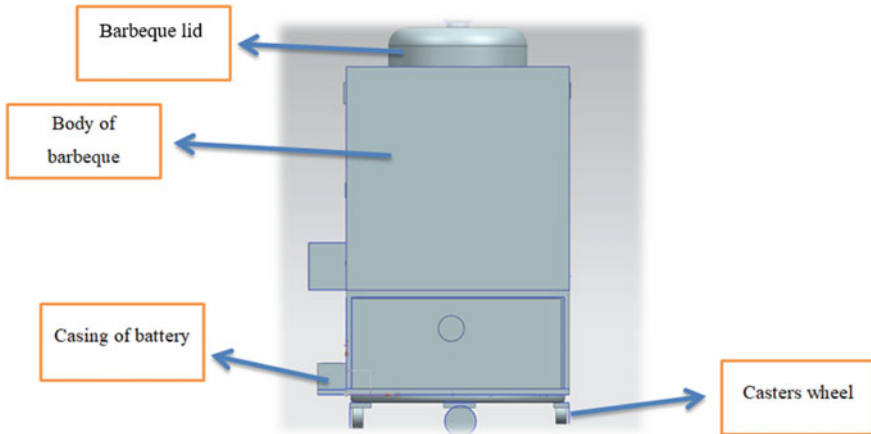
Fig. 1 Front view of the prototype

is able to be produce and recycle heat, and the quality of barbecuing in aspect of environmental. The concept of this barbecue manufacturing is to allow users to improve energy efficiency, avoid manual fanning, reduce time consumption, and be environmentally friendly.

2 Methodology

2.1 Design and Features of Model

The design of a portable charcoal barbecue with air ventilation system is divided into three different parts, which is charcoal port system, the cooker with air ventilation and hot rack. The 3D drawing of the barbecue set was designed using NX10 Modelling. Figure 1 shows the front view of the proposed system while Fig. 2a–c illustrated right, left and isometric views of the prototype, respectively.

2.2 Material Selection

Material selection was carried out to identify the ideal equipment for prototyping and to compare fuel types. The materials used in this study were decided based on price, size/dimension and quality and are summarized in Table 1.
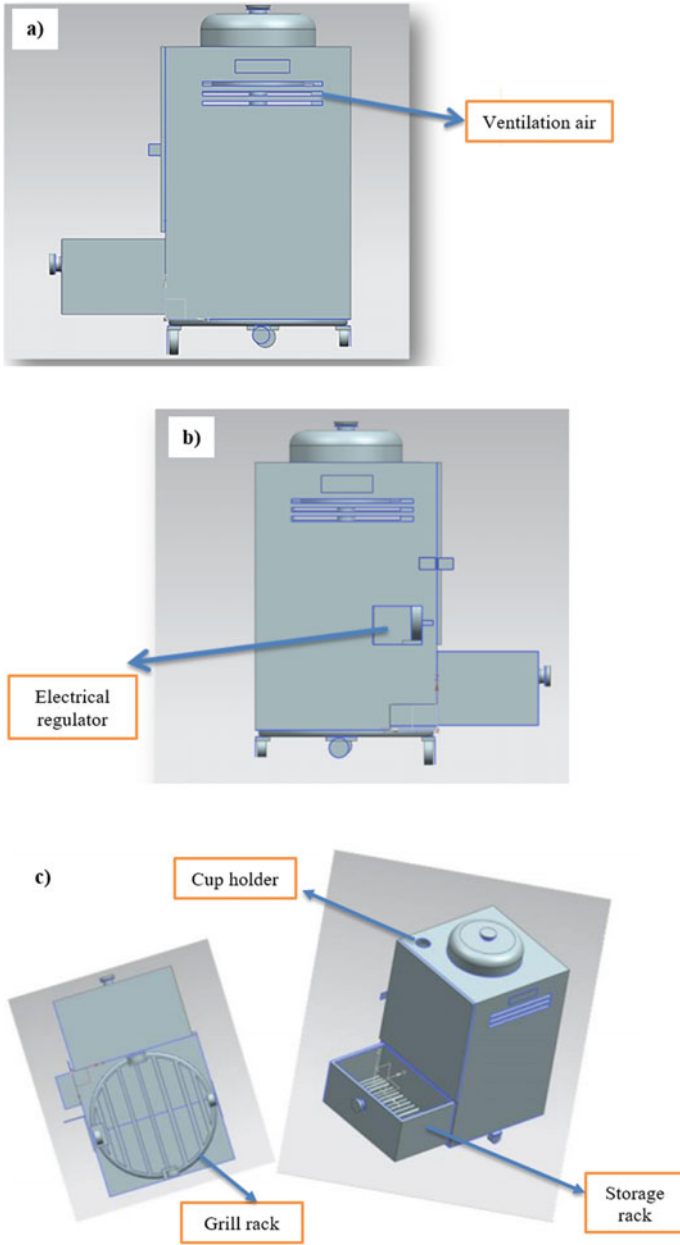
Fig. 2 **a** Right view, **b** left view and **c** isometric view of the prototype

Table 1 Material for charcoal barbecue with air ventilation system

Material	Quantity
Zink	10 kg
Barbecue bowl	1
Barbecue grill	1
Variable speed switch control	1
Blower	1
Coconut shell charcoal	3 kg
Casters wheels 2″	4
Battery 12 V	1

2.3 Fabrication Stage of Charcoal Barbecue with Air Ventilation System

The fabrication of the charcoal barbecue with air ventilation system was conducted in Engineering Technology Workshop at Universiti Malaysia Pahang. The prototype was made of zinc for the body part and stainless steel for the entire stove. The structure of the prototype was developed by a sizing process to get the right sizing, cutting, and assembly processes. The tools deployed in the fabrication process were grinder, welding machine, welder and rivet. The sizing of major components was provided in Table 2.

The manufacturing processes took place in a few stages starting with the construction of the bodywork where the frame was constructed using zinc material. The square shape of the zinc sheet was marked accordingly and cut into pieces of various sizes required depending on the design calculation as shown in Table 2. The workpieces were welded together to ensure rigidity, support and stability. Figure 3 shows the complete prototype of charcoal barbecue with air ventilation system fabricated in this work. As can be seen from this figure, there is a circular lid on top of the design that located the charcoal port (see Fig. 3c), while the hot rack storage consisted of drawer and a detachable grill shelf was attached to the front side. The close-up of this storage may be clearly seen on Fig. 3b. In this work, the charcoal container was made of stainless steel and the material was measured based on the design size. The charcoal chamber was perforated to allow transportation of air from the blower for effective supply of required air for the complete combustion. The purpose of the round shape design for charcoal and cooking surface is to improve heat distribution

Table 2 Sizing for major components

Components	Sizing
Body/Frame	36 cm (L) × 43 cm (W) × 38 cm (H)
Grill part	Diameter—26 cm
Charcoal port	Diameter—11 cm, Height—7 cm
Hot storage rack	33 cm (L) × 40 cm (W) × 13 cm (H)
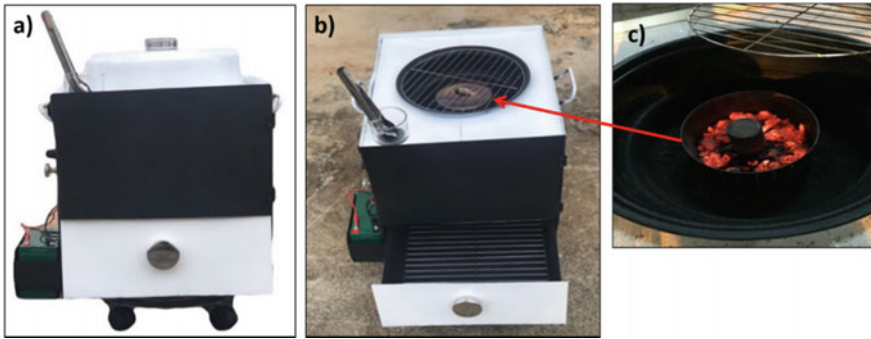
Fig. 3 a Front view and, **b** top view of the charcoal barbecue with air ventilation system together with **c** charcoal pot

inside the cooking area. It is believed that the rectangular design may lead to the overcooked parts on the food product due to the heat concentrated in the four corners of the rectangular shape. Otherwise, there is still argument stated that the rectangular shape of cooking area may lead to inefficient heat distribution because the heat comes from the corner of each edge whereas one corner absorbs more heat while the other release heat less than the other places. Therefore, it can be concluded that the choice of cooking shape influences the heat distribution in the cooking process. Other than that, the circular lid on top of the cooking surface was designed to induce the heat transfer by convection in the barbecue area. The air temperature in the grill area will be raised due to the convective heat transfer of the air apart from the direct heat comes from the coals. This will only happen when the lid is putting down and closing the grill area.

Another major component is the blower inside the body. It was measured and modified into desired shape for incoming air at the centre of a spinning impeller. As the impeller turns, it accelerates the air outwards from the impeller. The air was channeled through welded hoses and inserted into the charcoal port. The size of the blower is about 11 cm in diameter. The increased airflow created by the blower speeds up the ignition and heating of charcoal by channelling air through the charcoal port [8]. The manufacturing process was finally completed with the hot rack compartment to position the cooked foods to keep them warm. The commissioning of the electrical component took place after the prototype was manufactured. The electrical part is composed of a battery unit and an electric regulator. The battery used for the barbecue set has a 12-voltage capacity. The battery provides the necessary voltage to operate the fan to generate the air velocity. In the meantime, the electrical circuit works to regulate the speed of blower.

2.4 Performance Analysis

As the prototype was completed, three types of performance analysis were conducted to investigate blower performance, charcoal performance comparison and heat transfer analysis. During the performance analysis, few measurement devices were used such as thermal infrared contact thermometer, mini-anemometer as well as penetration stem dial thermometer. The performance analysis of the blower was conducted by adjusting the supply voltage to control the speed of the blower. This analysis is intended to monitor the minimum and maximum speeds that may be generated by the blower. This is because the heat generated by the charcoal can be controlled using the airflow provided by the blower. This analysis was repeated three times to determine the average speed.

Generally, the use of charcoal as a fuel in barbecuing determines the quantity of hot air produced. In this study, two types of charcoal were used for the barbecue, namely mangrove wood charcoal and coconut shell charcoal. The evaluation was done based on the hot air produced during the process and the smoke production. Meanwhile, in terms of the heat transfer analysis, two types of food samples (chicken and fish) were placed on the barbecue grill according to the time needed (12 and 8 min) for both items to be cooked accordingly. The temperatures T1, T2 and T3 were recorded using a K-type thermocouple probe to obtain the average temperature necessary for the calculation of the total heat transferred from the charcoal. This analysis was performed to determine temperature and quantity of heat transferred to food samples. Overall heat transfer was calculated using Eq. 1.

$$Q = m \times C_p \times \Delta T \tag{1}$$

where C_p is the specific heat capacity of the substance. In this study, the specific heat capacity for chicken and fish is 3.22 kJ/kg.K and 3.6 kJ/kg, respectively. m is the mass of the substance, and ΔT is the change in temperature between initial and final temperature of the substance.

3 Results and Discussion

3.1 Blower Performance Analysis

An air blower is a machine used to generate airflow at substantial pressure. The air flow generated by this fabricated barbecue is used to heat up the charcoal. The blower performance analysis was carried out by regulate the supply voltage to control the speed of blower. This analysis is executed to monitor the minimum and maximum speeds that can be produced by the blower. From Fig. 4, it can be seen that the higher the voltage, the greater the blower speed. The minimum supply voltage that can be
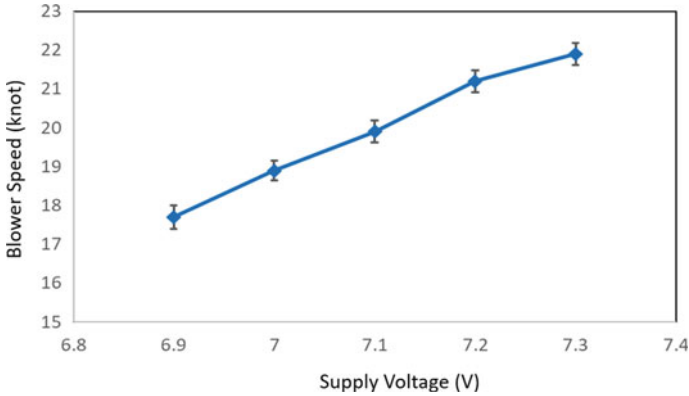
Fig. 4 Average blower speed versus supply voltage

adjusted using this system is 6.9 V and the blower speed was recorded at 17.7 knots after the power is turned on. Meanwhile, the blower speed was 21.9 knots when operating at the maximum voltage of 7.3 V. With the innovation of the air ventilation part, it is expected that the heat generated by the charcoal can be controlled by varying the blower speed. Generally, increasing the air velocity by the external force provided by the blower can dramatically improve the charcoal combustion process.

3.2 Performance Analysis on Charcoals

The air temperature caused by the charcoal emission was measured during thermal tests on a stainless steel cube as the sample product using a K-type thermocouple sensor. The effectiveness of two different kinds of charcoals was determined when it was fully ignited. The temperature of the hot air emitted by the charcoals was recorded every 2 min, for a total of approximately 20 min as shown in Fig. 5. Coconut shell charcoal attained a maximum temperature of 74.57 °C at $t = 10$ min. The temperature begins to fluctuate and then decrease when the experimental work is completed. The final air temperature was recorded at 67.80 °C at $t = 20$ min. As for mangrove wood charcoal, the temperature rises by about 64.57 °C at $t = 16$ min and decreases at the end of the process to 59.4 °C. The resulting temperature indicates that it was low and slow phase which is not ideal for the barbecue process.

The results of both charcoals showed that the coconut shell charcoal ignited faster and had a higher air temperature than the mangrove wood charcoal. During the barbecue, the coconut shell charcoal is observed to produce less smoke in the atmosphere than the mangrove wood charcoal. As reported in literature, coconut shell produces less ash (1.8%) with a moisture content of 5.56%, volatile matter of 70.82%, and fixed carbon of 21.8%, respectively, during the proximate analysis [9]. The studies state that low ash biomass can be considered a good fuel with a high
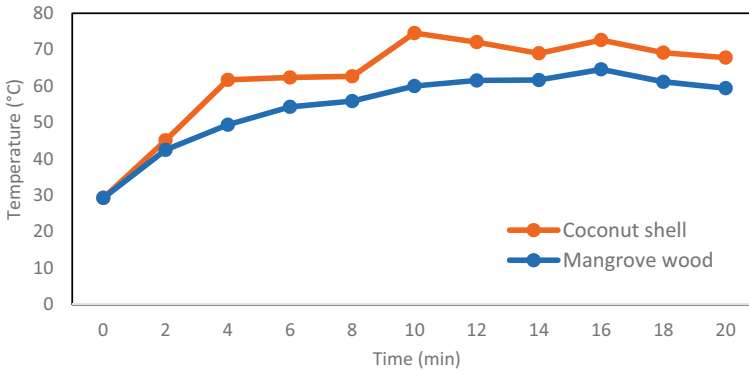
Fig. 5 Temperature of air emitted vs time for both charcoals

energy potential. To support the findings, a thermal analysis was conducted on food samples using chicken and fish, which have different meat properties.

3.3 Performance Analysis of Heat Transfer on Food Samples

Figures 6 and 7 show the overall heat transfer analysis on different types of food samples. The two figures show the heat transfer performance using coconut shell charcoal and mangrove wood charcoal as the selected type of fuel. The final heat transfer obtained in the chicken sample for coconut shell charcoal and mangrove wood charcoal were 16.99 kJ and 12.75 kJ, respectively. Meanwhile, as can be referred to Fig. 7, the final heat transfers for fish sample from the experiments were 22.92 kJ and 19.17 kJ, respectively. From this analysis, it can be observed that the
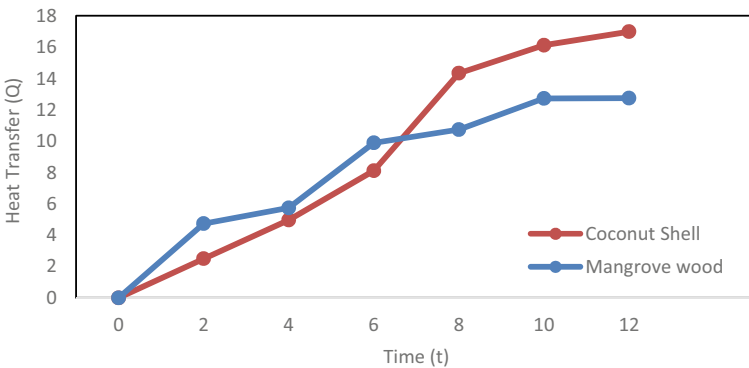
Fig. 6 Overall heat transfer versus time (chicken)
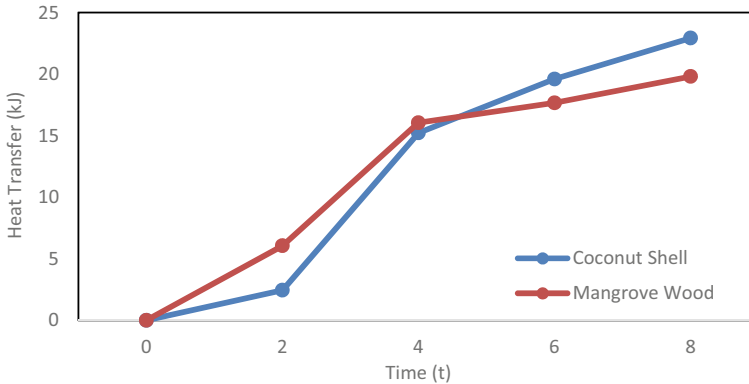
Fig. 7 Overall heat transfer versus time (fish)

coconut shell has high tendency to ignite faster and producing less smoke and ashes to the surrounding environment as compared to the mangrove wood.

The performance of heat transfer by coconut shell charcoal on different types of food samples is also higher on the two properties of the meat which is diverse from each other. These results are consistent with a previous study that found that coconut shell biomass exhibits a high fuel value index relative to other types of biomasses [9]. The higher value obtained could be attributed to its properties that produce a lower value of ash, a higher heating value and a high density of the feedstock material. From the overall analysis, it can be concluded that the coconut shell charcoal has a high propensity to ignite faster which helps to speed up the cooking process and produce less smoke as compared to mangrove wood charcoal.

4   Conclusion

In this work, the prototype of the proposed system was successfully manufactured using the chosen materials. The main purpose of choosing the right material is to minimize costs while achieving product performance targets. The final prototype was designed with special characteristics like portable configuration, force convection, easy handling and cleaning. The air ventilation system was applied to avoid manual fanning. In analyzing the performance of the manufactured system, two types of solid fuels were used, namely mangrove charcoal and coconut charcoal. According to the data presented, coconut charcoal outperformed mangrove charcoal in terms of heat transfer analysis and smoke emission.

References

1. Environmental Quality Act 1974, Department of Environmental Malaysia
2. Gyansah L (2012) Design, construction and modeling of a mechanical portable barbecue machine. Glob J Res Eng Mech Mech Eng 12(7):43–58
3. Taams S (2016) Designing a connected barbecue (Master). Delft University of Technology, Netherlands
4. Zhao Y, Tao P, Zhang B, Huan C (2020) Contribution of Chinese hot pot and barbecue restaurants on indoor environmental parameters. Aerosol Air Qual Res 20:2925–2940
5. Badyda A, Krawczyk P, Bihałowicz JS, Bralewska K, Rogula-Kozłowska W, Majewski G, Oberbek P, Marciniak A, Rogulski M (2020) Are BBQs significantly polluting air in Poland? A simple comparison of barbecues vs. domestic stoves and boilers emissions. Energies 13:6245
6. Wang L, Xiang Z, Stevanovic S, Ristovski Z, Salimi F, Gao J, Wang H, Li L (2017) Role of Chinese cooking emissions on ambient air quality and human health. Sci Total Environ 589:173–181
7. Lao JY, Wu CC, Bao LJ, Liu LY, Shi L, Zeng EY (2018) Size distribution and clothing-air partitioning of polycyclic aromatic hydrocarbons generated by barbecue. Sci Tot Environ 639:1283–1289
8. Oke PK (2013) Development of a multi-purpose roasting machine. Pacific J Sci Technol 14(2):48–52
9. Ahmad RK, Sulaiman SA, Yusup S, Dol SS, Inayat M, Umar HA. Exploring the potential of coconut shell biomass for charcoal production. Ain Shams Eng J. https://doi.org/10.1016/j.asej.2021.05.013

Effect of Voxel-Based Surface Mesh Size on Process Simulation for Metal Additive Manufacturing of Ti6Al4V Impeller of Centrifugal Compressor

Avez Shaikh, Ajinkya Shinde, Satish Chinchanikar, and Tanmay Deshpande

Abstract Additive manufacturing (AM) making radical changes in traditional manufacturing through innovation. The 3D printing modeling and simulation techniques are evolving to avoid difficulties and losses in manufacturing. A critical aspect of failure in metal 3D printing is due to design distortion and internal (residual) stresses. Simufact Additive is a simulation tool that has emerged to reduce process development time and produce high-quality parts by having prior information of the part distortion. Simufact Additive simulates and predicts structural behavior (stress, strain, failures, and distortion). This study analyzes the effect of voxel-based surface mesh size on the process simulation for metal additive manufacturing of Ti6Al4V impeller of the centrifugal compressor. The part is analyzed considering different mesh sizes to obtain highly accurate and quality components without design distortion. The analysis of simulated results shows that the increase in element size reduces the amount of distortion. Meshing and the simulation time observed as decreasing with the increase in element sizes.

Keywords Simufact additive · Additive manufacturing · Voxel-based meshing · 3D printing · Structural behavior

1 Introduction

3D printing or Additive Manufacturing's application in industry is vastly growing due to the instantaneous and accurate results it provides in product development. But it is costly, sluggish, and needs multiple approaches before the final product is ready. The need for speed and precision is needed in the process which can be achieved through simulation modeling and analysis. Many software has been developed that captures the whole procedure of modeling and gauge the simulation to the needs of the handler. The simulation and analysis carried out in this research paper are done with Simufact Additive [1].

A. Shaikh (✉) · A. Shinde · S. Chinchanikar · T. Deshpande
Mechanical Engineering, Vishwakarma Institute of Information Technology, Pune 411048, India
e-mail: avez.21820048@viit.ac.in

It is easy to work with and allows fast predictions about failures and stress in parts due to error or improper technology or manufacturing glitches. These predictions and simulations can address the problems in manufacturing through 3D printing. The errors or deterioration can be allowed through ineffectual forbearances or high-cost treatments. Residual stresses that are not required can cause self-distortion of the part during or post-production. Simulation in Simufact Additive allows users to digitally analyses and simulate the part with optimization such as required parameters, materials, environmental conditions, and creating or removing direction, support, etc. [2].

The software uses the finite element method to precisely approximate the stresses and distortions on the model or part. The finite elements are formed by the finishing element network. The most important part of the finite element analysis is whether the element size and number of elements used is sufficient for that analysis. If the element network is sufficient, and assuming other model inputs are correct then the outcome of the analysis is satisfactory. Finite element density is used to moderate the precision of the analysis which consist of element type and shape which highly affect the accuracy of the analysis [3]. There is abundant of work done in meshing and analysis on different models and with different materials. From medical applications to constructive approaches in different domains simulation with additive manufacturing to detect anomalies is growing. Introduction to the voxel-based point cloud representations is first-time given. There are key techniques for creating voxel-based point cloud representations to understand behavior and applications using voxel-based depictions [4].

In terms of material science, a new progressive damage model for 3D woven composites has been worked on with a depiction of volume cell with high fidelity is constructed. In this, Voxel and conformal mesh models of 3D woven composites are generated and then simulated on different environments to see the responses of materials and composites with a comprehensive comparison of damage simulations between the voxel and conformal models. It has pointed out that fake stress concentrations and artificial connections are induced by voxel mesh, which are identical to the real ones that could be induced in the part in real environment conditions [5]. With 3D printing already on the verge of becoming a traditional method for prototyping. Newer approaches such as 4D printing are on their way to disrupt the industry. A conceptual design framework for 4D printing has been proposed. It deals in voxel-based modelling and simulation of non-programmable shape-changing smart materials and composites. Their simulation and analysis can provide a quick evaluation of any material distribution behavior upon exposure to the stimulus and environment change.

High accuracy can be obtained in a high-density network only if there is no singularity region in the part. As the complexity of the model and its network elements increases the need for high specifications in the computer and the time required to complete increases. Whenever multiple trials and iterations have required this problem regarding time consumption will be encountered, especially for transient and non-linear analyses. The model used in this study is an impeller from a centrifugal compressor. Also, this study focuses on the voxel mesh and its advantages over

other mesh types. The dimensions of the part and finishing elements can be fully represented and worked upon. Different materials with different geometric properties of different objects can be inspected. The boundary conditions can be used simply. Though there are disadvantages like the difficulty of model connection designs, modeling assumptions, estimation of component interactions difficulty, and damping is usually ignored [6]. The voxel mesh is necessary for the disadvantages to being coped with and making the manufacturing of the part possible.

In this study, the Simufact Additive simulation tool has been used to predict structural behavior (stress, strain, failures, and distortion) of Ti6Al4V impeller of the centrifugal compressor considering the effect of voxel-based surface mesh size while the process simulation for metal additive manufacturing. The part is analyzed considering different mesh sizes to obtain highly accurate and quality components without design distortion. The analysis of simulated results is presented to reduce process development time and produce high-quality impellers by having prior information of the part distortion.

2 Metal Powder Bed Fusion

In the Metal Powder Bed Fusion process, high power energy sources i.e., lasers are used to produce parts layer by layer by the melting of finely sized metal powders. The first commercialized PBF process for metals was Selective Laser Sintering (SLS) which included sintering or fusing of regions of thin powder layers. Since then, various technological advancements have been done in the PBF process which has enabled the production of components with increased and better mechanical characteristics, performances, and properties. Thus, this led to subcategories of various processes under metal powder bed fusion technology [7].

2.1 Selective Laser Melting (SLM)

Selective Laser Melting (SLM) is a technology under the metal powder bed fusion AM process that employs using a laser that unintermittedly melts layers of metal powder under an inert atmosphere [8]. The noteworthy advantages of this AM process include having high flexibility in the manufacturing of components with high complexity both in terms of lattice structures and design. SLM's material research mostly prevails on Titanium alloys because of their high corrosion resistance, specific strength, and biocompatibility. With such process capabilities and material properties, SLM finds its applications widely in aerospace; space, biomedical and automotive fields [9–11].

2.2 *Direct Machine Laser Sintering (DMLS)*

Direct Metal Laser Sintering is a technology for the manufacture of metallic components directly from the 3D CAD Part/model. In DMLS mechanical properties of the components fabricated have been observed and studied by many researchers. The observations have concluded that DMLS can manufacture practical components in a small capacity. However, the properties of the components/parts manufactured through this process are inferior in quality as compared to components manufactured through other traditional manufacturing processes [12].

3 Process Simulation for Metal Additive Manufacturing

Software Process Simulation Modelling (SPSM) on models is a newer concept that is getting popular due to its multiple benefits and the fact that it is the solution to the disadvantages of 3D printing metal parts. The failures and internal stresses of a model can be analyzed without manufacturing the actual part through simulation. The process starts with a model or part that needs to be analyzed before mass production. First, it is voxel meshed, with different sizes such as 0.5, 1, 1.5, and 2 mm. A voxel signifies a value on a consistent grid in 3-D space. In short, Voxel mesh refers to the volumetric mesh structure. The solution is provided by separating the mesh pieces into three dimensions. The surface is laid after the surface mesh, the voxel mesh covers the entire surface. The residual stresses and distortions are calculated by the end of the analysis. The residual stresses can be reduced most of the orientation of the optimum part that can be determined and the support elements optimized along with editing environment data. The simulation armed with this information aims to analyze and reduce stress and distortions by adjusting voxel meshes along with element sizes which will result in lower distortion and after manufacturing less failure of the part. The software Simufact Additive works smoothly with the simulations and analysis part [13].

3.1 *Simufact Additive Software*

MSC Simufact Additive is a software specially developed for metal powder bed fusion additive manufacturing processes such as direct metal laser sintering (DMLS) Selective laser melting (SLM), laser beam melting (LBM) and electron beam melting (EBM) methods. The primary benefits of this software are that we can process simulate the complete AM process, including steps such as determination of various distortions and residual stresses, printing steps simulation, heat treatment, actual support cutting/removal and hot isostatic pressing (HIP). The software also uses efficient computational methods to predict: shrinkage, warpage, optimum location of

part placement., etc. The software provides the only solution of using a hexahedral element type for a voxel mesh. It enables the part to be built right the first time. For this study, we have used MSC Simufact Additive 1.0.

3.2 Materials and Methods

In this research paper, a case study component i.e., an impeller of the centrifugal compressor was used in the experiment. The main objective of this was to find the main effect of voxel size reduction of 3 predicted properties i.e., distortions, residual stresses, and effective strain in the final component before actually manufacturing it. Also, another main objective was to reduce the distortions in the simulated impeller part and to hence provide better manufacturing of the component. A generalized flowchart for the experimental process of performing the simulation is as shown in Fig. 1 [14].

In the very beginning the case study component i.e., the centrifugal impeller was imported into the software. The imported component must be always a CAD drawing in.stl format. (Fig. 2) The default metal powder fusion AM process was simulated i.e., SLM. The machine used for this process is EOS M 400 of dimensions 400 × 400 × 400 mm. The three process stages include building, simple cutting, and
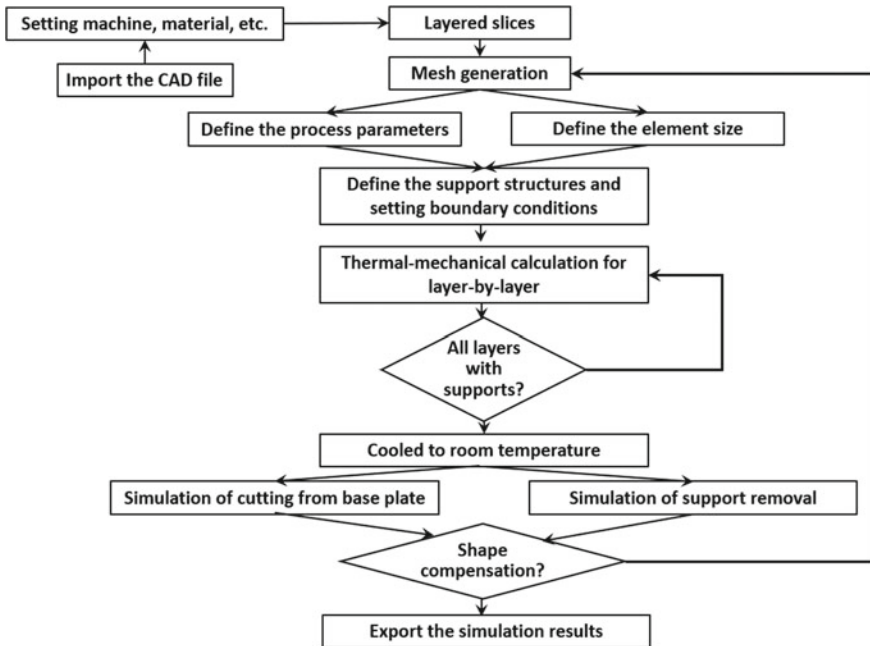
Fig. 1 Flowchart of simulation model [14]

Fig. 2 3D drawing of
impeller

support removal. The imported part is centered with distance from left and front as
82 and 4.2 mm from the bottom for all four simulations. The next process includes
generating supports for the impeller with a support radius of 0.25 mm and a critical
surface angle of 45°. A total of seventeen supports were generated as shown in Fig. 3.
The base plate material is X155CrVMo12-1_h. The metal powder used is Ti6Al4V,
and its material curves, composition, and constants were already predefined and as
depicted in Table 1.

The next step involves assigning all the supports for the support removal step. The
surface mesh for all four analyses is 2 mm. The layer thickness for each increment
is 0.03 mm. The properties for laser beam are beam width of 0.00015 mm, the
velocity of beam travel as 1 m/s, power as 200 W, and efficiency of 0.5. Impeller
with generated supports is as shown in Fig. 3a.

The next step involves defining the voxel mesh size and the voxel mesh parameter
size is the topic main focus of the research paper. The generated voxel mesh for
one of the sizes can be seen in Fig. 3b. As discussed, the software used hexahedral
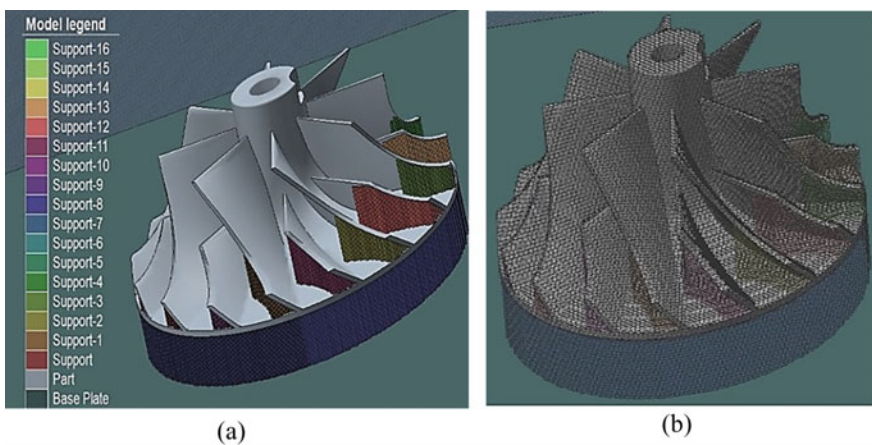
Fig. 3 a Impeller with generated supports and **b** voxel meshed impeller

Table 1 Ti6Al4V metal powder properties

Particulars	Values
Density	4.41 g/cm^3
Minimum wall thickness	0.3–0.4 mm
Maximum particle size layer thickness	d50 (DIN ISO 13320) 30 μm
Minimum temperature	293.15 K
Maximum temperature	1873.15 K
Material composition	Al (5.5–6.5%), V (3.5–4.5%), O < 2000 ppm (parts per million), N < 500 ppm, C < 800 ppm, H < 120 ppm, Fe < 2500 ppm, Titanium balance

elements also called voxel elements. The voxel size is defined as the edge length for the hexahedral i.e., voxel element. The size of elements represents the number of metal powder layers comprised. The minimum fraction for the parts and supports is 5 and 1%. The simulations were performed for the following voxel mesh sizes—0.5, 1, 1.5, and 2 mm.

The next step involved defining the solver properties i.e., parallelization, output division, and solver. Multiple cores were used i.e., six cores on Intel i7, 10th generation laptop, with features such as 16 GB RAM and 6 GB NVIDIA graphics card for computation. The domain decomposition feature inclines to use of multiple cores for process computation. The meshing time for different voxel meshes was also recorded. Finally, once the simulation was completed the different results for distortions, residual stresses, and effective strains were compared to draw conclusions and hence determine the effect of mesh sizes on the results.

4 Results and Discussion

All the simulations were performed to predict 5 important parameters for the metal PBF AM process that are total distortions, effective stress is also known as residual stresses, effective plastic strain, and mean normal stress.

- Distortion is the most common problem in additive manufacturing. Improper and Inconsistent shrinkages and accumulations during the additive manufacturing process drive the final distortion of the part. (Refer to Fig. 4 a, b which show the distortion comparison values between the analyzed simulation results for voxel mesh sizes of 1 mm and 1.5 mm, respectively).
- Effective stress is defined as stress, which depends mainly on 2 factors i.e., pore pressure and applied tension, which in turn controls the strength and strain behavior of the metal powder (Ti6Al4V). (Refer to Figs. 5a, b which shows the effective stress comparison values between the analyzed simulation results for voxel mesh sizes of 1 mm and 1.5 mm, respectively).
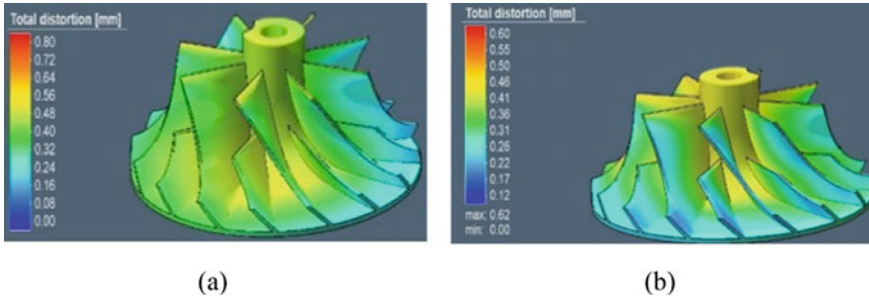
Fig. 4 Distortion for voxel mesh size of **a** 1 mm and **b** 1.5 mm
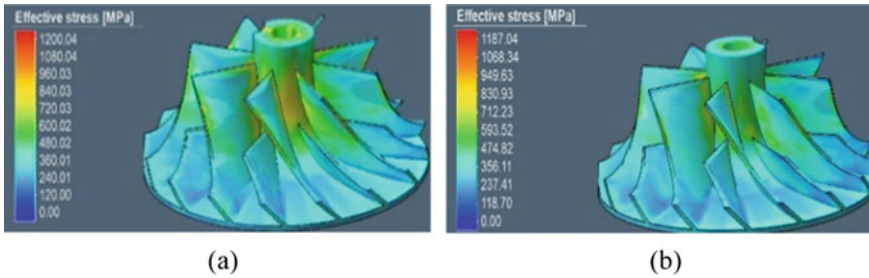
Fig. 5 Effective stress for voxel mesh size of **a** 1 mm and **b** 1.5 mm

- Effective plastic strain—The value of effective plastic strain is the integral of stepwise increments of plastic deformation for a period t. (Refer to Fig. 6a, b which show the distortion comparison values between the analyzed simulation results for voxel mesh sizes of 1 mm and 1.5 mm, respectively).

The predicted results for all four simulations are represented in Figs. 7 and 8. After performing simulations with four different voxel mesh sizes (0.5, 1, 1.5 and 2 mm), it was found that as the voxel mesh size is reduced more precise results were obtained.
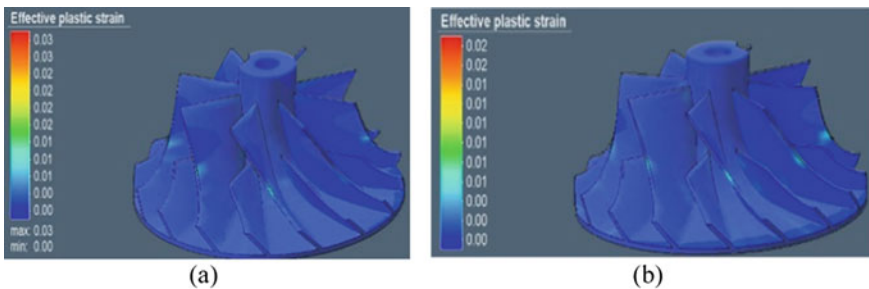
Fig. 6 Effective plastic strain for voxel mesh size of **a** 1 mm and **b** 1.5 mm
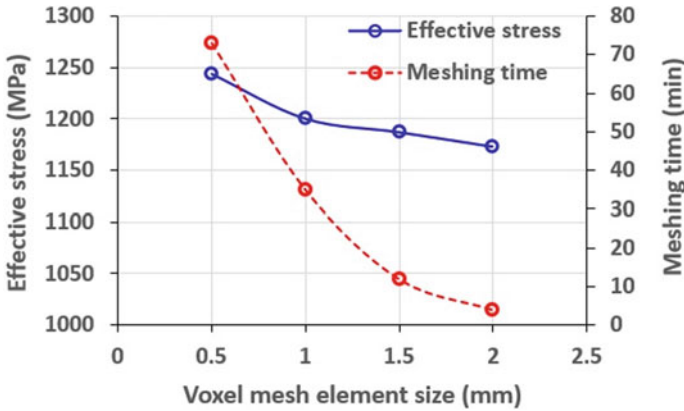
Fig. 7 Effect of voxel mesh size on effective stress and meshing time
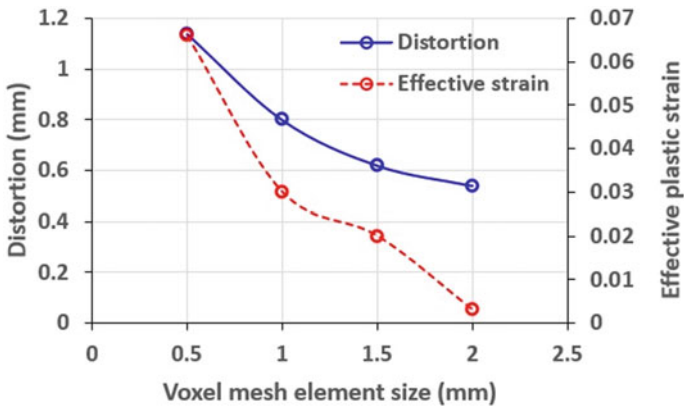
Fig. 8 Effect of voxel mesh size on distortion and effective plastic strain

Hence, the cause is that the more sensitive solution causes more deformation terms. It was also observed that if voxel mesh has an element size as small as the value, the experiments time will increase.

Figure 7 depicts the effect of voxel mesh size on effective stress and meshing time and Fig. 8 depicts the effect of voxel mesh size on distortion and effective plastic strain. It can be seen that voxel mesh element sizes and dimensions affect the numerical computation, analysis, and underlying final results. The simulated results show that varying voxel mesh size and constant surface mesh, i.e., with an increase in the element size, reduce the number of distortions, effective stress, effective strain, meshing, and the simulation time for each particular analysis.

5 Conclusion

Simulation modeling has multiple applications in pre-processing of additive manufacturing. It has the potential for a common standard in manufacturing industries. Distortion of parts through the production process constitutes a significant problem to MNCs, causing them to lose precious time and capital. Software like Simufact Additive is continuously improving to create a better-simulated environment for the user that tackles the disadvantages of Additive manufacturing. This study finds that voxel mesh element sizes and dimensions affect the numerical computation, analysis, and underlying final results. The simulated results from this study show that varying voxel mesh size and constant surface mesh, i.e., with an increase in the element size, reduce the number of distortions for each particular analysis. This study observed that finite element density, i.e., element type and shape are prominent metrics to control the accuracy of the predicted results. Effective stress, effective strain, distortion, meshing, and the simulation time observed as decreasing with the increase in element sizes. Finally, this study draws attention to that the future of pre-processing manufacturing lies within the lines of simulation modeling instead of the traditional practice of trial and error.

References

1. Litzkow J, Hwang IH, Mehmert P, Bernhardt R (2017) Simufact additive 1.0–a new era in simulating 3D-printing processes. In: Proceedings of the conference of the Korean society of precision engineering, pp 262
2. Çelebi A, Appavuravther EZ (2018) Analyzing the effect of voxel mesh and surface mesh application on residual stress by simufact additive software. Düzce Üniversitesi Bilim ve Teknoloji Dergisi 6(4):930–940
3. Jawade SA, Joshi RS, Desai SB (2020) Comparative study of mechanical properties of additively manufactured aluminum alloy. Mater Today: Proc
4. Sossou G, Demoly F, Belkebir H, Qi HJ, Gomes S, Montavon G (2019) Design for 4D printing: a voxel-based modeling and simulation of smart materials. Mater Des 175:107798
5. Beiges J, Chaumont M, Moreira CA, Cervera M, Codina R (2020) An adaptive finite element strategy for the numerical simulation of additive manufacturing processes. Addit Manuf:101650
6. Zheng T, Guo L, Tang Z, Wang T, Li Z (2021) Comparison of progressive damage simulation of 3D woven composites between voxel and conformal discretization models. Mech Mater 158:103860
7. Grasso M, Colosimo BM (2017) Process defects and in situ monitoring methods in metal powder bed fusion: a review. Meas Sci Technol 28(4):044005
8. Kruth JP, Froyen L, Van Vaerenbergh J, Mercelis P, Rombouts M, Lauwers B (2004) Selective laser melting of iron-based powder. J Mater Process Technol 149(1–3):616–622
9. Gong H, Rafi K, Gu H, Ram GJ, Starr T, Stucker B (2015) Influence of defects on mechanical properties of Ti–6Al–4 V components produced by selective laser melting and electron beam melting. Mater Des 86:545–554
10. Li P, Warner DH, Fatemi A, Phan N (2016) Critical assessment of the fatigue performance of additively manufactured Ti–6Al–4V and perspective for future research. Int J Fatigue 85:30–43
11. Sterling AJ, Torries B, Shamsaei N, Thompson SM, Seely DW (2016) Fatigue behavior and failure mechanisms of direct laser deposited Ti–6Al–4V. Mater Sci Eng, A 655:100–112

12. Anton J, Lars P (2016) Characterisation of carbon fibre-reinforced polyamide manufactured by selective laser sintering. Addit Manuf 9:7–13
13. Sunny S, Gleason G, Bailey K, Mathews R, Malik A (2021) Importance of microstructure modeling for additively manufactured metal post-process simulations. Int J Eng Sci 166:103515
14. Bian P, Shi J, Liu Y, Xie Y (2020) Influence of laser power and scanning strategy on residual stress distribution in additively manufactured 316L steel. Opt Laser Technol 132:106477

Review on Advanced CNC Controller for Manufacturing in Industry 4.0

Anbia Adam, Toong-Hai Sam, Kamran Latif, Yusri Yusof, Zohaib Khan, Danish Ali Memon, Yazid Saif, Noor Hatem, Maznah lliyas Ahmed, and Aini Zuhra Abdul Kadir

Abstract The aim of the next generation of Computer Numerical Control (CNC) is to provide few key elements such as interoperability, openness, and flexibility in order to adapt with Industry 4.0. The basic nature of the CNC software systems hinders the users to improve and modify to meet the various needs of conventional CNC machine to keep up with the function of current technology. However, throughout the years, research have been conducted to overcome this issue. From the decade review made in the paper, it shows that almost 80% of the enhanced system utilizes ISO 14649 as the preferred ISO data environment due to its interoperability in receiving feedback of information between the Computer Aided technologies (CAx) and 35% (majority) of the researchers preferred Windows as their Operating System due to its flexibility in allowing modules and programs supporting the CNC machine to be developed.

Keywords CNC · Industry 4.0 · STEP-NC · ISO 14649 · Manufacturing

A. Adam (✉)
Faculty of Engineering and Technology, Tunku Abdul Rahman University of Management and Technology, 53300 Kuala Lumpur, Wilayah Persekutuan Kuala Lumpur, Malaysia
e-mail: anbiaadam@gmail.com

Y. Yusof · Z. Khan · D. Ali Memon · Y. Saif · N. Hatem · M. lliyas Ahmed
Faculty of Mechanical and Manufacturing Engineering, Universiti Tun Hussein Onn Malaysia, UTHM, 86400 Parit Raja, Batu Pahat, Johor, Malaysia

T.-H. Sam
Faculty of Business, Communications and Law (FOBCAL), INTI International University, Persiaran Perdana BBN, Putra Nilai, 71800 Nilai, Negeri Sembilan, Malaysia

K. Latif
Faculty of Mechanical and Manufacturing Engineering Technology, Universiti Teknikal Malaysia Melaka, Jalan Hang Tuah Jaya, 76100 Durian Tunggal, Melaka, Malaysia

A. Z. Abdul Kadir
School of Mechanical Engineering, Faculty of Mechanical Engineering, Universiti Teknologi Malaysia, UTM Skudai, 81310 Skudai, Johor Bahru, Malaysia

1   Introduction

The Industry 4.0 is changing the landscape of manufacturing industry. The revolution of the manufacturing industry is increasing complexity of manufacturing process which is determined by the flexibility of the controller. A controller is the most important part of the CNC machine unit that is composed of two modules: hardware and software. The hardware module includes drives, NC card, Motion Control Card (MCC) and others. Whereas the software module is commonly known as interpreter. The function of interpreter is to translate the ISO data interface model instructions to the relative parts of the hardware module, so that the machine can perform corresponding linear or circular operations [1]. Current CNC controllers are only able to interpret ISO 6983 data interface model that is a low level language [2, 3]. However, STEP-NC is a high-level object-oriented data model that requires intelligence in a controller, which carries out tool paths generation, machining operations scheduling, optimization, inspection and other functions [4, 5]. Today's industries are equipped with many types of CNC machines with different controllers and multiple abilities to fulfil customer demands. However, the structure of commercial CNC systems are of closed nature that makes CNC unsuitable for modem manufacturing environment [6]. Therefore, the paper focusses on the review of the manufacturing controller that are enhanced throughout the years in order to achieve flexibility, interoperability, and openness to adapt with Industry 4.0.

2   Review on CNC System

The target for development of the CNC controller for recent researchers is to achieve adaptability, intelligence, optimization, interoperability, openness and flexibility [7–10]. There has been numerous attempts and efforts done by various party to enhance the use of CNC machine to be better at production and use. This review highlights on the previous methods and approaches applied for the development of this particular technology advancement for over a decade.

The proposed framework in 2011 by Peng et al. [11] for STEP-NC compliant controller with the development of knowledge base with Web Ontology Language (OWL) for the process planning in CNC controller has a novel STEP-NC compliant controller named OntoStep CNC, which could accept ISO 14649 machining models and then generate optimized tool path based on knowledge base and rules at the shop floor level. On the same year, Xu et al. [12] and his research team has introduced system open CNC based on PC and motion control card for the ability to interpret the ISO 6983 B-Spline curve. The system designed in C language that contains Graphical User Interface (GUI) for easy operation that utilize PLC for motion control and algorithm for B-Spline tool path generation via data extraction from ISO 6983 information. The prototype was composed of PC, GT400-SV motion control card,

card special Central Processing Unit (CPU) and PC CPU for master slave dual control mode, which communicates through PCI slot.

The next year, Long et al. [13] has taken way to improve the functionality and expansibility of the existing CNC interpretation technique through a new model of NC program interpreter which is proposed into three modules. With the control of the central management module, the modularized CNC interpreter module can call the tool path planning module directly. The prototype system uses Red Hat Linux controller to verify the validity of the proposed method. The experimental result that they have done shows that the new CNC interpreter system can improve the interpretation efficiency significantly. Meanwhile, Guo [14] and team taken the approach of using industrial PC to apply motion control card PCI-1243 which could control direction and velocity of step motor through human machine interface developed by Microsoft Visual Basic. However, it does not have interpreter to allow the system to be in STEP environment. In the same year, de Pacheo et al. [15] and team utilized PC with addition of microcontroller which receives machining information and forward the commands to the drives of the machine motors through compiler that interpreted the STEP-NC file to allow flexibility and efficiency.

Coming year, Khanna et al. [16] applied same method using microcontroller (Arduino) with the advancement of controlling 6-axis motor simultaneously. However, the research does not have interpreter to operate in STEP-NC environment which would take toll on flexibility of the machine. Other than that, Sivakumar and Dhanalakshmi [17] and team integrate CAD and CAM through feature extraction from STEP files for cylindrical parts to be further inspection process on FANUC commercial CNC system. Meanwhile Gutierrez and Álvares [18] has taken the way of using open source driver of Enhanced Machine Controller (EMC) also known as LinuxCNC in Linux PC to validate the machining feature of the output of the machine. On this year both Benavente and Zhang [19, 20] used SIEMEN CNC controller for the development of their research. Though the research differed through enablement of STEP file to the users via the Internet from [19], to allow users to perform a graphic simulation of the movement of the tools machining the component. On the other hand, Novak-Marcincin et al. [21] has taken approach of focusing of assembly task through the use of augmented reality to aid on manufacturing process. In spite of this, this approach lacked controlling aspect as compared to the latter research.

The following year, Sarhan [22] uses Arduino microcontroller and PC to develop NC controller called machine control unit (MCU) through use of MATLAB software which used as an image processing program to accomplish the boarder detection of the image and convert it into digital output (0 and 1) for each pixel by a number of functions. The pixels will bias an array for the image, which will be processed to instructions. These instructions will be sent to Arduino microcontroller by the MATLAB through Arduino cable (serial port). The Arduino microcontroller will generate the proper pulse trains to control the operation of stepper motors of the machine. Though, the system only able to control the motor without having any additional feature which could enhance the function of the existing machine. As

compared to Po et al. [23] that developed HITCNC from CATIA to interpret STEP-NC file directly and adaptively by making use of high-level information in the STEP-NC file and acquired data from the sensors. The research goes further with inspection aspect that enable the users to let the part either repaired or discarded. On the same year, Mohd Elias [24] begin the development of STEP-NC controller using PC to control the machining process through motion control card and UMI. The research was continued by Latif [1] with major improvements such as the addition of interpreter which allows the system to execute machining process under both ISO 6983 and ISO 14649 environment. Both research were fundamentally revolved around Denford Novamill CNC Milling Machine using extension PC for interface selection developed from LabVIEW which inspired the development of this research. Other addition such as report generation allowed the users to have full report of the machining process in Word of Pdf format for future reference that has become distinct factor between Latif [1] and Xiao [25]. In its framework, Xiao used CATIA to develop its controller that control servo motor as compared to stepper motor by Latif and Elias.

The year after that, Chang [26] developed G-Code generator for commercial milling system through application of augmented reality to provide an immersive experience in learning or teaching the planning phase, control system, and machining parameters of a functioning CNC machine without adding any other control or function to it. On the other hand, Shin et al. [27] used virtual machining model instead of AR to execute the same function with additional feature of machine monitoring data using MTConnect while adopting STEP-NC. The developed model is called STEP2M which operates for 2-axis turning machine process that can be virtually measured through its standardized interfaces. Hu et al. [28] also used MTConnect for monitoring data, with added sensors and motion controller through Open Modular Architecture Controller (OMAC). However, Álvares et al. [29] furthered the use of MTConnect to publish data over networks using the internet protocol to facilitate communication between controllers and devices on the shop floor.

The next year, Sang and Xu [30] came up with a framework named Control System as a Service (CSaaS) where the control system is detached from the machine tool and exists in the cloud, so that control of a machine tool becomes a cloud-based service. This gives a machine tool high flexibility and scalability. While, Lei et al. [31] proposes a closed-loop machining system based on extended STEP-NC data models which cover aligning and laser tracker measuring process. The system was developed using Microsoft Visual Studio and deployed on PC on the shop floor using TCP/IP communication protocol.

Following year, Zhao et al. [32] designed a cutting tool detection system using pattern recognition based on machine vision. Using coordinate system transform and stereo vision, the parameters which are defined in STEP-NC and position information of cutting tool are measured on industrial robot. Though, the system absent the controller and other aspects such as interpreter and simulation as done by Toquica et al. [33]. The system developed by Toquica also provides cloud manufacturing, and machine learning with database analytics using LinuxCNC on industrial robot. On contrary, Ye et al. [34] mapped the general standard STEP-NC to OWL to

describe machining process-related knowledge in a readable and comprehensible way in HBase storage for large-scale knowledge storage to apply cloud manufacturing in its system. Meanwhile, Kubota et al. [35] proposed solution for both online and offline machining parameter optimization through established machining knowledge based on STEP-NC data model with the capability of taking the physical variances between machine tools into account. Kubota applied the Cyber-Physical Machine Tool (CPMT) concept to gather the machining information for its base. Whereas, Othman et al. [36] used the knowledge base concept from IEC 61,499 for an automatic cutting tool selection module for an adaptive STEP-NC compliant controller instead of experience-based judgement by an expert manually.

The coming year, Afanasev et al. [37] proposed a framework of STEP-NC compliant manufacturing in a cloud environment using MTConnect. However, Zhao et al. [38] uses MTConnect to apply the virtual machining environment software named GrapeSim which functioned to estimate the machining state according to the accessed data from CNC with web server that allowing other devices to obtain the data as a data source of cloud manufacturing. While, Gao et al. [39] used EtherMAC for to communicate between hardware devices and the CNC machine. The system presented has several intelligent modules including interpreter and toolpath generator to further enhance the machining process for the system. Whereas, Liu et al. [40] proposed a STEP-compliant CAD/CNC system which consists of STEP-CAD and STEP-CNC. The research also introduced feature-oriented machining for 2.5D feature and freeform surface machining, wherein T-spline is introduced for the representation and data exchange of freeform surface. On the other hand, Zhao et al. [41] also uses 2.5D feature as demo workpieces for STEP-NC feature-oriented machining simulation method, which takes the workpiece blank as the combination of several machining features plus the workpiece, and implements customized algorithms for individual features which results in high efficiency with guaranteed accuracy and fidelity. Though, the simulation has no control over the motor and lack in cloud feature.

From this review, it has been observed that, there are a lot of effort which had been carried out for the implementation of STEP-NC data interface model (79.41%) by utilizing various techniques and tools as shown in Fig. 1. As discussed, the implementation was initiated on commercial CNC system but that was not able to provide full features of the STEP-NC because it translates the STEP data into G codes. Secondly, commercial machine units were found to be of closed nature. In order to overcome these issues, a STEP-NC Interpreted approach, and Open Access Controller (OAC) technology integration was suggested by various scholars as mentioned earlier. Most researchers prefer using PC operating systems such as Windows (35.29%), Linux (11.76%) as an alternative to vendor's commercial system (29.41%) as shown in Fig. 2 due to its flexibility to adapt to new commands and programs [42]. Based on the majority percentage of research that utilizes Windows as their preferred OS, it indicates that the CNC controller is getting widely improved and used on a more personal level. With the current technology's ability that is able to be performed on PC (AR, Compiler, Converter etc.) which can be connected to affordable microprocessor or microcontroller (Arduino, Raspberry Pi etc.), the future is set to see customized

Fig. 1 Percentage of ISO data environment by researchers
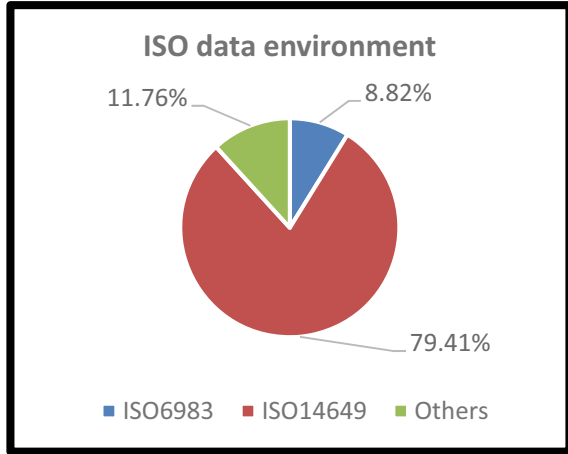
Fig. 2 Percentage of operating system for CNC by researchers
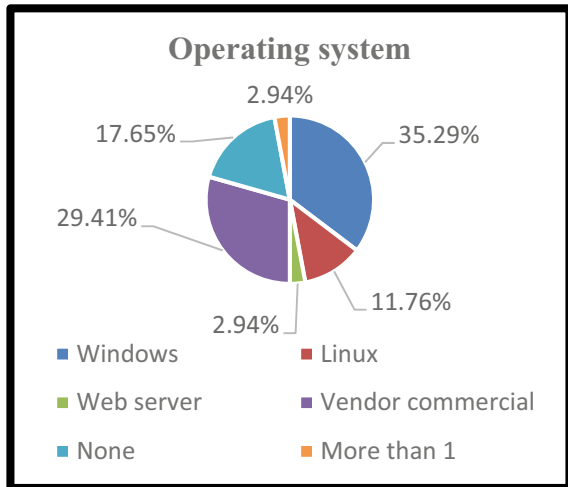
CNC controller with self-built CNC machine that could produce relatively small but useful machining products for home-use purposes.

3 Conclusion

This paper has distinctly reviewed the manufacturing controller over the decade. Although all of these techniques have some limitations in terms of control, hardware, software, modem functionalities and other factors. At present, there is not any STEP-NC system which has been yet fully commercialized, because the aim of next

generation CNC had not been fully achieved. However, STEP-NC has successfully enabled lots of modem functionalities into the CNC but there is more that is still to be achieved. This scenario indicates that the STEP based CNC development is a dynamic topic for research with almost 80% researchers utilizes ISO 14649 as its preferred ISO environment, in which various field need to be addressed such as HMI, interpreter, simulation, hardware configuration and many others. The utilization of OAC technology can enable some modern functionalities into current and future CNCs such as monitoring, shop floor data modification and inspection, thus preparing the future manufacturing controller to adapt with Industry 4.0.

References

1. Yusof Y, Latif K (2015) A novel ISO 6983 interpreter for open architecture CNC systems. Int J Adv Manuf Technol 80(9–12):1777–1786
2. Xu XW, He Q (2004) Striving for a total integration of CAD, CAPP, CAM and CNC. Robot Comput Integr Manuf 20(2):101–109
3. Xu XW, Newman ST (2006) Making CNC machine tools more open, interoperable and intelligent—a review of the technologies. Comput Ind 57(2):141–152
4. Kelvin H, Hascoet J-Y, Rauch M (2014) Modern mechanical engineering, no. January
5. Rauch M, Laguionie R, Hascoet JY, Suh SH (2012) An advanced STEP-NC controller for intelligent machining processes. Robot Comput Integr Manuf 28(3):375–384
6. Li B, Zhou YF, Tang XQ (2004) A research on open CNC system based on architecture/component software reuse technology. Comput Ind 55(1):73–85
7. Li P, Hu T, Zhang C (2011) A unified communication framework for intelligent integrated CNC on the shop floor. Procedia Eng 15:840–847
8. Mekid S, Pruschek P, Hernandez J (2009) Beyond intelligent manufacturing: a new generation of flexible intelligent NC machines. Mech Mach Theory 44(2009)
9. Yuhan W, Jun H, Ye L (2003) Study on a reconfigurable model of an open CNC kernel. J Mater Process Technol 138(1–3):472–474
10. Živanović S, Glavonjić M (2014) Methodology for implementation scenarios for applying protocol step-NC, no. March, pp 1–4
11. Peng L, Hu T, Zhang C (2011) STEP-NC compliant intelligent process planning module: architecture and knowledge base. Procedia Eng 15:834–839
12. Xu X, Wang L, Newman ST (2011) Computer-aided process planning—a critical review of recent developments and future trends. Int J Comput Integr Manuf 24(1):1–31
13. Long C, Dong Y, Han Z, Cong G, Lei D (2012) Design and implement of a modularized CNC interpreter based on the integration of tool path planning module. CCSAE 2012—Proc 2012 IEEE Int Conf Comput Sci Autom Eng 3:613–616
14. Lv C, Guo L, Li J (2012) Research of motion control system based on PCI-1243. In: Proceedings—2012 3rd international conference on digital manufacturing and automation, ICDMA 2012, pp 662–665
15. de Pacheco NO, da Hounsell MS, Carlos Ferreira JE (2012) Application of the step-Nc standard in a computer numerical controlled machining device. 5(Oct):713–723
16. Khanna A, Kumar A, Bhatnagar A, Tyagi R, Srivastava S (2013) Low-cost production CNC system. In: 7th International conference on intelligent systems and control, ISCO 2013, pp 523–528
17. Sivakumar S, Dhanalakshmi V (2013) A feature-based system for CAD/CAM integration through STEP file for cylindrical parts. Indian J Eng Mater Sci 20(1):21–26

18. Gutierrez ME, Álvares AJ (2013) Development of a Cnc router adherent to standard step-Nc based on the controller advanced machine (Emc2). In: 22nd International congress of mechanical engineering, no. Cobem, pp 8200–8213
19. Benavente JCT, Ferreira JCE, Goulart CM, De Oliveira VG (2013) A STEP-NC compliant system for the remote design and manufacture of mechanical components through the Internet. Int J Comput Integr Manuf 26(5):412–428
20. Zhang X, Nassehi A, Safaieh M, Newman ST (2013) Process comprehension for shopfloor manufacturing knowledge reuse. Int J Prod Res 51(23–24):7405–7419
21. Novak-Marcincin J, Barna J, Janak M, Novakova-Marcincinova L (2013) Augmented reality aided manufacturing. Procedia Comput Sci 25:23–31
22. Sarhan H (2014) A novel technique for controlling CNC systems. 4(5)
23. Po H, Hongya F, Zhenyu H, Dedong H (2014) A closed-loop and self-learning STEP-NC machining system, pp 1598–1603
24. Mohd Elias D (2014) Step-NC controller for 3-axis CNC milling machine. Universiti Tun Hussein Onn Malaysia (UTHM)
25. Xiao W, Zheng L, Huan J, Lei P (2015) A complete CAD/CAM/CNC solution for STEP-compliant manufacturing. Robot Comput Integr Manuf 31(1):1–10
26. Chang S-W, Yap KS, Yap HJ, Pai YS (2016) Development of an augmented reality-based G-code generator in a virtual CNC milling simulation. Int J Comput Sci Eng 5(2):63–72
27. Shin SJ, Woo J, Kim DB, Kumaraguru S, Rachuri S (2016) Developing a virtual machining model to generate MTConnect machine-monitoring data from STEP-NC. Int J Prod Res 54(15):4487–4505
28. Hu P, Han Z, Fu Y, Fu H (2016) Implementation of real-time machining process control based on fuzzy logic in a new STEP-NC compatible system. Math Probl Eng 2016
29. Álvares AJ, Paredes MEG, Ferreira JCE, Benavente JCT (2016) A web-based STEP-NC-compliant architecture for low cost 3D part manufacturing. Int J Manuf Res 11(1):1–27
30. Sang Z, Xu X (2017) The framework of a cloud-based CNC system. Procedia CIRP 63:82–88
31. Lei P, Zheng L, Xiao W, Li C, Wang D (2017) A closed-loop machining system for assembly interfaces of large-scale component based on extended STEP-NC. Int J Adv Manuf Technol 91(5–8):2499–2525
32. Zhao G, Zhang YX, Zhang PF, Xiao WL (2018) A STEP-NC compatible cutting tool detection system. IOP Conf Ser Mater Sci Eng 382(4)
33. Toquica JS, živanović S, Alvares AJ, Bonnard R (2018) A STEP-NC compliant robotic machining platform for advanced manufacturing. Int J Adv Manuf Technol 95(9–12):3839–3854
34. Ye Y, Hu T, Zhang C, Luo W (2018) Design and development of a CNC machining process knowledge base using cloud technology. Int J Adv Manuf Technol 94(9–12):3413–3425
35. Kubota T, Liu C, Mubarok K, Xu X (2018) A cyber-physical machine tool framework based on step-NC. Cie48 1(Dec):2–5
36. Othman MA, Jamaludin Z, Minhat M (2018) Automatic tool selection module for an adaptive CNC controller. In: Proceedings of innovative research and industrial dialogue'18, 2018, no. July, pp 90–91
37. Afanasev S, Zhao G, Xiao W (2019) Towards cloud-based STEP-NC to enhance interoperability in global manufacturing. IOP Conf Ser Mater Sci Eng 658(1)
38. Zhao G, Cao X, Xiao W, Zhu Y, Cheng K (2019) Digital twin for NC machining using complete process information expressed by StEP-NC standard. In: ACM international conference proceeding series, 2019
39. Gao W, Zhang C, Hu T, Ye Y (2019) An intelligent CNC controller using cloud knowledge base. Int J Adv Manuf Technol 102(1–4):213–223
40. Liu Y, Zhao G, Zavalnyi O, Cao X, Cheng K, Xiao W (2019) STEP-compliant CAD/CNC system for feature-oriented machining. Comput Aided Des Appl 16(2):358–368

41. Zhao G, Cao X, Xiao W, Liu Q, Jun MBG (2020) STEP-NC feature-oriented high-efficient CNC machining simulation. Int J Adv Manuf Technol 106(5–6):2363–2375
42. Khechekhouche A (2021) Mechanisms of a 3-axis CNC machine design and experiment, no. March

Improvement of Roof Shield Design Using TRIZ Method

R. B. Hoh, N. A. Alang, M. I. M. Ramli, J. Alias, and A. M. Romy

Abstract Factors such as poor aerodynamic shape, rigid roof and lack of attractiveness are the few factors that need to be taken into consideration for the roof shield design of a utility motorcycle. The purpose of this study is to improve the current design of the roof shield using TRIZ tools and techniques. The current design has some limitations due to the inventive parameters conflict of each component and causes engineering contradiction. Therefore, the TRIZ method is employed as a method to eliminate those inventive limitations. Function analysis is chosen as the initial step to determine the involved components and the components that are needed in the system. TRIZ method with the use of causes-effects chain analysis (CECA) then is applied by building the problem chain to obtain the potential effective cause. Using this approach, the engineering contradiction of the roof shield component is identified. Next, 40 inventive principles matrix in TRIZ, is applied to obtain a potential solution to the contradiction. Further brainstorm then is carried out to improve the design based on trigger potential inventive solution. The final conceptual design is sketched out and it is found that the overall design of the roof shield is improved in term of aerodynamic, flexibility and attractiveness.

Keywords Roof shield · Motorcycle · TRIZ · Function analysis · Cause and effect chain analysis

R. B. Hoh · N. A. Alang (✉)
Faculty of Mechanical and Automotive Engineering Technology, Universiti Malaysia Pahang, 26600 Pekan, Pahang, Malaysia
e-mail: azuan@ump.edu.my

M. I. M. Ramli
Automotive Engineering Center (AEC), Universiti Malaysia Pahang, 26600 Pekan, Pahang, Malaysia

J. Alias
Department of Mechanical Engineering, College of Engineering, Universiti Malaysia Pahang, 26300 Gambang, Pahang, Malaysia

A. M. Romy
Boon Siew Honda Sdn. Bhd., Persiaran Cassia Selatan 1, Kawasan Perindustrian Batu Kawan, 14100 Simpang Ampat, Pulau Pinang, Malaysia

271

1 Introduction

Demand for food delivery services has increased during COVID-19 pandemic, resulting an increase in the numbers of riders. In most countries, particularly in Malaysia, motorcycles are a common and convenient type of transportation preferred by the riders. However, bad weather such as rain and hot or sunny days is always a main factor that affects the rider's performance. A research study conducted by Ang et al. [1] states that there was a significant fatality in crash accidents for motorcycle riders.

A reliable, effective and scientific technique is necessary in analyzing and improving engineering design problems. It is essential to determine a suitable potential solution to the problems especially during the conceptual design stage before the product being commercialized. One of the well-known and powerful problem solving techniques is TRIZ [2]. TRIZ theory [3] was invented by Russian inventor led by Genrich Altshuller in the years 1946 to 1985. Over 200,000 pattern designs have been analysed and grouped into 40 rules. These 40 rules are defined as 40 inventive principles that are now widely implemented to trigger the inventive problems and potential solutions by analyzing the contradiction problem of the systems. In general, there are five causes analysis [4] introduced in TRIZ namely the Function Analysis, the Root Conflict Analysis (RCA+), the RelEvent Analysis, the Substance-Field (Su-Field Analysis) and the Trends of Evolution. The root cause analysis is an analysis in TRIZ which is usually conducted at the end of the causes-effects chain. Cause-Effect Chain Analysis (CECA) enables better understanding of the basic problem and the reasons for the existed problem [5]. In most designs, there will be a group of causes that come along with the problem. In this case, the trimming process allows for the elimination of unnecessary or irrelevant causes in order to minimize the complexity of the problem solving process.

Baharom et al. [6] employed the TRIZ method with RCA+ on zipper, Cliff and managed to trigger 26 inventive principles as the potential solutions for seven contradictions. They concluded that RCA+ offered a promising solution to improve the problem of the Cliff. In another study, Ekmekci and Koksal [2] applied the TRIZ method to find the potential solution to the moisture and cooling problem of pizza packet service. Several solutions have been identified based on the TRIZ principles. Yeop et al. [7] took a portable road debris collector as a product model to study the applicability of the TRIZ method. They concluded that the TRIZ method leads to creative thinking during the conceptual design stage [8].

This paper focuses on the enhancing the current roof shield design of utility motorcycle using the TRIZ method in order to improve the motorcycle performance especially during bad weather of rainy and sunny day and possibly reduces accident among motorcycle riders. The limitation of the current roof shield design is brainstormed and the potential solution gathered based on the TRIZ method is employed.

Fig. 1 Initial design of roof shield before applying TRIZ method

Roof shield

Roof-to-arm connection

Windscreen

Back support arm
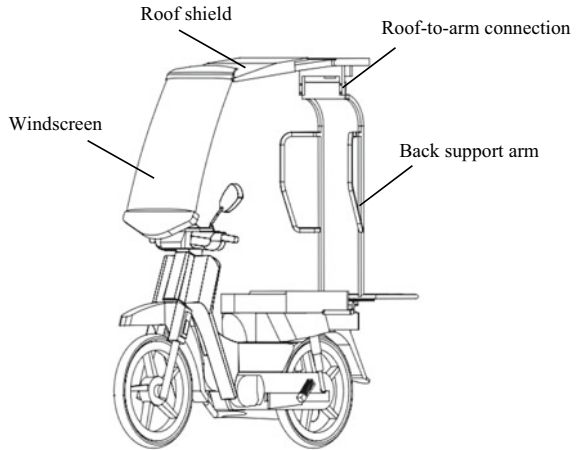
2 Description of Limitation of Current Design

The present paper focuses on the further improvement of the current design of roof shield that has been sketched during the conceptual design stage. At the beginning of this project, literature survey, group meeting, survey and data collection methods were carried out to generate the initial idea of the design. The collected data is compiled and is used as references for this study. The concept of the initial current design focuses on the performance, attractiveness, feasibility and light weight of the overall assembly parts. As shown in Fig. 1, there are a lot of limitations of the initial design such as lack of attractiveness, poor aerodynamic shape, long back support arm, complex mechanism and others. Hence, the TRIZ method is chosen to help eliminate those limitations.

3 Function Analysis and Modelling

Function analysis is an analysis which is widely applied in engineering design, business process and electrical process models for the understanding of how the components function and interact with each other in a system. In the present study, product structure modelling [9] that includes supersystem, subsystem or component and object is first identified. The interaction between the components is plotted into a function analysis diagram as shown in Fig. 2 whereby inserted blocks represent components and arrows represent functions. The diamond, rectangle and oval represent the supersystem, component and product, respectively. The irrelevant components have been removed from the system to minimize the complexity of the overall system.
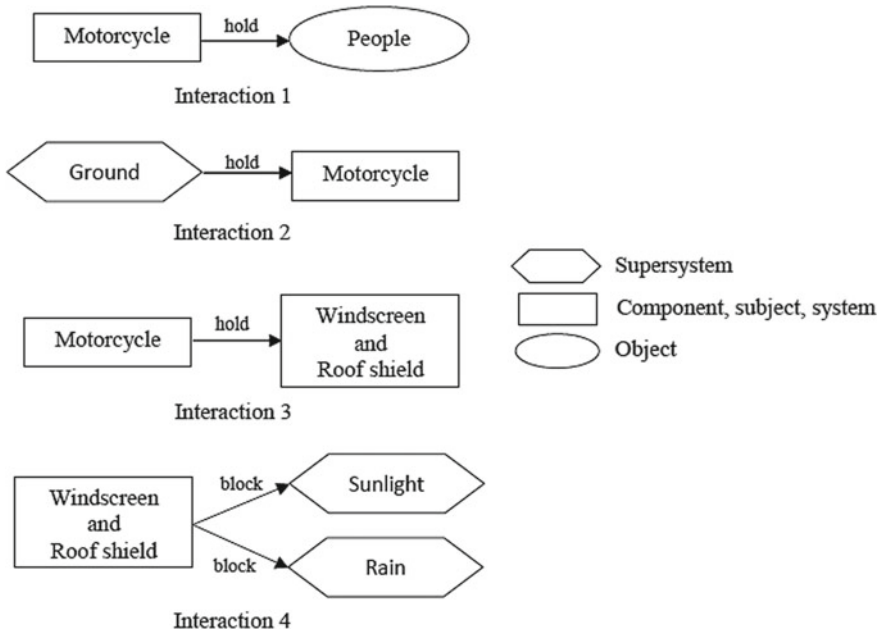
Fig. 2 Interaction analysis in the system

The modelling of component analysis is constructed to identify the supersystem and the components available in the system. The interactions between components are linked and connected together in the system for further analysis of either harmful or useful actions. Acquired analysis is collected to build the function model with a block of the components, as shown in Fig. 3. There are in total 19 relations that occur in the system whereby three (3) of the supersystem are harmful materials (dust, rain and sunlight) and two (2) are useful components which are namely the windscreen and roof that help to block the harmful materials.

4 TRIZ Method with Causes-Effect Chain Analysis (CECA)

In order to provide the solution for the engineering problem of the current design, it is required to identify the root cause of the particular problem. Therefore, the problem of the current initial design is brainstormed and listed as shown in Fig. 4. The potential effect of each problem is then identified. As shown in Fig. 4, four (4) main potential problems which are less performance (speed), unattractive, poor mechanism and poor visibility are analysed. The potential cause of each problem as well as the chain questions are drawn until the possible actual root cause is obtained. The information
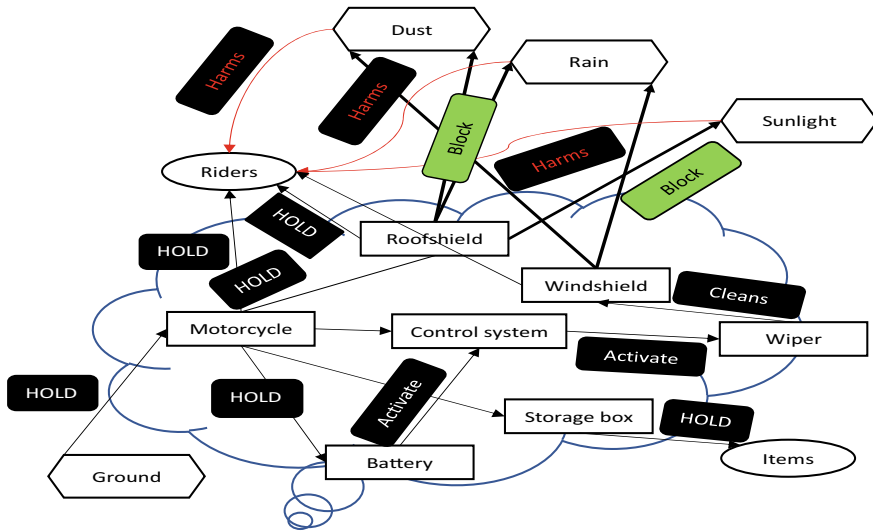
Fig. 3 Function model analysis of utility motorcycle with roof shield

from causes and effects chain analysis is then evaluated. The solution to the cause of the problem can be either useful or not, therefore critical justification is made for each solution. The cross-marks at the block in Fig. 4 indicate the problem that is irrelevant to the present study, therefore being eliminated from the next stage of evaluation.

Since the problem's root causes were identified by CECA analysis, deep understanding of worsening effects and improving effects is required to form into contradiction. A dotted line box is drawn in Fig. 4 to show one of the contradictions obtained from the CECA. Based on the function blocks located inside the dotted lines box, the opposite function occurred, for instance, the motorcycle performance increases (in terms of speed) by using light weight material but at the same time, a large storage box is required to enable more capacity space to store much items/delivery stuff but resulted in heavier weight. In this case, technical contradiction is introduced as both parameters need to be included in the system. Other technical contradictions then are identified based on the connection of problem root causes findings in the CECA diagram.

5 Technical Contradiction

A contradiction occurs when one parameter of a system has both positive and negative effects. A research by Petrov [10] showed the method to solve the contradiction in design. In this section, hypotheses made from the source of contradiction and its evaluation method is described. In the present study, the contradiction is divided into
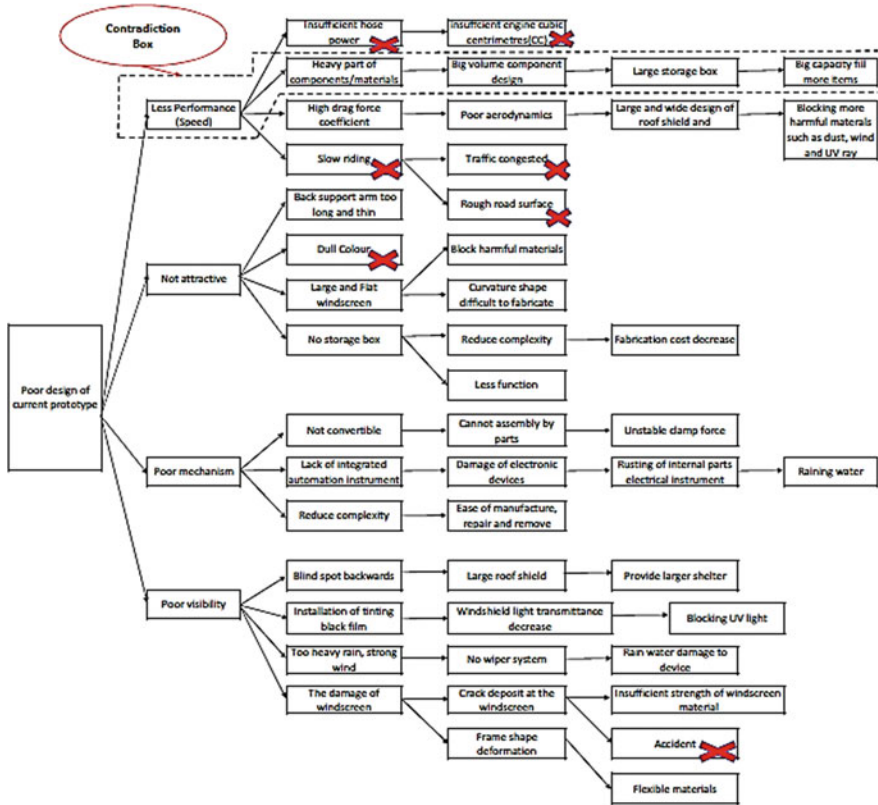
Fig. 4 Cause-effect chain analysis

worsening effects and improving effects which acted on the parameters (a factor that influences a system). In total, there are 40 parameters summarized in TRIZ. Technical contradiction is identified by matching the problem root causes and 39 parameters listed in TRIZ tools. The technical contradictions were arranged out as below:

1. Light weight material is perfect to be chosen for the component involved but it will affect the strength and cost (P1).
2. The wide and large area of the windscreen could block the wind, sunlight, dust and others, but it could affect the speed of the motorcycle due to the increment of drag force (P2).
3. Without a convertible roof, it will increase the stability and more ease of fabrication, but might lead to storing problem (P3).
4. Streamline design of aerodynamics shape could produce minimum drag force but it will be costly and time consuming to manufacture (P4).
5. The volume of the storage box can be larger to provide more storage capacity but it will affect the stability and space (P5).

6. Electronic device automation can reduce the manual operation, improve the versatility and function but at the same time, may lead to danger when exposed to water, especially during raining (P6).
7. Darkened windshield tint film is able to block sunlight, especially UV rays that may lead to healthy risk but it also will causes poor visibility (P7).
8. The back seat makes the design more attractive, multi-function design catches and gains the interest due to its unique appearance but reduces the strength to hold (P8).

The abovementioned technical contradiction is tabulated in Table 1. Each of the contradictions is analysed and the corresponding positive and negative effects, causes, action taken and contradiction parameters are also tabulated in Table 1. This contradiction is compared with TRIZ inventive principles to obtain the suitable parameter that relates to the problem caused. This contradiction parameter is important to determine the correct potential solution when applying the 40 inventive principles that will be discussed in the next section. In total, there are eight contradiction problems are found in the system which is represented by P1 to P8.

5.1 Contradiction Matrix

"Creative problem solving" [11] is a process that uses of contradiction matrix tools, morphological analysis and other TRIZ tools to generate ideas. This section explained the method of idea/problem solution generation for each contradiction discussed in previous section. The suitable parameter that causes the technical contradiction is identified then compared to the contradiction matrix in TRIZ. Since the matrix connects between the parameter and 40 inventive principles, the solution for each parameter can be easily triggered. In this study, there are 28 inventive principles have been suggested (when using the TRIZ matrix). Further justification and evaluation (based on the experience and literature study) then is made to determine which inventive principles are suitable to improve the design of the current roof shield. Note that are not all the inventive principles that suggested are useful and applicable. The summary of inventive principles triggered for each technical contradiction is tabulated in Table 2. The mapping between technical contradictions with inventive principles is shown in Fig. 5. A detailed explanation of how to employ the contradiction matrix or table can be found in literature [12].

6 Results and Discussion

Application of the TRIZ method with function analysis and (CECA) leads to 28 inventive principles (as concept references) that can be applied to improve the current design. From the total of 28 inventive principles, only 17 of them have the potential to

Table 1 List of technical contradiction for each criterion

	Root causes	Action	Positive effects	Negative effects	Parts	Parameter contradiction
P1	Less performance (Heavy object)	Change into light materials	Light weight, increase speed	Flexible but light material	Material selection	Weight, strength, speed
P2	Blocking harmful materials	Increasing Size of windscreen	Blocking area increases	Speed of motorcycle, weight increases due to large component	Windshield and frame	Size, weight, strength
P3	Poor mechanism (Not convertible)	Divide into parts	Ease for remove, ease for repair, easy to keep	Not enough strength to hold the parts, difficult to manufacture, increase complexity	All parts	Strength, complexity, shape, length of moving object, ease of repair, manufacture and remove
P4	Less performance (velocity)	Design good aerodynamics shape	Aerodynamics look, decrease drag force coefficient	Cost, difficult to manufacture	Front motorcycle appearance	Shape, angle, energy loss
P5	Not attractive (Lack of function)	Insert large capacity of storage box	Store large volume of items	Reduce stability due to centre of gravity increase, increase weight	Storage box	Volume, stability, weight
P6	Poor mechanism (Lack of integrated automation)	Automation and integrated instrument installed	Automatically operate	Cost, danger due to damage of electronic device	Electrical devices	Extend of automation, object generated harmful factors
P7	Poor visibility	Tinting windscreen	Block UV lights, good in reflect the sunlight, temperature	Illumination intensity, fabrication cost	Windscreen	UV damage, temperature, illumination intensity
P8	Not attractive design (long arm back seat)	Gain more attractive back seat design	Multifunction to grab the eyeballs for its unique design	Decrease strength due to too many components hold in a system	Back seat design	Adaptability/versatility, strength

Table 2 Summarized of inventive principle for each contradiction

Contradiction	Contradiction to solve	Inventive principles
P1	To decrease the weight of moving object without worsening the strength of materials	1, 35, 19, 39
	To decrease the weight of moving object without worsening ease of manufacture	27, 28, 1, 36
P2	To increase the surface area of moving object without worsening speed	29, 30, 4, 34
	To increase the surface area of moving object without increasing the weight	2, 17, 29, 4
P3	To improve the strength without worsening the system complexity	10, 4, 28, 15
	Improve ease of repair without worsening the ease of manufacture	1, 35, 11, 10
	To improve the shape without worsening the length of moving roof shield	29, 34, 5, 4
	Allow to decrease the volume without worsening the length	1, 7, 4, 35
P4	Improve the shape without worsening the speed	1, 31, 17, 28
	Increase the length without worsening the area of moving object	15, 17, 4
	Increase the shape without worsening ease of manufacture	32, 30, 40
	Improve the speed without worsening the length of moving object	13, 14, 8
P5	Increase the volume of moving object without worsening the stability	28, 10, 1, 39
	Improve the volume of object without worsening the weight	2, 26, 29, 40
P6	To extend automation without worsening ease of operation	1, 12, 34, 3
	To extend automation without worsening object generated harmful factors	2
P7	To improve illumination intensity without worsening the temperature	32, 35, 19
P8	To improve adaptability/versatility without worsening the strength	35, 3, 32, 6

fulfill the requirements of current design. These 17 inventive principles are tabulated in Table 3. The proposed solution that is related to the triggered inventive principles is brainstormed and followed by the improvement of the current design. Figure 6 shows the improved design of the roof shield and windscreen of a utility motorcycle after implementing the TRIZ.
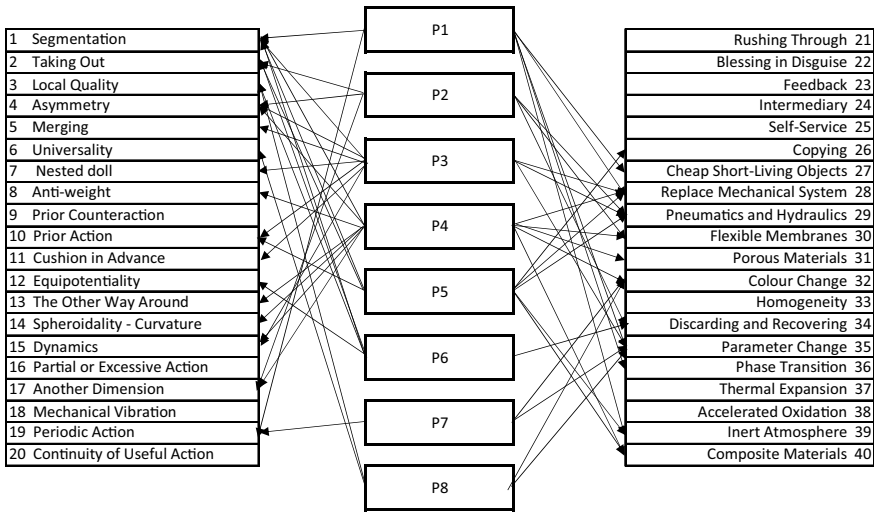
Fig. 5 The mapping of problem contradiction and inventive principles

7 Conclusion

The TRIZ method with function analysis and cause-effect analysis chain (CECA) has been implemented to improve the current design of the roof shield and windscreen of a utility motorcycle. It can be concluded that the method provides a systematic way to trigger various inventive solutions to address the problems with our current design. A total of 28 inventive principles have been triggered (based on 40 inventive principles matrix).However, only 17 of them have been further evaluated as a reference of engineering solution. The final design of the roof shield and windscreen of a utility motorcycle with aerodynamics shape roof shield and windscreen, simple yet attractive back seat design, multifunction storage box, convertible roof using of a pulley mechanism and sharp corners eliminated shows significant improvement compared to the initial design. Clearly, the TRIZ method with function analysis and CECA leads to creative and innovative solutions, resulting in significant improvement of the design.

Table 3 Inventive principle with potential solution

No.	Inventive principles	Potential solution
1	Segmentation	Assembly part (dividing into several parts) of roof shield
2	Taking out	Electrical harmful device eliminated to avoid the risk of injury
3	Local quality	Arrangement design inside storage box like lunchbox to fulfil more items
5	Merging	Roof shield connected to back part and windscreen
6	Universality	Back support as back seat and hold storage box
7	Nested doll	Roof shield will keep into storage box if not used
8	Anti-weight	Material selection like plastic, light aluminium
10	Prior action	Lubricants fitting at windshield (replace wiper system)
11	Beforehand cushioning	Windshield layer with a protective film
13	The other way around	Change stationary roof shield to moving parts
14	Curvature	Flatten the windshield and back seat parts so that more aerodynamics look
15	Dynamization	Convertible and adjustable length of roof shield parts
17	Another dimension	Design a multi-storage box to separate item keeping
26	Copying	Simulation analysis and safety assessment
28	Mechanical system	Pulley system to trigger the function
30	Flexible membrane and thin film	Thin roof shield and windshield
40	Composite materials	Thermoplastic composite materials
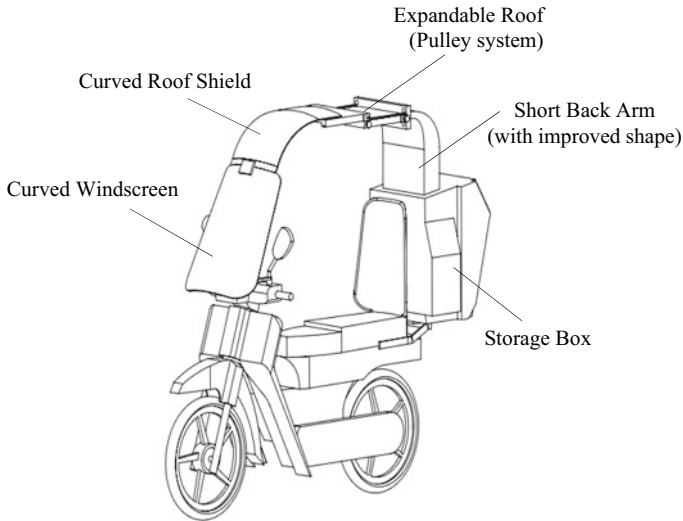
Fig. 6 Improved design of roof shield after implementing TRIZ method

References

1. Ang BH et al (2019) Self-regulatory driving and riding practices amongst older adults in Malaysia. Transp Res Part F Traffic Psychol Behav 62:782–795. https://doi.org/10.1016/j.trf.2019.03.014
2. Ekmekci I, Koksal M (2015) Triz methodology and an application example for product development. Procedia—Soc Behav Sci 195:2689–2698. https://doi.org/10.1016/j.sbspro.2015.06.481
3. Yi-Wen W (2009) Innovation design of products based on TRIZ theory. J Mach Des. [Online]. Available: http://en.cnki.com.cn/Article_en/CJFDTOTAL-JXSJ200902013.htm
4. Abramov O (2015) TRIZ-based cause and effect chains analysis vs root cause analysis
5. Lee M-G, Chechurin L, Lenyashin V (2018) Introduction to cause-effect chain analysis plus with an application in solving manufacturing problems. Int J Adv Manuf Technol 99. https://doi.org/10.1007/s00170-018-2217-1
6. Baharom MZ, Delbressine F, Toeters M, Feijs L (2017) The identification of contradictions in cliff: an automatized zipper prototype using the triz method with root conflict analysis (RCA+)
7. Yeop Wasir N, Shahrin S, Che Hassan MF (2020) Application of TRIZ method in a product design and development tertiary technical education course. Int J Emerg Trends Eng Res 8:2332–2337. https://doi.org/10.30534/ijeter/2020/21862020
8. Xue-Bin Y (2007) Model of the product conceptual design process to solve contradiction in TRIZ. Mach Des Manuf 2007. [Online]. Available: http://en.cnki.com.cn/Article_en/CJFDTotal-JSYZ200709088.htm
9. Bakker HM (2012) Improving software assistance for design engineers by integrating mathematical and function modeling

10. Petrov V (2019) Principles of resolving contradictions. In: TRIZ. Theory of inventive problem solving. Springer International Publishing, pp 89–137
11. Childs PRN (2018) 3—Ideation. In: Mechanical design engineering handbook, 2nd edn. Elsevier Science and Technology, UK
12. Hipple J (2012) The TRIZ contradiction table. In: The ideal result. Springer, New York, pp 105–130

Design and Development of a Pneumatic Non-explosive Quick-Stop Device for CNC Turning

Amiril Sahab Abdul Sani [ID]**, Shahandzir Baharom, Amirah Sakinah Mohd Rozlan, and Nur Shahida Azzahra Mohd Zamri**

Abstract In metal cutting, chip formation is both a fundamental and complex process. The workpiece material ahead of the cutting tool is deformed first in the primary shear zone and then in the secondary shear zone during the machining operation. The 'chip root' is the material included inside these two zones. A quick-stop device (QSD) is a research tool used to gather the chip-root samples. Prior to the development process, the QSD was developed to collect a frozen chip from the workpiece. The collected frozen chip needs to have minimal changes in its geometrical and metallurgical properties to reduce errors. The main objective of this research is to evaluate and analyze the performance of the newly developed pneumatic non-explosive QSD for the turning processes. QSD device was constructed to improve the machining operation which may include extending the tools' life expectancy, helps to select the proper tools for certain workpieces, and calculate the amount of friction and heat produced. The QSD design is constructed in CATIA and then simulated using explicit dynamics and statics structural analyses using the Finite Element Method in ANSYS. The complete fabricated QSD is then tested for machinability with surface roughness as the machining output and the data is compared with the normal cutting. Chip root formation of an orthogonal cutting experiment on an AISI 316L steel shows that the newly developed QSD may produce the required results of chip root formation.

Keywords AISI 316L · Chip formation · Chip root · CNC turning · Metal cutting · Quick-stop device

1 Introduction

Machining is a various process in which a piece of raw material experiences cutting and shape into the desired form. It experiences material removing process in a

© The Author(s), under exclusive license to Springer Nature Singapore Pte Ltd. 2022
A. S. Abdul Sani et al. (eds.), *Enabling Industry 4.0 through Advances in Manufacturing and Materials*, Lecture Notes in Mechanical Engineering,
https://doi.org/10.1007/978-981-19-2890-1_28

285

controlled condition. The process that have the common theme with this process is called as subtractive machining process. Machining is a process where manufacturing takes place on metal products but also can be used on other type of materials such as woods, plastics, ceramics, and composites [1, 2].

To approve various machining process, studies on analysis on chip formation has been conducted by much research throughout the year. Chip formation is a process of cutting material mechanically by using tools either saw, milling and lathe cutters. The formal study on chip formation has been conducted around World War 2, with the increase in demand of powerful and fast cutting machine tools. Pioneering in this topic of research was Kivima and Franz in 1952 and 1958, respectively [3, 4].

The formation of chip during machining is due to the removing of workpiece material into the desired shape and dimension. Rahim and Sasahara [5] indicated that the increment of cutting speed subsequently reduced the chip thickness. This is due to the high cutting energy and deformation strain rate. In addition, Rahim and Sasahara [6] stated that the chip thickness was increased as the feed rate increased due to a larger contact area between tool-chip interface. As a result of the increased friction, significant cutting temperatures and cutting forces were produced.

Bhuiyan et al. [7] showed that chip formation corresponded to the interaction with plastic deformation in the shear zone, which had a significant impact on tool life. The chip formation was significantly influenced by the formation mechanism and geometry. The increase in cutting speed, feed rate and depth of cut led to the increase in tool wear rate and plastic deformation of the workpiece material until the chip breakage. The chip formation mechanism, type of chips, chips material removal rate, the energy and temperature of the chips and rubbing action of the chips determined the tool wear. The use of QSDs enables for the extraction of the chip root as it strains in the actual process, although there is a tool–chip separation delay that depends on the QSD design. Also, in the QSD proposed by Chern [8], the tool-workpiece separation is also accomplished by utilizing the elastic stress of a spring and is aided by the cutting force.

To study the material behavior and the frictional properties of the material in the cutting zone, this study focuses on developing a pneumatic non-explosive, user friendly QSD that suits the study of chip root formation. This device is designed to be used for repeatable tests and with wide range of cutting parameters. It is also proposed for use not only for under-graduate but also for postgraduate university students, both local and international.

2 Methodology

In this work, a suitable workable design of a quick stop device is proposed after identifying it from several design available in literatures [9–11]. Next, a selection process is carried out using a metrics-based selection method following some critical criteria in designing a functioning QSD. The mechanisms of a QSD that have been identified will be analyzed, designed, and compared following the evaluation score.

Following on from the best-chosen design, a finite element analysis (FEA) is carried out on the design using a static structural analysis and an explicit dynamic analysis prior constructing and fabricating the QSD using CATIA and ANSYS software.

The important consideration in developing a QSD is the structural guidelines and parameters that need to be followed. According to Seyyed Hamed and Ebrahim [10], there are six important criteria to accomplish this goal, which are: 1. The quick-stop process must be immediate to enable the frozen chip collection at the selected cutting speed. 2. The vibration of the mechanism in operation must be kept minimum. 3. The QSD must act like a normal cutting tool. 4. It should be safe for use. 5. The time for setup must be minimum, and 6. The results of identical experiments must be reproducible, and the device should be built inexpensively.

Figure 1 depicts the exploded view of an assembled built of the QSD. The assembled part is then submitted for FEA analysis to CATIA (static analysis) and ANSYS for both statics structural analysis and an explicit dynamics analysis. In ANSYS, there are seven sections to be completed prior the simulation works, which are engineering data to select the material type to be used, geometrical parts for importing the design into ANSYS workspace (Space Claim) and the model sectioning for connecting all the simulation results into the geometrical part that marked the final analysis for establishing the final simulation results.

Machining experiment is conducted to test the newly fabricated QSD during turning experiment as shown in Fig. 2. A stainless-steel cylinder (AISI 316L) was used as the workpiece. The workpiece has an initial diameter of 65 mm and a length of 100 mm. The cutting insert used is an uncoated cermet (TNGG220408R) equipped on a tool holder of MTQNR2525M22. A fresh tool insert is used for each cutting pass to ensure sharp cutting edge is applied during cutting. The depth of cut was set at 1 mm with two levels of cutting parameters. Table 1 shows the complete machining parameter selected for this experiment. It followed the previous setup by Sani et al. [12].

Bill of Material: ASSEMBLY

Quantity	Part Number	Type
1	HOLDER PLATE	Part
1	QSD	Part
1	TURNING HOLDER	Part
1	SPRING STAND	Part
1	SPRING	Part
1	TRIGGER	Part
1	PNEUMATIC CYLINDER	Part
2	ELBOW	Part
1	LINKAGE	Part
1	BRACKET	Part
1	SPRING HOUSING	Part
1	PINN	Part
1	EJECTOR PIN	Part
1	LOCK PIN	Part
5	BOLT M10	Part
2	BEARING	Part
1	WASHER	Part
1	BOLT M08	Part
1	Trigger pin	Part
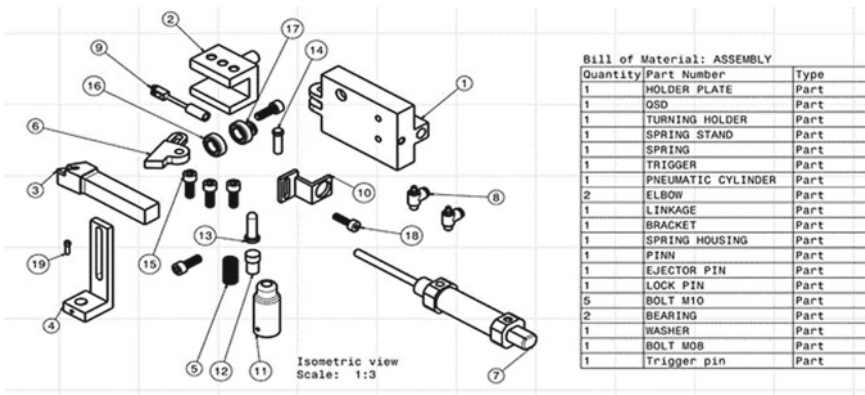
Fig. 1 Quick-stop device assembly in exploded view
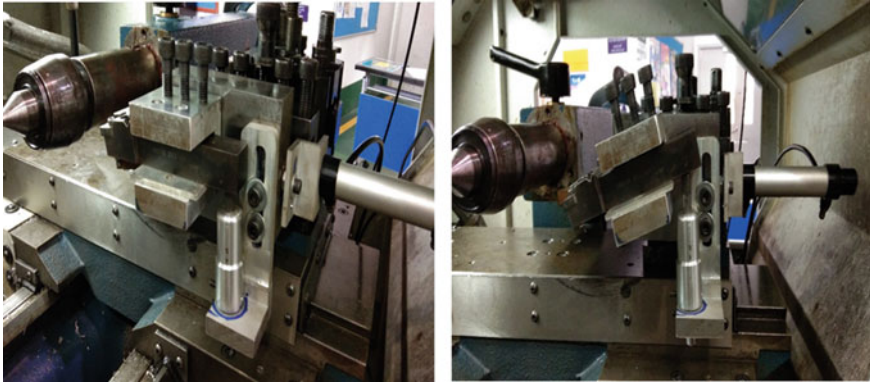
Fig. 2 Machining setup with the presence of QSD

Table 1 Machining condition

Description	Value
Cutting speed, v_c	120, 135, 150 m/min
Feed, f	0.12, 0.20, 0.25 mm/rev
Depth of cut, d	1 mm
Indexable insert	TNGG220408R (uncoated cermet)
Tool nose radius	0.8 mm
Tool rake angle, α	$-14°$
Tool clearance angle, γ	$0°$
Tool lead angle, κ	$-15°$
Tool entering angle, κr	$105°$
Tool holder	MTQNR2525M22 (Mitsubishi)

After each machining pass, the surface roughness was measured on the machined part using Surfcom with a cut-off length set at 0.8 mm. Five readings were recorded to get the average value of the roughness profile. A data comparison was carried out between cutting using the QSD and without using one. This data comparison will be used to identify the stiffness of the QSD structure that may act like a normal cutting tool. Chip root formation will also be analyzed at the end of the experiment to obtain the characteristics of the frictional and material behaviors at the deformation zones.

3 Results and Discussion

An explicit dynamics analysis was carried out to simulate the QSD deformation when the load is being exerted from the workpiece onto the cutting insert until the trigger is being released during the QSD mechanism. Based on the color contour
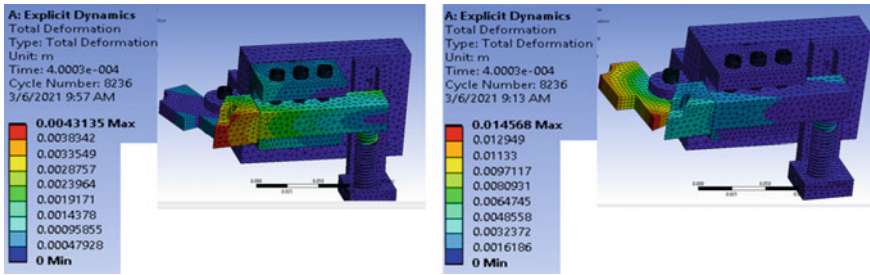
Fig. 3 Initial deformation of the QSD, left: before trigger is withdrawn, and right: trigger is withdrawn

in Fig. 3, the tool deformation on the tool holder tip is shown to be maximum at the tool cutting insert part and distributed evenly on the trigger surface just after the trigger is moving away from the tool holder, which marks the end of cutting (chip root collection). Figure 3 also depicts that the load exerted on the tool holder from the tool insert will activate the spring to subsequently compress to accommodate the force before the trigger is pulled away from the tool holder [13]. The load response on the trigger surface during the quick stop cutting mechanism will be used for further investigation during the static analysis of the QSD.

For the static structural analysis, the structural stresses distributed on the specific part of the QSD can be identified. The loads given during the static analysis are placed on the tool holder tip of the QSD in static condition (trigger is not activated), which varies from the lowest load of 800 N and up to a maximum load value of 10,000 N. The maximum physical deformation of the QSD structures after being simulated with the static loads are analyzed. Figures 4 and 5 present the findings of the equivalent stress and total deformation with the variation of the loads.

It is noted that, the increase of load generates the increment of stresses on the certain parts of the QSD structure. It is obvious that the trigger locking the tool holder prior the quick stop cutting mechanism bears the highest load for a fail-proof design consideration. In the machining experiment, the QSD trigger is attached with a pneumatic cylinder to enable the quick stop mechanism. When the trigger is activated by the pneumatic cylinder, the spring force that is compressed will exert on the tool holder bottom making it rotates away from the cutting zone, thus enabling the chip root collection.

Turning experiments were carried out following the cutting parameters given in Table 1 with the presence of QSD and without the QSD when cutting the AISI 316L cylinder. Surface roughness on the machined surfaces for both cutting conditions are compared. The results of the surface roughness are presented in Figs. 6, 7 and 8. The results of surface roughness values show that at higher cutting speed of 150 m/min and feed rate of between 0.12 and 0.20 mm/rev., the roughness values are comparable with the results from cutting without the presence of QSD. In addition, this could be further verified for higher cutting speed more than 150 m/min. Nevertheless, the higher feed speed of 0.25 mm/rev. shows a deviating result in which lower cutting speed
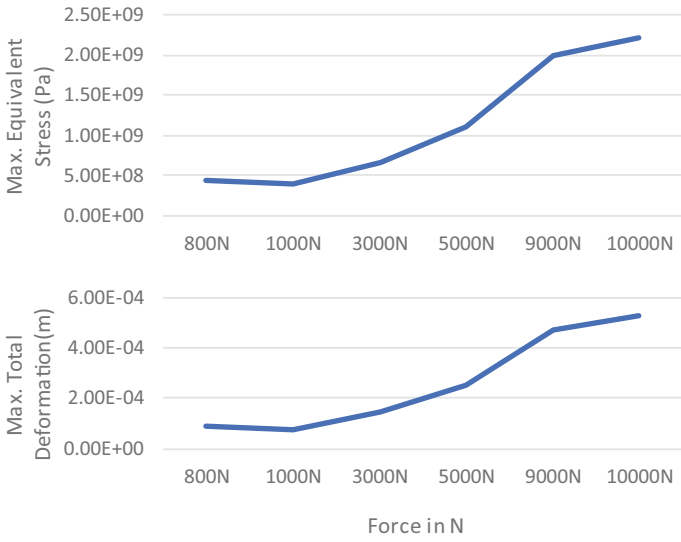
Fig. 4 The result of the maximum equivalent stress and the maximum total deformation
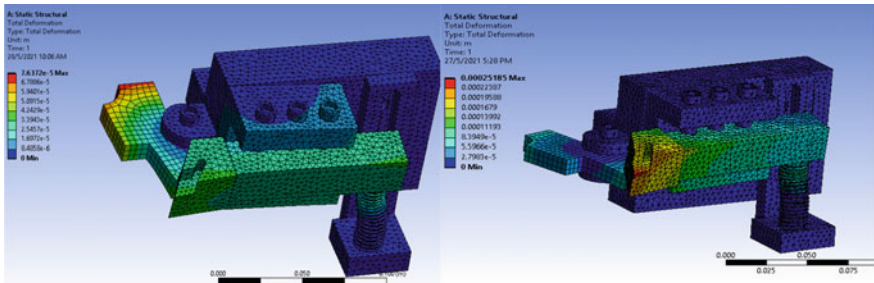
Fig. 5 The result of the total deformation at 1000 N (left) and 5000 N (right) of static load
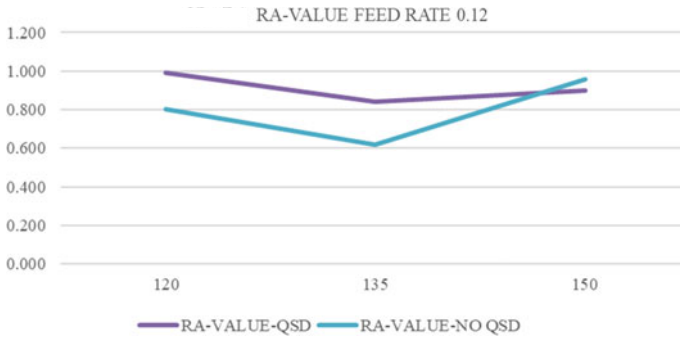
Fig. 6 Surface roughness at different cutting speed with constant feed rate of 0.12 mm/rev
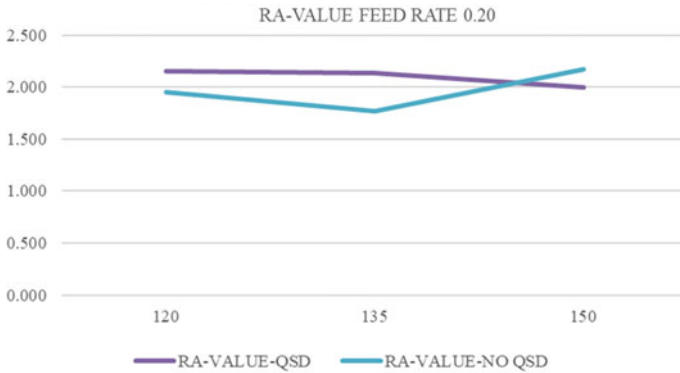
Fig. 7 Surface roughness at different cutting speed with constant feed rate of 0.20 mm/rev
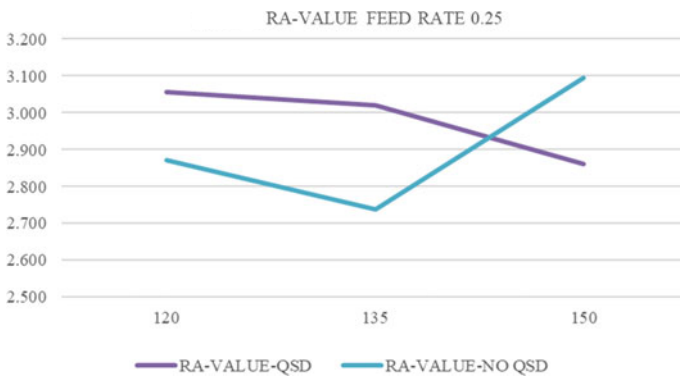
Fig. 8 Surface roughness at different cutting speed with constant feed rate of 0.25 mm/rev

of 120 m/min and higher cutting speed of 150 m/min depict the most comparable results of Ra values. It should be noted that the QSD being developed in this study provides positive results in the early stage of machining [13], thus can be used to study the chip root formation during the orthogonal cutting experiment considering the cutting parameters shown in Figs. 6 and 7.

Figure 9 shows the results of chip root collected from the orthogonal cutting of the AISI 316L stainless steel disc. It is observed that, the formation of built up edge (BUE) can be seen on the secondary shear zone, which indicates the material adhered on the sticking region of the cutting tool's rake face following a gradual formation of built up layer (BUL) that grows gradually as the metal shearing process is present [14, 15]. The BUL is moved from the tool surface to the front of the BUE, causing the BUE to become unstable and break up as it grows larger. This phenomenon repeats itself throughout the process of metal shearing (chip formation) until the cutting process is interrupted [8, 16].
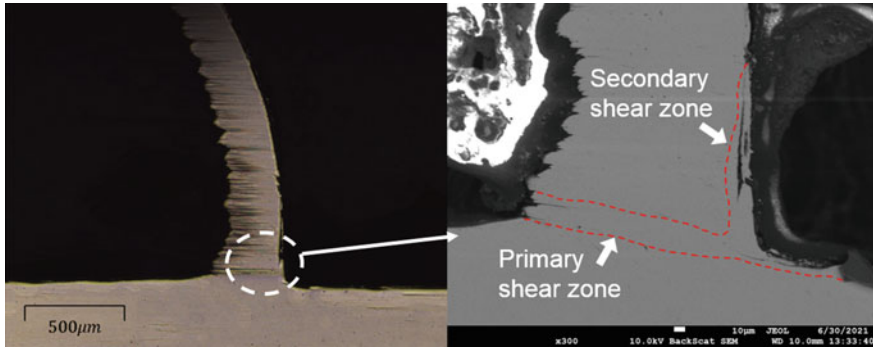
Fig. 9 Chip root formation at cutting speed of 150 m/min and feed rate of 0.12 mm/rev

4 Conclusion

In this study, a pneumatic non-explosive quick stop device (QSD) was successfully designed and developed to assist in investigating the frictional and material behavior of the workpiece during metal removing processes. In the design and development process, it is found that according to the FEA results, some important parameters that affect the quick stop mechanism are the force acting on the locking mechanism until the withdrawal of the trigger.

The experimental trial using the QSD shows a promising result, whereby the QSD could act almost likely as the tool holder without QSD at high cutting speed of 150 m/min and feed speed of 0.2 mm/rev. The results of surface roughness are found comparable for the machined surface being cut with and without the presence of the QSD.

The chip root collected at the end of the experiment concludes the ability of the QSD that can work well during the investigation of collecting chip root. It is also essential to be noted that the manufacturing process of the QSD does not require high cost and does not require a long time to complete it. With the application of a pneumatic system, the QSD is easy and safe to be used for any level of operator.

References

1. Anuj Kumar S, Arun Kumar T, Amit Rai D (2016) Effects of minimum quantity lubrication (MQL) in machining processes using conventional and nano fluid based cutting fluids: a comprehensive review. J Clean Prod 127:1–18
2. Brinksmeier E, Meyer D, Huesmann-Cordes AG, Herrmann C (2015) Metalworking fluids—mechanisms and performance. CIRP Ann—Manuf Technol 64(2):605–628
3. Vorm T (1976) Development of a quick-stop device and an analysis of the frozen-chip technique. Int J Mach Tool Des Res 16:241–250
4. Brown RH (1976) A double shear-pin quick-stop device for very rapid disengagement of a cutting tool. Int J Mach Tool Des Res 16(2):115–121
5. Rahim EA, Sasahara H (2011) Investigation of tool wear and surface integrity on MQL machining of Ti-6AL-4V using biodegradable oil. Proc Inst Mech Eng, Part B: J Eng Manuf 225(9):1505–1511
6. Rahim EA, Sasahara H (2011) A study of the effect of palm oil as MQL lubricant on high speed drilling of titanium alloys. Tribol Int 44(3):309–317
7. Bhuiyan MHS, Choudhury IA, Nukman Y (2012) An innovative approach to monitor the chip formation effect on tool state using acoustic emission in turning. Int J Mach Tools Manuf 58:19–28
8. Chern GL (2006) Development of a new and simple quick stop device for the study on chip formation. Int J Mach Tools Manuf 45:853–859
9. Dung NTQ (2019) Analysis and fabrication of a mechanical quick-stop for research on chip formation in hard turning process. Appl Mech Mater 889:87–94
10. Seyyed Hamed MA, Ebrahim A (2016) Analysis of chip removal operations via new quick-stop device. Mater Manuf Process 31(13):1782–1791
11. Pereira RBD, Braga DU, Santos CL, Ribeiro SY, Neves FO (2011) Design of quick-stop device easy and safe to operate for chip formation study on turning. In: International congress of mechanical engineering
12. Sani ASA, Erween AR, Safian S, Hiroyuki S (2019) Machining performance of vegetable oil with phosphonium- and ammonium-based ionic liquids via MQL technique. J Clean Prod 209:947–964
13. Awopetu OO (2017) Development of a universal quick stop device for lathe machine. J Sustain Technol 8:107–116
14. Gu L (2018) Mechanism study on adiabatic shear fracture induced isolated segment formation during high-speed machining. Procedia CIRP 77:348–350
15. Saeid A, Mohammad L, Hossein P, Mohsen K (2017) Characterization of vibratory turning in cutting zone using a pneumatic quick-stop device. Eng Sci Technol, an Int J 20:403–410
16. Jaspers SPFC, Dautzenberg JH (2002) Material behaviour in metal cutting: strains, strain rates and temperatures in chip formation. J Mater Process Technol 121(1):123–125

Designing, Manufacturing and Testing of New Radiator

Gautam Gupta, Pratik Sidkar, and Bikramjit Sharma

Abstract To guarantee the smooth running of a vehicle under factor load conditions, one of the critical frameworks which are vital is the cooling system. For years, this component somehow got very little attention and hence very little innovation in the designing and manufacturing took place. This paper presents the more efficient automobile radiator which has been designed, simulated, and manufactured. The 3D model of circular radiator is designed and optimized in SolidWorks. Flow simulation tool in SolidWorks is used for airflow analysis of fans to find the optimal radiator structure. To virtualize the effect of different parameters like velocity, pressure, and temperature of the water on both the radiators, they have been simulated in Ansys. This research aims to do an experimental comparison between an ordinary radiator and a modified radiator. The radiator with curved pipes is designed, given a circular shape, resulting in a temperature drop of 37% more than the ordinary radiator.

Keywords Heat exchanger · Automobile · SolidWorks · Fabrication · Simulation

1 Introduction

The radiator is a pivotal component of automobile cooling systems, as it exchanges the heat of water by the air forced over the radiator by a fan. Radiator functions as heat exchanger, removing heat from the water produced by engine and circulate it by moving heat to the surrounding air. In an automobile, a radiator is a segment of the cooling framework that does a significant job in moving the warmth from parts to the climate through its perplexing framework and working. It is a cross-flow radiator that is compelled to remove the heat from engine to the atmosphere passed up by axial fan. A vehicle goes at different scopes of speed. The quicker it ventures, the more remarkable the engine requirements to produce, and subsequently the better the cooling cycle must be. The radiator is essential for cool-down arrangement of

G. Gupta (✉) · P. Sidkar · B. Sharma
Department of Mechanical Engineering, Thapar Institute of Engineering and Technology, Patiala, Punjab 147004, India
e-mail: ggupta2_be15@thapar.edu

the engine and in automobiles the radiators used are generally a cross-stream heat exchanger. Main reason for the use of airflow is to eliminate the heat and the cooled fluid from the radiators reenters the engine.

Heavy loaded vehicle engines generate more power and heat. These vehicles required high performance cooling system for more durability of engine. However, engine's cooling system is cardinal component of the cooling system. To analysis its air flow, a flow simulation is used to design a radiator with most utilization of air. In the I.C. engines, heat is rejected by crossing of a fluid known as coolant. The coolant absorbs generated as it ingests the heat conveyed in the engine. After that it is circled back to the engine in a shut circle. The life of engine, execution, and general security are guaranteed because of successful engine cooling. The Engines have changed our lifestyle and vision towards transportation.

From zooming cars to faster airplanes, we have progressed significantly. In spite of the fact that the requirement for more grounded engines in more bound spaces has caused issues of heat dissemination in the engines. Engine cooled fluid is generally a water-based product; however, it may likewise be oil as well. It isn't unexpected to utilize water for driving the coolant to circle, and moreover for a pivotal fan to constrain air towards radiator. In this paper, 3D model is conceived and fabricated with minimal manufacturing processes to produce the final product. Then, it is empirically compared with the regular automobile radiator.

2 Literature Review and Objectives

Earlier study [1] shows the CAD drawing with maximum utilization of air flow and implemented heat transfer studies to demonstrate effective efficiency of radiator. Figure 1 shows a square-formed radiator with a fan gave which regulates air in a circular region. If the sides of the radiator are equal to D (Diameter of Fan), the viable area of such radiator is equivalent to D^2. The progression of air from the fan
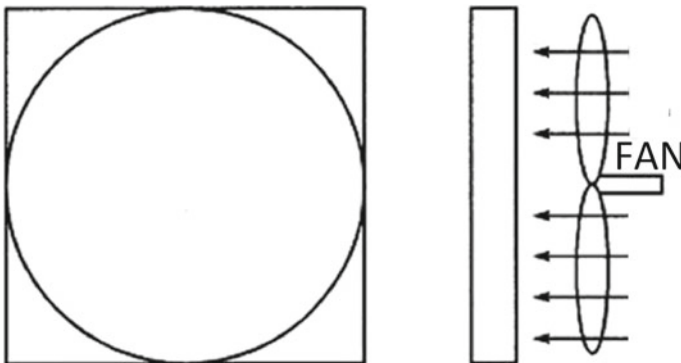
Fig. 1 Air-cooled square shaped heat exchanger [1]

will be of region area $(\pi/4)\,D^2 = 0.76\,D^2$. The difference between the area of both the regions would be as $\{D^2 - (\pi/4)\,D^2\} = 0.24\,D^2$. To beat the downsides of this regular design, a new shaped design is proposed to acquire effective working of the radiator. The air-flow simulation has been performed and illustrated, further in paper.

CFD has been performed in reference to some previous studies. The CFD with air flow simulation performed by Yao et al. [2] on engine's cooling fan presents velocity and pressure distribution simulated in SolidWorks. CFD results were introduced in [3] as velocity vectors and path lines, which gave genuine stream qualities of air around the fan for various sharp edge directions. Three radiators have been compared in [4] on the basis of different graphs governed from the CFD analysis. Comprehensive study on louvered fins in [5] have been used for this experiment.

Studies have done by Trivedi and Vasava [6] demonstrating simulation of the mass flow-rate of air passing across the tubes of an automobile radiator. CFD investigation in [7] for both helical sort pipes and straight pipes of the radiator at the radiator, for all liquids and thermal analysis examined in Ansys. Helical shaped tubes are taken for CFD analysis in [8] on two distinct pitches. A study in [9] aim to analyze the heat-exchanger could be improvement by changing certain dimensions. The fundamental target shown in [10] is to plan the vehicle radiator with surface zone thickness (SAD) with expanded heat transfer coefficient, decreased expense, and diminished weight utilizing CFD.

Heat transfer analysis of a car heat-exchanger is realized for the scope in [11], at variable speed of the air hitting the heat-exchanger with ethylene glycol as fluid. The pressure-drop and heat-transfer characteristics of $Zn–H_2O$ and $ZnO–H_2O$ Nano-fluids in [12] have been experimentally proven. An investigation in [13] taken between various coolants, water, and others as combination of water with propylene-glycol has also been completed. Tests were directed in [14] on a solitary pass cross-stream smaller heat exchanger by varying the different boundaries, such as, inlet temperature, the flow-rate, and speed of air. The experimental setup in [15] is also used in this research to compare the outlet temperature of water in both radiators to analyze the efficiency of radiator.

Bunch of hypothetical parametric and affectability examinations in [16] on the heat-exchanger dependent on the Effectiveness-NTU strategy. Two kinds of cross-flow radiators have been manufactured in [17] that have been built up to precisely anticipate the presentation of the radiator. A rectangular radiator is been constructed in [18] on the basis of design and material selection. A heat transfer study in [19] for the radiator are analyzed, to compare the inlet and outlet temperatures of the fluids in the radiator.

CFD investigation by Prasad and Prasad [20] on elongated and louvered fins radiator with half fraction of ethylene glycol and half fraction of water combination as liquid poured display better heat transfer. Temperature, pressure and mass rate distribution of the fluid and air has been evaluated [21] to analysis the different types of materials (Aluminum (Al), Al-Si-Mg alloy and Graphite flakes-metal alloy) used for Radiator. DFMA methodology in [22] is used in this experiment to fabricate the new radiator by designing and manufacturing each part separately and assembled.

The helical coils having more heat transfer coefficient than straight pipes shown by Xin and Ebadian [23], helical pipe design for heat exchanger is widely used in the industries A study by Jayakumar et al. [24] on helical pipes-based heat exchanger concludes that in order to predict the value of fluid-to-fluid heat-transfer for any coolant, few conditions such as constant wall-temperature and heat-flux are in applied. CFD and mathematical investigation by Ladumor et al. [25] to improving heat-exchanger proficiency.

3   Materials and Methods

First and foremost, a 3D model of a fan is designed in SolidWorks with seven blades and a rotational central hub as shown in Fig. 2. In this model, each blade of fan has length 40 mm and of central hub radius 25 mm. The diameter of rotational liquid area is 130 mm. Rotational axis of axial fan is referred as Y-axis and the synchronizing origin is situated at center of fan. The Computational domain is $140 \times 200 \times 140$ mm^3. The rotational speed is 600 RPM and the air flow is selected as fluid domain. Figures 3 and 4 show the velocity flow trajectory with the lines and arrow are assigned as 80 mm length of line and 250 arrows respectively.

Based on [1] CAD drawing, 3D models of all the individual parts of radiator are created in SolidWorks as shown in Fig. 5. These parts are designed individually, which helps to fabricate the model according to the designed parts and then assemble them all. A study in [5] and [20] shows comprehensive study on louvered fins that used for this experiment. The assembled radiator is shown in Fig. 6. After the circular

Fig. 2 Model of fan in SolidWorks
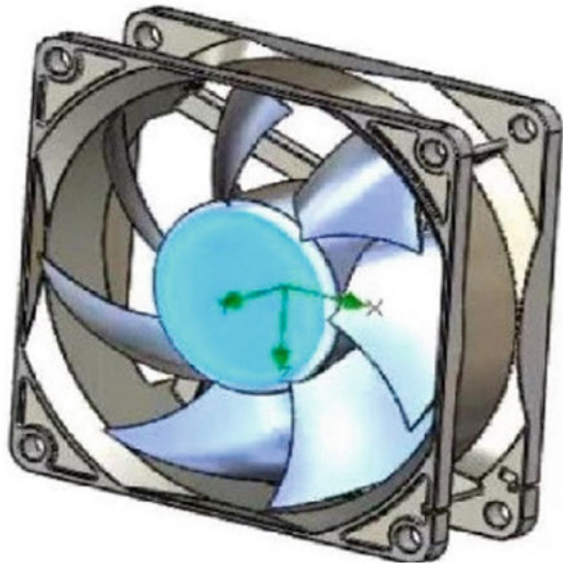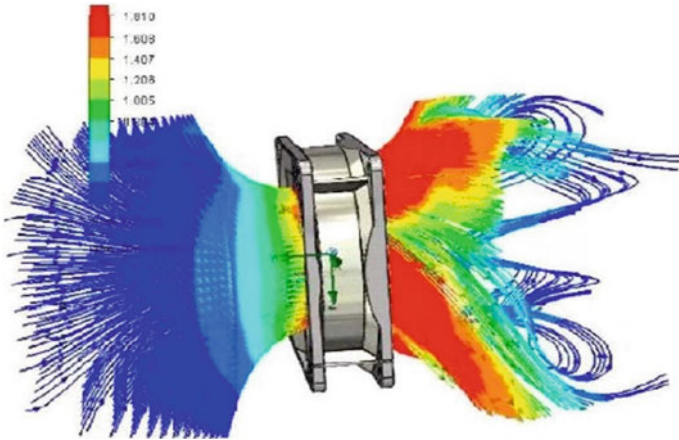
Fig. 3 Flow simulation on fan (side view)
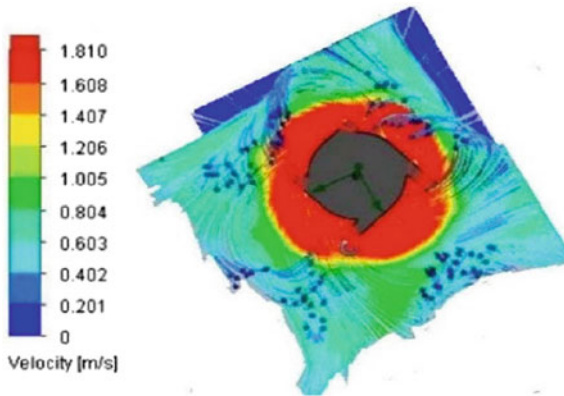
Fig. 4 Flow simulation of fan (front view)
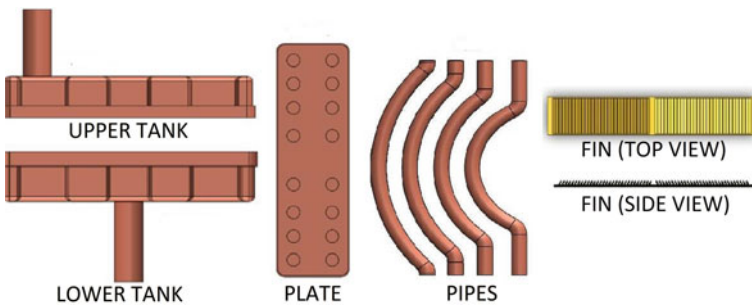
Fig. 5 Individual parts of circular radiator
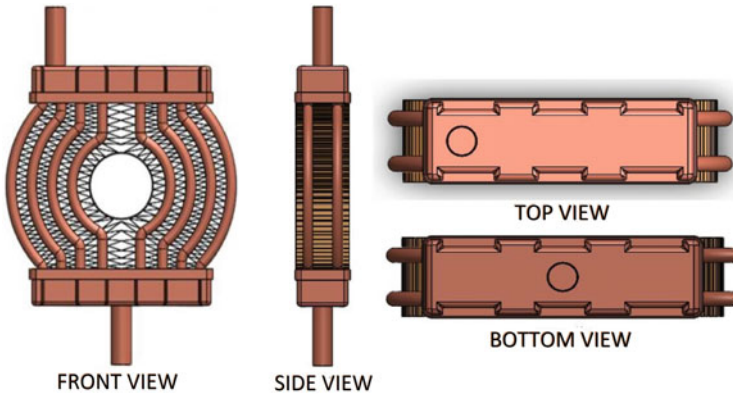
Fig. 6 Assembled modified circular radiator

radiator has been designed in SolidWorks, it than simulated with different parameters like velocity, pressure and temperature of water.

Firstly, the effect of velocity of water shown in Figs. 7 and 8 with front-view and top-view of the circular radiator respectively, using velocity vectors is simulated in Ansys. Secondly, the pressure effect of water on the circular and ordinary radiator is shown in Figs. 9 and 10 respectively, which was simulated in Ansys. Thirdly, the temperature effect or simulation of the water on the circular and ordinary radiator is shown in Figs. 11 and 12 respectively, which was simulated in the Ansys. Here, "Temp." is referred as temperature here, which is used to describe Figs. 11 and 12.

The simulations help to improve and optimize the design of the circular radiator before fabrication. The observations noted with the above simulation are that the
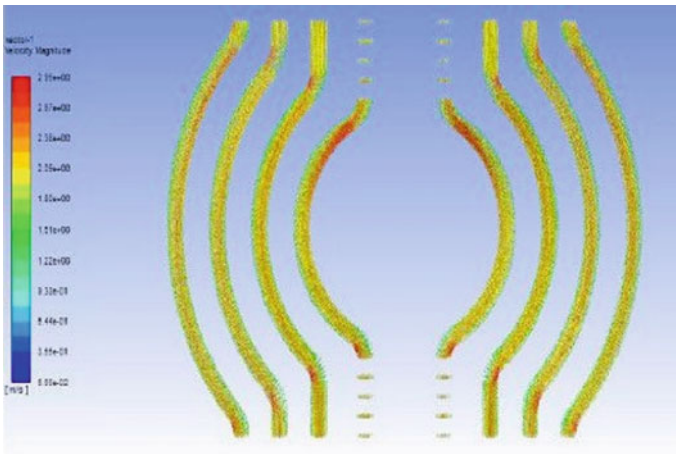
Fig. 7 Velocity simulation (front view)
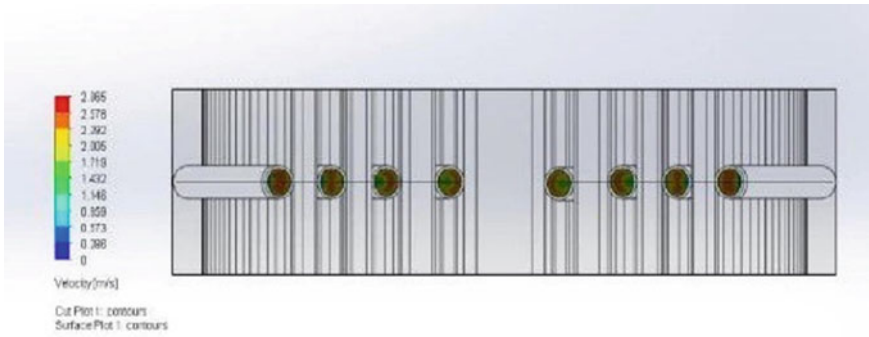
Fig. 8 Velocity simulation (top view)
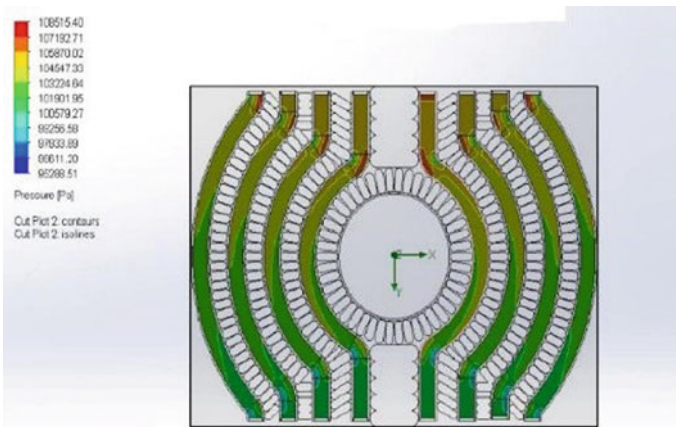
Fig. 9 Pressure simulation on circular pipes

regions indicated by red are the regions that present the velocity higher than 2 m/s. The velocity changes at each curve, the outer curve of the pipe having slightly larger radius have velocity range of about 1.2–1.5 m/s.

Then, each part is fabricated in the workshop according to the 3D drawing with the required and optimal manufacturing processes from the raw material. Copper is used for manufacturing tanks and pipes whereas, fins are made of aluminium. Tanks are fabricated by using copper sheet that was moulded under the press machine. Pipes are framed from copper sheet, which are formed between huge rollers under extensive pressure to create the hollow pipes with required diameter. Fins are manufactured in the fin press machine with width of 7.5 mm.

After completion of all the parts, next step is for assembly of all the products to get finalize desired product. Final step for fabrication is to assemble all the individual
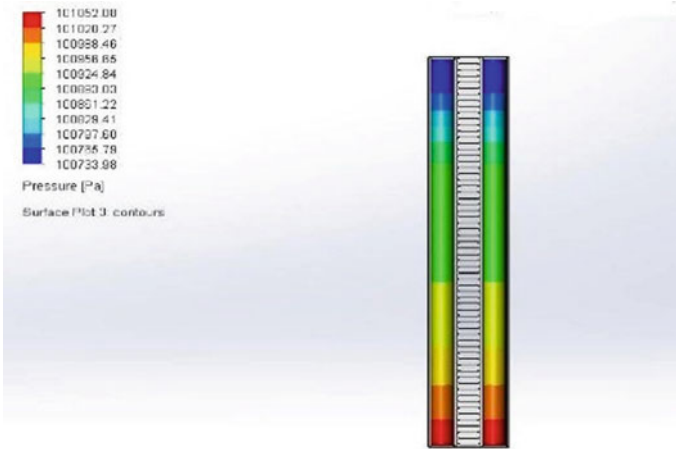
Fig. 10 Pressure simulation on straight pipes
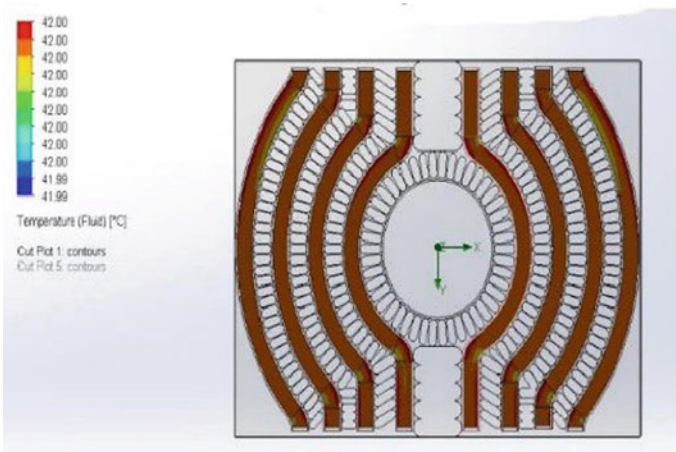
Fig. 11 Temp. simulation on circular pipes

parts. Tanks & pipes are joined together using copper brazing, and fins placed between the pipes to complete the fabrication of the radiator as shown in Fig. 13. Similarly, an ordinary radiator is also manufactured with same dimensions of tanks and same gap between tank but straight pipes brazed for assembly such that core of the radiator would be 130×130 mm^2 as shown in Fig. 14.
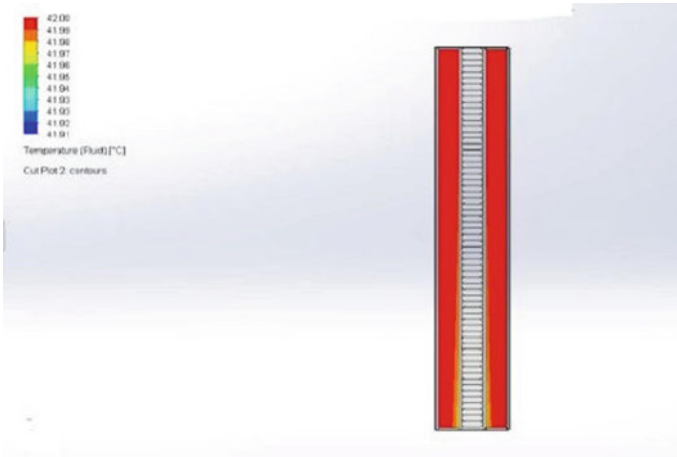
Fig. 12 Temp. simulation on straight pipes

Fig. 13 Fabricated circular radiator

4 Experimentation

Figure 15 shows the experiment setup, posted by Peyghambarzadeh et al. [15] is utilized in this paper. Arrangement incorporates a capacity tank, streamline pipes, a heater, a stream meter, a diffusive pump, a table fan and a both the radiators. The pump gives steady stream of heat exchange of 8 L/min. The working fluid is filled with 16 L in the storage tank. Five layered insulated tube with 1.5 cm in diameter.

For warming the working liquid, an electrical boiler rod was used to maintain the fluid temperature 42 °C that was measure with the digital thermometer. The overall

Fig. 14 Fabricated ordinary radiator
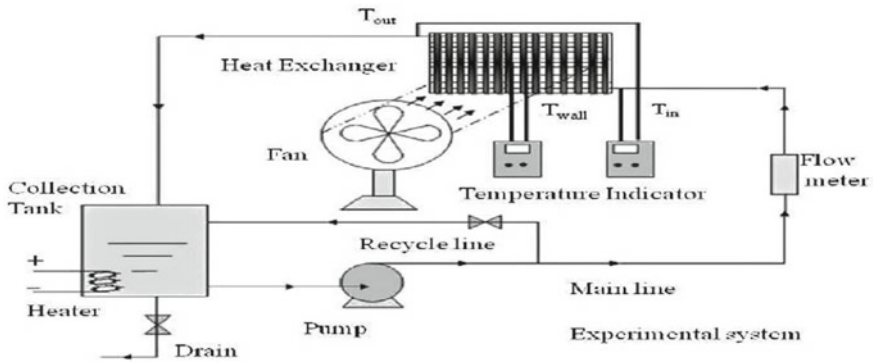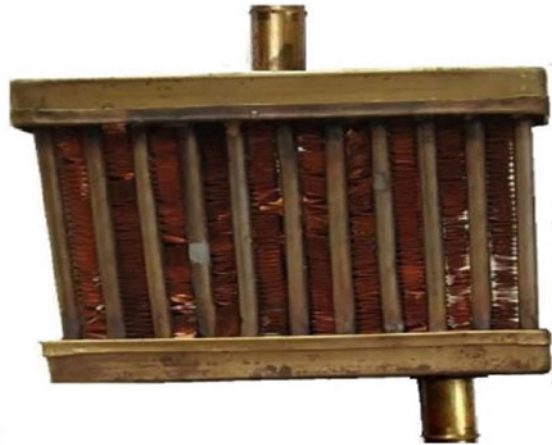
Fig. 15 Schematic of experimental setup [15]

volume and temperature of circulating fluid is constant in all the experiments. The speed of table fan is 600 RPM that was measured with tachometer. Two thermocouples (both K-type) were utilized for heat-exchanger inlet and outlet temperature readings. Thermocouples were attached with silicon paste at both the ends of radiator.

The thermocouple presented the reading of both the points in °C. Thermocouples are thoroughly calibrated with the precision has been assessed to be 0.1 °C. Experiment was firstly conducted on ordinary radiator till the temperature of the outlet was measured to be stable and cannot be decreased further. And then, using same measured and setup it was conducted on new modified radiator. In order to, check the precision of the experiment, it was conducted 10 times on each radiator and average of all the reading was compared to meet the conclusion.

5   Results and Discussion

All the reading calibrated from the thermocouple are converted and presented into graph form. Figure 16 shows graph of the ordinary radiator performed with the constant inlet temperature of 42 °C and resultant outlet temperature is noted as 38.5 °C. Whereas, Fig. 17 shows the graph of the modified radiator performed with the constant inlet temperature of 42 °C with resultant outlet temperature is noted as 37.2 °C. The "Temperature" vs "Time" graphs are presented in Figs. 16 and 17. Each unit of the X-axis represents 0.5 s and each unit in Y-axis represents 1 °C. The gradual decrease of the second curve (outlet curve) presents the downfall of temperature that is affects the temperature of the first curve (inlet curve) due to external flow through fan.

The experimental setup on each radiator was continued till the outlet temperature become stable and constant. The outcome of the experiment was in noted to be as expected; the outlet temperature of modified radiator is less as compared to the outlet temperature of ordinary radiator. During testing, it is observed that there was no significant change in the temperature in both the designs after passing water. This is primarily due to the small size of the prototype. One thing we were able to observe in the design physically is the pressure drop in the outlet of the curved pipes. Since there is more convection in the curved fin the temperature drop in the modified radiator was more after applying the air through the fan. The differences between temperatures on the outlet of both the radiators are the final outcome of the experiment.
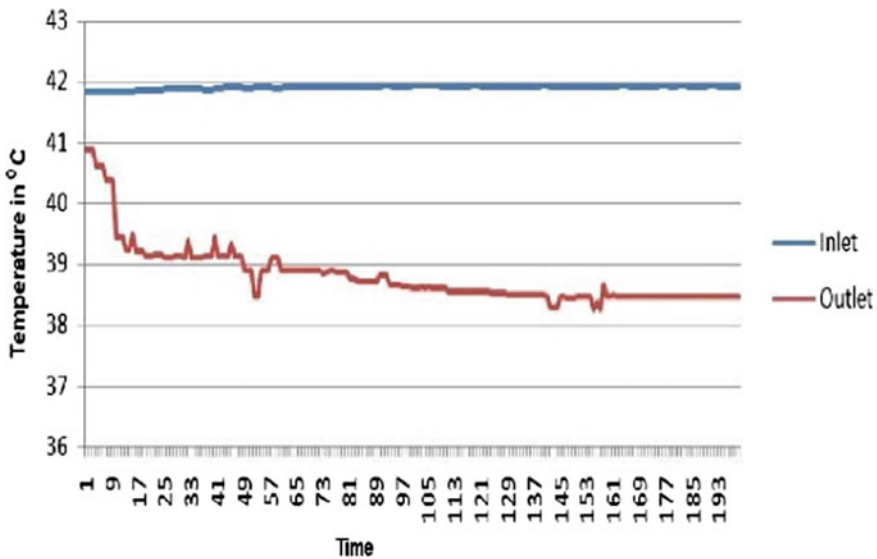
Fig. 16   Temperature graph of old radiator
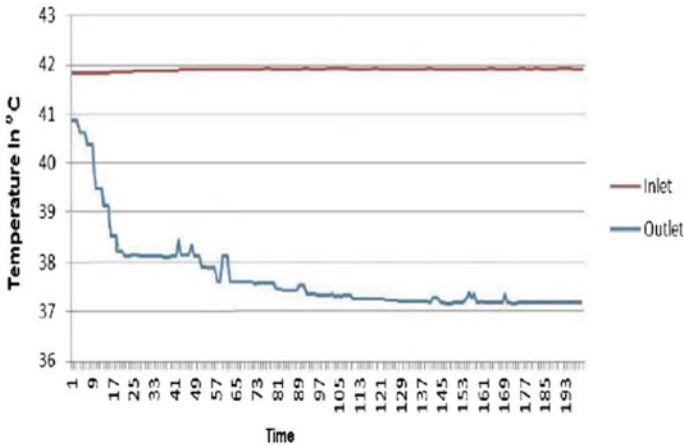
Fig. 17 Temperature graph of new radiator

6 Conclusion

Two different designs of the radiator, one straight and other with curved pipes has been compared in this paper. In modified radiator or circular radiator, it was observed that there was a temperature drop of 4.8 °C while in straight pipes or ordinary radiator the temperature drop in the water was 3.5 °C. Hence, the efficiency of the modified radiator is more and is more optimal as it utilized more air produced by fan. Clearly, the resulting difference in a temperature drop is of 1.3 °C more than the ordinary radiator.

References

1. Chavan DK, Tasgaonkar GS (2013) Study, analysis and design of automobile radiator (heat exchanger) with CAD drawings and geometrical model of the fan. Int J Mech Prod Eng Res Dev 3(2):137–146
2. Yao Y, Zhang WM, Shi BQ, Wang CZ (2011) Experiment and simulation research of engine cooling fan in dump truck. Proc 2011 Int Conf Electron Mech Eng Inf Technol (EMEIT 2011) 2(9):742–745. https://doi.org/10.1109/EMEIT.2011.6023202
3. Jain S, Deshpande Y (2012) CFD modeling of a radiator axial fan for air flow distribution. 6(11):1085–1090
4. Hanmanthu B (2019) Enhancement of heat transfer rate in single fin type radiator with CFD simulation. XII(Xii):288–301
5. Erbay LB, Doğan B, Öztürk MM (2017) Comprehensive study of heat exchangers with louvered fins. Heat Exch—Adv Featur Appl. https://doi.org/10.5772/66472
6. Trivedi PK, Vasava NB (2012) 10.1.1.672.4493. 1(6):1–4
7. Rajan RK, Pramod Kumar P (2017) CFD analysis of heat transfer coefficient for helical radiator with different coolant. 6(32):6486–6493
8. Kayastha KS (2015) CFD simulation and heat transfer analysis of automobile radiator using helical tubes. Int J Eng Res Dev 11(01):2278–2367

9. Patel HB, Dinesan D (2015) Performance analysis of an automobile radiator using CFG. Int J Inno Res Sci Technol 1(12):318–322
10. Senthilkumar G, Ramachandran S, Purusothaman M (2010) Indigenous development of automobile radiator using CFD. In: Proceedings of international conference on frontiers in automobile and mechanical engineering—2010, FAME-2010, pp 373–376. https://doi.org/10.1109/FAME.2010.5714862
11. Mounika P, Sharma RK (2017) Performance analysis of automobile radiator. 2(May 2016):257–263
12. Sonage BK, Mohanan P (2015) Miniaturization of automobile radiator by using zinc-water and zinc oxide-water nanofluids. J Mech Sci Technol 29(5):2177–2185. https://doi.org/10.1007/s12206-015-0438-x
13. Yadav JP, Singh BR (2015) Study on performance evaluation of automotive radiator. SAMRIDDHI: A J Phys Sci Eng Technol 2(2):47–56. https://doi.org/10.18090/samriddhi.v2i2.1604
14. Sharma S (2018) Fabricating an experimental setup to investigate the performance of an automobile car radiator by using aluminum/water nanofluid. J Therm Anal Calorim 133(3):1387–1406. https://doi.org/10.1007/s10973-018-7224-9
15. Peyghambarzadeh SM, Hashemabadi SH, Jamnani MS, Hoseini SM (2011) Improving the cooling performance of automobile radiator with Al_2O_3/water nanofluid. Appl Therm Eng 31(10):1833–1838. https://doi.org/10.1016/j.applthermaleng.2011.02.029
16. Bargal MHS, Abdelkareem MAA, Wang Y (2019) Parametric sensitivity analysis of automobile radiator performance. IOP Conf Ser Mater Sci Eng 563(4). https://doi.org/10.1088/1757-899X/563/4/042038
17. Harris C, Kelly K, Wang T, McCandless A, Motakef S (2002) Fabrication, modeling, and testing of micro-cross-flow heat exchangers. J Microelectromech Syst 11(6):726–735. https://doi.org/10.1109/JMEMS.2002.806025
18. Yadav RJ (2019) Design and material selection of an automobile radiator. Int J Appl Eng Res 14(10):60–63
19. Carl M, Guy D, Leyendecker B, Miller A, Fan X (2012) The theoretical and experimental investigation of the heat transfer process of an automobile radiator. 2012 ASEE Gulf Southwest Ann Conf 1(128):1–12
20. Prasad P, Prasad LSV (2017) Cfd analysis on louvered fin. Int Res J Eng Technol 4(1):1458–1462. [Online]. Available: https://irjet.net/archives/V4/i1/IRJET-V4I1265.pdf
21. Gopinath C, Poovazhagan L (2019) Design and analysis of fluid flow and heat transfer in a crossflow radiator as changing the fin and tube material. Int J Recent Technol Eng 8(1):332–340. https://doi.org/10.2139/ssrn.3511928
22. Boothroyd G (1994) Product design for manufacture and assembly. Comput Des 26(7):505–520. https://doi.org/10.1016/0010-4485(94)90082-5
23. Xin RC, Ebadian MA (1996) Natural convection heat transfer from helicoidal pipes. J Thermophys Heat Transf 10(2):297–302. https://doi.org/10.2514/3.787
24. Jayakumar JS, Mahajani SM, Mandal JC, Vijayan PK, Bhoi R (2008) Experimental and CFD estimation of heat transfer in helically coiled heat exchangers. Chem Eng Res Des 86(3):221–232. https://doi.org/10.1016/j.cherd.2007.10.021
25. Ladumor RJ, Gajjar PVY, Araniya PKK (2015) A review paper on analysis of automobile radiator. Int Conf Multidiscip Res Pract I(Viii):411–415

Temperature and Heat Flow Analysis in a Drying Chamber Through Finite Element Method

Nurul Hasya Md Kamil, Ahmad Shahir Jamaludin, Mohd Nizar Mhd Razali, and Abdul Nasir Abd. Ghaffar

Abstract Food production sectors have changed, transitioning from micro-enterprises and traditional, family-run operations to enormous investments and highly sophisticated industrial processes. However, the raw materials for food manufacturing are still derived from local farming or fishing. Thus, advancements in food technology are necessary to minimize spoiling, where it can reduce the strain on employees in processing food quickly. It is well recognized that the drying process of food, particularly fruits, is an essential production operation in the industry. The current drying technique is time and costly, as it takes several hours for the food or fruit to dry completely. Understanding the drying phenomena requires heat flow and temperature distribution studies within a drying chamber. It is expected that, by understanding the influence of design parameters on a drying chamber, it would be possible to use it more efficiently and enhance output. The aim of this study is to analyze the food preserving using the method of conventional drying through temperature and humidity observation, by modelling the behavior of temperature and heat flow inside a drying chamber through Finite Element Method and validate the modelled condition with a commercially available drying chamber. A specific FEM modelled is designed and tested with various parameters to understand the heating behavior, along with actually drying process with the commercially available drying chamber. From the study, various fruit/food/material has variety of drying rate due to surface properties (pore size, thickness etc.). From the FEM analysis, from the increasing heat flux, heating effective range increases because of increasing heat flow rate. Decreasing fin gap, heat flux requirement decreases because of increasing heating effectiveness, yet material cost increases, plus with decreasing inlet air speed will decrease the heat flux requirement, but will increases the drying chamber heating time to reach the required temperature.

N. H. Md Kamil · A. S. Jamaludin (✉) · M. N. Mhd Razali
Faculty of Manufacturing and Mechatronic Engineering Technology, Universiti Malaysia Pahang, 26600 Pekan, Pahang, Malaysia
e-mail: shahir@ump.edu.my

A. N. Abd. Ghaffar
Faculty of Electrical and Electronic Engineering Technology, Universiti Malaysia Pahang, 26600 Pekan, Pahang, Malaysia

1 Introduction

Nowadays, food production industries had become modernized, from micro size enterprise, traditional, family-run production to large investment and highly technological industrial processes. However, the material source for food production are still based on local farming or fishery. Thus, it is required to advances in food technology in order to avoid spoilage, where it can lessen the burden of workers in processing food rapidly [1]. The preservation of food dates back to when Cro-Magnon humans preserved food by smoking it for the first time about 15,000 BC during Ice Age, where heat is one of the fundamental key of food preservation [2]. Sun drying is also the earliest food preservation process and conventionally used. The optimal usage of power, cost reduction and the reduced environmental impact are the extremely lucrative facets of the industry [2, 3]. Correspondingly, the complexity to gain an appropriate drying method and the design of the dryer have a significant impact on the consistency, form, size and moisture content of the final product, had led to the development of drying process sustainability in academic and industries [1, 4–7].

It is well understood that drying is carried out mainly by two steps: the transfer of moisture from the inside to the outside of a material and the moisture evaporation from the higher temperature material surface to the ambience [2, 4, 5]. Any external factors are closely related to water, such as humidity, friction, shape and type of the exposed flow velocity, temperature and surface area. The drying method is still an exclusive area for technologists and researchers to study and thoroughly, considering the increase in the number of studies and technological advancements. Efforts to make the drying process clearer for all users ought to be maintained; this is a dynamic physical phenomenon, but needed to promote the product's consistency [1, 5]. One of the modern problems for study in this area is the use of knowledge of thermodynamics and transport phenomena to explain balance and kinetic drying [2, 8–10]. Food products can now be dried by air, by super-heated steam, by vacuum, by inert gas or by direct application of heat. Depending on the quality of the material, the ideal form of the finished product, the particular form, and so on, there are many types of dryers. Dehydration is a method in which the vaporized heat is passed to the water in the food [1, 5, 11, 12].

The easiest and cheapest drying technique is sun drying. It is used for foods such as corn, rice, sultanas and raisins that are high in volume. The downside of sun drying is that the processor has very little control over the conditions of drying and the dried fruit consistency. Additionally, processors use an artificial dryer to make better quality dried fruits. According to the various needs of the customer, there are many types of dryer available (solar, petrol, electric, biomass powered) [3, 13]. Using drying as a food preservation process, depending on the equipment, the moisture content of the fruit and the humidity in the air, different amounts of drying time can result. It

is stated that, fruits drying process should be prevented from reaching hard or brittle condition, where the fruit must be leathery and pliable for consumption [14, 15].

It is known that drying process of food, especially fruits, is one of the important manufacturing process in the industry. Currently available drying process is time and cost consuming, where it is needed for several hours for the food or fruit to reach the desired dryness. It is needed to understand the drying phenomenon through heat flow and temperature distribution analysis inside a drying chamber. It is expected that, by understanding the effect of design parameter in a drying chamber, it can be used effectively and increase the productivity. Thus, the aim of the study is to model the behavior of temperature and heat flow inside a drying chamber through Finite Element Method.

2 Methodology

It is needed to simplified the design of an actual product to be fit into Finite element simulation to make it possible. The software that will be utilized is ANSYS V19.1 Workbench's FLUENT Module. In this module, it is required to model the fluid component of a design as solid. For the case of the drying chamber, the internal air body and external 1 m front, above and back is designed as a single body. The model is show in Fig. 1. The simulation is considered as a continuous singular air
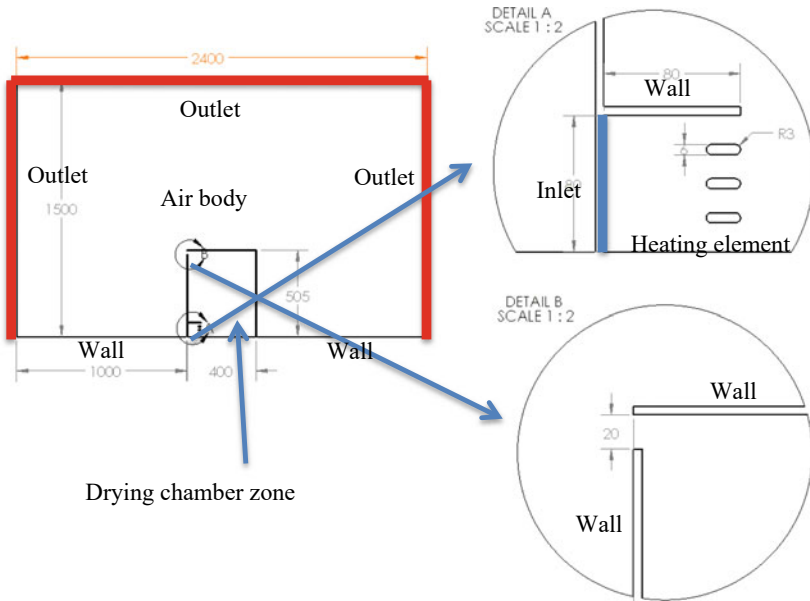
Fig. 1 Drying chamber FEM model

Table 1 Simulation condition

Heating temperature (°C)	70–120
Heating time (min)	10, 20, 30, 60
Air speed (m/s)	2.0
Heat flux (W/m^2)	50, 500, 6400, 10,000
Fin distance (mm)	0.5, 1.0, 2.0, 3.0
Fin material	Aluminium

body compared to separating between inside chamber and outside chamber. Several considerations need to be clarified for FEM such as following:

- Air inlet
- Air outlet
- Air body
- Wall
- Heating element
- Air vent between drying chamber and environment
- Air speed and temperature from the inlet
- Wall thermal properties are neglected.

Additionally, Table 1 shows additional simulation conditions required to generate data required for the study.

3   Results and Discussion

3.1   FEM Estimation on the Effect of Heat Flux onto Air Heating Behavior

Figure 2 shows the FEA model for heat transfer behaviour from fin. Temperature distribution surrounding the fin can be observed from Fig. 2, where for each temperature profile is generated from the input heat flux parameter. It is needed to estimate the maximum heat flux that makes aluminium fin melt, which is at 660 °C. It can be observed that, with the increasing heat flux input, the maximum temperature incurred by the aluminium fin is increasing.

It can be observed from the input heat flux, 10,000 W/m^{2}K has shown temperature over the melting point of the aluminium, while 6400 W/m^{2}K has shown the temperature of 500 °C, which is under the aluminium melting point temperature. This is due to, with the increasing heat flux, the rate of heat transfer increases, thus increase the overall aluminium fin temperature. From linear interpolation, it can be estimated that the maximum input heat flux possible for the design is shown as following;
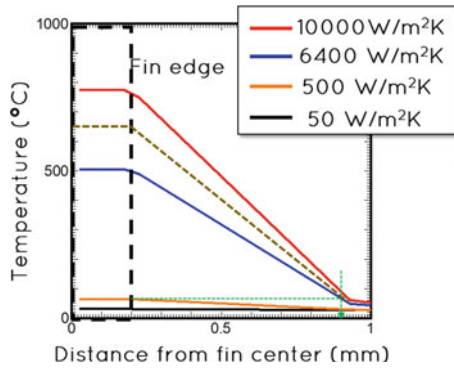
Fig. 2 Effective distance of temperature increment from fin

$$\frac{775 - 505}{10000 - 6400} = \frac{660 - 505}{\phi_e - 6400}$$

$$\phi_e = 8467\left[\text{W/m}^2\text{K}\right]$$

By taken consideration of 90% efficiency, as the 8467 W/m²K heat flux input, the aluminium starting to melt; it is suggested to set the heat flux input up to 90% of the maximum permissible heat flux, which is 7560 W/m²K. The distance of effective drying temperature of 70 °C needed to be estimated. It can be observed that, with the increasing heat flux, the effective distance for the fin to raise the air temperature increases. This is due to, with the increasing heat flux, the amount of heat transferred from fin to air is increased, thus increase the effective range of heating. It can be estimated that, for the heat flux between 6400 and 10,000 W/m²K, the distance between effective temperature will be between 0.56 and 0.64 mm. Based on the calculated maximum permissible heat flux value of 7560 W/m²K, through linear interpolation, the maximum effective distance can be obtained as the following;

$$\frac{0.64 - 0.56}{10000 - 6400}(7560 - 6400) + 0.56 = 0.586 \text{ [mm]}$$

The different of permissible maximum heat flux 7560 W/m²K and 6400 W/m²K is only around (0.586–0.56)/0.56 * 100% = 4.6%, thus it can be considered that lower heat flux is better, and the distance chosen should be the easier to be fabricated, which is 0.5 mm * 2 = 1 mm distance between fin.
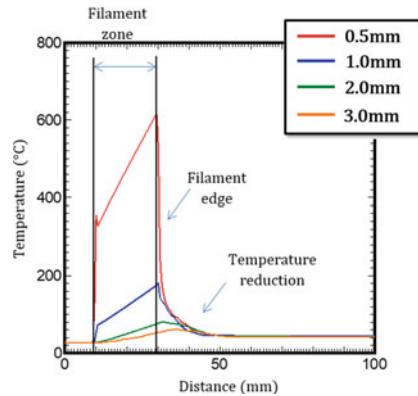
Fig. 3 The highest temperature and temperature profile

3.2 FEM Estimation on the Effect of Fins Distance onto Air Heating Behaviour

The highest temperature and the temperature profiles are shown in Fig. 3 for the heat flux input of 6400 W/m^{2}K for various fins distances. It is observed that the air is heated while passing through the space between fins, and still maintain heated after a certain distance but with reduced temperature. With similar heat flux, smaller gap fins show high temperature increment when the air speed is fixed. With a smaller gap, the heat is accumulated effectively, and the air is heated instantly. However, smaller gap means more material, and more material means higher cost. It is observed that 1 mm fin gap design estimated higher temperature for the same heat flux value of 6400 W/m^{2}K, where it is assumed that more contact area and effective heating zone increase the amount of heat absorbed by air that pass through the fin.

When the heat flux is reduced proportionally to 4400 W/m^{2}K, the effective drying temperature is obtainable. Thus, it is assumed that, by decreasing the gap between fin, plus with an extra number of fin to conduct the heat from the heating element, the contact surface is increased; reducing energy needs to heat the supplied air.

3.3 FEM Estimation on the Effect of Air Speed onto Air Heating Behavior

The process shown in Fig. 3 is extended to 100 s to observe the temperature stability inside the chamber, plus with additional supplied air speed parameter, as shown in Fig. 4. Interestingly to see that, with the same heat flux, lower air speed will increase the maximum internal chamber's stable temperature. However, lower air speed will also increase the time needed for the drying chamber to reach its stable temperature. It
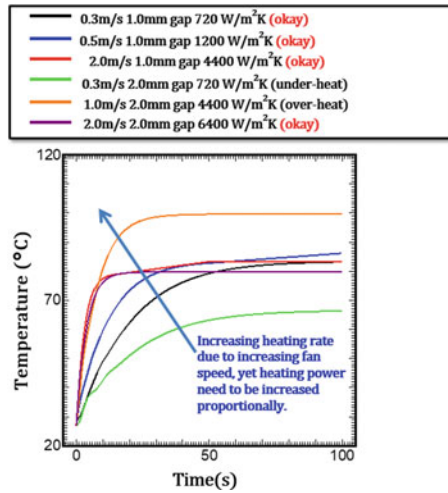
Fig. 4 Extended air heating time in the drying chamber

is assumed that it is possible to gain higher effectiveness up to 500%, when comparing between higher heat flux higher air speed with lower heat flux lower air speed drying chamber setting.

4 Conclusion

The study had proven that Finite Element Method can help to understand the behaviour of heating in a drying chamber. Following are the conclusion that can be made throughout the analysis.

- Increasing heat flux, heating effective range increases due to increasing heat flow rate.
- Decreasing fin gap, heat flux requirement decreases due to increasing heating effectiveness, yet material cost increases.
- Decreasing inlet air speed will decrease the heat flux requirement, but will increases the drying chamber heating time to reach the required temperature.

References

1. Hazervazifeh A, Nikbakht AM, Moghaddam PA (2016) Novel hybridized drying methods for processing of apple fruit: energy conservation approach. Energy 103:679–687
2. del Real-Olvera J (2016) Introductory chapter: principles of sustainable drying. In: Sustainable Drying Technologies
3. Adiletta G, Russo P, Senadeera W, Di Matteo M (2016) Drying characteristics and quality of grape under physical pretreatment. J Food Eng 172:9–18
4. Dehnad D, Jafari SM, Afrasiabi M (2016) Influence of drying on functional properties of food biopolymers: from traditional to novel dehydration techniques. Trends Food Sci Technol 57:116–131
5. Karam MC, Petit J, Zimmer D, Baudelaire Djantou E, Scher J (2016) Effects of drying and grinding in production of fruit and vegetable powders: a review. J Food Eng 188:32–49
6. Santacatalina JV, Soriano JR, Cárcel JA, Garcia-Perez JV (2016) Influence of air velocity and temperature on ultrasonically assisted low temperature drying of eggplant. Food Bioprod Process 100:282–291
7. Tajudin NH, Tasirin SM, Ang WL, Rosli MI, Lim LC (2019) Comparison of drying kinetics and product quality from convective heat pump and solar drying of Roselle calyx. Food Bioprod Process 118:40–49
8. Aral S, Beşe AV (2016) Convective drying of hawthorn fruit (Crataegus spp.): effect of experimental parameters on drying kinetics, color, shrinkage, and rehydration capacity. Food Chem 210:577–584
9. Pasban A, Sadrnia H, Mohebbi M, Shahidi SA (2017) Spectral method for simulating 3D heat and mass transfer during drying of apple slices. J Food Eng 212:201–212
10. Takougnadi E, Boroze T-ET, Azouma OY (2020) Effects of drying conditions on energy consumption and the nutritional and organoleptic quality of dried bananas. J Food Eng 268:109747
11. Onwude DI, Hashim N, Chen G (2016) Recent advances of novel thermal combined hot air drying of agricultural crops. Trends Food Sci Technol 57:132–145
12. Sasongko SB, Hadiyanto H, Djaeni M, Perdanianti AM, Utari FD (2020) Effects of drying temperature and relative humidity on the quality of dried onion slice. Heliyon 6(7)
13. Pornpraipech P, Khusakul M, Singklin R, Sarabhorn P, Areeprasert C (2017) Effect of temperature and shape on drying performance of cassava chips. Agr Nat Resour 51(5):402–409
14. Barreiro JA, Sandoval AJ (2020) Kinetics of moisture adsorption during simulated storage of whole dry cocoa beans at various relative humidities. J Food Eng 273:109869
15. Yu F, Li Y, Wu Z, Wang X, Wan N, Yang M (2020) Dehydration of wolfberry fruit using pulsed vacuum drying combined with carboxymethyl cellulose coating pretreatment. LWT 134:110159

Preparation and Water Absorption Analysis of Polyurethane Foam Reinforced Sawdust Composites

Tristan Joey Benjamin, Lih Jiun Yu, Darrell Arvin Thomas Raymond, and Nai Yeen Gavin Lai

Abstract Water absorption and structure of polyurethane foam being reinforced with sawdust was conducted by comparing the structure of the foam, which were the cell wall thickness and the cell size, against the properties of the foam which was the water absorbing and retention of the foam. The reason for reinforcing the foam with the filler is because polyurethane is not a water absorbing material and by reinforcing it with filler, that is water absorbent, it will help the polyurethane to be more water absorbent. Besides, this research will also determine the changes on the mechanical properties of the polyurethane foam. The combination of Polyol and Methylene Diphenyl Isocyanate (MDI) produced the Polyurethane Foam. The filler, sawdust, was then reinforced into the mixture and left to be hardened. Once hardened, the foam underwent multiple tests such as water absorption test and water retention test. This is to determine if the property change is a positive change or a negative change. It was found that, with the increase in cell size and cell wall thickness, there was an increase in water retention of the foam. As for the cell size and wall thickness of the foam, there was a decrease in water absorption, up till a certain amount of added filler content, then the water absorption increased.

Keywords Polyurethane foam · Sawdust · Mechanical Properties and Structure · Water Absorption and Retention

T. J. Benjamin · L. J. Yu (✉) · D. A. Thomas Raymond
Faculty of Engineering, Technology and Built Environment, UCSI University Kuala Lumpur Campus, No. 1, Jalan Menara Gading, UCSI Heights (Taman Connaught), 56000 Cheras, Kuala Lumpur, Malaysia
e-mail: yulj@ucsiuniversity.edu.my

N. Y. G. Lai
Faculty of Science and Engineering, University of Nottingham Ningbo China, 199 Taikang East Road, Ningbo 315100, China

1 Introduction

Polyurethane (PU) is a composite of polymer that are linked together through carbamate (urethane) joins [1]. Polyurethane is known to be a thermosetting polymer which means it would not soften easily. Therefore, polyurethane is commonly use in daily household items such as furniture, bed mattress and seating materials such as car seats and office chairs. Polyurethane is also a type of synthetic polymer that is produced by reacting monomers [2]. The monomers present contain a responding end groups which causes the diisocyanate (OCN-R-NCO) to form a reaction with the diol (HO-R-OH). It begins with having a linking between the two molecules at both ends which are reactive alcohol (OH) and reactive isocyanate (NCO). Therefore, the groups that were formed react more with other monomers hence forming a greater and lengthier molecule chain.

Sawdust, also known as wood dust, are mostly found to be the waste product of woodwork such as sanding, drilling, sawing and milling. Sawdust mostly consists of fine fragment of wood which can be sometimes lighter than dust. Moreover, sawdust consists mostly of cellulose, hemicelluloses, lignin and a small percentage of external materials. Chemical compounds also contribute to the creation of sawdust such as carbon, oxygen, hydrogen and nitrogen.

As of 2016, over 5.3 million tons of polyurethane foam were demanded to be used in furniture and has been increasing as time passes [3]. However, most polyurethane are hydrophobic and are not able to absorb water very well. Researcher Yu et al. [4] found that only 8% of water can be absorbed in comparison to the weight of the polyurethane foam. Furthermore, sawdust is disposed as a waste in timber industry, logging of trees in forest produces around 17% of sawdust [5] which is then just left on the ground.

In the past, many researchers conducted experiments to reinforce foam with fillers aimed to improve the properties of polyurethane. In Czlonka et al. [6] research on polyurethane foam reinforced with polyhedral oligomeric silsesquioxanes (POSS), it was found that the strength of the foam increased when 0.5 wt% of filler was added but decreased when anything more than 1.5 wt% of filler was added due to the uneven distribution of filler of the foam. In another research, where potato protein acted as the filler for the polyurethane foam, it was found that the by adding 0.1wt% of filler the strength of the foam increased but increasing the filler content any more caused a decrease in foam strength. This was due to the addition of filler which caused the number of closed cells to increase [7].

The main objective of this work is to investigate the effects of the incorporation of sawdust on to polyurethane on its water capabilities through image analysis. The correlation between the structural properties of the sawdust-polyurethane composite and the filler content was done in order to improve the water absorption properties of the closed-cell polyurethane composite.

Table 1 Polyurethane and polyurethane composite with varies sawdust filler

Sample	Filler (wt%)
Reference Sample (C)	0
Sample 1 (S1)	1
Sample 2 (S2)	2
Sample 3 (S3)	3
Sample 4 (S4)	4

2 Methodology and Experimental Setup

2.1 Preparation of Polyurethane Foam and Sawdust Filler

Polyurethane foam (PU foam) is prepared in two parts, Part A (VORACOR CD1095 Polyol which comes with a catalyst, HCFC-141b) and Part B (PAPI 27 Polymeric MDI). Both the parts are weighted separately using an electronic scale and then poured into the mixing cup. The mixture would then be allowed to rise freely at a stable condition at room temperature. The foam was left for 24 h in stable conditions to be allowed to fully form before taking any measurements and analysis and conducting any tests.

For preparation of sawdust polyurethane composite, the fine sawdust filler without surface treatment (1–4 wt%) was incorporated to the mixture of polyurethane during mixing process (Table 1). The ratio used in Part A and Part B was 1:0.65. Part A, Part B and the filler was then stirred until the mixture was fully mixed and was left for 24 h for curing to become solid state, before taking any measurements or conducting any tests.

2.2 Characterisation

Microstructure analysis

The structure of the polyurethane foam in this experiment relates to the pore size and the cell wall thickness. The sample microstructure was captured by using the Olympus BX51 at 10 × magnification. Image J software was used to determine the size of the cell and the thickness of the cell.

Water Absorption Test Characterisation

The water absorption test was conducted according to the ASTM D370 standards procedure. After that, the samples were immersed in water for 24 h and measured the mass. The water absorption was determined from the changes of mass over the pre-condition mass in percentage. Data was recorded up to 7 days.

Water Retention Test Characterisation

The same foams that were used in the water absorption test were used to conduct the water retention test. The foams samples that were immersed into water were later weighed at every 24th hour and continued being immersed in water for 7 days.

3   Results and Discussion

3.1   Cell Size and Cell Wall Thickness

The diameter of the cell and the thickness of wall were analyzed as there was a built-in measuring system in the Image J software from the microscope images of all samples as shown in Fig. 1. The PU foam cell structure was illustrated in schematic diagram Fig. 2. The cell size and wall thickness and average value obtained are shown in Table 2. It is clear that the average cell size will reduce when more sawdust filler was added into the mix. This is because the pores are generally in closed cell position. The addition of the sawdust filler into the mixture restricted the growth of foam during the expansion process, resulting in small cell size. This observation was in agreement with Czlonka et al. [6] and Lyu et al. [7], which suggested that the uneven distribution of fillers impacted the foaming process. Upon addition of sawdust filler, it was found that the strut wall thickness is reduced but then gradually increases when additional filler content was added. Such phenomena were due to fillers acting as nucleating site to promote the growth of wall thickness.

3.2   Relationship Between Cell Size and Water Absorption

Figure 3 shows a graph of the pore size against the water absorption of the polyurethane foam on 7th day. It was shown that the addition of 1 wt% and 2 wt% of the sawdust filler had caused a decrease in water absorption of around 500 percent compared to the reference sample (C). On the other hand, with the inclusion of 3%wt and 4%wt of the sawdust filler into the foam, the absorption rate of the foam increased by approximately 625 to 657 percent compared to 2 wt% sample (S2).

The water absorption of the foam had decreased for samples 0 wt%, 1 wt% and 2 wt%. This could be due to the number of closed cells because of the addition of sawdust filler. The filler behaves as a blockage that prevents most water particles from being absorbed by the foam [8]. Therefore, preventing the water particles from penetrating into the matrix of the foam thus limits the amount of water that the polyurethane foam can absorb. When the sawdust filler content increased to 3 wt% and 4 wt%, the water absorption increased to a slightly higher level than the reference sample (C). The reason behind this is due to the cell structure that is not uniform. The excess amount of filler content that causes the change to the foam structure will
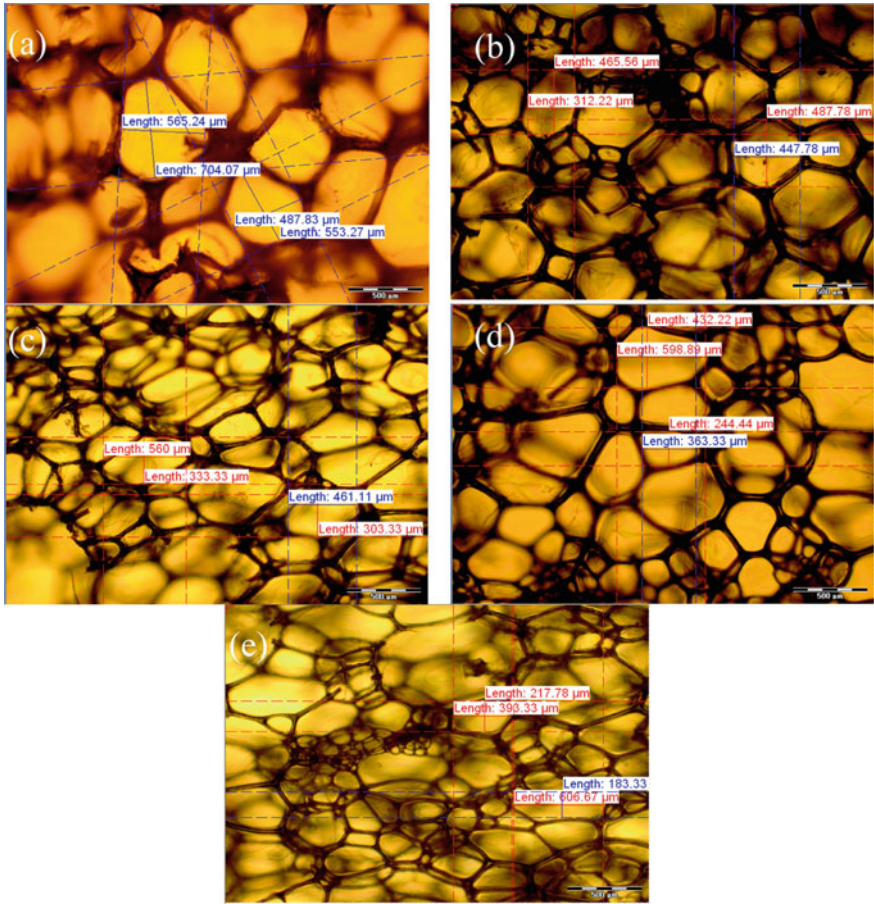
Fig. 1 Cell Size Diameter of PU Foam **a** C, **b** S1, **c** S2, **d** S3, **e** S4 (bar scale = 500 μm)

Fig. 2 Cell structure diagram
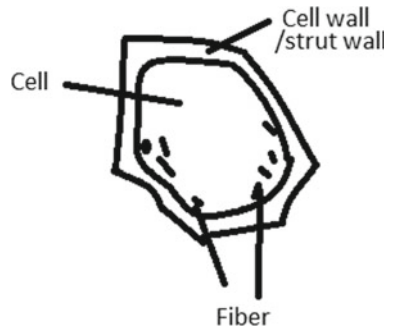
Table 2 Cell size average diameter and thickness

Specimen	C	S1	S2	S3	S4
Average cell size diameter (μm)	577.603	428.365	414.443	409.970	350.278
Average thickness (μm)	53.240	28.090	34.848	47.248	67.045
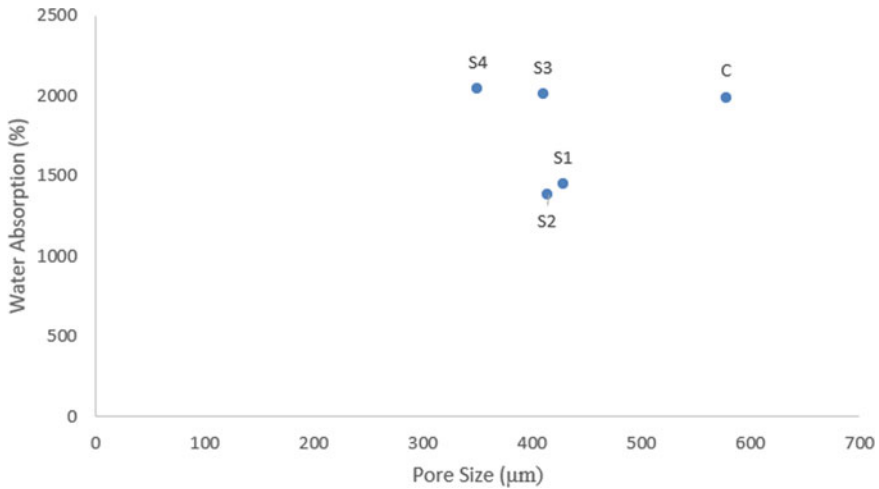
Fig. 3 Pore size of cell against water absorption of PU foam

eventually cause the cell structure to break [9]. The change in the foam structure creates more voids in the foam, which allows for water intake of the foam.

3.3   Relationship Between Cell Size and Water Retention

Figure 4 shows the graph of the cell size against the water retention of the polyurethane foam composite. With the increase in sawdust filler content, there was an increase in the water retention of the PU foam. Thus, a quadratic function is shown in Fig. 4.

The control sample could retain the second-highest amount of water in the foam relative to other samples. This is because there was no filler in the foam, the mixture's viscosity is low and allowing the foam to grow without any constraints. Hence, larger cells were able to form, and water can travel through the foam easily. Water increases the pore size, leading to an increase in the permeability of the foam [10]. For the foams that contained filler content, the increase in water retention could be attributed to the foam's cellular structure. The filler creates a disturbance in the cell structure, which eventually causes the cell wall to break [11]. Therefore, there is a disturbance to the foams matrix in which changes the foams forming process and eventually
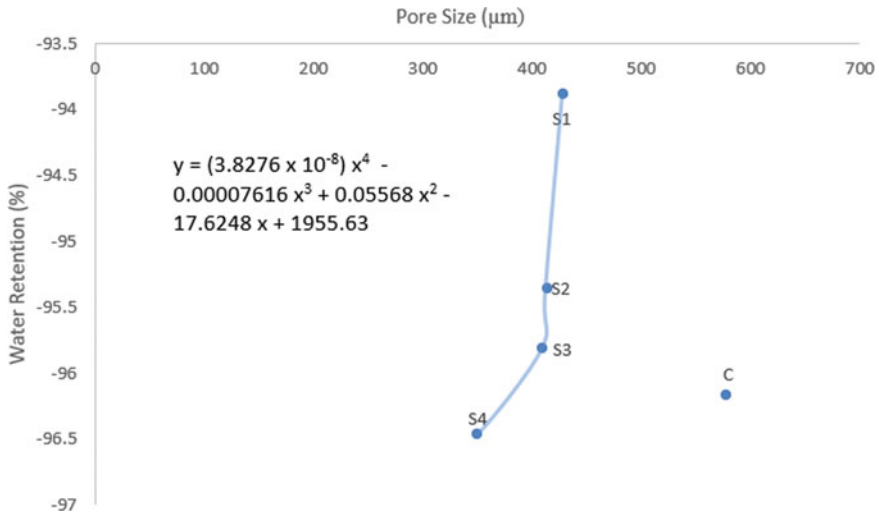
Fig. 4 Pore size of cell against water retention of PU foam

causing defects to the cell structure [12]. Thus, more water can be concealed in the cell structure of the foam.

3.4 Relationship Between Cell Wall Thickness and Water Absorption

Figure 5 shows the thickness of cell wall against the water absorption of the foam. It is clear that for the 0 wt%, 1 wt% and 2 wt% sawdust filler content samples, a decrease in water absorption of up to 541 percent compared to the cure sample was observed. However, for the sample with filler content of 3 wt%, an increase in water absorption is seen, similar to the reference sample (C).

When the filler content is 1 wt% and 2 wt% of sawdust filler, there was less water absorption. This can be due to the sawdust being a natural fibre. As the cell walls are symmetrical, the sawdust filler blocks the water from entering and exiting the foam. Sawdust filler acts as a blockage for the water as it is a natural fibre which has multiple layers of cellulosic microfibrils [13]. This causes water to take more time to penetrate the cell walls when moving in and out of the foam. As for the sawdust filler content of 3 wt% and 4 wt%, it was shown that there was an increase in water absorption. This could be because of the lamellae and plateau of the cell walls becoming thicker. As the walls become thicker, more irregular shapes starts to form in the foam [14] and because sawdust has hydrophilic properties [15], it will allow more water to be retained in the foam.
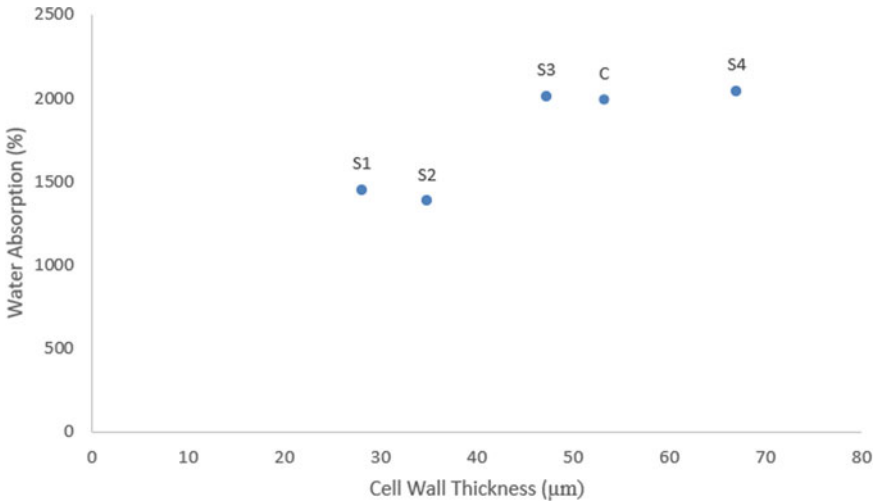
Fig. 5 Thickness of Cell wall against Water Absorption of PU foam

3.5 Relationship Between Cell Wall Thickness and Water Retention

Figure 6 shows the thickness of the cell wall against the water retention of the foam. Referring to the figure, the increase in sawdust filler from 1 wt% to 4 wt%, increases

$$y = 0.00001339x^4 - 0.002615x^3 + 0.188x^2 - 5.9404x - 25.7176$$
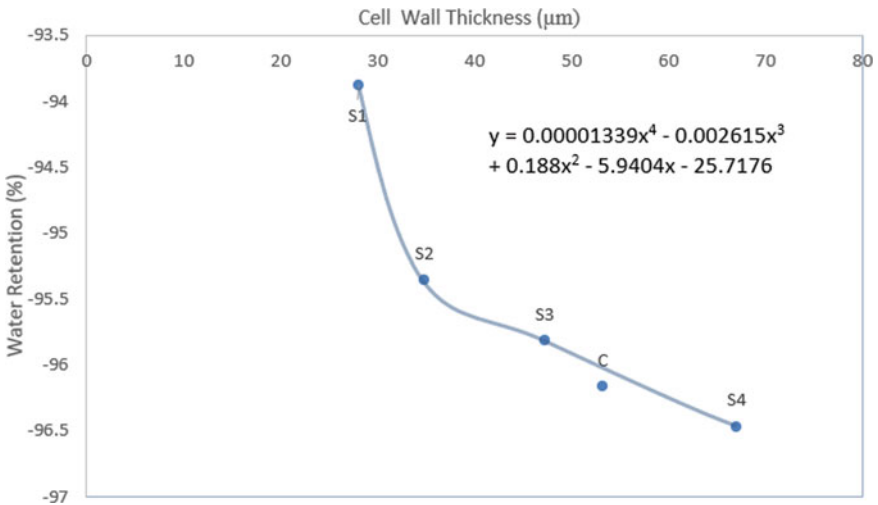
Fig. 6 Thickness of cell wall against water retention of PU foam

the cell wall and the water retention of the foam. A polynomial equation was shown in the Fig. 6.

The filler shown to have an increase of water retention with the cell walls increasing in size. This reasoning can be because of the fillers' properties. Sawdust contains cellulose fibers which allows the water to stay in three areas which are the lumen of the fiber, the cell walls and the spaces between the polyurethane and the fiber [16]. Thus, with the increase in sawdust filler, there is also an increase in the three areas as confirmed by Lin et al. [17]. This will allow the foam to create more space which will allow more water to be absorbed as well as retained by the foam. The reference sample (C) was shown to retain the second highest amount of water retention compared to the rest of the samples. This can be due to the theory of the foams' cellular structure. Since there is no presence of filler, the foam will be able to grow freely creating more open cells to be formed [18]. This allows more water to be retained in the foam due to the thick walls created by the foams' growth.

4 Conclusion

In this study, varying amounts of sawdust filler were used to reinforce the polyurethane foam. The addition of sawdust filler have a considerable effect on the water absorption properties of the material. The study shows that with the increased amount of filler content, there is an increase of the cell wall thickness, enabling an increase in water retention of all the foams. However, this was not the case for water absorption. It was observed for the cell size that the addition of sawdust filler of 1 wt% and 2 wt% had caused a decrease in water absorption. There was an increase in water absorption rate for the samples of sawdust filler of 3 wt% and 4 wt%. Similar results were observed in the cell wall thickness against the water retention rate. The reasoning behind the observations could be due to the filler acting as a barrier that prevents water from entering the foam. With the addition of more filler (in the 3 wt% and 4 wt% samples), it causes a deformation in the foam structure, leading to water being stored in the voids created by the filler. It was suggested that no surface treatment was performed on the saw dust. The study is limited to 1–4 wt% as high filler content resulting high viscosity of the mixture and restricted the foaming process. Further work could be focus on the usage of different saw dust particle size and treated saw dust particles.

References

1. Chauhan NPS, Nirmala KJ, Punjabi PB, Ameta R (2015) Polyuretanes: silicone-polyurethane copolymers. https://doi.org/10.1081/E-EBPP-120050554
2. Polyurethane (2020) How products are made. http://www.madehow.com/Volume-6/Polyurethane.html. Accessed 14 Apr (2020)
3. Properties P, Production P, Market, Uses (2019) Plastic Insight. https://www.plasticsinsight.com/resin-intelligence/resin-prices/polyurethane/. Accessed 14 Apr (2020)
4. Yu Y-J, Hearon K, Wilson TS, Maitland DJ (2011) The effect of moisture absorption on the physical properties of polyurethane shape memory polymer foams. Smart Mater Struct 20:085010
5. Jenkins JH (1933) Percentage of waste resulting from the conversion of the tree into lumber in the Southeastern Coast region of British Columbia
6. Czlonka S, Strakowska A, Strzelex K, Adamus-Wlodarczyk A, Kairyte A, Vaitkis S (2019) Composites of rigid polyurethane foams reinforced with poss. Polym 11(336)
7. Czlonka S, Bertino MF, Strzelec K (2018) Rigid polyurethane foams reinforced with industrial potato protein. Polym Test 68:135–145
8. Lyu Y, Yu LJ, Badri KH, Zulkoffli Z, Sajuri Z, Zulkefly MZF, Tarawneg MA (2020) Characterization of biomass-reinforced biopolyol based polyurethane foams. Int J Nanoelectronics Mat 13:95–106
9. Członka S, Strąkowska A, Kairyte A, Kremensas A (2020) Nutmeg filler as a natural compound for the production of polyurethane composite foams with antibacterial and anti-aging properties. Polym Test 86
10. Fawzi T, Yu LJ, Badri KH, Sajuri Z, Al-Talib AAM, Noum SYE (2021) Sodium hydrogen bicarbonate and water as blowing agent in palm kernal oil based polyol polyurethane foam. Mater Today Proc 30:993–998
11. Min LY (2020) Paper pulp reinforced polyurethane growing media. UCSI Univeristy, Thesis
12. Gu R, Konar S, Sain M (2012) Preparation and characterization of sustainable polyurethane foams from soybean oils J Am Oil Chem Soc 2103–2111
13. Bledzki AK, Gassan J (1999) Composites reinforced with cellulose based fibres. Prog Polym Sci 24(2):221–274
14. Xue B-L, Wen J-L, Sun R-C (2014) Lignin-Based rigid polyurethane foam reinforced with pulp fiber: synthesis and characterization. ACS Sustain Chem Eng 1474–1780
15. Islam MN, Islam MS (2013) Characterization of chemically modified sawdust-reinforced recycled polyethylene composites. J Thermoplast Compos Mater 28(8):1135–1153
16. . Karmaker AC, Hoffmann A, Hinrichsen G (1994) Influence of water uptake on the mechanical properties of jute fiber-reinforced polypropylene. J Appl Polym Sci 54(12):1803–1807
17. Lin Q, Zhou X, Dai G (2002) Effect of hydrothermal environment on moisture absorption and mechanical properties of wood flour. J Appl Polym Sci 85(14)
18. Thirumal M, Khastgir D, Singha N, Manjunath BS, Naik YP (2008) Effect of foam density on the properties of water blown rigid polyurethane foam. J Appl Polym Sci

Water Absorption and Tear Resistance Properties of Polyurethane Foam Reinforced with Recycled Paper Pulp

Ka Kit Lee, Lih Jiun Yu, Isaac Yu Jin Kwa, and Khang Wei Tan

Abstract The closed cell polyurethane foams acquire low surface hydrophilic characteristics in general. The incorporation of recycled paper pulp in polyurethane foams could significantly improve the water absorption and mechanical properties of the composite. In this study, the results revealed that the samples with 4 wt% of recycled paper pulp showed a significantly higher value in tear strength with an extension of 34.396 mm at break. The microstructure of samples was found in closed cell structure, they tends to reduce in cell size, i.e. from 577.60 µm to 390.28 µm after the addition of recycled paper pulp (from 0 wt% to 4 wt%). It was also revealed that the water absorption rate over a 7 days span was decreased despite the increase of filler content of the recycled paper pulp. Nevertheless, the water retention rate was improved significantly when the filler content of the recycled paper pulp increased.

Keywords Polyurethane (PU) · Polyurethane foams (PUFs) · Recycled paper pulp (RPP)

1 Introduction

Polyurethane foams (PUFs) are playing an important role in our daily life. They are developing to be versatile, and the sales of the commonly used products made of PUFs is continuously expanding in worldwide market [1]. It was evaluated that the overall worldwide consumption of PUFs was approximately RM 264.59 Billion in 2017 and it was anticipated to be RM 345.94 Billion in 2021 [2]. The PUFs are versatile and flexible. They can be used in various applications such as motor-vehicle,

---

K. K. Lee · L. J. Yu (✉) · I. Y. J. Kwa
Faculty of Engineering, Technology and Built Environment, UCSI University Kuala Lumpur Campus, No. 1, Jalan Menara Gading, UCSI Heights (Taman Connaught), 56000 Cheras, Kuala Lumpur, Malaysia
e-mail: yulj@ucsiuniversity.edu.my

K. W. Tan
School of Energy and Chemical Engineering, Xiamen University Malaysia, 43900 Sepang, Selangor, Darul Ehsan, Malaysia

manufacturing and construction [3]. PUFs can be easily obtained with affordable price. They are also durable and they do not wear out easily.

PUFs as insulating materials is the most widely used rigid PUFs in the current worldwide market due to its closed cell structure and hydrophobic nature which shows very little susceptibility to water uptake [4]. They post very low water absorptivity owing to the closely arranged cell structures which does not allow water to absorb. For open cell polyurethanes, water are permeable into the inner structure. However, the mechanical properties is weaken attributed to its structure characteristic. Reinforcing material is mixed into rigid PUFs mixture to reinforce the structure with some other enhanced properties. It is possible to modify mechanical characteristics and water absorbing characteristics physically, without changing the chemical structure of the rigid PUFs. PUFs acquired minimum surface hydrophilic characteristic [5]. The recycle paper pulp (RPP) has been chosen as a reinforcing material due to its great water absorbing characteristics [6]. Furthermore, reusing recycle paper pulp into alternative application is also a green approach to reduce material wastes.

This research study was conducted by incorporating varies RPP content into the PUFs via a one-step mixing method. Characterization was performed on the RPP/PUFs in terms of theirs morphology, water absorption properties and tear resistance properties.

2 Methodology and Experimental Setup

2.1 Sample Preparation

Figure 1 showed the research flow chart of this work. Polyurethane foam (PUF) consisted of two components, where Part A (VORACOR CD1095 Polyol) and Part B (PAPI 27 Polymeric MDI) in the mixing ratio of 1: 0.65 was prepared. Recycled paper pulps (RPP) were prepared from wet grinding, drying and sieving process. The

Fig. 1 Research flow chart
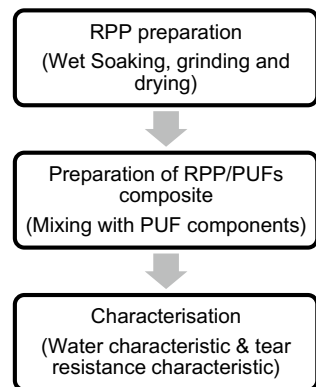
Table 1 Sample label and recycle pulp content

Sample name	Recycle paper pulp content (wt%)
CS	0
RS1	1
RS2	2
RS3	3
RS4	4

RPP/PUF composite were prepared by incorporating 0 wt%- 4 wt% RPP into the Part B, prior to the PUF foaming process. The mixture were allowed to foam and settle for a day before characterization. The samples were labelled as in Table 1.

2.2 Analysis and Testing of Polyurethane

Microstructure

The microstructure images of RPP/PUF composite were captured using optical microscope Olympus-BX51. Image analysis software Image J was used for image processing to obtain the morphology data.

Tear Resistance Test

Tear strength measurement of PUFs incorporated with RPP was conducted following the ASTM-D3574 Test F procedure. The RPP/ PUFs composite was cut into 152.4 mm × 25.4 mm × 6 mm (L × W × T). Then, both side of sample was clamp at respective jaw grips of machine symmetrically. A tear force of 46 kN and ramp speed of 500 mm/min was set. The results were recorded after the samples were torn completely.

Water Absorption Test

Water absorption test of PUFs incorporated with RPP was managed following ASTM-D570 procedure. The PUFs reinforced with RPP was cut into 42.5 mm (d) × 25 mm (h). Samples were pre-heated in oven at 60 °C to remove excessive moisture prior to weight measurement. Then, the samples were submerged in water, and soaked for a day to weight the water content in the sample. Water absorption test was repeated daily up to 7 days. The water absorption percentage was calculated based on the daily changes of the wet samples over the pre-heated sample's weight. The water absorption data on the 7th day was used in analysis.

Water Retention Test

The samples from the water absorption test were withdrew from the water and placed on net to dry naturally. The weight measurement was taken daily up to 7 days. The water retention percentage was calculated based on daily changes of water retained

sample's weight over the pre-dry sample's weight. The water retention data on the 7th day was used in analysis.

3   Results and Discussion

3.1   The Effect of Recycled Paper Pulp Loading On Polyurethane Foam Properties

Microstructure

The PUFs cell structure images of RPP/PUF samples were shown in Fig. 2. Cell size measurement was taken on the individual window of the PUF surface. The average cell size was tabulated in Table 2. From Fig. 2 and Table 2, it showed that the control sample (without filler) acquired highest average diameter and biggest in cell size. This is due to the low viscosity of the mixture in the absence of reinforcement material. The absence of RPP allowed cells to grow freely without any interference from viscosity [7]. It was noticeable that the cell size was reduced when the reinforcement material was incorporated into the system. This allowed the air bubbles to grow simultaneously and nucleated during the synthesis process. With increase of RPP content in PUFs, it changed the nucleation growth from homogenous to heterogeneous which reduced the nucleation's barrier.

With increase of filler content, the filler particles tends to agglomerate, distorted the cell growth hence resulting in cell dysplasia [8]. As a results, RS 4 with the highest filler content exhibited smallest cell size due to the rupture of structure in cell contributed by the high viscosity in the mixture. The agglomeration was found to be more exaggerated accumulate near the cell struts when higher RPP was incorporated.

Tear resistance test

The sample tear resistance results are displayed in Table 3. From Table 3, the samples with higher RPP content experienced longer extension length before the sample break. RS 4 was recorded to have highest extension value in all samples. The higher extension length at break was attributed to the microstructure presented. RS 4's microstructure displayed largest number of closed cells with smallest average cell size (Table 2). The existence of large number of closed cells with thick wall and struts highly enhanced the structure of PUFs [9]. Furthermore, RS 4 consists high filler content (4 wt%), it was found to have agglomeration distributed near the cell walls, possibly contributed positive mechanical reinforcement effects to the composite, resulted improvement in the sample's tear resistance. In general, the tensile strength of fiber reinforced PUFs were increased with increase of fiber loading [8]. An evenly scattering of reinforced material within the fibre-matrix could strengthened the walls and struts resulting in greater mechanical properties [9]. However, it was found that the changes of filler content had no significant impact on the load at break for all
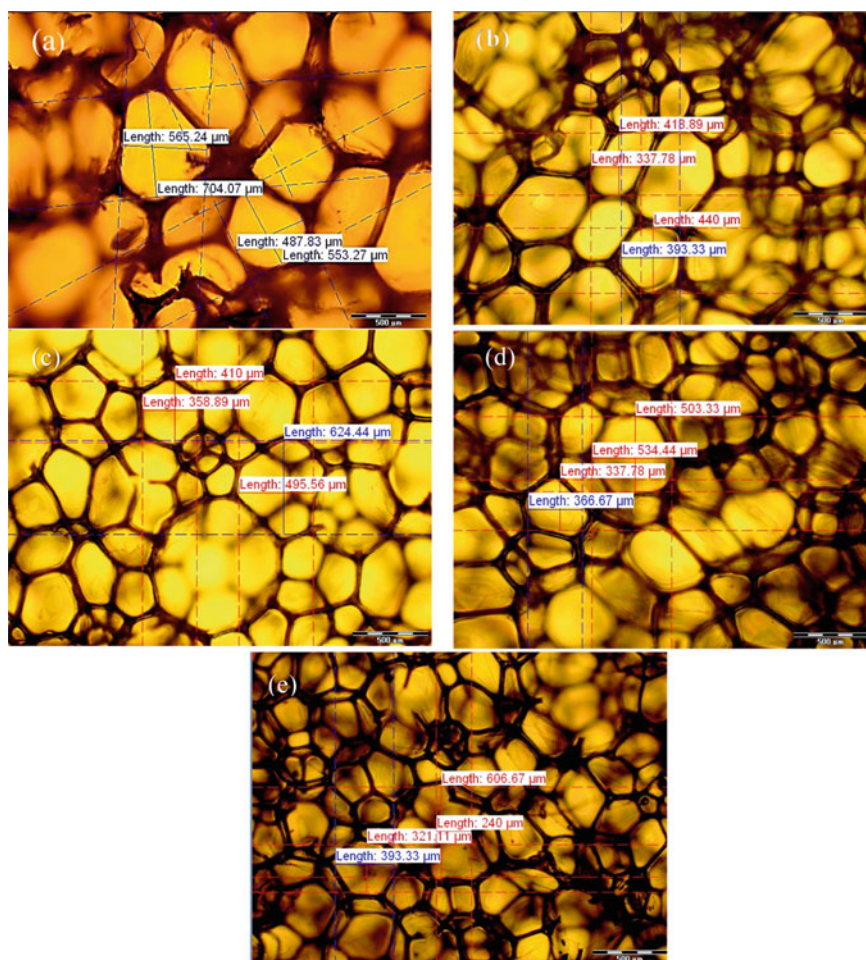
Fig. 2 Microstructure of RPP/PUF samples: **a** CS, **b** RS1, **c** RS2, **d** RS3, **e** RS4, scale bar = 500 (μm)

Table 2 Average diameter of cells of fabricated samples

PUFs	Average size diameter (μm)
CS	577.60 ± 78.43
RS 1	397.50 ± 38.23
RS 2	472.22 ± 100.54
RS 3	435.56 ± 80.96
RS 4	390.28 ± 136.20

Table 3 Tear test of
RPP/PUF samples

Sample	Extension (mm)	Load at break (N)
CS	19.397	46.739
RS 1	21.895	46.552
RS 2	21.896	46.451
RS 3	32.730	46.715
RS 4	34.396	46.612

RPP/PUFs samples. It was suggested that the slippage of short fiber RPP occurred during tearing process, the load might not be sufficiently transferred between the fiber-matrix.

The Relationship between Cell Size and Water Absorption

The relationship between cell size and water absorptivity rate of every reinforced samples shown in Fig. 3. It can be seen that increment of RPP filler content has no significant improvement in water absorption, where the incorporation of RPP showed lower water absorption rate, as compared to control sample. For closed cell structure PUFs, samples with cell size range between 400 and 500 µm, water absorptivity characteristics can be considered similar. There was a sudden hike in graph when cell size reached 577.6 µm, in which the water absorptivity rate increased significantly. The control sample acquired a larger cell size which allowed water to enter the cell structure easier [10]. This explains why control sample experiences highest water absorption uptake in comparison to other samples.

From Fig. 3, the addition of RPP from 1 wt% to 2 wt% caused reduction in water absorption rate, whereas the addition of reinforcing material increased the water absorption rate. The results was in disagreement with Ibrahim et al. [11], where
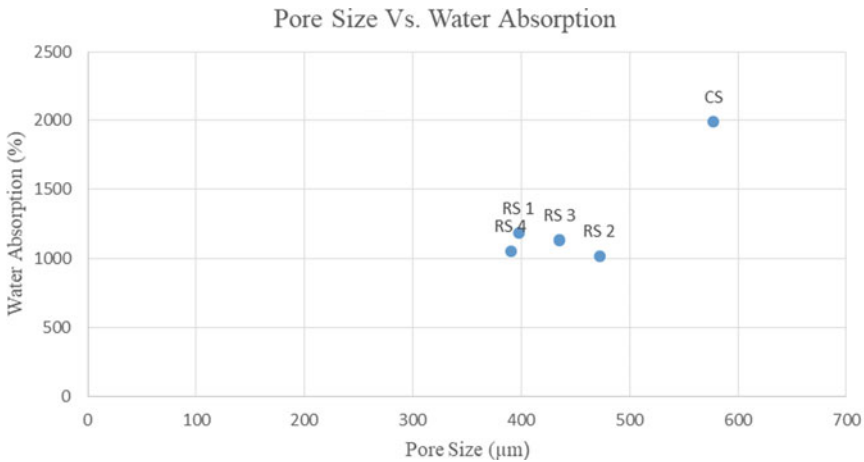
Fig. 3 Cell size versus water absorption

the water uptake rate of the empty fruits palm/recycle paper pulps increased with increase of recycle paper pulp content. This could be attributed to the reinforced material (RPP) acting as a barrier which stop water from entering the cell structure at low concentration. Nevertheless, with excess supply of reinforced material, it caused deformation in cell structure of PUFs which would eventually allow more water to store in voids created by the reinforcing material.

The Relationship between Cell Size and Water Retention

The relationship between the cell size and water retention rate of each reinforced samples was shown in Fig. 4. From Fig. 4, with cell size ranged from 400 µm to 500 µm, the water retention was fluctuating within a small range (i.e. 7–8%). There was a drastic decrement when the cell size reached 600 µm; the water retention rate decreased significantly. The genuine PUFs suffered greatest water loss among all the samples. From Fig. 4, the reinforced samples were recorded to have more favourable water retention rate compared to genuine PUFs. This could be due to the more compact and smaller cell size which increased the holding capacity of fluid in PUFs, the water molecules were encapsulated within the cell structure. As mentioned earlier, the absence of RPP as nucleation sites in genuine PUFs allowed cells to grow freely without interference from viscosity. This would cause genuine PUFs to acquire opened and bigger cell size. Thus, allowing water to enter and leave cell structure easily. The bigger cell size would form canals throughout the PUFs to ease the water drainage. Furthermore, RPP is a water absorbent which is rich in hemicellulose that help to retain more water [12], holding the moist within the cell structure thus delaying the evaporation process and drying rate process.
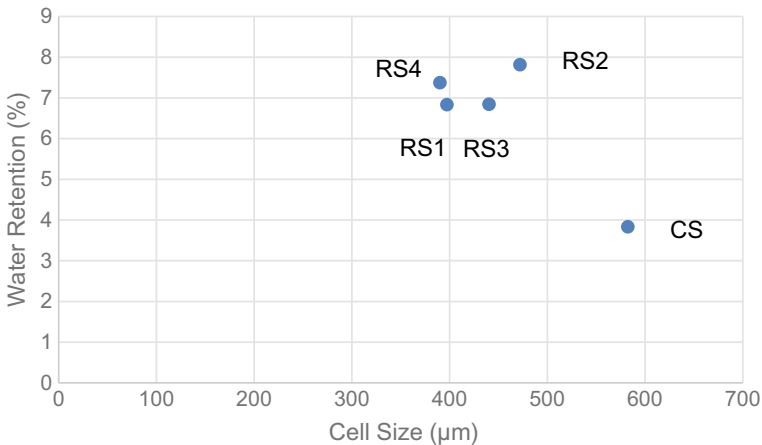
Fig. 4 Cell size versus water retention

4 Conclusion

Increment of RPP content improve the tear resistance, the samples experienced longer extension before break. The addition of RPP content has no signification improvement in water absorption and water retention properties. This could be explained that close cell structure formation of the synthesized PUFs. Addition of RPP decreased the cell size of PUFs, limiting the water molecules to permeable through the close cell structure. For water retention properties, RPP reinforced samples showed better water retention properties than control sample due to encapsulating effect of the cell structure and water absorption effect of the RPP. Further work could be done on the open cell structure PUFs in order to improve water absorption properties.

References

1. Zieleniewska M, Leszczynski MK, Kuranska M, Prociak A, Szczepkowski L, Krzyzowska M, Ryszkowska J (2015) Preparation and characterisation of rigid polyurethane foams using a rapeseed oil-based polyol. Ind Crops Prod 887–897
2. Gama NV, Ferreira A, Barros-Timmons A (2018) Polyurethane foams: past, present and future. Materials 1–35
3. Nikje MM, Noruzian M, Moghaddam ST (2015) Investigation of FE_3O_4/AEAP supermagnetic nanoparticles on the morphological, thermal and magnetite behavior of polyurethane rigid foam nanocomposites. Polimery 26–32
4. Kong LY, Li Y, Qiu FX, Zhang T, Guo Q, Zhang XY, Yang D, Xu J, Xue MW (2017) Fabrication of hydrophobic and oleophilic polyurethane foam sponge modified with hydrophobic AL_2O_3 for oil/water separation. J Ind Eng Chem 1–7
5. Oluwole OI, Avwerosuoghene OM (2015) Effects of cassava starch and natural rubber as binders on the flexural and water absorption properties of recycled paper pulp based composites. Int J Eng Technol Innovation 255–263
6. Bugosh J, Wilmington D (1960) Hydrophilic polyurethane foam structure and process. United States Patent Office, pp 1–4
7. Madaleno L, Pyrz R, Crosky A, Jensen LR, Rauhe JM, Dolomanova V, Norman J (2013) Processing and characterization of polyurethane nanocomposites foam reinforced with montmorillonite-carbon nanotube hybrids. Composites Part A 1–7
8. Lyu Y, Yu LJ, Badri KH, Zulkoffli Z, Sajuri Z, Zulkefly MZF, Tarawneg MA (2020) Characterization of biomass-reinforced biopolyol based polyurethane foams Int J Nanoelectronics Mat 13:95–106
9. Czlonka S, Sienkiewicz N, Kairyte A, Vaitkus S (2019) Colored polyurethane foams with enhanced mechanical and thermal properties. Polym Test 1–11
10. Czlonka S, Sienkiewicz N, Strakowska A, Strzelec K (2018) Keratin feathers as a filler for rigid polyurethane foams on the basis of soybean oil polyol. Polym Test 1–48
11. Ibrahim R (2003) Structural, mechanical and optical properties of recycled paper blended with oil palm empty fruit bunch pulp. J Oil Palm Res 29–35
12. Azevedo CA, Rebola SMC, Domingues EM, Figuriredo FML, Evtuguin DV (2020) Relationship between surface propertoes and fiber network paramenter of Eucalyptus Kraft pulps and their absorption capability. Surfaces 3:265–281

Influences of the Gate System Design on the Plastic Injection Molding Process

J. B. Saedon, Siti Sarirah Binti Mohamad Noh, and M. S. Adenan

Abstract Many factors influenced the final product of an injection molding process. All the factors are needed to be optimized to able to use the most optimum choice and produce a defect-less product. In this study, a series of gate system designs on the syringe's body was analyzed with a fixed dimensions and parameters values to obtain the most ideal design. The model was developed on CAD software, and the gate system was built in the CAE software. There were three different designs of the gate system; Design 1, Design 2, and Design 3. Then, a series of results were discussed and compared between all three designs. The main focused was how each design influenced the results, the whole process, and hence the final product itself. It was found that Design 2 was the most reliable gate system design. A design that has one injection location on each syringe and it's located at a discreet point of the body's surface.

Keywords Plastic injection molding · Gate system design · Gate location

1 Introduction

The plastic injection molding process is a commonly used process among plastic materials. It is a 300 billion market in the world that produces up to five million tons globally each year [1]. Although the process is costly at the beginning, it is already balanced out with having a low running cost for many years to come [2]. Thus, the process is preferably used across many industries in the world.

Plastic injection molding like many other processes has many factors that needed to be considered. A lot of past papers done in optimization analysis were to find optimum parameters for the product intended. Optimization is crucial to prevent

J. B. Saedon (✉) · S. S. B. Mohamad Noh · M. S. Adenan
School of Mechanical Engineering, Universiti Teknologi MARA, 40450 Shah Alam, Selangor, Malaysia
e-mail: jurisaedon41@uitm.edu.my

unnecessary defects occurred on products. Warpage, shrinkage, and weld lines formation are among the common defects in the process. It is very essential to optimize the process to have a consistent product quality [3].

Some of the major parameters that significantly influenced most defects are melt and mold temperature, holding pressure, injection pressure, injection time, and cooling time [3]. An example of the connection between the parameters and the defects is when given a low injection temperature and pressures, it will result in incomplete filling of the polymer. In other words, it caused a short shot, where the incompleteness is due to air existence inside the mold [4]. Other than that, having too much of a clamping force will also lead to insufficient air not able to vent out of the mold and ended up with a short shot defect as well [5].

Conversely for thin-walled products, injection speed, melt temperature, mold temperature, and injection pressure are insignificant factors to aid the warpage defect [6]. Warpage is mainly caused by the shrinkage variations on products during the injection process. A bad setup of the sprue-runner-gate system also can affect the part to warp excessively [7]. Unsuitable use of the size and geometry of the runner and gate system also can affect the internal and external parts of the product [8].

Many overlook the importance of having an optimized design of the gate system too. According to Mehdi Moayyedian, the cross-section of the gate is important to minimize the visible blemishes on the product and also to have a better flow of the molten pallets into the cavities [8]. The gate cross-section should also be small in size to prevent it from leaving a visible mark when demolding. Also, to avoid overfilled and underfilled in the mold, the runner dimensions must always be larger than the part attached [9].

Thus, this study aims to find the influences the gate system designs have on a disposable syringe's body. The gate system will be developed using a CAE software; Autodesk MoldFlow Insight and all dimensions and parameters will be fixed since the main aim is to observe the influence of the designs. The analysis results will show how each defect varies in each gate design and select which design is better among the three designs.

2 Methodology

2.1 Phase I: CAD Development

In this phase, the syringe's body was developed using CAD software; CATIA V5R21. This 3D model as shown in Fig. 1 was drawn out using the dimension from an existing disposable syringe. The syringe's body is only 70 mm in length with a thickness of 1 mm and a volume capacity of 5 ml.

The material used for this disposable syringe's body is Polypropylene (PP). It is a very common material to be used for disposable syringes and many other medical applications like pill containers, specimen bottles, etc. PP also was chosen because

Fig. 1 Developed 3D Model
of Syringe Body
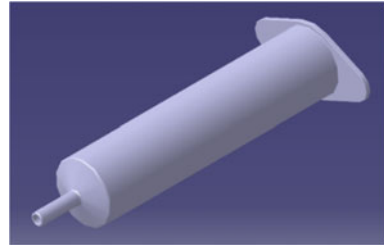
Table 1 Mechanical
Properties of Polypropylene
(PP)

Parameter	Value
Melt temperature (°C)	200–300
Injection mold temperature (°C)	10–80
Heat deflection temperature (°C)	157
Tensile strength (MPa)	55.2
Shrink rate (%)	1.5–3.0
Density (kg/m	904–908
Young modulus, E (MPa)	3520

of its good in bacterial and high chemical resistance. Table 1 shows some of the
mechanical properties for the used material; polypropylene.

2.2 Phase II: Developing the Gate System

The current research will have three types of runner designs, each with a different
injection location. All three designs have the same dimensions throughout the simu-
lation which are shown below in Table 2. The gate used in this research was the
tunnel gate shape. The dimensions for the gate system were chosen based on the
consideration of the gate shape which the tunnel gate usually acquired 50–80% of
the injected wall. While the runners were kept in union dimension despite in Design
1 and 2 have branch runners. This is to easier dictate which design has the most influ-
ence on the process wholly. The gate system was developed using a CAE software;
Autodesk MoldFlow Insight.

Table 2 Gate system dimensions

Sprue		Runner		Side Gates	
Orifice diameter	2.5 mm	Diameter	5 mm	Orifice diameter	2.5 mm
Included angle	3°			Included angle	7.07 mm
Length	30 mm			Angle	15°

A gating suitability analysis has been done before positioning the injection location on all three designs. The analysis result was shown in Fig. 2. The deep blue color remarked the best position to place the injection sprue. While the red color remarked the worst position to place the injection point.

As shown in the figures, Fig. 3a shows Design 1 of the gate system. In this design, the syringes were positioned in one horizontal line and were placed at the worst point area for injection location. Each syringe was connected by the runner and had each side gate on both sides of the plunger hole. This design was to test out the efficiency of using two side gates on each syringe instead of one. Although the gating suitability analysis has marked the area in.

Meanwhile, Design 2 and Design 3 are shown in Fig. 3b, c respectively, they were stacked in parallel, and the side gates were reduced to one at each syringe. The Design 2 injection location was also situated at the worst point area which was at the
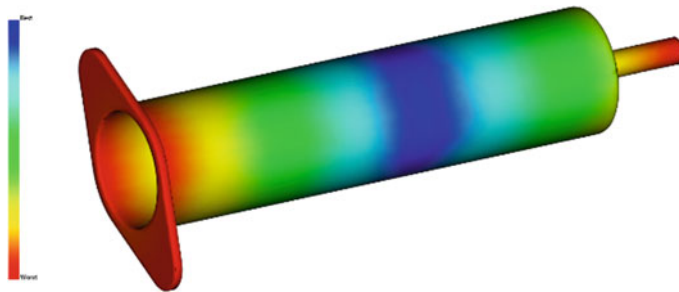
Fig. 2 Gating suitability analysis
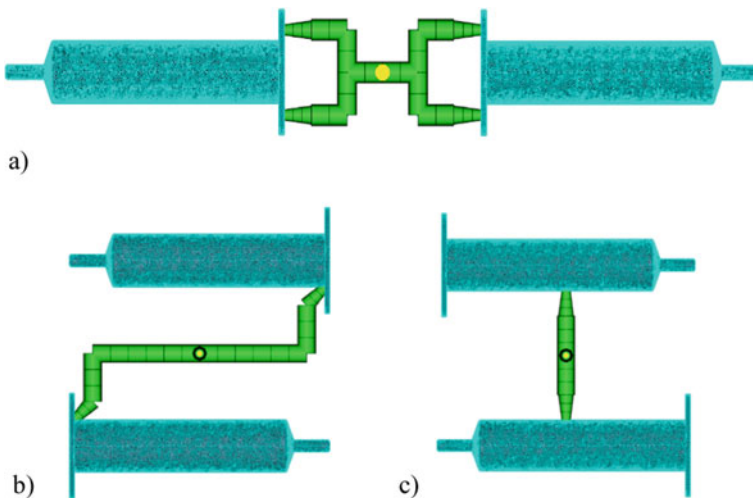
Fig. 3 Gate system design: **a** design 1; **b** design 2; **c** design 3

Table 3 Parameters value for the analysis

Parameters	Unit	Values
Mold Temperature	°C	50
Melt temperature	°C	220
Flow rate	cm^3/s	50
Injection pressure	Mpa	9
Cooling time	s	20

end corner of the barrel. For Design 3, the injection location was placed at the best location using a simple runner design that connected both syringes in the middle of the barrel.

Both Design 1 and 2 have been placed in the red zone location, although it was marked as the worst area. This is to fulfill the purpose of aesthetics features in the product. Since the best injection location would disturb the labeling on the barrel part of the syringe's body, Design 1 and 2 will be testing out the gate design in a more discreet position on the syringe's body. While Design 3 will be used to observe gate position on said best injection location.

2.3 Phase III: Simulation Process on CAE Application

Last but not least, for the third phase, the simulation analysis on those three designs had taken place. The simulation was also done in the same software to develop the gate system; Autodesk MoldFlow Insight.

All the simulations were done in the Fill + Pack + Warp sequence. The syringe has meshed with 123,703 elements. The parameter values which had the same values throughout three design analyses were filled on the process settings tab. The values can be referred on Table 3.

3 Experimental Results and Discussion

3.1 Fill Time

For this fill time result, it will show the time duration of the design took to become a finished product through the injection molding process.

As shown in Fig. 4, those are the results taken from each gate system design. For Design 1, the fill time was at 0.0267 s while for Design 2 was the longest among them was at 0.0323 s and the least one was Design 3 at 0.0233 s having a slight difference with Design 1.
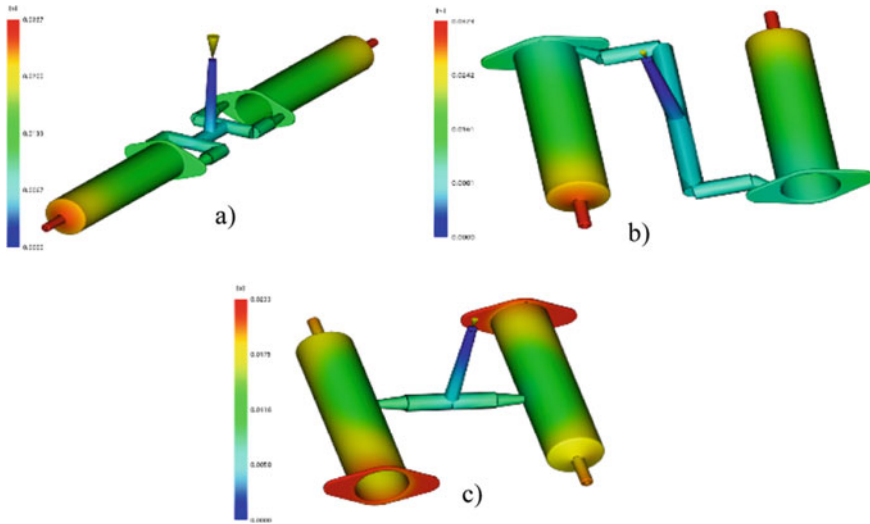
Fig. 4 Fill time results: **a** design 1, **b** design 2, **c** design 3

From the results, it can be observed that Design 3 has the shortest fill time. That shows a good sign for using a gate design that has a simple and forward runner connecting the syringes. Similarly shown by the result comparison done in the past paper by Yathish Kumar, whereby using a direct sprue for the type of gate produces the fastest fill time than the others tested [10].

A faster fill time is what to be achieved for in manufacturing mass products. Although having a slight difference of 0.001 s, it could make a huge difference in the total product produced in a day. Thus, for the gate system, the design should be taken in mind to be as simple as it could to achieve a good and least fill time.

3.2 Air Traps

Next is about air traps result. Air traps can cause short shot defects which usually occurred around the corner of a thin-walled product. These air traps are air bubbles that are stuck in between the product wall.

The air traps that occurred in the three designs can be seen circled in red in Fig. 5. All three designs showed that the air bubbles were on a similar area which was on the corner tip of the hub and at the corner of the plunger hole. However, only on Design 3 that the air bubbles were visible on some part of the barrel part of the syringe.

In comparison, all three designs have quite severe air bubbles trapped on the corner of the syringes' wall. Although air traps in inevitable, having the right gate system design could impose a great difference on the product [11].
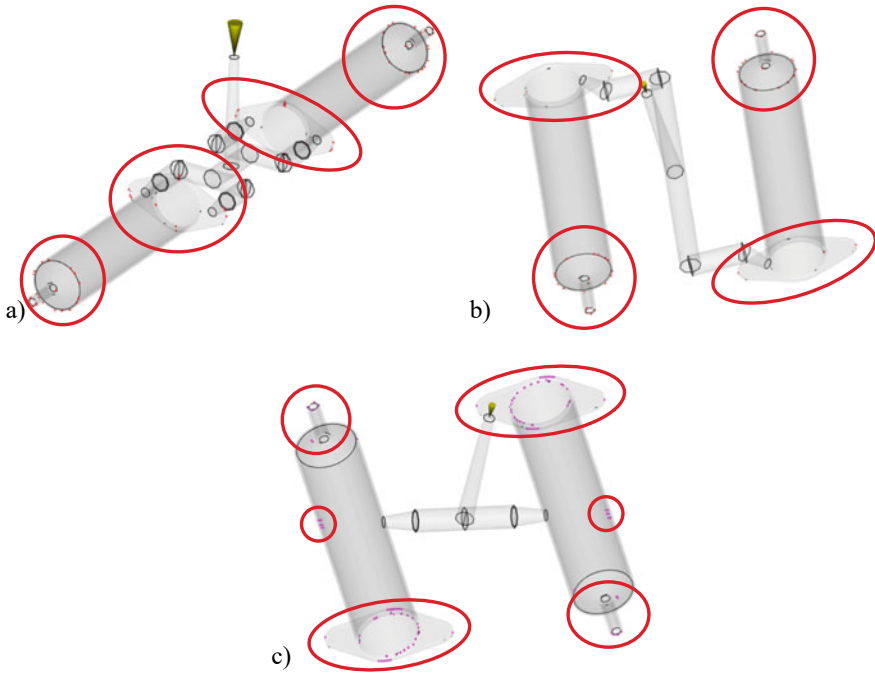
Fig. 5 Air traps result: **a** design 1; **b** design 2; **c** design 3

Design 3 had the most air bubbles on the syringe's body, despite having the fastest fill time among the three designs. This is due to the placement of the injection location where only Design 3 had the location on the barrel part of the body instead of on the area of the plunger hole. Thus, this can be said that injection location is important in reducing unnecessary air bubbles.

3.3 Weld Lines

Weld lines are one of the common defects in the injection molding process. This defect happened when two molten plastic injected intercept each other. It also easily occurs on a weak spot area of a product [12].

As shown in Fig. 6, weld lines in red circles occurred the most in Design 3. The corner had become the weak spot for the syringe because of the presence of air bubbles. Meanwhile, Design 2 has the least weld lines among the three.

Weld lines can also easily occurred when there is more than one injection location [12]. This explains why Design 2 has slightly fewer weld lines than Design 1. Although Design 3 has only one injection location on each syringe, the corner around the plunger hole has become a weak part due to the existence of air bubbles.
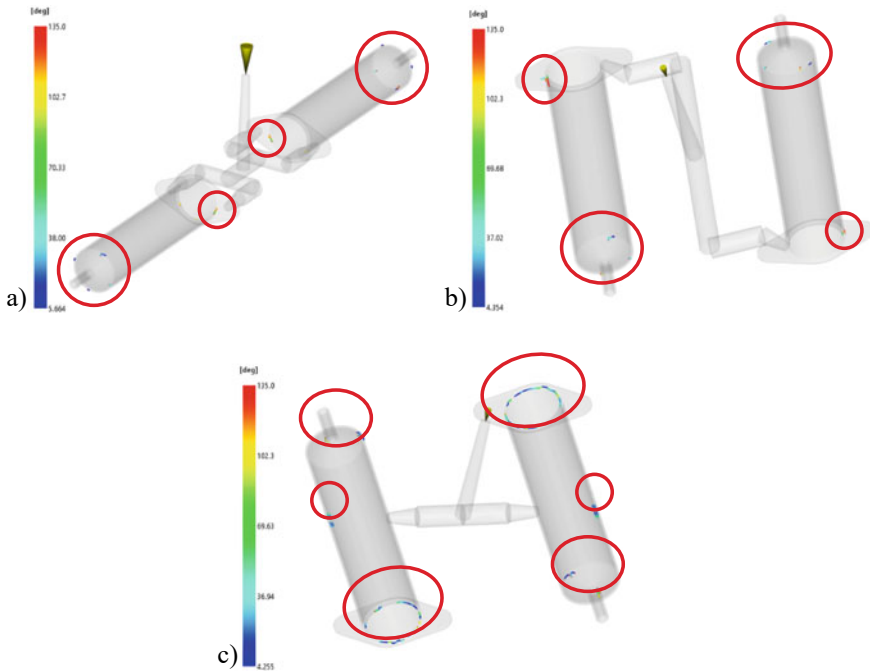
Fig. 6 Weld lines results: **a** design 1, **b** design 2, **c** design 3

In Design 2 and Design 1, the effect of using one or two injection locations can be seen around the plunger hole. In Design 2, the weld lines were spotted only on the opposite of the injection location whilst on Design 1 there were three spots of weld lines along the ring.

3.4 Sink Marks

In this result of sink marks, it is to observe at which part that will have a coagulated surface due to internal part of the wall had solidified first before the surface does. Sink marks usually occurred on the thick wall and are also detrimental defects for aesthetic products [13].

Based on Fig. 7, all three results showed the sink marks in the red circles occurred similarly at the corner that connects the syringe's barrel and the plunger hole. Designs 1, 2, and 3 had sink marks shaded at 0.0115 mm, 0.0121 mm, and 0.0246 mm each respectively.

Since sink marks are visible on the surface of the product, it is crucial to minimize them down to none. The sink marks position will affect the plunger to function properly with the syringe's body. Based on the results, Design 1 has the smallest sink
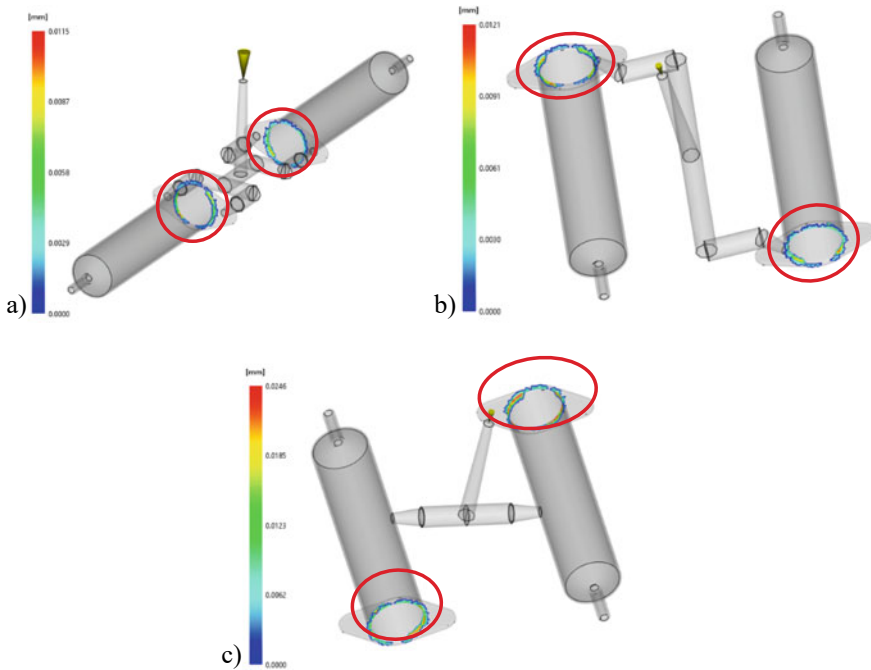
Fig. 7 Sink marks results: **a** design 1; **b** design 2; **c** design 3

marks on the syringe's surface, while Design 3 has the most among the three. This shows that having a two-injection location helps to reduce the sink marks better than one injection location.

3.5 Warp: Deflection All Effects

Last but not least for the result is the deflection or warp analysis. Warpage can be meant as a deformation of the product. It is the most common defect that happened in the plastic injection molding process.

For these three gate system, it can be seen as that the deflection occurred were not that significant. Based on Fig. 8, the worst reading in red-colored for Design 1, Design 2, and Design 3 were 0.1272 mm, 0.1285 mm, and 0.1246 mm respectively. Whilst for the minimum reading in deep blue color was 0.0225 mm, 0.0356 mm, and 0.0007 mm.

As seen in the results above, all three designs showed a very minimal deflection. Design 3 has the most minimal deflection of them all. All the readings were almost similar to each other and the pattern shown on the figures showed most of the least reading of deflection only.
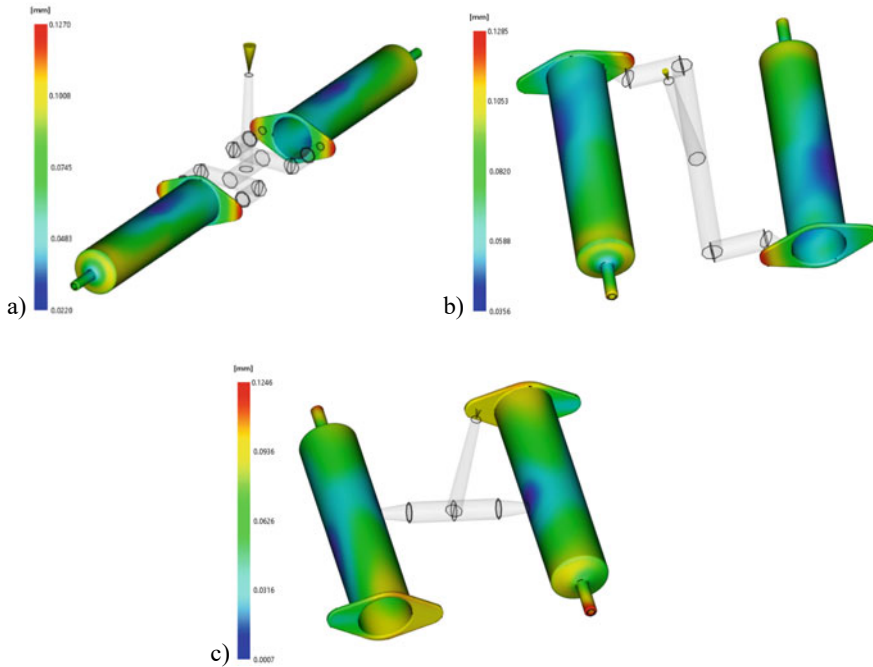
Fig. 8 Warp results: **a** design 1, **b** design 2, **c** design 3

Thus, from the result, it can be gathered that the gate system design does not affect significantly the deflection results.

4 Conclusion

In a nutshell, Design 1 has the least sink marks while Design 2 has fewer air bubbles trapped in the syringes and fewer weld lines among the other two. Design 3, has the fastest fill time and also the least deflection occurred on the syringe's body.

However, even though Design 3 may be the fastest in fill time, it has one other detrimental defect and that is on the gate system design itself. Although it was placed in the best position of injection location, the runner will leave out an obvious mark on the barrel surface after demolding. A simple runner is what to be achieved but a smooth body surface is crucial for syringes to have labels print out on their surface later on.

For Design 2, although not having the least fill time among the three, it triumphed on having the least air traps and weld lines. On the design side, although it is situated on the worst point for injection location, the position is much more discreet in having the inevitable mark from the gate system design.

Thus, this concludes that Design 2 is a more reliable gate system design and influenced a better-produced product for this simulation study. Any future works can be done in actual experimental work to proof the simulations studies done in this research.

References

1. Injection molding: The definitive engineering guide (n.d.) Retrieved 20 Jan 2021, from https://www.3dhubs.com/guides/injection-molding/#useful-resources
2. Ghazali WM, Idris DMND, Sofian AH, Siregar JP, Basrawi MF (2018) Gate location and injection analysis of a spur gear. MATEC Web Conf 225:1–10. https://doi.org/10.1051/matecconf/201822506012
3. Farooque R, Asjad M, Rizvi SJA (2020) A current state of art applied to injection moulding manufacturing process—a review. Mater Today Proceed 43:441–446. https://doi.org/10.1016/j.matpr.2020.11.967
4. De Miranda DA, Nogueira AL (2019) Simulation of an injection process using a cae tool: assessment of operational conditions and mold design on the process efficiency. Mater Res 22(2). https://doi.org/10.1590/1980-5373-MR-2018-0564
5. Huang MS, Nian SC, Chen JY, Lin CY (2018) Influence of clamping force on tie-bar elongation, mold separation, and part dimensions in injection molding. Precis Eng 51(September 2017):647–658. https://doi.org/10.1016/j.precisioneng.2017.11.007
6. Huang Y-T, Huang C-F, Peng B-Y, Chang C-W, Cheng H-C, Lin Y, Shen YK, Wang H (2020) Experimental and numerical study determining the warpage phenomenon of thin-wall injection molding. Adv Polym Technol 2020:1–13.https://doi.org/10.1155/2020/2914801
7. Nian SC, Wu CY, Huang MS (2015) Warpage control of thin-walled injection molding using local mold temperatures. Int Commun Heat Mass Transfer 61(1):102–110. https://doi.org/10.1016/j.icheatmasstransfer.2014.12.008
8. Moayyedian M, Abhary K, Marian R (2015) Improved gate system for scrap reduction in injection molding processes. Procedia Manuf 2(February):246–250. https://doi.org/10.1016/j.promfg.2015.07.043
9. Kale PD, Darade PD, Sahu AR (2021) A literature review on injection moulding process based on runner system and process variables. IOP Conf Ser Mater Sci Eng 1017(1). https://doi.org/10.1088/1757-899X/1017/1/012031
10. Kumar KRY, Nagaraja R (2014) Significance of mold filling analysis for finding optimal gate location in injection molding process for bobbin. Manufacturer 4(4):1–8
11. Mold M (2018) Troubleshooting short shot in plastic injection molding—midstate mold. Midstate Mold Eng. https://www.midstatemold.com/troubleshooting-short-shot-in-plastic-injection-molding/
12. Blog M (2018) Weld line in injection molding cause troubleshooting. Mechanicalengblog. https://mechanicalengblog.com/weld-line-in-injection-molding-cause-troubleshooting/
13. Knack O (2015) 11 Injection molding defects and how to prevent them. Retrieved 17 July 17 2019, from https://www.intouch-quality.com/blog/injection-molding-defects-and-how-to-prevent

Optimization of Quick Release Hanging Hook Design and Fabrication Using 3D Printing

K. Saptaji, M. A. Prayogo, H. N. Fauzah, L. A. Nugroho, C. L. Chan, and F. Triawan

Abstract 3D printing technology has been widely applied for academic research and industries. The 3D printing can be used for reverse engineering purpose such as to produce an existing object, components, or products. It can also be used to modify product development, such as improving simple or complex designs with higher endurance for its function. In this study, a quick release hanging hook design was developed and a prototype was fabricated using 3D printing with a thermoplastic material such as PLA. The quick release hanging hook needs to fulfill some requirements such as ease to be inserted and released from the bottom side of the pegboard, fit into 12.7 mm diameter of the hole and 3.81 mm pegboard thickness, and being able to carry and hold a minimum of 7 kg load. The 3D design was built and simulated to determine the strength. The simulation result by ANSYS software shows the maximum stress was not exceeded the yield strength of the PLA material and has a safety factor of 1.7. The proposed design was 3D printed using the FDM process and successfully achieved the 7 kg minimum load.

Keywords 3D printing · Finite element simulation · Fused deposition modeling (FDM) · Design optimization · Quick release hanging hook

1 Introduction

Additive manufacturing or 3D printing is widely used for fabricating complex geometries or structures from 3D model data [1, 2]. 3D printing is becoming a popular fabrication method to produce various plastic products ranging from small to large

K. Saptaji (✉) · M. A. Prayogo · H. N. Fauzah · L. A. Nugroho · F. Triawan
Department of Mechanical Engineering, Faculty of Engineering and Technology, Sampoerna University, Jakarta 12780, Indonesia
e-mail: kushendarsyah@sampoernauniversity.ac.id

M. A. Prayogo · H. N. Fauzah · L. A. Nugroho · C. L. Chan
Department of Aerospace and Mechanical Engineering, College of Engineering, The University of Arizona, Tucson, USA

sizes, especially in the innovation stage [3–5]. This "layer-by-layer" additive manufacturing technique allows customized products [6] and minimizes material use [7]. For instance, it has been applied for rapid prototyping purposes in robotics, medical, and vehicle components [8–10]. The application of 3D printing becomes broader due to the sharply decreased of cost in the past five years, while its performance has notably increased [11]. In addition, many developments of new 3D printing machines using various mechanisms have been performed such as using H-Bot [12]. Therefore, the 3D printing machine is suitable for product prototyping.

One of the products that can be produced by 3D printing is a custom quick release hanging hook used in a pegboard. In recent years, the combination of a pegboard and the hook is a popular choice to hang a variety of objects. It is space-saving, displayable, affordable, portable, neat, etc. Fused Deposition Modelling (FDM) is one of the additive manufacturing methods for printing 3D-designed objects layer by layer which having low-cost and can be conducted with various materials, such as Polylactic Acid (PLA), Acrylonitrile butadiene styrene (ABS), *thermoplastic polyurethane (TPU)* [13].

This paper aims to design and optimize quick release hanging hooks and fabricate the prototype using a 3D printing. The proposed hanging hook is specified for a heavy-duty pegboard installed on the ceiling. The requirements of the hook design can be installed and removed in few seconds, released from the pegboard bottom side only, and capable of holding a minimum of 7 kg weight. Each hole of the pegboard has a 12.7 mm diameter and 3.81 mm thickness. The present work can be used as a case study in learning the manufacturing processes course, mainly additive manufacturing topics and its application in rapid prototyping for engineering students.

2 Methodology

The method to produce a quick release hanging hook can be divided into the following stages, (i) concept design, (ii) finite element simulation, (iii) 3D printing, and (iv) load testing. The designing process was conducted by a literature review study from various resources. The designing process was conducted using SolidWorks software. Subsequently, a stress analysis simulation of the design was conducted to obtain and understand the distribution of stress when the load was applied to the object. The hanging hook design was then fabricated using 3D printing. Once the prototype was ready, load testing was conducted by installing the 3D printed proposed quick release hanging hook onto the ceiling pegboard dan applying the load on the hanging hook. The testing performed to confirm that the proposed quick release hanging hook can fulfill the requirements and validate the simulation results.
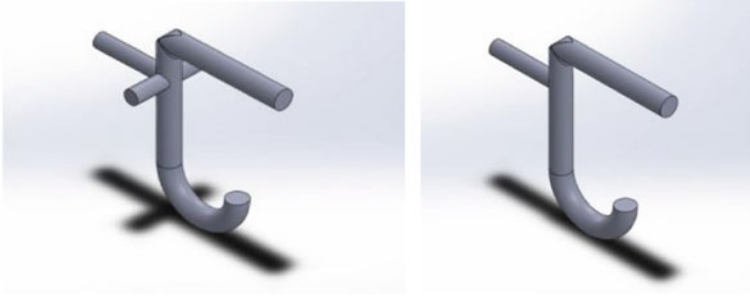
Fig. 1 Design candidate 1 (left) and candidate 2 (right) of the quick release hanging hook

2.1 Concept Design

There are specific requirements of the design for the hanging hook used for the ceiling pegboard. As the pegboard is installed at the ceiling, the hanging hook can only have access from the bottom, which means it can only be installed or uninstalled from the bottom side of the pegboard. Moreover, it also must fit into a 12.7 mm diameter of hole and 3.81 mm pegboard thickness. The hanging hook must be easily inserted and released from the pegboard (quick release hanging hook). In addition, this hanging hook must carry and hold a minimum of 7 kg load.

In this study, the iterative process of designing was conducted in which resulted in two design candidates. The 3D model of the hook was developed using SolidWorks software. The two design candidates are shown in Fig. 1.

The proposed design was inspired by the letter "J." However, it was added with additional features for the ease of installation and removal from the pegboard. In addition, the elements were also added to make sure the hanging hook can carry the required load. Each design has a diameter of 8.0 mm, which met the design's requirement, where it has to be fit into a 12.7 mm pegboard's hole, while the additional features have a diameter of 6.0 mm. However, design candidate two is selected as the final design due to its simplicity, and also it is expected to be easier for fabrication using 3D printing. Figure 2 shows the detailed dimensions of the design candidate 2.

2.2 Finite Element Analysis

The finite element simulation was conducted using ANSYS workbench software. The static structural analysis was used to determine the capability of the design to hold at least 7 kg of load. Polylactic Acid (PLA) is selected as the material for the hanging hook, similar to the material for 3D printing. The material properties of Polylactic Acid (PLA) are shown in Table 1.
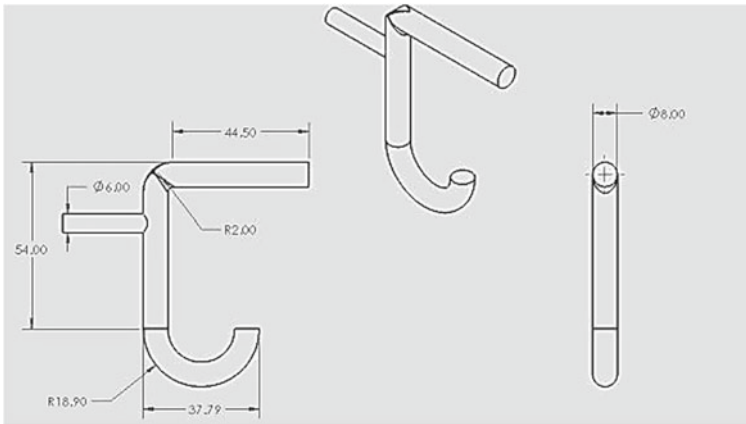
Fig. 2 The dimension of the design candidate 2 (in mm)

Table 1 Material properties for PLA

Properties	Value	Unit
Density	1.25e − 06	kg/mm^3
Poisson's Ratio	0.3	–
Young's Modulus	3.45	GPa
Thermal Conductivity	0.000144	W/mm °C
Specific heat	1.19e + 06	mJ/kg °C
Tensile Yield Strength	54.1	MPa
Tensile Ultimate Strength	59.2	MPa

The simulation setup with the boundary conditions and applied load is shown in Fig. 3. The top part is set to be fixed since the actual application of the upper part is placed into the pegboard hole. At the same time, the load applied at the bottom part with a force of 68.67 N or equal to 7 kg.

2.3 3D Printing Process

The fused deposition modeling (FDM) 3D printing method is used to fabricate the proposed hanging hook design prototype. Anycubic I3 Mega is used for printing the design with the filament material selected is *Polylactic Acid (PLA)* (Fig. 4). In order to fulfill the requirements, the 3D printed heavy-duty hanging hook was made of 100% PLA. PLA, a biodegradable thermoplastic, is made out of fermented plant starch [14, 15]. This material was chosen because of its commonness and had high tensile strength [16, 17]. Even though build orientations and heat treatment also affect the mechanical properties of 3D printed PLA material, especially the yield strength,
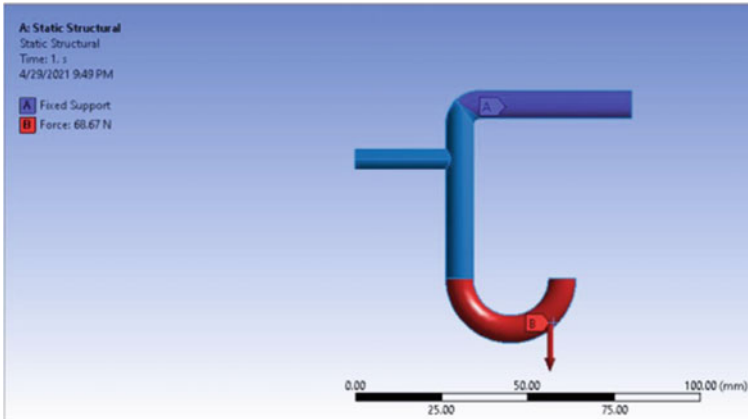
Fig. 3 Boundary conditions used for static structural analysis

Fig. 4 Anycubic I3 Mega
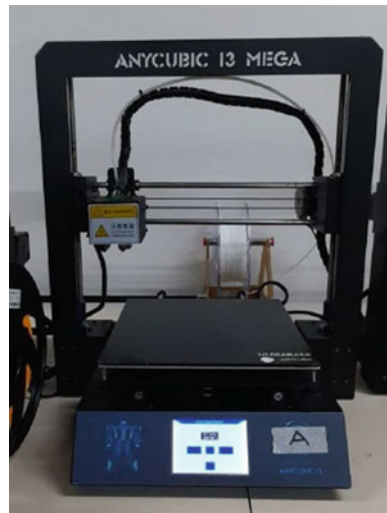
ultimate strength, and elastic modulus [18]. In addition, PLA can also be recycled and be used again as a 3D printing filament [19]. It is known that the price of plastic 3D printing materials such as PLA and ABS is considered to be low around $21.00 per kg. Then, the design file created in Solidworks and simulated in ANSYS had then converted the format to *.stl* to be used for 3D printing. Subsequently, CURA software was used to set the 3D printing parameters.
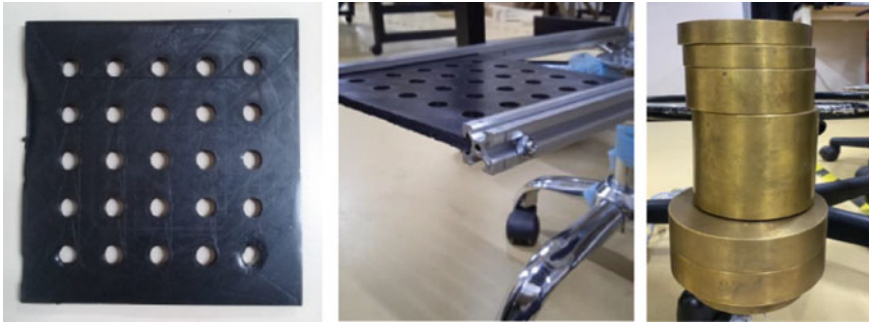
Fig. 5 Pegboard used in this experiment (left), pegboard positioned vertically to represent when installed in the ceiling (middle) and 7 kg load (right)

2.4 Load Testing

Experimental work conducted to examine the performance of the 3D printed quick release hanging hook. The hanging hook tested to observe the easiness during the insert and release from the bottom of the pegboard as one of the design requirements (quick release). In addition, once the hanging hook settled in the pegboard from the bottom, a load of about 7 kg was hanged at the bottom part of the hanging hook for testing the hanging hook's strength. Figure 5 shows the pegboard and load used in this experiment.

3 Results and Discussion

The selected design candidate, design candidate two, was analyzed using ANSYS workbench, fabricated using 3d printing process and load testing.

3.1 Finite Element Simulation

The static structural simulation result presented in Fig. 6. As can be seen in Fig. 6, the maximum stress occurred is 31.423 MPa. The maximum stress is at the elbow located at the upper section of the hanging hook. The maximum stress occurred at that location because this elbow has a right angle (90°) and located at the upper side and periphery of the pegboard hole. This position can be considered as critical and high-stress concentration. In addition, the maximum stress value does not exceed the tensile yield strength value of the PLA material. It implies that this design can withstand the 7 kg applied load.
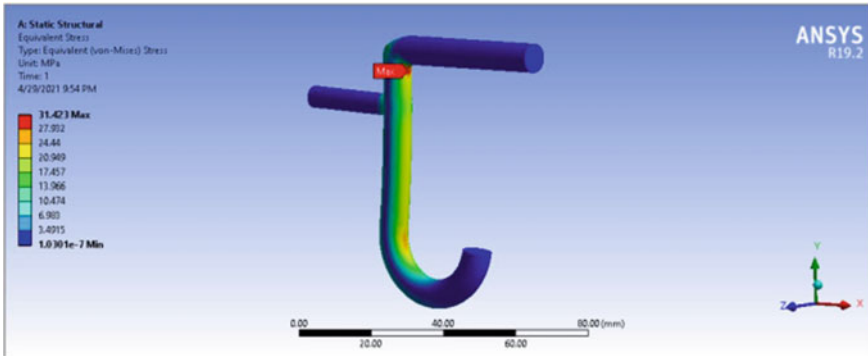
Fig. 6 Static structural simulation result

The safety of factors can also be calculated using ANSYS software. The safety factor is presented in Fig. 7. The safety of factor value obtained from the simulation is approximately 1.7 with attaching a load of 68.67 N. It implies that the proposed design can hold 7 kg + 70% of 7 kg or equal to 11.9 kg load. However, the simulation performed in the ideal condition with no defect or internal crack during the printing process. The defect or internal damage may affect the strength of the hanging hook. Hence, the maximum allowable load for the hanging hook is less than 11.9 kg, but it can still hold 7 kg of load.
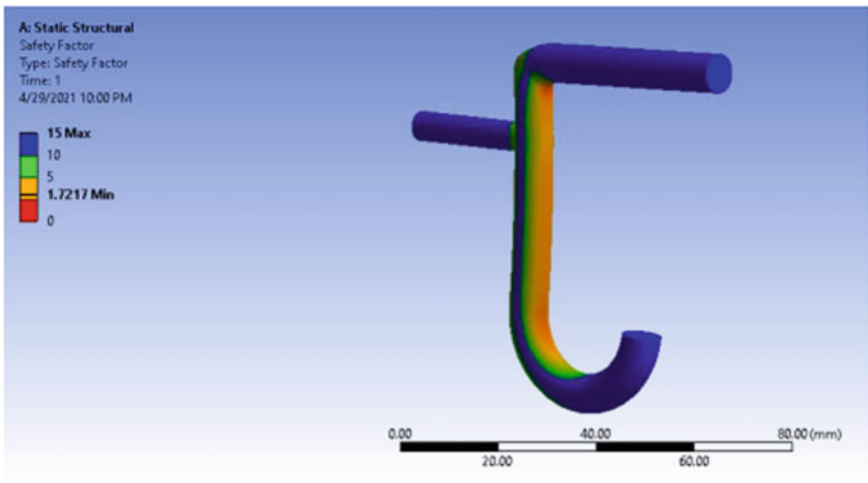
Fig. 7 Safety of factor analysis of the design

3.2 3D Printing Process

The 3D printing process using Anycubic I3 Mega is shown in Fig. 8. The printing parameters used are layer thickness of 0.2 mm, infill density of 70%, infill pattern zig zag, print speed of 50 mm/s, time of 44 min, and temperature of 200 °C. The selection of parameters can affect the hanging hook capability in carrying the load. Increasing the layer thickness could affect the strength, modulus elasticity, and loads that can be accommodated by the hanging hook [20]. The density determines the mechanical strength and stiffness of the design and the material filling in making the layers [16, 21]. The higher the value of density, the more compact and solid the object. However, the weight of the hook would be higher and decrease the design effectiveness; therefore, the density chosen to be 70%. Figure 9 shows the 3D printed hanging hook. The hook has a "J" letter with dimensions of 8 mm of thickness and 9 g of weight.

Fig. 8 Printing process
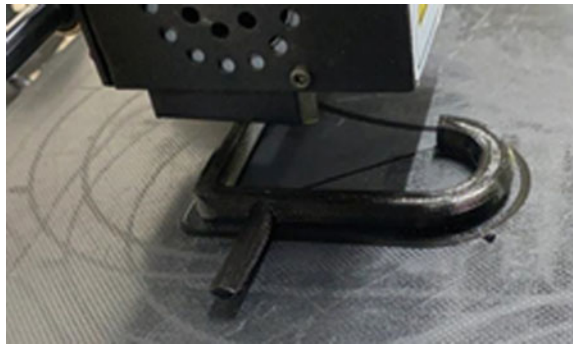
Fig. 9 Result of 3D printing

Fig. 10 Pegboard position during the test (left), installation of hanging hook onto the pegboard from the bottom (middle), load testing applied on the hanging hook (right)

3.3   Load Testing

After the printing process, a load testing experiment was conducted. The load testing was performed to confirm the design fulfilled the requirements and hung with a load of about 68.67 N or 7 kg. Figure 10 shows the experimental setup. The pegboard was positioned horizontally, and then the hanging hook was inserted from the bottom hole of the pegboard. Practically, during the insertion and removal, the 3D printed hanging hook was considered a quick and convenient process without effort. The insertion and removal time for the hanging hook is around 2 s. It proves that the proposed design fulfilled the requirement of "quick release."

Figure 10 also shows the proposed quick release hanging hook was tested with the 7 kg load. The load was applied by tying up the cylindrical weight to a rope. Another end of the rope was used to tie up to the hanging hook. The hanging hook was able to carry the required load without failure. Hence the design of the quick release hanging hook was successful in fulfilling the strength requirement.

4   Conclusion

In this work, a prototype of a hanging hook that can quickly be inserted and released from the bottom part of the horizontal pegboard was developed and fabricated. The proposed design was able to fulfill the requirements defined as (i) can be easily inserted, and release from the bottom side of the pegboard (quick release hanging hook), (ii) fit into 12.7 mm diameter of a hole, and 3.81 mm pegboard thickness, and able to carry and (iii) hold a minimum of 7 kg load. The simulation result shows the maximum stress does not exceed the yield strength of the PLA material and has a

safety factor of 1.7. The proposed design was 3D printed using the FDM process and successfully achieved the 7 kg minimum load. In addition, the present work could also be helpful for lecturers in demonstrating the application of 3D printing in rapid prototyping to mechanical engineering students.

References

1. Ngo TD, Kashani A, Imbalzano G, Nguyen KTQ, Hui D (2018) Additive manufacturing (3D printing): a review of materials, methods, applications and challenges. Compos Part B Eng 143:172–196
2. Gokhare VG, Raut DN, Shinde DK (2017) A review paper on 3D-printing aspects and various processes used in the 3D-printing. Int J Eng Res Technol 6
3. Candi M, Beltagui A (2019) Effective use of 3D printing in the innovation process. Technovation 80–81:63–73
4. Shahrubudin N, Lee TC, Ramlan R (2019) An Overview on 3D printing technology: technological, materials, and applications. Procedia Manuf 35:1286–1296
5. Fan D et al (2020) Progressive 3D printing technology and its application in medical materials. Front Pharmacol 11:122
6. Sun (2020) Preliminary study on personalized customization service platform based on 3D printing technology* BT. In: Proceedings of the 4th international conference on culture, education and economic development of modern society (ICCESE 2020), pp 1440–1443
7. Liu Z, Jiang Q, Zhang Y, Li T, Zhang H-C (2016) Sustainability of 3D printing: a critical review and recommendations
8. Castiblanco PA, Ramirez JL, Rubiano A (2021) Smart materials and their application in robotic hand systems: a state of the art. Indones J Sci Technol 6(2)
9. Triawan F, Denatra G, Djamari DW (2020) Quasi-static compressive properties and behavior of single-cell miura origami column fabricated by 3D printed PLA material. Int J Sustain Transp Technol 3:66–73
10. Oladapo BI, Ismail SO, Afolalu TD, Olawade DB, Zahedi M (2021) Review on 3D printing: fight against COVID-19. Mater Chem Phys 258:123943
11. Rayna T, Striukova L (2021) Assessing the effect of 3D printing technologies on entrepreneurship: an exploratory study. Technol Forecast Soc Change 164:120483
12. Hadisujoto B, Wijaya R (2021) Development and accuracy test of a fused deposition modeling (FDM) 3D printing using H-Bot mechanism. Indones J Comput Eng Des (IJoCED) 3(1)
13. Wilson S, Thomas R, Mary N, Bosco ET, Gopinath A (2021) Development and fabrication of fused deposition modelling 3D printer. IOP Conf Ser Mater Sci Eng 1132(1):012019
14. Catana D, Pop M-A, Brus D-I (2021) Comparison between the test and simulation results for PLA structures 3D printed, bending stressed. Molecules 26(11):3325
15. Kim H, Park E, Kim S, Park B, Kim N, Lee S (2017) Experimental study on mechanical properties of single- and dual-material 3D printed products. Procedia Manuf 10:887–897
16. Rismalia M, Hidajat SC, Permana IGR, Hadisujoto B, Muslimin M, Triawan F (2019) Infill pattern and density effects on the tensile properties of 3D printed PLA material. J Phys Conf Ser 1402:44041
17. Hanon MM, Marczis R, Zsidai L (2021) Influence of the 3D printing process settings on tensile strength of PLA and HT-PLA. Period Polytech Mech Eng 65(1):38–46
18. Fatchurrohman N, Noor Hamdan NNN, Gebremariam MA, Saptaji K (2020) Investigation on the effect of build orientation and heat treatment on tensile strength and fracture mechanism of FDM 3D printed PLA BT—iMEC-APCOMS 2019, pp 461–465
19. Babagowda RSK, Goutham MR, Srinivas Prasad KR (2018) Study of effects on mechanical properties of PLA filament which is blended with recycled PLA materials. In: IOP Conf Ser Mater Sci Eng 310:12103

20. Nugroho A, Ardiansyah R, Rusita L, Larasati IL (2018) Effect of layer thickness on flexural properties of PLA (PolyLactid Acid) by 3D printing. J Phys Conf Ser 1130(1)
21. Giri J, Chiwande A, Gupta Y, Mahatme C, Giri P (2021) Effect of process parameters on mechanical properties of 3d printed samples using FDM process. Mater Today Proc

Prediction of the Creep Behavior of P91 Steel at 873 K Using Continuum Damage Mechanics Model

Imam Ul Ferdous, N. A. Alang, and J. Alias

Abstract Creep deformation is one of the life-limiting factors for the high-temperature components. As a result, there is a considerable amount of interest in predicting the creep rupture life of the high-temperature component during the design stage. The present paper intends to predict the creep rupture behaviour of the P91 steel using the Kachanov's continuum damage mechanics (CDM) at 873 K. The uniaxial creep rupture test was conducted at 873 K using three specimens, extracted from a commercial P91 steel pipe. Two different sets of material parameters for short-term and long-term creep prediction were determined using experimental data and NIMS data, respectively. Using the estimated material constants, creep behaviour in terms of creep strain–time and time to rupture at different stress levels have been predicted. In the case of lower stress level (long-term creep), Kachanov's CDM model underestimates the creep rupture life, whereas, for higher stress levels (short-term creep) the predicted data showed a good agreement with the experimental data except for the stress of 145 MPa which may attribute by the transition of creep damage mechanism. It is worth to be noted that, all the predicted lives are fall within a factor of two.

Keywords Continuum damage mechanics · Creep · Creep strain rate · P91 steel · Rupture

1 Introduction

Numerous material design innovations have resulted from the urge for more efficient power generation. Because of the high creep and fatigue strength, adequate oxidation resistance, and reasonable price, the usage of martensitic 9–12% Cr steels for thermal

I. U. Ferdous · N. A. Alang (✉)
Faculty of Mechanical and Automotive Engineering Technology, Universiti Malaysia Pahang, 26600 Pekan, Pahang, Malaysia
e-mail: azuan@ump.edu.my

J. Alias
Department of Mechanical Engineering, College of Engineering, Universiti Malaysia Pahang, 26300 Gambang, Pahang, Malaysia

359

power plant components has expanded dramatically in recent decades [1]. P91 or T91, which contains 9% chromium and 1% molybdenum, is one of these steels. It contains alloying elements such as Nb and V, which combine to generate fine, stable carbides and carbonitrides precipitates [2]. By interrupting dislocation movement and delaying plastic deformation by blocking grain boundary sliding [3], preserving finer grains during austenization [4, 5], and prolonging the initiation of tertiary creep stage [6], these improve its high temperature creep strength.

In the thermal and nuclear power generation industries, P91 steel is a significant structural material for steam generator applications. The steel has been chosen for manufacturing the major components like a tube, steel pipe, and thick section tube-plate in the steam generators for having high-temperature mechanical properties [7]. It exhibits better creep, tensile and low cycle fatigue than the conventional steels containing Cr content up to 9% i.e., plain 9Cr-1Mo steel and other steel like 2.25Cr-1Mo [8]. P91 steel shows some degree of creep strength degradation at very long creep duration, thus high and low-stress regimes in terms of stress dependence of minimum creep strain rate and rupture life is usually observed [9].

The creep deformation of a material in its creep area is inevitable after a certain time. Ultimate material failure due to creep deformation cannot be avoided in this case but can be controlled through correct system design and regular monitoring. For that reason, it is necessary to establish a prediction model to predict the rupture life of the component's material for avoiding abrupt accidents and ensuring flawless operation of the plant. In the recent past, different approaches have been made to describe the creep behavior in martensitic steels. The approach based on the CDM model was made by McLean et al. [10], Yin et al. [11], and Semba et al. [12] to describe the creep behavior. But it is worth to be noted that, though it offers an obvious advantage for the computation; it can offer poor extrapolation if there were more than one damage mechanism are operating in the stress/temperature regime because it requires a large number of parameters to predict the rupture life.

In the present study, the Continuum Damage Mechanics approach has been implemented to predict the rupture life of P91 steel. The necessary material parameters are determined by plotting the best fit curve for minimum creep strain rate against stress (A and n) and rupture life against stress (M and υ), and matching the predicted creep curve with the experimental curve. The results are compared and the reasons for possible deviations are investigated.
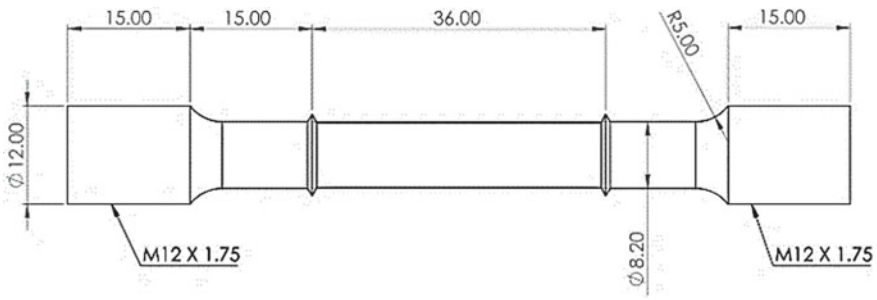
Fig. 1 Detailed dimension of plain creep specimen

2 Methodology

2.1 Material and Specimen

Three plain specimens were extracted from the commercial P91 steel pipe in the longitudinal direction. The detail of the specimen's geometry, which is used for in-house creep testing is shown in Fig. 1. Additional plain bar creep rupture data is taken from the literature [13, 14].

2.2 Creep Rupture Testing

The creep rupture test was carried out according to the suggested test procedure enlisted in the standard ASTM E139 [15]. A dead-load creep testing machine was used to carry out the tests, which had a lever ratio of 1:50. Figure 2 shows the accessible uniaxial creep testing machine in Universiti Malaysia Pahang and its integrant parts. The machine was equipped with a furnace and a temperature controller to provide a controlled high-temperature environment around the specimen. The specimen was placed inside the furnace using lower and upper grip (Fig. 2b). The elongation of the material in the longitudinal direction was measured using LVDT (Linear variable differential transformer), which was installed using a clamp holder. There were three K-type thermocouples, which were embedded in the furnace at three suitable locations; top, middle and bottom to measure the temperature of the specimen. The specimen was heated to 600 °C and ensured the uniform temperature distribution for the entire specimen. Then the pre-defined load was applied through the lever. It was taken care of that the deviation between all thermocouples should not exceed 2 °C during the test. The creep displacement data were collected every 2 min during the primary stage and during the secondary stage, the increment was for every 10 min. The test was continued until the specimen gets ruptured (Fig. 3). Table 1 shows the test matrix for the creep test.
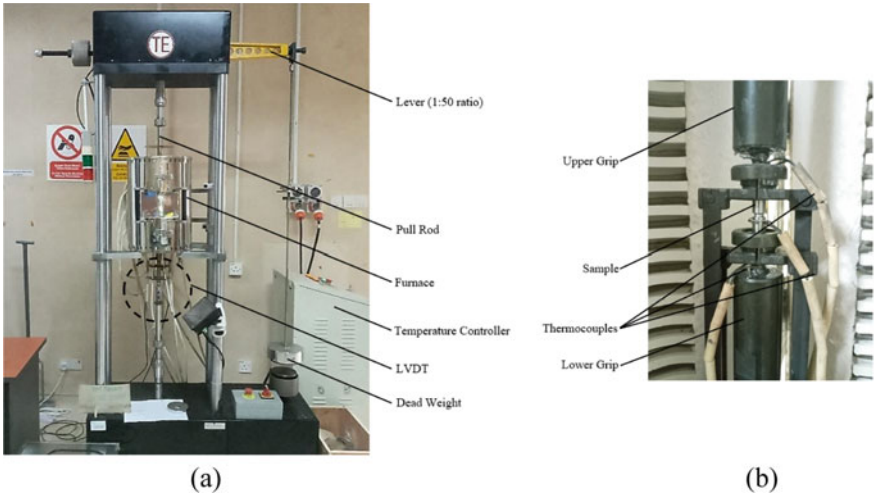
Fig. 2 Experimental setup: **a** overall and **b** close-up on creep specimen

Fig. 3 Fractured specimen of P91 steel

Table 1 Test matrix for creep rupture testing

Specimen type	Temperature, T (°C)	Net stress, σ (MPa)	
Plain	600	100	[13]
		110	
		120	
		145	[14]
		160	
		170	Experimental data
		180	
		190	

2.3 CDM Approach

In this study, an empirically-based CDM model has been used to predict the rupture life of the P91 steel. The model was first introduced by Kachanov [16] and Rabotnov [17] to quantify the tertiary stage of creep in the 1950s.

The term creep damage is coined by engineers to explain the progressive loss of load-bearing capacity under the influence of high stress and temperature which manifests itself as a tertiary creep. However, the reduction of the strength of the material can be initiate due to various mechanisms of degradation (grain boundary cavitation, dynamic subgrain coarsening, and mobile dislocation multiplication), but the engineering solution introduced by Kachanov [16] was to implement a single empirical parameter which attempts to address all these damage mechanisms. In the model, he incorporated a power-law creep rate formulation with a power law-dependent damage evolution equation.

Under the domination of secondary creep, the overall deformation of the material can be described by steady-state creep strain rate or minimum creep strain rate, $\dot{\varepsilon}_m$ and is expressed by:

$$\dot{\varepsilon}_m = A\sigma^n \tag{1}$$

Equation (1) is also known as Norton power law. The deformation mechanisms are different in the short- and long-term creep. For that reason, bi-linear power-law lines are suitable to describe the minimum creep strain rate versus stress data. In such a case, two-regimes Norton law relation can be expressed by Eq. (2).

$$\dot{\varepsilon}_m = A\sigma^n \quad \begin{Bmatrix} A = A_S \text{ and } n = n_S \text{ if } \sigma > \sigma^* \\ A = A_L \text{ and } n = n_L \text{ if } \sigma \leq \sigma^* \end{Bmatrix} \tag{2}$$

Here, σ^* is the stress at the transition between the two linear lines. The subscript S and L denote short and long-term creep, respectively. Within the creep regimes, a similar form of bi-linear power-law representation of the creep deformation can be applied to relate the rupture time to applied stress and is expressed as:

$$t_r = M\sigma^{-v} \quad \begin{Bmatrix} M = M_S \text{ and } v = v_S \text{ if } \sigma > \sigma^* \\ M = A_L \text{ and } v = v_L \text{ if } \sigma \leq \sigma^* \end{Bmatrix} \tag{3}$$

The values of M and v can be obtained by plotting the rupture life data against applied stress in the double-logarithm scale and the slope of the linear best fit line is v and the intercept is log (M).

Incorporating the creep damage parameter, ω with the Norton power law, Kachanov described the tertiary creep behavior of the material. The creep strain rate and the damage rate based on Kachanov's CDM model can be expressed by Eqs. (4) and (5), respectively. When the damage parameter, $\omega = 0$, the Norton power law creep relation takes place and Eq. (4) reduces to Eq. (1).

$$\dot{\varepsilon}_c = A\left(\frac{\sigma}{1-\omega}\right)^n \tag{4}$$

$$\dot{\omega} = B'\frac{\sigma^\chi}{(1-\omega)^{\phi'}} \tag{5}$$

Here, B', ϕ', and χ are material constants. Now, considering constant stress, integrating Eq. (5), assuming the rupture life, t_r as a function of applied stress, σ and applying the proper limits, Eq. (7) can be obtained.

$$\int_{\omega=0}^{\omega=1} (1-\omega)^{\phi'}d\omega = \int_{t=0}^{t=t_r} B'\sigma^\chi dt \tag{6}$$

$$t_r = \frac{\sigma^{-\chi}}{B'(1+\phi')} \tag{7}$$

Comparing Eq. (7) with Eq. (3), the following relations are obtained:

$$\chi = \upsilon \tag{8}$$

$$M = \frac{1}{B'(1+\phi')} \tag{9}$$

Furthermore, for constant stress, integrating Eq. (5) and applying $t = 0$, $\omega = 0$ and $t = t$, $\omega = \omega$ the following equations can be obtained:

$$\int_{\omega=0}^{\omega=\omega} (1-\omega)^{\phi'}d\omega = \int_{t=0}^{t=t} B'\sigma^\chi dt \tag{10}$$

$$\omega = 1 - \left[1 - B'(1+\phi')\sigma^\chi t\right]^{\frac{1}{(1+\phi')}} \tag{11}$$

Now, substituting the value of ω into the Eqs. (4) and (12) can be obtained by further integration:

$$\varepsilon_c = \frac{A\sigma^{(n-\chi)}}{B'(n-\phi'-1)}\left(\left[1 - B'(1+\phi')\sigma^\chi t\right]^{(\phi'+1-n)/(\phi'+1)} - 1\right) \tag{12}$$

The creep curves are first predicted according to the Eq. (12) and the determination of material parameters are discussed in Sect. 2.4. In this CDM model, for determining the long-term creep, material parameters are derived from the long-term creep data from the literature, because in-house long-term creep testing is impossible to be conducted.

It is worth to be noted that, in the present approach, microstructural parameters such as Z-phase coarsening, change in MX (precipitates) growth, damage caused by dislocation network, and subgrain coarsening, etc. have not been considered.

2.4 Initial Parameters

There are two sets of material parameters are needed to be calibrated to predict the rupture life of the material using the CDM model. One set for short-term creep rupture life ($\sigma >125$ MPa) and one set for long-term creep rupture life ($\sigma < 125$ MPa), where $\sigma < 125$ MPa is the transition between two creep mechanisms. It is considered that the creep deformation obeys the Norton power-law relation as given in Eq. (2). The mean data curve was plotted for minimum creep strain rate against stress data and the corresponding value of A and n has been determined (Fig. 4). Similar bi-linear law was applied to determine the value of M and v by fitting the mean data curve for rupture time against stress data (Fig. 5). A total of 43 NIMS [18] creep data were analyzed to determine the long-term creep constants. On the other hand, 3 experimental creep data were used to determine the short-term creep constants. The value of ϕ' was determined by the trial-and-error method. The creep curves were first determined using an arbitrary value of ϕ'. This value was varied until the predicted curve fitted to the experimental creep curve. Table 2 tabulates the material constant for the CDM model.
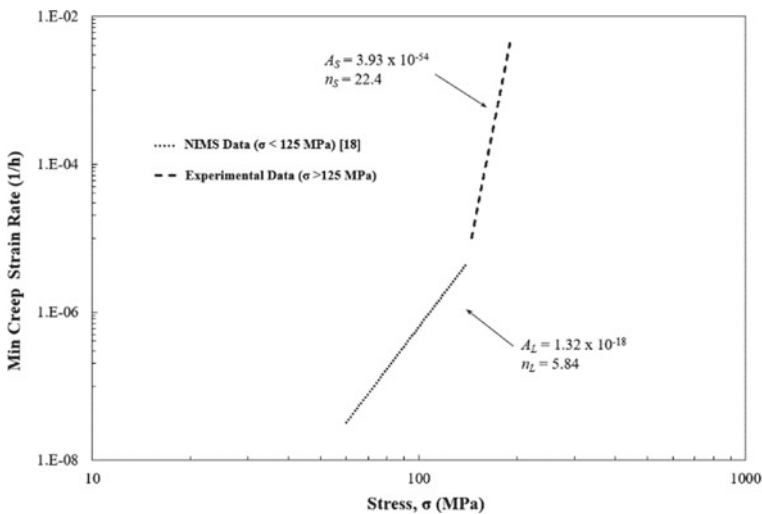
Fig. 4 Minimum creep strain rate vs stress of Grade 91 steel
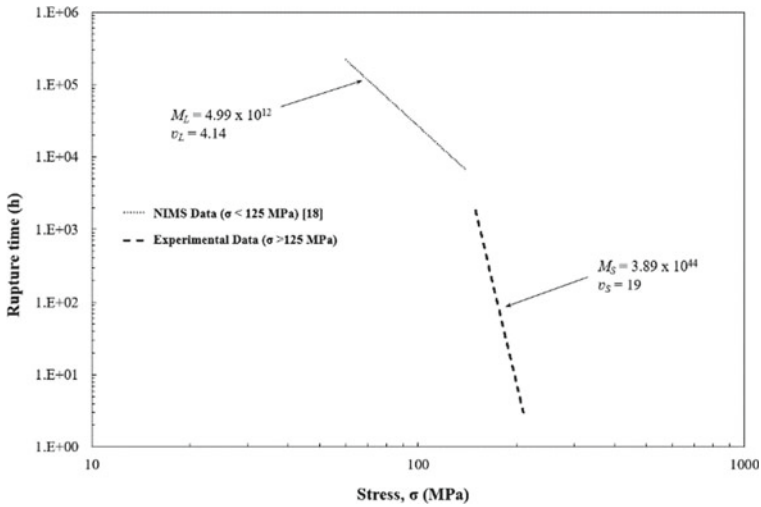
Fig. 5 Rupture time versus stress of P91 steel

Table 2 Optimized material parameters

CDM Parameters	M (MPa$^\chi$h)	A (MPa^{-n}h^{-1})	B (MPa$^{-\chi}$h^{-1})	n	χ	ϕ'
Optimized Value (short-term)	3.89×10^{44}	3.93×10^{-54}	1.35×10^{-46}	22.4	19	18
Optimized Value (long-term)	4.99×10^{12}	1.32×10^{-18}	4.01×10^{-14}	5.84	4.14	4

3 Results and Discussion

Figures 6, 7 and 8 compares the predicted creep rupture life obtained using the CDM model to the experimental creep rupture life. The experimental creep strain vs. time for 100, 110, and 120 MPa along with the predicted creep strain-time data has been shown in Fig. 6. From the figure, it can be observed that the prediction underestimates the rupture life. In that case, the material parameters are obtained using literature (NIMS) data [18], because it is inconvenient to perform the long-term test (which may take several years) in the university laboratory. In the literature (NIMS) data, different material conditions (different chemical composition, different heat treatment, different batch, etc.) are considered, which may lead to the deviation to the prediction. Creep strain-time data has also been predicted using short-term material parameters at 145 and 160 MPa and compared with the corresponding experimental data in Fig. 7. The proposed CDM model predicts quite well for the stress level 160 MPa but overestimates the rupture life for the stress level 145 MPa. Noted that when the stresses decrease or approaching the long-term creep, as in the case of stress 145 MPa, the CDM model overestimates the creep strain which may
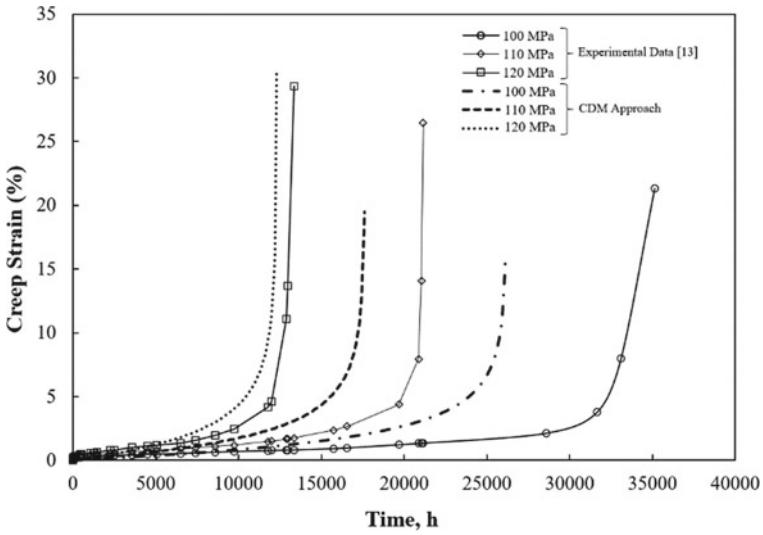
Fig. 6 Comparison of predicted and experimental creep strain–time data for 100, 110, and 120 MPa at 873 K
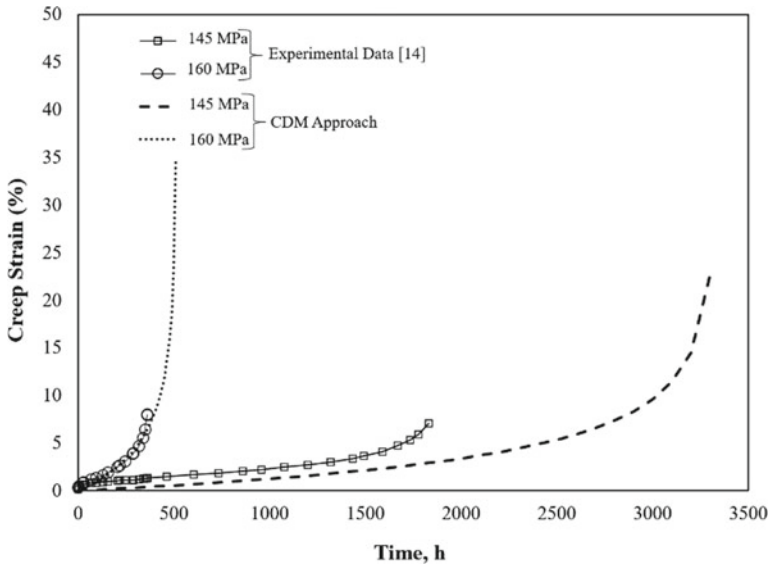
Fig. 7 Comparison of predicted and experimental creep strain–time data for 145 and 160 MPa at 873 K
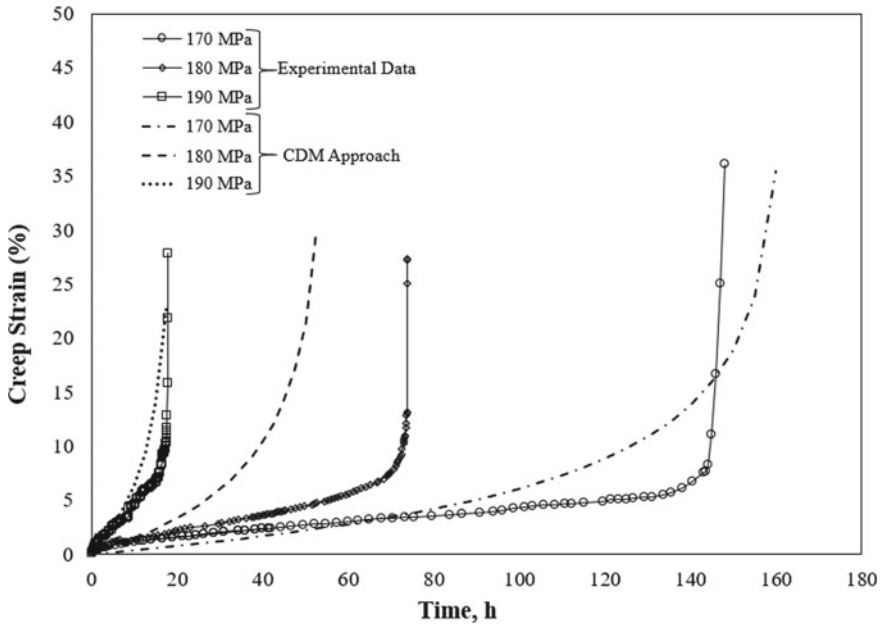
Fig. 8 Comparison of predicted and experimental creep strain–time data for 170,180, and 190 MPa at 873 K

imply the transition between two creep mechanisms. Prediction of creep strain-time has also been determined for relatively high stresses. Figure 8 compares the prediction and experimental data for the stress level 170,180, and 190 MPa. It can be observed from the figure that, the prediction showed a good match for 170 MPa and 190 MPa but significantly underestimate the rupture life for the stress level of 180 MPa. Table 3 shows the ratio of the predicted rupture life to the experimental rupture life. It can be noticed from the table that; the ratio doesn't exceed 2. Figure 9 compares the predicted rupture life to the experimental rupture life. All the predicted life data are within the factor of ± 2 of the experimental value. Zhao et al. [19] applied the scatter

Table 3
Prediction-experimental ratio

Stress level (MPa)	Prediction/experiment
100	0.74
110	0.83
120	0.92
145	1.80
160	1.42
170	1.08
180	0.71
190	0.97
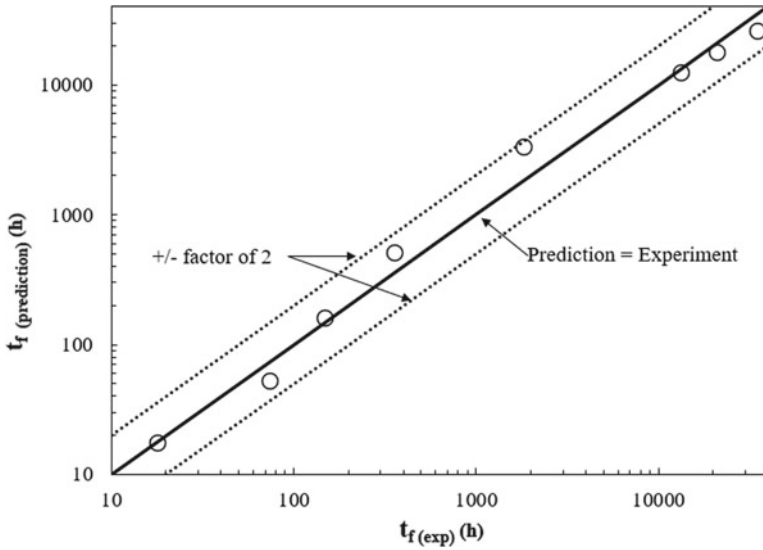
Fig. 9 Comparison between CDM predicted and experimental rupture life of P91 steel

band factor of ± 2 to observe the accuracy of the prediction method to investigate the creep rupture behavior of notched P92 steel. In another study, Chen et al. [20] applied the same scatter band factor to compare the accuracy of the prediction to the experimental results.

As mentioned before, in this CDM approach, microstructural parameters are excluded during analysis. There is a considerable amount of effort made by many researchers to include these parameters to predict the rupture life more accurately. Ashby and Dyson [21] came with the idea of a physically-based CDM model in with the mechanism of microstructural degradation was induced into the mathematical framework of CDM. The physically-based CDM model followed four steps: (i) Damage mechanism identification. (ii) Defining the mechanism using a dimensionless variable. (iii) Adding each variable within a kinetic equation. (iv) Evaluating each equation for each variable. In another study [22], for 9–12% Cr steel, nucleation and growth of laves phase were considered during implementing the CDM model. Yadav et al. [23] predicted the rupture life of P91 steel using a hybrid concept, coupling physical model (microstructural evaluation) to CDM approach. In another study, Nandi et al. [24] used the CDM model proposed by Hore et al. [25] and added additional microstructural parameters to evaluate the rupture life of P91 steel. Christopher et al. [8] also used the physically-based CDM model to predict the creep behavior of P91 steel. In his study, coarsening of dislocation networks and precipitates were considered and kinetic creep law containing microstructural parameters was used to calculate the total creep damage. Considering all these microstructural parameters into the CDM model is likely to improve the overall prediction, however, the model

becomes relatively complex and the determination of every parameter may lead to a calculation error.

4   Conclusion

An empirical Kachanov's CDM model has been employed to predict the creep behaviour and rupture life of P91 steel. Different material parameters had been implemented to predict the rupture life at different stress levels; short- and long-term creep. For predicting short-term creep rupture, the material parameters were optimized using experimental data. On the other hand, data from literature was employed for long-term creep rupture prediction. The deviation between the predicted and experimental values have been observed for both higher and lower stress level, which may indicate the transition between damage mechanism. Overall, the predicted life for all cases considered in the present study is within the factor of ± 2 of experimental result. It is worth to be noted that in this approach, microstructural parameters were excluded during prediction.

References

1. El-Desoky OE, Abd El-Azim ME, ElKossy MR (2019) Analysis of creep behavior of welded joints of P91 steel at 600 °C. Int J Press Vessel Pip 171:145–152. https://doi.org/10.1016/j.ijpvp.2019.02.008
2. Guguloth K, Roy N (2017) Creep deformation behavior of 9Cr1MoVNb (ASME Grade 91) steel. Mater Sci Eng A 680:388–404. https://doi.org/10.1016/j.msea.2016.10.112
3. Pelleg J (2017) Creep in ceramics. https://doi.org/10.1007/978-3-319-50826-9_4
4. Ren F, Tang X (2017) Study on creep behavior of Grade 91 heat-resistant steel using theta projection method. AIP Conf Proc 1890:652–656. https://doi.org/10.1063/1.5005205
5. Benaarbia A, Xu X, Sun W, Becker AA, Jepson MAE (2018) Investigation of short-term creep deformation mechanisms in MarBN steel at elevated temperatures. Mater Sci Eng A 734:491–505. https://doi.org/10.1016/j.msea.2018.06.063
6. Guguloth K, Roy N (2018) Study on the creep deformation behavior and characterization of 9Cr-1Mo-V-Nb steel at elevated temperatures. https://doi.org/10.1016/j.matchar.2018.10.011
7. Gorash Y, Mackenzie D (2017) On cyclic yield strength in definition of limits for characterisation of fatigue and creep behaviour. Open Eng 7:126–140. https://doi.org/10.1515/eng-2017-0019
8. Christopher J, Choudhary B (2019) Prediction of long-term creep behaviour of Grade 91 steel at 873 K in the framework of microstructure-based creep damage mechanics approach. Int J Damage Mech 28:877–895. https://doi.org/10.1177/1056789518796118
9. Erten DT, Nguyen TT, Jeong TM, Yoon KB (2017) Creep deformation and rupture behaviour of service exposed P91 weld and base steel measured by miniature tensile creep testing. Mater High Temp 34:425–433. https://doi.org/10.1080/09603409.2017.1381497

10. McLean M, Dyson BF (2000) Modeling the effects of damage and microstructural evolution on the creep behavior of engineering alloys. J Eng Mater Technol 122:273–278. https://doi.org/10.1115/1.482798
11. Yin YF, Faulkner RG (2006) Continuum damage mechanics modelling based on simulations of microstructural evolution kinetics. Mater Sci Technol 22(8):929–936. https://doi.org/10.1179/174328406X102426
12. Semba H, Dyson B, McLean M (2008) Microstructure-based creep modelling of a 9%Cr martensitic steel. Mater High Temp 25:131–137. https://doi.org/10.3184/096034008X354873
13. Kimura K, Kushima H, Sawada K (2009) Long-term creep deformation property of modified 9Cr-1Mo steel. Mater Sci Eng A 510–511:58–63. https://doi.org/10.1016/j.msea.2008.04.095
14. Swei M, Sedmak AS, Petrovski B, Golubovi ZZ, Sedmak SA, Katini M, Azzabi KI (2019) Creep crack growth behavior of P91 steel weldments. Therm Sci 23:1203–1209. https://doi.org/10.2298/TSCI170729240S
15. ASTM E139-11 (2011) Standard method for conducting creep, creep-rupture, and stress-rupture tests of metallic materials. Annual book of ASTM standards
16. Kachanov LM (1958) Time of the rupture process under creep conditions. Nank SSR Otd Tech Nauk 8:26–31
17. Rabotnov YN (1959) On the mechanism of creep rupture. Issues Strength Mater. Struct 5–7
18. Sawada K, Kimura K, Abe F et al (2014) Data sheets on the elevated-temperature properties of 9Cr–1Mo–V–Nb steel tubes for boilers and heat exchangers. (ASME SA-213/SA-213M Grade T91), 9Cr–1Mo–V–Nb steel plates for boilers and pressure vessels (ASME SA-387/SA-387M Grade 91) and 9Cr–1Mo–V–Nb steel seamless pipe for high temperature service (ASME SA-335/SA-335M Grade P91). NIMS Creep Data Sheet No. 43A. Natl Inst Mater Sci. https://doi.org/10.11503/nims.1047
19. Zhao L, Alang N, Nikbin K (2018) Investigating creep rupture and damage behaviour in notched P92 steel specimen using a microscale modelling approach. Fatigue Fract Eng Mater Struct 41:456–472. https://doi.org/10.1111/ffe.12713
20. Chen S, Wei D, Wang J, Wang Y, Jiang X (2020) A new fatigue life prediction model considering the creep-fatigue interaction effect based on the Walker total strain equation.https://doi.org/10.1016/j.cja.2020.06.001
21. Ashby MF, Dyson BF (1984) Use of CDM in materials modeling and component creep. In: Advances in fracture research
22. Wert C, Zener C (1950) Interference of growing spherical precipitate particles. J Appl Phys 21:5–8
23. Yadav SD, Scherer T, Prasad Reddy GV, Laha K, Sasikala G, Albert SK, Poletti C (2018) Creep modelling of P91 steel employing a microstructural based hybrid concept. Eng Fract Mech 200:104–114. https://doi.org/10.1016/j.engfracmech.2018.07.027
24. Nandi S, Vikrant KSN, Pavan AHV, Singh K, Ghosh RN (2013) Creep modelling of P91 steel for high temperature power plant applications. Procedia Eng. 55:751–755. https://doi.org/10.1016/j.proeng.2013.03.326
25. Hore S, Ghosh RN (2011) Computer simulation of the high temperature creep behaviour of Cr–Mo steels. Mater Sci Eng A 528:6095–6102

The Impact of a Decrease in Energy Reserve to Production Ratio on Malaysia's Energy Security

Saleh Shadman ⓘ **, Christina Chin May May** ⓘ **, Novita Sakundarini** ⓘ **, and Eng Hwa Yap** ⓘ

Abstract With the rapid growth of population and increase in energy demand, there is a high demand for fossil fuels to meet the supply needs. In this research, the decreasing impact of fossil fuels reserves to the production ratio (R/P) is studied using the system dynamics approach of modelling. A total of 3 dimensions, namely, availability of energy, socio-economy, and environmental sustainability, was studied with their relevant indicators. Three causal loop diagrams (CLDs) were combined to form one final CLD, followed by converting the CLD to a stock and flow diagram (SFD). The SFD is simulated to draw the significant findings of this research. The decreasing reserves of fossil fuels can threaten the economic growth subsequently the nation's social well-being. Per this, it is vital to understand how energy security is impaired if such a scenario arises. The simulation results suggest that there will be a decrease in energy consumption, growth in economic health, and energy intensity due to a decrease in the R/P ratio. Energy efficiency seems to improve due to more careful use of lower supply in this scenario; however, it is not an indication of improved technological applicability or energy-efficient technologies. Energy policies such as the national depletion policy need to be curated to control the current usage of fossil fuels and introduce renewable energy sources faster to the energy mix to reduce dependency on fossil fuels.

Keywords Energy security · System dynamics · Environmental sustainability · Socio-economy · Energy reserves · Energy policy

S. Shadman (✉) · C. Chin May May · N. Sakundarini
University of Nottingham Malaysia, Jalan Broga, 43500 Semenyih, Selangor, Malaysia
e-mail: saleh1shadman@gmail.com

E. Hwa Yap
School of Robotics, XJTLU Entrepreneur College (Taicang), Xi'an Jiaotong-Liverpool University, Suzhou 215123, Jiangsu, People's Republic of China

1   Introduction

This research continues the work done by Shadman et al. [1] to quantify the impact of energy shortage on Malaysia's energy security (ES). This study created a system dynamics model based on 3 dimensions of Malaysia's ES, namely availability of energy, socio-economy, and environmental sustainability. These 3 dimensions have been critical in the ES research of Malaysia and have been discussed in several ES studies that were based on Malaysia e.g. [2–7]. The model comprises 3 causal loop diagrams (CLDs) that have been combined to form the final CLD and followed by the formation of the stock and flow diagram (SFD) to quantify the desired indicators. In this study, the impact of decreasing reserve to production ratio for different fuel types has been studied to draw policy implications and recommendations to ensure this scenario can be tackled well in the future.

The scenario selected in this study is the reduction of energy reserve to production ratio by half of its original value to understand how and to what extent it can affect Malaysia ES. This is a hypothetical scenario based on the assumption that energy reserves will deplete eventually if alternative sources of energy especially renewables are not included at a faster rate in the energy mix for total primary energy supply (TPES) and power generation. The studies of Chatri et al. [8] and Foo. [4] have discussed the importance of the existing oil, natural gas, and coal reserves for Malaysia. Khattak et al. [2] have stated that Malaysia's oil reserves are maturing and oil production within the country is declining at a steady rate due to an increase in consumption in economic activities within the nation. Hamzah et al. [9] have stated that Malaysia coal's reserves and production in 2016 were 1938.37 Mt and 2.414 million Mt consecutively where most of the coal mining activities are located in Sarawak, Sabah, and Selangor. The national depletion policy was introduced in 1980 to safeguard the existing natural resources especially the natural gas and oil reserves of Malaysia [10–12]. The manufacturing of crude oil was restricted to 630,000 barrels per day (BPD) and the consumption of gas in peninsular Malaysia was restricted to 32,000 million standard cubic feet per day.

This paper firstly discusses Malaysia's ES dimensions, and the indicators by creating a causal link between the indicators in the Vensim SD tool. The data collection method consists of a questionnaire survey that asks true/false questions to develop causal relations between the dimensional indicators. The overall results are discussed based on the simulation of the model that gives quantitative results for energy consumption, energy efficiency, growth in economic health, and energy intensity. In the end, policy implications are recommended to ensure that the existing reserves can be safeguarded for a longer period by the sustainable use of the existing reserves and the addition of RE sources at a faster rate in the energy mix.

2 Methodology

This study employs a mixed-method approach that has been conducted from the past study by the same researchers [13]. The methods have been discussed in-depth and adopted and followed for this research as well [13]. The qualitative data collection was conducted by surveying 117 participants from the energy and sustainability sector in Malaysia with a total of 33 questions. While quantitative data was collected from the energy statistics handbook published by the regulatory bodies of energy in Malaysia [14], energy reports by the Energy Commission, and the International Energy Agency (IEA) [15, 16].

The CLDs are created in Vensim by developing the causal relation between the indicators through the qualitative data collected. The CLD is then converted into an SFD where the quantitative data are given input in the respective chosen variables: reserve to production ratio, energy wastage, energy cost, and energy efficiency. The respective indicators in the model have been defined by equations and units in this case to standardise the units have been converted to a percentage for all the indicators. There are two assumptions according to Morecroft and Sterman (1994): (1) flows within processes are continuous, and (2) flow does not have a random component [17]. With these two assumptions in mind, one can consider any stock and flow system hence, the following SFD was created from its respective CLD. The following section illustrates and explains the CLD and SFD generated in this research.

3 Causal Loop Diagram and Stock Flow Diagram

This section illustrates the CLDs created based upon the questionnaire survey conducted with 117 participants. The CLD was categorized into three segments to better understand the causal relationship between each of the dimensional indicators of ES in this research.

3.1 Causal Loop Diagram (CLD)

The CLD in Fig. 1 comprises of 3 balancing feedback loops with energy reserve to production ratio and imported energy as common indicators in 2 different loops. The loops give a clear indication here that imported energy does have an impact on the energy reserve to production ratio and hence the short-term ES. Also, energy import increases energy dependency hence, it can impair the growth in economic health and country's unemployment. Figure 1 is very critical to this research as it defines most of the key indicators within the energy availability and socio-economy dimension.

Figure 2 shows how energy cost is related to energy consumption, energy intensity, growth in economic health, and country's unemployment. These variables are
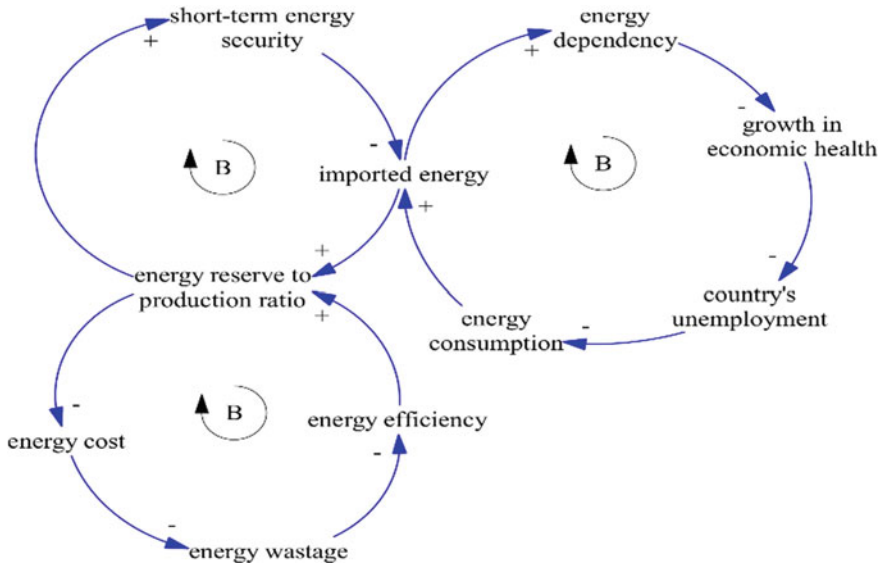
Fig. 1 CLD of energy availability and energy efficiency
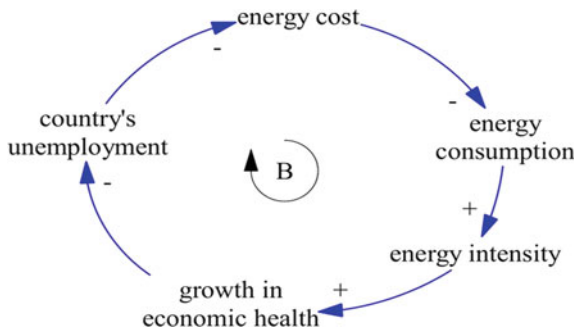
Fig. 2 CLD of energy cost and the indicators that are directly affected by the energy cost

simulated using SFD in Fig. 5. This figure shows a single balancing loop with 5 variables in it, where ' + ' shows the positive influence in the relation between the variables and vice versa for '-' sign.

While Fig. 3 shows the CLD of environmental and social impact and this CLD also holds a very key role in this research. It comprises 2 balancing loops and 1 reinforcing loop in with environmental impact, energy consumption, and RE in the energy mix as the common indicators in the 3 loops. The environmental and social impacts are often neglected or given lower priority in ES assessment for developing nations. In this research, these dimensions have been given equal importance and defined in detail as per Fig. 3.
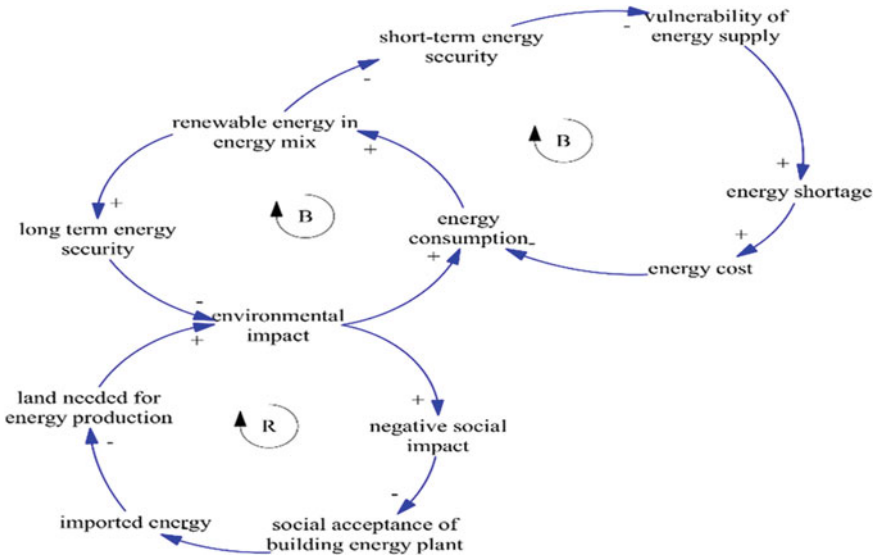
Fig. 3 CLD of environmental and social impact that the increase of RE has on other indicators

3.2 Stock and Flow Diagram (SFD)

In SD modelling, the equations that define the indicators, units, and input values are very important thus need to be defined accurately. Stocks in SFD are also known as 'levels' which represent accumulation in a system that determines the current state of the system [18]. SFD in Fig. 5 was a conversion of Fig. 4 by assigning these stocks, flows and by equating the variables. There are 2 assigned stocks, energy production to reserve ratio, and environmental impact in the SFD. Imported energy, short-term ES, land needed for energy production, and negative social impact are the flows. The unemployment rate, energy intensity, percentage of vulnerability, percentage of renewable energy, initial GDP are the external variables. The validation of the model is conducted by engaging stakeholders through semi-structured interviews (SSI's). Input from each of the 16 stakeholders interviewed collected are modelled and modified according to the most common changes suggested throughout this validation process.

4 Simulated Scenario, Results, and Discussion

This section discusses the reason behind the selection of the scenario and the results of the simulation. The overall discussion of the results is also presented in this section.
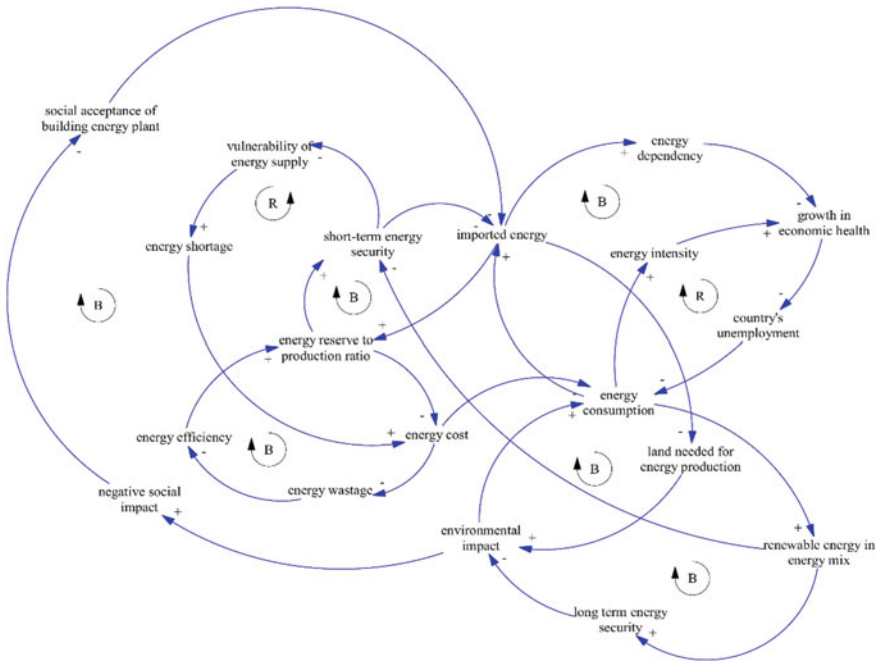
Fig. 4 Combination of CLD's 1, 2, and 3 to create the overall CLD
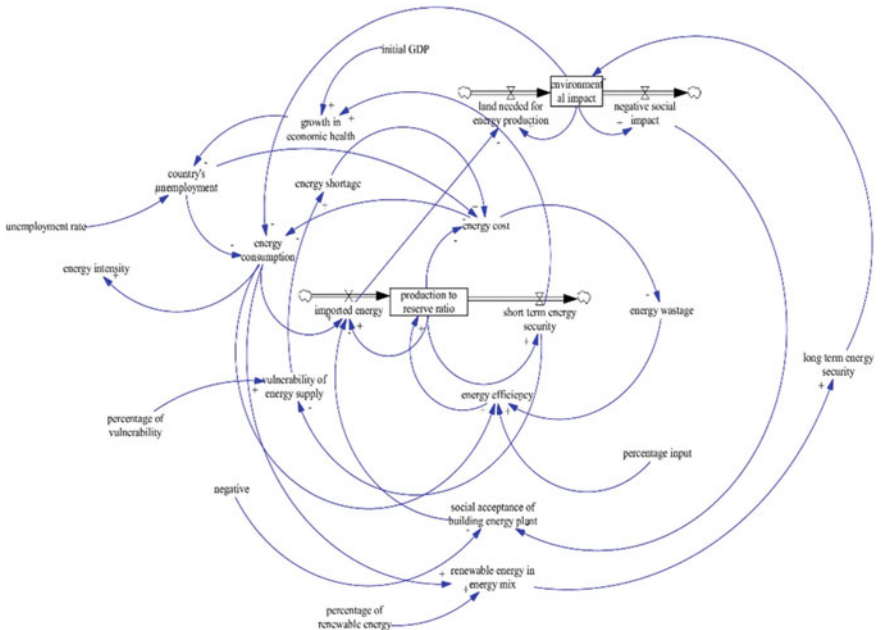
Fig. 5 SFD conversion from CLD simulating different scenarios
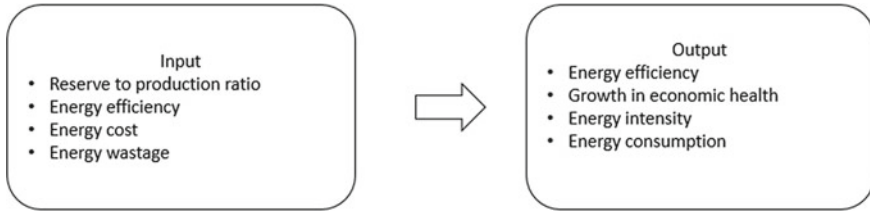
Fig. 6 The inputs and output variables measured using the SD model

4.1 Reduction in Energy Reserve to Production Ratio by 50%

This is a hypothetical scenario created is based on the assumptions of decreasing reserves in the nation. The dependency on energy imports and the usage of fossil fuel makes up over 90% of the energy mix in Malaysia which can be threatening to the availability of energy in the future. To avoid this scenario to come to reality there must be a consolidated policy on the prudent use of fossil fuels and adding alternative RE sources in the energy mix. It is of utmost importance to do so, as the reserves are not going to be everlasting and at some point in time there would be added pressure on the nation's reserve margins. This is not desirable from the R/P point of view which impairs the energy availability dimension of ES severely. Figure 6 below shows the input variables and the expected output variables that have been quantified through the simulation.

The input values are taken from the quantitative data from the energy statistics of Malaysia [14]. These input variables gave the simulated results for the 4 output variables depicted in Fig. 6. The results are discussed in the following section.

4.2 Scenario Results

Figure 7 represents the results of the simulation of the SFD. These graphical representations depict how the 4 output variables change over a period of 5 years from 2015 to 2020. The input variables for the SFD and the values are extracted from Table 1.

4.3 Discussion

The reduction of the energy reserve to production ratio has caused energy consumption to decrease drastically. This is because with a decreasing reserve the usage must be constricted to ensure that it supports the existing reserves longer. As the energy reserve to production ratio decreases, the energy cost increases to a great extent since

Fig. 7 Graphs for the desired output variables of the research
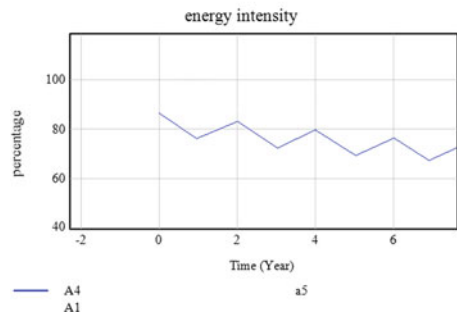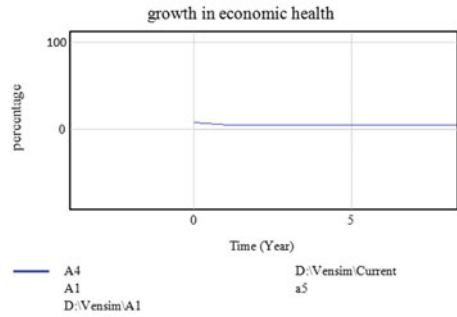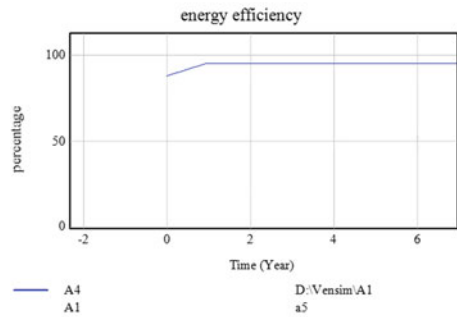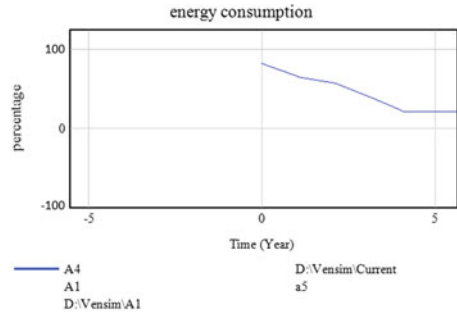
Table 1 Value of input variables for SFD

Input (2015)	Value (%)
Reserve to production ratio	600.9615
Energy efficiency	89.49
Energy cost	31.23
Energy wastage	10.51

a 50% reduction is set. This increase in energy cost will reduce the energy consumption to the minimum point set from the simulation. Energy cost and consumption do have direct causation of effect as affordability is impaired with higher cost, hence reducing the usage. Energy efficiency is expected to hit its maximum limit in a year. The energy cost which had increased drastically due to the reduction of the reserve to production ratio has indirectly caused lower energy wastage. It has caused the energy efficiency to increase drastically, but this is not necessarily an indication of improved efficiency due to the improved applicability of technology or efficiency in handling the existing reserves. This indicator signifies the careful use of energy due to low reserves and hence low supply within the different sectors which improves the efficiency.

Whereas the true definition of improved efficiency has to come from more energy-efficient technological advancement within various industries e.g., manufacturing processes, efficient and energy-saving vehicles, household appliances, etc. The growth in economic health is expected to hit a low point of 3%. This in which is expected due to the decrease in energy consumption, energy intensity, and increasing energy dependency due to the increase in imported energy. Energy intensity has seen a decrease from 88% (2015) to only an approximation of 70% (2020). The effect of the decrease of energy reserve to production will harm the economic health of Malaysia by putting Malaysia's energy supply in a more vulnerable state. A reduction in supply will only be detrimental to the growing demand as explained earlier due to the growth of population and increase in economic activities. Not fulfilling the demand for energy needs will not only affect the economic health of the country but equally the consumer confidence.

5 Conclusion

The results of this study suggest that a decrease in the R/P ratio to half of its current value can have a drastic impact on energy consumption due to a decrease in reserve and also energy intensity. Out of the 4 output indicators that have been studied energy consumption and energy intensity will deteriorate the most while growth in economic health is not impaired to great extent but it still shows a decline. The key policy implications that can be suggested from this research are;

i.   The efficient use of existing natural resources i.e. coal, oil, and natural gas will be crucial for the sustainability of these resources. This can be controlled through policies like the 1980 National Depletion Policy that can be modified and curated to meet the current needs.

ii. The addition of RE at a faster rate in the energy mix will be crucial to take the load off the fossil fuel sources. There are several challenges in integrating RE in the energy mix especially the intermittency to integrating RE in the national grid [19]. Despite these, the Malaysian government is implementing new approaches and policies to tackle and ensure a total of 31% RE can be added to the TPES by 2025 [20].

iii. ES needs a separate policy profile or section in the future "Malaysia Plan or RMKE" to ensure that these challenges can be highlighted, the measures to tackle them can be discussed robustly and through a data-driven approach.

References

1. Shadman S, Chin CMM, Sakundarini N, Yap EH (2021) Quantifying the impact of energy shortage on malaysia's energy security using a system dynamics approach. Springer, Singapore, pp 143–154
2. Khattak MA et al (2018) Global energy security and malaysian perspective: a review. Prog Energy Environ 6:1–18
3. Sharifuddin S (2014) Methodology for quantitatively assessing the energy security of malaysia and other southeast asian countries. Energy Policy 65:574–582
4. Foo KY (2015) A vision on the opportunities, policies and coping strategies for the energy security and green energy development in Malaysia. Renew Sustain Energy Rev 51:1477–1498
5. Sovacool BK, Mukherjee I, Drupady IM, D'Agostino AL (2011) Evaluating energy security performance from 1990 to 2010 for eighteen countries. Energy 36(10):5846–5853
6. Sahid EJM (2018) Energy security in Malaysia: aquantitative analysis. Int J Eng Technol 7(4):400–403
7. Sahid EJM, Sin TC (2019) Energy security in ASEAN region: a case study of Malaysia energy security performance with renewable energy implementation. J Adv Res Fluid Mech Therm Sci 61(2):190–201
8. Chatri F, Yahoo M, Othman J (2018) The economic effects of renewable energy expansion in the electricity sector: a CGE analysis for Malaysia. Renew Sustain Energy Rev 95(June):203–216
9. Hamzah N, Tokimatsu K, Yoshikawa K (2019) Solid fuel from oil palm biomass residues and municipal solid waste by hydrothermal treatment for electrical power generation in Malaysia: a review. Sustain 11(4):1–23
10. Chong C, Ni W, Ma L, Liu P, Li Z (2015) The use of energy in Malaysia: tracing energy flows from primary source to end use. Energies 8(4):2828–2866
11. Chaudhry P, Tewari VP (2010) Environmental education using Nek Chand's Rock Garden in the city of Chandigarh. Int J Environ Sustain Dev 9(1–3):30–36
12. Rahman Mohamed A, Lee KT (2006) Energy for sustainable development in Malaysia: Energy policy and alternative energy. Energy Policy 34(15):2388–2397
13. Shadman S, Chin CMM, Sakundarini N, Yap EH, Velautham S (2021) Methodological review of malaysia's energy security measurement: a systems approach using stakeholder engagement. IOP Conf Ser Mater Sci Eng 1092(1):012032
14. Statistics E (2017) Energy statistics handbook
15. Energy Commission (Malaysia) (2017) Energy Malaysia. Suruhanjaya Tenaga 12:3

16. IEA (2016) Statistics_IEA, International energy agency
17. System Analysis I Compendium for students (2009)
18. Osgood N, Introduction to stocks & flows state of the system : stocks ('levels', 'state variables', 'compartments')
19. Shadman S, Chin CMM (2021) The role of current and future renewable energy policies in fortifying Malaysia' s energy security: PESTLE and SWOT analysis through stakeholder engagement. 16:1–17
20. Energy Commission Malaysia (2021) Report on peninsular generation development plan 2020

Ionization Characteristic of Different Gases Inside Zinc Oxide Target During Sputtering Process Simulated Using SRIM Software

N. S. M. Nazri, M. H. Mamat ⬢, N. Parimon, M. F. Malek, M. K. Yaakob, A. B. Suriani, A. Mohamed, M. K. Ahmad, N. Nayan, I. B. Shameem Banu, N. Vasimalai, M. Y. Ahmad, and M. Rusop

Abstract The aim of the paper is to study a distribution of ions inside a zinc oxide (ZnO) target during sputtering process using different gases. The plots of ion distribution were obtained from the simulation results using Stopping and Range of Ions in Matter (SRIM)-2013 software. Generally, the SRIM software is utilized to calculate a variety of parameters related to ion beam implantation and ion beam processing of materials. Simulation of ion beam sputtering is a necessary to analyze the ionization characteristics of different ions from different gases inside ZnO target during

N. S. M. Nazri · M. H. Mamat (✉) · N. Parimon · M. Rusop
NANO-ElecTronic Centre (NET), School of Electrical Engineering, College of Engineering, Universiti Teknologi MARA, 40450 Shah Alam, Selangor, Malaysia
e-mail: mhmamat@uitm.edu.my

M. H. Mamat · M. F. Malek · M. Rusop
NANO-SciTech Lab (NST), Center for Functional Materials and Nanotechnology, Institute of Science (IOS), Universiti Teknologi MARA, 40450 Shah Alam, Selangor, Malaysia

N. Parimon
Faculty of Engineering, Universiti Malaysia Sabah, 88400 Kota Kinabalu, Sabah, Malaysia

M. F. Malek · M. K. Yaakob
Faculty of Applied Sciences, Universiti Teknologi MARA, 40450 Shah Alam, Selangor, Malaysia

A. B. Suriani · A. Mohamed
Nanotechnology Research Centre, Faculty of Science and Mathematics, Universiti Pendidikan Sultan Idris, 35900 Tanjung Malim, Perak, Malaysia

M. K. Ahmad · N. Nayan
Microelectronic and Nanotechnology–Shamsuddin Research Centre (MiNT-SRC), Faculty of Electrical and Electronic Engineering, Universiti Tun Hussein Onn Malaysia, 86400 Batu Pahat, Johor, Malaysia

I. B. Shameem Banu · N. Vasimalai
School of Physical and Chemical Sciences, B.S. Abdur Rahman Crescent Institute of Science & Technology, Vandalur, Chennai 600048, India

M. Y. Ahmad
Nanorian Technologies Sdn. Bhd., No. 40, Jln Kajang Perdana 3/2, Taman Kajang Perdana, 43000 Kajang, Selangor, Malaysia

sputtering process for a thin film deposition. The results show that Radon, Krypton, and Xenon gases were the best gases to sputter high density of ZnO target in this simulation. The depth of ion during sputtering process is shown and discussed. The result indicates that depth of ion diffused into the target material decrease as the density of the target increases. These results are important to find suitable gases for ZnO sputtering and at the same time prolonging the target lifespan.

1 Introduction

Zinc oxide (ZnO) widely known for its uniqueness properties as a material that can be used to different technological application purposes. Due to extensive research and studies, ZnO materials have been known to have a lot of functionalities such as sensors, solar cell, and many other semiconductor device [1–7]. ZnO has a lot of advantages including high energy band gap (3.37 eV), high exciton binding energy (60 meV), and can be prepared by various fabrication processes at low cost [8, 9]. The solutions-based growth, chemical vapor deposition, physical vapor deposition, and thermal evaporation processes have mostly been used to prepare ZnO nanostructure-based devices [10–15]. The use of composite and doping materials will enhance the performance of the device significantly, which can be achieved by various techniques including sputtering process [16–18].

Many nanotechnological applications and electronic industry use a sputtering process for their device fabrication [19, 20]. The sputtering process is not only popular and used in nanotechnology industries but also used in aviation and medical applications [21, 22]. The sputtering is a process of ejecting atoms from a solid or liquid target by bombarding it with energetic particles, generally ions. Collisions between incident energetic particles and/or the resulting rebound atoms and surface atoms initiate the sputtering process. The sputter yield is the ratio of the number of expelled atoms by sputters to the number of incoming particles and is a measure of the rate at which surface atoms are removed. The sputter yield determines the number of atoms released from the surface per incident ion and it is a key indicator of the sputtering process' efficiency. The energy of the incident ions, their masses, and the masses of the target atoms, as well as the solid's bond energy, are amongst the important factors that influence the deposition of thin film using sputtering method. The sputtering process is described in Fig. 1.

In this paper, ZnO target was bombarded with ions from different gases and the ionization characteristic of the gas inside the target during sputtering process was observed by The Stopping and Range of Ions in Matter (SRIM) software. In General, the Monte Carlo simulation code SRIM (originally Transport of Ions in Matter (TRIM) software) is utilized to calculate a variety of parameters related to ion beam processing of materials. The behavior and performances of different ions based on different gases could be analyzed using this software. SRIM is a complex
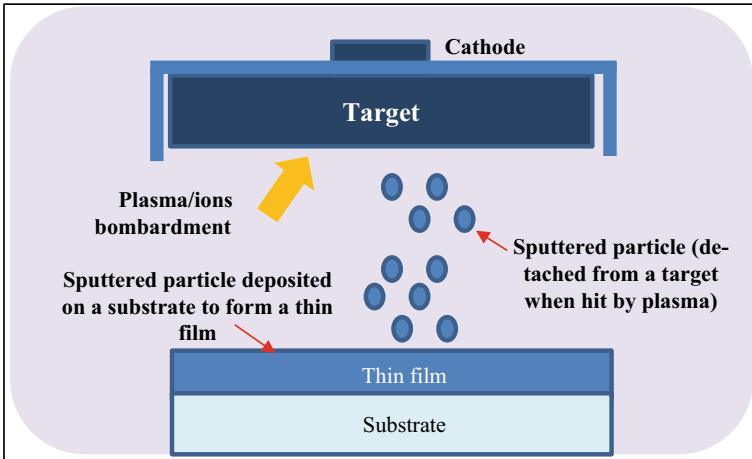
Fig. 1 Schematic of the sputtering process

programmed that not only describes the range of ions that can enter matter, but also many other aspects of the damage done to the target throughout the slowing-down process. It displays the ions penetration into the target in full animation, as well as recoil cascades and target atoms mixing. The sputtering process normally uses argon gas or mixture of gases to deposit ZnO thin films. However, the impact of the ion's bombardment on the ZnO target is rarely studied. Consequently, the ZnO target is easily damaged due to excessive ions bombardment and uncontrolled ionization process of the gas inside the target. Therefore, the simulation of ion beam sputtering is a necessary to analyze the ionization characteristics of different gases inside ZnO during sputtering process. The simulation results will guide an actual fabrication process on the use of appropriate gas for the deposition process for the ZnO target density given. Therefore, the objectives of this paper are: (1) to perform simulation of ions bombardment on the ZnO target using different gases base on SRIM-2013 software and (2) to study the ionization characteristic of different gases inside ZnO target with different ZnO target densities during sputtering process.

2 Experimental Procedure

2.1 Software Setup

The simulation software used to analyze the ionization characteristic of different gases was SRIM. Ziegler developed a program, which was initially released in 1985 [23]. SRIM is a collection of computers programmed that calculate ion-matter interactions. The program transport of ions in matter forms the basis of SRIM (TRIM).

SRIM calculates the interactions of energetic ions with amorphous targets and displays them statistically and graphically, making the ion beam process more understandable. The simulation of the ions was done using SRIM-2013 software. To use this software, there were three things need to be considered:

1. Which ion data will be use?
2. What the density of target material?
3. Will the target be amorphous after the implant?

   The simulation had been carried out by the following steps:

- Steps 1: The type of ion data is selected. The ion data used for sputtering with ZnO target were set to 8 types, which are Argon, Helium, Xenon, Neon, Krypton, Radon, Nitrogen and Oxygen.
- Steps 2: Name the target layers as ZnO and set the width to 1000 Å.
- Steps 3: The density of ZnO was varied from 0.4283 g/cm^3 to 4.283 g/cm^3.
- Steps 4: Zinc element and Oxygen element were selected to the layer.
- Steps 5: The input parameters were saved, and the simulation of sputtering using SRIM software was conducted.
- Steps 6: After a few moments, the ionization characteristics were analyzed. Then, the calculated parameters were displayed, and all the data were collected.

   The results of the simulations are presented and discussed in this paper. The results were collected for 8 types of gas ions with differents ZnO target density. However, the ion energy was fixed for each simulation process at 10 keV. Therefore, the results are only discussed based ion range and depth of ion diffusion.

2.2   Data Collecton and Analysis

The software produces the distribution of ion inside ZnO target during sputtering. From the simulation results, there were data that successfully collected including ion range, straggle of ion, backscattered ion, transmitted ion, ionization energy and ionization recoils energy. From this data, the sputtering process using different ions could be analyzed.

3   Result and Discussion

Figure 2 shows projected longitudinal range of ions for different gases versus ZnO target density. The results show that different ions give different ionization characteristics inside ZnO target in form of ion range values. The ion range plot for ions produced by Neon, Oxygen, and Nitrogen gases show almost identical patterns with ion range value increases when the target density increases from 0.4283 g/cm^3 up to 1.2849 g/cm^3. However, the ion range value decreases as the target density is further
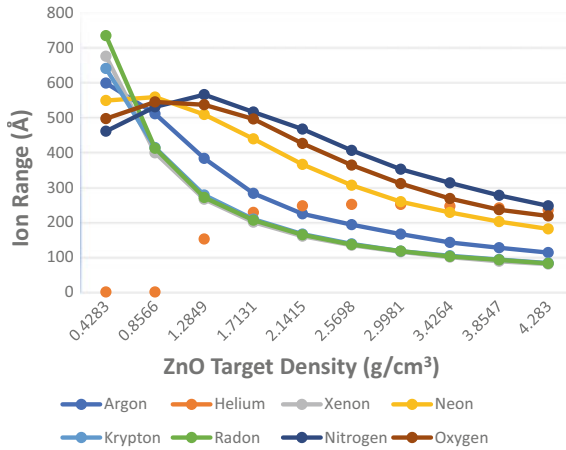
Fig. 2 Projected longitudinal range of ions for different gases versus ZnO target density

increased to 4.283 g/cm^3. For Argon, Radon, Krypton, and Xenon gases, the ion range shows decreased value when the target density increases from 0.4283 g/cm^3 to 4.283 g/cm^3. Meanwhile, for Helium gas, no ion range was recorded at the low ZnO target density up to 0.8566 g/cm^3. However, the ion range increases gradually when the target density increases to 2.1415 g/cm^3 and become almost constant when the target density increases up to 2.1415 g/cm^3. From the plot in Fig. 2, it could be observed that the longitudinal range of ion almost constant for all gases with the value less than 500 Å at the ZnO density of 4.283 g/cm^3. The Radon ion shows the highest longitudinal range at target density of 0.4283 g/cm^3 but decreases as the density of ZnO increases. The radon ion also shows the lowest longitudinal range at the highest target density of 4.283 g/cm^3. Meanwhile, the helium ion shows the lowest longitudinal range at target density of 0.4283 g/cm^3 but the longitudinal ion range increases as the density of the ZnO target increases. Generally, for all gases except Helium, it could be sumarized that the longitudinal range of ion decreases as the target density increases.

Table 1 shows the result of the range of ion that diffused into ZnO during sputtering process for Radon and Xenon. These two gases had the highest diffused depth in the target material at ZnO density of 0.4283 g/cm^3 but subsequently reduced as the target density increased up to 4.2830 g/cm^3. Generally, the commercially available ZnO target has the theoretical density of approximately 5.61 g/cm^3. However, this study aims to investigate the condition of gas ionization characteristics inside ZnO target that has lower density compared to commercial target. The low target density often found in the self-made ZnO target, which prepared using limited lab facility and less controlled environments. Therefore, this study is important to investigate the impact of ions bombardment on the ZnO target at low density particularly for self-made target.

Table 1 Longitudinal ion range for Radon and Xenon ions at different ZnO target densities

ZnO target density (g/cm^3)	Ion range (Å)	
	Radon	Xenon
0.4283	735	676
0.8566	412	399
1.2849	271	266
1.7131	206	200
2.1415	164	160
2.5698	136	134
2.9981	117	115
3.4264	102	100
3.8547	92	88
4.2830	82	80

The ZnO target material has been bombarded with different gases ions but in this result only Radon gas is discussed as it has the highest value for longitudinal ion range for the lowest density of ZnO target. Figures 3a–j show the simulation results of sputtering process using Radon gas on ZnO target with different density values. For the first simulation in Fig. 3a, the density of ZnO was set to 0.4283 g/cm^3 and the result of the simulation was the range of ion diffused into ZnO with the value of 735 Å. Diffusion of Radon ion during sputtering process recorded as the highest due the mass of the ion of 222 amu, which is the heaviest compared to other gases. From this result in Fig. 3a–j, it is shown that the density of target material has inverse relation with the depth of the ion diffusion. The higher the density of target material, the shorter the diffusion of the ions inside ZnO target. Theoretically, energy also play significant role for sputtering process and have a direct relationship with ion depth but as the energy of ions was set to constant (10 keV), it will not be considered in this simulation results.

The ions must have a material-dependent minimum energy to evict an atom from the target (typically 30–50 eV). The sputtering yield rises over this point. At low target density, gas ions at high energy are diffused much deeper into the target and hardly accumulated on surface. Therefore, during this condition, the yield of the sputtering is not in the optimum condition. The achievable momentum transfer is determined by the mass ratio of the ion and target atom. When the mass of the target and the ion are almost equal, maximum yield is reached for light target atoms. The maximal yield changes to ever greater mass ratios between the ion and the target atom as the mass of the target atoms grows.

Based on these results, the best gases for sputtering process would be Radon, Krypton, and Xenon at high density ZnO target. This is because the projected ion range for these gases decreases a lot as the density of the target increases. As the projected ion range are lower, it will preserve the target material after the sputtering process. By looking at the pattern of projected ion range of Radon Krypton, and Xenon gases, the ion range decreases more with the increase of target density and
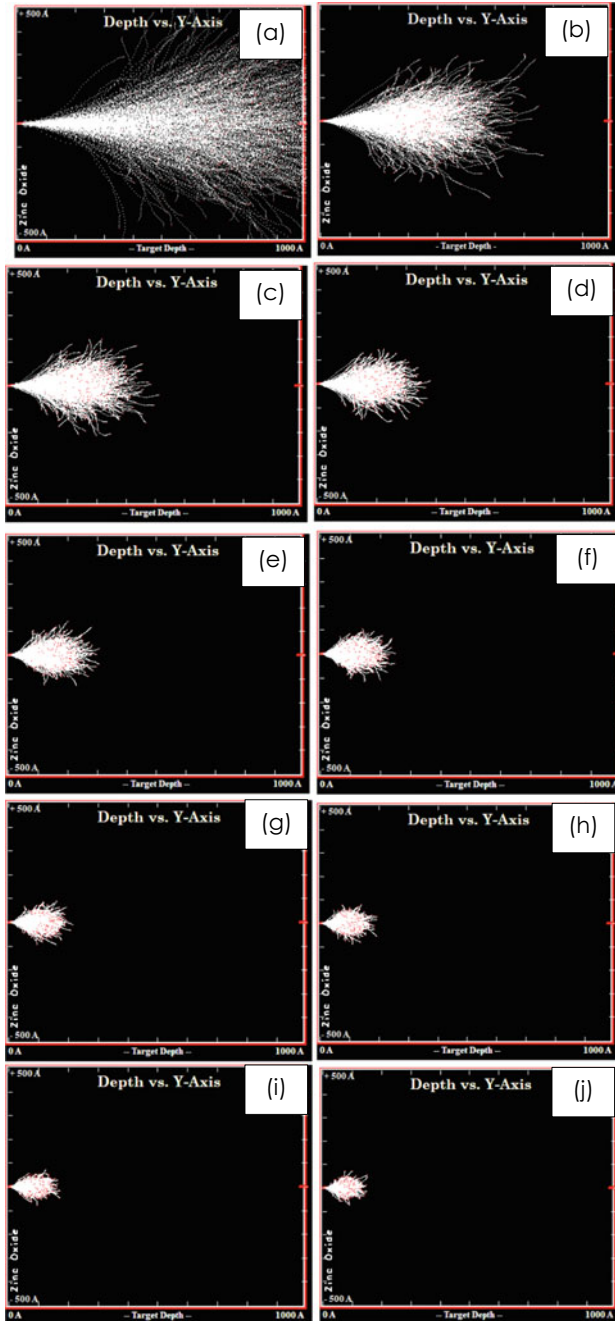
Fig. 3 The depth of Radon ion diffused inside various densities of ZnO target during sputtering process (Inside ZnO target with density of **a** 0.4283 g/cm^3, **b** 0.8566 g/cm^3, **c** 1.2849 g/cm^3, **d** 1.7131 g/cm^3, **e** 2.1415 g/cm^3, **f** 2.5698 g/cm^3, **g** 2.9981 g/cm^3, **h** 3.4264 g/cm^3, **i** 3.8547 g/cm^3, and **j** 4.283 g/cm^3)

only touch the surface of the target material, which is necessary to protect the ZnO target from damage and prolonging lifespan of the target. In addition, these gases also have small kinetic energies which are beneficial to produce smooth and high quality ZnO thin film. Nagata et al. reported that ZnO thin film deposited using Xenon plasma shows better quality and smoother surface compared to those deposited using Argon plasma [24]. They reported that Xenon plasma has lower electron temperature than that of the Argon plasma. Moreover, the recorded ion density in the Xenon plasma is higher than the ion density in the Argon plasma. These characteristics enables the deposition of high quality of ZnO thin film on the substrate.

The results produced by the SRIM simulation may differed to that of simulated by other software due to the different model used. The SRIM uses the Ziegler-Birsack-Littmark (ZBL) interatomic potential model [25]. Other software such as OKSANA and MARLOWE use screened Coulomb potential model [26]. The limitation of this software probably to get the good and accurate results at low energies of sputtering process (below 1 keV), where the surface effects are vital. However, this research conduct at high energy sputtering of 10 keV, in which the surface effects suffer the loss of their impact, particularly at normal incidence. Therefore, these results could be used as a guide to conduct a physical experiment on ZnO sputtering at high energy.

4   Conclusion

This simulation confirmed that the density of ZnO target and depth of projected ion have an inverse relationship. The lower the density, the deeper the ion will diffuse into the target. The deeper the diffusion, the worse effect would be received by the sputtering target. The sputtering process is a physical process that causes a solid material to vaporize by blasting it with energized ion bombardment. The ion beam processing is a common technique for forming thin films on materials, engraving processes, white material erosion, and analytical techniques. In conclusion, the Radon, Krypton, and Xenon gases were identified as the best gases for sputtering process for high ZnO target density in this simulation, which shown by low ion ranges to indicate high ion accumulation on the target surface.

References

1. Haghparas Z, Kordrostami Z, Sorouri M, Rajabzadeh M, Khalifeh R (2021) Highly sensitive non-enzymatic electrochemical glucose sensor based on dumbbell-shaped double-shelled hollow nanoporous CuO/ZnO microstructures. Sci Rep 11:344

2. Rasool A, Santhosh Kumar MC, Mamat MH, Gopalakrishnan C, Amiruddin R (2020) Analysis on different detection mechanisms involved in ZnO-based photodetector and photodiodes. J Mater Sci: Mater Electron 31:7100–7113

3. Ismail AS, Mamat MH, Yusoff MM, Malek MF, Zoolfakar AS, Rani RA, Suriani AB, Mohamed A, Ahmad MK, Rusop M (2018) Enhanced humidity sensing performance using Sn-Doped ZnO nanorod Array/SnO₂ nanowire heteronetwork fabricated via two-step solution immersion. Mater Lett 210:258–262

4. Malek MF, Sahdan MZ, Mamat MH, Musa MZ, Khusaimi Z, Husairi SS, Md Sin ND, Rusop M (2013) A novel fabrication of MEH-PPV/Al: ZnO nanorod arrays based ordered bulk heterojunction hybrid solar cells. Appl Surf Sci 275:75–83

5. Bhati VS, Hojamberdiev M, Kumar M (2020) Enhanced sensing performance of ZnO nanostructures-based gas sensors: A review. Energy Rep 6:46–62

6. Liu C, Wu W, Zhang D, Li Z, Ren G, Han W, Guo W (2021) Effective stability enhancement in ZnO-based perovskite solar cells by MACl modification. J Mater Chem A 9:12161–12168

7. Mamat MH, Che Khalin MI, Nik Mohammad NNH, Khusaimi Z, Md Sin ND, Shariffudin SS, Mohamed Zahidi M, Mahmood MR (2012) Effects of annealing environments on the solution-grown, aligned aluminium-doped zinc oxide nanorod-array-based ultraviolet photoconductive sensor. J Nanomaterials 2012:189279

8. Mohamed R, Rouhi J, Malek MF, Ismail AS, Alrokayan SAH, Khan HA, Khusaimi Z, Mamat MH, Mahmood MR (2016) Sol gel synthesized zinc oxide nanorods on single and co-doped ZnO seed layer templates: morphological, optical and electrical properties. Int J Electrochem Sci 11:2197–2204

9. Md Sin ND, Mamat MH, Malek MF, Rusop M (2014) Fabrication of nanocubic ZnO/SnO₂ film-based humidity sensor with high sensitivity by ultrasonic-assisted solution growth method at different Zn: Sn precursor ratios. Appl Nanosci 4:829–838

10. Müller R, Huber F, Töws M, Mangold M, Madel M, Scholz J-P, Minkow A, Herr U, Thonke K (2020) High-Quality ZnO layers grown by CVD on sapphire substrates with an AlN Nucleation Layer. Cryst Growth Des 20:3918–3926

11. Mamat MH, Hafizah NN, Rusop M (2013) Fabrication of thin, dense and small-diameter zinc oxide nanorod array-based ultraviolet photoconductive sensors with high sensitivity by catalyst-free radio frequency magnetron sputtering. Mater Lett 93:215–218

12. Malek MF, Mamat MH, Soga T, Rahman SA, Abu Bakar S, Ismail AS, Mohamed R, Alrokayan SAH, Khan HA, Mahmood MR (2015) Thickness-controlled synthesis of vertically aligned c-axis oriented ZnO nanorod arrays: effect of growth time via novel dual sonication sol–gel process. Jpn J Appl Phys 55:01AE15

13. Ponja SD, Sathasivam S, Parkin IP, Carmalt CJ (2020) Highly conductive and transparent gallium doped zinc oxide thin films via chemical vapor deposition. Sci Rep 10:638

14. Mamat MH, Malek MF, Hafizah NN, Asiah MN, Suriani AB, Mohamed A, Nafarizal N, Ahmad MK, Rusop M (2016) Effect of oxygen flow rate on the ultraviolet sensing properties of zinc oxide nanocolumn arrays grown by radio frequency magnetron sputtering. Ceram Int 42:4107–4119

15. Zainizan Sahdan M, Hafiz Mamat M, Salina M, Khusaimi Z, Noor UM, Rusop M (2010) Heat treatment effects on the surface morphology and optical properties of ZnO nanostructures. Phys Status Solidi C 7:2286–2289

16. Mamat MH, Sahdan MZ, Amizam S, Rafaie HA, Khusaimi Z, Rusop M (2009) Optical and electrical properties of aluminum doped zinc oxide thin films at various doping concentrations. J Ceram Soc Jpn 117:1263–1267

17. Suriani AB, Dalila AR, Mohamed A, Mamat MH, Malek MF, Soga T, Tanemura M (2016) Fabrication of vertically aligned carbon nanotubes–zinc oxide nanocomposites and their field electron emission enhancement. Mater Des 90:185–195
18. Mohamed A, Ardyani T, Abu Bakar S, Sagisaka M, Umetsu Y, Hamon JJ, Rahim BA, Esa SR, Abdul Khalil HPS, Mamat MH, King S, Eastoe J (2018) Rational design of aromatic surfactants for graphene/natural rubber latex nanocomposites with enhanced electrical conductivity. J Colloid Interface Sci 516:34–47
19. Sobri M, Shuhaimi A, Hakim KM, Ganesh V, Mamat MH, Mazwan M, Najwa S, Ameera N, Yusnizam Y, Rusop M (2014) Effect of annealing on structural, optical, and electrical properties of nickel (Ni)/indium tin oxide (ITO) nanostructures prepared by RF magnetron sputtering. Superlattices Microstruct 70:82–90
20. Najwa S, Shuhaimi A, Ameera N, Hakim KM, Sobri M, Mazwan M, Mamat MH, Yusnizam Y, Ganesh V, Rusop M (2014) The effect of sputtering pressure on structural, optical and electrical properties of indium tin oxide nanocolumns prepared by radio frequency (RF) magnetron sputtering. Superlattices Microstruct 72:140–147
21. Behera A, Rajak DK, Kolahchi R, Scutaru M-L, Pruncu CI (2020) Current global scenario of Sputter deposited NiTi smart systems. J Market Res 9:14582–14598
22. Geyao L, Yang D, Wanglin C, Chengyong W (2020) Development and application of physical vapor deposited coatings for medical devices: a review. Procedia CIRP 89:250–262
23. Ziegler JF, Biersack JP, Ziegler MD (2008) SRIM, the stopping and range of ions in matter. SRIM Company
24. Nagata T, Ashida A, Fujimura N, Ito T (2004) The effects of Xe on an rf plasma and growth of ZnO films by rf sputtering. J Appl Phys 95:3923–3927
25. Shulga VI (2018) Note on the artefacts in SRIM simulation of sputtering. Appl Surf Sci 439:456–461
26. Robinson MT, Torrens IM (1974) Computer simulation of atomic-displacement cascades in solids in the binary-collision approximation. Phys Rev B 9:5008–5024

Zinc Oxide Based Resistive Type Humidity Sensor Performance Enhancement Through Doping, and Composite Strategy: An Initial Assessment

A. S. R. A. Subki , **M. H. Mamat** , **A. Manut** , **M. D. Birowosuto** ,
M. Z. Musa , **M. Y. Ahmad, and M. Rusop**

Abstract Pristine zinc oxide (ZnO) has various limitations that severely limit the development of ZnO as humidity sensors. However, doping, co-doping, and the implementation of composite structures are excellent methods for improving ZnO nanostructures' structural, optical, and electrical properties. This review will reveal and discussed various dopant impurities and effects of composite formation employed by preceding researchers to enhance the performance of humidity sensing of resistive type humidity sensor based on ZnO as sensing material. We are inspired to present this study and evaluate the improvement in humidity sensing performance considering there are limited review papers that address this topic.

Keywords Humidity sensor · Zinc Oxide · Nanostructure · Doping · Composite

A. S. R. A. Subki · M. H. Mamat (✉) · A. Manut · M. Z. Musa
NANO-Electronic Centre (NET), School of Electrical Engineering, College of Engineering, Universiti Teknologi MARA, 40450 Shah Alam, Selangor, Malaysia
e-mail: mhmamat@uitm.edu.my

M. H. Mamat · M. Rusop
NANO-SciTech Lab, Centre for Functional Materials and Nanotechnology, Institute of Science (IOS), Universiti Teknologi MARA, 40450 Shah Alam, Selangor, Malaysia

A. S. R. A. Subki
Faculty of Electrical and Electronic Engineering Technology, Universiti Teknikal Malaysia Melaka, Hang Tuah Jaya, 76100 Durian Tunggal, Melaka, Malaysia

M. D. Birowosuto
CNRS International NTU THALES Research Alliances (CINTRA), Research Techno Plaza, 50 Nanyang Drive, Border X Block, Singapore 637553, Singapore

M. Y. Ahmad
Nanorian Technologies Sdn Bhd, No 40, Jln Kajang Perdana 3/2, Taman Kajang Perdana, 43000 Kajang, Selangor, Malaysia

1 Introduction

As natural occurrence, humidity occurs as a result of the presence of moisture in the air. An excellent humidity sensor can be specified centered on criteria such as higher sensitivity, dependency on operating temperature, minimum response time, good repeatability, and lower hysteresis, longer shelf life with sufficient durability, capacity to handle pollutants, and low production cost [1]. Typical humidity sensors are constructed from a variety of materials, with metal oxide semiconductors being one of the most prominent. This is due to substantial ratio of surface-to-volume, non-toxicity, minimal cost, superior sensitivity, simplicity in fabrication, fast response with improved sensitivity, and decent thermal and chemical stability.

Zinc oxide (ZnO) has drawn a lot of attentions from researchers that study its potential as a sensing material due to its availability and configurable surface structure, wide resistivity range, and excellent chemical and thermal durability [2]. ZnO is an inorganic semiconductor of the II-VI type with ionicity that exists on the boundary between covalent and ionic semiconducting materials. At room temperature (T = 300 K) ZnO exhibits a wide and directly energy gap of 3.37 eV and 3.437 eV at low temperature (T = 4 K) with 60 meV of relatively significant exciton energy [3].

Various parties are doing experiments and analysis with the objective of improving the performance of ZnO-based resistive humidity sensors, primarily in terms of sensitivity, response/recovery time, and stability, with varying degrees of success. Doping is an intriguing and realistic method for modifying various semiconductor materials. Doping is a mechanism by which extrinsic components are inserted into the intrinsic structure to enhance and change their basic properties, such as structural, optical, and electrical properties. Principle of doping is shown as in Fig. 1. Composite, in another way, is coupling two types of semiconductor materials that owns dissimilar energy band gaps which permitted recombination of electron–hole pairs that directly modified material properties. Nevertheless, a review on effect of doping and formation of
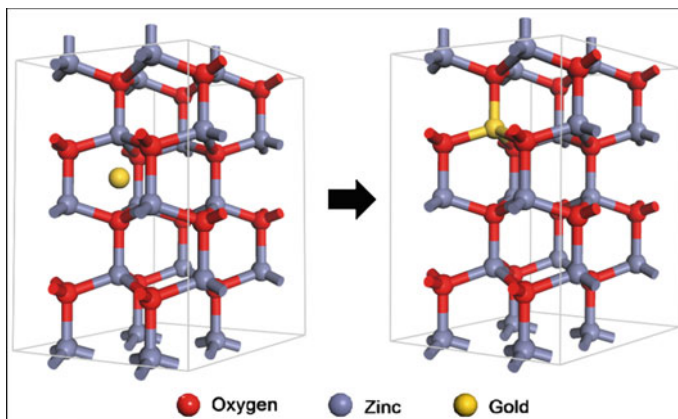
Fig. 1 ZnO doping with gold (Au) impurity [4]

composite strategy to improved ZnO-based resistive type humidity sensor remained scarce. Herein, recent progress on the ZnO-based resistive type humidity sensor on effect of doping impurities and formation of composting strategy is presented, reviewed, and discussed.

2 Effect of Doping

The pristine ZnO possess a minimal specific surface area, poor electron mobility and deficiency of hydrophilic functional groups on its surface, thus, strictly limits ZnO progression as suitable material for humidity sensing [5]. Doping is the act of adding specific amount of impurity into a host material. The doping process will alter the structural properties, surface morphology, electrical conductivity properties of ZnO through integration with transition and post-transition metals [6, 7]. In other words, doping is an optimal solution to address these deficiencies and to enhance the nature of pristine ZnO.

2.1 Single Doping Strategy

For instance, ZnO was reported to be doped with numerous kinds of elements, but several impurities such Al, Sn, Cu, Au, W and F reported to have a significant impact on ZnO-based humidity sensor. Table 1 summarized the performance and its improvement of ZnO based humidity sensing at various doping impurities element.

Kundu et al. developed a highly responsive resistive humidity sensor constructed from porous aluminum-doped ZnO (Al: ZnO, AZO) thin films [8]. In this study, the doping concentration varying from 0 to 5 at.% and then the thin films are calcined 500 °C to optimize crystallinity, electrical and optical features. According to morphological analysis, the samples are porous, and the surface porosity increases as the Al doping concentration increases. The nanoporous structure is crucial in the aggregation and adhesion of foreign particles on the film's surface. The analysis for humidity sensing performance found that the highest responsivity value of 733 and sensitivity of 0.3 MΩ/%RH are obtained from a 5 at.% AZO sample. In regards of response/recovery time, the 5 at.% AZO samples perform the best in terms of humidity response across the whole relative humidity range. The response peaks in each cycle are nearly identical, indicating that the AZO sensor has good repeatability.

Humidity sensing based on aluminum oxide (Al_2O_3) doped ZnO nanomaterials synthesized through solid state chemical route has been successfully studied by Misra et al. [9]. According to their studies, samples in pellet form containing Al_2O_3 doped ZnO nanocrystalline powders with different weight percentage (wt.%) of Al_2O_3 in ZnO were prepared and upon exposure to humidity, the pellet resistance reduced when relative humidity (RH) continued to increase. The best sensitivity of 14.98 MΩ/%RH is achieved with the sample containing 15 wt.% of Al_2O_3 in ZnO and

Table 1 ZnO based humidity sensing performance and its improvement at various doping impurities element

Doping technique	Doping impurity	Response/recovery	Sensitivity	Sensitivity calculation	Refs.
Single dopant element	Aluminium	250 / 202	0.3 (↑**8%**)	$\Delta R/\Delta\%RH$	[8]
	Aluminium Oxide	85 / 286	14.98 (↑**15%**)	$\Delta R/\Delta\%RH$	[9]
	Tin	250 / 35	3.36 (↑**25%**)	R_a/R_{rh}	[10]
	Tin Oxide	74 / 212	32.16 (↑**62%**)	$\Delta R/\Delta\%RH$	[11]
	Copper	32 / 47	39.14 (↑**47%**)	$\Delta R/\Delta\%RH$	[12]
	Gold	28 / 118	20.73 (↑**80%**)	$\Delta R/\Delta\%RH$	[13]
	Tungsten	45 / 105	1.44 (↑**42%**)	$\Delta R/R_{rh}$	[14]
	Fluorine	8 / 25	226 (↑**20%**)	R_a/R_{rh}	[15]
Co-dopant element	Al+F	7 / 24	247 (↑**25%**)	R_a/R_{rh}	[16]
	Y+Al	15 / 50	15 (↑**5%**)	R_a/R_{rh}	[17]

annealed at 700 °C. In term of response and recovery time, the sample with 15 wt.% of Al_2O_3 in ZnO response/recovery time were clocked at 85 and 286 s, respectively. They also indicate, in a span of 6 month, the sensing element sensitivity are within 2% different in cyclic repeatability.

Sensing film based on tin (Sn) doped zinc oxide (TZO) for humidity sensing application were successfully fabricated by Ismail et al. [10]. These nanorod arrays of Sn were synthesized at various Sn concentrations varying from 0.6 to 3 at.%. Upon exposure to humidity absorption and desorption process, the humidity sensor doped with Sn up to 1 at.%, its sensitivity increased from 1.55 to 3.36 and plummeted to 1.36 as concentration reached 3 at.%. Based on their experiment, all of these findings revealed that TZO has a significant potential for humidity-sensor applications and optimizing doping element concentrations is critical.

Pallet samples containing various wt.% of SnO_2 dopant element in ZnO were prepared by solid-state reaction route for humidity sensing studies by Misra and his co-workers [11]. According to morphological studies, as the annealing temperature increased, porosity of the material increases, resulting in clusters of SnO_2 doped in ZnO. The large pores link the inter-granular pores and this arrangement facilitates water vapour adsorption and desorption process. As for humidity sensing experiment, compared to sensors based on pure and other concentration of SnO_2-doped ZnO nanomaterials, the sensor based on 15 wt.% SnO_2-doped ZnO nanomaterials had the superior sensing behaviour. The response and recovery time for 15 wt.% SnO_2-doped ZnO were clocked quicker (74/212 s) compared to other samples with the sensitivity of 32.16 MΩ/%RH. Apart from that fabricated sensor possess feature such lower hysteresis, less ageing impact, and excellent repeatability.

Other works by Misra and Pandey, using copper sulphate as dopant source, copper (Cu) doped ZnO nanomaterial were prepared for humidity sensing analysis [12]. According to evidence from micrograph images, as the temperature rises, the porosity of the material increases, resulting in the formation of clusters for Cu doped ZnO. At 600 °C annealing temperature, grains of nanocomposites produced are distributed all over the substrate, forming a network of pores. They found that Cu-doped ZnO thin films annealed at 600 °C surpass all other prepared samples, with a sensitivity of 39.14 MΩ/%RH and quick response time of 32 s and a recovery time of 47 s. They conclude when compared to pristine ZnO, Cu-doped ZnO nanomaterial has higher adsorption and desorption rates, which results in higher sensitivity, lower hysteresis, faster response/recovery time, and superior reproducibility.

Using hydrothermal method at low processing temperature, pristine and Au nanoparticle-modified (ANM) ZnO nanorods were successfully prepared by Young and Lai [13]. According to micrograph analysis, the surfaces of the ANM ZnO nanorods, were rough because the Au nanoparticles were adsorbed on the surfaces of the ZnO nanorods. As for humidity sensing analysis, the structures of both humidity sensors displayed strong photo-to-dark current contrast ratios and rapid response and recovery times. According to their experimental findings, the ANM ZnO nanorods humidity sensor outperformed the pure ZnO nanorods humidity sensor in terms of humidity sensing performance with the contrast ratios of photo-to-dark current, response time, and recovery time were 20.73, 28 s, and 118 s, respectively. They conclude that deposited Au nanoparticles might significantly improve humidity sensing.

By varying different molar ratio of sodium tungstate dihydrate as source of dopant, Verma and his workfellow efficaciously synthesized pure and tungsten (W) doped ZnO nanocrystals through the co-precipitation procedure [14]. Based on morphological studies, the nanostructures are distinguished by interconnected inter-necked grains and capillary pores that provide a large specific area and available sites for water molecule infiltration. As for humidity sensing performance, the humidity sensing characteristics are strongly reliant on the W concentration. In the 10 to 90%RH range, a nano-sensor doped with 1.75 mol.% W exhibits the highest sensitivity of 1.44 with considerable swift response and recovery times of 45 and 105 s, respectively. All of these features contribute to the credibility of W-doped ZnO-based humidity sensor for usage in a practical context.

Algun studied the effect of varying the fluorine (F) doping concentration on the humidity sensing properties of F-doped zinc oxide (FZO) structures that were synthesized using a combination of the sol-gel and dip coating method [15]. Nevertheless, the crystallinity of the FZO thin films is increased with 2 mol.% of F dopant concentration which due to the probability of filling oxygen vacancies with F anions. Based on morphological study, homogeneous and uniform surfaces consisting of nano-sized grains and capillary pores. In term of electrical characteristic, the resistance of all samples decreases as the relative humidity level rises. With 2 mol.% the amount of F doping, this sample displays a remarkable superior sensitivity (226) compared to the other FZO sample and an undoped ZnO. Other humidity sensing performance, such as stability, reproducibility, response/recovery time, also indicate an excellent

result in contrast to undoped ZnO. F doping reduces response time, and response and recovery times for 2 mol.% sample is the best recorded at 8 s and 25 s, respectively.

2.2 Co-doping Strategy

Co-doping is a potential method for effectively tuning dopant populations, electronic attributes, and magnetic properties. It can improve the solubility of dopants and the stability of targeted defects [18].

Based on the results of previous studies [15], Algun and Ackay study the humidity sensor performances of aluminum (Al) and fluorine (F) co-doped zinc oxide (AFZO) nanostructured thin films with varying Al concentrations by maintaining the F doping concentration at 2 mol.% [16]. According to micrograph image, the formation and presence of capillary pores will help promote the process of water molecule adsorption on the surface of an AFZO film. At a concentration of 1 mol.% of Al dopant, the crystallinity of AFZO film improved. The electrical properties of an AFZO nanostructured suggest a significant improvement compared to FZO films. They revealed that with 1 mol.% of Al, the sensor had the highest sensitivity of 247. Apart from that, all AFZO sensors demonstrated outstanding resistance measurement stability over time with insignificant quantity of hysteresis. The recorded response/recovery time were 7 and 24 s, respectively. They observed that aluminum doping improves the humidity sensor properties of the previous FZO nanostructured thin films.

Uzar et al. in their work were successfully prepared Yttrium/Aluminium (Y/Al) co-doped zinc oxide-based humidity sensor [17]. The Al concentration was kept constant at 0.5%, while the Y element was varied from 0.5 to 2%. According to micrograph images, Al and Y co-doped ZnO are in tiny clamped rectangular and dot-shaped structures with free of cracks and uniform in appearance. According to the humidity sensing testing, the resistance of a Y/Al-doped ZnO sample changes as the %RH being changed from 25 to 95%. According to the experimental results, the resistances of AZOY thin films rise and response time shortened when the RH percentage increases. They summarized, as Y concentration increases, the electrical changes of AZOY films against humidity become more noticeable.

3   Effect of Composite

The formation of ZnO composite is another way to increase the performance of humidity sensors. Composite materials are assembled by merging and combining two or more materials with different and unique characteristics. The different materials in the composite work together to give the unique composite properties such superior physical and chemical capabilities when compared to the individual materials.

On work related to tin oxide, Velumani et al. synthesis and grown SnO_2 thin films and ZnO/SnO_2 composite thin films on cleaned soda-lime glass substrates [19]. For

the characterization of the humidity sensing performance, compared to pure SnO_2, the improvement in impedance is related to the adsorption of water molecules at both the ZnO and SnO_2 surface sites, resulting in a cumulative impact. In term of response time, the composite ZnO/SnO_2 based sensors exhibit faster response time which recorded at roughly 21 s. Compared to composite structure, the pure SnO_2 based humidity sensors possess nearly three-time better sensitivity calculated at (1.10 $\pm$ 0.079) kΩ/%RH. Finally, the stability of the composite sensor was analyzed shows the negligible variation in the impedance over the tested period.

In their most recent works, Velumani and his colleague further their investigation on pure and composite thin films based on ZnO and SnO_2 [20]. For humidity sensing performance analysis, the result exhibits that ZnO/SnO_2 based composite films show a greater shift in impedance with regard to the RH levels which offer greater humidity sensing characteristics compared to pure ZnO based sensors. Compared to their previous works [19], the prepared composite films had the fastest response time of 17 s. However, they found that the prolonged desorption of water molecules from the sensing surface accounted for the poor recovery times recorded at 65 s. The ZnO rich composite sensors possesses better sensor response of 95% and sensitivity of 8.6 $\pm$ 0.5 kΩ/%RH with acceptable hysteresis of 2.9%. Apart from that, the result shows that the hysteresis for sensing mechanism prepared via sol-gel method is far better compared to sample prepared with reactive magnetron sputtering (4.3%).

Using gold (Au) nanoparticle to modified ZnO nanosheets structure, Yu et al. synthesis and fabricated humidity sensor [21]. They indicated, with 0.5 mM of chloroauric acid as Au source, Au/ZnO composite based humidity sensor displays nearly 5 orders of magnitude fluctuation in impedance manifestation with better linearity compared to pure ZnO when tested in a range of RH from 11 to 95%. Apart from that, the response time and recovery time of Au/ZnO composite based humidity sensors recorded at 16 s and 28 s, respectively and observed faster compared to pure ZnO as well as constricted hysteresis loop (~3.0%). The Au/ZnO based humidity sensor possess a good repeatability, fast response, and identical response curves over four cycles. In terms of resistance stability, minimal changes in resistance might be seen over time and suggest that Au/ZnO nanosheets could improving the performance of ZnO humidity sensors.

At low temperatures, coral-like CuO nanostructures were hydrothermally synthesized by Zainelabdin and his co-workers via selective growth on ZnO nanorods [22]. As for humidity sensing performance characterization, the humidity sensing properties of the nanocoral CuO/ZnO-based humidity sensor show a significant linear reduction in direct current resistance. They also found that the nanocoral based humidity sensor disclose the highest sensitivity factor of ~6045 among available data for the constituent materials and demonstrates fast dynamic response to humidity variations with response and recovery time recorded at 6 s and 7 s, respectively. However, the CuO/ZnO NC RH sensor has a comparatively substantial hysteresis effect of 21%, implying that the NC RH sensor requires additional design improvement.

Jagtap et al. in their works reported the synthesis of ZnO nanoparticles through ammonium zincate bath and sodium zincate bath [23]. In term of humidity sensing performance, they discovered that films made with sodium zincate bath have higher

sensitivity than films made with ammonium zincate bath. They conclude that by varying TiO_2 percentage, sensitivity toward humidity is found to increased significantly. The sensitivity recorded for 10 wt.% TiO_2 added ZnO films prepared via sodium zincate bath were 11.34 $M\Omega$/%RH with response and recovery time logged at 10 s and 60 s, respectively. Finally, they concluded the prepared humidity sensor has good repeatability, low hysteresis, and good reproducibility.

Pandey and his co-worker prepared the nanocomposite powder pellets by mixing TiO_2 pure powder with pure ZnO powder [24]. Based on their humidity characterization analysis, they discovered that as the relative humidity rises the pellets resistance decreases significantly. Moreover, they conclude with addition of TiO_2 to ZnO, the overall sensitivity decreases. On the other hand, for the sensing element with the 15 wt.% of TiO_2 in ZnO produces best results with a sensitivity of 9.08 $M\Omega$/%RH. However, the sensitivity for pure ZnO-based humidity sensor are much higher (12.89 $M\Omega$/%RH). In contrast, the hysteresis for the prepared humidity sensor with the 15 wt.% of TiO_2 in ZnO produces the lowest of all, which is within 2%, with less effect of ageing and good reproducibility. The logged response and recovery times of this sensing element are the lowest at 84 s and 396 s, respectively. They observed that the respond and recovery time for ZnO–TiO_2 nanocomposite are shorter than humidity sensor based on pure ZnO sensing elements (128 s, 452 s), but higher than ZnO–Cu_2O nanocomposite based humidity sensor (76 s, 196 s) [25].

ZnO–WO_3 nanocomposite pallet were synthesized by Shakya and his associates, and their humidity sensing characteristics have been studied and reported [26]. They observed that the resistance of the sensing materials was found to decrease with increase in relative humidity. They observed the humidity sensor with 5 wt.% of ZnO showed highest sensitivity recorded at 20.95 $M\Omega$/%RH. Compared to other sample at different ZnO weight percentage annealing temperature, the response and recovery time is far better for 5 wt.% ZnO-doped WO_3 composites that have been annealed at 600 °C. They finally conclude that 5 wt.% of ZnO–WO_3 composite also shows better stability and reproducibility, lower hysteresis, and less reaction to aging.

Zhang and his colleague have been successfully developed and fabricated resistive-type humidity sensor based on coated hierarchical ZnO/MWCNTs/ZnO nanocomposite film [27]. Based on their analysis, the measured resistance of the sensor is ranging from 5.94 to 8.10 $k\Omega$ with a sensitivity of 24.8 Ω/%RH. They also found that that the sensor demonstrated small hysteresis, acceptable repeatability over five exposure/recovery cycles repeatedly, and swift response-recovery characteristics (4 s and 34 to 74 s). They also suggested the potential sensing mechanism for the produced sensor was credited to the ZnO/ MWCNTs/ZnO nanostructures itself and interlayer swelling effects. The research data showed that the suggested film sensor is extremely sensitive toward RH and have potential material for humidity sensors.

The effect of the hexamethylenetetramine (HMT) on the UV and humidity sensing capabilities of nanocomposite consists of ZnO and cellulose (ZCN) were studied investigated by Sahoo and his co-worker [28]. As RH was increased, they identified a considerable variation in ZnO-cellulose nanocomposites impedance. With 0.9 wt.% of HMT concentration of synthesized ZCN sensor, the impedance declined

to 2.888×10^5 Ω in 90%RH from 2.24646×10^8 Ω in 40%RH. As a result, the calculated sensitivity of the nanocomposite to humidity was 4.487 MΩ/%RH. Aside from that, the ZCN humidity sensor exhibited impressive repeatability and little fluctuation in impedances, indicating that the ZCN sensor device is stable over time. According to these findings, the ZnO-cellulose nanocomposite can be utilized to construct humidity sensors.

Tomer et al. synthesized $ZnO\text{-}SiO_2$ nanocomposites for purpose of detecting relative humidity (RH) at room temperature [29]. Based on their experimental findings, the sensor utilizing in situ loading process exhibits superior impedance changes along with excellent linearity, and good repeatability. The sensor exhibits rapid response and recovery time recorded at 15 s and 16 s, respectively with sensor marginal to negligible hysteresis of 1.2%. In over a span of 30 days, the sensor shows outstanding consistency, stability and a satisfactory variation in impedance is measured. To conclude, they suggested that their study will pave the way for the fabrication of high-performance RH sensors using $ZnO–SiO_2$ hybrid nanocomposite.

4 Conclusion

A study at the most recent improvements and development of ZnO resistive type humidity sensors has been presented. According to the reported results, the doping and formation of composite strategy is relevant for enhancing the favorable characteristics of the pristine ZnO structure. An enhancement such reduced crystallite, high-quality surface structure and porosity, an abundance of oxygen-containing functional group sites, lower surface resistance to alleviate higher electromobility, and a high concentration of free carrier all contribute to the improved performance of ZnO-based resistive humidity sensors. Obviously, thanks to the excellent efforts of researchers on this subject, ZnO has a tremendous potential to become a very efficient humidity sensing material. However, there are still voids to be filled in order to increase the device's performance even further.

References

1. Najeeb MA, Ahmad Z, Shakoor RA (2018) Organic thin-film capacitive and resistive humidity sensors: a focus review. Adv Mater Interfaces 5(21):1–19
2. Yu Z, Zhang H, Li Z (2019) Effects of pH on high-performance ZnO resistive humidity sensors using one-step synthesis. Sensors 19(23):5267

3. Hahn YB (2011) Zinc oxide nanostructures and their applications. Korean J Chem Eng 28(9):1797–1813
4. Cajzl J et al (2020) Creation of gold nanoparticles in ZnO by ion implantation–DFT and experimental studies. Nanomaterials 10(12):1–21
5. Ismail AS et al (2019) Structural modification of ZnO nanorod array through Fe-doping: ramification on UV and humidity sensing properties. Nano-Structures and Nano-Objects 18:100262
6. Yang H et al (2017) Stable and fast-response capacitive humidity sensors based on a ZnO nanopowder/PVP-RGO multilayer. Sensors (Switzerland) 17(10)
7. Chou CC, Shih LH, Chang SJ (2020) The study of humidity sensor based on Li-doped ZnO nanorods by hydrothermal method. Microsyst Technol 9
8. Kundu S, Majumder R, Ghosh R, Pal Chowdhury M (2019) Superior positive relative humidity sensing properties of porous nanostructured Al:ZnO thin films deposited by jet-atomizer spray pyrolysis technique. J Mater Sci Mater Electron 30(5):4618–4625
9. Misra SK, Pandey NK, Shakya V, Roy A (2015) Application of undoped and Al_2O_3-doped ZnO nanomaterials as solid-state humidity sensor and its characterization studies. IEEE Sens J 15(6):3582–3589
10. Ismail AS et al (2018) Modulation of Sn concentration in ZnO nanorod array: intensification on the conductivity and humidity sensing properties. J Mater Sci Mater Electron 29(14):12076–12088
11. Misra SK, Pandey NK (2016) Analysis on activation energy and humidity sensing application of nanostructured SnO_2-doped ZnO material. Sens Actuators A Phys 249:8–14
12. Misra SK, Pandey NK (2016) Study of activation energy and humidity sensing application of nanostructured Cu-doped ZnO thin films. J Mater Res 31(20):3214–3222
13. Young SJ, Lai LT (2021) Investigation of a highly sensitive Au nanoparticle-modified ZnO nanorod humidity sensor. IEEE Trans Electron Devices 68(2):775–779
14. Verma V, Pandey NK, Gupta P, Singh K, Singh P (2021) Humidity sensing enhancement and structural evolution of tungsten doped ZnO nanosensors fabricated through co-precipitation synthesis. Phys B Condens. Matter 619(March):413224
15. Algün G (2018) Humidity sensing properties of fluorine doped zinc oxide thin films. J Mater Sci Mater Electron 29(19):17039–17046
16. Algün G, Akçay N (2019) Enhanced sensing characteristics of relative humidity sensors based on Al and F co-doped ZnO nanostructured thin films. J Mater Sci Mater Electron 30(17):16124–16134
17. Üzar N, Algün G, Akçay N, Akcan D, Arda L (2017) Structural, optical, electrical and humidity sensing properties of (Y/Al) co-doped ZnO thin films. J Mater Sci Mater Electron 28(16):11861–11870
18. Zhang J, Tse K, Wong M, Zhang Y, Zhu J (2016) A brief review of co-doping. Front Phys 11(6)
19. Velumani M, Meher SR, Alex ZC (2018) Impedometric humidity sensing characteristics of SnO_2 thin films and SnO_2–ZnO composite thin films grown by magnetron sputtering. J Mater Sci Mater Electron 29(5):3999–4010
20. Velumani M, Meher SR, Alex ZC (2019) Composite metal oxide thin film based impedometric humidity sensors. Sens Actuators B Chem 301(September):127084
21. Yu S, Zhang H, Chen C, Lin C (2018) Investigation of humidity sensor based on Au modified ZnO nanosheets via hydrothermal method and first principle. Sens Actuators B Chem 287(October):526–534
22. Zainelabdin A et al (2012) CuO/ZnO Nanocorals synthesis via hydrothermal technique: Growth mechanism and their application as Humidity Sensor. J Mater Chem 22(23):11583–11590
23. Jagtap S, Priolkar KR (2013) Evaluation of ZnO nanoparticles and study of ZnO-TiO_2 composites for lead free humidity sensors. Sens Actuators B Chem 183:411–418
24. Pandey NK, Tiwari K, Roy A (2012) ZnO–TiO_2 nanocomposite: Characterization and moisture sensing studies. Bull Mater Sci 35(3):347–352
25. Pandey NK, Tiwari K, Roy A (2011) Moisture sensing application of Cu_2O Doped ZnO Nanocomposites. IEEE Sens J 11(9):2142–2148

26. Shakya V, Pandey NK, Misra SK, Roy A (2017) Electrical and optical properties of ZnO-WO$_3$ nanocomposite and its application as a solid-state humidity sensor. Bull Mater Sci 40(2):253–262
27. Zhang D et al (2016) Humidity-sensing properties of hierarchical ZnO/MWCNTs/ZnO nanocomposite film sensor based on electrostatic layer-by-layer self-assembly. J Mater Sci Mater Electron 27(3):2481–2487
28. Sahoo K, Mohanty B, Biswas A, Nayak J (2020) Role of hexamethylenetetramine in ZnO-cellulose nanocomposite enabled UV and humidity sensor. Mater Sci Semicond Process 105(May):104699
29. Tomer VK, Duhan S, Sharma AK, Malik R, Nehra SP, Devi S (2015) One pot synthesis of mesoporous ZnO-SiO$_2$ nanocomposite as high performance humidity sensor. Colloids Surfaces A Physicochem Eng Asp 483:121–128

Potential of Microparticles Graphitize Coconut Shell Charcoal with Low Ball Milling Time

Hafsa Omar, Nur Syazwani Abdul Malek, Nurfazianawatie Mohd Zain, Zuraida Khusaimi, Saifollah Abdullah, M. Rusop, and Noor Asnida Asli

Abstract Coconut shell charcoal is a reliable and eco-friendly agro waste material in order to produce carbon materials due to it containing a high percentage of carbon at more than 50%. Smaller particle size of graphite based coconut shell formed a high quality graphene oxide by reducing oxidation time during chemical synthesis. Coconut shell charcoal (CSC) powder was produced by mesh using mortar, then ball milled using for four different speeds of 250 rpm, 350 rpm, 450 rpm and 550 rpm at low ball milling time, 1 h. Particle size analysis of graphite from CSC powder was measured using Particle Sizer and Micro-Raman spectroscopy was also utilized. The particle size of carbon particle synthesize via ball mill at 250 rpm mill was observed to have z-average of 1466 nm compared to particle size before ball mill which is z-average 2759 nm. Milling speed at 550 rpm shows the smallest particle size at z-average 1355 nm with existence of D-peak, G-peak and also highest 2D-peak from Raman analysis. All samples of CSCp were graphitize coconut shell charcoal due to the existence of a broad Raman resonance peak of D band at 1339 cm^{-1}, G band at 1589 cm^{-1} and 2D region.

Keywords Coconut shell · Carbon powder · Ball Milling · Particle size · Raman spectroscopy

H. Omar · N. S. A. Malek · N. M. Zain · Z. Khusaimi · S. Abdullah · M. Rusop · N. A. Asli (✉)
Centre for Functional Materials and Nanotechnology, Institute of Sciences, Universiti Teknologi MARA, Shah Alam, Selangor, Malaysia
e-mail: asnida1462@uitm.edu.my

H. Omar · N. S. A. Malek · N. M. Zain · Z. Khusaimi · S. Abdullah · N. A. Asli
Faculty of Applied Science, Universiti Teknologi MARA, 40450 Shah Alam, Selangor, Malaysia

M. Rusop
NANO-ElecTronic Centre (NET), School of Electrical Engineering, College of Engineering, Universiti Teknologi MARA, 40450 Shah Alam, Selangor, Malaysia

1 Introduction

For many years, Coconut has been planted in almost every country in Asian region due to its use especially in the food industry. However, it becomes an agro wastes from household and food processing industries when the outer parts of the coconut fruit were peeled and thrown [1]. This agro waste can turn into environmental pollution as it can get incinerated and lead to release large amounts of carbon dioxide (CO_2). Coconut shell (CS) is a very reliable and eco-friendly material, can be transformed to powder form structure and synthesis into natural carbon source by heating it in high temperature, thus pyrolysis to turn it into coconut shell charcoal [2]. Coconut shell charcoal (CSC) is a renewable natural resource and C-amorphous material which can be turned into natural carbon. Natural carbon which contains the highest oxygen to carbon ratio influences the properties of Graphene oxide, thus affecting the application in future (GO) [2, 3]. In natural carbon such as CS, the oxygen percentage were around 30% compared to carbon at more than 50% [4]. Graphite is known to be in three forms which are amorphous structure at around 70–80%, another structure which is crystalline flakes at 90–98%. It also can be in formed of crystalline lump, or vein at 90–99% [5, 6]. Furthermore, graphite from agro waste has been chosen as starting material to be used in order to form graphene oxide because it is low cost, more structured, higher strength and others [7, 8].

The process of turning bulk CS into CS powder, then synthesis into graphite, top down method has been suggested nowadays by researchers around the world. Ball milling, which is one of the top down approaches, produces three types of species that can be distinguished in different forms such as nanoparticles, flakes/slabs, and unground micro-sized particles [9]. The top-down method can reduce material particle size with an initial size of a few micrometers into nano-particles with a size in the range of 40–200 nm [10]. Ball milling (BM) is a simple, reproducible, and eco-friendly method for converting bulk materials to the nanometer range [9]. Nanomaterials have a great advantage because the small size of particles leads to large surface area which affects applications in device performance.

The advantage of reducing particle size and shape of carbon powder is because its application affects the oxidation time of graphene oxide formed by hummer's method. Based on research done by Shojaeenezhad et al., oxidation time for synthesis of graphene oxide decreases with the reduction of particle size [11]. The particle size also significantly altered the characteristic of coating material in its application [12]. Synthesis of nanomaterials through mechanical milling are dependent on the charge ratio, rate of rotation of vial, brittleness of materials used, milling duration [13], size of the milling balls and materials of which the balls are made. In this research, we study systematically the influence of ball milling speed to reduce the particle size of local coconut shell charcoal.

2 Materials and Method

The experimental methodology consists of two processes which are the preparation of graphite nanoparticles and also the characterization.

2.1 Preparation of Graphite Nanoparticle

Coconut shell charcoal (CSC) was obtained from east coast Malaysia. Coconut shell charcoal powder (CSCp) was produced by meshing the CSC using mortar. The CSCp were ball milled using planetary ball mill, model: PM 200 RESTCH for four different speeds which are 250 rpm, 350 rpm, 450 rpm and 550 rpm. In this research, ball milling was using a zirconia ball with weight of 4.81 g at 1 h milling time.

2.2 Characterization

Particle size analysis of graphite from local CSCp was measured using ZETA NANO SIZER-S. Micro-Raman spectroscopy was utilized using Jobin Yvon (model DU420A-OE-325). X-ray diffraction analysis was done to study the structural properties of CSC powder before and after ball milled using model brand PANanalytical X'pert PRO.

3 Results and Discussion

The particle size distribution can be observed as in Fig. 1 for all four samples. From Fig. 1, it can be observed that the particle size distribution was non-homogeneous. However, there is an improvement in particle size distribution as the ball milling speed increases to 400 rpm. The particle size distribution in Fig. 1 was observed to be approximately at micrometer range. This will be discussed in more detail in Table 1. Collisions between steel ball and particle inside the ball mill grinding jars can generate particle friction which gives rise to abrasion or particle breakage that will lead to particle fragmentation [14]. However, due to the extent collision between particles is dependent on various factors such as material structure which is either its crystalline or amorphous, thus affecting the particle size distribution of CSCp.

Table 1 tabulates the particle size of mesh CSCp and varied speed CSCp from 250 rpm, 350 rpm, 450 rpm and 550 rpm. There was some reduction of particle size about 1674 nm between samples of CSCp mesh and CSCp after the ball milled at a low speed of 250 rpm. It was observed that an increase of ball milling speed from 250 to 450 rpm caused the particle size of CSCp to increase. Increasing ball
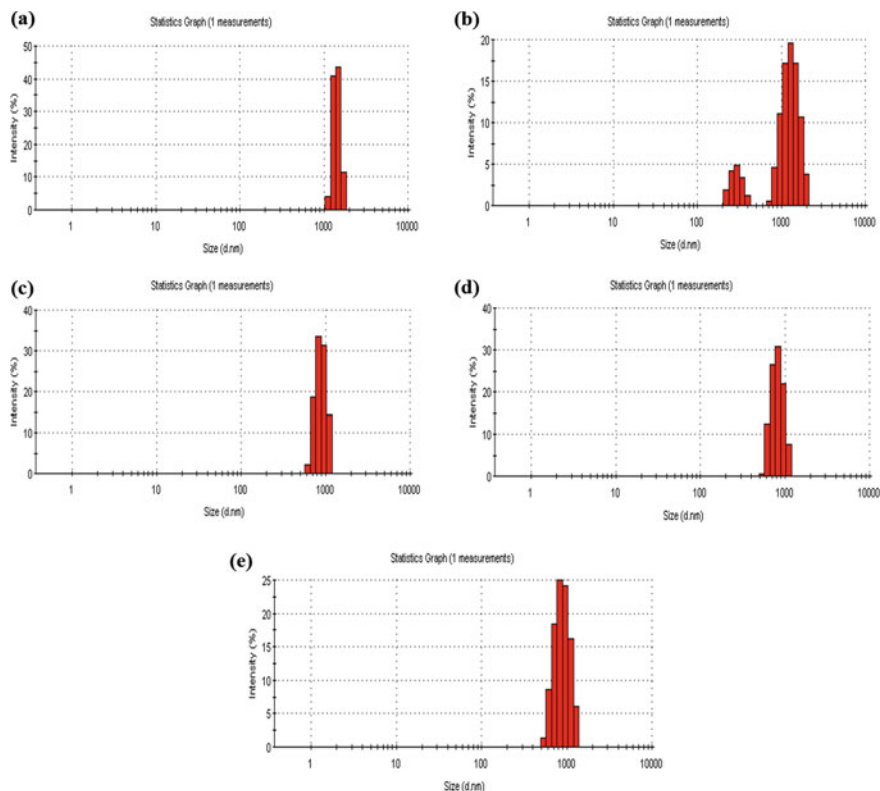
Fig. 1 Particle size analysis for graphite from local coconut shell charcoal (CSCp) **a** control sample-mesh **b** 250 rpm **c** 350 rpm and **d** 450 rpm and **e** 550 rpm

Table 1 Coconut shell charcoal particle size analysis after initial mesh and ball mill using steel ball for different speed

	Speed (rpm)	Weight (g)	Time (min)	Z-Average (d/nm)
Mesh	–	5	1 h	2790
Ball mill	250			1466
	350			1720
	450			1577
	550			1355

mill speed resulted in deterioration of the agglomeration of nanoparticles [15]. The kinetic energy of the steel ball inside the jar is proportional to the rotation speed [16]. As the rotation speed increases, the kinetic energy of the steel ball increases. The decrease in particle size happens as a result from the complicated dynamic interaction of the steel balls and turbulent slurry inside the grind jar during the ball mill process
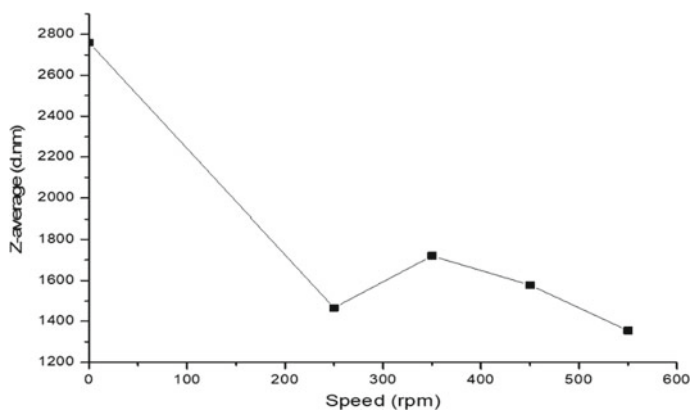
Fig. 2 Particle size analysis for graphite from local coconut shell charcoal (CSC)

compared to CSCp mesh. At a certain size of ball used, a higher rotation speed (rpm) yields a finer average particle size because of the higher number of rotations within a given period of milling time (12 h). Based on research done by H. Shin et. al, the optimized rotation speed of the mill using ~2 mm will achieve average particle size (d_{50}) around 840 nm at 153 rpm [16]. However, the milling time to achieve such average particle size was longer which is 12 h compared to our study, 30 min.

Figure 2 shows the graph of particle size analysis from CSCp by meshing process and CSCp after ball mill. From Fig. 2, the reduction of particle size obviously appeared after the CSCp were ball milled at 250 rpm speed. It can be observed that decreasing in particle size as there is an increment in milling speed led to an increase in surface area (high surface energy) of the coconut shell charcoal particle [17]. However, the z-average of sample 250 rpm seems to have smaller value than the next milling speed at 350 rpm and 450 rpm. This is due to light scattering during particle sizer analysis where more to a small portion of large particle size hence give a higher z-average for sample 350 rpm. One or two individual large particles may scattered more light than a distribution of smaller particle [18]. Corresponding to Fig. 1c which shows that sample 250 rpm particle size distribution is non-homogeneous. Higher speed of ball milling at a short time gave a smaller particle size [9]. This situation can be observed as the milling speed increased to 550 rpm, the particle size decrease to the smallest z-average at 1355 nm. Size reductions were observed to stop and particle size increases because of aggregation particles due to the effect of Van der Waal force and Coulomb electrostatic force acting on particle [19].

In order to investigate the existence of the stone-like shape of carbon particles, a non-destructive measurement of Raman spectroscopy was performed for all five samples. Figure 3 shows Raman spectroscopy analysis of CSCp after mesh which shows the existence of D peak, G peak and 2D peak at 1339.65 cm^{-1}, 1589 cm^{-1} and 2681 cm^{-1}. G peak is corresponding to the ordered sp^2-hbridized carbon bonds in the lattice, while D peak indicates the presence of the edge basal defects or other impurities in the carbon materials. Raman spectroscopy was done to prove that CSCp
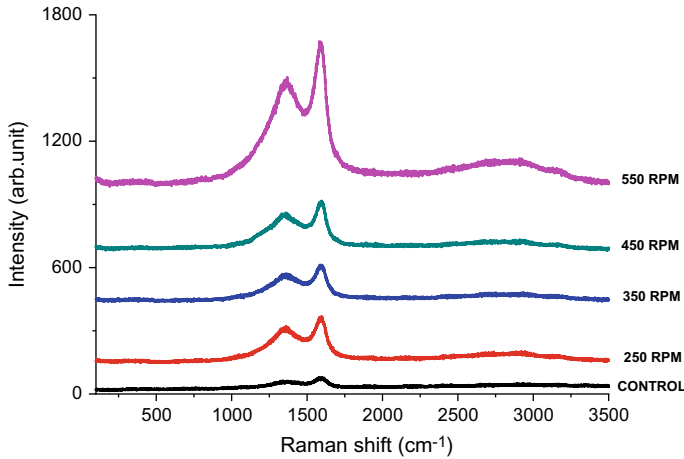
Fig. 3 Raman spectroscopy of CSCp control sample (mesh) and ball milling at milling speed 250 rpm, 350 rpm, 450 rpm and 550 rpm

is a carbon material based on the existence of the Raman resonance peak of D, G and 2D peak [20]. The broad D peak and G peak reveal that it is an amorphous carbon [21]. Conversion of a particle to a smaller size by using mechanical exfoliation will promote a high number of crystalline defects [22]. This can be observed as the milling speed increases, the D-band peak increases gradually. The increment of D-peak intensities indicate the transformation of in-plane sp^2 carbon to disordered tetrahedral sp^3 carbon domains [23].

Table 2 tabulated data on the intensity and also the Raman shift of five different samples. In this research, milling at 550 rpm shows less disordered carbon structure at I_D/I_G of 0.7937 compared to others milling speed. I_D/I_G, the intensity ratio between the D-peak and G-peak is used to characterize defect content of the ball mill carbon based CS. As the milling speed increases, there is a formation of nanosized particles with a less disordered structure [24]. There is an increase of 2D peak of samples that was milled compared to the MESH sample which shows a better exfoliation of

Table 2 Raman spectroscopy analysis on reducing size of carbon particle based coconut shell from ball milling

Speed (rpm)	Intensity			Raman shift	
	I_D	I_G	I_D/I_G	D-peak	G-peak
Mesh	60.102	77.419	0.7763	1358.140	1601.550
250	213.922	263.837	0.8108	1358.136	1588.372
350	192.275	226.071	0.8505	1358.136	1589.982
450	220.543	274.533	0.8033	1358.139	1595.348
550	675.127	850.594	0.7937	1364.341	1588.372

carbon based CSC [25]. It can be observed that there is a large difference at 153.82 for the ID value of mesh compared to ball milling. Based on Mendoza et.al, intensity of D peak can exhibit an amount of defect in carbon structure because of the vibrational modes that comes from the disorganized region near particle edges, lattice defects and vacancies [24].

4 Conclusion

In this paper, graphite microparticles were successfully synthesized using ball milled at different milling speeds. Particle size analysis was done successfully and it can be concluded that at 550 rpm is the optimal ball milling speed for sample CSCp as it has the smallest particle size. CSCp, which is a mesh reduces the particle size and and shows as an amorphous graphites particle proved by Raman spectroscopy as the existence of three bands which are D, G and 2D. For future work, more parameters suggest to be done in order to achieve nanoparticle size of CSCp.

References

1. Wachid FM, Perkasa AY, Prasetya FA, Rosyidah N, Darminto (2014) Synthesis and characterization of nanocrystalline graphite from coconut shell with heating process. AIP Conf Proceed 1586(1):202-206
2. Supeno M, Siburian R (2020) New route: convertion of coconut shell tobe graphite and graphene nano sheets. J King Saud Univ-Sci 32(1):189–190
3. Mahmoudi E, Ang WL, Ng CY, Ng LY, Mohammad AW, Benamor A (2019) Distinguishing characteristics and usability of graphene oxide based on different sources of graphite feedstock. J Colloid Interface Sci 542:429–440
4. Rosi M, Viridi S (2018) Reduction the oxygen content of the coconut shell char produced by using simple pyrolysis method. In: IOP conference series: materials science and engineering, vol 395, no 1, p 012024
5. Sujiono EH, Zabrian D, Dahlan MY, Agus J, Amin BD (2021). Fabrication and characterization of graphite powder based on coconut shell waste. Mater Today Proc
6. Yang Q, Geng Y, Dong H, Zhang J, Yu X, Sun L, Chen Y (2017) Effect of environmental regulations on China's graphite export. J Cleaner Prod 161:327–334
7. Bello SA, Agunsoye JO, Hassan SB (2015) Synthesis of coconut shell nanoparticles via a top down approach: assessment of milling duration on the particle sizes and morphologies of coconut shell nanoparticles. Mater Lett 159:514–519
8. Sun L, Fugetsu B (2013) Mass production of graphene oxide from expanded graphite. Mater Lett 109:207–210
9. Hashaikeh R (2018) Insight into ball milling for size reduction and nanoparticles production of HY zeolite. Mater Chem Phys 220:322–330

10. Hou TH, Su CH, Liu WL (2007) Parameters optimization of a nano-particle wet milling process using the Taguchi method, response surface method and genetic algorithm. Powder Technol 173(3):153–162

11. Shojaeenezhad SS, Farbod M, Kazeminezhad I (2017) Effects of initial graphite particle size and shape on oxidation time in graphene oxide prepared by Hummers' method. J Sci Adv Mater Dev 2(4):470–475

12. Arun S, Hariprasad S, Saikiran A, Ravisankar B, Parfenov EV, Mukaeva VR, Rameshbabu N (2019) The effect of graphite particle size on the corrosion and wear behaviour of the PEO-EPD coating fabricated on commercially pure zirconium. Surf Coat Technol 363:301–313

13. Bello SA, Agunsoye JO, Adebisi JA, Anyanwu JE, Bamigbaiye AA, Hassan SB (2017) Potential of carbonised coconut shell as a ball-milling interface for synthesis of aluminium nanoparticles. Ann Fac Eng Hunedoara 15(2):149

14. Farizhandi AAK, Zhao H, Chen T, Lau R (2020) Evaluation of material properties using planetary ball milling for modeling the change of particle size distribution in a gas-solid fluidized bed using a hybrid artificial neural network-genetic algorithm approach. Chem Eng Sci 215:115469

15. Jalili F, Zhiani M, Kamali S (2018) Preparation and evaluation of a new hybrid support based on exfoliation of graphite by ball milling for Ni nanoparticles in hydrogen evolution reaction. Int J Hydrogen Energy 43(46):21187–21195

16. Shin H, Lee S, Jung HS, Kim JB (2013) Effect of ball size and powder loading on the milling efficiency of a laboratory-scale wet ball mill. Ceram Int 39(8):8963–8968

17. Jeffry SNA, Jaya RP, Hassan NA, Yaacob H, Mirza J, Drahman SH (2018) Effects of nanocharcoal coconut-shell ash on the physical and rheological properties of bitumen. Constr Build Mater 158:1–10

18. Hallett FR (1994) Particle size analysis by dynamic light scattering. Food Res Int 27(2):195–198

19. Krishna S, Patel CM (2019) Preparation of coconut shell nanoparticles by wet-stirred media milling. Mater Lett 257:126738

20. Couzi M, Bruneel JL, Talaga D, Bokobza L (2016) A multi wavelength Raman scattering study of defective graphitic carbon materials: the first order Raman spectra revisited. Carbon 107:388–394

21. Robaiah M, Rusop M, Abdullah S, Khusaimi Z, Azhan H, Asli NA (2017) Synthesis graphene layer at different waste cooking palm oil temperatures. In: AIP conference proceedings, vol 1877, no 1, p 030008. AIP Publishing LLC

22. Mendoza-Duarte JM, Robles-Hernández FC, Gomez-Esparza CD, Miranda-Hernández JG, Garay-Reyes CG, Estrada-Guel I, Martínez-Sánchez R (2020) Exfoliated graphite preparation based on an eco-friendly mechanochemical route. J Environ Chem Eng 8(5):104370

23. Sharma S, Susan D, Kothiyal NC, Kaur R (2018) Graphene oxide prepared from mechanically milled graphite: effect on strength of novel fly-ash based cementitious matrix. Constr Build Mater 177:10–22

24. Mendoza-Duarte JM, Bocanegra-Bernal MH, Martínez-Sánchez R, Estrada-Guel I (2013) Raman spectroscopy and microstructural study of natural graphite processed by high-energy ball mill. Microsc Microanal 19(2):1596–1597

25. Baqiya MA, Nugraheni AY, Islamiyah W, Kurniawan AF, Ramli MM, Yamaguchi S, Cahyono Y (2020) Structural study on graphene-based particles prepared from old coconut shell by acid–assisted mechanical exfoliation. Adv Powder Technol 31(5):2072–2078

Fault Detection for Automotive Coil Spring Using Signal Processing Analysis

M. H. Mohammed Faozi, Ahmad Razlan Yusoff, Mohd Zuhaifi Zainol, and Zubair Khalil

Abstract Shock absorber failure can be easily detected during shock absorber utilization in the vehicle. The failure usually happened due to crack propagation under fatigue life of compress and extend operation. To prevent any failures during utilization it is preemptive to detect any possible fault during manufacturing quality check inspection process. However, it is very difficult to do full check to all finished product due to high time consumption they require. In order to shorten the time, automated checking method are desire. In this study, automotive coil spring health are recognized using signal processing analysis to enable automated line quality check inspection. Fatigue testing machine was use to excite the spring in order to create signal needed in the processing analysis. The analysis was carried out using excitation signal detected along cycle time. Output data for both healthy and faulted springs (pre-inserted cracked) were processed and compared using signal processing analysis. This method shown an accurate consistency for fault detection of crack occurred in automotive spring where the number of peaks and valley of the signal as well as their maximum values not only able to show defective characteristics but also the severity degree of the defect where higher number and frequency density are more severe than not. This method will definitely able to shorten time needed for quality check inspection of cracks when applied in fabrication line compared to conventional method using naked eyes where micro cracks are very hard to detect.

Keywords Shock absorber · Crack · Signal processing · Detect crack · Fast fourier transforms · Coil Spring

M. H. Mohammed Faozi · A. R. Yusoff
College of Engineering, Universiti Malaysia Pahang, Kampus Gambang, Kuantan, Pahang, Malaysia

M. Z. Zainol · Z. Khalil (✉)
Faculty of Manufacturing and Mechatronic Engineering Technology, Universiti Malaysia Pahang, Pekan, Malaysia
e-mail: zubair@ump.edu.my

1 Introduction

The automobile suspension systems have received a considerable amount of interest from the academicians and automotive industries for their performance characteristics. It includes study the relationship among road handling, against suspension comfort and stability. The automobile suspension mechanism is a system that is commonly implemented to automobiles that mechanically prevents the vehicle body from ground shocks in order to minimize the longitudinal harmful vibration conveyed to the passenger and to retain continuous interaction with the road wheel [1, 2].

Shock absorbers are one of the many parts of an automobile. Its primary aim is not only to have the best efficiency, but also to last longer lifespan of the product. Shock absorbers minimize the movements of a vehicle and car wheels by eliminating the energy stored in the springs or torsion bars. Therefore, the car and the driver would not be impacted by this transportation disruption. Shock absorbers channel kinetic energy from the suspension by generating heat and dissipate them. The majority of new shock absorbers are susceptible to velocity. The shock absorber's resistance is calculated by the caster angle, suspension rpm, and number and scale of the piston hole. Passive dampening happens when the suspension accelerates which ensures the shock absorbers produce passive dampening [3, 4].

The shock absorber spring is an essential and indispensable safety device. The basic idea of the shock absorber work depends on facing the vibration of the car's body while driving, thus ensuring that the car does not swing. It also ensures that there is good adhesion and traction to the road surface so the car does not deviate from the lane [5, 6]. In essence, the automobile's drivers are subjected to a great level of vibrations. They work consistently numerous hours on the car, particularly during the bustling working time. These working conditions not just mischief the wellbeing state of the driver, yet in addition make early exhaustion and diminish his effectiveness. Then again, present necessities for lower cost in car manufacturing prompts a significant prerequisite for better manufacturing method [7]. Under these conditions, improving the ride comfort and ride safety of autos is a requirement. This improvement might be accomplished by designing a system for detecting fault on shock absorber helical springs at a higher efficiency.

Faults of the vehicle suspension system directly affect the stability and safety of the vehicle consequently endangering passenger's life. Over the last few years, researchers have researched the process of detecting and diagnosing faults in suspension components. Xiaoyi Hu has studied how to apply a fault diagnostic approach based on a vehicle dynamics model and dynamic response signal processing technology to locate and identify faults in vertical damping components [8]. Shock absorber spring will eventually wear out over time. Proportionally to how much it wears, shock absorber spring will not function as well as it did at the beginning [9, 10].

Currently, inspection for cracks on coil spring are done manually. This would not only be time consuming, but additionally due to that only randomize sampling can be done. Thus increasing the risk of faulted spring to be overlooked. This may

compromise comfort of the passenger and eventually leading to more severe problem with vehicle handling and safety. It would mean that the driver will lose control of the vehicle and crash into accidents. In this paper, study on possibility of automated inspection method to detect faulted spring with cracks with higher frequency and accuracy. The method will enable us to recognize them before they reach to their critical points of complete failure.

2 Methodology

This study was done using SAE9254 spring steel. It is manufactured for automotive suspension which were supplied by our industrial collaborator. It is commonly used material for suspension due to its properties of high resistance to stress and heat. With heat treatment its tensile strength increased to 2018 N/mm^2. This shock absorber coil springs is specifically for the use of mid-size compact town car. Its chemical composition is shown in Table 1.

Table 2 shown the spring's detail specification. Vertical-type push-pull based Fatigue testing machine as shown in Fig. 2 was used in this study to force spring subject into compressions and tensions to intentionally imitate the automotive vibration motion on the road. Springs were initially compressed from its original length of 275 mm to its full bound at 126.3 mm. Then, pull to full rebound at 246.9 mm. The cycle of spring excitation was done for about 100 cycles per set and maintained at 1 Hz constantly throughout the test. Experimental settings used in the study is shown in Table 3. It is required to create the appropriate vibration motion for the shock absorber springs at several compressions and tensions. Coil spring samples

Table 1 Chemical composition of SAE9254 spring steel (wt %)

Element	wt %
C	0.58
Mn	0.63
P	0.009
S	0.008
Si	1.37
Cr	0.62

Table 2 Spring specifications

Wire diameter (mm)	14.3	±0.06
Mean coil diameter (mm)	101.7	±2
Effective no. of coil (turns)	6.3	±0.05
Spring rate (N/mm)	63	
Free height (mm)	275	
Average Hardness (HV)	585–615	

Table 3 Experimental settings

Spring condition	Displacement (mm)	Stress (MPa)	Load (N)
Full bound (maximum)	126.3	994	8858
Full rebound (minimum)	246.9	140	1260

in three different health conditions prepared for this study. The first one is healthy without any cracks and in good condition. One small size crack was intentionally inserted into the second spring sample using super drill. While the third spring has two cracks that can be seen with naked eye. Figure 1 shows the spring sample and the location of the cracks made in the second and third springs at the second last turn as indicated.

Fig. 1 Shock absorber coil spring

3rd spring's crack is at red and yellow

2nd spring's crack is at red

Sensor PCB352c33 are placed here on the upper die
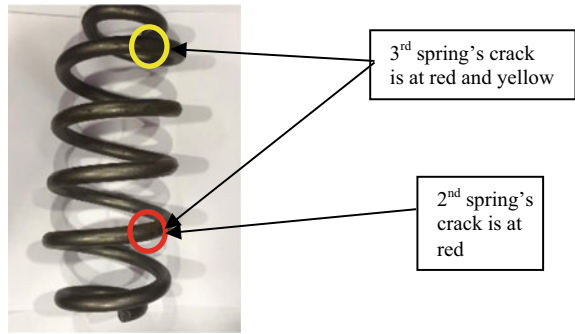
Fig. 2 Fatigue testing machine

Fig. 3 Sensors placement
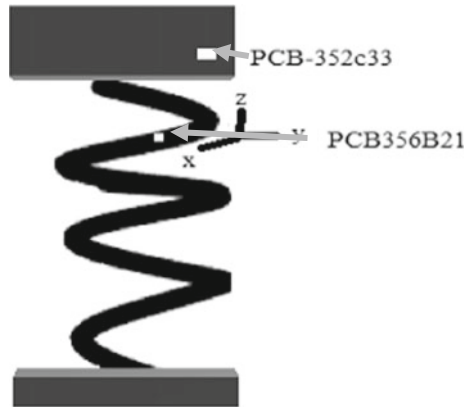
Data Acquisition (DAQ) is used for measurement that is electronic or physical such as voltage, current, temperature, noice, vibration and tone. Two different sensors used were accelerometer sensors (PCB352c33) with sensitivity of 100 mv/g and a dynamic range of peak, and accelerometer sensor (PCB356B21) with a sensitivity of 10 mv/g and a dynamic range of peak to determine the vibration of the coil and vibration of the jig. They are placed into position as shown in Fig. 3. All data will be shown in acceleration, velocity and displacement against time (s). It will be displayed as original output data to match real time estimation for real application. The analysis outcome of this study will be use as reference and validation purposes when this quality checking method is applied into one of the steps for finalizing finished products.

2.1 Data Analysis and Calculation

Data gathered were analysed and displayed using LabVIEW software. By plotting the filter block to filter the signal, the signal will be accelerated by connecting the acceleration to the Fast Fourier Transform (FFT) block to obtain frequency. Additionally, FFT functions was used to calculate velocity and displacement:

$$X(\omega) = \frac{1}{2\pi} \int_{-\infty}^{\infty} x(t)e^{-i\omega t} dt \tag{1}$$

And

$$(t) = \int_{-\infty}^{\infty} X(\omega)e^{-i\omega t} d\omega \tag{2}$$

To obtain velocity from equation:

$$v = \int_0^t a\,dt \tag{3}$$

To obtain displacement from equation:

$$s = \int_0^t v\,dt \tag{4}$$

3 Results and Discussion

3.1 First Shock Absorber Spring (Healthy Condition)

This spring is in healthy condition without any cracks. The acceleration signal, velocity and displacement of this spring are as follow. Figure 4 shows the acceleration of the spring in time domain. As shown in the figure, maximum acceleration peak response of the spring does not exceed 200 m/s² while high density responds are uniformly kept under 50 m/s². Figure 5 shows the Velocity of the first spring in Time domain. As shown in the figure the velocity is stable and uniform at all cycles and has no obvious peak disturbance. The velocity range for peak is 1250 mm/s and valley is −750 mm/s.
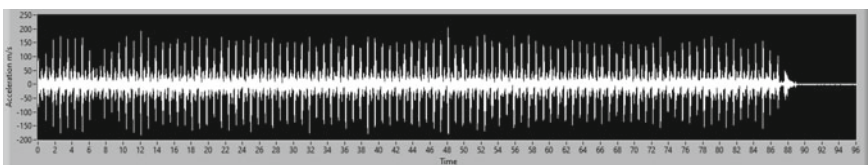
Fig. 4 Acceleration in time domain (s)
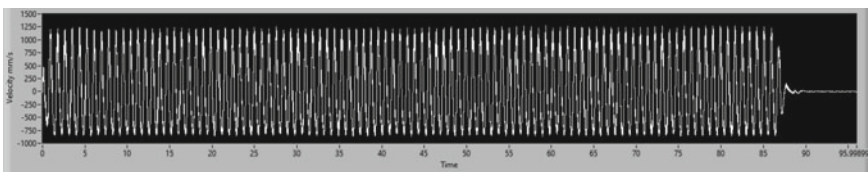
Fig. 5 Velocity in time domain (s)
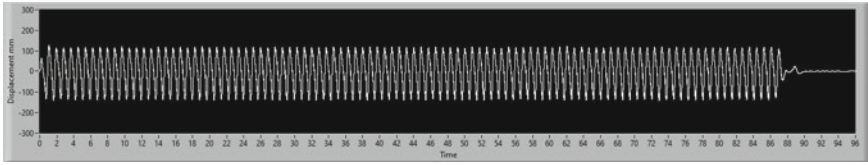
Fig. 6 Jig displacement in time domain (s)
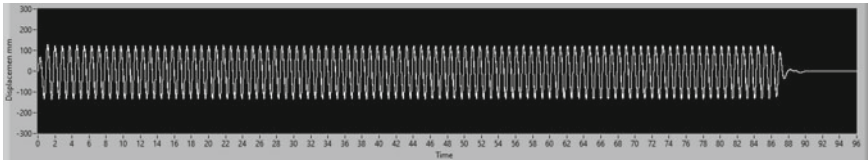
Fig. 7 Spring displacement in time domain (s)

Figures 6 and 7 show the displacement of the machine Jig and the spring in Time domain. Displacement of both Jig and spring shown a similar pattern of simple harmonic motion where there was no peak disturbance. The maximum displacement is 125 mm. The amplitude shown in the output are very closed to the full bound displacement of the coil spring. These output will be our based reference to compare the other springs with it.

3.2 Second Shock Absorber Spring (with One Crack)

This spring has one crack. The acceleration signal, velocity and displacement of this spring are as follow: Fig. 8 shows the acceleration of the spring in time domain. The acceleration shown noise with high density averagely at about $250 \, \text{m/s}^2$. Compared to healthy sample, it has shown an increase of 500% for high density region. Maximum acceleration of the spring is peak is around $400 \, \text{m/s}^2$, while valley is about $-300 \, \text{m/s}^2$. Figure 9 shows the velocity of this spring in Time domain. While the amplitude for velocity's second sample for peak is averagely the same as healthy output while valley shown a deeper value of $-1200 \, \text{mm/s}$, line density was observed to be thicker. This is
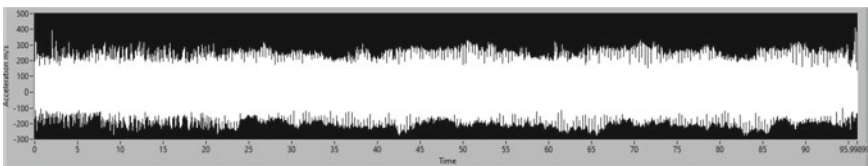
Fig. 8 Acceleration in time domain (s)
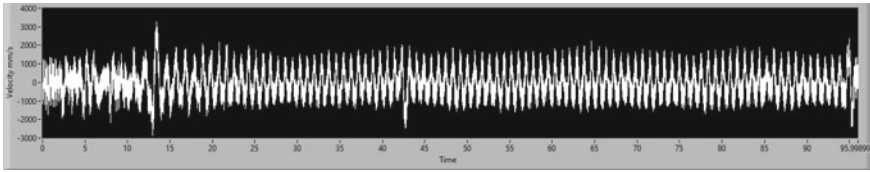
Fig. 9 Velocity in time domain (s)
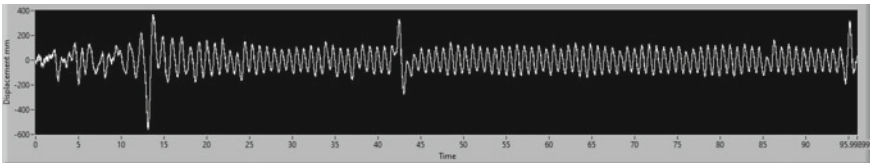
Fig. 10 Jig displacement in time domain (s)
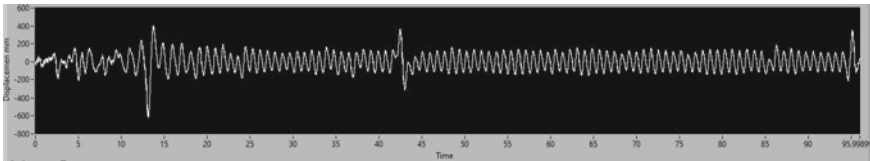
Fig. 11 Spring displacement in time domain (s)

due to higher resistance from the unstable excitation of the coil spring. The maximum velocity which come from one of the peak located at about 13 s is 3000 mm/s and valley is −3000 mm/s. Figure also shown two obvious peaks and three valleys. Figures 10 and 11 show the displacement for jig and spring in time domain. As we have in healthy sample, both output data displayed an almost similar pattern to one another. The average amplitude is about 200 mm which increase 200% from healthy displacement motion. Displacement output displayed 3 peaks and 3 valleys located at 13 s, 43 s, and 96 s. First peak at cycle 13 with compression 600 mm and tension 400 mm, second peak at cycle 43 with ±400 mm and lastly at cycle 96 with compression 200 mm and tension 400 mm. The maximum peak valley shown and increase of at about 300% compare to full bound and rebound actual height.

3.3 Third Shock Absorber Spring (Severely Cracked Condition)

This spring has two cracks. The acceleration signal, velocity and displacement of this spring are as follow: Fig. 12 shows the acceleration of the spring in time domain.
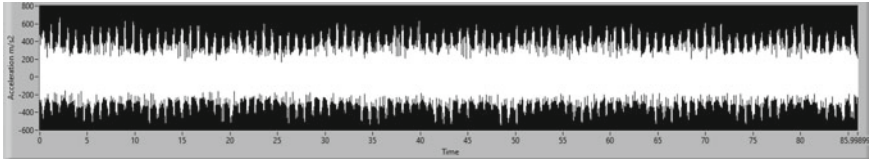
Fig. 12 Acceleration in time domain (s)
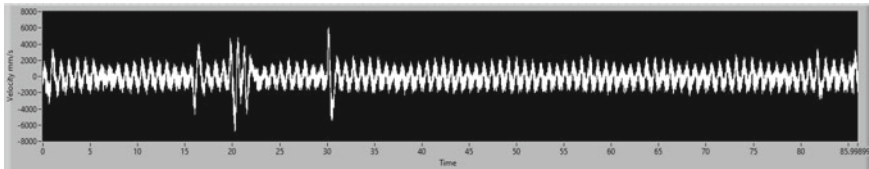
Fig. 13 Velocity in time domain (s)

Acceleration's high density region shown an average of range in between ±300 m/s^2. It increases a bit compared to sample no 2. However, the maximum peaks and valley increase by 180% to show values up to 650 m/s^2. Figure 13 shows the Velocity of this spring in Time domain. It is averagely ranging about ±2000 mm/s with denser line compared to sample no 2. We can observe 8 peaks with maximum velocity about 6000 mm/s forward and 7 valleys with maximum value of -7000 mm/s. Comparing these to sample no 2, we have an extra 6 peaks and 4 valleys which could be translated to severity of defect in third samples. Figure 14 and 15 show the displacement for jig and spring in time domain. Displacement shown an average values of ±200 mm. This is comparable to sample no 2. Meanwhile, the motion shows 6 peaks with maximum value of about 1000 mm and 5 valleys with maximum value of -800 mm.
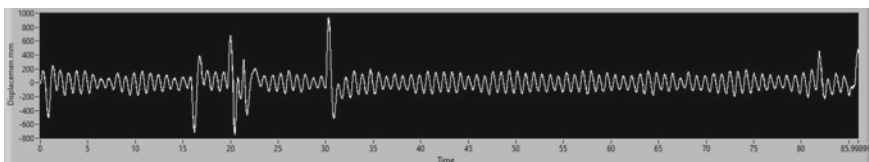
Fig. 14 Jig displacement in time domain (s)
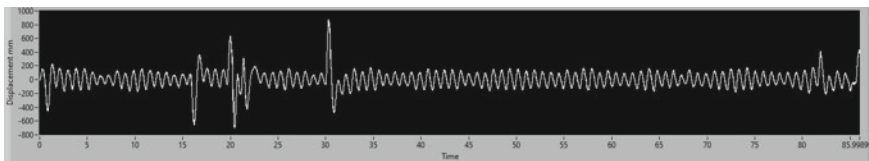
Fig. 15 Spring displacement in time domain (s)

Table 4 Comparison of the coil springs in term of acceleration

Spring	High density region (m/s^2)	Maximum peak value (m/s^2)	Maximum valley value (m/s^2)
Sample No 1 (Healthy)	± 50	200	-200
Sample No 2 (1 Crack)	± 250	400	-300
Sample No 3 (2 Cracks)	± 400	650	-650

The increase in number of peaks and valleys as well as their maximum values are due to the two cracks. Therefore, owing to previous statement, we can safely assume undoutedly that health conditions and the level of defects severity of the coil springs could be determine using these sets of data. This are also agreed by Liu et al. [11].

3.4 Summaries and Discussion

All the observation mentioned above are summarized in Tables 4, 5 and 6. They show the differences between the acceleration, velocity and displacements of the coil springs. To summarize our findings, healthy springs displayed low noise signal even

Table 5 Comparison of the coil springs in term of velocity

Spring	No of peaks	Maximum peak value (mm/s)	No of valleys	Maximum valley value (mm/s)
Sample No 1 (healthy)	n/a	n/a	n/a	n/a
Sample No 2 (1 crack)	2	3000	3	-3000
Sample No 3 (2 cracks)	8	6000	7	-7000

Table 6 Comparison of the coil springs in term of displacement

Spring	No of peaks	Maximum peak value (mm)	No of valleys	Maximum valley value (mm)
Sample No 1 (healthy)	n/a	n/a	n/a	n/a
Sample No 2 (1 crack)	3	400	3	-600
Sample No 3 (2 cracks)	6	1000	5	-800

for high density region for acceleration amplitude. For both velocity and displacement signals, they shown a simple harmonic motions without any singularity in the signals. On the other, sample no 2 shown a significant increase in acceleration, velocity and displacement signals in term of maximum peak and valley number, as well as their values. Furthermore, sample no 3 shown a consistency in data value because the enhancement in terms of peak and valley numbers and its maximum values can be plainly observed. According to B. Liu, the peaks and valleys occurs in the signals can be related to resonance frequency [11]. When peaks and valleys occurs in displacement, velocity and acceleration, frequency that occur during push or pull force are almost equivalent to resonant frequencies of the systems, and the frequencies would be significantly larger compare to nonresonance frequencies as suggested by Donskoy and Sutin [12]. Due to their characteristics of overloading stress and load into certain focus point, instead of essential desired function for coil springs to evenly distributing forces and energies while converting them from and to kinetics and potential energies to maintain stability and safety of the vehicle, the resonance can be said to be the undesirable elements that should be avoided at all cause. They would also lead to accidents in worse cases.

4   Conclusion

Finally, the objectives of this study have been successfully achieved. The system to detect the fault on shock absorber coil springs has been introduced. Using this, cracks availability including micro-cracks on coil spring surface which are very difficult to detect can be easily have been detected based on differences from signal observed. Additionally, since the data output from jig and spring shown an almost 100% similarities, for future application, there will be no need to attach sensors onto coil springs. Thereby enhancing the easiness of quality check inspection and even decreasing time consumption required.

As conclusion, by measuring the vibration of the coil springs and analysing their signal, springs health conditions can be evaluated. The more severe their faults, it will show denser response compare to healthy sample. The results of this study will definitely help early detection during final quality check at productions lines. Consequently, will help keeping only the healthy suspension system in good condition are released. This can be achieved by doing a higher frequency inspection with higher precision despite shorter time required. This will definitely lead to better quality of shock absorber in the market. As a results, the safety and wellness of driver and passengers' life can be ensured.

For further studies, it is recommended to study more into cracks propagation due to repeated action of compress and tensile of the coil springs during its utilization. This will further enhance the accuracy of analysis.

References

1. Vu TNL, Dung D, Van T, Van N, Hai PT (2017) Analytical design of PID controller for enhancing ride comfort of active vehicle suspension system. In: Proceedings—2017 international conference on system science and engineering, ICSSE 2017, pp 305–308
2. Sreenivasan M et al (2020) Finite element analysis of coil spring of a motorcycle suspension system using different fibre materials. Mater Today Proc xxxx
3. Kou B, Zhang C, Yan B, Cao H (2008) Detent force analysis and suppression of electrical shock absorber. In: 2008 IEEE vehicle power and propulsion conference VPPC 2008, pp 8–11
4. Shaikh ZK (2017) Experimental study of helical compression spring. Int J Eng Technol Sci Res 4(12):970–975
5. Kommalapati (2013) design evaluation of a two wheeler suspension system for variable load conditions. Int J Comput Eng Res 03(4)
6. Moreda (2017) Automatic air suspension in cars. J Inf Knowl Res Mech Eng 4(2)
7. Kosec L et al (2015) Failure analysis of a motor-car coil spring. Case Stud Eng Fail Anal 4(October):100–103
8. Hu X (2017) Study on dynamic behavior of CRH380B type high speed vehicle with suspension component failures. In: Proceeding 2016 IEEE international wheelset congress IWC 2016, pp 151–155
9. Koutromanos I (2017) Fundamentals of finite element analysis: linear finite element analysis
10. Omar M, El-kassaby MM, Abdelghaffar W (2017) A universal suspension test rig for electro-hydraulic active and passive automotive suspension system. Alexandria Eng J 56(4):359–370
11. Liu B, Yang J, Gang T (2020) Analysis of sound and vibration interaction on a crack and its use in high-frequency parameter selection for vibro-acoustic modulation testing. Mech Syst Signal Process 143:106835
12. Donskoy D, Sutin A, Ekimov A (2001) Nonlinear acoustic interaction on contact interfaces and its use for nondestructive testing. NDT&E Int 34(4):231–238

Simulation of Stress and Deflection in Cutting Tool of End Milling Using Finite Element Analysis

Haslina Abdullah ⓘ **, Muhammad Nur Ariff Zulkifli,**
Mohamad Shukri Zakaria ⓘ **, and Norfazillah Talib** ⓘ

Abstract Excessive stress in a machining process will lead to the failure of the cutting tool. In addition, it will cause the deflection of the cutting tool. In this paper, a simulation procedure based on Finite Element Method has been performed to analyse the stress distribution and deflection in the cutting tool of the end milling process. A three-dimensional model of a 2-flute flat end milling cutting tool has been developed using Solidwork software, and Abaqus software has been used to simulate the cutting tool. Static analysis has been implemented, and a concentrated force has been applied at the tip of the cutting tool. The value of deflection is determined by the magnitude of the total displacement. Based on the simulation, the result shows that the maximum stress occurred at hthe cutting tool's edge. The maximum value for stress is 3.11×10^3 Pa and While the maximum value for total displacement is 3.546×10^{-7}. In conclusion, by applying the finite element method, the deflection of the cutting tool can be predicted by analyzing the stress and displacement.

Keywords Stress distribution · Tool deflection · Finite element method

1 Introduction

End milling is a valuable tool and one of the most popular metal removal operations throughout the milling process. It is frequently utilized in industrial industries such as automotive and aerospace, where quality is critical in producing slots, dies, pockets, and slots. The cutter in end milling revolves on an axis vertical to the workpiece [1]. As a result, one of the most significant elements influencing cutting cost is the appropriate selection of cutting parameters for the milling process [2]. Predictions

H. Abdullah (✉) · M. N. A. Zulkifli · N. Talib
Faculty of Mechanical Engineering and Manufacturing, Universiti Tun Hussein Onn Malaysia, 86400 Parit Raja, Johor, Malaysia
e-mail: haslinaa@uthm.edu.my

M. S. Zakaria
Fakulti Kejuruteraan Mekanikal, Universiti Teknikal Malaysia Melaka, Hang Tuah Jaya, Durian Tunggal, Melaka, Malaysia

of numerous parameters such as cutting pressures, stresses, and temperature are crucial in selecting tool material and design prior to production to guarantee an effective machining process. To ensure the machining process's efficiency, many things need to be considered, for instance, tool deflection, cutting force, and chatter. The production of tool deflection and high cutting force will cause the failure of the machining process [3]. Many methods are employed to estimate tool deflection and cutting forces, such as developing a cutting force model, simulation using FEM, and experimental work. For example, Moges et al. [4] and Huo et al. [5] have been developed of cutting force model to predict the cutting force and tool deflection. This model has been developed based on the two-dimensional condition of the machining process and been verified by using experimental work. Nghiep et al. [6] use Taguchi method to predict and improve the tool deflection in end milling based on several machining parameters. Based on the experiments, it is found that tool deflection can be decreased by adjusting the levels of factors which is lubrication, radial depth of cut, axial depth of cut, and feed of cut. On the other hand, the Finite element method is also one of the methods to predict the cutting tool deflection by analyzing the stress distribution in the cutting tool. This method has been widely used in the machining process neither in the milling nor turning process. The FEM provides findings to the actual values and, therefore, it is now a well-accepted numerical method [7, 8].

Guo et al. [9] has applied FEM to predict the effect of deflection on the temperature of the cutting tool. Then, the results were validated using experimental work. Ismail and Tajalla [10] also use FEM to investigate parameters such as cutting speed and rake angle on stress and temperature. Pratap and Patra [11] claimed that an accurate prediction of cutting forces in micro-end milling is necessary to increase the efficiency of the machining process. Therefore, a finite element method has been applied using ABAQUS/Explicit software to predict the cutting forces in micro-end milling by consideration of tool edge radius effect, thermo-mechanical properties, and failure parameters of the workpiece material. Like Ozel and Altan [12], a finite element method has been used to study the cutting process and predict chip flow, cutting forces, tool stresses, and temperatures. However, the simulation is focused on side milling using a flat end milling operation. While Mebrahitom et al. [13] was performed a finite element analysis to predict the cutting forces using Finite Element Analysis on two flute HSS flat end mill. The finite element analysis was performed based on the interaction between the Aluminum workpiece and high-speed steel tool cutter. However, the model of the cutting tool is in 2-Dimensional, and the flute model has been disregarded.

Generally, there are many simulations of two-dimensional (2D) model has been conducted using finite element method have been proposed and verified due to challenges that exist in constructing 3D numerical cutting models [14–16]. In this research, FEM will be utilized to study the stress distribution and deflection on the three-dimensional of the cutting tool in the end milling machining process. Typically, end milling deflections were measured in proportion to force, resulting in static deflections [17, 18]. Cutting forces during the end milling process causes tool deflection and machined surface form inaccuracy. This study aims to develop a simulation procedure to determine the deflection and stress in a cutting tool of the milling
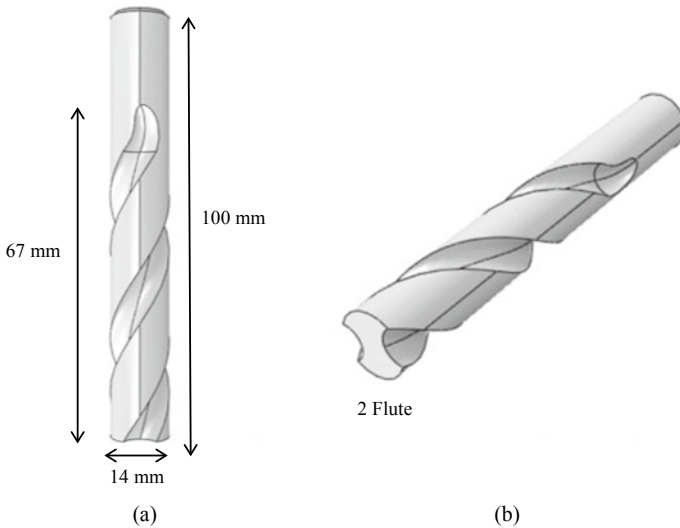
Fig. 1 Flat end mill cutting tool **a** front view **b** three-dimensional view

process. The simulation on cutting force and tool deflection of cutting tool for milling process has been performed using Abaqus software based on Finite Element Method (FEM).

2   Methodology

2.1   Development of Three-Dimensional Cutting Tool

This study has constructed the flat end milling cutting tool using Solidwork software, as shown in Fig. 2. The type of cutting is a two flute end mill cutting tool. This cutting tool is used in the process of roughing end milling process. Even though [19, 20] has stated that the number of the flute had influenced the stress distribution in the cutting tool, this study only focused on the two flute only. Then, this cutting tool model has been saved as STEP for the importing process in Finite Element software (Fig. 1).

2.2   Simulation Using Finite Element Method

In this study, Abaqus software has been implemented to analyze the stress and deflection in the end milling cutting tool. The model that has been saved in Step format has been imported in Abaqus because it contained more 3D data and part geometry
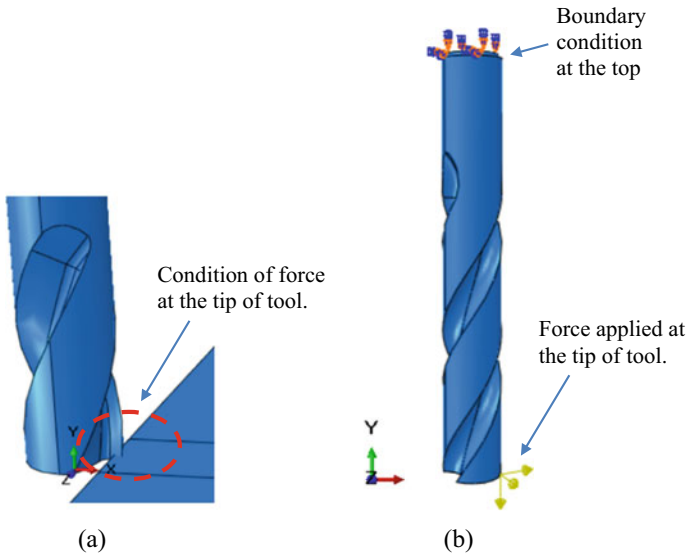
Fig. 2 **a** Condition of force in end milling **b** force and boundary condition applied on cutting tool

than IGES. The STEP format is adaptable, practical and should remain a trusted 3D CAD. The next step is defining the material properties of the cutting tool. The material cutting tool is High-Speed Steel. Table 1 has illustrated the material properties for the cutting tool, which is based on stainless steel material. In Abaqus, the material has been defined as the Elastic mechanical behaviors.

A concentrated loading force has been applied at the tip of the cutting tool To analyze the stress distribution and the deflection of the cutting tool. The value of force has been obtained based on the experimental work conducted by Jiang et al. [21]. Figure 2 shows the applied loading on the tip of the cutting tool, consisting of concentrated force in 3 directions: Fx, Fy, and Fz. The value for Fx, Fy, and Fz are 167.34 N, 161.05 N, and 77.35 N, respectively. This loading is applied with the assumption that the cutting tool has touched the workpiece during the end milling process, as shown in Fig. 2a. Then, the boundary condition has been applied on top of the cutting tool based on encastre boundary condition. This condition is ensuring the top of the cutting tool constrains all active structural degrees of freedom in the region specified. The boundary condition acts as a spindle to hold the cutting tool at the top surface. For the meshing process, the tetrahedral type, which is 0.01 has

Table 1 Material properties of the cutting tool

Parameters	Value
Modulus of elasticity, E(GPa)	200
Poisson's ratio, v	0.33
Density, ρ (Kg/cm^3)	7870

Fig. 3 Tetrahedral meshing
of cutting tool

been chosen suitable with the structure of the tool, as shown in Fig. 3. The selection
of meshing parameters was consistent with this research in a FEM simulation [22].

3 Results and Discussion

In this research, a linear static analysis has been implemented to study the stress
distribution and deflection of the cutting tool under concentrated forces. It is essential
to know the magnitude of stress. When the value exceeds the tool material fatigue
strength, it will cause the failure of the cutting tool. So, it is crucial to predict the
location and modes of the failures. A path has been created called trued distance
along with the cutting tool in order to determine the magnitude and the location of
the maximum stress, as shown in Fig. 4. Based on the graph, the maximum stress
has occurred at the tip of the cutting tool with the magnitude 3.11×10^3 Pa and the
value is constant when the length of the cutting tool is about 3 mm. This simulation
found that the critical location that has experienced the higher stress is the tip of the
cutting tool. Similar results were also obtained by Wu et al. [23]. Generally, many
factors influence the stress in the cutting tool, such as the parameters of the cutting
parameters, which are axial dept of cut, radial depth, spindle speed, feed per tooth,
and the workpiece material [24]. Though, in this study, these parameters are not
considered. The stress distribution is only focusing due to the concentration applied
on the tip of the cutting tool. However, the simulation procedure developed in this
study can still predict the stress distribution and the location of the maximum stress.

   Figure 5 shows the total displacement along the true distance based on concen-
trated forces at the edge of the tool. The true path distance is similar to the path
to obtain the magnitude of stress. The highest displacement is occurred at the tip
with the magnitude 3.54×10^{-7} mm. Then the displacement is gradually decreased
when the length of cutting too is increasing. A comparison of displacement has been
made to observe the magnitude in each axis. Based on the Fig. 6, it can be seen
that the highest displacement has occurred on the x-axes. This is due to the highest
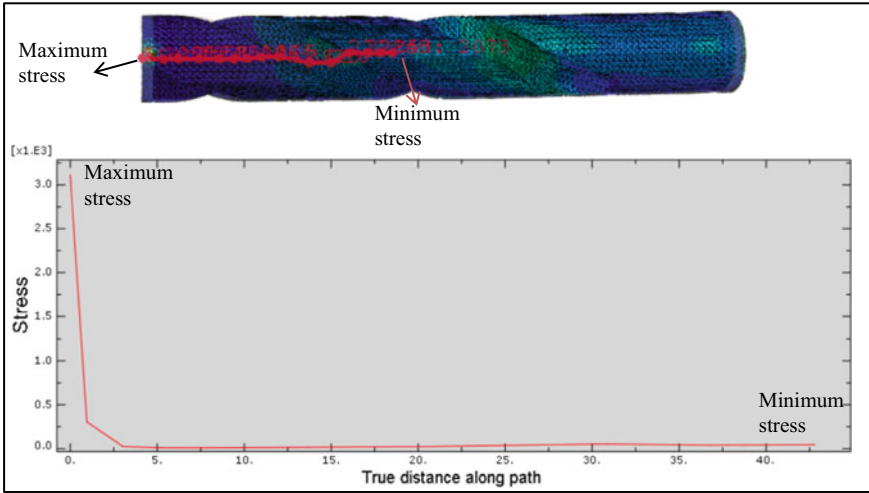
Fig. 4 Stress distribution along path true distance
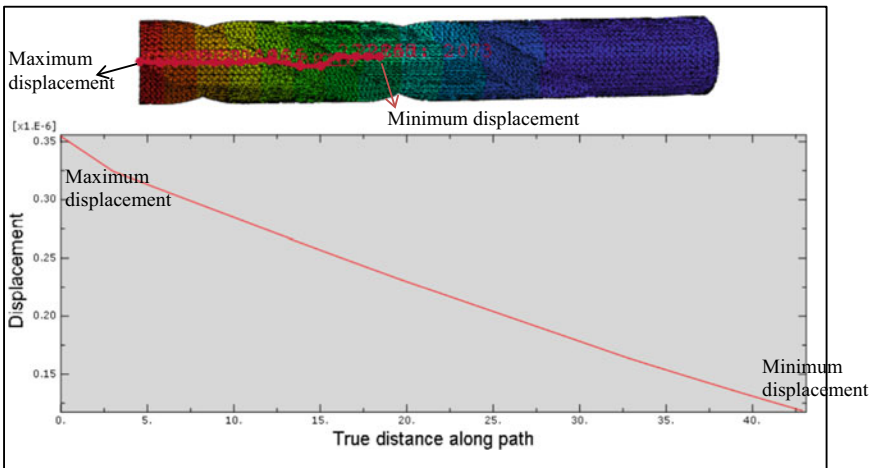
Fig. 5 Displacement distribution along path true distance

magnitude of force has been applied. The tool deforms elastically under a cutting load, and this is satisfies the conditions of small deflection, Hooke's law, and the superposition principle [9]. Based on Kiyak et al. [25], the deflection of cutting tool is expressed by the value of cutting force, tool overhang, modulus of elasticity, and the scalar moment of inertia. Based on the analytical method, "If an elastic structure is subjected to n loads $\vec{F}_{c1} \vec{F}_{c2} \vec{F}_{c3}, \ldots \vec{F}_{cn}$, the deflection x_j of the point of application of $\vec{F}_{cj}$; measured along the line of action of $\vec{F}_{cj}$, can be expressed as the partial derivative of the strain energy of the structure with respect to the load $\vec{F}_{cj}$" [26].
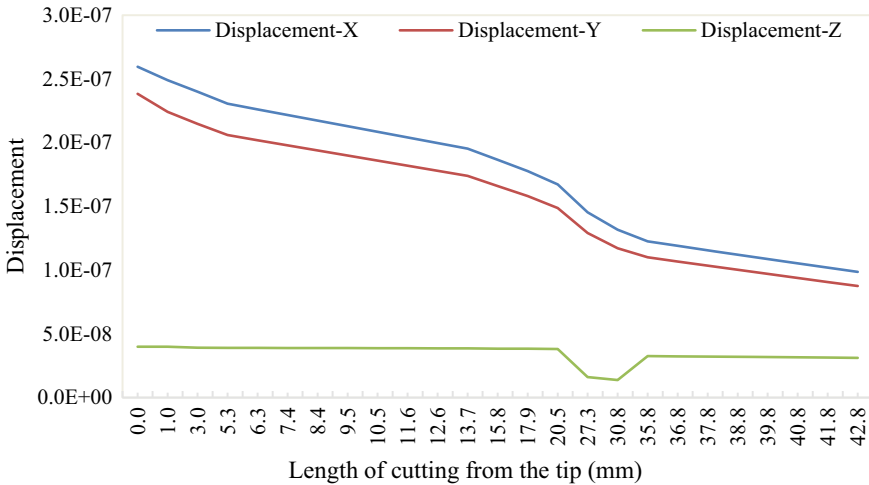
Fig. 6 Comparison displacement distribution along path true distance

Therefore, to analyze the deflection in the cutting tool of milling, the displacement has been considered in this study.

In order to analyze the magnitude of deflection in the cutting tool, the results of simulation FEM has been compared analytically with the formulation of tool deflection that has been proposed by Guo et al. [9] and Budak [17], as shown in Eq. 1. The location of boundary condition and applied loading at the end mill in the model are demonstrated in Fig. 7. However, in this study, the magnitude of the force is defined by the total force acting on the tip of the cutting tool. To predict the magnitude of tool deflection, Budak [17] defined Eq. (1) to predict deflections of tools for given geometric parameters and density. The constant C and N for the 2-flute end mill are 7.93 and 0,974, respectively. Based on the comparison, it has been found that the percent error between the value of calculating tool deflection using the formula with the magnitude obtained from FEM is 24.54%. The percent error occurred because the simulation is based on three-dimensional while the formula of the tool deflection does not specify all the force acting on the cutting tool. Furthermore, the meshing of the cutting tool is not tiny that cause the result obtained are not optimum. It can

Fig. 7 Deflection model of
end milling of cutting tool
[17]
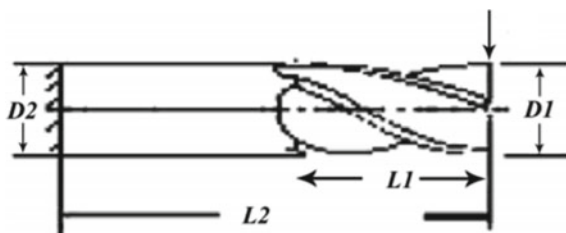
cause the difference of value obtained from the Abaqus software with calculation using formula.

$$deflection_{\max} = C \frac{F_R}{E} \left[\frac{L1^3}{D1^4} + \frac{\left(L2^3 - L1^3\right)}{D2^4} \right]^N \tag{1}$$

where is;

D1   mill diameter
D2   shank diameter
L1   flute length
L2   overall length.

4   Conclusion

A Finite Element Analysis simulation procedure has been performed to study the distribution of stress and displacement in the cutting tool for the end milling process. Based on the simulation, it has been found that the stress distribution is highest at the tip of the cutting tool due to the application of concentrated force. Similar to displacement, the magnitude is decrease proportional to the length of the cutting tool starting from the tip of the cutting tool. Though some parameters were not considered during the simulation, such as cutting speed, feed rate, and axial depth, the static analysis can still predict the stress and displacement distribution.

References

1. Joshua OS, David MO, Sikiru IO (2015) Experimental investigation of cutting parameters on surface roughness prediction during end milling of aluminium 6061 under MQL (Minimum quantity lubrication). J Mech Eng Autom 5(1):1–13
2. Daniyan IA, Tlhabadira I, Daramola OO, Mpofu K (2019) Design and optimization of machining parameters for effective AISI P20 removal rate during milling operation. Procedia CIRP 84:861–867
3. Mamedov A, Ehsan Layegh KS, Lazoglu I (2013) Machining forces and tool deflections in micro milling. Procedia CIRP 8:147–151
4. Moges TM, Desai KA, Rao PVM (2018) Modeling of cutting force, tool deflection, and surface error in micro-milling operation. Int J Adv Manuf Technol 98(9–12):2865–2881
5. Huo D, Chen W, Teng X, Yang CL, Yang K (2017) Modeling the influence of tool deflection on cutting force and surface generation in micro-milling. Micromachines 8(6):188
6. Nghiep TN, Sarhan AAD, Aoyama H (2018) Analysis of tool deflection errors in precision CNC end milling of aerospace Aluminum 6061-T6 alloy. Meas: J Int Meas Confed 125:476–495

7. Duran A, Nalbant M (2005) Finite element analysis of bending occurring while cutting with high speed steel lathe cutting tools. Mater Des 26(6):549–554

8. Suraidah S, Ridzuwan M, Asmelash M, Azhar A, Mulubrhan F (2020) End milling finite element method for cutting force prediction and material removal analysis. IOP Conf Ser: Mater Sci Eng 788(1)

9. Guo Y, Ye W, Xu X (2021) Numerical and experimental investigation of the temperature rise of cutting tools caused by the tool deflection energy. Machines 9(6):122

10. Ismail AI, Tajalla GUN (2019) Machining simulation of Ti-6Al-4V alloy using finite element method (FEM). In: CEVT 2019—proceeding: 6th international conference on electric vehicular technology 2019, pp 119–123

11. Pratap T, Patra K (2017) Finite element method based modeling for prediction of cutting forces in micro-end milling. J Inst Eng (India): Ser C 98(1):17–26

12. Ozel T, Altan T (2000) Process simulation using finite element method—prediction of cutting forces, tool stresses and temperatures in high- speed flat end milling. Int J Mach Tools Manuf 40:713–738

13. Mebrahitom A, Choon W, Azhari A (2017) Side milling machining simulation using finite element analysis: prediction of cutting forces. In: 6th International conference of materials processing and characterization (ICMPC 2016) Side. Vol 4. Elsevier Ltd., pp 5215–5221

14. Sun S (2014) A study of different FEM techniques for modelling 3d metal cutting process with an emphasize on ALE and Cel formulations. December

15. Song X, Li A, Lv M, Lv H, Zhao J (2019) Finite element simulation study on pre-stress multi-step cutting of Ti-6Al-4V titanium alloy. Int J Adv Manuf Technol 104(5–8):2761–2771

16. Li ZL, Tuysuz O, Zhu LM, Altintas Y (2018) Surface form error prediction in five-axis flank milling of thin-walled parts. Int J Mach Tools Manuf 128(February):21–32

17. Budak E (2006) Analytical models for high performance milling. Part I: Cutting forces, structural deformations and tolerance integrity. Int J Mach Tools Manuf 46(12–13):1478–1488

18. Duan X, Peng F, Yan R, Zhu Z, Huang K, Li B (2016) Estimation of cutter deflection based on study of cutting force and static flexibility. J Manufact Sci Eng, Trans ASME 138(4)

19. Norrdin NA, Saedon JB, Kasim MS (2018) Simulation of tool flute geometry influences the micro-end milling operation. In: Proceedings of mechanical engineering research day 2018, May, pp 50–51

20. Roushan A, Rao US, Vijayaraghavan L (2020) Prediction of cutting force in micro-end-milling by a combination of analytical and FEM method. J Micromanuf 3(1):28–38

21. Jiang Z, Jia M, Liu P (2017) Experimental study on milling force in processing Ti6Al4V thin-walled part. In: 6th International conference on measurement, instrumentation and automation (ICMIA 2017) 154(Icmia), pp 486–515

22. Davoudinejad A, Tosello G, Parenti P, Annoni M (2017) 3D finite element simulation of micro end-milling by considering the effect of tool run-out. Micromachines. 8(6):1–20

23. Wu Q, Zhang Y, Gao X, Fang L (2012) Investigation of tool deflection of solid carbide end mill in cutting process. Appl Mech Mater 163:95–99

24. Ji C, Sun S, Lin B, Fei J (2018) Effect of cutting parameters on the residual stress distribution generated by pocket milling of 2219 aluminum alloy. Adv Mech Eng 10(12):1–15

25. Kiyak M, Kaner B, Sahin I, Aldemir B, Cakir O (2010) The dependence of tool overhang on surface quality and tool wear in the turning process. Int J Adv Manuf Technol 51(5–8):431–438

26. Beer F, Johnston R (2020) Mechanics of materials, 8th edn.-SI. Vol 53

The Effect of Heat Treatment to Additive Manufacturing Material AlSi10Mg: A Review on Microstructure and Mechanical Properties

S. P. Tan, M. S. Shaari, Akiyuki Takahashi, and M. R. M. Akramin

Abstract Additive Manufacturing (AM) ameliorates the traditional techniques in the manufacturing process. The focus of the material used in this technique is AlSi10Mg. This is because the AlSi10Mg alloy has a low density and high-performance characteristic. The material used for AM to fabricate an end product has gained attention from both industries and researchers. This is to develop a completely novel technique in studying and optimizing material properties. Hence, this technique's maturity needs strong literature support on mechanical properties affected by post-process for wider customized application. Meanwhile, the change of microstructure affected by post-process is also essential to understand the properties of the changed factor. Therefore, the post-processes, which are often applied to conventional cast aluminium alloy, are investigated. This paper reviews the effect of the post-process on microstructural behaviour and material properties. The tensile and ductility are the main concern for the mechanical properties and the effect of fatigue crack growth of AM material. This paper aims to understand the changes in properties and the relationship between microstructure and mechanical properties that are affected by post-process. This is because AM technology will revolutionize the manufacturing of goods and markets in future.

Keywords AlSi10Mg · Metallic additive manufacturing · Heat treatment

1 Introduction

Three-dimensional (3D) printing is getting popular nowadays, better known as additive manufacturing (AM). AM is defined as "a process of joining materials to make

S. P. Tan · M. S. Shaari (✉) · M. R. M. Akramin
Faculty of Mechanical and Automotive Engineering Technology, Universiti Malaysia Pahang, 26600 Pekan, Pahang, Malaysia
e-mail: shamil@ump.edu.my

A. Takahashi
Department of Mechanical Engineering, Faculty of Science and Technology, Tokyo University of Science, 2641 Yamazaki, Noda-shi 278-8510, Chiba-ken, Japan

objects from 3D model data, usually layer upon layer, as opposed to subtractive manufacturing methodologies" [1]. The AM process fabricates a 3D object by progressively adding material layer by layer from a computer-aided design (CAD) model, which is why it is called additive manufacturing [2]. AM is totally a different method compared to traditional machining in 3D printing. Here, casting and forging processes, where the material is removed from a stock item (subtractive manufacturing) or filled and shaped into a mold and dies, compresses and hammers [3]. The study has shown that AM brings more convenience and cost efficiency to manufacturing industries.

Additive Manufacturing has to progress from fast prototyping and quick tooling to assembling applications [4]. The benefits of AM consist of (i) allowing new manufacturing design parts with flexible, uncommon and complex geometric for internal structures [4, 5], (ii) high strength to low weight ratios [6], (iii) near-zero material waste and (iv) reduction of expensive tooling and less material lost [2]. The AM process also fabricates the model with high quality and low defect risk of complicated parts without geometrical constraints [7]. Therefore, the AM process is nowadays becoming a more and more popular trend in industrial applications. AM process is commonly applied on fabricating freedom and near-net-shape lightweight components [8].

There exist a few AM processing systems such as direct metal laser sintered (DMLS), selective laser melting (SLM), electron beam melting (EBM), selective laser sintering (SLS), laser engineered net shaping (LENS) and laser metal deposition (LMD) [9]. The laser processes heating alloy metals, which consolidate through a rapid solidification process. The materials used for these manufacturing techniques are strictly con-trolled. Several types of metals are routinely applied in the AM process such as titanium [10], stainless steel [11], nickel [12] and aluminium alloys [2].

Aluminium alloy is of great interest for powder bed fusion (PBF) AM manufacturing. In the AM material range, the common metal used is AlSi10Mg alloy. This is because the material is readily cast with good mechanical properties such as high strength and low density [13]. In addition, Al–Si alloy has good mechanical properties, lightweight metal, high corrosion resistance, abundant material, and cost-effectiveness. Therefore, Al–Si alloy is commonly used in aviation and automotive industries and is available for powder-bed fusion AM [14]. However, numerous common Al-alloys are not accessible for the powder-bed fusion AM process. This is because of high thermal conductivity, poor flowability, wide solidification range and a strong tendency to form oxide scales [15].

The reason industries holding AM process back and do not prefer 3D printing is due to the investing cost versus output yield in the long run. The cost of outputs is highly dominated by initial machined cost. Then, the costing will only be marginally trended down as more and more parts are printed over a long period of time. It takes time to print a single piece to scale up the manufacturing, which implies that the manufacturer needs to buy additional machines, which helps in cost reduction. This turns our traditional economies of scale on their head. Therefore, if the price of raw material and 3D printer machine costs could be reduced with constant supply, the

manufacturer can lower the cost and be accessible for more parts by 3D printing. As mentioned, a complicated hollow structure is now possibly created by AM process with near-zero material waste and less material loss. Therefore, some researchers studied the performance of products by comparing virgin and recycled AM material powders, which is AlSi10Mg. The studies were studied on microstructure, mechanical properties, and characterization such as chemical and phase composition, surface oxide content, as well as crystal size. The result showed that the characteristics and microstructure of samples manufactured from virgin and recycled powders had an almost very high similarity. This slightly different strengthening mechanism in identical samples was due to a slightly different microstructure [16, 17]. Observed that, the particles of AlSi10Mg are getting more spherical and particle size getting smaller after several times reused.

Development and proper post-processing for AM product may improve the capability of AM components [18]. Meanwhile, conventionally cast AlSi10Mg alloy normally contains coarse needle-shaped silicon as well as magnesium that contains precipitates. The size of silicon precipitates is affected by the material's ductility and needs to be refined [19]. This is due to the distance between Si–Si particles, which increases after post-process. Therefore, the strength is reduced, but the ductility increases [20]. At the same time, Li et al. [21] reported the localized stress and strain reduction induced by the increase in the size of Si particles. Subsequently, the AM is powder-based before the manufacturing process. Therefore, solution heat treatment is needed to reduce the stress concentration of the AlSi10Mg due to laser sintering. By manufacturing products with AM technology, the process involves numerous potential effects due to microstructure and residual stresses. This study presents the review on the effect of microstructural behaviour and material properties of AlSi10Mg by heat treatment.

2 Effect of Heat Treatment Process

The heat treatment process is the common post-process applied to end products in aluminium industries. This process is to enhance or customize the character of the end product to particular specifications according to the application. The treatment consists of heat treating, quenching and natural or artificial ageing [22]. These processes are usually applied to different types of heat treatment processes, which are T4 to T6. Somehow, the stress relief process (TS) was also applied before the heat treatment process. This annealing treatment is to reduce the residual stress from the internal structure. The most common post-process for Al–Si–Mg alloys is categorized at T6 heat treatment. T6 is often performed to products of AlSi10Mg to disintegrate the anisotropy due to the progressive layer by layer building method. Basically, these processes are applied to conventional aluminium alloy products for enhanced performance on the mechanical properties of end products [23].

The heat treating process can simultaneously change the structure of AlSi10Mg alloy into homogenized, spheroidized Si phase and dissolve soluble phases containing

Mg or other trace elements [24]. In heat treating of AlSi10Mg alloy, the heating temperature is commonly set at the range between 450 and 550 °C. Then, the quenching process is applied, which submerged AlSi10Mg alloy into an agitated liquid to rapid cool down to around 200 °C. Quenching can hold the transformed structure resulted during high temperature and inhibit the structure into precipitation. Next, the natural or artificial ageing process is applied after quenching in the T6 heat treatment process. Ageing provides a uniform dispersion of precipitates to the alloy. Natural ageing occurs at room temperature, while artificial ageing is performed at a higher temperature, 150–210 °C. Meanwhile, a few types of heat treatment processes have been studied for AlSi10Mg alloys, such as annealing, in which the temperature applied is between 200 and 500 °C [18, 25, 26]. Overall, the time taken for the T6 heat treatment of AM material is similar to the cast component [27–29]. Nevertheless, the peak hardening during the ageing process applied in AlSi10Mg alloy is seldom reported. Therefore, the relationship between the post-process effect of the mechanical properties and microstructure behaviour on AlSi10Mg alloys is important to powder-bed fusion AM material. The following will discuss the microstructural behaviour and mechanical properties changed by the heat treatment process for a better understanding.

2.1 Microstructure

The heat treatment process is able to refine the grain structure and homogenous AlSi10Mg alloy in microstructure [29]. Li et al. [6] reported that, the calculated solubility of Si particles in an aluminium matrix is rated to be 8.89% for the as-built specimens. The solubility of Si particles in the Al matrix decreases rapidly when solution temperature increases. Moreover, the solubility appears to further decrease after going through artificial ageing. Heat treatment changes the microstructure by rapid precipitating Si particles forming a spheroidized Si. This formation caused a reduction in interfacial energy [22].

In a study by Zhou et al. [31], Si particles' precipitation gets coarser and increases in size after heat treatment. At the same time, the boundaries of melt pools have obscured after heat treatment [32]. After Si particles get coarser, the distance between Si particles increases and the Si content in Al decreases. Figure 1 showed the microstructure change on AlSi10Mg alloy in terms of an as-built, annealed, and heat-treated process. Figure 1a, c compared melt pools' size and observed that the size gets coarser after annealing. This also happened to Si particle size and formed precipitate, as shown in Fig. 1d. After heat treatment, melt pools disappeared (see Fig. 1e) and found a formation of Fe-containing intermetallic phase (see Fig. 1f). During the additive manufacturing process, AlSi10Mg alloy is fabricated with fast solidification of the cooling rate that can reach up to 107 °C/s [33]. Meanwhile, the traditional manufacturing process is around 102 °C/s or even lower [34]. This rapid solidification process caused the Si particle in AlSi10Mg alloy to form spherical eutectic silicon, with a tiny scale that is nano in size [35]. Therefore, the
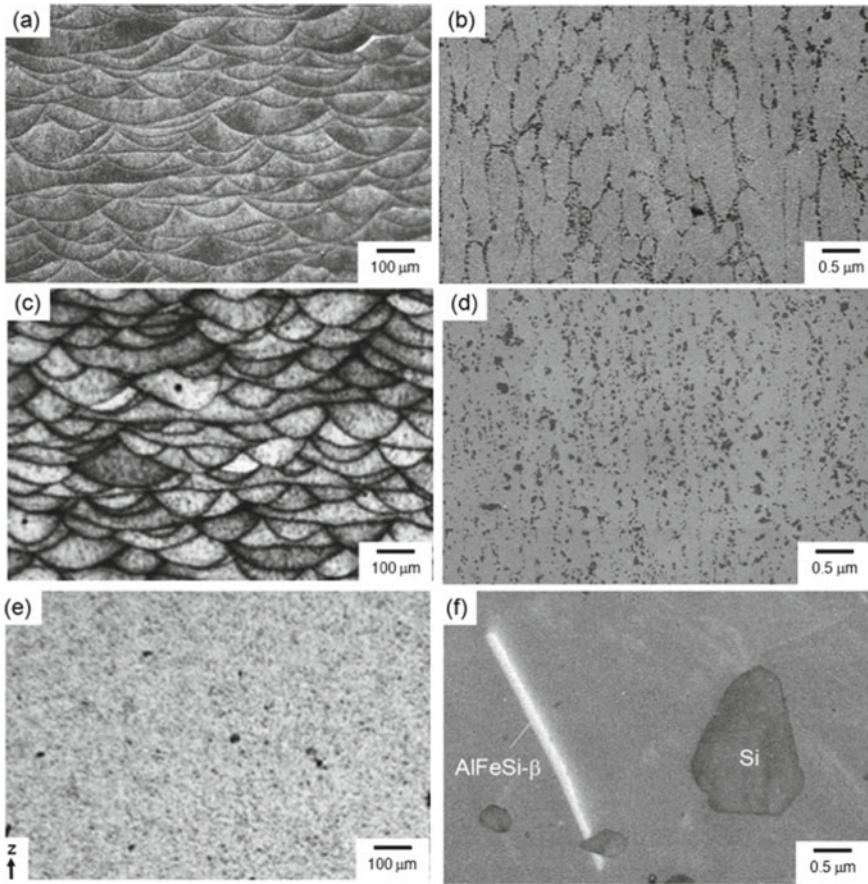
Fig. 1 **a**, **c**, **e** Optical micrographs and **b**, **d**, **f** microstructure images of the AlSi10Mg alloy samples under SEM: **a**, **b** as-built, **c**, **d** annealed at 300 °C for 2 h, **e**, **f** heat-treated at 530 °C for 6 h [30]

AM process produces an ultrafine microstructure, which causes the as-built alloy to perform in high mechanical properties. This as-built alloy also found a high volume of grain boundaries capable of preventing the dislocation effect [36]. Furthermore, the progressive layer by layer stacking manufacturing method caused the alloy to undergo a "self-quenching" treatment. The alloy cooled down rapidly, then formed a small melt pool. Then, the subsequent layer deposition reheats the alloy, acting like an artificial ageing; thus, encouraging precipitation of Mg_2 Si formed [20, 37].

In Fig. 2, the Al is a domain material with Si particles located in the Al matrix. After heat-treated, Mg is more distributed compared to Si. Meanwhile, the content of Mg is higher than Si. This is due to the formation of Mg_2Si precipitate. As mentioned, heat treatment is a common post-process to enhance microstructure and mechanical properties. Therefore, the change of microstructure affects mechanical properties and
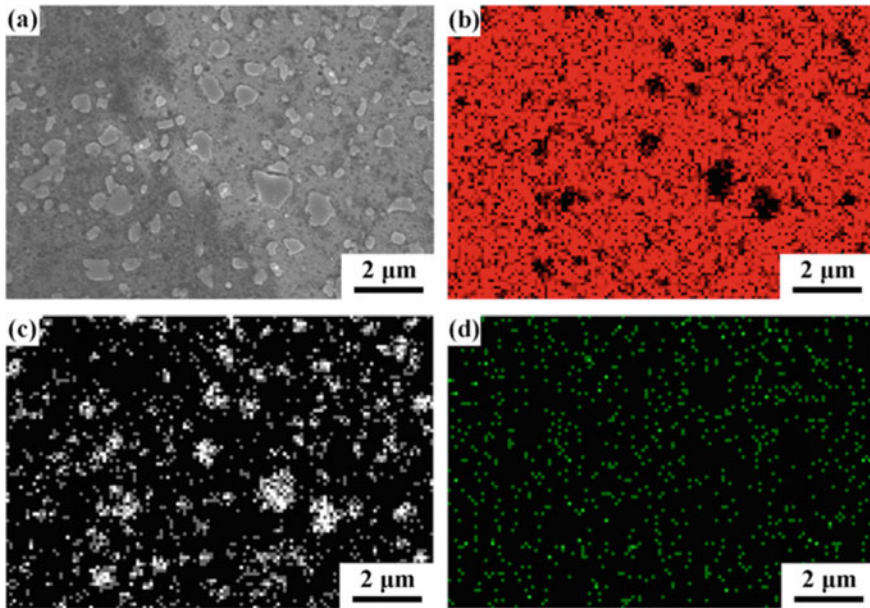
Fig. 2 Microstructure of heat treated AlSi10Mg alloy under EDX analysis **a** SEM image and corresponding EDX maps of **b** Al; **c** Si; and **d** Mg [6]

performance of AlSi10Mg alloy after heat-treated to be discussed in the following section.

2.2 Mechanical Properties

In the meantime, to achieve demanded quality, output capacity, and capability of the product, cost-efficiency is also crucial in this modern market world to ensure the manufacturer's sustainability. However, AM is currently known as a high-cost technique compared to the traditional machining or casting method [38]. Therefore, the manufacturer wishes to optimize the mechanical properties to achieve the optimized performance of AlSi10Mg alloy.

Several mechanical properties of AlSi10Mg alloy fabricated by the AM process have been studied, such as tensile behaviour, hardness, and fatigue performance. For example, Read et al. [39] and Tradowsky et al. [29] highlighted that AM process fabricated higher tensile strength AlSi10Mg alloy than the casting manufacturing method. Some research put efforts to improve AM material on refining microstructure to enhance the mechanical properties of AlSi10Mg alloys between as-built state and proceeded heat treatment [6, 40, 41]. The as-built Al–Si alloys usually show a "fish-scale" arrangement structure on build-direction and columnar pattern opposite the

built direction. This "fish-scale" structure occurs due to the formation of a melt pool [29]. From the previous study, Li et al. [21] found that the mechanical properties such as tensile and elongation of AlSi10Mg alloys can be manipulated by controlling the size of Si with specific heat treatment.

Furthermore, Li et al. [6] also revealed that the mechanical properties could be enhanced when AlSi10Mg alloy consists of fine cellular grain Al with nano-sized Si produced by high cooling rates. Yet, some studies found that heat treatment is no longer guaranteed to improve tensile strength. After heat treatment, the result of tensile is decreased [23, 28, 32, 42] but ductility of AlSi10Mg was improved [6, 21, 39]. This is because the number of Si particles decreases, causing the distance between Si particles to increase, which reduces localized stress and strain [21]. Hence, the effect of heat treatment for AM material is significant to be determined since it might lead to the improvement of fatigue crack growth. This is due to heat treatment modifying the mechanical properties of the material's strength and ductility.

2.3 Fatigue

Most of the structural failures occur due to the growth of fatigue crack [41]. There are two phases which are the initiation period and propagation period in fatigue life. Figure 3 shows the typical fatigue life phases. Fatigue is a type of progressive process. Once defected, the process is initiated within the initiation period. Then, this process accelerates rapidly until it fails. There are several methods of studies carried out by the researchers in predicting fatigue life. The process of choosing the fatigue life model is an important decision where each of the models has its own function. Moreover, further research is needed to determine the integrity of the AM materials based on the microstructural and fatigue crack growth behaviour of AM materials. This is to ensure the safety and the reliability of the AM technology to be used as an end-product. The fatigue property of a model changes mostly due to the transformation of microstructure [26]. As previously mentioned, the heat treatment process of spheroidized and discontinuities of Si particles reduces fatigue strength.
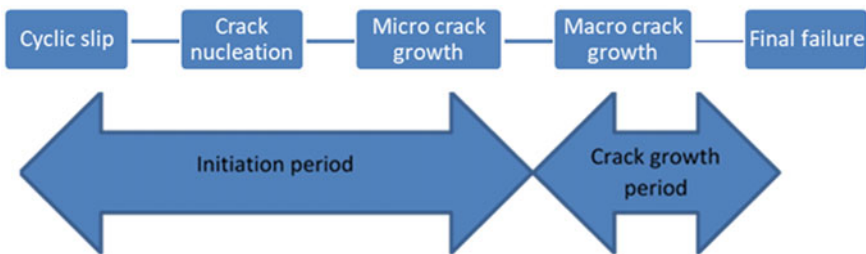
Fig. 3 The typical fatigue life phases

Fatigue life is also affected by other factors such as porosity, manufacturing platform parameters, building directions and stress ratio of cyclic loading [42].

In addition, further research is needed to determine the integrity of the AM materials based on the microstructural and fatigue crack growth behaviour. This is to ensure the safety and the reliability of the AM technology to be used as an end-product. The complex nature of the fatigue process makes it a challenge for engineers to analyze it using the conventional finite element method (FEM). A conventional fatigue computation has to remesh the whole geometry for each crack propagation. Therefore, S-version FEM is introduced into this study. S-version FEM is rather more of a method created as an alternative to solve the finite element problem. S-version FEM employs the superimposed FEM proposed by the local fine mesh onto the global mesh [43]. It creates a fine mesh at the locality of the crack tips. The benefits of using computational analysis help reduce the time, design cycle and cost of raw material. Therefore, this research is significant to determine fatigue crack growth behaviour for AM materials.

3   Conclusion

AM brings convenience and efficiency to manufacturing industries. Moreover, 3D printing brings convenience to manufacturing industries and no limits to creativity for a designer. The complicated involvement of many steps of the process is simplified into a single process to complete. Meanwhile, the end product of this technique may need a significant amount of post-processing, such as heat treatment. Therefore, the mechanical properties and microstructure behaviour of the AlSi10Mg alloys is currently essential to determine a better agreement of the post-processing of this alloy. However, the validity of the effect on the range of different heat treatment processes versus microstructure and mechanical behaviour on fatigue property has not been carried out. AM process allows the manufacturer to create a design that was once deemed impossible. This will be a fascinating meeting of material science and machines in the manufacturing industry.

References

1. Gorelik M (2017) Additive manufacturing in the context of structural integrity. Int J Fatigue 94:168–177
2. Herzog D, Seyda V, Wycisk E, Emmelmann C (2016) Additive manufacturing of metals. Acta Mater 117:371–392

3. Hamzah HH, Keattch O, Covill D, Patel BA (2018) The effects of printing orientation on the electrochemical behaviour of 3D printed acrylonitrile butadiene styrene (ABS)/carbon black electrodes. Sci Rep 8(1)
4. Gibson I, Rosen D, Stucker B (2015) Additive manufacturing technologies: 3D printing, rapid prototyping, and direct digital manufacturing, 2nd edn. Springer, New York
5. Wang Z, Wu W, Qian G, Sun L, Li X, Correia JAFO (2019) In-situ SEM investigation on fatigue behaviors of additive manufactured Al-Si10-Mg alloy at elevated temperature. Eng Fract Mech 214:149–163
6. Li W, Li S, Liu J, Zhang A, Zhou Y, Wei Q, Yan C, Shi Y (2016) Effect of heat treatment on AlSi10Mg alloy fabricated by selective laser melting: microstructure evolution, mechanical properties and fracture mechanism. Mater Sci Eng, A 663:116–125
7. Liu YJ, Liu Z, Jiang Y, Wang GW, Yang Y, Zhang LC (2018) Gradient in microstructure and mechanical property of selective laser melted AlSi10Mg. J Alloy Compd 735:1414–1421
8. Casati R, Nasab MH, Coduri M, Tirelli V, Vedani M (2018) Effects of platform pre-heating and thermal-treatment strategies on properties of alsi10mg alloy processed by selective laser melting. Metals 8(11):954
9. Hölker-Jäger R, Tekkaya AE (2017) Additive manufacture of tools and dies for metal forming. In: Laser additive manufacturing: materials, design, technologies, and applications. Elsevier Inc., pp 439–464
10. Attar H, Calin M, Zhang LC, Scudino S, Eckert J (2014) Manufacture by selective laser melting and mechanical behavior of commercially pure titanium. Mater Sci Eng, A 593:170–177
11. Murr LE, Martinez E, Amato KN, Gaytan SM, Hernandez J, Ramirez DA, Shindo PW, Medina F, Wicker RB (2012) Fabrication of metal and alloy components by additive manufacturing: examples of 3D materials science. J Market Res 1(1):42–54
12. Jia Q, Gu D (2014) Selective laser melting additive manufacturing of Inconel 718 superalloy parts: densification, microstructure and properties. J Alloy Compd 585:713–721
13. Kikuchi M, Wada Y, Shimizu Y, Li Y (2012) Crack growth analysis in a weld-heat-affected zone using S-version FEM. Int J Press Vessels Pip 90–91:2–8
14. Tang M, Pistorius PC, Beuth JL (2017) Prediction of lack-of-fusion porosity for powder bed fusion. Addit Manuf 14:39–48
15. Hu LL, Yu TX, Gao ZY, Huang XQ (2008) The inhomogeneous deformation of polycarbonate circular honeycombs under in-plane compression. Int J Mech Sci 50(7):1224–1236
16. Hadadzadeh A, Baxter C, Amirkhiz BS, Mohammadi M (2018) Strengthening mechanisms in direct metal laser sintered AlSi10Mg: comparison between virgin and recycled powders. Addit Manuf 23:108–120
17. Del Re F, Contaldi V, Astarita A, Palumbo B, Squillace A, Corrado P, Di Petta P (2018) Statistical approach for assessing the effect of powder reuse on the final quality of AlSi10Mg parts produced by laser powder bed fusion additive manufacturing. Int J Adv Manuf Technol 97:2231–2240
18. Fousová M, Dvorský D, Michalcová A, Vojtěch D (2018) Changes in the microstructure and mechanical properties of additively manufactured AlSi10Mg alloy after exposure to elevated temperatures. Mater Charact 137:119–126
19. Cáceres CH, Davidson CJ, Griffiths JR (1995) The deformation and fracture behaviour of an AlSiMg casting alloy. Mater Sci Eng, A 197(2):171–179
20. Hadadzadeh A, Amirkhiz BS, Mohammadi M (2019) Contribution of Mg_2Si precipitates to the strength of direct metal laser sintered AlSi10Mg. Mater Sci Eng, A 739:295–300
21. Li XP, Wang XJ, Saunders M, Suvorova A, Zhang LC, Liu YJ, Fang MH, Huang ZH, Sercombe TB (2015) A selective laser melting and solution heat treatment refined Al-12Si alloy with a controllable ultrafine eutectic microstructure and 25% tensile ductility. Acta Mater 95:74–82
22. Sjölander E, Seifeddine S (2010) The heat treatment of Al-Si-Cu-Mg casting alloys. J Mater Process Technol 210(10):1249–1259
23. Girelli L, Tocci M, Gelfi M, Pola A (2019) Study of heat treatment parameters for additively manufactured AlSi10Mg in comparison with corresponding cast alloy. Mater Sci Eng, A 739:317–328

24. Moustafa MA, Samuel FH, Doty HW (2003) Effect of solution heat treatment and additives on the microstructure of Al-Si (A413.1) automotive alloys. J Mater Sci 38(22):4507–4522
25. Rosenthal I, Shneck R, Stern A (2018) Heat treatment effect on the mechanical properties and fracture mechanism in AlSi10Mg fabricated by additive manufacturing selective laser melting process
26. Zhang C, Zhu H, Liao H, Cheng Y, Hu Z, Zeng X (2018) Effect of heat treatments on fatigue property of selective laser melting AlSi10Mg. Int J Fatigue 116:513–522
27. Fiocchi J, Tuissi A, Bassani P, Biffi CA (2017) Low temperature annealing dedicated to AlSi10Mg selective laser melting products. J Alloy Compd 695:3402–3409
28. Aboulkhair NT, Maskery I, Tuck C, Ashcroft I, Everitt NM (2016) The microstructure and mechanical properties of selectively laser melted AlSi10Mg: the effect of a conventional T6-like heat treatment. Mater Sci Eng, A 667:139–146
29. Tradowsky U, White J, Ward RM, Read N, Reimers W, Attallah MM (2016) Selective laser melting of AlSi10Mg: Influence of post-processing on the microstructural and tensile properties development. Mater Des 105:212–222
30. Takata N, Kodaira H, Sekizawa K, Suzuki A, Kobashi M (2017) Change in microstructure of selectively laser melted AlSi10Mg alloy with heat treatments. Mater Sci Eng, A 704:218–228
31. Zhou L, Mehta A, Schulz E, McWilliams B, Cho K, Sohn Y (2018) Microstructure, precipitates and hardness of selectively laser melted AlSi10Mg alloy before and after heat treatment. Mater Charact 143:5–17
32. Wang LF, Sun J, Yu XL, Shi Y, Zhu XG, Cheng LY, Liang HH, Yan B, Guo LJ (2018) Enhancement in mechanical properties of selectively laser-melted AlSi10Mg aluminum alloys by T6-like heat treatment. Mater Sci Eng, A 734:299–310
33. Yu G, Gu D, Dai D, Xia M, Ma C, Chang K (2016) Influence of processing parameters on laser penetration depth and melting/re-melting densification during selective laser melting of aluminum alloy. Appl Phys A Mater Sci Process 122(10):1–12
34. Lu L, Nogita K, Dahle AK (2005) Combining Sr and Na additions in hypoeutectic Al-Si foundry alloys. Mater Sci Eng, A 399(1–2):244–253
35. Chen Z, Lei Y, Zhang H (2011) Structure and properties of nanostructured A357 alloy produced by melt spinning compared with direct chill ingot. J Alloy Compd 509(27):7473–7477
36. Aboulkhair NT, Tuck C, Ashcroft I, Maskery I, Everitt NM (2015) On the precipitation hardening of selective laser melted AlSi10Mg. Metall Mater Trans A 46(8):3337–3341
37. Jägle EA, Sheng Z, Wu L, Lu L, Risse J, Weisheit A, Raabe D (2016) Precipitation reactions in age-hardenable alloys during laser additive manufacturing. JOM 68(3):943–949
38. Liu J, Chen Q, Liang X, To AC (2019) Manufacturing cost constrained topology optimization for additive manufacturing. Front Mech Eng 14(2):213–221
39. Read N, Wang W, Essa K, Attallah MM (2015) Selective laser melting of AlSi10Mg alloy: process optimisation and mechanical properties development. Mater Des 65:417–424
40. Wu J, Wang XQ, Wang W, Attallah MM, Loretto MH (2016) Microstructure and strength of selectively laser melted AlSi10Mg. Acta Mater 117:311–320
41. Bufford DC, Stauffer D, Mook WM, Syed Asif SA, Boyce BL, Hattar K (2016) High cycle fatigue in the transmission electron microscope. Nano Lett 16(8):4946–4953
42. Larrosa NO, Wang W, Read N, Loretto MH, Evans C, Carr J, Tradowsky U, Attallah MM, Withers PJ (2018) Linking microstructure and processing defects to mechanical properties of selectively laser melted AlSi10Mg alloy. Theoret Appl Fract Mech 98:123–133
43. Fish J (1992) The s-version of the finite element method. Comput Struct 43(3):539–547

Awareness and Perception of the Environmental Sustainability of Beverage Packaging Materials

Nai Yeen Gavin Lai, Kok Hoong Wong, Fangfang Zhu, Tong Sun, Rafael Rivero, Zhuo'er Li, and Lih Jiun Yu

Abstract Sustainability is an important issue, and there are growing concerns on what could be done to achieve it better. Beverage packaging materials have an important task to safely hold its content and allow for convenience in consuming drinks by the consumer. However, after consumption, it becomes an environmental sustainability concern. This paper investigated university-educated young consumers' awareness, and perception of the impact different beverage packaging material choices have on environmental sustainability through a mixed methods action research approach. Prospective participants of the study were invited through the students' network and contact. The participants were requested to complete a survey with multiple choice answers and an opinion scale on various areas related to the environmental sustainability of beverage packaging. Conventional plastic-based beverage packaging materials were in the opinion of the majority of the surveyed consumers, to be most detrimental to the environment. However, that might not be the real case, as evident from the results of life cycle analysis (LCA) studies on several different beverages and packaging materials. It was noted that the students and alumni do care about environmental sustainability. However, there is some confusion among the respondents on how they could contribute effectively in their daily activities to the sustainability goal. Some still lack practical knowledge that can guide their purchasing decisions and disposal practice for consumed packaging. Some propositions for future actions and research on improving awareness and actions were provided.

Keywords Sustainability · Packaging materials · Engineering education · LCA

N. Y. G. Lai (✉) · K. H. Wong · F. Zhu · T. Sun · R. Rivero · Z. Li
Faculty of Science and Engineering, University of Nottingham Ningbo China, 199 Taikang East Road, Ningbo 315100, China
e-mail: gavin.lai@nottingham.edu.cn

L. J. Yu
Faculty of Engineering, Technology and Built Environment, UCSI University, Kuala Lumpur Campus, No. 1, Jalan Menara Gading, UCSI Heights (Taman Connaught), 56000 Cheras, Kuala Lumpur, Malaysia

1 Introduction

Sustainability is an important concept with increasing efforts seen by governments around the globe in implementing measures that will help the world grow more sustainably. Consumer personal consumption purchases directly impact a nation's GDP and, more importantly, sustainability efforts [1]. Consumer purchase behaviors and actions have direct consequences on the quest for sustainability [2]. Consumers who have become aware of the importance of sustainability may choose to select products labeled with information implying "sustainability" or, in their opinion, will be able to help with the sustainability cause. In a context of sustainability and need of a circular economy, studies on consumers purchasing behavior on common goods and services has been an important research topic because any changes to this influencing factor would have a significant impact to the success of environmental initiatives that involves supply and demand [3, 4]. One of the prevalent initiatives is promoting sustainability in packaging materials usage and their waste control, as outlined in the European Union Directive on Packaging and Packaging Waste (Directive 94/62/EC). For beverage industry, packaging not only plays an important role in preserving the quality of the liquid it contains, but it is also a marketing tool and communication instrument between the industry and consumers. Aesthetical aspect of a packaging, such as shape, graphic design and color has been used for product promotion by differentiating its appearance from its competitors [5]. Packaging also conveys important information to consumers, such as shelf life, ingredients, nutritional content and place of manufacture. Thus, the design of a packaging has a significant influence on consumer decision process.

Considerable amount of new design guidance have been introduced to packaging industry, for example, several design frameworks for sustainable packaging have been proposed, with coverage ranging from efficient use of material, energy and water to the inclusion of life cycle analysis tool for assessment of environmental impact caused by the packaging material [6, 7]. Beverage industries have realigned their strategy toward the three pillars of sustainability, i.e. economic, environment and social, because by doing that they can gain competitive advantages to meet the demand of modern "green consumers". Many beverage companies, such as PepsiCo, Coca-Cola and Nestlé, have published their goals to improve sustainability of their packaging materials. These goals are collectively listed in a database shared by the Sustainable Packaging Coalition [8]. To achieve these goals, such as "Making 100% of our packaging recyclable globally by 2025, Cola-Cola" [8], companies have to address multiple aspects of design issues simultaneously, which include sustainable sourcing, weigh reduction, increasing use of recycled and/or biodegradable materials, reusability and design for improved recovery. Inevitably, all these require substantial amounts of financial commitment and thus in return the companies expect increased market share and customer satisfaction within a reasonable timeframe.

Consumer buying decisions have been modelled by many studies [9] and can be divided into several steps, which include need recognition, information search, evaluation of alternates, purchase and post-purchase behavior [10]. It has been reported

that the design of a packaging, in particular its visual appearance, has a significant effect on such buying decisions and can influence consumer's perceptions about the product quality and its appeal. Packaging imagery has been widely known to be one of the important elements that affects packaging visual appearance. A well designed image can attract consumer's attention quickly and the information the image trying to transmit can be processed with less cognitive efforts, which is more efficient compared to textual printings [11]. Packaging color also has a strong positive correlation to consumer buying decisions [12]. Despite color psychology is complex and personal, a great deal of efforts have been directed towards understanding its contribution to brand identity and sale value [13]. Packaging material is another contributing factor to consumer buying decision, but in a quite unique way, as the perception is built mostly on haptic contact. A packaging with good visual appeal but made of flimsy material will not be pleasing to the hand and thus negatively affecting the buying decision [14].

Despite the beverage industry has devoted considerable efforts in promoting sustainable packaging, and substantial number of existing literatures on relationship between packaging design and consumer buying decisions are available, there have been few studies investigate which features of sustainable packaging have the most influential effects on consumer buying decisions. In recent years, many environmental labels have been proposed and used on beverage packaging, aiming to communicate the importance and benefit of sustainable practices. However, it was reported that some consumers still confused with the various environmental labels used and difficult to link their buying decision to sustainable packaging [15, 16]. In this study, we focused on university-educated young consumers' awareness and perception of the design of sustainable beverage packaging.

Universities attract and nurture talents that will have a profound impact on the world. Universities and institutions of higher learning have an important role in promoting the sustainable development cause, and more universities are embracing sustainability [17]. The institutions are teaching students about the importance of sustainability through their programs offerings and embed the principle of sustainability in their operations, mission, and strategy [18, 19]. By including sustainability topics into its programs and demonstrating sustainability values in all that it does, the universities seek to influence their students and graduates to become aware and champion sustainability measures.

University students are well educated and will have substantial purchasing power in the marketplace upon graduation. These young adults are a key market for beverage producers, and the consumption of all types of beverages is growing steadily. However, there is an important issue with the growth trend: the increased usage of packaging for the beverages and the disposal or treatment needed to handle the growing amount of waste. From the authors' own experience, consumed drink bottles are among the most common disposals on campus litter bins.

This study will assess the students' perception of the environmental sustainability of different beverage packaging options commonly found in China. The study had also explored the participants' choice of beverage packaging options and willingness to adjust their options in the interest of environmental sustainability through an online

survey. A further in-depth interview was conducted with the participants to explore how they have learned about the importance of sustainability and how it has guided or influenced their purchasing decision of everyday goods like beverages.

2 Methodology

This study adopts the action research approach to study environmental sustainability concerns. Action research is a participatory method that is context-specific and problem-focused based on a partnership between action researchers and participants directly involved in the change process [20]. Action research is one of the three key research paradigms for insider research on own organization settings [21]. The authors (academics and students) are all part of the higher education community highly passionate about sustainability. The focus of the study on beverage packaging materials was initiated due to the authors' observations on the growing consumption and disposal of takeaway beverage cups and bottles in higher education institutions. For data collection, the study had adopted mixed method research approach. Mixed method approach involves the collection of both quantitative and qualitative data in a single inquiry or study which is suited for answering a wide range of research questions [22]. Additionally it has been noted that the mixed method approach is aligned closely with that of action research [23, 24]. Quantitative research was carried out in the form of an online questionnaire survey, and qualitative research was carried out in the form of a face-to-face interview with participants. The advantages of using an online questionnaire include geographical reach, relatively low cost, and the ability to reach a considerable amount of respondents [25]. Although face-to-face interviews are time-consuming and laborious, the answers obtained were more detailed based on the open-ended questions [26]. Therefore up to 15 respondents were invited and participated in the follow-up interview sessions.

The participants in this study were invited from the personal contact and networking of the students based on a convenience sampling approach. All of the participants were current or recent graduates of an institution of higher learning in China. The survey question was adapted from [27, 28] and supplemented with details that suit the locality of the study. The online questionnaire consisted of four sections. In the first section, five questions mainly investigate the participants' awareness and perception of environmental sustainability. The second part investigates how strongly the participants feel about environmental protection when they purchase packed beverages. The third section of the online questionnaire explores the respondents' awareness and knowledge of some common labeling information found on beverage packaging, particularly those related to its disposal instruction and environmental impact. The participants were required to choose the correct answer according to the meaning of the eleven different labels. The answer choices available to the respondents were in two primary forms. When the questions relate to their perception or opinion on sustainability, they will choose the alternatives on a 1–7 scale, where 1 = completely disagree (very environmentally unsustainable) and 7 = completely agree

(very environmentally sustainable). The other questions are in the multiple-choice format, where the respondent will need to select the best answer/s that represents their view. The questionnaire was hosted and distributed using the China popular online survey platform wjx (www.wjx.cn). A total of 243 valid and complete questionnaires were received in this study.

The last part of the questionnaire covers the respondents' demographics and background information and asks if they are willing to participate in a follow-up in-depth interview related to the topic. Further in-depth interview with a total of fifteen participants was completed. The interview consisted of thirteen semi-structured questions related to the topic and was arranged to gain insights from the respondents.

3 Results and Discussion

The information collected from the online survey is analyzed, presented, and reflected along the four key components mentioned in the methodology. Further related inputs collected from the face-to-face interview sessions will also be included and linked to the survey findings. The key notable findings are presented as follows.

3.1 Background Information of the Respondents

The 243 respondents participated in this study age between 18 and 28 years old, where 50.62% are male, and 49.38% are female. The respondents are currently students or have recently graduated from their undergraduate or post-graduate university education. The following are some of the selected key responses to the questions covered in the questionnaire.

3.2 Awareness and Views on Environmental Sustainability

Figure 1 shows that about 68% of the respondent feels that the ecological environment around them was getting better. On the other hand, about 12% of the respondents did not have an opinion or is unclear about the condition. This clearly shows that the majority of the respondents believe that the ecological environment is getting better. It is not surprising as in the authors' own experience, the environment and pollution in the local vicinity has improved over the years. There are continuous efforts by the local authorities and city government in improving cleanliness, reducing pollution activities, and minimizing littering in the streets. As mentioned by a number of the interviewees, they had participated and supported waste separation activities driven by their university and local government. However, as highlighted by the interview participants as well, the news and social media posting of environmental issues and
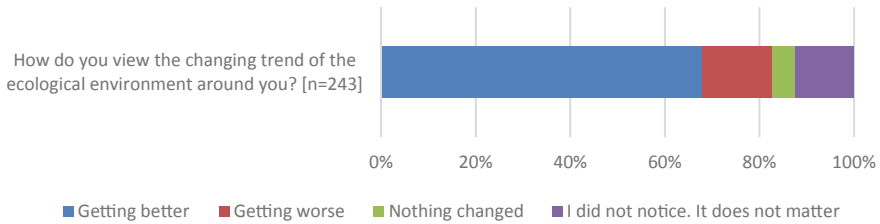
Fig. 1 Opinion on the ecological environment

disasters happening around the world is less pleasing and is of a concern to them. They periodically watch and read about the increasing impact of climate change, pollution, and disasters happening in different places around the globe. This has made them becoming more concerned about the environment.

Figure 2 illustrates the participant's awareness towards environmental protection, where the respondents are asked to rate their agreement on a scale of 1–7 on several environmental-related issues. The data shows that about 94% of the respondents agree that "Sustainable development is the most important factor in environmental protection." Up to 78% of the respondents disagree with the notion of "The packaging design is more important than its environmental friendliness." A further 63% of the respondent finds it challenging to classify and separate wastes.

Interestingly about 72% of the participants had felt that packaging pollution imposes more severe problems than food waste. From the responses, it is evident that the respondents feel strongly about sustainability and the concept of sustainable development. However, they may find it difficult to sustain the activities needed to ensure sustainable living voluntarily. As mentioned in the interview sessions, the
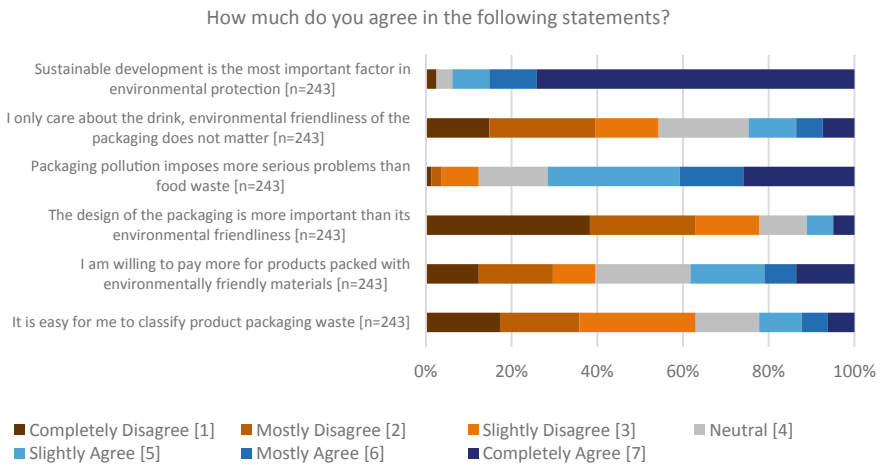
Fig. 2 Agreement with environmental sustainability related statements

students had participated, and some had volunteered to support the government initiative of municipal waste separation at the source. Others have indicated that they are aware of the waste separation initiative and think it is good for the environment. However, they only comply and follow it as it is a strictly enforced requirement in their dorm or residential community. They might not have acted to separate their litter if not for the requirement set.

3.3　Beverage Packaging and Environmental Problems

For the next research question, each respondent can select more than one option; hence a total of 993 responses was received from 243 respondents. As shown in Fig. 3, only 3.7% of respondents did not think that beverage packaging can cause environmental problems. 72.8% of the respondents chose water pollution. This shows that the respondents believe that the consumption of beverage packaging can cause various kinds of environmental problems. Many respondents had associated the use of plastic beverage packaging with the pile-up of plastic litter in the ocean and the micro plastic pollution of the seas. Likely this is due to the continuous media and environmental organizations coverage of plastics threat on the marine ecosystems [29]. Other forms of environmental issues such as climate change, ozone layer destruction, and biodiversity reduction were also in the opinion of many respondents due to the increasing usage of beverage packages that are not properly managed. While some of these issues may be directly linked to the overuse and poor disposal of beverage packages, factors like ozone depletion may not be so. The respondent may have a general impression that the packaging is responsible for environmental issues but may not be so clear on the exact cause and mechanism of how damage
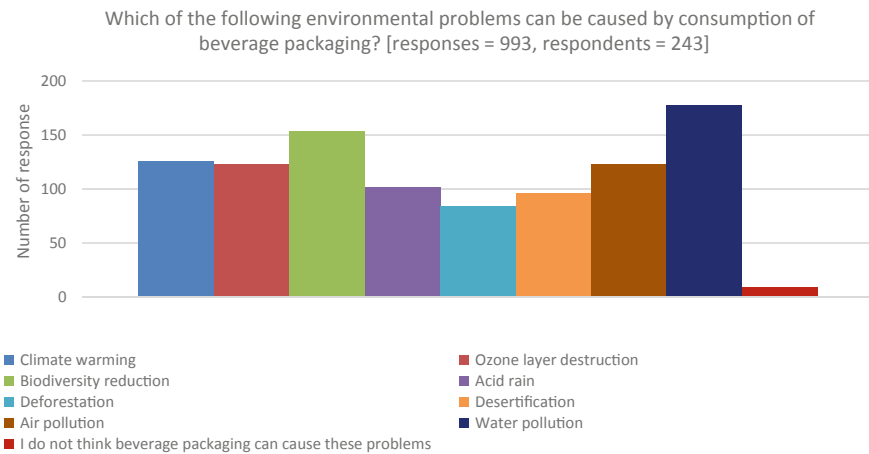
Fig. 3 Environmental issues related with the increase of beverage packaging use

to the environment occurs, as seen in the in-depth interview responses. A notable comment shared by the interviewees relates to the fact that the increased usage of beverage packaging materials (and all materials) will burden the available resources in the world. There are only finite materials and resources available.

Figure 4 shows the perception of the respondent on some of the aspects that makes the beverage packaging material more sustainable. It was seen the majority of the respondents agree that all the listed features or characteristics will make beverage packaging more environmental friendly. The top choices of the respondent are; beverage packaging that is compostable or biodegradable, material that can be recycled, and beverage packages that can be reused for other purposes. On the other hand, the option with minor support relates to beverage packaging that can be returned and refilled. The interview responses support the findings presented in this figure. Interviewees had shared that they least prefer the use of reusable bottles or cups as they feel the convenience of getting a drink on the go is important for
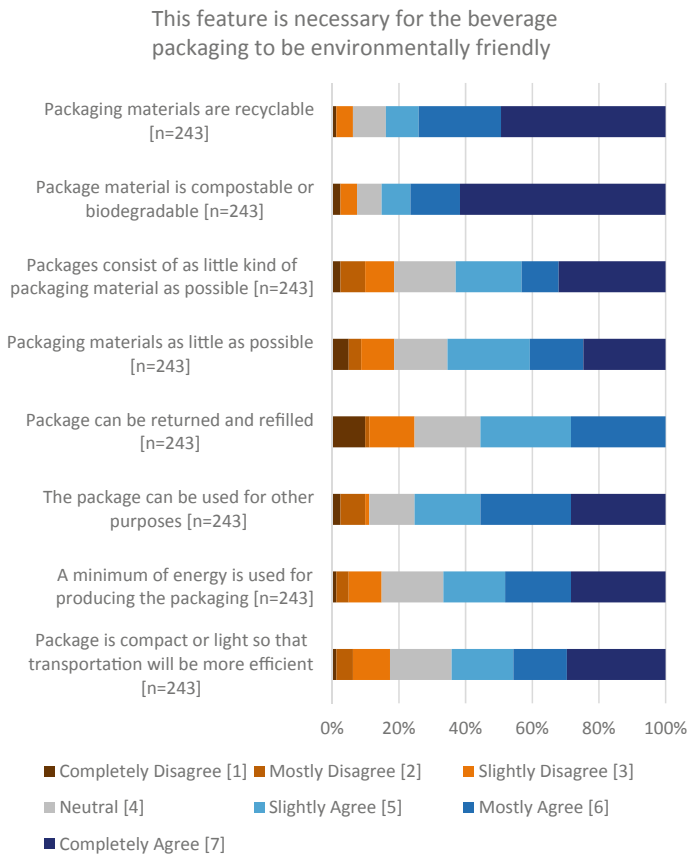
Fig. 4 Characteristics of more environmental sustainable beverage packaging

them. They have shared that the use of their own containers usually is for drinking water, and many outlets that prepare drinks like milk tea do not offer the options to customers to bring their own cup or container. Although recyclability after use is listed as one of the top choices, some interview respondents had a cautious view of the practice. "It (recycling) is not as simple as many people think" was a quote from one of the respondents. Recycling is a complicated process, and many factors affect its viability and success [30]. It is even more complicated when recycling food and beverage-related packaging materials as there are stringent safety and health requirements. The recycling process also consumes energy, and this, as mention earlier, leads to the depletion of natural resources.

On which type of packaging material the respondents think is more environmentally friendly, bio based plastic was listed as the clear choice as seen in Fig. 5. On the other far end, conventional petroleum-based plastic was rated as the least environmental friendly beverage packaging material. Glass, metal and Tetra Pak beverage packaging materials are in between the two extremes. The interview response provides further insights into the views of the students and graduates that participated in this study. Although they are not clear on the technical specification and process for biodegradable plastics, the interviewees had shared that they had the impression that bio based plastic is easily degradable and will return as nourishment to the earth. Therefore they feel it would be beneficial for the environment. Apart from the bio based plastic, the findings here actually diverge from an LCA study
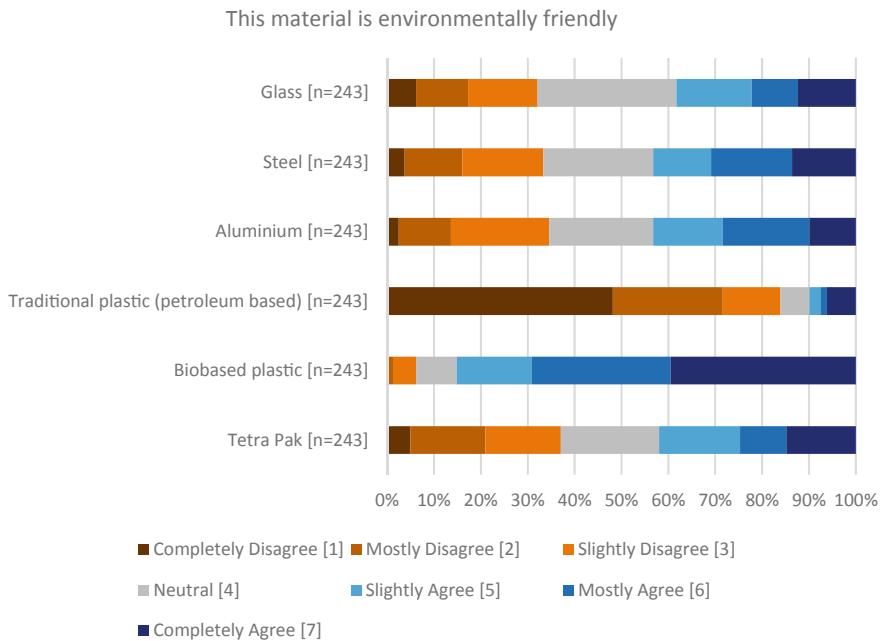
Fig. 5 Beverage packaging materials that is environmental friendly

on several different packaging options for some of the common beverages available. According to the LCA study by Brock and Williams [31] PET and HDPE plastics were found to be listed in the middle in terms of harm caused to the environment for the use in a variety of common liquid beverages. The findings are in line with the earlier findings by Gujba and Azapagic [32] on a variety of packaging materials for beverages. Plastic has been branded to be evil, but that may not necessarily be the truth as it offers more benefits and is better for the environment than some of its alternatives [33]. A more recent LCA study compared the more sustainable material option for outdoor drinking bottles. It was determined that the single-use PET plastic bottles were a better choice than a refillable aluminum bottle with the appropriate cleaning and washing needs factored [34].

The next question presented the respondents with a selection of common beverages. They were required to rate if the packaging is environmentally friendly and their willingness to purchase that beverage with the particular packaging using the scale of 1–7. The average scores of each beverage are presented in Fig. 6. It is evident from the response that the respondent's motivation to purchase a beverage or drink is not predominantly affected by the type of packaging materials. The trend observes here is supported by further insights from the interview sessions. The interviewees mentioned that their drink preference, the convenience of purchase, and cost influence their regular beverage consumption when outside. The environmental impact of the type of packaging materials is not a critical consideration. According to the feedback,
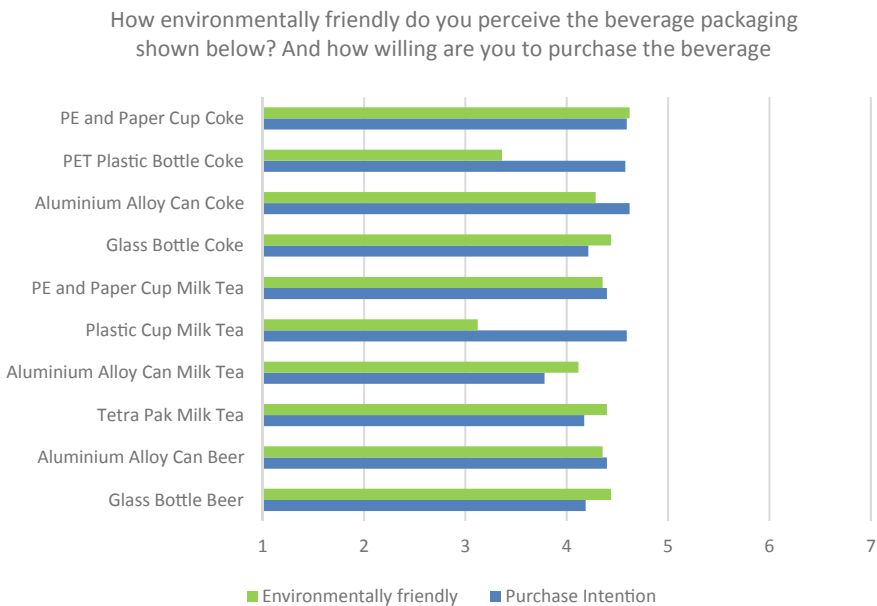
Fig. 6 Perceived environmental friendly qualities of the beverage packaging material and willingness to purchase the beverage

they would help to dispose of the bottles and package in the correct litter bin as part of their effort to protect the environment. However, most of the interviewees admitted that they do not know well about the technical details about the recycling process and how much the sorting of waste for recycling will impact sustainability. They have been encouraged to do it, so it must be good another student had mentioned.

3.4 Awareness on Beverage Packaging Label Logo Information

Figure 7 shows that most respondents are familiar with the PITCH-IN (do not litter) symbol, followed by the Food Quality and Safety Sign and the Universal Recycling Symbol, where 70.37%, 58.02%, and 54.32% of the respondents got it correct, respectively. Other than those three logos, the percentage of correct answers of other labels falls below 50%. This hints that most respondents still lack knowledge and understanding of environmental-related information presented on beverage packaging. In comparison to an earlier study of the European general public [27], the number of correct identification for ecolabels and logo on beverage packaging is higher in this study. In China, it is not all beverages sold have logos or ecolabels in their products. Ecolabels are also not covered extensively in the educational system. This explains why most respondents do not know the meaning behind most of them. It is worth noting that some beverage producers with sustainability concepts in mind
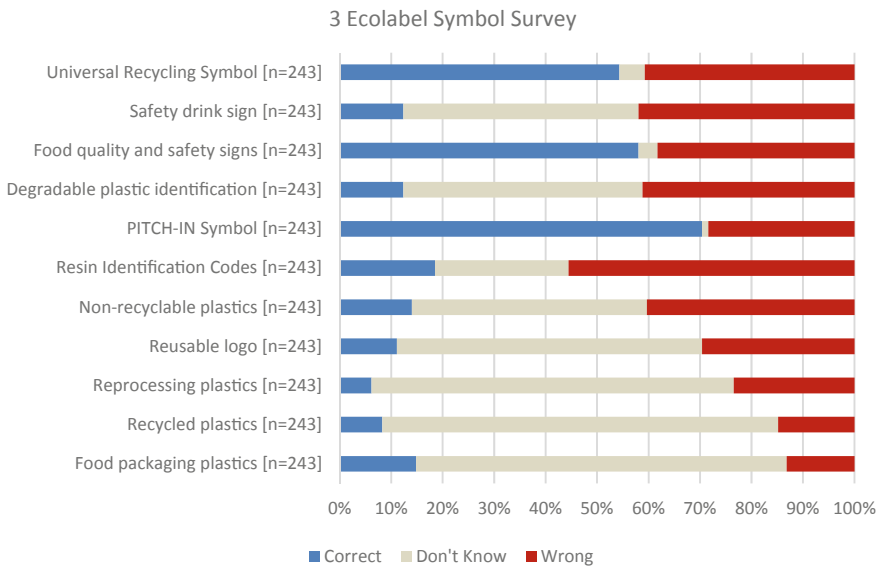
Fig. 7 Beverage packaging label logo information

do include ecolabels on their products. This might help in making their product to stand out and ideally to attract consumers with a strong sustainable living principal. The interviewees had mentioned that they have seen some of the logo on some of the drinks they have purchased before and have learned about it from various sources. However, they are sometimes confused by the logo as they are rather "small" on print, and some of the information provided is not directly beneficial for them.

Participants to this study were also probed on their willingness to pay more for beverage products which are deemed more sustainable. These beverages can be packed using more environmental friendly packaging material and have the information clearly labelled on them on the possible environmental impact. Majority of the interviewees have indicated that they are willing to spend a little more if it will help environmental sustainability through their purchases. However, it was emphasized that the amount must be small relative to their purchase amount and it must not be a noticeable burden to their finances. Not everyone will want to pay more for their products and how much more will depend on the segment of customer or background [35].

4 Conclusion and Reflections

Sustainability is an important issue to be addressed, and higher learning institutions can influence their community to contribute better and support its success. This mixed-methods action research had explored the university students' and graduates' awareness and perception of the common beverages packaging materials on environmental sustainability. As sustainability is emphasized as an important part of university education today, it was anticipated that the young consumers participating in this study would have a high level of awareness and knowledge regarding environmental sustainability. The finding shows that the majority of the respondents do feel strongly and are aware of the concept of environmental sustainability. However, their perceptions of what is environmentally sustainable may not always be based on scientific facts and evidence, as seen in some of the survey responses and interview feedback. The media and environmental organizations' campaigns have deeply impacted their views on sustainability. There have been lots of talks about the negative impact of plastic without further clarification on the even worst impact of non-plastic alternatives. As seen in the literature, a number of LCA studies had indicated that there are far worst packaging material choices for the beverages when considering the impact on the environment. Even single-use plastic bottles could still be used sustainably if proper disposal and recycling are considered. The respondents could correctly identify the more common and obvious labels and logos on beverage packages related to environmental sustainability. The correct rate was also higher relative to a similar study for the general population in a European setting. It is seen that although young adults understand and embrace the concept of sustainability, more is needed to equip them with practical knowledge on how to act and contribute to the

sustainability agenda. This is evident in this study when discussing beverage packaging, which is a common everyday product. The authors seek to reflect and explore different approaches and opportunities to enhance higher education sustainability education. Further practical and actionable information on sustainability should be encouraged in higher education settings. As seen in this study, students can participate in sustainability research and initiate projects with academics to deliver positive change to the broader community.

References

1. Clift R, Sim S, Sinclair P (2013) Sustainable consumption and production: quality, luxury and supply chain equity. Treatise on sustainability science and engineering. Springer, pp 291–309
2. Tukker A et al (2010) The impacts of household consumption and options for change. J Ind Ecol 14(1):13–30
3. Chen C-C, Chen C-W, Tung Y-C (2018) Exploring the consumer behavior of intention to purchase green products in belt and road countries: an empirical analysis. Sustainability 10(3):854
4. Lin ST, Niu HJ (2018) Green consumption: environmental knowledge, environmental consciousness, social norms, and purchasing behavior. Bus Strateg Environ 27(8):1679–1688
5. Reimann M et al (2010) Aesthetic package design: a behavioral, neural, and psychological investigation. J Consum Psychol 20(4):431–441
6. Grönman K et al (2013) Framework for sustainable food packaging design. Packag Technol Sci 26(4):187–200
7. Lewis H (2012) Designing for sustainability. Packaging for sustainability. Springer, pp 41–106
8. Sustainable Packaging Coalition. Packaging Sustainability Goals. 2021 [cited 2021 7/7/2021]; Available from: https://sustainablepackaging.org/goals/?member
9. Prasad RK, Jha MK (2014) Consumer buying decisions models: a descriptive study. Int J Innov Appl Stud 6(3):335
10. Qazzafi S (2019) Consumer buying decision process toward products. Int J Sci Res Eng Dev 2(5):130–134
11. Smith V, Barratt D, Sørensen HS (2015) Do natural pictures mean natural tastes? Assessing visual semantics experimentally. Cogn Semiotics 8(1):53–86
12. Abdullah M, Kalam A, Akterujjaman S (2013) Packaging factors determining consumer buying decision. Int J Human Manage Sci (IJHMS) 1
13. Kumar JS (2017) The psychology of colour influences consumers' buying behaviour–a diagnostic study. Ushus J Bus Manage 16(4):1–13
14. Ferreira B, Capelli S (2012) The effects of the haptic perception of packaging texture in product perceptions. In: Athens: ATINER'S conference paper series, No: BUS2012-0171
15. Juwaheer TD, Pudaruth S, Noyaux MME (2012) Analysing the impact of green marketing strategies on consumer purchasing patterns in Mauritius. World J Entrepreneur Manage Sustain Dev
16. Scott L, Vigar-Ellis D (2014) Consumer understanding, perceptions and behaviours with regard to environmentally friendly packaging in a developing nation. Int J Consum Stud 38(6):642–649
17. Wigmore-Álvarez A, Ruiz-Lozano M (2012) University social responsibility (USR) in the global context: an overview of literature. Bus Prof Ethics J 31(3/4):475–498
18. Lopez YP, Martin WF (2018) University mission statements and sustainability performance. Bus Soc Rev 123(2):341–368
19. Deus RM, Battistelle RAG, da Silva GHR (2016) Sustainability insights from the mission statements of leading Brazilian Universities. Int J Educ Manage

20. Waterman H et al (2001) Action research: a systematic review and guidance for assessment. Health Technol Assess (Winchester, England) 5(23):iii–157
21. Brannick T, Coghlan D (2007) In defense of being "native": the case for insider academic research. Organ Res Methods 10(1):59–74
22. Creswell JW, Clark VLP (2017) Designing and conducting mixed methods research. Sage Publications
23. Ivankova N, Wingo N (2018) Applying mixed methods in action research: methodological potentials and advantages. Am Behav Sci 62(7):978–997
24. Menon S, Hartz-Karp J (2020) Applying mixed methods action research to explore how public participation in an Indian City could better resolve urban sustainability problems. Action Res:1476750320943662
25. Devine Wright P (2005) Beyond NIMBYism: towards an integrated framework for understanding public perceptions of wind energy. Wind Energy 8(2):125–139
26. Schultze U, Avital M (2011) Designing interviews to generate rich data for information systems research. Inf Organ 21(1):1–16
27. Boesen S, Bey N, Niero M (2019) Environmental sustainability of liquid food packaging: Is there a gap between Danish consumers' perception and learnings from life cycle assessment? J Clean Prod 210:1193–1206
28. Korhonen V (2012) Package value for LOHAS consumers-results of a Finnish study. In: 18th IAPRI world packaging conference, 2012. DEStech Publications, Inc San Luis Obispo California
29. Stafford R, Jones PJS (2019) Viewpoint—ocean plastic pollution: a convenient but distracting truth? Mar Policy 103:187–191
30. Reck BK, Graedel TE (2012) Challenges in metal recycling. Science 337(6095):690–695
31. Brock A, Williams I (2020) Life cycle assessment and beverage packaging. Detritus 13:47–61
32. Gujba H, Azapagic A (2011) Carbon footprint of beverage packaging in the United Kingdom. Towards life cycle sustainability management. Springer, pp 381–390
33. Klemeš JJ, Fan YV, Jiang P (2021) Plastics: friends or foes? The circularity and plastic waste footprint. Energy Sources, Part A: Recov Util Environ Effects 43(13):1549–1565
34. Tamburini E et al (2021) Plastic (PET) vs bioplastic (PLA) or refillable aluminium bottles–what is the most sustainable choice for drinking water? a life-cycle (LCA) analysis. Environ Res 196:110974
35. Laroche M, Bergeron J, Barbaro-Forleo G (2001) Targeting consumers who are willing to pay more for environmentally friendly products. J Cons Mark

A Preliminary Study on the Interest and Initiatives Toward Industry 4.0 Among OEMs in Automotive Industry, Malaysia

Ungku Shamir Hamzah and Muhammed Nafis Osman Zahid ⓘ

Abstract This is an organizational study on a group of companies which are vendors to Original Equipment Manufacturer (OEMs) in the automotive industry in Malaysia. The writer seeks to study on these companies' awareness and plans in adopting the Industry 4.0. Key personnel from selected subsidiaries of this group of companies were given questionnaires to provide answers on the awareness, familiarity, plans and important elements in adopting Industry 4.0. Most of the respondents were aware and familiar of Industry 4.0 and do have some plans in its implementation as well as able to identify the challenges and important elements in its implementation. However, most of them are still of the opinion that they are able to move forward into the future without having to implement Industry 4.0.

Keywords Industry 4.0 awareness · Industry 4.0 challenges · Automotive industry

1 Introduction

Industry 4.0, is the infusion of smart technology into the present-day manufacturing environment. It is the merging of physical and digital technologies, such as the Internet of Things (IoT), Artificial Intelligence (AI) and Cognitive Computing (CC). Cyber-physical systems such as sensors for collecting data to be analysed to improve daily operations and the creation of Big Data from the cumulation of all the data will provide valuable real-time information that can be used for problem solving and decision making.

Automation of production, digitisation of operational information combined with better communication technology will upgrade the production line and the supply chain to a much higher level. Artificial intelligence will enable factory equipment to self-optimise and self-configure in performing complex production and delivery activities more efficiently and more cost effectively [1].

U. S. Hamzah · M. N. O. Zahid (✉)

Faculty of Manufacturing and Mechatronic Engineering Technology, Universiti Malaysia Pahang, 26600 Pekan, Pahang, Malaysia

e-mail: nafis@ump.edu.my

The first industrial revolution in the nineteenth century was the development from farming to factory production. The second industrial revolution from 1850s to World War I was the introduction of steel, electrification of factories and mass production. The third industrial revolution from the late 1950s to the late 1970s refers to the change from analogue, mechanical, and electronic technology to digital technology. The fourth industrial revolution is now the movement towards digitisation.

The main objective of Industry 4.0 is to develop a smart manufacturing platform for industrial-networked information applications. This enables manufacturing firms of all sizes to gain easy and affordable access to modelling and analytical technologies that can be customised to meet their needs [2].

1.1   To Be Industry 4.0 Compliant

Industry 4.0 connects digital and physical technologies hence, main focus being Machine to Machine—M2M, Internet of Things (IoT), Artificial Intelligence (AI), Robotics and Cloud Computing enabling factories to become more automated and self-monitoring as the machines within are given the ability to analyse and communicate with each other without the need for human intervention. All these features will create a more adaptable, responsive and unified production with the ability to make informed decisions. The human factor of the factory can be redeployed to perform other tasks.

An Industry 4.0 factory plant or a manufacturing system must be able to integrate interoperability, achieve information transparency, possess technical assistance and decentralised decision-making [3]:

- Interoperability—is an environment whereby machines, devices, sensors and people are all connected and able communicate with one another.
- Information transparency—is the technology that provides operators with vast amounts of useful information needed to make appropriate decisions.
- Technical assistance—is the shifting of human role of from an operator of machines to a problem solver and decision maker. Systems with the ability to help people in decision-making and problem-solving and to assist people with tasks that are too difficult or unsafe for humans to do.
- Decentralized decision-making—Interconnection and information transparency allow for operators to make decisions both inside and outside of production facilities. In short, it is the ability to directly make simple decisions and become as autonomous as possible.

The above environment can be achieved with the implementation of the 9 components of Industry 4.0; Internet of things, Cloud computing, System integration, Simulation, Additive manufacturing, Autonomous robots, Big data, Augmented reality and Cybersecurity. These are integral parts for the formation of a Smart Factory. However, it is also important to note that not all should be implemented at one time. The basic premise of Industry 4.0 is to take every manufacturing process and import

it into one single system where the workflow, maintenance and management of every machine, process or even a factory's entire shop floor can be monitored and controlled from a remote or collocated hubs. At the very least, Internet of Things, Big Data and Autonomous Robotics should be considered. And lastly, Cybersecurity is ultimately essential to ensure overall system security.

Adding IoT capabilities, wireless connectivity and sensor opens up various potentials such as autonomous maintenance and installation processes that significantly reduces human error, equipment and installation failures, raw material shortages and poor productivity of production line or robotic manufacturing processes. Big data analyses and simulation can be done for planning and forecasting. All these promise the result to significantly reduce costs and make the operation more efficient. The following fundamental factors to a successful implementation:

- Good and affordable internet access is the basis in developing system and applications. This will provide opportunities in creating new business models.
- High processing power and digital storage which can potentially drive the manufacturing of high technology products. With high processing power, even a small smartphone can run a variety of functions.
- An education system that prepares and exposes students to Industry 4.0 as early as the primary level. Early exposure is helpful to develop skilled manpower that caters to the job market.

1.2 The Importance and Challenges of Industry 4.0

According to Deloitte, companies in Germany and the US, expect Industry 4.0 to bring many advantages, stretching from improved competitiveness to a reversal of the trend to relocate production to low-wage countries and the opening of more domestic production locations in Europe and North America [4]. Reshoring (the process of returning the production and manufacturing of goods back to the company's original country) is already a contributor to increased demand for robots in Europe and North America [5]. A 2016 executive survey by PwC [6] revealed that:

- Respondents expect to significantly increase their portfolios of digital products and services; many expect to be at an advanced level in this area by 2020.
- Over the next five years, the companies surveyed expect to increase annual revenues by an average of 2.9% and reduce costs by an average of 3.6% p.a.
- Customers will be at the centre of the changes to value chains, products and services. Products, systems and services will be increasingly customised to customer needs, and many say they plan to use data analytics to understand and meet their customer's needs. Those who are able to establish successful Industry platforms first, will have a significant advantage over competitors.
- The survey respondents say that their biggest implementation challenge is not the right technology, it is a lack of digital culture and skills in their organisation.

- Data fuels Industry 4.0 and successful data analytics is the prerequisite for successful implementation of digital enterprise applications.
- Half of the surveyed companies have established dedicated data analytics functions, either on a corporate level to bundle talent or on a business unit level to remain close to the operational business.
- Industry 4.0 will create digital networks and ecosystems that in many cases will span the globe, but still retain distinct regional footprints.
- The research suggests that global industrial products companies will invest US $907 billion per year through to 2020. The major focus of this investment will be on digital technologies like sensors or connectivity devices, as well as on software and applications like Manufacturing Execution Systems (MES).

However, it has to be noted that digital transformation often involves the adoption of Disruptive Technologies. A disruptive technology is one that displaces an established technology and shakes up the industry or a ground-breaking product that creates a completely new industry [7].

While major focus of investment will be on digital technologies, companies must also invest in training their employees, hiring new specialists and driving organizational change [8]. For small and medium-sized enterprises, all these technologies can be very challenging. Some manufacturers do not feel their operations are big enough, the pace of change is too fast, the large capital expenditure was not budgeted and their unique selling proposition or niche might be affected. Deloitte Global in their reported even senior business executives and government agency leaders from around the world say they are lacking confidence in their organizations' readiness to influence and harness Industry 4.0's opportunities in their organisations [9].

Companies must consider a list of variables before making a decision—the technologies of choice, the cost of the investment, the items/areas to be transformed, the deployment of these new technologies, the talent and knowledge to know the best ways to adopt it and the impact this adoption on the overall business [10].

Back home in Malaysia, 98.5% of business establishments are SMEs which comprise of various type of businesses. There are 907,065 establishments of SMEs in Malaysia. SME contributes 36.6% of Malaysia's GDP in 2016 [11]. As in theory, smaller companies should be able to implement Industry 4.0 easier and more cost effectively, improving productivity within SMEs, would definitely have a positive impact towards the country.

In conclusion, while the advantages Industry 4.0 can help vendors in their business growth and overcome the obstacles and future challenges, evaluation of technologies available in the market that are suitable and affordable to the vendors for the adoption of Industry 4.0 technologies is equally very important [12].

2 Methodology

The method of research is based on gathering primary data from a survey via the use of questionnaires. The questionnaire was developed based on the following flow (Fig. 1).

The questionnaire has 13 questions of which 9 questions are Binary in nature; Yes/No answers and the rest are Categorical in nature; specific outcome answers. The questions are divided into 4 basic categories; the first being the applicability, awareness and interest of the respondents towards Industry 4.0. In this category respondents were asked first and foremost whether Industry 4.0 is applicable in their industry. Next is on their awareness, familiarity and interest in the concept.

The second category is on the important features of Industry 4.0. Respondents were asked what the most important area of Industry 4.0 to start off with, should it be on top of their existing legacy system and what are the benefits that are expected from implementing this system.

The third category is the planning for Industry 4.0 implementation. respondents were asked about their plans, training and strategies on Industry 4.0 and the last category the challenges and drivers, whereby respondents were asked about their implementation affordability, assistance from government or OEMs and the relevance of Industry 4.0 in their going concern.

The population of the research is Ingress Automotive Component Group of Companies, which comprise of subsidiaries which are vendors to major car manufacturers in Malaysia, Thailand, Indonesia and India. The targeted companies are:

- Ingress Technologies Sdn Bhd—one of the biggest subsidiaries in the Ingress group of companies, a tier-1 vendor for Perodua, Proton and Honda Malaysia.
- Talent Synergy Sdn Bhd—a system integrator company focusing on Industrial automation and industry 4.0 solution provider.
- Ingress Katayama Technical Centre—design and manufacture moulds, dies, jigs and toolings for the automotive industry.

Fig. 1 The categories of the question proposed in the questionnaire
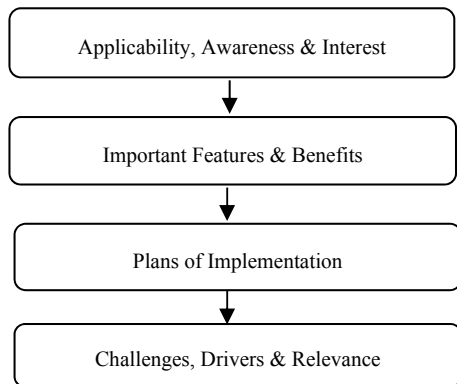
- Ingress Corporation Berhad MIS Department—to provide the strategy for IT direction and service deliveries towards the organization and its users within the Ingress group of companies.

These companies were chosen for reasons of their familiarity with Industry 4.0 and their vast network of customers, Tier-2 vendors, sub-contractors and partners who have similar exposure with Industry 4.0. Five (5) respondents of managerial positions were selected from each of the above companies. All the respondents were males, age ranging from 35 to 45 years and have good background in IT and manufacturing. The mode of answer for the questions is show in Table 1.

Table 1 The mode of answer used in the questionnaire

Questions	Mode
Is Industrial 4.0 applicable to the vendors?	Yes
In your opinion, what is the awareness level of Industry 4.0 among the vendor community?	Aware, familiar and interested
What would be the most important area of Industrial 4.0 for vendors to implement as a start?	Inter-operability (machines, devices, sensors and people that connect and communicate with one another)
Should Industrial 4.0 be implemented on top of the present legacy system?	Yes
What would be the real benefit of Industrial 4.0?	Competitiveness
Does your company have plans already for the adoption of Industrial 4.0?	Yes
Does your company already started training for Industrial 4.0?	Yes
Which areas should vendor start strategising in their future plan of implementing Industrial 4.0	Equal mode for every answers - Manpower planning/Capital investment budgeting/Knowledge and information gathering/Initiate discussion and sharing plans with OEMs or Tier-1
Can you afford to implement Industrial 4.0?	No
Should vendor wait for the government sponsorship to adopt Industrial 4.0?	Equal mode for both Yes/No
Should the OEM help the vendors in the implementation of Industrial 4.0?	Yes
Should the OEMs include the vendors in their implementation of Industrial as being part of their value chain supply?	Yes
Would vendors not having any feature of Industrial 4.0 will still be relevant to the Industry?	Yes
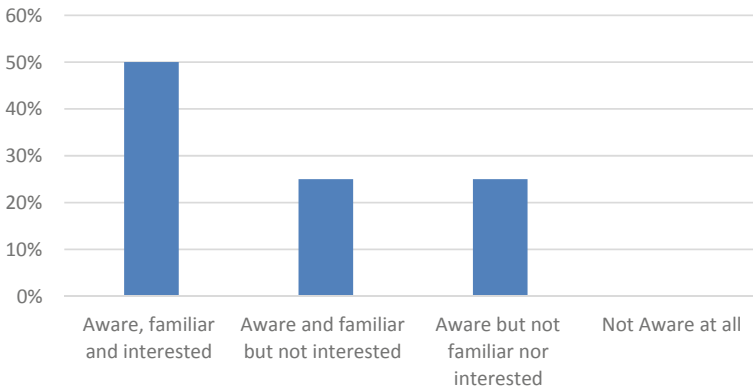
Fig. 2 Awareness level of Industry 4.0 within the organization

3 Results and Discussion

3.1 Applicability, Awareness and Interest Towards Industry 4.0

All respondents were in agreement that Industry 4.0 is applicable to their companies. This is not surprising as the topic on Industry 4.0 is quite well known due to the government initiatives in promoting the concept. However, in terms of interest, only half of the respondents are actually interested in Industry 4.0. (Fig. 2). Further efforts are still required to get the buy-ins from these people or maybe a more proven and existing smart factories are required to be highlighted to showcase their success stories in Industry 4.0. The level of awareness is further tested for relationship with having plans to implement Industry 4.0. The result yielded a positive 0.856 which indicated a strong relationship. The test implies that awareness level of Industry 4.0 has a strong relationship with having plan for it. Companies that are familiar with Industry 4.0 tend to plan for its implementation.

3.2 Important Features and Benefits of Implementing Industry 4.0

In term of what would be the most important area of Industry 4.0 for vendors to implement as a start; majority of the respondents opted Inter-operability (Fig. 3), which is the obvious and generally understood concept of Industry 4.0. However, Industry 4.0 should be implemented 'on top' of their existing system. Most of the respondents also believed Industry 4.0 will provide competitiveness to their company. In manufacturing, the capability of information and accessing real-time data has
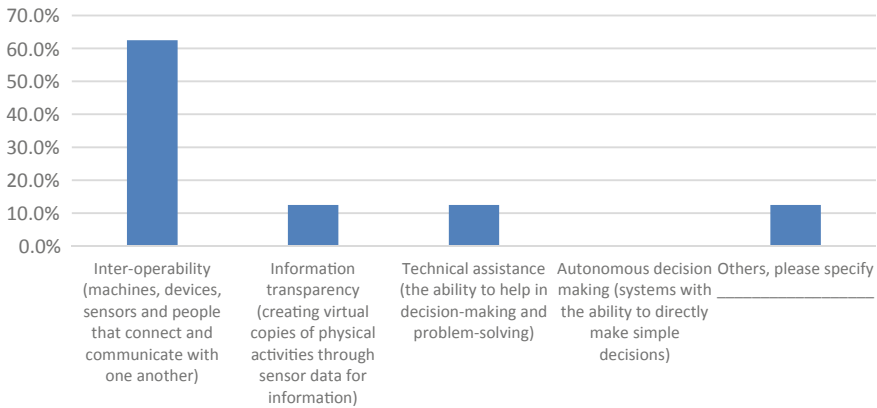
Fig. 3 Most important area of Industry 4.0 to implement

the potential to improve production resulting in more effective and more reliable operations. The goal of Industry 4.0 is to achieve low-cost production efficiencies while leveraging automation. It also allows the company to share information with within its organization, customers and suppliers accurately and quickly.

3.3 Plan of Implementation

In this third category, the majority of the respondents do have plans for Industry 4.0 and have already started some sort training for it. However, in terms which area to start the implementation (in their organisation) their opinions were equally spread between manpower planning, capital investment planning, knowledge and information gathering and initiate discussion with OEMs or Tier-1 (Fig. 4). Training employees is normally required for any implementation of new technologies. Human capital must be trained in order to implement, operate, and maintain the automated systems properly and to ensure their continuous operation [13]. On the other hand, the development and introduction of Industry 4.0 technologies may require substantial investment which rise the concern of the availability of financing and government support for small and medium-sized enterprises. This has always been a common issue among the vendors [14]. Other pre-development initiatives involve Cyber-Physical Systems (CPS) which typically requires the use of knowledge-based and intelligent information approaches. IT infrastructure support is often based on the analysis and reuse of the information and knowledge contained in the manufacturing processes and CPS and their production units. Hence, data gathering is also important [15]. Lastly, by the end of the day, true to the marketing concept, a business entity's main objective is to serve its customer needs. The implementation of Industry 4.0
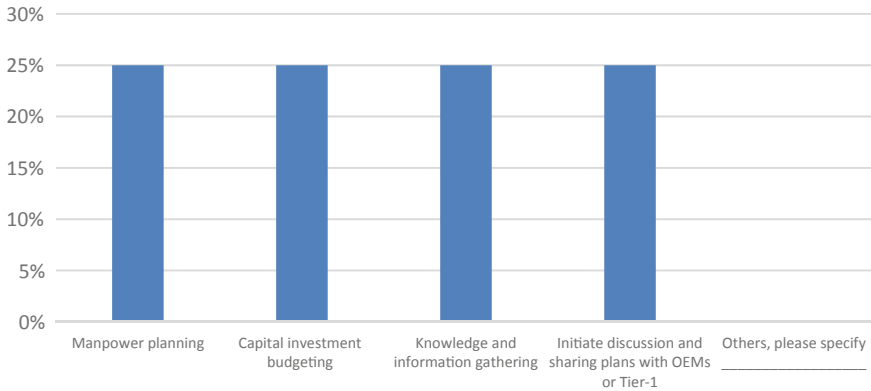
Fig. 4 Area to start strategizing in implementing Industry 4.0

technologies within the supply chain is important in order to collaborate and exchange information with the automotive OEM in real time [16].

3.4 Challenges, Drivers and Relevance in Implementing Industry 4.0

Most of the respondents were of the opinion that they are unable to afford implementing Industry 4.0. However, despite this opinion, the respondents were equally divided on whether government assistance is required. Instead, most believe that it is the OEMs that should assist the vendors and the adoption of Industry 4.0 should be done within the supply chain. Being able to afford Industry 4.0 and the awareness of the concept were tested for relationships. The result yielded 0.389 which indicated positive relationship however, a weak one. In this test, Industry 4.0 awareness has a weak relationship with the company's ability to afford implementing it. High level of awareness is impeded by the opinion of not being able to procure the Industry 4.0 technology.

Lastly and perhaps the most intriguing, most respondents were still of the opinion that even without Industry 4.0, vendors will still be relevant in the automotive industry. The level of awareness was test for any relationship with the opinion of the respondents on the relevancy of their company not having Industry 4.0. The result yielded a negative −0.522 which indicated no relationship. Industry 4.0 awareness does not necessary indicate the respondents' belief in its relevancy in the going concern of the company.

From the above, the analysis showed that all respondents are aware and have some understanding of Industry 4.0, however affordability is the main issue and half of the respondents seek government and OEMs assistance in implementing Industry 4.0. Finally, perhaps the most significant finding is that most respondents still believe

vendors will still be relevant without adopting Industry 4.0. somewhat giving an indication that most of the vendors are still not very serious in adopting the Industry 4.0; promoting the belief that Industry 4.0 may end up as a passing trend within the industry.

4   Conclusion

Industry 4.0 has the potential to affect long-term positive change in manufacturing. Vendors should constantly monitor the new developments and update their strategies that take advantage of these new opportunities in order to remain competitive. Awareness of this concept is very high in most respondents. What the vendors want are opportunities to test out and acquire these new technologies to lessen the risk in the process of adoption and enable them to decide for themselves the most appropriate technology for their businesses. Most importantly vendors need to find a cost-effective way to integrate new technologies with their legacy systems. Support from the Government and OEMs is important to ensure success in the implementation of Industry 4.0. Last but not least, more demonstrations on the Industry 4.0 application systems to further familiarize the automotive vendor community on its relevance in the future.

References

1. Saqib S, Cang S, Yu H, Li Y (2016) Management approaches for industry 4.0, 5309–5310. https://doi.org/10.1109/CEC.2016.7748365
2. Moore M (2019) What is industry 4.0? Everything you need to know. https://www.techradar.com/news/what-is-industry-40-everything-you-need-to-know
3. Ranta K (2009) Industry 4.0 and challenges manufacturers face
4. (2014) Deloitte: Industry 4.0 challenges and solutions for the digital transformation and use of exponential technologies
5. Burns A (2015) New statistics from the international federation of robotics illustrate converging patterns of data, efficiency and demand. http://siteselection.com/onlineInsider/uncaged.cfm
6. 2016 Global Industry 4.0 Survey: what we mean by Industry 4.0/Survey key findings/Blueprint for digital success, Industry 4.0: building the digital enterprise available at https://www.pwc.com/gx/en/industries/industries-4.0/landing-page/industry-4.0-building-your-digital-enterprise-april-2016.pdf
7. Christensen CM (2011) The innovator's dilemma. Harper Business, Reprint edn
8. Ngotngamwong R (2020) Artificial intelligence and its impacts on employability. 21(2):51–53. ISSN 2651-1762
9. Deloitte Global (2018) The fourth industrial revolution is here—are you ready?. https://www2.deloitte.com/content/dam/Deloitte/tr/Documents/manufacturing/Industry4-0_Are-you-ready_Report.pdf
10. Schroder C (2016) The challenges of industry 4.0 for small and medium-sized enterprises, 11 & 12
11. SME Corp. Malaysia Homepage. https://www.smeinfo.com.my/. Last accessed 20 July 2021

12. Ingaldi M, Ulewicz R (2019) Problems with the implementation of industry 4.0 in enterprises from the SME sector, 3
13. Sima V, Gheorghe IG, Subić J, Nancu D (2020) Influences of the industry 4.0 revolution on the human capital development and consumer behavior: a systematic review, 4
14. Schröder C (2016) The challenges of industry 4.0 for small and medium-sized enterprises, 16
15. Toroa C, Barandiarana I, Posadaa J (2015) A perspective on knowledge based and intelligent systems implementation in Industrie 4.0, 367
16. Soares MC, Ferreira CV, Murari TB (2021) Supply chain resilience and industry 4.0: an evaluation of the Brazilian northeast automotive OEM scenario post COVID-19, 4

Analysis of Driver Behaviour (Sleepiness) Using Microsleep Detector Device (MDD)

Nur Atiqah Nabila Binti Hazman, Nor Fazli Adull Manan, and Ahmad Khushairy Bin Makhtar

Abstract Microsleep happens when a sleepy individual is attempting to resist sleep and stay awake. Microsleep also can occur while a person is driving, which will significantly increase the risk of a fatal collision. Thus, detecting microsleep and prevent from happening is become very crucial nowadays. This project aims to develop an effective Microsleep Detector Device (MDD) equipped with a warning system before a driver falls asleep on the wheel. An experiment was conducted to observe the symptoms of drivers such as yawning, rubbing eyes, body incline to the front while driving, and map with Karolinska Sleepiness Scale (KSS). A total of ten respondents (Mean Age = 24 Years Old, SD = 0.4) participated in the experiment. They had experienced a total of 4 sessions with 30 min of driving per session on a driving simulator. An alarm was set based on the Eye Aspect Ratio (EAR) of the individual participants if the EAR value exceeds the threshold. The result of EAR shows that that the respondents were getting sleepy after an hour of driving. The results of KSS showed KSS's level of participants increased from level 5 to level 6 after one hour of driving. Overall, the MDD performance result indicates the average value of (M:5), implying that the device can detect the respondent's EAR. The KSS level slightly declines from level 6 to level 5 just after the warning system is triggered. In a nutshell, microsleep can affect the performance as well as safety of drivers. These show that the device will increase the alertness of micro- sleep while driving, which eventually reduces the number of accidents.

Keywords Microsleep · Eye aspect ratio · Karolinska sleepiness scale

1 Introduction

Microsleep is a transitional state between waking and sleeps in which vigilance, or the capacity to maintain one's attention on a task, is generally decreased. This can be a significant issue when performing tasks that require sustained attention,

N. A. N. B. Hazman · N. F. Adull Manan · A. K. B. Makhtar (✉)
School of Mechanical Engineering, Universiti Teknologi Mara, Shah Alam, Malaysia
e-mail: ahmadkhushairy@uitm.edu.my

such as driving [1]. Detection microsleep can be divided into two categories which are visual features and non-visual features. The visual features were focusing the techniques by using computer visions. Based on previous studies, visual features can be divided into eye state analysis, eye blinking analysis, mouth, and yawning analysis, and facial expression analysis [2, 3]. Besides, a drowsy individual can be identified by their gaze pupil movements [4]. It was evident that a sleepy person has a more restricted gaze region than an alert person. Additionally, a drowsy person has fewer saccadic movements than when they are awake. Subsequently, a fatigued individual can be identified by the eyelids' movement [4]. Drowsy individuals blink significantly slower than awake individuals. A fatigued individual will close their eyes for a more extended period than an awake individual. To put it simply, a drowsy person has a longer duration of eye closure than an alert person [2].

The research concentrated on facial landmark detectors for determining the contours of the eyes and eyelids [5]. The eye aspect ratio (EAR) was derived from the detected images to estimate the eye-opening state [6]. If an eye is open, the EAR has been mostly constant. When an eye is closed, the EAR approaches zero. Because both eyes blink in perfect sync, the EAR of both eyes is averaged [5]. The face must be detected using a Viola-Jones face detector available in the OpenCV library to detect the eye landmarks [7].

Additionally, subjective measures can be used to analyze driver's sleepiness. There were five standardized subjective fatigue or sleepiness methods to analyze sleepiness, such as Karolinska Sleepiness Scale (KSS), Visual Analogues Scale (VAS), and Epworth Sleepiness Scale (ESS) [8]. Subsequently, KSS has become the most widely used tool for subjective self-assessment of microsleep in recent years. KSS consists of a 9-point scale at first (1 = extremely alert, 2 = very alert, 3 = alert, 4 = rather alert, 5 = neither alert nor sleepy, 6 = some signs of sleepiness, 7 = sleepy, but no difficulty remaining awake, 8 = sleepy but some difficulty to keep awake, and 9 = extremely sleepy, great difficulty to keep awake, fighting sleep). However, a modified version of KSS contains one other item: 10 = extremely sleepy. Thus, the modified KSS will be mating with the fatigued driver.

Existing microsleep detection methods are unsuitable for use while driving, as the device or components will be attached to the driver's body. Thus, the purpose of this research is to develop a MDD capable of detecting the driver's eye aspect ratio (EAR) while driving. The proposed MDD employs a camera mounted directly in front of the driver, which is more conducive to use while driving. Additionally, this study concentrated on the warning system. Therefore, once the driver exhibits signs of sleepiness, MDD will activate the alarm. Following that, the driver's behavior will be classified using the Karolinska Sleepiness Scale (KSS).

2   Project Methodology

2.1   Microsleep Detector Device (MDD) Development

The working mechanism of the MDD for the entire process, starting from initialization to the warning system. The experiment starts with detecting the face using a Vio-la-Jones face detector available in the OpenCV Library. Next, the device received input from the camera attached to the driver and processes the frame captured for microsleep detection (Fig. 1).

Previous studies have based their criteria on facial landmark detectors to localize the eyes and eyelid contours. First, as landmarks detected in the image with face, the EAR was derived from an estimate of the eye openness state. Then, each video frame is computed; the eye landmarks are detected. Finally, the EAR between the height and width of the eye is calculated based on the Eq. 1, where p1 till p6 are the

Fig. 1 Flowchart of microsleep detector device (MDD)
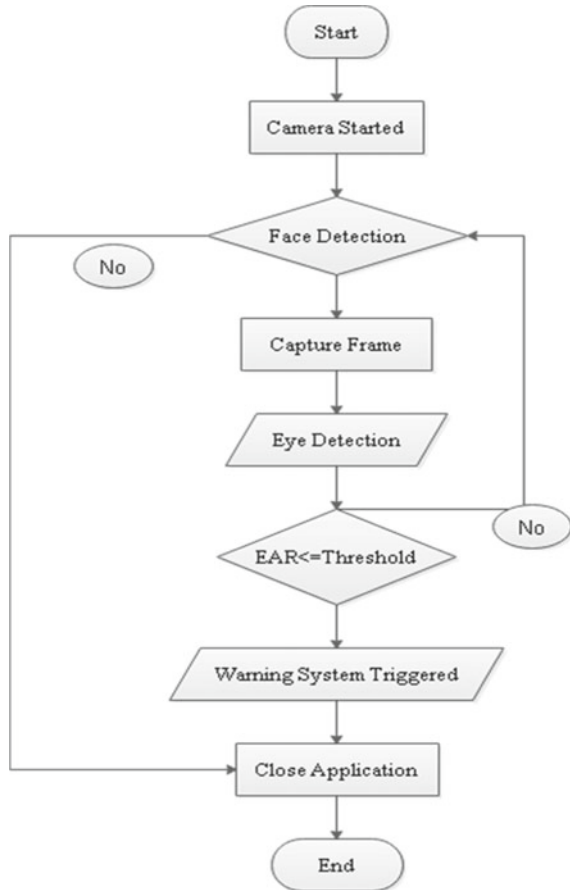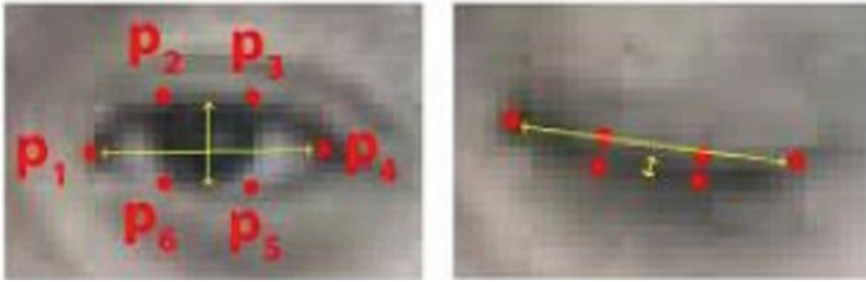
Fig. 2 Eye landmark [5]

2D landmark locations, depicted in Fig. 2.

$$EAR = (|(\|p2 - p6\|)| + \|p3 - p5\|)/(2\|p1 - p4\|) \tag{1}$$

The value of EAR is constant when the eyes are opened and getting close to value zero when the driver is closing their eyes. Thus, the device collects EAR data for both eyes synchronously and averaged the value to find the threshold for every respondent. Subsequently, the EAR threshold for every respondent had been stored in the device to proceed with the warning system. As the value EAR of each respondent equaled or exceeded the threshold for five milliseconds, the alarm will be triggered to alert the driver.

2.2 Participants

The experiment was conducted with five male and five female drivers between the ages of 25 and 24 years old (Mean = 24.2, SD = 0.422). The experienced driving of respondents showed between one to eight years, which proved they had a valid driver's license. All the respondents have no record of smoking behavior, and their blood pressure is normal, which will not affect their performance during the experiment.

2.3 Experiment Setup

The experiment was carried at the Ergonomic Laboratory of the Faculty of Mechanical Engineering, UiTM, Shah Alam. A driving simulator was set up before the experiments start, as illustrated in Fig. 3. The MDD's camera module has been mounted on the top of the computer to capture video of the driver, as shown in Fig. 3.
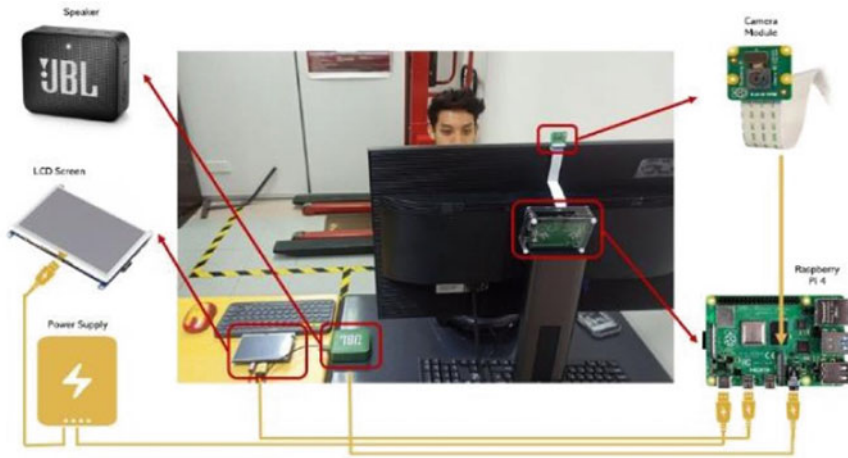
Fig. 3 Layout of device

Next, the respondent's blood pressure and temperature were recorded to ensure that they were in excellent health during the experiment. Subsequently, the respondent has been explained the procedure of the experiment. Thus, the respondent is given a consent form to ensure that the respondent agrees to participate in the experiment. Following that, before the experiments start, the respondent's information, such as age, height, weight, and driving experience, was collected via General Questionnaire.

2.4 Experiment Procedure

After developing a device capable of detecting the EAR, an experiment on microsleep was conducted. The experiment procedure comprises four sessions within two and half hours. The duration for every session is 30 minutes following 10 minutes breaks. In all sessions, the participants were required to drive in driving simulator environment. The driving condition and environment is the same throughout the sessions. Following that, the first session starts with taking value EAR, and observed the driver's behaviour simultaneously. Value EAR is taken by MDD for every 150 frames. Thus, every five minutes for 30 minutes, the researcher observed the driver's behaviour using the modified KSS and recorded the frequency of their behaviour. The first session's procedure is repeated until the third session.

Following that, the experimental procedure for the fourth session is continued with the warning alarm system. The third session's mean value of EAR was set in as threshold. The warning system is triggered during the fourth session when the threshold value exceeds the EAR. Following the completion of the fourth session, the respondent was required to complete a Google Form regarding feedback on the device's performance.

Table 1 Modified karolinska sleepiness scale (KSS)

Level	4	6		7		8	
		6.0	6.5	7.0	7.5	8.0	8.5
Criteria of micro sleep	Alert	Some sign of sleepiness	Some sign of sleepiness	Sleepy, but no effort to keep awake	Sleepy, but no effort to stay awake	Sleepy, but some struggle to stay awake	Sleepy, but some effort to stay awake
Behavior	Driving with one hand	Having a conversation or singing	Yawning one time while driving	Yawning two times while driving	Rubbing eyes	Yawning over three-time while driving	Body incline to the front while driving

2.5 Driver Behaviour Sleepiness Scale

The driver behaviour sleepiness scale has been mating with the criteria of KSS accordingly, as shown in Table 1. The KSS level of this experiment ranges from 4 to 8, with drivers exhibiting specific behaviours such as yawning, conversing, and rubbing their eyes, as illustrated in Table 2.

2.6 Statistical Analysis

IBM SPSS Statistic was used to analyze all the respondents' data after being sorted out in Microsoft Excel. IBM SPSS Statistic analyzed the data to reveal the significant result in each measurement. Repeated measure ANOVA and univariate measure ANOVA were used to analyze the Eye Aspect Ratio (EAR) and observed KSS level and Questionnaire as the software will determine the significance for the data that have been entered is less than ($p < 0.05$). The significance level or alpha level of 0.5 (5%) has been selected to run the test of all results in this experiment. Repeated measure ANOVA was used to determine the statistical significance in all gender results and univariate measure ANOVA was used to determine the statistical significance in the overall result of all participants. Wilk's lambda is a test statistic that's reported in how well each level of independent variable contributes to the model.

Table 2 Driver behavior

	Driver behaviour	Explanation
1	Having conversation of singing	The drivers have a conversation with people or sing while driving
2	Driving with one hand	The drivers suddenly change their driving style from both hands to one hand
3	Yawning one time while driving	The driver yawning one time for over 5 s
4	Rubbing eyes	The driver rubbing their eyes over 2 s
5	Body incline to the front while driving	The driver moved the body towards the steering wheel

3 Results and Discussion

3.1 Physiological Measurement (EAR)

A repeated-measures ANOVA was conducted with EAR of session one till three, as the within-subjects factor. The results of the repeated measure ANOVA indicated a significant value of EAR on every session, Wilks' Lambda $= 0.718$, $F(18, 978) = 9.795$, $p < 0.05$, $\eta^2 = 0.153$.

Figure 4 illustrates the average value of EAR from session one to session three, separated by gender. The results of the repeated measure ANOVA indicated a significant value of EAR on every session, Wilks' Lambda $= 7.305$, $F(2.000, 497) = 9.795$, $p < 0.05$, $\eta^2 = 0.029$. Thus, from session one to session three, a male's EAR value trend is increasing. However, the female EAR increased from session one to session two but decreased slightly from session two to session three. An evaluation of this result suggests that males are not sleepy during driving for the entire experiment as they are accustomed to driving for a prolonged time. This can be demonstrated that
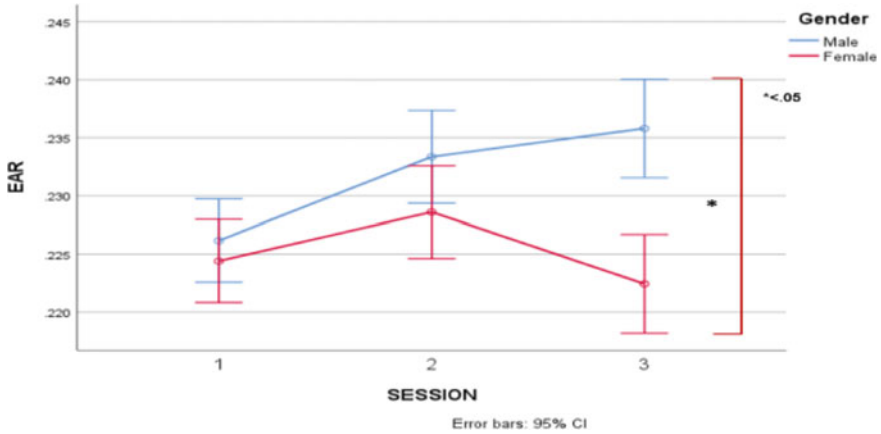
Fig. 4 Line graph of mean EAR by gender

female drivers are more sleepy than male drivers. For the whole experiment, the difference in EAR values between genders was statistically significant ($p = 0.003$). Gender has been shown to profoundly affect lifestyles, stress levels, and, more broadly, all aspects of human behavior [9]. To illustrate this issue, homeostatic pressure to sleep increases more quickly in females, leading to a more decisive necessity for sleep in females than in males [10].

Figure 5 present the analysis of the overall mean ten respondents for each session. The results of the repeated measure ANOVA indicated a significant value of EAR on every session, Wilks' Lambda $= 0.974$, $F(2.000, 498.000) = 6.752$, $p < 0.05$, $\eta^2 = 0.026$. The value of EAR is slightly level up from session one to session two. This is
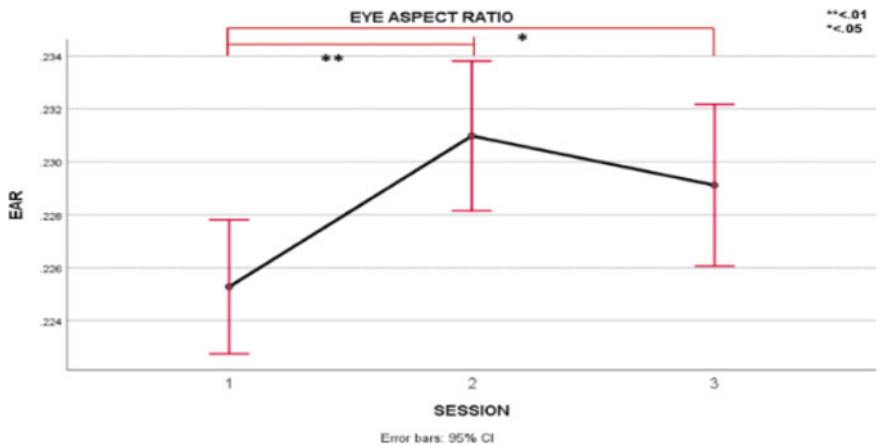
Fig. 5 Line graph of mean EAR for the entire session

plausible given the respondent's excitement while driving the simulator for the first time.

The pairwise comparison revealed a significant value between session one and session two ($p = 0.000$). The graph indicates that the growth rate from session two to session three is noticeably slower. Therefore, this provides evidence that the respondent is getting sleepy after an hour of driving. The result of EAR is higher at session three than session one, which session three is supposedly lower. This is because the respondent begins the experiment with drowsy state as they sleep at 5 a.m. According to a previous study, drivers become sleepy when they get little sleep prior to driving [11].

3.2 Subjective Measurement (KSS)

A repeated-measures ANOVA was conducted with KSS of sessions one, two, three, and four, respectively, as the within-subjects factor. Also, ten respondents as between-subjects factors. The results of the repeated measure ANOVA indicated a significant value of KSS on every session, Wilks' Lambda $= 0.381$, $F(27, 140.827) = 2.042$, $p < 0.05$, $\eta^2 = 0.275$.

Figure 6 illustrates the average value of KSS from session one to session three, separated by gender. The results of the repeated measure ANOVA indicated a significant value of KSS on every session, Wilks' Lambda $= 0.964$, $F(3.000, 56.000) = 0.696$, $p < 0.05$, $\eta^2 = 0.036$. The trend line of male's KSS increased dramatically from session one to session three. An evaluation of this analysis proves that the male's driver is alert at the first session but changed to neither alert nor sleepy at
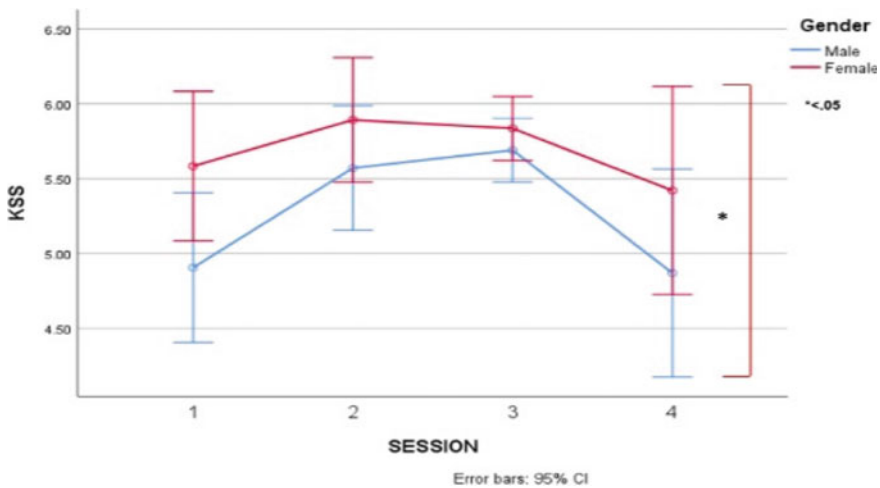
Fig. 6 Line graph of mean KSS by gender

session three. Throughout the experiment, the male driver demonstrated microsleep behavior. Additionally, the trendline of female's KSS also increased up noticeably from session one to session three. Thus, the female driver's KSS at session one is significantly different than the male driver's KSS, indicating that the female driver is trying to stay alert while driving. Thus, overall, the genders had affected the KSS level during driving. As was the scenario in session four, a warning system was installed to alert the drowsy driver. Therefore, the KSS level is expected to decrease between sessions three and four for both female and male drivers. What can be seen is that the male KSS level decreases, indicating a transition from sleepiness to alertness. Following that, the female KSS level gradually decreased which neither awake nor sleepy while driving. To summarize, the graph indicates that they return to the same state as in session one for female drivers but are more alert than in session one for male drivers after the warning system is triggered.

Figure 7 depicts the average value of KSS for each session from one to four, based on the mean of ten respondents. The results of the repeated measure ANOVA indicated a significant value of EAR on every session, Wilks' Lambda $= 0.849$, $F(3.000, 57) = 3.366$, $p < 0.05$, $\eta^2 = 0.151$. The KSS level shows increasing value from session one to session three. According to the driver behavior sleepiness scale, drivers begin to exhibit signs of sleepiness such as yawning while driving (Table 3). What this chart clearly shows is the steadily maintained KSS level from session two to session three. This would be to say; the respondent exhibited the same level of KSS. Following that, the graph demonstrates a slight decrease between sessions three and four. The KSS level decreases due to the driver's alertness while driving when the warning alarm sounds. Following that, the significance value between sessions one and two is $p = 0.013$ which is significant. The same holds for session one, and session
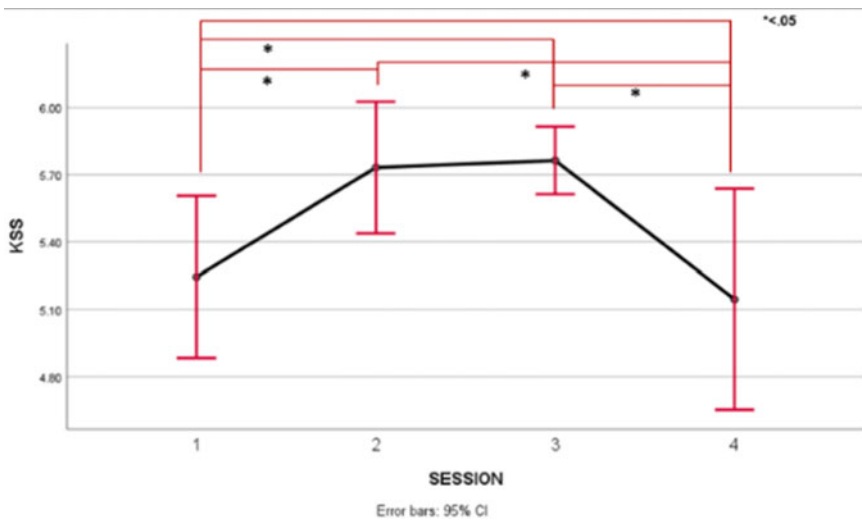
Fig. 7 Line graph of mean KSS for entire experiment

three demonstrated a statistically significant value ($p = 0.008$). This indicated that the more hours spent driving, the higher the KSS level. This is due to the presence of a warning system during session four. This hypothesis is remarkably similar between sessions three and four, as indicated by the p-value ($p < 0.016$). Based on previous research, the participants who were in sleepy conditions, the sleepiness scale reported increasing, which leads to falling asleep [11].

3.3   Performance of Microsleep Detector Device (MDD)

Figure 8 depicted an average response to a questionnaire during an experiment. The results of the repeated measure ANOVA indicated a significant value of the questionnaire's answer, Wilks' Lambda $= 0.106$, $F(4.000, 6.000) = 12.702$, $p < 0.05$, $\eta^2 = 0.894$. The average value of ten respondents' responses regarding the camera's position is (M:2), which disagrees with the statement. According to the respondent, the camera's position did not obstruct them while driving because the camera was not attached to their body. Therefore, the respondent can drive the simulator without any obstruction.

Following that, the device's performance affirms the answer of (M:5), strongly agreed. Once the warning alarm is triggered after the threshold exceeds the EAR, the device's performance can be justified. Additionally, the device can detect the respondent's face and ear while driving. Furthermore, the MDD can detect the EAR even if the respondent is wearing spectacles. Regarding that, the question is about the alarm's performance. The average response of ten respondents was (M:5), which is strongly
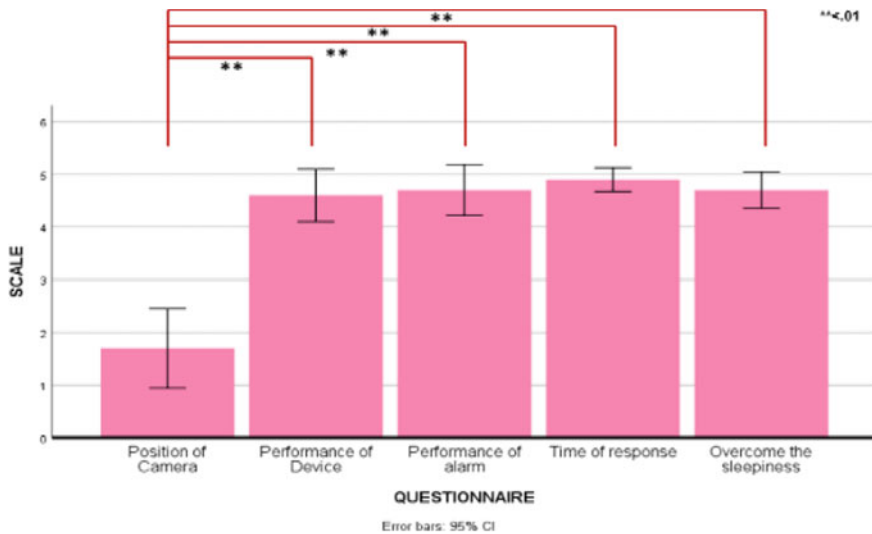
Fig. 8 Bar chart of questionnaire's answer

agreed on such. The warning is triggered during the fourth session following the threshold setting in MDD. Thus, when the threshold was maintained for five milliseconds, the warning system sounded. Furthermore, the respondent is intent about the time of response. When the threshold exceeds the EAR, the warning system does not delay. Finally, the respondent agreed unequivocally that MDD could overcome microsleep. This is demonstrated when the respondent's KSS level drops slightly from session three following the triggering of the warning.

4   Conclusion and Recommendation

In a nutshell, the physiological and subjective measurement analysis of driver behaviour (sleepiness) was indicated. The physiological measurements were focused on the driver's eye aspect ratio EAR by using MDD, while the subjective measurements using the KSS and a questionnaire. The EAR demonstrates statistical significance for each subject as $p < 0.05$. The analysis of EAR by gender statistically significant as the research concluded female drivers are more drowsy than male drivers. Furthermore, the EAR of ten respondents indicating statistical significance as the drivers become drowsy, their EAR approaching to zero. Next, the results of KSS were statistically significant for each subject, which means they tend to sleepy during driving. The statistical result of gender for KSS also showed significant value as male drivers showed more fatigue behaviour than female drivers. Additionally, the mean of KSS for ten respondents also showed the statistical result as $p < 0.05$. This demonstrates that the longer the driving hour, the higher the KSS level. The KSS level of the drivers decreasing as the warning system was triggered.

However, there is still room for improvement to present a great result to MDD and analyse driver behaviour (sleepiness). The MDD can be improved by utilizing advanced technology and a high-quality camera module to capture high-resolution video frames. Additionally, to capture genuine microsleep, the number of video frames should be reduced to 35. Subsequently, a suitable environment should be created for drivers to experience the actual driving situation, leading to microsleep. Finally, the number of respondents should be increased to 50, as the number of respondents is critical for accurately representing the population. Overall, this research confirms previous findings and presents novel findings that aid in evaluating existing technologies and inform future development of microsleep detection systems. In this sense, this research contributes to the evolution of tailored technology for microsleep detection and warning based on the characteristics of individual drivers.

References

1. Picot A, Charbonnier S, Caplier A (2008) On-line automatic detection of driver drowsiness using a single electroencephalographic channel. In: Proceedings 30th annual international conference IEEE engineering in medicine and biology society EMBS'08—personalized healthcare through technology, pp 3864–3867. https://doi.org/10.1109/iembs.2008.4650053
2. Kaplan S, Guvensan MA, Yavuz AG, Karalurt Y (2015) Driver behavior analysis for safe driving: a survey. IEEE Trans Intell Transp Syst 16(6):3017–3032. https://doi.org/10.1109/TITS.2015.2462084
3. Islam A, Rahaman N, Ahad M (2019) A study on tiredness assessment by using eye blink detection. J Kejuruter 31(2):209–214
4. Zhao Q, Yuan X, Tu D, Lu J (2015) Eye moving behaviors identification for gaze tracking interaction. J. Multimodal User Interfaces 9(2):89–104. https://doi.org/10.1007/s12193-014-0171-2
5. Cech J, Soukupova T (2016) Real-time eye blink detection using facial landmarks. Center for Machine Perception, Department of Cybernetics. Faculty of Electrical Engineering, Czech Technical University in Prague, pp 1–8
6. Mart N, Mart N, Seepold R (2019) ECG sensor for detection of driver's drowsiness, vol 00. https://doi.org/10.1016/j.procs.2019.09.366
7. Maior CBS, das Chagas Moura MJ, Santana JMM, Lins ID (2020) Real-time classification for autonomous drowsiness detection using eye aspect ratio. Expert Syst Appl 158:113505. https://doi.org/10.1016/j.eswa.2020.113505
8. de la Lopez OJ et al (2012) Development of a system to test somnolence detectors with drowsy drivers. Procedia—Soc Behav Sci 48:2058–2070. https://doi.org/10.1016/j.sbspro.2012.06.1179
9. Soares S, Monteiro T, Lobo A, Couto A, Cunha L, Ferreira S (2020) Analysing driver drowsiness: from causes to effects. Sustain 12(5):1–12. https://doi.org/10.3390/su12051971
10. Colten HR, Altevogt BM, Institute of Medicine Committee on Sleep Medicine and Research (2006) Sleep Physiology. Accessed: 20 June 2021. [Online]. Available: https://www.ncbi.nlm.nih.gov/books/NBK19956/
11. Kareem A (2003) Review of global menace of road accidents with special reference to Malaysia—a social perspective. Malaysian J Med Sci 10(2):31–39

Evolution of Archwires in Orthodontics: A Short Review

Md. Abdul Alim , **C. W. Ng** , **and M. F. Razali**

Abstract A plethora of archwires were introduced in the research of orthodontics throughout the previous centuries. The materials and mechanical characterization of orthodontic archwire is one of the popular topics in orthodontics research. Numerous literatures that described the developments of the specific or selective properties of archwire are readily available. After study through the existing literatures, we found that there is still a lackage of proper review article which gradually describes its evolution in orthodontics. This article summarizes its origins and features in short form, which will give an insight to the readers about the research and development of orthodontic archwire.

Keywords Archwire · Orthodontics · Biomaterials

1 Introduction

Treatment of teeth malocclusion could have a significant influence on oral and dental health, as well as on an individual's appearance, leading to an appealing smile that can boost psychological self-esteem and confidence. Orthodontic therapy is one of the oldest methods of teeth repositioning. The involvement and emergence of dental materials in the orthodontic discipline began with Edward Hartley Angle's (1855–1930) initial orthodontic uses of gold and steel wire alloys. Angle is regarded as the founder of contemporary orthodontics. Most of the materials and technologies utilized in orthodontic practice today would have been unimaginable during Edward Angle's lifetime [1, 2].

During the orthodontic treatment using fixed appliance therapy, archwires are the major source of the applied force to initiate the tooth movement. The orthodontic force is originated from the strain recovery of the deflected archwires after placement into the slots of dental brackets and buccal tubes. As the orthodontic archwires are

Md. A. Alim · C. W. Ng · M. F. Razali (✉)
School of Mechanical Engineering, Universiti Sains Malaysia, Engineering Campus, 14300 Nibong Tebal, Pulau Pinang, Malaysia
e-mail: mefauzinizam@usm.my

made of a variety of metals and alloys, understanding the fundamental materials properties is critical when selecting the wires for treatment. The mechanical characteristics of a material are controlled by a number of elements, including intrinsic properties, which is the alloy's composition, and extrinsic properties, which are the macroscopic features (diameter, length). Three key qualities of archwires determine their clinical utility: strength, stiffness, and elastic range. Over the last century, materials science has improved at a tremendous speed. In the orthodontics field, advancements have been made in materials and ideologies [3, 4].

Since there are currently a number of alloys utilized in orthodontic archwire, the development of the archwire and its compositions needs to be understood. In this article, we reviewed the materials available on these various archwire systems and assemble the knowledge for choosing wire during orthodontic treatment at the particular treatment stage. It is important to note that the main focuses in this article are the orthodontic archwires that made of metals and alloys. While some polymers have also been employed into the development of esthetic orthodontic archwires, for instance, polyphenylene polymers, the respective types of orthodontic archwire are not discussed in the present article. Among the different type of alloys, more attention will be given to nickel titanium (NiTi) orthodontic archwires, as NiTi alloy possesses the remarkable shape memory behavior that made it a popular candidate in orthodontic applications. The pseudoelasticity of NiTi shape memory alloy allow it to deliver light and continuous force throughout the strain recovery from large deflection, thereby generating more physiological tooth movement without affecting the patient's comfort [5–8].

2   Materials and Manufacturing

The orthodontic archwires are made by various types of materials. Silver, gold, stainless steel (SS), cobalt, chromium, nickel, titanium, beta titanium, alpha titanium, copper, timolium, niobium, and other fundamental materials are listed in the literature. The manufacturing of archwire begins with the casting of an alloy with proper composition. The ingot is then subjected to a series of wire drawing processes until the cross section is appropriately sized. Square or rectangular cross sections will always have corner rounding. This can make a significant contribution to archwire bracket torque delivery, especially when the wires are tightly engaged in the bracket slots. Heat treatments are required throughout the manufacturing process to remove the considerable work hardening that happens during the different phases of mechanical reduction. Certain atmospheric conditions are required to produce titanium-containing orthodontic wires as it is reactive with oxygen in air. After heating the alloy, the wires are drawn or rolled [9].

3   Evolution of Archwires

3.1   Gold Archwires

Edward Angle began using nickel silver alloys in his orthodontic equipment in 1887. Prior to 1950, precious metals such as gold and gold alloys were often utilized for orthodontic purposes. It was possible to change their stiffness by approximately 30% by the heat treatment. Gold has excellent corrosion resistance, but it is soft, malleable, and ductile in its purest form. After hardening in heat treatment, the modulus of elasticity rises by around 5%. To improve its mechanical characteristics, various metals including silver, copper, palladium, platinum, nickel, and zinc were utilized to cast the gold alloys with higher strength. Biocompatibility and formability of gold wires are good. Soldering is simple, and solder junctions are also corrosion-resistant [10].

3.2   Stainless Steel (SS) Archwires

Dr. F Hauptmeyer, the company's dentist, introduced stainless steel into dentistry in 1919 at Krupp's Dental Polyclinic in Germany. Stainless steel (SS) also possessed superior corrosion resistance, work-hardening capabilities, and a low frictional magnitude, making it the industry standard. Wrought structural wires have a high modulus of elasticity, making them ideal for orthodontics. Norris Taylor and George Paffenbarger presented steel as a gold replacement at the AAO Conference in 1931. Archie Brusse, the founder of Rocky Mountain Orthodontics, proposed the clinical use of stainless steel in orthodontics for the first time in 1933. Stainless steel was first used in the manufacturing of orthodontic equipment in Brazil in the late 1940s. By the 1960s, gold had mostly been replaced by SS [11].

3.3   Cobalt-Chromium Archwires

The Elgin Watch Company created a cobalt-chromium alloy with the composition of Cobalt (40%), Chromium (20%), Silver (16%), and Nickel (14%) in the 1940s. The introduction of cobalt-chromium-nickel alloy into orthodontic was done by ELGIN national enterprise in the 1950s, while the alloy was named as "Elgiloy". It was available in four tempers like-soft, ductile, semi-robust, and resilient. Elgiloy's corrosion resistance is derived from a thin passivating chromium oxide coating on the wire surface, similar to stainless steel alloys. These wires were cheap while having good tarnish and corrosion resistance. The joining of the wires can be achieved by soldering (with fluoride fluxes) and welding [12, 13].

3.4 Nickel Titanium (NiTi) Archwires

In 1972, the NiTi alloy that is suitable for clinical was developed by Unitek Corperation under the trade name of Nitinol (Nickel Titanium Naval Ordinance Laboratory). High resilience, restricted formability, shape memory or heat memory, and pseudoelastic or superelasticity are all characteristics of this material. NiTi alloys have two main crystalline phases at different temperature. The austenite phase has a B2 cubic structure that is similar to the body centered cubic structure (BCC) at higher temperatures. On the other hand, the martensite phase has a monoclinic B19' crystal structure at lower temperatures. Additionally, the intermediate rhombohedral phase (R-phase) that is capable to postpone the austenite-to-martensite phase transition could be originated after work hardening or thermomechanical treatment of NiTi alloy [14].

3.5 Chinese NiTi Archwires

It was developed in 1978 by Dr. Hua Cheng Tien and colleagues at Beijing's Nonferrous Metal Research Institute. Chinese NiTi wires offer a high degree of flexibility and shape memory recovery. The springback is very substantial, and the low stiffness characteristics have received widespread clinical endorsement for initial alignment. The magnitude of its springback is 1.6 and 4.4 times higher as compared to nitinol and stainless steel wires, respectively, in different types of deformation. The wire has a strength of 73% that of steel wire and 36% that of ordinary nitinol. It comes with a broad range of effects and back-strokes. Clinically, Chinese NiTi is suitable for upright, labial, and lingual tooth movements that need significant deflections [15, 16].

3.6 Japanese NiTi Archwires

Furukawa Electric Co. Ltd. of Japan discovered a new kind of NiTi alloy in 1978, which Miura et al. published in 1986. This NiTi austenitic alloys is known as Japanese NiTi acrhwires for active user. It demonstrates superelasticity produced via stress-induced martensitic transformation (SIM). Clinically, they provide physiological movement and improved patient comfort by using mild continuous power. In Japan, NiTi is known as Sentalloy [17].

3.7 Alpha and Beta Titanium Archwires

AJ Wilcock Jr developed these wires in 1988, claiming that they were very resilient while yet being formable. Like SS and NiTi orthodontic wires, titanium exhibits various crystalline structures at different temperatures. The stable form of alpha titanium has the hexagonal closed pack crystal structure at temperatures below 885 °C. but beta titanium exhibits bcc structure at higher temperatures. At room temperature, the elastic modulus and yield strength of Alpha-titanium are about 110 GPa and 40 MPa, respectively. Before reaching its yield point, beta titanium could be bent 105% farther or double the distance of SS. Although beta titanium can't be soldered, it can be bonded to itself with very little strength loss [18].

3.8 Supercable Archwires

It was discovered by Hanson in 1993. It was identified that It's a seven-stranded, coaxial NiTi that improves flexibility while lowering wire strength. These wires are simple to connect to densely packed teeth. It has a number of benefits, including better anchoring control, less patient discomfort, and less drilling. The propensity of wires at extraction points to sprout, break, and unravel, as well as the inability to deal with curves, stairs, or helices, are all disadvantages [19, 20].

3.9 Copper NiTi Archwires

Copper NiTi was invented by Rohit Sachdeva and Suchio Miyasaki in 1994. By reducing hysteresis and providing a precise temperature for transformation, they constitute the next generation of super-elastic and memory wires. Copper NiTi wires have a loading force of approximately 20% less than titanium nickel wires. The bracket slot is therefore simpler to utilize since it may be easier to handle the wire and so produces less stress and discomfort for the patient. Around the remaining area, however, the force decrease produced by NiTi is less than that caused by NiTi alloys. This illustrates how NiTi copper works in clinical efficiency by acting like teeth near to the target site. The additional copper element in the composition allowed for precise transformation temperature characteristics to be incorporated throughout the manufacturing process. This built-in precision is designed to control the physician, particularly during the early stages of treatment, in a way that no other force delivery technique can. These wires are classified as follows and are put at four distinct transformation temperatures for four different strength levels, allowing doctors to deal [21].

3.10 Titanium Nobium Archwires

Dr. Rohit Sachdev first presented it in early 1995. Ormco is the manufacturer. Although Ti-Nb is flexible and simple to work with, it has the same working range as stainless steel. It has a rigidity of 20% less than TMA and 70% less than stainless steel. Ti-Nb wire has a wider plastic range, comparable activation and deactivation curves, and a low spring back. It has a bending stiffness that is 48% less than stainless steel and a spring back that is 14% less than stainless steel. Can quickly bend a steel wire in unusual ways while avoiding excessive force levels [22].

3.11 Other Types of Archwires

Literature reveals several more significant archwire types. Australian archwires, Biotwist NiTi archwires, BioForce archwires, BioForce with ionguard archwires, Orthocosmetic elastinol archwires, Marsenol archwires, Nitanium tooth toned archwires, Nitinol complete control archwires, and various coated archwires are among the most well-known. The year of development is unclear, however these ground are extremely important to the researchers [23–30].

4 Conclusions

In the last few decades, a variety of new wires and alloys have entered into the field of orthodontics. These wires offer a broad range of mechanical properties and improved flexibility in orthodontic therapy. There may not be many new wires on the market for the physicians. This article gives an overview of several archwire features. It may be more useful to utilise the favourable features of a certain wire type chosen to meet the requirements of the patient. We can observe that a single type of archwire could not satisfy all the orthodonticist's needs. As time goes by, some of the alloys may lost their popularity in orthodontic applications, and eventually get replaced by other type of alloys with more favourable mechanical properties and functionality. Nevertheless, it is undeniable that these alloys have played an important role in the development and evolution of orthodontic archwire. To discover the "perfect" materials for archwire, we still have a long way to go. But since materials science and technology progresses so quickly, it is very likely that we will see substantial advancements in the archwires soon. The attention may be shifted from metals and alloys to polymers in the future, as the manufacturing and production of polymer archwires could be more cost-effective, and the polymers are capable to contribute to the aesthetic properties of archwire while having the similar properties with the metals and alloys.

References

1. Malik N, Dubey R, Kallury A, Chauksye A, Shrivastav T, Kapse BR (2015) A review of orthodontic archwires. J Orofacial Res 5:6–11
2. Berkhout JH, Ram AHN (2019) Recent advancements in spectrophotometric pka determinations: a review. Indian J Pharm Educ Res 53(4):S475–S480
3. Cardoso C, Quintão A, Helena I, Portella V (2009) Orthodontic wires: knowledge ensures clinical optimization. Dent Press J Orhtod 14(6):144–157
4. Kusy RP (2002) Orthodontic biomaterials: from the past to the present. Angle Orthod 72(6):501–512
5. Liaw YC, Su YYM, Lai YL, Lee SY (2007) Stiffness and frictional resistance of a superelastic nickel-titanium orthodontic wire with low-stress hysteresis. Am J Orthod Dentofac Orthop 131(5):12–18
6. Wilkinson PD, Dysart PS, Hood JAA, Herbison GP (2002) Load-deflection characteristics of superelastic nickel-titanium orthodontic wires. Am J Orthod Dentofac Orthop 121(5):483–495
7. Zhou HM, Shen Y, Zheng W, Li L, Zheng YF, Haapasalo M (2012) Mechanical properties of controlled memory and superelastic nickel-titanium wires used in the manufacture of rotary endodontic instruments. J Endod 38(11):1535–1540
8. Turpin DL (2010) American journal of orthodontics and dentofacial orthopedics: editor's comment. Am J Orthod Dentofac Orthop 137(5):578
9. Wang LM, Liu LH, Yang H, Wang LY, Xiu GQ (2002) Melting and fabrication of NiTi shape-memory alloy wires. Mater Sci Forum 394–395:297–300
10. de Oliveira LF, da Silva LH, Maeda FA, Triviño T (2020) Efeito de diferentes soluções ácidas na corrosão de Arcos Niti ou Aço. Odonto 26(52):27
11. Harini R, Kannan MS (2020) Orthodontic arch wires-a review. Eur J Mol Clin Med 7(8):1804–1810
12. Kusy RP (1997) A review of contemporary archwires: their properties and characteristics. Angle Orthod 67:197–208
13. Ingram SB, Gipe DP, Smith RJ (1986) Comparative range of orthodontic wires. Am J Orthod Dentofac Orthop 90(4):296–307
14. Pious N, Krishnan RV, Patni V, Mhatre A (2021) Review of superelastic archwires in orthodontics. Trends Biomater Artif Organs 35(1):91–94
15. J. D. E (1951) The American journal of orthodontics. Am J Orthodon Dentofac Orthop 37(7):534
16. Jacobson A (2001) Orthodontic materials: scientific and clinical aspects. Am J Orthod Dentofac Orthop 119(6):672–673
17. Bradley TG, Brantley WA, Culbertson BM (1996) Differential scanning calorimetry (DSC) analyses of superelastic and nonsuperelastic nickel-titanium orthodontic wires. Am J Orthod Dentofac Orthop 109(6):598–597
18. Donovan MT, Lin JJJ, Brantley WA, Conover JP (1984) Weldability of beta titanium arch wires. Am J Orthod Dentofac Orthop 85(3):207–216
19. Berger J (1997) Archwire hooks for the SPEED system. J Clin Orthod 31(6):354–357
20. Philip N, Sunny S, George LA, Antony P (2016) Newer orthodontic archwires: imparting efficacy to esthetics. Int J Oral Dent Health 2(2):102
21. Dalstra M, Melsen B (2004) Does the transition temperature of cu-niti archwires affect the amount of tooth movement during alignment? Orthod Craniofac Res 7(1):21–25

22. Buehler WJ, Gilfrich JV, Wiley RC (1963) Effect of low-temperature phase changes on the mechanical properties of alloys near composition TiNi. J Appl Phys 34(5):1475–1477
23. Miles PG (2005) SmartClip versus conventional twin brackets for initial alignment: is there a difference? Aust Orthod J 21(2):123–127
24. Nathani R, Daigavane P, Shrivastav S, Kamble R, Gupta D (2015) Esthetic arch wires—a review. Int J Adv Res 3(12):743–751
25. Tonner RIM, Waters NE (1994) The characteristics of super-elastic Ni-Ti wires in three-point bending. Part l: The effect of temperature. Eur J Orthod 16(5):409–419
26. Abdelrahman RS, Al-Nimri KS, Al Maaitah EF (2015) A clinical comparison of three aligning archwires in terms of alignment efficiency: a prospective clinical trial. Angle Orthod 85(3):434–439
27. Vimalathithan RR (2013) Is nickel titanium superior to multistranded stainless steel wire in aligning crowded lower anteriors? a comparative in-vivo study. IOSR J Dent Med Sci 9(3):47–51
28. West AE, Jones ML, Newcombe RG (1995) Multiflex versus superelastic: a randomized clinical trial of the tooth alignment ability of initial arch wires. Am J Orthod Dentofac Orthop 108(5):464–471
29. Sandhu SS, Shetty VS, Mogra S, Varghese J, Sandhu J, Sandhu JS (2012) Efficiency, behavior, and clinical properties of superelastic NiTi versus multistranded stainless steel wires a prospective clinical trial. Angle Orthod 82(5):915–921
30. Evans TJ, Jones ML, Newcombe RG (1998) Clinical comparison and performance perspective of three aligning arch wires. Am J Orthod Dentofac Orthop 114(1):32–39

Design and Analysis of Carbon Fiber Composite Chassis for Off-Road

A. Ridzuan Abd Hamid and J. J. Chong

Abstract Off-road buggy implemented with carbon fiber as a chassis material is proposed to replace conventional steel such as AISI 1018 carbon steel. This research aimed to design high strength and lighter off-road buggy chassis. Three concepts have been proposed, modelled in computer-aided design, and then compared using the Pugh method through impact analysis by determining the strength of chassis. The results are tabulated in the decision matrix and found out that Design 1 has attained the highest score. Design 1 achieved a score of 2.625, Design 2 is 0.803, and -3.318 for Design 3. A total of 13 samples consists of 12 carbon fiber composite and one carbon steel analysed through tensile simulation. The sample with ply orientation $[0/-30/60/90]_S$ achieved the highest tensile strength and three times compared to carbon steel. Furthermore, the analysis continued by simulating 12 ply orientations for every impact condition to select a set of orientations. The ply orientation is $[90/45/0/-45]_S$ for the front, $[0/-30/60/90]_S$ for the rear, $[45/-45/0/90]_S$ for the side, $[90/45/0/-45]_2$ for the top, and $[45/-45/0/90]_S$ for the bottom. The implemented chassis with carbon fiber composite compared with carbon steel. The investigation found carbon fiber composite is weaker and less stiff than carbon steel in an impact. Nevertheless, carbon fiber composite provides a significant mass reduction of 81.23% in chassis and 17.79% for overall chassis with components. Carbon fiber composite chassis offers excellent energy absorption compared to conventional steel, which is safer for drivers and passengers.

Keywords Carbon fiber · Off road buggy · Conceptual design · Pugh method · Ply orientation

A. R. Abd Hamid (✉) · J. J. Chong
Department of Mechanical Engineering, Faculty of Engineering, Technology and Built
Environment, UCSI University, 56000 Cheras, Kuala Lumpur, Malaysia
e-mail: amar@ucsiuniversity.edu.my

1 Introduction

The definition of carbon fiber classified as having carbon content with a minimum of 92 wt % and fiber have a content minimum of 99 wt %. The atoms in carbon fiber-connected in long-chain [1]. Carbon fiber has a diameter of about 5–10 microns and consists mainly of carbon atoms. Generally, carbon fiber has excellent resistance of temperature, high stiffness, and high tensile strength [2]. Carbon fiber has a lower density than steel, meanwhile at a higher strength than steel [3]. In a study on carbon fiber fabric, unidirectional fabric found nearly achieved more than twice the tensile strength of the woven fabric [4]. Most of the time, carbon fiber composite tube is using unidirectional fabric and woven fabric act as aesthetics purpose on the top layer. The epoxy resin used for the fabrication of carbon fiber composite provides mechanical strength by holding the fibers together [5]. The mechanical properties of resin can enhance through the change of resin matrix [6]. Besides, reinforcement of fiber such as polymer, metal, and plastic able to strengthen the properties [7]. The carbon fiber composite has characteristics of great strength-to-weight and stiffness-to-weight ratio [8]. Laminated carbon fiber composite is more vulnerable to damage such as tension, compression, tensile, and impact [9]. In laminated composite, the designed composite should always situate to load direction, which is parallel to fiber direction to avoid mechanical failure [10]. The increase of lamination thickness will cause a reduction in strength and stiffness [11]. The effect of the number of laminates in tensile strength is minor compared to the fiber orientation [7]. The increase of laminates improves the tensile modulus rather than strength [12]. The off-road vehicle is known to be any form of a vehicle capable of travelling up and down paved or gravel surfaces [13]. Off-road buggy, which is an off-road vehicle often physically described by having rigid chassis and pneumatic tires with flexible suspension [14]. The off-road buggy is commonly used steel as the chassis frame. The research project investigates the implementation of carbon fiber composite on the space frame chassis. The Carbon fiber is lighter than steel which able to reduce overall vehicle weight by 60% and improve fuel efficiency by 30% [15]. Chassis made of carbon fiber composite able to achieve high stiffness and rigidity [16]. The load transfer due to the weight able to affect the acceleration of a vehicle [17]. The acceleration defined as the change of velocity over time. Under the same force, the vehicle with lower mass resulted in higher acceleration [18]. The reduction of load transfer may improve the handling grip and acceleration as well as deceleration time [19]. Carbon fiber epoxy has an excellent energy absorption criterion which is approximate 250 and 20 kJ/kg for steel. The carbon fiber composite does not behave like steel in an impact which bent. The carbon fiber composite break when the exerted force is large [18]. The carbon fiber composite able to reduce the acceleration of a vehicle in an impact [20]. The research aims to design a chassis which is high strength and lightweight.

2 Methodology and Experimental Setup

2.1 Conceptual Design Selection

Three chassis designs are proposed, and the selection process is determined through Pugh method. A total of six criteria are calculated and to be analysed using CAE method. The six criteria are front impact, rear impact, side impact, roll over, torsional and centre of gravity [21]. The analysis in this section only studied the chassis. Hence, components mass is ignored. The calculation of force for front impact, rear impact, side impact, and roll over used Eqs. (1), (2), and (3) [22]. For roll over condition, velocity is calculated by using Eq. (4) due to free fall and torsional scenario load used in the Eq. (5) [23]. The centre of gravity (CG) height is determined in CAE and impact time taken as 0.1 s.

$$W = \left(0.5 \times M \times V_{final}^2 - 0.5 \times M \times V_{initial}^2\right) \tag{1}$$

$$s = t \times V_{maximum} \tag{2}$$

$$W = F \times s \tag{3}$$

$$M \times g \times h = 0.5 \times M \times V_{initial}^2 \tag{4}$$

$$G = M \times g \tag{5}$$

Pugh method result shows that Design 1 attained the highest score of 2.625 based on Table 1. Hence, Design 1 is selected.

Table 1 Pugh method result

Analysis	Design 1	Design 2	Design 3
Front impact	0.179	−1.179	1
Rear impact	−1.462	0.462	1
Side impact	1	0.205	−1.205
Roll over	0.908	1	−1.908
Torsional	1	−0.102	−0.898
CG height	1	0.417	−1.417
Total	2.625	0.803	−3.328

2.2 Material Selection

Carbon fiber composite of low tensile modulus is selected because 230 GPa tensile modulus is a common carbon fiber epoxy used in the research project. Higher tensile modulus can provide better material properties, especially in strength analysis, but the price is costly. Hence, 230 GPa tensile modulus carbon fiber epoxy is selected. The material for off-road buggy chassis in this research used two types of carbon fiber fabric which is unidirectional and woven. The woven is used on the top layer for an aesthetic purpose. Meanwhile, the bottom layer is unidirectional for better strength AISI 1018 carbon steel which is one of the conventional materials, is analysed to compare with carbon fiber composite. The material properties of carbon fiber epoxy of woven and unidirectional, which is required in CAE analysis are extracted from Ansys engineering data [24]. AISI 1018 carbon steel which is one of the conventional materials is selected, to compare with carbon fiber composite [25].

2.3 Tensile Simulation Method

The analysis of studying the material is carried out through the tensile simulation to measure the strength and stiffness of the material. The tensile simulation procedure is conducted through ASTM D3039 standard, which is designed for composite material [26]. The dimension and material parameters for tensile simulation is shown in Table 2. There are 13 samples for the analysis, which consist of 12 carbon fiber composite samples with different ply orientation and one carbon steel sample. The samples are listed in Tables 3 and 4.

Table 5 shown the simulation parameters for the tensile simulation sample. The simulation study on the normal stress and strain in the tensile direction [27]. The total deformation of the sample also being investigated [28]. The applied load and displacement data is used to determine the stiffness [29]. The total deformation from the simulation is known as displacement and stiffness able to determine the rigidity of a material. Equation (6) is used to calculate the stiffness follow by Eq. (7) to find out the average stiffness.

Table 2 Material parameters for tensile simulation sample

Material parameters
Ply material: Epoxy carbon unidirectional (230 GPa) prepreg
Epoxy carbon woven (230 GPa) prepreg
Ply thickness: 0.3 mm
Total woven thickness: 0.3 mm
Total unidirectional thickness: 2.1 mm

Table 3 Ply orientation sample of carbon fiber composite

Sample	Ply orientation
SP-1	[45/−45/0/90]₂
SP-2	[45/−45/0/90]ₛ
SP-3	[0/90/45/−45]₂
SP-4	[0/90/45/−45]ₛ
SP-5	[90/45/0/−45]₂
SP-6	[90/45/0/−45]ₛ
SP-7	[−45/0/45/90]₂
SP-8	[−45/0/45/90]ₛ
SP-9	[30/−30/0/60]₂
SP-10	[30/−30/0/60]ₛ
SP-11	[0/−30/60/90]₂
SP-12	[0/−30/60/90]ₛ

Table 4 Tensile simulation sample for carbon steel

Sample	Material
SP-13	Carbon steel

Table 5 Simulation parameters for tensile simulation sample

Simulation parameters
Fixed support: On top of the sample grip
Remote force: Varies from 10 kN, 20 kN, 30 kN, 40 kN, and 50 kN
Remote displacement: Free at X-axis direction

$$\text{Stiffness} = \frac{\text{Applied force}}{\text{Displacement}} \qquad (6)$$

$$\text{Average stiffness} = \frac{\Sigma\,\text{Stiffness}}{5} \qquad (7)$$

2.4 Structural Analysis Method

The structural analysis of chassis is initiated by simulating with all the orientation ply to study the strength and stiffness. The orientation is chosen based on the criteria of deformation, stress and strain for every analysis. An optimum set of orientation gathered from every analysis is combined to form a new group of orientation set that suitable for each part. On the other hand, the mass of components is determined by including the major components of an off-road buggy. The chassis mass in Table

Table 6 Chassis mass

Components	Chassis mass (kg)	Component mass (kg)	Total mass (kg)
Carbon fiber composite chassis	28.85	548	576.85
Carbon steel chassis	153.7	548	701.70

6 is the summation of mass for components and chassis. The weight of chassis is determined in Anasys. Hence, the applied load shown in are calculated by using Eqs. (1), (2), (3), (4), and (5).

3 Results and Discussion

3.1 Tensile Simulation

A comparison of tensile strength for 13 samples has shown in Fig. 1. Overall, ply orientation of SP-12 has the highest strength among 13 samples, which is 2943.7 MPa. The ply orientation of SP-12 is $[0/-30/60/90]_S$. The maximum strength achieved by SP-13 at 50 kN load is only 883.32 MPa. SP-12 has a strength three times more than SP-13. The histogram in Fig. 2 show SP-13, which is carbon steel have higher rigidity compared to other samples. This meaning to say SP-13 is most rigid because able
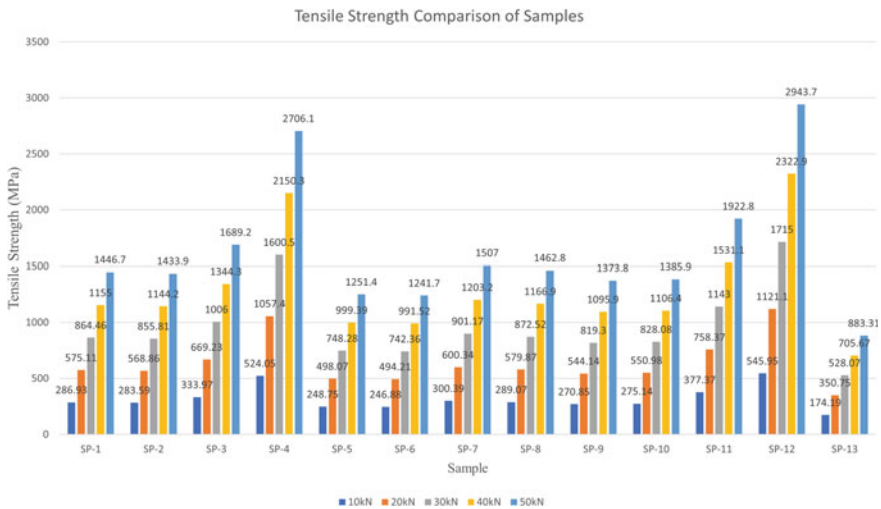
Fig. 1 Tensile strength comparison of samples
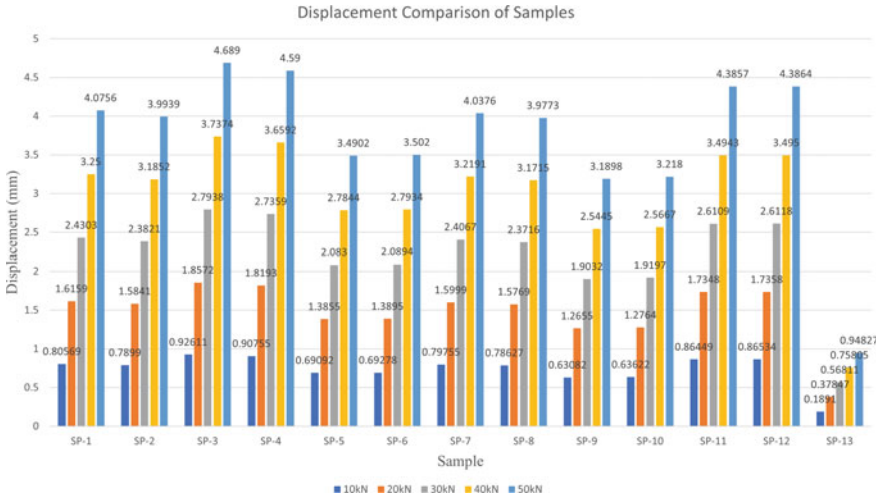
Fig. 2 Displacement comparison of samples

to resist the deformation when the load is applied. This show previous discussion is correct where the stiffness of the sample measures by the displacement. The sample with higher displacement has lower stiffness. According to SP-3, stiffness is the lowest, which is 10.7342 MN/m, as shown in Fig. 3. Meanwhile, SP-13 with the lowest displacement is the most rigid with a stiffness value of 52.8055 MN/m. This show that carbon steel sample is at least three times stiffer than carbon composite
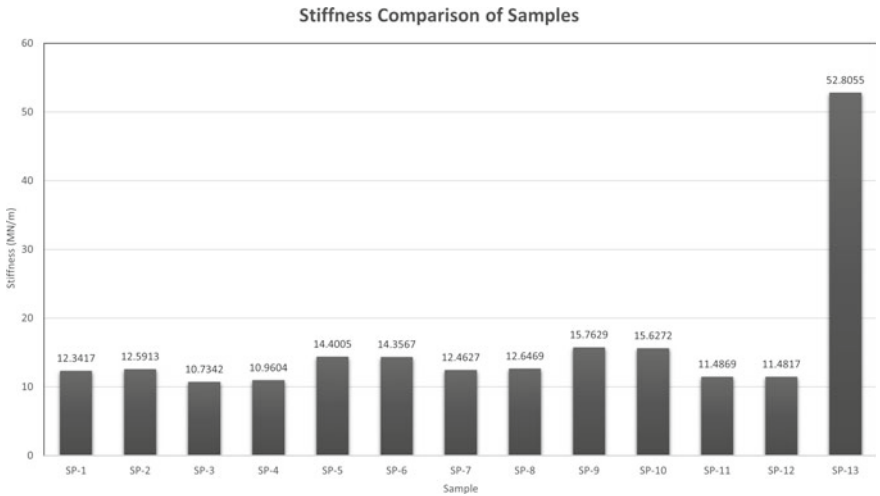
Fig. 3 Stiffness comparison of samples
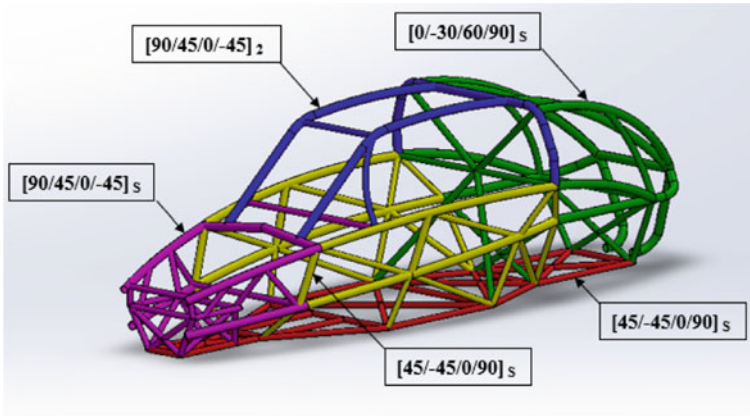
Fig. 4 Chassis ply orientation

samples. The analysis results proved that carbon fiber composite has high tensile strength but not in stiffness. The carbon steel is rigid than carbon fiber composite.

3.2 Ply Orientation Selection

Ply orientation selection was conducted by analysing the chassis in several conditions such as front impact, rear impact, side impact, roll over, and torsional. Ply orientation which has lowest exerted strength from the applied load, is selected. Figure 4 represents the selected ply orientation implemented into chassis.

3.3 Chassis Comparison Analysis

Table 7 shows tabulated maximum total deformation, equivalent stress and elastic strain which acquired from the impact analysis.

Table 8 shows the mass comparison of carbon fiber composite with carbon steel. Reduction of chassis mass can enhance performance and energy efficiency.

4 Conclusion

Off-road buggy implemented with carbon fiber composite as a chassis material found out to be a new study. At the end of this research, three proposed objectives have successfully met. Three designs proposed for the implementation of carbon fiber

Table 7 Simulation data comparison

Analysis	Material	Maximum total deformation (mm)	Maximum equivalent stress (MPa)	Maximum elastic strain (mm/mm)
Front impact	Carbon fiber composite	3.78420	245.47	0.00566030
	AISI 1018	0.88374	249.47	0.00135360
Rear impact	Carbon fiber composite	34.5610	909.56	0.01727700
	AISI 1018	6.83400	557.03	0.00292360
Side impact	Carbon fiber composite	7.01730	236.43	0.00612980
	AISI 1018	1.38870	190.89	0.00096194
Roll over	Carbon fiber composite	3.10230	136.10	0.00350660
	AISI 1018	0.61369	96.86	0.00053849
Torsional	Carbon fiber composite	19.6460	500.66	0.01384000
	AISI 1018	3.54600	428.47	0.00217500

Table 8 Mass comparison

Components	Carbon fiber composite (kg)	AISI 1018 carbon steel (kg)	Mass reduction percentage (%)
Chassis	28.85	153.7	81.23
Chassis with components	576.85	701.70	17.79

composite for off-road buggy chassis with CAD drawing. The three designs underwent thorough design selection with Pugh method to determine the strength of the chassis by analysed through CAE method. The highest strength design found to be Design 1, which achieved a score of 2.625, Design 2 is 0.803, and −3.318 for Design 3. Hence, Design 1 is selected. The observation found out that number of structural members, design, and geometry affect the strength of chassis. The study of carbon fiber composite and conventional material strength and stiffness are referred to ASTM D3039 method. The carbon fiber composite with different ply orientation analysed through a tensile simulation which mainly to study the strength and conventional material such as AISI 1018 carbon steel used for comparison. Despite the stiffness, carbon fiber composite has favourable strength aspect. The carbon fiber composite sample with the ply orientation $[0/-30/60/90]_S$ achieved the highest strength found out to be three times higher strength than carbon steel sample. Design 1 underwent multiple simulations to analyse and study the strength of chassis with 12 ply orientations. The analysis measures the strength of ply orientation from five analysis and

then, implemented into the chassis. Design 1 successfully implemented with four different ply orientations. Thorough simulation has conducted for every analysis to determine the strength and stiffness by observing the deformation, stress, and strain. The results compared with conventional material such as AISI 1018 carbon steel. The findings of the analysis found out carbon fiber composite chassis is weaker than carbon steel chassis. The carbon fiber composite has low strength due to the impact force is parallel to the fiber direction. The research also found out that carbon fiber composite chassis is less stiff than carbon steel chassis. Despite all the limitations, the benefits for the implementation of carbon fiber composite found out during the research. The weakness of impact strength has led to excellent energy absorption, which able to provide higher safety for passengers. On the other hand, an overall mass reduction of 81.23% of chassis mass and 17.79% which include the major components which able to improve acceleration performance. Not to forget, energy efficiency in terms of fuel consumption due to lightweight. The findings of the analysis can be understood as the implementation of carbon fiber composite to an off-road buggy chassis is not impact resistant. Whereas the lightweight criteria of carbon fiber composite chassis able to improve acceleration performance. The implementation of carbon fiber composite is mainly designed for lightweight and energy absorption purpose.

References

1. Johnson DJ (1990) Structure and properties of carbon fibers, 1st edn. Kluwer Academic Publishers, London, pp 43–72
2. Bhatt P, Goe A (2017) Carbon fibres: production, properties, and potential use. J Mater Sci Res 14(1):52–57
3. Liu Y, Kumar S (2012) Recent progress in fabrication structure, and properties of carbon fibers. Polym Rev 52(3):234–258
4. Eksi S, Genel K (2017) Comparison of mechanical properties of unidirectional and woven carbon, glass, and aramid fiber reinforced epoxy composites. Acta Phys Pol, A 132(3):879–882
5. Broughton WR, Koukoulas T, Woolliams P, Williams J, Rahatekar SS (2013) Assessment of nanoparticle loading and dispersion in polymeric materials using optical coherence tomography. Polym Test 32(7):1290–1298
6. Grosbras PL, Paluch B, Brieu M (2013) Characterization of free edge effects: influence of mechanical properties, microstructure, and effects. J Compos Mater 47(22):2823–2834
7. Kinloch AJ, Mohammed R, Taylor AC, Sprenger S, Egan D (2006) The interlaminar toughness of carbon-fibre reinforced plastic composites using 'hybrid-toughened' matrices. J Mater Sci 41(15):5043–5046
8. Rahmani H, Najafi SH, Ashori A (2014) Mechanical performance of epoxy/carbon fiber laminated composites. J Mech Manuf 33(8):733–740
9. Shokrieh M, Daneshvar A, Akbari S (2013) The use of carbon nanofibers for thermal residual stress reduction in carbon fiber/epoxy laminated composites. Carbon 59(1):255–263
10. Kaleemulla KM, Siddeswarappa B (2009) Influence of fiber orientation on the in-plane mechanical properties of laminated hybrid polymer composites. J Reinf Plast Compos 29(12):1900–1914
11. Zhang K, Gu Y, Li M, Zhang Z (2014) Effect of rapid curing process on the properties of carbon/ epoxy composite fabricated using vacuum assisted resin infusion molding. Mater Des 54(1):624–631

12. Shi F, Dong X (2011) 3D numerical simulation of filling and curing processes in non-isothermal RTM process cycle. Finite Elem Anal Des 47(7):764–770
13. Off-Road Vehicle Act (1985) New Brunswick acts and regulations. Attorney General, New Brunswick, Canada
14. Satinder S, Beant S (2014) Design, optimization, and statistical crash analysis of chassis frame for off road vehicle. Int J Automobile Eng Res Dev 4(6):7–12
15. Othman R, Ismail NI, Pahmi MAH, Basri HM, Sharudin H, Hemdi AR (2018) Application of carbon fiber reinforced plastics in automotive industry: a review. J Mech Manuf 1(1):144–152
16. Eurenius CA, Danielsson N, Khokar A, Krane E, Olofsson M, Wass J (2013) Analysis of composite chassis. Thesis. Sweden: Chalmers University of Technology
17. Milliken D, Milliken W (1995) Race car vehicle dynamic. Society of automotive engineers
18. Masilamani R, Dhandapani NV, Kumar KV, Mani KT (2017) A review on usage of carbon fiber reinforced plastics in automobiles. Int J Pure Appl Math 117(20):537–544
19. Crolla D, Deakin A, Hanley R, Ramirez J (2000) The effect of chassis stiffness on race car handling balance. SAE technical paper
20. Wang T, Li Y (2015) Design and analysis of automotive carbon fiber composite bumper beam based on finite element analysis. Adv Mech Eng 7(6):1–12
21. Mahonaran, Kailashnath (2013) Design and development of tubular space frame for BAJA. Germany: University of Siegen
22. Sati BK, Upreti P, Tripathi A, Batra S, and, (2016) Static and dynamics analysis of the roll cage for an all-terrain vehicle. Imp J Interdiscip Res 2(6):43–51
23. Patangray TN, Patil HD (2018) Static analysis of the roll cage of all-terrain vehicle. Int Res J Eng Technol 5(8):451–457
24. Ansys® Academic Research Material, Release 19.2, Ansys workbench, engineering data composites.
25. More A, Chavan C, Patil N, Ravi K (2017) Design, analysis, and optimization of space frame chassis. Int J Eng Technol 9(2):1411–1421
26. ASTM International (2000) ASTM D3039 / D3039M–00 - Standard test method for tensile properties of polymer matrix composite material. Annu Book ASTM Stand 15(3):105–116
27. Hamzah AF, Saad NA, Hamzah MS (2014) Numerical and experimental investigation for tensile properties of polyphenylene sulfide basis composite material. Project paper. Babylon University, Iraq
28. Vangala R, Devaiah M, Rajendar N, Raju K (2019) Comparison of mechanical properties for carbon, E-glass, and hybrid (carbon and E-glass) composites. Int J Mech Eng Technol 10(2):407–417
29. Nirbhay M, Dixit A, Mira RK, Mali HS (2014) Tensile test simulation of CFRP test specimen using finite elements. Int Conf Adv Manufact Mater Eng 5(1):267–273

Recent Progress on Titanium Dioxide-Based Humidity Sensor: Structural Modification, Doping, and Composite Approach

M. Z. Musa , **M. H. Mamat** , **N. Vasimalai** , **A. S. R. A. Subki** ,
H. Hassan , **M. F. Malek** , **M. Y. Ahmad, and M. Rusop**

Abstract Advancement to the performance of humidity sensor is an importance subject due to its diverse role in multitude of applications. The trend shows that researchers are using various approaches to tackle the performance issues of humidity sensor. This paper reviews recent progress on the improvement of titanium dioxide-based humidity sensor performance through structural modification, doping and composite effect. These three approaches have seen tremendous success in elevating the humidity sensing performance of titanium dioxide-based humidity sensor in term of higher sensitivity, shorter response/recovery time, and higher stability. The main advantages of the modified nanostructures are that they offer huge surface area which is beneficial for the adsorption of water molecules and directional pathway

M. Z. Musa · M. H. Mamat (✉) · A. S. R. A. Subki
NANO-Electronic Centre (NET), School of Electrical Engineering, College of Engineering, Universiti Teknologi MARA, 40450 Shah Alam, Selangor, Malaysia
e-mail: mhmamat@uitm.edu.my

M. H. Mamat · M. F. Malek · M. Rusop
NANO-SciTech Laboratory, Centre for Functional Materials and Nanotechnology, Institute of Science (IOS), Universiti Teknologi MARA, 40450 Shah Alam, Selangor, Malaysia

M. Z. Musa
Center for Electrical Engineering Studies, Universiti Teknologi MARA Cawangan Pulau Pinang, Permatang Pauh Campus, 13500 Permatang Pauh, Pulau Pinang, Malaysia

H. Hassan
Center for Chemical Engineering Studies, Universiti Teknologi MARA Cawangan Pulau Pinang, Permatang Pauh Campus, 13500 Permatang Pauh, Pulau Pinang, Malaysia

N. Vasimalai
Department of Chemistry, B.S. Abdur Rahman Crescent Institute of Science and Technology, Vandalur, Chennai 600 048, India

A. S. R. A. Subki
Faculty of Electrical and Electronic Engineering Technology, Universiti Teknikal Malaysia Melaka, Hang Tuah Jaya, 76100 Durian Tunggal, Melaka, Malaysia

M. Y. Ahmad
Nanorian Technologies Sdn Bhd, No. 40, Jalan Kajang Perdana 3/2, Taman Kajang Perdana, 43000 Kajang, Selangor, Malaysia

for the flow of charge carrier. Meanwhile, doping and formation of composite have contributed by having a positive synergistic effect in term of hydrophilicity, electrical conductivity, surface reactivity etc. In this work, efforts to improve the humidity sensing performance by various researchers working on this material are presented and discussed.

Keywords Humidity sensor · Titanium dioxide · Nanostructure · Doping

1 Introduction

The importance of metal oxide semiconductors is growing with each passing year. Materials such as ZnO, NiO, SnO, MgO etc. are constantly at the centre of research subject from researcher from all over the world. This is due to the advantageous properties of metal oxides namely their non-toxicity, high chemical stability, intrinsic high sensing characteristic, low cost, and their abundance in nature. These compounds are formed when the electron from metal element is released to the oxygen atom resulting in oxides with different bonds and electronic structures [1].

One such metal oxide is titanium dioxide (TiO_2) or titania. TiO_2 is semiconductor with bandgap energy of 3.0–3.2 eV [2]. Since the discovery of its photocatalytic capability in 1972 [3], interest in this compound continue to rise. Furthermore, in 1988, Gratzel et al. [4] have introduced a new type of solar cell which utilizes TiO_2 as the photoanode in dye-sensitized solar cell. Nowadays, TiO_2 have found its way in various type of application such as pollutant degradation photocatalyst [5], photochemical water splitting, UV photosensor [6], biosensors [7], and chemical sensors [8].

One of the important chemical sensors is the humidity sensor. It is a device which can detect the level of water molecules in the air. It is used in wide variety of fields such as home appliances, agricultural, weather forecasting, and health monitoring. In the light of recent advancement in Internet of Things (IoT) and fourth industrial revolution (IR 4.0), the trend of application is shifting toward interconnected sensors and wearable devices. Depending on the transduction mechanism, humidity sensor can be divided into several types namely resistive, capacitive, and optical [9]. Humidity is often expressed in term of relative humidity (RH). It can be defined as the ratio of the amount of water vapour present in the atmosphere to the maximum amount that the atmosphere can hold [10]. RH is usually stated in unit of percentage.

Experimental works and analyses are being carried out by numerous groups with the aim to promote the performance of TiO_2-based humidity sensor mainly in term of sensitivity, response/recovery time, hysteresis, linearity and stability with various degree of success. However, a comprehensive review on this subject remained scarce. Herein, recent progress on the TiO_2-based humidity sensor is presented and discussed. Emphasis is placed on efforts which were based on structural modification, doping process and composite formation with other materials.

2   Effect of Different Types of Nanostructures

It is widely considered that humidity sensing mechanism are largely influenced by the structural or the shape of the material [11]. Herein, various kind of structures and their effects to the performance of humidity sensor are discussed.

2.1   TiO$_2$ 1-D Nanostructure

1-D nanostructured material refers to a material with one of its dimensions is larger than the other two dimensions. These materials usually are associated a very high aspect ratio. Examples of these type of structure includes nanorods [12], nanowires, nanotubes, and nanofibers. This type of structure offers good carrier transport along its structural axis. The direct pathway of the movement of electron or hole enable faster response with high sensitivity.

Jyothilal et al. [13] have reported on the fabrication of humidity sensor using slanted TiO$_2$ nanorods produced using electron beam evaporation. They have achieved high sensitivity with fast response and recovery time of 145 and 120 ms respectively. It is suggested that the morphology has helped increase the carrier concentration leading to improved protonic conduction. Their sensor also showed promising potential as breath analyzer.

TiO$_2$ nanotube structure have been tested by Farahani et al. [14] as the humidity sensor. They have claimed that the structure is super-hydrophilic, allowing full absorption of water molecules. Their sensor recorded responsivity of 300%.

Meanwhile, Li et al. [15] have experimented with humidity sensor made of TiO$_2$ nanowires. Sensitivity of 280 pF/% RH was recorded at low RH (7% RH to 33% RH). It is supposed that the cross-linked nanowire structure improves charge conduction leading to the increase in sensitivity at low RH environment.

2.2   TiO$_2$ 2-D Nanostructure

2-D nanostructures are made of with thin layer structure. Nanosheet, nanowall, nanobelt, nanodisk, and nanoflakes are some of the examples of 2-D nanostructure. These types of structures were also being utilized to increase the performance of humidity sensor. For example, 2-D graphene [16, 17], NiO [18], WS$_2$ [19] and MoS$_2$ [20] have shown promising result as humidity sensor.

However, the use of TiO$_2$ 2-D structure for the application of humidity sensor remained scarce. One report on TiO$_2$ nanosheet-based ultrasensitive humidity sensor have been published by Gong et al. [21]. The ultrathin petal-like structure shortened transporting paths and increase contact area between sensing material and electrodes. The self-assembled TiO$_2$ nanosheet yielded a nanoporous structure with high specific

surface area. It is also argued that the ultrathin structure is rich with oxygen vacancy defect which is beneficial for humidity absorption. Up to 10 times improvement in sensitivity value was observed from the fabricated device.

2.3 TiO$_2$ 3-D Nanostructure

3-D nanostructures usually encompassed three categories which are 3-D spatial ensembles of 1-D or 2-D nanostructure, 3-D nanoporous structures and 3-D hierarchical nanostructured materials [22]. Examples of this type of structure are nanoflower [23], nanoball, nanocube and interconnected pores. They are usually credited as having the largest surface area. Zhang et al. [24] reported on the quartz crystal microbalance (QCM) type humidity sensor using hollow ball, nanosphere and nanoflower TiO$_2$. The hollow ball structure which has the largest surface area showed the highest sensitivity of 33.8 Hz/%RH.

Similar nanoflower structure was also reported by Jeong et al. [25] who have fabricated resistive type humidity sensor with sensitivity of 485.7 RH%$^{-1}$. Urchinlike structure have been reported by Wang et al. [26]. Figure 1 shows the examples of different types of TiO$_2$ nanostructures, and Table 1 gives a summary of TiO$_2$ nanostructure-based humidity sensor.
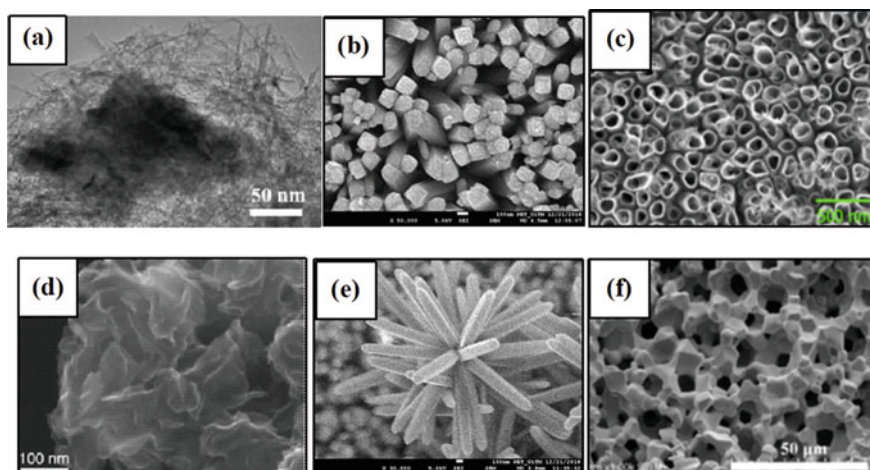

Fig. 1 Examples of different types of TiO$_2$ nanostructures: **a** TiO$_2$ nanowire, **b** TiO$_2$ nanorod, **c** TiO$_2$ nanotubes, **d** TiO$_2$ nanosheet, **e** TiO$_2$ nanoflower, **f** TiO$_2$ interconnected pores. Reproduced with permission from [15, 21, 27, 28]

**Table 1** Summary of TiO_2 nanostructure-based humidity sensor

Structure type	Structure	Preparation method	Sensor type	Sensor performance	References
1-D	Nanorods	Electron beam evaporation	Resistive	Response time 145 ms Recovery time 210 ms	[13]
	Nanotubes	Anodization	Voltage	Sensitivity 300	[14]
	Nanowires	Alkali oxidation	Impedance	Sensitivity 280 pF/% RH	[15]
2-D	Nanosheet	Surfactant self-assembly	Impedance	Sensitivity 4-order of magnitude	[21]
3-D	Interconnected pores	Emulsion template	Impedance	Sensitivity 4-order of magnitude	[28]
	Nanoflower	Solution immersion	Resistive	Sensitivity 196	[29]
	Nanoflower	Hydrothermal and gravure printing	Resistive	Sensitivity 485.7 RH%$^{-1}$	[25]

3 Effect of Doping

Doping is the act of adding specific amount of impurity into a host material in order to improve its properties. In the case of TiO_2, the doping could be divided into metal and non-metal doping. Dopant properties such as atomic radius and electronegativity would influence the effectiveness of a doping process [30].

3.1 Metal Doping

Li et al. [31] reported on the doping of niobium (Nb) into TiO_2. The pentavalent Nb^{5+} ion is a donor and will donate electron based on the following equation:

$$Nb_2O_5 \xrightarrow{2TiO_2} 2Nb_{Ti}^{\cdot} + 4O_o + 1/2O_2 + 2e'$$
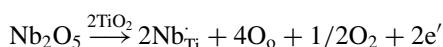
This type of reaction would increase the electron concentration of TiO_2. Since electron conduction is responsible for the humidity detection mechanism, this has resulted in improved sensitivity of up to 13,705 pF/%RH in a capacitive-type humidity sensor.

Quartz crystal microbalance (QCM)-type humidity sensor made of Ru-doped TiO_2 nanofiber have been reported by Farzaneh et al. [32]. Using density functional

Table 2 Summary of doping effect on TiO$_2$-based humidity sensor

Dopant type	Dopant	Sensor type	Sensor performance	References
Metal	Nb	Capacitive	13,705 pF/%RH	[31]
	Ru	QCM	Four times more sensitive than undoped TiO$_2$	[32]
	Co	Resistive	Sensitivity five orders of magnitude	[33]
Non-metal	N	Resistive	Sensitivity five orders of magnitude	[34]
	GO	Optical	0.47 dB/%RH	[35]

theory (DFT) calculation, they have managed to show that the Ru-doped TiO$_2$ have significantly larger surface reactivity compared to undoped TiO$_2$. This have helped increase the water absorption ability, leading to the increase in sensitivity.

Meanwhile, Li et al. [33] presented Co as the dopant for TiO$_2$ for the application of resistive-type humidity sensor. Substitution of Ti^{4+} with Co^{2+} creates many defect sites and reduces the grain size, effectively increasing the humidity sensing performance.

3.2 Non-metal Doping

Humidity sensing properties could also be improved by doping with non-metal elements. Li et. al. [34] has reported on the N doping of ordered mesoporous TiO$_2$. Through XPS analysis, the resulting material showed the presence of Ti^{3+} defect sites. The defect sites would react with water molecules, releasing additional electron to the structure which would improve the sensitivity.

The sensitivity of optical-type humidity sensor could also be increased through non-metal doping as demonstrated by Ghadiry et al. [35] who added graphene oxide (GO) in TiO$_2$ solution which were then drop-casted on waveguides. GO helps in the diffusion of water molecules which bring significant changes to the refractive index. Table 2 shows the summary of doping effect on TiO$_2$-based humidity sensor.

4 Effect of Composite

Another approach to improve the performance of humidity sensor is through the formation of TiO$_2$ composite. Since it is quite challenging to simultaneously produce all the desired properties in a single material, synthesis of composite material has been gaining considerable attention [36]. Among the composite types which are commonly used are layered, core–shell, random mixture, and decoration structure. Composite materials are interesting as they often exhibit improved physical and chemical properties compare to each of the material alone.

Table 3 Summary of TiO$_2$ composite-based humidity sensor

Composite	Sensor type	Sensor performance	References
TiO$_2$/ZnO	Impedance	Sensitivity 0.4 orders of magnitude	[37]
TiO$_2$/VOPcPhO	Capacitive	Better sensitivity, lower hysteresis and reduced absolute threshold value	[41]
TiO$_2$/PVDF	Capacitive	Response time 45 s, recovery time 11 s	[39]
TiO$_2$/PLA	Capacitive	Response time 40 s, recovery time 20 s	[42]
CoTiO$_3$/TiO$_2$	Resistive	Sensitivity 157.23	[11]
TiO$_2$/NaNbO$_3$	Resistive	Sensitivity 125,512	[36]

Araujo et al. [37] have reported on the TiO$_2$/ZnO composite-based humidity sensor. Their result showed improved performance in term of increased sensitivity. Both metal oxides complimented each other properties. TiO$_2$ compensated the low hydrophilicity of ZnO while ZnO nanostructure improve the overall surface area of the sensor. TiO$_2$ naturally have high hydrophilicity because of the presence of Ti^{3+}/Ti^{4+} interface sites which is associated with dissociative transfer of water molecules [38].

Polymer is another material capable of forming beneficial composite with TiO$_2$. Mallick et al. [39] formed TiO$_2$ composite with polyvinylidene fluoride (PVDF) for the application of humidity sensor. They reported that the addition of TiO$_2$ increases the hydrophilicity of the sensor. Moisture absorption and settling were reported to increase at a more hydrophilic surface, leading to increase in the sensitivity of capacitive humidity sensors [40].

Some researcher worked with TiO$_2$ and organic-inorganic hybrid nano-composites, VOPcPhO [41]. Formation of this composite helped produced uniform voids across the surface of the material which are favourable for the absorption of moisture content. These voids also increase the surface porosity as evidenced through atomic force microscopy (AFM) result.

Adding a p-type semiconductor to n-type TiO$_2$ could form heterojunction structure as shown by Lu et al. [11]. Carrier transportation could be increased significantly through the decrease of electron current path at the heterogenous interface. Si et al. [36] reported a similar result when using TiO$_2$/NaNbO$_3$ nanocomposite. In their work, detection of humidity was achieved through the reduction of potential barrier height of the heterojunction due to the transfer of electrons from NaNbO$_3$ to TiO$_2$ upon exposure to moisture. Table 3 shows the summary of TiO$_2$ composite-based humidity sensor.

5 Conclusion

A review on the recent progress of the development of TiO$_2$-based humidity sensor have been presented. Engineering the shape of TiO$_2$ nanostructures into 1-D, 2-D

and 3-D could bring advantageous properties to the performance of humidity sensor. In addition, doping process and formation of composite have also been shown to contribute to the increased performance of humidity sensor. Clearly TiO_2 have a very good potential to become a very efficient humidity sensing material thanks to the commendable effort by researcher on this subject. However, there are still gaps to be explored to further improve the performance of the device.

References

1. Victor NS, Leão ESA (2019) Metal oxide heteronanostructures prepared by electrospinning for the humidity detection: fundamentals and perspectives. J Mater Sci Chem Eng 7:43–54
2. Kalb J, Folger A, Zimmermann E, Gerigk M, Trepka B, Scheu C, Polarz S, Schmidt-Mende L (2019) Controlling the density of hydrothermally grown rutile TiO_2 nanorods on anatase TiO_2 films. Surf Interfaces
3. Fujishima A, Honda K (1972) Electrochemical photolysis of water at a semiconductor electrode. Nature 238(5358):37–38
4. O'Regan B, Grätzel M (1991) A low-cost, high-efficiency solar cell based on dye-sensitized colloidal TiO_2 films. Nature 353(6346):737–740
5. Tayel A, Ramadan AR, El Seoud OA (2018) Titanium dioxide/graphene and titanium dioxide/graphene oxide nanocomposites: synthesis, characterization and photocatalytic applications for water decontamination. Catalysts 8(11)
6. Yusoff MM, Mamat MH, Abdullah MAR, Ismail AS, Malek MF, Zoolfakar AS, Al Junid SAM, Suriani AB, Mohamed A, Ahmad MK, Shameem Banu IB, Rusop M (2020) Coupling heterostructure of thickness-controlled nickel oxide nanosheets layer and titanium dioxide nanorod arrays via immersion route for self-powered solid-state ultraviolet photosensor applications. Measurement 149:106982
7. Shetti NP, Bukkitgar SD, Reddy KR, Reddy CV, Aminabhavi TM (2019) Nanostructured titanium oxide hybrids-based electrochemical biosensors for healthcare applications. Colloids Surf B 178:385–394
8. Barreca D, Carraro G, Comini E, Gasparotto A, Maccato C, Sada C, Sberveglieri G, Tondello E (2011) Novel synthesis and gas sensing performances of CuO–TiO_2 nanocomposites functionalized with Au nanoparticles. J Phys Chem C 115(21):10510–10517
9. Yusoff SFAZ, Lim CS, Azzuhri SR, Ahmad H, Zakaria R (2018) Studies of Ag/TiO_2 plasmonics structures integrated in side polished optical fiber used as humidity sensor. Results Phys 10:308–316
10. Blank TA, Eksperiandova LP, Belikov KN (2016) Recent trends of ceramic humidity sensors development: a review. Sens Actuators B Chem 228:416–442
11. Lu J, Liang K, Xu C, Wang X, Haibo O, Huang J, Feng L (2019) Humidity sensor based on heterogeneous $CoTiO_3$/TiO_2 film with vertically aligned nanocrystalline structure. Vacuum 163:292–300
12. Musa M, Mamat MH, Othman MA, Shameem IB, Vasimalai N, Malek MF, Rusop M (2020) Enhanced sensitivity of humidity sensor prepared using vertically aligned v-doped TiO_2 nanorods array. J Electr Electron Syst Res 17:68–73
13. Jyothilal, Shukla G, Walia S, Kundu S, Angappane S (2020) Humidity sensing and breath analyzing applications of TiO_2 slanted nanorod arrays. Sens Actuators A Phys 301:111758
14. Farahani E, Mohammadpour R (2020) Fabrication of flexible self-powered humidity sensor based on super-hydrophilic titanium oxide nanotube arrays. Sci Rep 10(1):13032
15. Li N, Jiang Y, Zhou C, Xiao Y, Meng B, Wang Z, Huang D, Xing C, Peng Z (2019) High-performance humidity sensor based on urchin-like composite of Ti_3C_2 MXene-derived TiO_2 nanowires. ACS Appl Mater Interfaces 11(41):38116–38125

16. Saqib M, Khan SA, Ur Rehman, HMM, Yang Y, Kim S, Rehman MM, Kim WY (2021) High-performance humidity sensor based on the graphene flower/zinc oxide composite. Nanomaterials (Basel) 11(1)
17. Hassan G, Sajid M, Choi C (2019) Highly sensitive and full range detectable humidity sensor using PEDOT: PSS, methyl red and graphene oxide materials. Sci Rep 9(1):15227
18. Parimon N, Mamat MH, Shameem Banu IB, Vasimalai N, Ahmad MK, Suriani AB, Mohamed A, Rusop M (2020) Fabrication, structural, optical, electrical, and humidity sensing characteristics of hierarchical NiO nanosheet/nanoball-flower-like structure films. J Mater Sci Mater Electron 31(14):11673–11687
19. Dwiputra MA, Fadhila F, Imawan C, Fauzia V (2020) The enhanced performance of capacitive-type humidity sensors based on ZnO nanorods/WS$_2$ nanosheets heterostructure. Sens Actuators B Chem 310:127810
20. Ze L, Yueqiu G, Xujun L, Yong Z (2017) MoS$_2$-modified ZnO quantum dots nanocomposite: synthesis and ultrafast humidity response. Appl Surf Sci 330–336
21. Gong M, Li Y, Guo Y, Lv X, Dou X (2018) 2D TiO$_2$ nanosheets for ultrasensitive humidity sensing application benefited by abundant surface oxygen vacancy defects. Sens Actuators B Chem 262:350–358
22. Zhao H, Lei Y (2020) 3D nanostructures for the next generation of high-performance nanodevices for electrochemical energy conversion and storage. Adv Energy Mater 10(28):2001460
23. Musa MZ, Mamat MH, Vasimalai N, Shameem Banu IB, Parimon N, Hassan H, Malek MF, Rusop M (2021) Humidity sensing performance of V: TiO$_2$ 3D nanostructure-based humidity sensor. IOP Conf Ser Earth Environ Sci 682(1):012073
24. Zhang D, Chen H, Li P, Wang D, Yang Z (2019) Humidity sensing properties of metal organic framework-derived hollow ball-like TiO$_2$ coated QCM sensor. IEEE Sens J 19(8):2909–2915
25. Jeong H, Noh Y, Lee D (2019) Highly stable and sensitive resistive flexible humidity sensors by means of roll-to-roll printed electrodes and flower-like TiO$_2$ nanostructures. Ceram Int 45(1):985–992
26. Wang Z, Xiao Y, Cui X, Cheng P, Wang B, Gao Y, Li X, Yang T, Zhang T, Lu G (2014) Humidity-sensing properties of urchinlike CuO nanostructures modified by reduced graphene oxide. ACS Appl Mater Interfaces 6(6):3888–3895
27. Bindra P, Hazra A (2019) Selective detection of organic vapors using TiO$_2$ nanotubes based single sensor at room temperature. Sens Actuators B Chem
28. Wang X, Li J, Li Y, Liu L, Guan W (2016) Emulsion-templated fully three-dimensional interconnected porous titania ceramics with excellent humidity sensing properties. Sens Actuators B Chem 237:894–898
29. Musa MZ, Mamat MH, Vasimalai N, Shameem Banu IB, Malek MF, Ahmad MK, Suriani AB, Mohamed A, Rusop M (2020) Fabrication and structural properties of flower-like TiO$_2$ nanorod array films grown on glass substrate without FTO layer. Mater Lett 273:127902
30. Umar AA, Saad SKM, Umar MIA, Rahman MYA, Oyama M (2018) Advances in porous and high-energy (001)-faceted anatase TiO$_2$ nanostructures. Opt Mater 75:390–430
31. Li TY, Si R, Sun J, Wang S, Wang J, Ahmed R, Zhu G, Wang C (2019) Giant and controllable humidity sensitivity achieved in (Na+Nb) co-doped rutile TiO$_2$. Sens Actuators B Chem 293:151–158
32. Farzaneh A, Esrafili MD, Mermer Ö (2020) Development of TiO$_2$ nanofibers based semiconducting humidity sensor: adsorption kinetics and DFT computations. Mater Chem Phys 239:121981
33. Li Z, Haidry AA, Gao B, Wang T, Yao Z (2017) The effect of co-doping on the humidity sensing properties of ordered mesoporous TiO$_2$. Appl Surf Sci 412:638–647
34. Li Z, Haidry AA, Dong B, Sun L, Fatima Q, Xie L, Yao Z (2018) Facile synthesis of nitrogen doped ordered mesoporous TiO$_2$ with improved humidity sensing properties. J Alloy Compd 742:814–821
35. Ghadiry M, Gholami M, Lai CK, Ahmad H, Chong WY (2016) Ultra-sensitive humidity sensor based on optical properties of graphene oxide and nano-anatase TiO$_2$. PLoS ONE 11(4):e0153949

36. Si R, Xie X, Li T, Zheng J, Cheng C, Wang C (2020) TiO_2/$NaNbO_3$ heterojunction for boosted humidity sensing ability. Sens Actuators B Chem 309:127803
37. Araújo ES, Libardi J, Faia PM, Oliveira HPD (2017) Humidity-sensing properties of hierarchical TiO_2:ZnO composite grown on electrospun fibers. J Mater Sci Mater Electron 28(21):16575–16583
38. Poonia E, Mishra PK, Kiran V, Sangwan J, Kumar R, Rai PK, Tomer VK (2018) Aero-gel assisted synthesis of anatase TiO_2 nanoparticles for humidity sensing application. Dalton Trans 47(18):6293–6298
39. Mallick S, Ahmad Z, Touati F, Shakoor RA (2019) Improvement of humidity sensing properties of PVDF-TiO_2 nanocomposite films using acetone etching. Sens Actuators B Chem 288:408–413
40. Najeeb MA, Ahmad Z, Shakoor RA (2018) Organic thin-film capacitive and resistive humidity sensors: a focus review. Adv Mater Interfaces 5(21):1800969
41. Azmer MI, Aziz F, Ahmad Z, Raza E, Najeeb MA, Fatima N, Bawazeer TM, Alsoufi MS, Shakoor RA, Sulaiman K (2017) Compositional engineering of VOPcPhO-TiO_2 nanocomposite to reduce the absolute threshold value of humidity sensors. Talanta 174:279–284
42. Mallick S, Ahmad Z, Touti F, Bhadra J, Shakoor SA, Al-Thani NJ (2018) PLA-TiO_2 nanocomposites: thermal, morphological, structural, and humidity sensing properties. Ceram Int 44(14):16507–16513

Integration of Analytic Hierarchy Process Technique and Knowledge-Based System to Prioritize Essential Critical Risk Factors Using the Web-Based Approach

Fazilah Abdul Aziz, Nik Mohd Zuki Nik Mohamed, and Ahmad Nasser Mohd Rose

Abstract Web-based expert systems have proved an exceptional tool for creating intelligent decision-making systems based on experts' knowledge and opinions. This work presents an approach for assessing ergonomics risk factors based on integrating the analytic hierarchy process (AHP) method and knowledge-based system (KBS) using a web-based interface approach. A web-based ergonomics assessment system (W-BEAS) was developed and validated by comparing the assessment results using the existing method risk priority number (RPN). Physical, psychosocial, individual and organizational ergonomics are the four critical factors prioritized by the W-BEAS. Arrangements of priority weight and rank position obtained by W-BEAS and RPN provided reasonable evidence of validity for prioritizing the critical risk factors. Validation results prove that the W-BEAS can produce outcomes relative to the current ergonomics assessment approach. W-BEAS is capable of assessing complex ergonomics risk factors and continuing to support better workplace ergonomics. In addition, the W-BEAS employs a macro-ergonomics approach to evaluate the multi-factorial risk related to WMSD. Through W-BEAS, workers can share their knowledge and concern with the system to prioritise critical risk factors more accurately. A field study was conducted using for the first time an integrated web-based system as an intervention tool in assessing workplace ergonomics risk. Workers used it independently without personal expert training. Results indicated that workers could evaluate their workplace hazards anywhere and anytime.

Keywords Work related musculoskeletal disorders (WMSD) · Ergonomics risk factor · Analytical hierarchy process (AHP) · Knowledge-based system (KBS) · Web-based expert system (WBES)

F. Abdul Aziz (✉)
Faculty of Manufacturing and Mechatronics Engineering Technology, Universiti Malaysia Pahang, 26600 Pekan, Pahang, Malaysia
e-mail: fazilahaa@ump.edu.my

F. Abdul Aziz · N. M. Z. Nik Mohamed · A. N. Mohd Rose
Mechanical Engineering Department, College of Engineering, Universiti Malaysia Pahang, 26300 Kuantan, Pahang, Malaysia

1 Introduction

Any company intending to compete entirely in their respective industries should prioritize employee wellness [1, 2]. The workplace has a direct impact on employee health. The productivity and efficiency of work organizations have an impact on employee wellness as well. Because of the critical role of humans in industry, these facts demonstrate that workplace ergonomics plays an essential part in long-term sustainability. Workplace ergonomics, linked to safety and health concerns, demand an organizational strategic direction to attain long-term viability [3]. Furthermore, a better working environment for workers is linked to long-term development [4]. Workers will be endangered by work-related musculoskeletal diseases (WMSDs) if their physical abilities do not match the job's physical requirements due to inadequate workplace ergonomics. WMSDs are painful muscle, tendon, and nerve disorders. Because of their widespread use and detrimental impact on job productivity, WMSDs have resulted in economic losses worldwide [5]. As a result, holistic systems and strategies linking workplace ergonomics management to long-term organisation growth are required.

The importance of researching workplace ergonomics risk factors and creating musculoskeletal disorders (MSD) prevention techniques has grown. The MSD hazard and risk factors can be decreased early in developing a new product and process employing risk management in the organization [6]. In addition, the majority of MSD disorders are caused by a combination of risk factors [7]. To recognise critical risks and eliminate crucial risk factors, occupational safety and health (OSH) practitioners need a decision instrument that includes a systematic, participative ergonomics and risk-based method. As a result, this study employs a systematic approach using the analytic hierarchy process (AHP), one of the multi-criteria decision analysis techniques (MCDA), in a decision-making aid for multi-factorial investigations. The AHP is a structured approach based on mathematics and psychology for preparation and analysing complex decisions. AHP also is an effective and powerful technique for decision making [8]. Moreover, AHP can measure and synthesise many criteria [9] and helpful in complex issues [10].

In the ergonomics field, knowledge-based systems (KBS) have been used in a variety of ways. KBS is a software program that generates and employs a knowledge base to undertake complicated issues. KBS can collaborate with or take the place of human experts in workplace ergonomics assessments [11]. KBS, or computer-based information systems, can represent expert knowledge. KBS can achieve the level of skill required to resolve workplace hazard situations at an expert level [12]. Moreover, using KBS in ergonomics assessments can help workers rapidly and properly discard various risk concerns [13]. Employees and employers must have ergonomic knowledge and be informed of workplace ergonomics assessments to avoid the risk. Hence, KBS is critical in promoting proactive ergonomics to improve an organization's long-term sustainability in work activities, workplaces, and working environments.

Table 1 The AHP uses a pair-by-pair comparison scale

Importance intensity	Score	Meaning	Description
1	1	Equally vital	Two elements influence the property in equal measure
2	3	The importance of one over the other is moderate	One has a minor advantage over the other based on experience and judgment
3	5	Importance is essential or significant	Experience and judgement vastly prefer one over the other
4	7	The significance is enormous	An element is heavily favoured, and its domination may be seen in action
5	9	Extremely vital	One of the most significant levels of affirmation is evidence that favours one element over another
Reciprocals		When one of the numbers mentioned above is chosen for the activity i opposed to j; the activity j analysed to I is set to its inverse	
Ratio		Rates resulting from requiring constancy in decisions	

Adapted from Saaty [8]

Many academics have worked on KBS to evaluate the ergonomic risk associated with WMSD [14–16]. Most KBSs for ergonomics assessments operate on a stand-alone mode that performs its function without a network link. Consequently, this study combines the AHP approach, KBS, and a web-server application to construct a web-based ergonomics assessment system (W-BEAS). Web-based apps are applications that use a web browser to communicate with a remote server. W-BEAS is a computer software tool that uses the internet to imitate ergonomics experts' critical thinking abilities.

This study, which contributes to the ergonomics risk assessment literature and practice, demonstrates the use of a W-BEAS in deciding the essential workplace risk factors connected to WMSD.

2 AHP and KBS are Integrated to Create a W-BEAS

2.1 AHP Technique for Critical Risk Factor Prioritization

Workplace risk factors connected to physical, organizational, and psychosocial components have been linked to WMSDs, which reduce workers' wellness and well-being [2, 17–19]. A macro-ergonomic assessment approach includes individual (IF), organizational (OF), physical (PhyF), and psychosocial (PsyF) variables to assess the critical WMSD risk factors. There are four primary factors and 26 sub-factors in the AHP (refer to Fig. 1 and Table 3). Figure 1 describes the formation of the

Table 2 W-BEAS validation members' demographic information

Demographic dimension		Freq.	%
Working time	Normal	3	15
	Shift	17	85
Working position	Supervisor	13	65
	Executive	3	15
	Engineer	3	15
	Assistant manager	0	0
	Manager	1	5
Working department	Production assembly	5	25
	Production stamping	4	20
	Engineering	4	20
	Safety, health, and environment	3	15
	Logistics	4	20
	Shift	17	85
Working experience (years)	11–15	2	10
	16–20	18	90
	> 20	0	0
	Shift	17	85
Education level	SPM	12	60
	Certificate	2	10
	Diploma	5	25
	Degree	1	5
Age (years)	25–34	0	0
	35–44	14	70
	45–55	6	30
Gender	Male	20	100
	Female	0	0

AHP. Procedures to detecting ergonomic risk factors and sub-factors and a pairwise comparison to determine priority weight are included in the AHP structure.

The AHP model includes procedures for identifying ergonomic risk factors and sub-factors and a pairwise comparison to determine weight. The AHP process included the following steps:

1. Designing a decision form and conducting pair-wise comparisons, users were required to determine the significance of risk factors between certain ergonomic factors and sub-factors. Table 1 presents a mathematical scale for pairwise comparisons. This method included the formation of the square matrix $A_{n \times n}$. Equation 1 represents the $A_{n \times n}$.
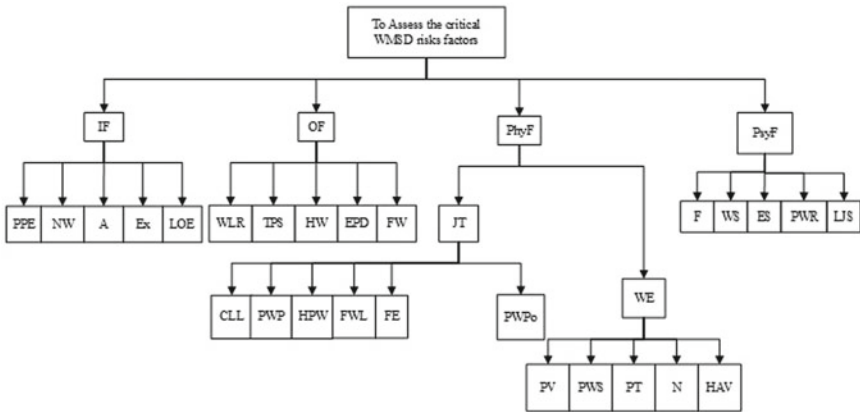
Fig. 1 The hierarchy for critical risk factors correlated to WMSD

$$A_{n \times n} = \left[a_{11}a_{21}a_{12}a_{22} \cdots a_{1n}a_{2n} \vdots \ddots \vdots a_{n1}a_{n2} \cdots a_{nn} \right] \tag{1}$$

where a_{ij} was the factor in the pair-wise comparison matrix. It delivered the comparative importance of criterion i concerning criterion j. Matrix $A_{n \times n}$, $a_{ij} = 1$ when $i = j$ and $a_{ij} = \frac{1}{a_{ij}}$ when $i \neq j$.

2. Combining the results. The method outputs a vector of local weights or priorities for every risk factor based on the overall goal. The Geometric mean (GM_i) was used to calculate the aggregate expert judgments.

$$GM_i = \left[\prod_j^n a_{ij} \right]^{\frac{1}{n}}, \tag{2}$$

where $n =$ number of members.

3. Determining the local weights. The Eqs. (3) and (4) can define the principal Eigenvector and Eigenvalues individually.

$$w_i = \frac{GM_i}{\sum_{i=1}^n GM_i}, \tag{3}$$

$$\lambda_{\max} = \frac{\sum_i^n w_i}{n}, \tag{4}$$

where $n =$ number of factors.

4. Confirming the pair-wise comparison's consistency. Equations (5)–(7) can be used to describe the consistency index (CI) and consistency ratio (CR).

Table 3a and b The RPN technique and the W-BEAS prioritized risk factors are compared

Ergonomic risk factors	W-BEAS		RPN	
	Priority Weight (%)	Ranking	Priority Weight (%)	Ranking
(a)				
Individual				
Negligence of workers (NW)	21	2nd	22	2nd
Improper use of personal protective equipment (PPE)	13	4th	16	4th
Level of education (LOE)	45	1st	29	1st
Working experience (Ex)	17	3rd	22	2nd
Age (A)	4	5th	11	5th
Total	100		100	
Organisational				
High workload (HW)	17	2nd	22	2nd
Worker lack of rest (WLR)	10	4th	16	4th
Frequent workdays (FW)	9	5th	11	5th
Exposure to physical demands (EPD)	50	1st	29	1st
Tight production schedule (TPS)	14	3rd	22	2nd
Total	100		100	
Physical-Job task factors				
Work that requires a lot of lifting (FWL)	8	6th	13	5th
Lifting and carrying (CCL)	15	3rd	15	3rd
Working conditions are poor (PWPr)	10	5th	10	6th
Work that is physically demanding (HPW)	14	4th	15	3rd
Effort put forth in a job assignment with a lot of force (FE)	28	1st	27	1st
Working posture is poor (PWPo)	25	2nd	20	2nd
Total	100		100	
(b)				
Physical-workplace and equipment				
Insufficient ventilation in the workplace (PV)	7	5th	12	5th
Inadequate working conditions (PWS)	23	2nd	24	2nd
In the workplace, the temperature is too hot (PT)	16	3rd	18	3rd
Noise in working environment (N)	14	4th	16	4th
Hand arm vibration (HAV)	39	1st	31	1st
Total	100		100	
Psychosocial				
Fatigue (F)	15	4th	16	4th

(continued)

Table 3a and b (continued)

Ergonomic risk factors	W-BEAS		RPN	
	Priority Weight (%)	Ranking	Priority Weight (%)	Ranking
Work stress (WS)	7	5th	11	5th
Emotional stress (ES)	18	2nd	22	2nd
Frustration with work-related and unrelated (FWR)	18	2nd	22	2nd
Low job support (LJS)	42	1st	29	1st
Total	100		100	

$$CI = \frac{\lambda_{\max} - n}{n - 1}, \tag{5}$$

$$\lambda_{\max} = \sum_{i=1}^{n}\left[\left(\sum_{i=1}^{n} GM_i\right)(w_j)\right], \tag{6}$$

where $\lambda_{\max}$ is the maximum eigenvalue and n is the number of factors

$$CR = \frac{Consistency\,index\,(CI)}{Random\,index\,(RI)} \leq 0.10, \tag{7}$$

If the CR value is less or equal to 0.1, it is acceptable. It must be replaced if the subjective judgment is more than 0.1 or 10%.

2.2 Integrated W-BEAS Design

W-BEAS' core structure consists of a user interface (UI), an AHP inference engine (IE), and a knowledge base. W-BEAS was served with XAMPP as the AHP IE, and the database used MySQL. W-BEAS contains three parts: UI, a web server (WBS), and a KBS database, as presented in Fig. 2.

The integrated web-based system is divided into five main components, as shown in Fig. 3:

a. Database—after user retrieval, all factor information is recorded and stored in the knowledge database.
b. Input process—refers to the user's preference for studying data retrieved from a database.
c. Processing of data—the server performs the consistency test and calculates each component and sub-factor weights using the AHP method.
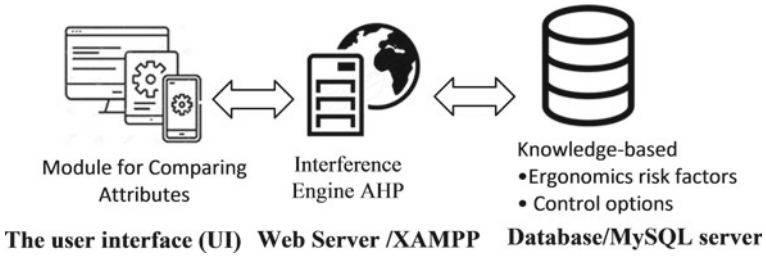d. Process of output—the ergonomic risk factors and sub-factors connected to WMSD are prioritized.
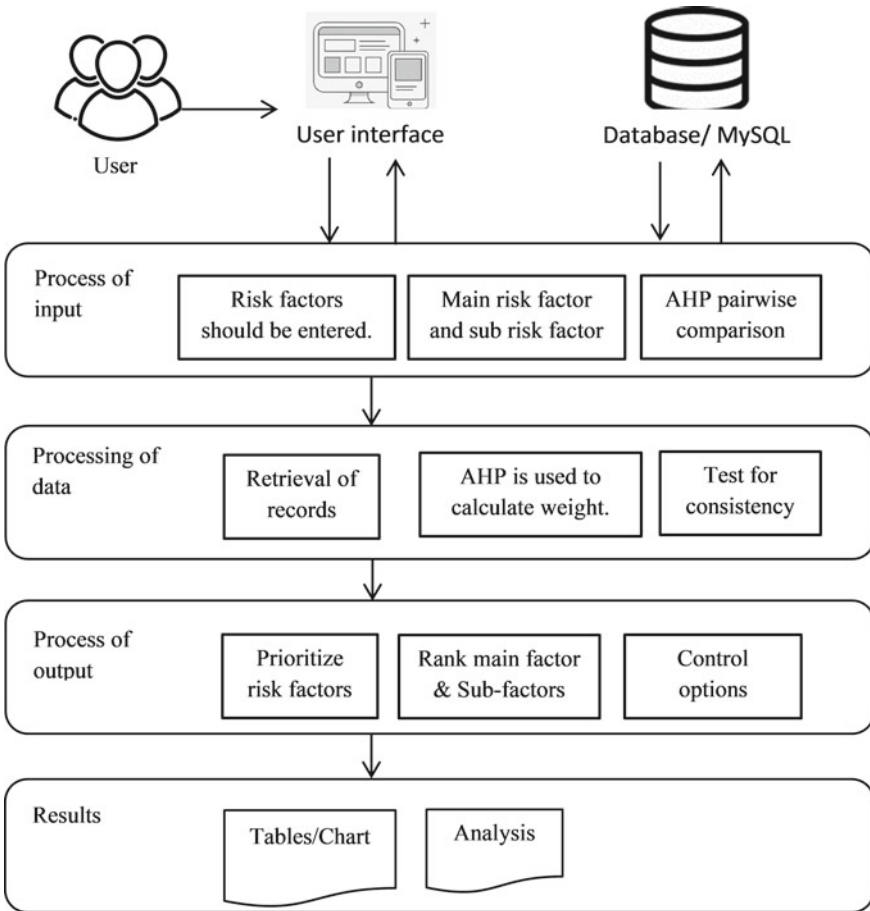
Fig. 2 The structure of W-BEAS

Fig. 3 Parts of the W-BEAS integrated system and their functionalities

e. Analyze and report the results of the ergonomics evaluation in the form of charts and tables.

2.3 W-BEAS User Interface

Figures 4, 5 and 6 depict the W-BEAS interface. Before logging into the system, users were required to register (see Fig. 4). The comparison module page opened

Fig. 4 A page for registering system

Fig. 5 System home page

ERGONOMICS RISK FACTORS

When you are considering the ocupational ergonomics risk factors in the early phase of project, which one do you think is more important to make improvement and how many important than the others?

First Pair					Values					Second Pair
	9	7	5	3	1	3	5	7	9	
Individual Factors	O	O	O	O	O	O	O	O	O	Organizational Factors
Individual Factors	O	O	O	O	O	O	O	O	O	Physical Factors
Individual Factors	O	O	O	O	O	O	O	O	O	Psychosocial Factors
Organizational Factors	O	O	O	O	O	O	O	O	O	Physical Factors
Organizational Factors	O	O	O	O	O	O	O	O	O	Psychosocial Factors
Physical Factors	O	O	O	O	O	O	O	O	O	Psychosocial Factors

NEXT ➤

Fig. 6 Ergonomics risk factors comparison module in system

after logging in. Every questionnaire was addressed in this module under different potential threats, and the scale was determined.

3 Validation of W-BEAS

3.1 Validation Method

The primary goal of the W-BEAS was to demonstrate the efficacy and logic of the proposed web-based expert system in practice. The W-BEAS was validated using real-world data. The validation method compares the results collected by the W-BEAS and the existing assessment method, risk priority number (RPN).

The W-BEAS validation was carried out at a local automotive component manufacturer, with twenty senior personnel chose based on expertise, abilities, and work experience. The demographic data of the W-BEAS validation respondents is presented in Table 2.

This study employed the RPN method to determine the weights of factors and sub-factors for validation reasons. RPN is the current failure mode and effect analysis to rank each failure mode. The W-BEAS was validated using the RPN procedures listed below:

Step 1: The workplace risk factors were assessed by assessing the Likelihood (L) of the risk happening, using a scale of 1 = rare, 2 = unlikely, 3 = likely, and 4 = almost certain.

Step 2: The workers were required to examine the severity (S) of risk factors if any relevant incident occurred, using a scale of 1 = minor/negligible, 2 = moderate, 3 = major, and 4 = severe/catastrophic.

Step 3: The following equation was adopted to measure the risk priority number (RPN).

$$RPN = L \times S \tag{8}$$

Each risk factor's priority weight percentage was determined.

3.2 Validation Results

The findings of the W-BEAS and RPN are compared in Table 3a and b. Refer to Table 3, the first-place rank of risk factors estimated by the W-BEAS and RPN methods is comparable. The rank arrangement reveals a slight variance for the sub-risk variables of individual, organization, and physical-job task. On the other hand, ranked risk factors differently by only one position deemed unimportant. ES must usually exhibit reasonable efficiency at some stage during development [20].

These results show that the W-BEAS can produce results that are comparable to the current assessment method. These validation results are similar to a previous study done by Falamarzi et al. [21] in that the developed web-based system percentages of answers were equivalent to those produced by the previous system. W-BEAS, on the other hand, produced more precise results [22]. Also, it improved the effectiveness of the ergonomics assessment method [23, 24]. Besides, the W-BEAS provides a more thorough indicator of WMSD risk variables than other techniques by employing a macro-ergonomics approach.

These results show that the W-BEAS can produce results that are comparable to the current assessment method. These validation results are similar to a previous study done by Falamarzi et al. [21] in that the developed web-based system percentages of answers were equivalent to those produced by the previous system. W-BEAS, on the other hand, produced more precise results [22]. Also, it improved the effectiveness of the ergonomics assessment method [23, 24]. Besides, the W-BEAS provides a more thorough indicator of WMSD risk variables than other techniques by employing a macro-ergonomics approach.

4 Conclusions

A web-based expert system was produced and validated for this study, using practical online ergonomics assessment advantages. This W-BEAS is valid and reliable in prioritizing the critical workplace risk factors. W-BEAS will help the OSH practitioners identify the critical risk factors needed to resolve the hazards at the workplace.

This study indicates that workers are provided with a flexible ergonomics assessment system through a web-based approach. The worker can assess their ergonomics workplace individually at anywhere and anytime.

Workers must be informed of the critical risk factor of their workplaces and make plans to prevent the WMSD. W-BEAS support the organization to protect and promote the worker's well-being and workplace sustainability. Thus, the results of this validation proof of concept suggest that a W-BEAS appears to be a promising straightforward alternative to the partly expensive and time-consuming expert training. We intend to apply the procedure illustrated in this paper to some other classification problems arising in different sectors for further research.

References

1. Falck AC, Rosenqvist M (2012) What are the obstacles and needs of proactive ergonomics measures at early product development stages? An interview study in five Swedish companies. Int J Ind Ergon 42:406–415. https://doi.org/10.1016/j.ergon.2012.05.002
2. Zare M, Bodin J, Cercier E, Brunet R, Roquelaure Y (2015) Evaluation of ergonomic approach and musculoskeletal disorders in two different organizations in a truck assembly plant. Int J Ind Ergon 50:34–42. https://doi.org/10.1016/j.ergon.2015.09.009
3. Abdullah NH, Wahab E, Shamsuddin A, Aziati N, Hamid A, Kamaruddin NK (2016) Workplace ergonomics and employees' health: a case study at automotive manufacturer. 917–923
4. Maia LC, Alves AC, Leão CP (2012) Design of a lean methodology for an ergonomic and sustainable work environment in textile and garment industry. In: ASME 2012 international mechanical engineering congress and exposition. American Society of Mechanical Engineers Digital Collection, pp 1843–1852
5. Liu L, Chen SG, Tang SC, Wang S, He LH, Guo ZH, Li JY, Yu SF, Wang ZX (2015) How work organization affects the prevalence of WMSDs. Biomed Environ Sci 28:627–633. https://doi.org/10.3967/bes2015.088
6. Maakip I, Keegel T, Oakman J (2016) Prevalence and predictors for musculoskeletal discomfort in Malaysian office workers: investigating explanatory factors for a developing country. 53:252–257
7. Occhipinti E, Colombini D (2016) A toolkit for the analysis of biomechanical overload and prevention of WMSDs: criteria, procedures and tool selection in a step-by-step approach. Int J Ind Ergon 52:18–28. https://doi.org/10.1016/j.ergon.2015.08.001
8. Saaty TL (2008) Decision making with the analytic hierarchy process. Int J Serv Sci 1:83. https://doi.org/10.1504/IJSSCI.2008.017590
9. Russo RDFSM, Camanho R (2015) Criteria in AHP: a systematic review of literature. Procedia Comput Sci 55:1123–1132. https://doi.org/10.1016/j.procs.2015.07.081
10. Das SK, Patyal VS, Mukhopadhyay S (2017) Development and validation of a re-modified work-style short form questionnaire for assessment of stress in medical practitioners working in Indian hospitals. Theor Issues Ergon Sci 18:95–109. https://doi.org/10.1080/1463922X.2016.1154228
11. Qutubuddin SM, Hebbal SS, Kumar AC (2012) computer assisted system for enhancing the application of ergonomics in manufacturing systems. Int J Ergon 2:1–11

12. Leo Kumar SP (2017) State of the art-intense review on artificial intelligence systems application in process planning and manufacturing. Eng Appl Artif Intell 65:294–329. https://doi.org/10.1016/j.engappai.2017.08.005

13. Dansie C, Bloswick DS (2013) Ergonomic risk assessment based on a bayesian-optimised expert system Richard Sesek. Int J Hum Factors Model Simul 4:23

14. Pavlovic-Veselinovic S, Hedge A, Veselinovic M (2016) An ergonomic expert system for risk assessment of work-related musculo-skeletal disorders. Int J Ind Ergon 53:130–139. https://doi.org/10.1016/j.ergon.2015.11.008

15. Savino M, Mazza A, Battini D (2016) New easy to use postural assessment method through visual management. Int J Ind Ergon 53:48–58. https://doi.org/10.1016/j.ergon.2015.09.014

16. Shavarani SM, Korhan O (2015) Expert system assessment of work-related musculoskeletal disorders for video display terminal users. Appl Res Qual Life 10:205–216. https://doi.org/10.1007/s11482-014-9307-5

17. Widanarko B, Legg S, Devereux J, Stevenson M (2014) The combined effect of physical, psychosocial/organisational and/or environmental risk factors on the presence of work-related musculoskeletal symptoms and its consequences. Appl Ergon 45:1610–1621. https://doi.org/10.1016/j.apergo.2014.05.018

18. Yazdani A, Wells R (2018) Barriers for implementation of successful change to prevent musculoskeletal disorders and how to systematically address them. https://doi.org/10.1016/j.apergo.2018.05.004

19. Roquelaure Y, Bodin J, Ha C, le Manac'h AP, Descatha A, Chastang JF, Leclerc A, Goldberg M, Imbernon E (2011) Personal, biomechanical, and psychosocial risk factors for rotator cuff syndrome in a working population. Scand J Work Environ Health 37:502–511. https://doi.org/10.5271/sjweh.3179

20. O'Keefe M, Balci O, Smith E (1987) Validation of expert system performance. http://eprints.cs.vt.edu/archive/00000043/. https://doi.org/10.1109/MEX.1987.5006538

21. Falamarzi A, Borhan MN, Rahmat RAOK (2014) Developing a web-based advisory expert system for implementing traffic calming strategies. Sci World J 1–16. https://doi.org/10.1155/2014/757981

22. Kumar S, Mishra RB (2010) Web-based expert systems and services. Knowl Eng Rev 25:167–198. https://doi.org/10.1017/S0269888910000020

23. Asensio-Cuesta S, Bresó A, Saez C, García-Gómez J (2019) Robustness and findings of a web-based system for depression assessment in a university work context. Int J Environ Res Public Health 16:644. https://doi.org/10.3390/ijerph16040644

24. Qattawi A, Mayyas A, Abdelhamid M, Omar MA (2013) Incorporating quality function deployment and analytical hierarchy process in a knowledge-based system for automotive production line design. Int J Comput Integr Manuf 26:839–856. https://doi.org/10.1080/0951192X.2013.799780

Static Structural Analysis of Auxetic Structures for Sports Protective Gears

Ritul Varrdhan , **Jitendra Bhaskar** , **and Anand Kumar**

Abstract Man-made auxetic structures improve mechanical properties and energy absorption ability of structure without any weight penalty. Both these properties of structures are highly suitable for sports gear in view to reduce weight reduction of safety items for players without burden on their body. The objective of this paper is to design and simulate effective auxetic structures for improved sports gear to absorb high impact energy. Three types of structures based on diamond, honeycomb and re-entrant auxetic structures are used for analysis. Based on positive and negative aspects of each selected auxetic structures, three hybrid auxetic structures are considered for protective gears. The value of equivalent von-Mises stresses and specific energy absorption of diamond and re-entrant is found to be higher than any other sample structure. Higher the value of equivalent von-Mises stress, higher will be the stiffness. Hence, hybrid structure of diamond and re-entrant may provide better protection than conventional open cell polyethane foam based sports protective gears.

Keywords Energy absorption · Equivalent von-Mises stress · Relative density

1 Introduction

Material with a negative Poisson's ratio is termed auxetic material. These auxetic materials can be utilized in sport protective gears as they expand laterally when stretched and shrink when compressed [1]. Due to negative Poisson's ratio many other mechanical properties such as fracture toughness [2], synclastic curvature [3], indentation resistance [4, 5], energy absorption [6, 7], etc. of material and structure also change. More and more auxetic materials and structures are being introduced for

---

R. Varrdhan · J. Bhaskar · A. Kumar (✉)
Department of Mechanical Engineering, Harcourt Butler Technical University, Kanpur, Uttar Pradesh, India
e-mail: anandk@hbtu.ac.in

J. Bhaskar
e-mail: jbhaskar@hbtu.ac.in

different applications such as medical implants, shoes, body armors, shock absorbers, etc. [8].

Nallavan opined that auxetic materials may be good replacement of traditional materials for sports personal protective equipments. These are lighter in weight, comfortable and have good energy absorption [9]. Ingrole reported that auxetic materials with negative Poisson's ratio may be embedded in protective equipments as they absorb high impact forces [10]. Recent researches done by Bronder et al. on auxetic structures are mostly focusing on the optimizing the fabrication methods and improving its energy absorption abilities [11].

The objective of this research paper is to optimally design auxetic structures for quality sport protective equipment. Three types of structures are simulated-diamond, honeycomb and re-entrant and their hybrids- diamond and re-entrant, diamond and honeycomb and re-entrant and honeycomb with suitable boundary conditions. It mainly focuses on comparing von-Mises stresses and energy absorption capability of the auxetic structures for their performance evaluation. The auxetic structures with high energy absorption capability may be used in helmets, batting pads, knee and elbow pads, etc.

2   Methodology

2.1   Materials

Acrylonitrile butadiene styrene (ABS) is the material chosen for simulation and analysis. ABS is an engineering thermoplastic which consist of crosslinking of poly(styrene-co-acrylonitrile) and polybutadiene. It is broadly used to make plastic products due to its remarkable qualities such as high impact resistance, toughness and good processing characteristics. The properties of ABS used are: Young's modulus, E = 2.2 GPa; yield strength, σ_{ys} = 31 MPa; Poisson's ratio, v = 0.35 and density, ρ = 1.05 g/cm^3 [10].

2.2   Modelling

Three important auxetic structures based on diamond, honeycomb and re-entrant (Fig. 1) are considered for proposed research work. Effort has been made to explore the possibilities of hybrid auxetic structures by coupling important features of two auxetic structures in one. Hybrid structures such as diamond and re-entrant, diamond and honeycomb and re-entrant and honeycomb are shown in Fig. 2. 3D geometric models are created using ANSYS SpaceClaim 2021 R1 software. Specific dimensions for each structure geometry is listed in Table 1.
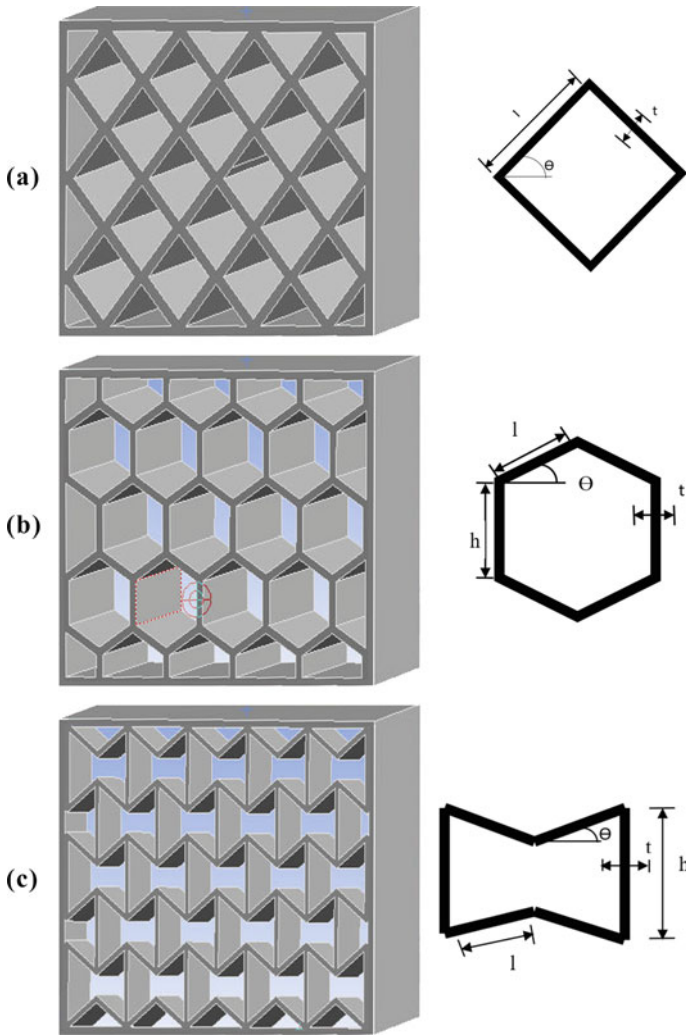
Fig. 1 Schematic diagram of auxetic structures: **a** Diamond; **b** Honeycomb; **c** Re-entrant

Six different auxetic structures are modelled through software-diamond, re-entrant, honeycomb and their hybrids-diamond and re-entrant, diamond and honeycomb and re-entrant and honeycomb. The structures are imported in Finite Element Analysis software as ".scdoc" format. FEM of each sample is done through "ANSYS 2021 R1" under workbench GUI in static structural project schematic. Each sample is loaded with a compressive force of 500 N and bottom and side of case are fixed as a boundary condition. The material selection is done manually. The meshing for each structure is listed in Table 2.
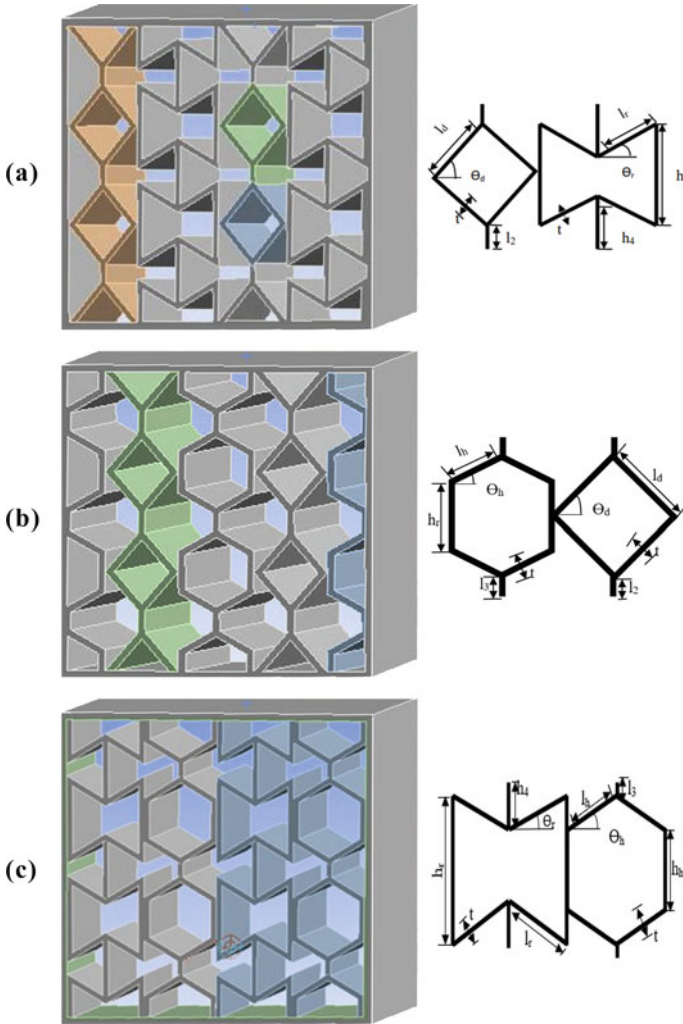
Fig. 2 Schematic diagram of hybrid auxetic structures: **a** Diamond and Re-entrant; **b** Diamond and Honeycomb; **c** Re-entrant and Honeycomb

2.3 Relative Density

Relative density of auxetic structure is used to measure the stiffness of the structure [12]. Increase in the relative density leads to an increase in the capability to resist the load applied on the structure. Relative density of each structure is calculated using Eqs. 1 to 6 [13]:

For diamond structure:

Table 1 Dimension of each unit cells

Sample	Dimensions of unit cell
Diamond	l = 5 mm, Θ = 50°, t = 1 mm
Honeycomb	l = 5 mm, h = 5 mm, Θ = 30°, t = 1 mm
Re-entrant	l = 8 mm, h = 11 mm, Θ = 30°, t = 1 mm
Diamond and Re-entrant	l_d = 9.79 mm, Θ_d = 50°, l_r = 8 mm, h_r = 15 mm, Θ_r = 30°, l_2 = 1.6 mm, h_4 = 5.3 mm, t = 1 mm
Diamond and Honeycomb	l_d = 6 mm, Θ_d = 50°, l_h = 5 mm, h_h = 5 mm, Θ_h = 30°, l_2 = 1.6 mm, l_3 = 1.29 mm, t = 1 mm
Re-entrant and Honeycomb	l_r = 8 mm, h_r = 15 mm, Θ_r = 30°, l_h = 7.5 mm, h_h = 7.5 mm, Θ_h = 30°, l_3 = 1 mm, h_4 = 5 mm, t = 1 mm

where, l = length of sides, Θ = inclination angle of side, h = height of sides t = thickness of sides

Table 2 Quality of mesh

Physics preference	Non-linear mechanical
Element order	Quadratic
Element size	2 mm

$$\rho = \frac{2lt}{2lcos\,\theta sin\,\theta} \tag{1}$$

For honeycomb structure:

$$\rho = \frac{(2l + h)t}{2l\cos\theta(l\sin\theta + h)} \tag{2}$$

For re-entrant structure:

$$\rho = \frac{(2l + h)t}{2l\cos\theta(h - l\sin\theta)} \tag{3}$$

For diamond and re-entrant structure:

$$\rho = \frac{((4l_r + h_r) + 4l_d + (h_4 + l_2))t}{2l_r\cos\theta_r(h_r - l_r\sin\theta_r) + 2l_d^2\sin\theta_d\cos\theta_d + (h_4 + l_2)t} \tag{4}$$

For diamond and honeycomb structure:

$$\rho = \frac{((4l_h + h_h) + 4l_d + (l_3 + l_2))t}{2l_hcos\theta_h(h_h + l_h sin\theta_h) + 2l_d^2\sin\theta_d\cos\theta_d + (l_3 + l_2)t} \tag{5}$$

For re-entrant and honeycomb structure (Table 3):

Table 3 Calculated relative densities of different auxetic structures

Sample	Relative densities
Diamond	0.2031
Honeycomb	0.2309
Re-entrant	0.2783
Diamond and Re-entrant	0.5023
Diamond and Honeycomb	0.3840
Re-entrant and Honeycomb	0.4007

$$\rho = \frac{((4l_r + h_r) + 4l_h + (l_3 + h_4))t}{2l_r \cos\theta_r (h_r - l_r \sin\theta_r) + 2l_h^2 \sin\theta_h \cos\theta_h + (l_3 + h_4)t} \tag{6}$$

2.4 Energy Absorption

One of the main charateristics of these structures is their energy absorbing capabilities. The overall energy absorbed during the compression has been calculated for each sample manually. Total energy absorbed (W) is calculated by integrating the nominal stress–strain curves and is determined by Eq. 7. Specific energy absorbed (W_s) by the materials is calculated using Eq. 8 [14].

$$W = \int_0^\epsilon \sigma(\epsilon) d\epsilon \tag{7}$$

$$W_s = \frac{\int_0^\epsilon \sigma(\epsilon) d\epsilon}{\rho * \rho_{mat}} \tag{8}$$

where, ρ is relative density and ρ_{mat} is denstiy of ABS material (1.05 g/cm^3).

3 Results and Discussion

Stress, strain, deformation and strain energy are analyzed through ANSYS 2021R1 software after due meshing and applying boundary conditions (Fig. 3).

Figure 4 illustrates deformation in different structures on application of 500 N load. Diamond and re-entrant and diamond and honeycomb have small amount of distortion due to densification of structures at the region where the load is applied.

Stress and strain generated on all the structures on application of 500 N load is different. The maximum stress is seen in diamond and re-entrant in comparison to
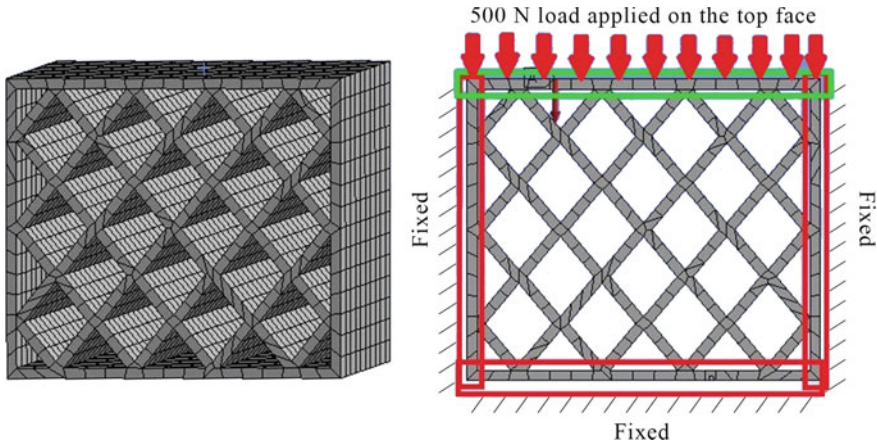
Fig. 3 **a** Meshed model of diamond structure; **b** boundary condition and load application on diamond structure

other samples. Higher the relative density, higher will be the stiffness as these structures collapse within themselves and sustain greater load due to high densification at that region [10]. It is clear from Fig. 5 that structures with lesser relative density have lesser stifffness. Hence, hybrid structure of diamond and re-entrant structure is the stiffest structure due to its greater density.

The specific energy absorbed by each structures is calculated using Eq. 8. It is seen that diamond and re-entrant hybrid has highest specific energy absoption. Figure 6 indicates that the structures with high stiffness will have higher energy absorption capacity. It means that higher the stiffness (i.e. ability to resist deformation when load is applied), it will absorb more energy.

4 Conclusions

The static structural compressive analysis is performed on different auxetic structures namely diamond, honeycomb, re-entrant, and their hybrids. Hybrid structure of diamond and re-entrant is proved to be best. From all the data recorded, it is observed that the diamond and re-entrant structure has high relative density and densifies most on the application of load making it most stiff. It has the highest capability to absorb the energy.

Based on stress analysis, three hybrid combinations of auxetic structures i.e. diamond and re-entrant, diamond and honeycomb, re-entrant and honeycomb were considered for their energy absorbing capacity. Diamond and re-entrant structure shows highest energy absorbing capacity. Diamond and re-entrant can be very useful for designing sports protective gears due to its better stiffness and energy absorption capacity.
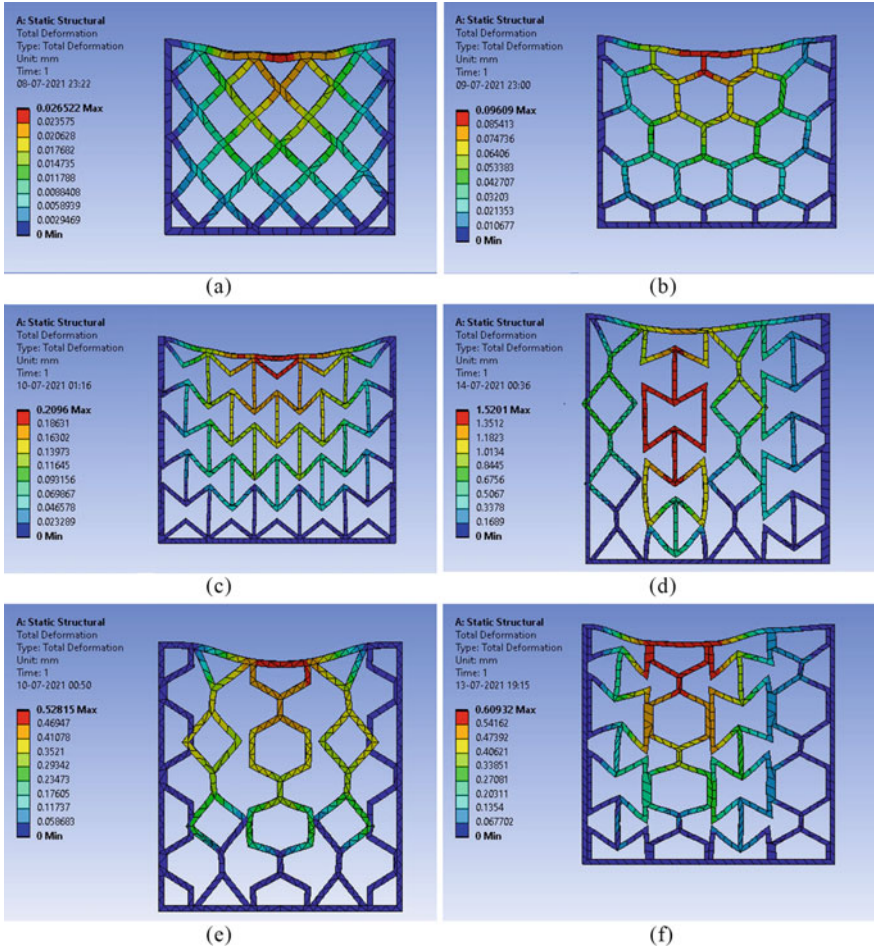
Fig. 4 Total deformation in structures on application of force **a** Diamond; **b** Honeycomb; **c** Re-entrant; **d** Diamond and Re-entrant; **e** Diamond and Honeycomb; **f** Re-entrant and Honeycomb
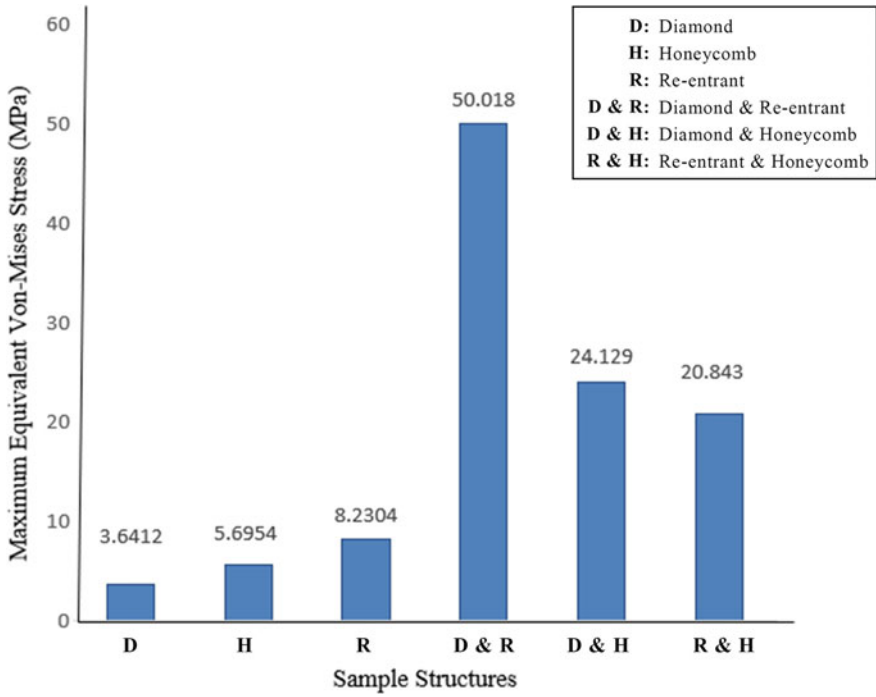
Fig. 5 Maximum equivalent von-Mises stresses (MPa) for different auxetic structures
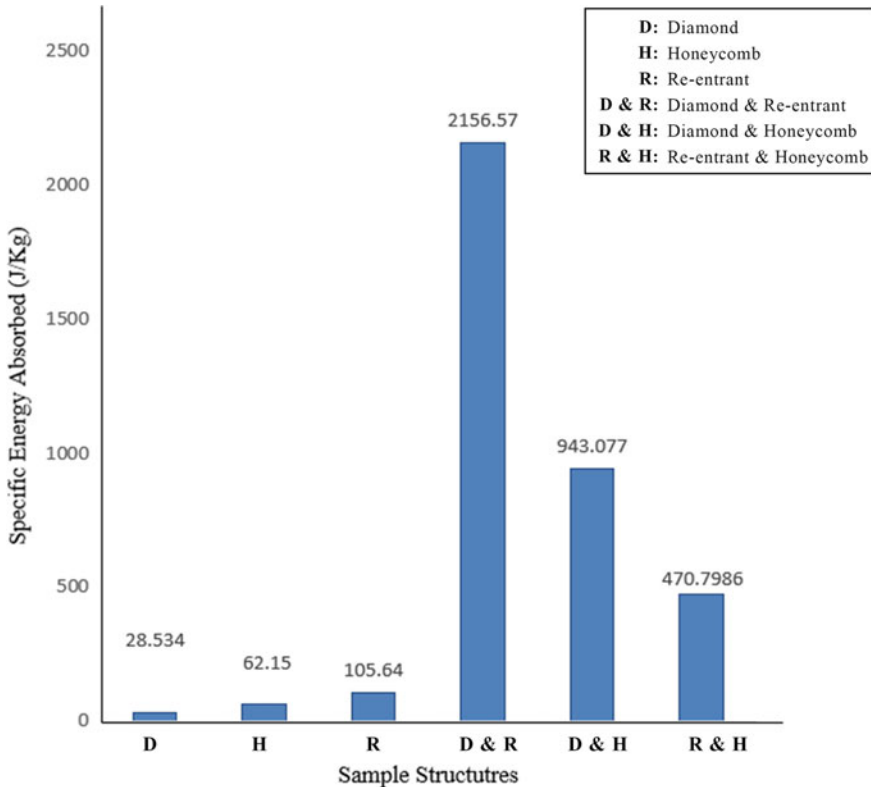
Fig. 6 Specific energy absorbed (J/Kg) for different auxetic structures

References

1. Wang Z, Hu HF (2014) Auxetic materials and their potential applications in textiles. Text Res J 84(15):1600–1611
2. Choi JB, Lakes RS (1996) Fracture toughness of re-entrant foam materials with a negative Poisson's ratio: experiment and analysis. Int J Fract 80:73–83
3. Lakes R (1987) Foam structures with a negative Poisson's ratio. Science 235:1038–1040
4. Argatov II, Guinovart-Díaz R, Sabina FJ (2012) On local indentation and impact compliance of isotropic auxetic materials from the continuum mechanics viewpoint. Int J Eng Sci 54:42–57
5. Coenen VL, Alderson KL (2011) Mechanisms of failure in the static indentation resistance of auxetic carbon fibre laminates. Phys Status Solidi B 248:66–72
6. Imbalzano G, Tran P, Ngo TD, Lee PVS (2016) A numerical study of auxetic composite panels under blast loadings. Compos Struct 135:339–352
7. Jiang L, Hu H (2017) Low-velocity impact response of multilayer orthogonal structural composite with auxetic effect. Compos Struct 169:62–68
8. Miller W, Hook PB, Smith CW, Wang X, Evans KE (2009) The manufacture and characterisation of a novel, low modulus, negative Poisson's ratio composite. Compos Sci Technol 69(5):651–655
9. Nallavan G (2020) Impact of recent developments in fabrication of auxetic materials on safety and protection in sport. AIP Conf Proc 2271(1):030006

10. Ingrole A (2018) Auxetic and hybrid structure designs and advanced manufacturing study for energy absorption improvements. Doctoral dissertation, The Florida State University
11. Bronder S, Adorna M, Fíla T, Koudelka P, Falta J, Jiroušek O, Jung A (2021) Hybrid auxetic structures: structural optimization and mechanical characterization. Adv Eng Mater 23(5):2001393
12. Sahu SK, Badgayan ND, Sreekanth PR (2020) Numerical investigation on the effect of wall thickness on quasistatic crushing properties of nylon honeycomb structure. Mater Today Proc 27:798–804
13. Shruti M, Hemanth NS, Badgayan ND, Sahu SK (2021) Compressive behavior of auxetic structural metamaterial for lightweight construction using ANSYS static structural analysis. Mater Today Proc 38:12–17
14. Gibson LJ, Ashby MF (1999) Cellular solids: structure and properties. Cambridge University Press

Cutting Strategy of Polymer Composite Material for Aerospace Engineering Application

Amiril Sahab Abdul Sani [ID]**, Ahmad Zafir Zainuddin, and Mohd Shahneel Saharudin** [ID]

Abstract Despite the popular use of hybrid fibers in polymer composite in aerospace applications, it comes with a price where it is expensive and has a complex process to produce. A new alternative method of using nanocomposite using natural fiber such as Epoxy/Graphene is getting placed in the industry. However, the natural fiber has a hygroscopic characteristic. The minimum quantity lubrication (MQL) method was approached for this research to investigate the machinability behavior of the Graphene/Epoxy nanocomposite. The cutting force was also investigated to see the effect of different coatings material of the flat-end mill cutters when machining the Epoxy/Graphene nanocomposites. Despite having various acetone doses in the Epoxy/Graphene specimens, the results show that the MQL technique has a favorable impact on the surface finish and that the TiAlN-coated tungsten carbide tool has a constant cutting force during slot milling. Furthermore, the addition of acetone into the nanocomposite may assist in decreasing the build-up edge on the tool cutting edge, lowering the risk of the tool failure.

Keywords Epoxy · Flat-end milling · Graphene · MQL · Nanocomposite · Synthetic ester

1 Introduction

Polymer composite materials has been proven to be flexible and adaptable engineering materials for various type of engineering applications such as Aerospace engineering. The focus of aerospace engineering is the research and development of aircraft and spacecraft. Among the application of aerospace engineering that is

A. S. Abdul Sani (✉) · A. Z. Zainuddin
Faculty of Manufacturing and Mechatronic Engineering Technology, Universiti Malaysia Pahang, 26600 Pekan, Pahang, Malaysia
e-mail: amiril@ump.edu.my

M. S. Saharudin
Universiti Kuala Lumpur Malaysia Italy Design Institute (UniKL MIDI), Taman Shamelin Perkasa, 119 Jalan 7/91, 56100 Kuala Lumpur, Malaysia

widely used is the flight vehicle such as aeroplane, shuttles, etc. Composite materials are lightweight materials and thus, they are normally used for everything in structural applications and components of all aircrafts and spacecraft such as gliders, hot air balloon gondolas, fighter planes, space shuttles and passenger jets. The structure of the material used in this air vehicles demands high specific stiffness, high specific strength and high degree of dimensional stability to withstand under wide range of temperature and higher altitude atmospheric pressure as well as the applied structural load during operations.

In the recent decades, the use of air travel has been increased drastically worldwide. To meet the high demand, a higher production rate of the machining is compulsory. The most critical technique for producing better surface quality is the machining parameters of cutting speed, feed rate and cutting depth. Nicolais et al. states in their studies that for cutting and machining polymer composites, a combination of small depth of cut, smaller feed rate and high cutting force can produce better surface finish [1]. Meanwhile, for micro-milling of nano-polymer composites, Shyha et al. concluded in their studies that the feed rate influenced the cutting force while the cutting speed has little to no effect on cutting force [2]. Also, a negligible tool wear on cutting edge were obtained from the addition of nano-filler of up to 1% weight of filler fraction. The tool bits are also as much as important as those three parameters. According to studies by Xu et al., they highlighted that the TiAlN-coated tungsten carbide drill bit has better wear resistance to catastrophic failure than diamond-coated tungsten carbide drill bit despite having a similar cutting condition applied [3]. In terms of fiber orientation, studies by He et al. showed that the friction coefficient for milling dependent on fiber cutting angle [4].

John & Kumaran stated that, at constant feed rate, chilled air machining outperforms dry machining in terms of delamination and surface roughness [5]. Xu et al. investigated and found that a lower drilling torque and less energy consumption can be obtained under the minimum quantity lubrication (MQL) machining which was contributed by the lower frictional force occurred at the tool-hole wall interface [6]. MQL has been shown to have a positive influence on the geometric precision of composite holes.

Minimum Quantity Lubrication (MQL) or also known as Micro-lubrification is an alternative to the use of traditional metal working fluids in machining. When chips are ejected, the excellent lubricity of a good MQL lubricant guarantees that much of the heat generated from metal sliding friction is transmitted to the chip and departs the interface. This heat lubrication and transfer keeps the cutting tool cooler for longer and reduces tool wear. It is common for machinists to have double the tool life after using MQL. The swarf or chips from cutting with MQL are practically dry and can be recycled for greater benefit and without washing. With MQL, before secondary operations take place, sections also do not need any cleaning. Hydrogen-bonded liquid media are more likely to induce environmental stress cracking (ESC) in polymers. Which also mean vegetable oil are more suitable for polymers since vegetable oil has little to less water content. Many MQL lubricants are highly distilled bio-based (plant) oils and are fully safe for skin contact and have the added advantage of organic and environmentally sustainable materials [7].

The objectives of this research are to compare the machinability behaviors of nanocomposites (Epoxy/Graphene) under various cooling and cutting conditions in terms of cutting force, surface quality and morphology as well as the build-up edge formation on the different coated flat-end mill cutters.

2 Methodology

There are three types of Epoxy/Multi-Layer Graphene Nanocomposites used as the material specimens in this work. A 0.1 wt.% of multi-layer graphene of 12 nm average thickness (purity 99.2%) was added in acetone at different concentrations of 0, 25 and 50 ml before being sonicated in a sonicating bath for 30 min prior mixing it with the epoxy resin. The preparation procedure is discussed thoroughly by Saharudin et al. in [8]. A monolithic (neat) epoxy is used as the control specimen sample in this investigation. Figure 1 shows the material specimens before the machining processes take place, which are (A) Monolithic Epoxy, (B) Epoxy/Graphene-0 ml Acetone, (C) Epoxy/Graphene-25 ml Acetone and (D) Epoxy/Graphene-50 ml Acetone. Each specimen was in the shape of a cuboid with a dimension of 80 mm in length, 10 mm in width and 3 mm of thickness. The specimens were tested on a Vickers Micro-hardness Tester following the ASTM E384 standard for measuring the surface hardness of each specimen. The hardness test specifies an initial load, P of 0.05 kg divided by the indentation diagonal area, A in mm^2 after 20 s indentation time. Equation 1 depicts the Vickers microhardness calculation method according to the standard specification.
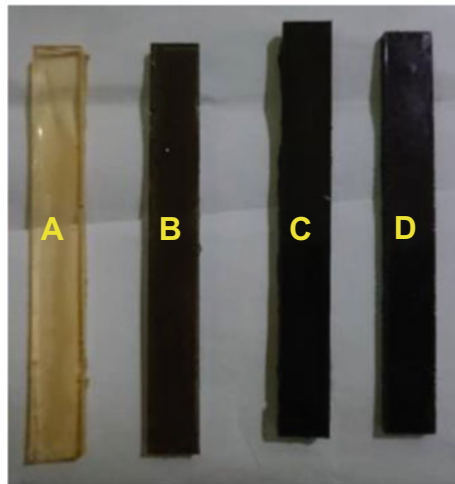

Fig. 1 Material specimens of **a** Monolithic epoxy; **b** Epoxy/graphene-0 ml acetone; **c** Epoxy/graphene-25 ml acetone; and **d** Epoxy/graphene-50 ml acetone

Table 1 Machining and MQL parameters

Items	Description
End mills	4 flute, Tungsten carbide
End mill diameter	3 mm
Coatings	AlTiN (HRC50), TiSiN (HRC60), TiAlN (HRC55), Uncoated (HRC55)
Cutting speed, v_c	35 m/min
Feed rate, f	25 mm/rev
Axial depth of cut, a_p	0.5 mm
Cutting length	10 mm per pass (4 passes each set)
MQL condition	Pressurized air, MQL-synthetic ester (MQL-SE)
MQL pressure and flowrate	0.4 MPa at 15 ml/hr

$$HV = \frac{100P}{A} \tag{1}$$

Surface roughness of the specimens is measured using a perthometer (Surfcom Touch 50) both before and after the slot milling operations. The cut-off length, λ_c was set at 0.8 mm with the measurement length of 5.6 mm according to the EN ISO 4287 standard.

Four different coatings of 4-flutes, 3 mm diameter tungsten carbide flat-end mill cutters are used for the machining tests. Table 1 depicts the cutting parameters of the slot milling experiments. For this experiment, the slot millings were conducted on MAKINO KE-55 CNC vertical milling machine which has a maximum power of 5.6 kW, maximum spindle speed of 4000 rpm, a positioning accuracy of 25–100 μm. The machine has a table width of 375 mm and a table length of 800 mm with traverse and crossing distances of 548.64 mm and 320.04 mm, respectively.

All four different types of Graphene/Epoxy nanocomposites will undergo a total of 16 sets of experiment following the machining parameters shown in Table 1. For each set of experiment a new specimen and tool bit are used. The first 12 sets of experiments use the three coated cutting bits with pressurized air while the last four will use the uncoated milling cutter lubricated by the Synthetic Ester (SE) through the MQL condition as the lubrication method. The pressurized air and the micro-lubrication of SE is delivered to the cutting zone using a MQL device (Kuroda Ecosaver KEP-WR) through a nozzle orifice diameter of 2.5 mm and the distance from the nozzle tip to the tool cutting edge between 50 to 55 mm. Figure 2 illustrates the machine configuration of the milling operations. The machining process starts at the entry region towards the end point (negative X-direction) with the up-milling procedure is taken place at the entry point (conventional milling).

All the test specimens and the tool bits are then analyzed with video measuring microscope and digital microscope to capture the tool morphologic and surface topography before and after the machining tests.

Fig. 2 Machining setup, nozzle distance and cutting path

3 Results and Discussion

The surface hardness and roughness results of the material specimens are shown in Figs. 3 and 4, respectively. According to Saharudin et al., the hardness of the nanocomposite prepared without acetone is higher compared to the Vickers micro-hardness of the monolithic epoxy [9]. The initial surface roughness of the specimens recorded a different results variation. The monolithic epoxy has a rougher surface compared to the other nanocomposites and the smoother surface is shown by the nanocomposite prepared without acetone, specimen B.
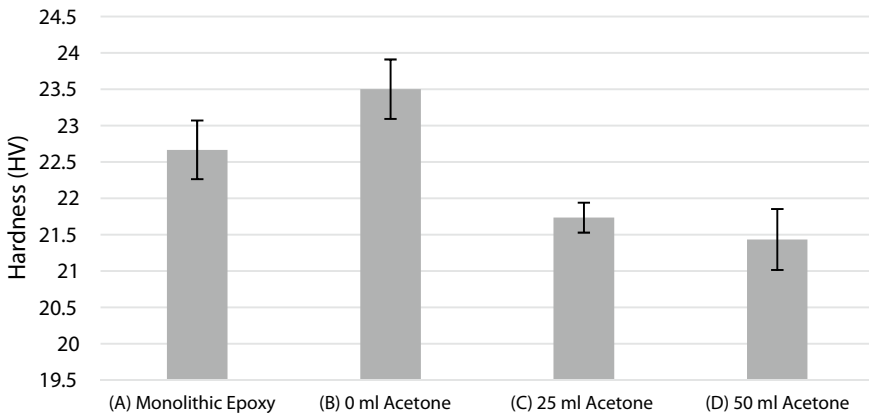
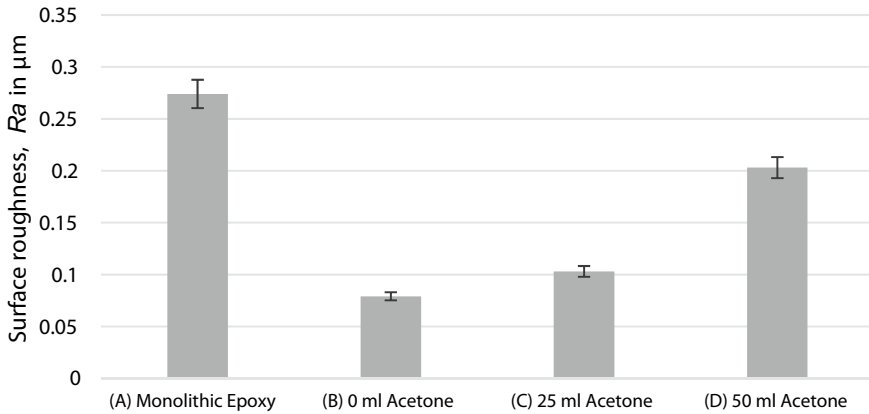**Fig. 3** Vickers hardness of monolithic epoxy and its nanocomposites

Fig. 4 Surface roughness results of the specimens before milling

The cutting force results of all specimens during milling operation using different coatings of flat-end mill cutters are presented in Fig. 5. The specimen of Epoxy/Graphene-25 ml Acetone (specimen C) shows that the cutting forces remain at a constant trend of below 6 N for all coated and uncoated tungsten carbide tools compared to the other results. In addition, the milling with MQL-SE lubrication using uncoated tools presented a consistent trend of low cutting forces (between 3.9 and 5.6 N) for all specimen materials. This finding also corroborates with the report from Skopp and Klaffke, whereby low cutting forces were produced when cutting using uncoated tungsten carbide tool under MQL condition [10]. It can be noted that MQL does have a positive influence on nanocomposite machining.

The cutting forces produced by TiAlN-coated tools with pressurized air show a comparable good trend of results with the uncoated tools. TiAlN is reported to have
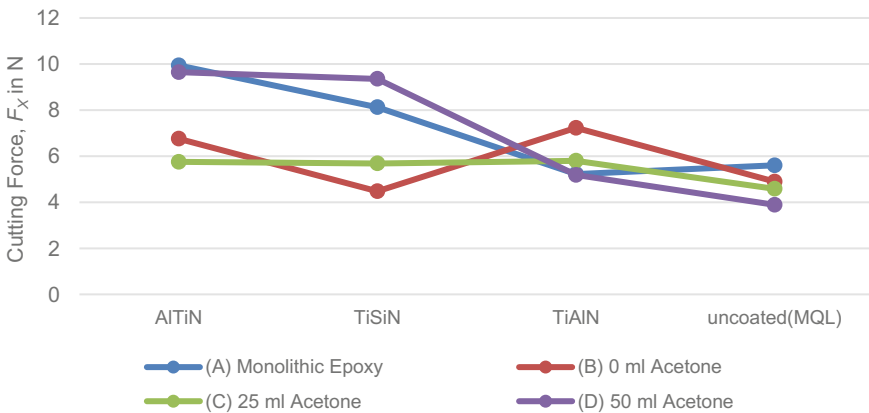

Fig. 5 Cutting Force, F_X with respect to different tool coatings

a very high thermal stability of up to 1000 °C, thus this coating can sustain high cutting temperature generated at the cutting zone, which subsequently resulted in lower tool wear rate and cutting forces as compared to the other coated and uncoated flat-end mill tools [11]. Additionally, Ji et al. [12] reported that lower cutting energy consumption can be obtained under MQL condition with TiAlN coated-tool due to the reduced frictional forces acting at the tool-hole wall interface.

The surface roughness, R_a results after the milling operation can be seen in Fig. 6. The machined surface of the specimen A using AlTiN-coated carbide tool has a rougher surface compared when using other cutting tools. At high cutting speed of 35 m/min, the AlTiN-coated carbide tool experiences extreme frictional conditions that results in rapid tool wear as well as higher cutting forces compared to TiAlN and the uncoated + MQL-SE [11]. With TiSiN-coating, the slotted surface was found with clean cut alongside with uncoated tungsten carbide tool under MQL-SE condition. As for the machined surface using TiAlN-coated flat-end mill cutter, minor thermal damage is found at the exit of the slot as shown in Fig. 7. Different coating materials provide different tribo-mechanical interactions between the tool-workpiece sliding interfaces, which indicate the difference in surface friction produced by the coatings material on the tool-workpiece sliding surfaces [13].

Thermal damages can be seen on the machined surfaces of specimen B despite having been machined using different type of coated flat-end mill cutter especially when using the TiAlN-coated tungsten carbide tool. A better surface finished is presented on specimen C when using TiAlN-coated cutting tool in high pressurized air condition as well as when using the uncoated tool in MQL-condition as shown in Fig. 7. The TiAlN coated carbide tool may reduce the sliding friction between the TiAlN coated surfaces while cutting the workpiece specimen C (dispersed in 25 ml Acetone) compared to the material that has 0 ml Acetone dispersant (specimen B). The highly concentrated multi-layered graphene nanoparticles in the epoxy of specimen B may increase the frictional behavior of the workpiece when being cut by the different coated carbide tools [13].
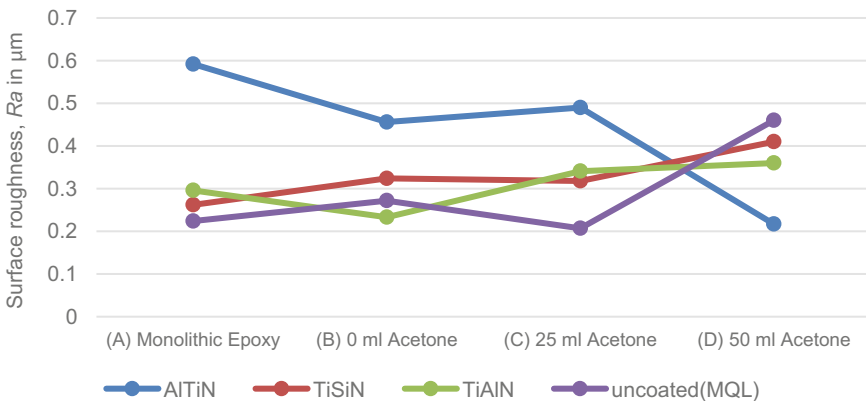

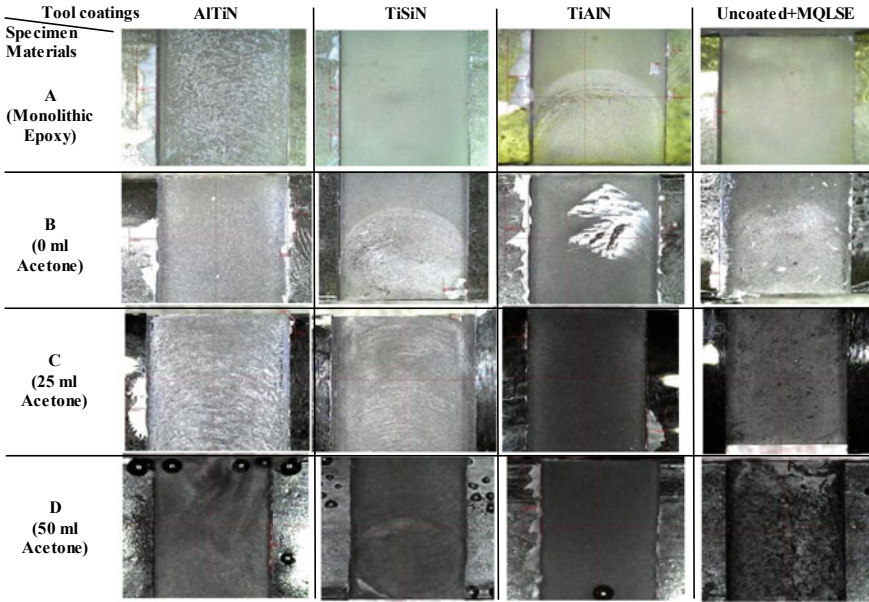**Fig. 6** Surface roughness results on the machined surfaces for all specimens after milling

Fig. 7 Optical images of the machined surfaces at 4th pass on all specimens' materials

The machined surfaces on specimen D is seen to be having a similar pattern of surface damage when compared to all the other cutting conditions. The presence of higher acetone volume in the specimen D reduces the dynamic storage modulus, E' as well as contributing to the presence of high porosity, which could degrade the mechanical properties of the specimen [8]. However, the topographical image after machining with the uncoated tungsten carbide tool in MQL-SE condition shows a rougher surface compared to the other cutting tools as presented in Figs. 6 and 7. The uncoated tool may increase the material adhesion of specimen D at the chip-tool interface as the cutting temperature increases while removing the workpiece material, thus increases the tool wear and material's build-up at the cutting zone, which produces rougher surface conditions (0.46 μm) compared to that of the other coated cutting tools that cut the same specimen's material [13].

4   Conclusion

In this paper, a comparative study was performed on the machinability properties of Epoxy/Graphene nanocomposites under various tool coatings and lubrication conditions in terms of cutting force, surface quality and morphology on different specimen materials using flat-end milling processes. Based on the results and findings acquired, the conclusion can be summarized as follows:

- Less cutting force and lower surface roughness were obtained from MQL-SE condition machining except for Epoxy/Graphene-50 ml Acetone (specimen D).
- Cutting Epoxy/Graphene-25 ml Acetone (specimen C) with uncoated tungsten carbide in MQL-SE condition give the best surface finish (0.207 μm).
- Epoxy/Graphene-25 ml Acetone (specimen C) is much easier to cut compared to other specimens even using different coated carbide cutting tools.
- The TiAlN-coated tungsten carbide tool produces a more consistent cutting forces compared to the other coated cutting tools despite having to cut different material specimens.
- AlTiN, TiSiN and TiAlN-coated flat-end mill cutters produce better surface finish compared to the uncoated cutting tool when cutting the Epoxy/Graphene-50 ml Acetone (specimen D).
- Acetone volume influenced the material adhesion on the tool-workpiece interfaces with higher acetone dosage being added in the nanocomposite, less material adhesion is found on the cutting tool's edge.

References

1. Sheikh-Ahmad JY, Davim JP (2012) Cutting and machining of polymer composites. In: Nicolais L (ed) Wiley Encyclopedia of Composites, pp 648–658
2. Shyha I, Fu G, Huo D, Le B, Inam F, Saharudin MS, Wei J (2018) Micromachining of nano-polymer composites reinforced with graphene and nano-clay fillers. Key Eng Mater 786:197–205
3. Xu J, Ji M, Paulo Davim J, Chen M, El Mansori M, Krishnaraj V (2020) Comparative study of minimum quantity lubrication and dry drilling of CFRP/titanium stacks using TiAlN and diamond coated drills. Compos Struct 234:111727
4. He Y, Sheikh-Ahmad J, Zhu S, Zhao C (2020) Cutting force analysis considering edge effects in the milling of carbon fiber reinforced polymer composite. J Mater Process Technol 279:116541
5. John KM, Kumaran T (2019) The techniques employed in milling of CFRP to reduce material damages. Int J Innov Technol Exploring Eng 9(2S2), 396–398 (2019).
6. Xu J, Ji M, Chen M, El Mansori M (2020) Experimental investigation on drilling machinability and hole quality of CFRP/Ti6Al4V stacks under different cooling conditions. Int J Adv Manuf Technol 109:1527–1539
7. Abdul Sani AS, Jamaluddin NA, Jamaludin AS, Talib N (2021) Calophyllum-Inophyllum from Pahang Malaysia as biolubricant feedstock for industrial application. In: Recent trends in manufacturing and materials towards industry 4.0, pp 441–449. Springer, Singapore
8. Saharudin MS, Hasbi S, Okolo C, Wei J, Jusoh AR (2019) The processing of epoxy/multi-layer graphene nanocomposites: effects of acetone on properties. J Eng Sci Technol 14(6):3131–3142
9. Saharudin MS, Shyha I, Inam F (2016) Viscoelastic and mechanical properties of multi-layered-graphene polyester composites. In: ICAME2016—2nd international conference on advances in mechanical engineering, Istanbul, Turkey, pp 1–5

10. Skopp A, Klaffke D (1998) Aspects of tribological testing of diamond coatings. Surf Coat Technol 98(1–3):1027–1037
11. Kulkarni AP, Sargade VG (2015) Characterization and performance of AlTiN, AlTiCrN, TiN/TiAlNPVD coated carbide tools while turning SS 304. Mater Manuf Processes 30:748–755
12. Ji M, Xu J, Chen M, El Mansori M (2020) Effects of different cooling methods on the specific energy consumption when drilling CFRP/Ti6Al4V stacks. Procedia Manufact 43:95–102
13. Kumar CS, Patel SK (2018) Performance analysis and comparative assessment of nano-composite TiAlSiN/TiSiN/TiAlN coating in hard turning of AISI 52100 steel. Surf Coat Technol 335:265–279

Evaluation of Oxidative and Thermal Stability of Base Oil for Automotive Application

Najmuddin Mohd Ramli, Mohd Sabri Mahmud, Mohd Khairul Nizam Mohd Zuhan, Musfafikri Musa, and Mohd Najib Razali

Abstract Base oils make up the majority of the content of engine oils and substantially impact the overall performance of the finished lubricant product. The oxidative and thermal stability of the base oil are critical factors in defining the quality of automobile lubricating oil. Thus, it is critical to understand the degrading behavior of base oils and engine oils. The oxidative and thermal stability of several base oils and engine oil were thoroughly investigated in this study. Three distinct types of base oil (base 1, 2 and 3) and motor oil were produced and physically characterized. The samples were dried in a drying oven at atmospheric pressure and 150 °C for 24 h. The impact of heat treatment on the samples' oxidative stability was investigated using a Fourier Transform Infrared Spectrometer (FTIR). The thermogravimetric analysis was used to determine the samples' thermal stability (TGA). The study was done in an inert atmosphere using nitrogen gas and a 10 °C min^{-1} heating rate from 30 to 900 °C. The experimental results indicate that base oils and engine oil resisted oxidation since no apparent chemical structural alteration was seen following 24-h heat treatment. Meanwhile, engine oil demonstrated the most outstanding onset temperature of 298 °C, followed by base oil three (276 °C), base oil two (275 °C), and base oil one (262 °C). Additionally, the TGA profile revealed that engine oil had the highest thermal stability at 5, 50, and 90% weight loss. Base oil three, base oil two, and base oil one all followed this pattern. Nonetheless, further research is

N. Mohd Ramli · M. N. Razali (✉)
Faculty of Chemical & Process Engineering Technology, Universiti Malaysia Pahang, 26300 Gambang, Pahang, Malaysia
e-mail: najibrazali@ump.edu.my

M. S. Mahmud
Department of Chemical Engineering, Universiti Malaysia Pahang, 26300 Gambang, Pahang, Malaysia

M. Musa
MNR Multitech Sdn. Bhd., K02 Ground Floor, Kompleks UMP Holdings, 26300 Gambang, Pahang, Malaysia

M. K. N. Mohd Zuhan
Pusat Pengajian Diploma, Universiti Tun Hussein Onn, Hab Pendidikan Tinggi Pagoh, KM1, Jalan Panchor, Johor Pagoh, Malaysia

necessary to better understand the mechanisms at action and assist in creating an industry-specific optimal solution.

Keywords Base oils · Engine oil · Oxidative stability · Thermal stability · Infrared spectra

1 Introduction

Automotive lubricant formulation is a complicated process [1]. It is a carefully blended base oil with additives such as phenolic antioxidants, viscosity modifiers, friction modifiers, corrosion inhibitors, and dispersants [2–6]. The oxidative and thermal stability of lubricating oils is evaluated by the chemical reaction of base oil and different additives [7–9]. Base oils are the primary element of lubricants, typically accounting for more than 90% of the composition. As a result, the base oil composition and characteristics considerably impact the final lubricant's performance [10, 11]. Base oils are derived from several diverse sources, and their compositional differences directly affect lubricant performance. They are broadly classified into mineral, semi-synthetic, and fully synthetic. Lubricating oils begin as one or more of these three primary types before added additives [12, 13]. All-mineral base oils are conventional fuels derived from crude oil refining. Typically, paraffinic waxes are extracted from oils during the refining process, and an extra process is required to generate semi-synthetic oils.

Generally, synthetic oils are long-chain esters of low molecular weight poly-alpha-olefins (PAO) [14]. The effects of base oils and engine oil on oxidative and thermal stability were examined in this study. Oxidation stability is a chemical response that happens when lubricating oil comes into contact with oxygen. The escalation of oxidation rate is dependent upon temperatures, water, acids, catalysts and time. The ageing period of lubricating oil is likewise shortened when the temperature rises. Oxidation also affects the corrosion, anti-wear and viscosity properties of the lubricating oil. Hence, it is essential to evaluate the oxidative and thermal stability of base oil to ensure the quality and performance of the lubricating oils are protected [15]. The mechanism of base oil and engine oil deterioration in this paper has been studied in depth using standard thermogravimetric methods in an inert environment. In addition, the impact of heat treatment on the oxidative stability of base oils and engine oil was investigated using a Fourier Transform Infrared Spectrometer (FTIR).

Table 1 Physical characterization of base oils and engine oil

Parameter	Unit	Method	Value			
			Base 1	Base 2	Base 3	Engine oil
Colour	–	Visual	Clear	Clear	Clear	Yellowish
Density @ 15 °C	$\frac{g}{mL}$	ASTM D 4052	0.83	0.85	0.84	0.87
Viscosity @ 40 °C	cSt	ASTM D 445	18.18	29.32	34.57	107.00
Viscosity @ 100 °C	cSt	ASTM D 445	4.25	5.47	6.36	14.50
Viscosity Index	–	ASTM D 2270	144.90	124.70	136.90	138.00
Flash point	°C	ASTM D 92	240.00	238.00	238.00	> 215.00

2 Experimental

2.1 Materials

All oil samples were obtained from a Malaysian source based in Selangor. The samples' technical characteristics are presented in Table 1.

The physical characteristics of three base oils and engine oil are summarized in Table 1. This physical characteristic demonstrates unequivocally that motor oil has a maximum viscosity between 40 and 100 °C. Additionally, all samples had a viscosity index (VI) of greater than > 120. This parameter is critical because it provides information on the variation in the viscosity of lubricating oil as a function of temperature changes. Therefore, a more excellent VI value is preferred since it implies a slower rate of viscosity change [16]. Meanwhile, a low VI value indicates a significant degree of viscosity fluctuation, significantly increasing mechanical friction and wear caused by film loss [17].

2.2 Fourier Transform Infrared Spectrometer (FTIR)

10 mL of oil from each sample was dried in a drying oven at atmospheric pressure and 150 °C for 24 h. The functional groups were then examined using a Nicolet iS5 FTIR Spectrometer equipped with an iD7 ATR by Thermo Fischer Scientific, United States of America. Alkane, carbonyl, and hydroxyl groups are some of the most prevalent functional groups found in lubricating oil. The samples were scanned within a frequency range of 4000–500 cm^{-1} [18].

2.3   Thermogravimetric Analysis

The evaporation of volatile components and breakdown of the lubricating oils show the oil stability. The samples were evaluated using the ASTM E2550 technique on a TA Instruments TGA Q500. The study was done utilizing nitrogen gas blanketing to create an inert environment. A 20 mg of material from each sample was placed in a pan and heated at a rate of 10 °C min^{-1} between 30 and 900 °C [18].

3   Results and Discussion

3.1   Oxidative Stability of Base Oil by Using FTIR

At 150 °C, the FTIR spectra of fresh and heated oil samples for 24 h are shown in Fig. 1a–d. As can be observed, each sample contains numerous firm peaks. The typical frequency distributions are assigned to the functional categories indicated in Table 2 [19–22]. Infrared spectroscopy was used to see the vibration or absorption of CH_2 and CH_3 in all four lubricants that correspond to aliphatic hydrocarbon groups.
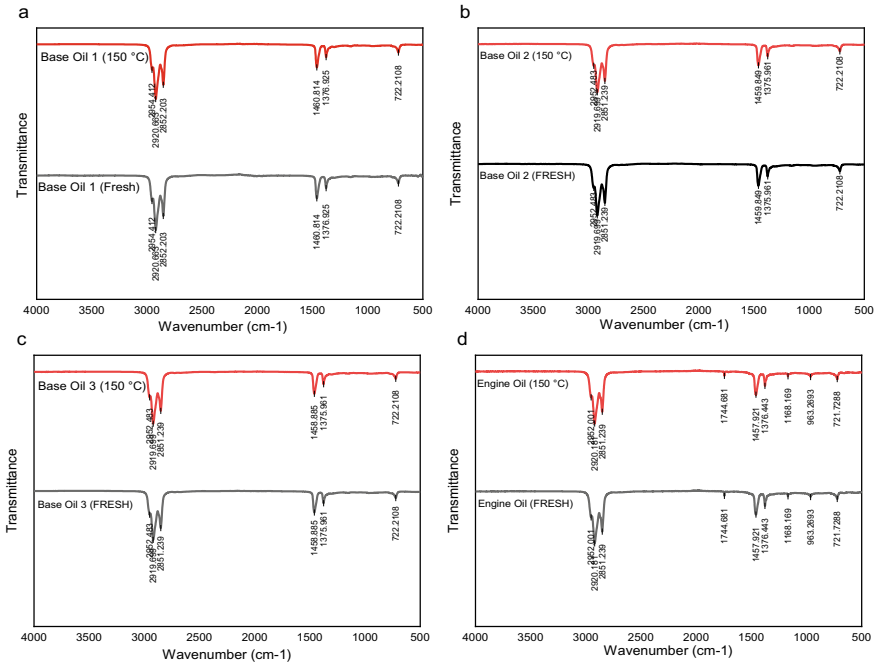

Fig. 1   FTIR spectra for three different base oils and engine oil

Table 2 FTIR spectra assignment for base oil one, base oil two, base oil three, and engine oil

Type	Functional group assignment	Group	Frequency range (cm^{-1})
Aliphatic hydrocarbon	Asymmetric CH$_3$ stretching vibration	$-$CH$_3$	~ 2952.07
	Asymmetric CH$_2$ absorption	$-$CH$_2-$	~ 2919.53
	Symmetric CH$_2$ absorption	$-$CH$_2-$	~ 2851.15
	Asymmetric CH$_3$ deformation vibration	$-$CH$_3$	~ 1458.02
	Symmetric CH$_3$ vibration	$-$CH$_3$	~ 1376.19
	Rocking absorption of $-$(CH$_2$)$_n-$ (4 or more CH$_2$ in a row)	$-$CH$_{2n}-$	~ 721.57
Olefin	Carbon-Hydrogen Deformation $-$CH=CH$-$ (trans)	$-$CH $=$ CH$-$	963.65
Aliphatic ester	Saturated C=O Stretch	C $=$ O	1744.68
	C$-$O$-$C in long-chain saturated fatty acid	C $-$ O $-$ C	1168.21

At 2952 and 1458 cm^{-1} the CH$_3$ asymmetric stretching and deformation vibration occurs, the CH$_3$ symmetric vibration band arises at 1376 cm^{-1} and CH$_2$ asymmetric and symmetric absorption bands appear at 2920 and 2851 cm^{-1}. A sharp and robust band was seen at 721 cm^{-1} suggesting that rocking absorption of four or more CH$_2$ in a row. This band indicates the abundance of samples containing long-chain aliphatic compounds. Three additional peaks were identified in Fig. 1d of engine oil that corresponded to the olefin and aliphatic ester functional groups. The peak at 963.65 cm^{-1} corresponded to the deformation of CH=CH, the saturated C=O stretch at 1744.68 cm^{-1} and C$-$O$-$C in long-chain saturated fatty acids at 1168.21 cm^{-1}. These findings combined engine oil with a base oil comprising long-chain alkanes, saturated fatty acid esters, and olefin.

Additionally, Fig. 1a–d demonstrated no significant differences in the infrared spectra of heated and fresh oil samples, with no new powerful, distinctive peaks appearing throughout the whole wavelength range. Additionally, absorbances at 2951, 2919, 2852, 1459, 1376, and 721 cm^{-1} indicated that long-chain alkanes, carbonyl compounds, and unsaturated hydrocarbons remained prevalent in the aged oils. Gan et al. previously discovered that the O$-$H stretching vibration recorded at 3645 cm^{-1} declined with increasing temperature until it was no longer detectable, suggesting that phenolic antioxidants were consumed constantly. At 300 °C, the C=C stretching vibration was discovered, indicating that long-chain hydrocarbons were broken down into olefins and other compounds due to temperature [23]. Jiabao et al.

said that when the lubricant undergoes thermal ageing, the peaks at a range of 1715 and 1736 cm^{-1} typical of the C=O bond produced by oxidation would arise [24].

As seen in Fig. 1a–c, the peaks that correspond to the C=O bond do not appear in the FTIR spectrum. As a result, the C=O bond would not appear following the 24-h heating period at 150 °C. Meanwhile, the engine oil spectrum from Fig. 1d revealed the presence of peaks at 1744.681 and 1168.169 cm^{-1} new engine oil was ascribed to the C=O (aliphatic ester) and C=C deformations, respectively (olefin). Additionally, there are no significant changes in the spectra following the heat treatment technique. The FTIR data suggest that oxidation of the motor oil via the production of C=O did not occur during the heat treatment since the saturated C=O stretching is already present in the new engine oil. In other words, no apparent change in the chemical structure occurs at the above-mentioned operating conditions. Additionally, this study demonstrated that the long-chain hydrocarbon did not degrade into olefin during heat degradation. No phenolic antioxidant was used in the base and engine oils due to the absence of vibration or absorption of the phenolic component using infrared spectroscopy.

3.2 Thermal Stability of Base Oil by Using Thermogravimetric Analysis (TGA)

The traditional weight loss curves for all the samples base oil one, base oil two, base oil three, and engine oil were done using inert gas at a constant heating rate of 10 °C min^{-1} from 30 to 900 °C, as shown in Fig. 2. All samples decompose in a single stage, with base oil one and engine oil including residue following heat breakdown. The wide temperature range over which breakdown occurs showed that these materials had a broad molecular weight distribution [25]. Additionally, figure two demonstrated that all lubricants began to deteriorate at temperatures above 200 °C. The weight loss distributions of all samples throughout the specified temperature range are summarized in Table 3. According to Table 3, engine oil exhibited the highest thermal stability at 5, 50, and 90% weight loss. Base oil three, base oil two, and base oil one all followed this pattern. Nik et al. hypothesized that weight variations in specimens might be caused by the creation and breakdown of physical and chemical interactions at high temperatures [26].

Meanwhile, TGA curves were utilized to determine the samples' onset temperatures. The TGA degradation onset temperature is used to assess the samples' resistance to thermal deterioration. It is calculated by extending the horizontal baseline of TGA curves and intercepting the curve with the tangent. The higher decomposition onset temperature implies more excellent thermal stability [27]. According to Fig. 2, engine oil has the most excellent onset temperature of 298 °C, followed by base oil three (276 °C), base oil two (275 °C), and base oil one (262 °C). As revealed by FTIR spectroscopy, the presence of aliphatic ester confirms the enhanced thermal stability of engine oil. Ester molecules are inherently polar, which provides them
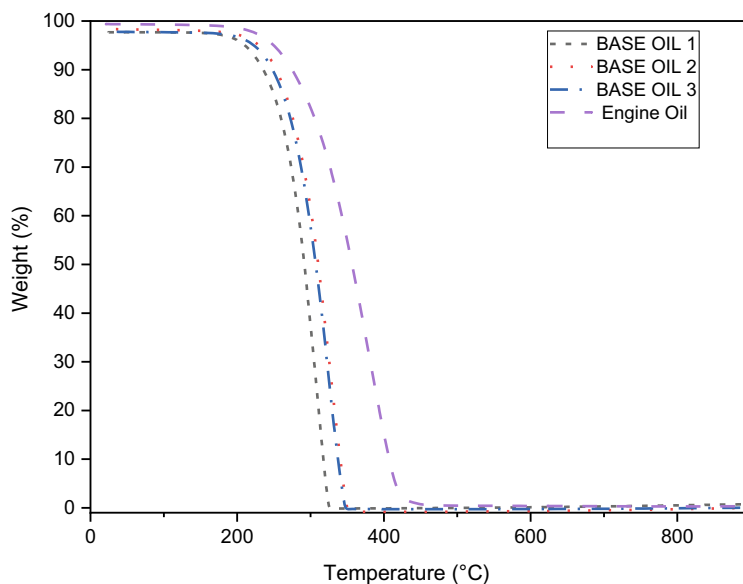
Fig. 2 Weight loss of lubricating oils by using TGA

Table 3 The distribution of weight loss of all samples at stipulated temperature range

Lubricating oil	$T_{5\%}$ (°C)	$T_{50\%}$ (°C)	$T_{90\%}$ (°C)	T_{onset}(°C)	T_{final}(°C)	Residue (%)
Base 1	210.46	291.52	317.47	262.00	324.00	0.70
Base 2	222.73	307.09	337.41	275.00	344.00	0.00
Base 3	229.74	310.43	340.60	276.00	349.00	0.00
Engine oil	249.82	356.63	407.27	298.00	418.00	0.35

an attraction for one another in the liquid form. This implies they are less prone to evaporation and so contribute to the engine oil's thermal stability [19].

The data in Fig. 2 and Table 3 indicated that high viscosity oils had more excellent thermal stability than low viscosity oils. This is confirmed because base oil one has the lowest viscosity, followed by base oil two, three, and engine oil. This resulted in a significant connection between oil viscosity and heat stability. In addition, due to an olefin viscosity modifier, the engine oil has a greater viscosity, typically composed of Ethylene Propylene (EP) copolymers. This copolymer reduced the concentration of oxidatively labile tertiary protons, increasing the lubricating oil's thermal stability [28].

4   Conclusion

According to the initial results and discussions, the following deductions may be attained:

(1)   There is no alteration in the FTIR spectra of all heated samples compared to the fresh samples. Furthermore, no new peaks emerged at the required temperature range of 150 °C for 24 h, suggesting that all the lubricating oils are not prone to oxidation. The FTIR spectra further highlighted that no phenolic antioxidant compounds are being utilized in all lubricating oils.

(2)   TGA is a reliable technique for the thermal stability study. All lubricating oil starts to deteriorate around 200 °C. The engine oil has the most excellent onset temperature of 298 °C, followed by base oil three, base oil two, and base oil one. The onset temperature for the base oils is comparable to the engine oil.

(3)   TGA findings also revealed that engine oil demonstrated the highest thermal stability at 5, 50, and 90% weight loss, followed by base oil three, base oil two, and base oil one. The increased thermal stability in engine oil is attributed to the presence of aliphatic ester.

(4)   It is advised that numerous additives are utilized to evaluate the influence of additives on lubricating oil performances.

References

1.   Meena KR, Dhiman R, Singh K, Kumar S, Sharma A, Kanwar SS, Mondal R, Das S, Franco OL, Mandal AK (2021) Purification and identification of a surfactin biosurfactant and engine oil degradation by Bacillus velezensis KLP2016. Microb Cell Fact 20:1–12. https://doi.org/10.1186/s12934-021-01519-0

2.   Wu P, Chen X, Zhang C, Zhang J, Luo J, Zhang J (2021) Modified graphene as novel lubricating additive with high dispersion stability in oil. Friction 9:143–154. https://doi.org/10.1007/s40544-019-0359-2

3.   Cyriac F, Tee XY, Poornachary SK, Chow PS (2021) Influence of structural factors on the tribological performance of organic friction modifiers. Friction 9:380–400. https://doi.org/10.1007/s40544-020-0385-0

4.   Zhan W, Jia D, Jin YL, Duan HT, Li J, Liu J (2020) Synthesis and evaluation of amines/phenolics antioxidant for TMPTO base oil. Ind Lubr Tribol 72:46–53. https://doi.org/10.1108/ILT-02-2019-0053

5. Moriceau G, Lester D, Pappas GS, O'Hora P, Winn J, Smith T, Perrier S (2019) Well-defined alkyl functional poly(styrene-co-maleic anhydride) architectures as pour point and viscosity modifiers for lubricating oil. Energy Fuels 33:7257–7264. https://doi.org/10.1021/acs.energy fuels.9b01470

6. Noor El-Din MR, Mishrif MR, Kailas SV, Suvin PS, Mannekote JK (2018) Studying the lubricity of new eco-friendly cutting oil formulation in metal working fluid. Ind Lubr Tribol 70:1569–1579. https://doi.org/10.1108/ILT-11-2017-0330

7. Sneha E, Rani S, Arif M (2019) Evaluation of lubricant properties of vegetable oils as base oil for industrial lubricant. IOP Conf Ser Mater Sci Eng 624. https://doi.org/10.1088/1757-899X/624/1/012022

8. Owuna FJ (2020) Stability of vegetable based oils used in the formulation of ecofriendly lubricants—a review. Egypt J Pet 29:251–256. https://doi.org/10.1016/j.ejpe.2020.09.003

9. Higgins CL, Filip SV, Afsar A, Hayes W (2019) Evaluation of thermal and oxidative stability of three generations of phenolic based novel dendritic fuel and lubricant additives. React Funct Polym 142:119–127. https://doi.org/10.1016/j.reactfunctpolym.2019.06.009

10. Nour AH, Elamin EO, Nour AH, Alara OR (2021) Dataset on the recycling of used engine oil through solvent extraction. Chem Data Collect 31:100598. https://doi.org/10.1016/j.cdc.2020.100598

11. Konishi M, Washizu H (2020) Understanding the effect of the base oil on the physical adsorption process of organic additives using molecular dynamics. Tribol Int 149:105568. https://doi.org/10.1016/j.triboint.2019.01.027

12. Kim HM, Spikes H (2020) Correlation of elastohydrodynamic friction with molecular structure of highly refined hydrocarbon base oils. Tribol Lett 68:1–14. https://doi.org/10.1007/s11249-020-1265-5

13. Hong HS, Engel C, Filippini B, Slocum S, Qureshi F, Higuchi T (2017) Challenging conventional wisdom by utilizing group II base oils in fuel efficient axle oils. SAE Int J Fuels Lubr 10:857–863. https://doi.org/10.4271/2017-01-2356

14. Ashmawy AM, Elnaggar ESM, Mohamed MG, Hamam MC (2020) Preparation and evaluation of new liquid crystal compounds as flow improvers for waxy crude oil. J Dispers Sci Technol 0:1–15. https://doi.org/10.1080/01932691.2020.1841000

15. Kovalsky BI, Bezborodov YN, Lysyannikova NN, Kravtsova EG, Lysyannikov AV, Shram VG (2019) Research of engine and transmission oils for thermo-oxidative stability with cyclic temperature changes. IOP Conf Ser Mater Sci Eng 537. https://doi.org/10.1088/1757-899X/537/6/062074

16. Epelle EI, Otaru AJ, Zubair YO, Awele OJ (2017) Improving the viscosity index of used lubricating oil by solvent extraction. Int Res J Eng Technol. www.irjet.net

17. Stanciu I (2017) Viscosity index improvers for multi-grade oil of copolymers polyethylene-propylene and hydrogenated poly (isoprene-co-styrene). J Sci Arts Year 17:771–778

18. Mahmud MS, Ishak S, Razali MN, Abdul Aziz MA, Musa M (2019) Grease quality issues on middle voltage switchgear: corrosivity, resistivity, safety and ageing. IIUM Eng J 20:216–228. https://doi.org/10.31436/iiumej.v20i1.995

19. L.R. Rudnick, Lubricant Additives Chemistry and Applications, Second Edi, CRC Press, Delaware, Usa, 2008. http://objdig.ufrj.br/64/teses/883343.pdf.

20. Pan J, Cheng Y, Yang J (2016) Structural degradation of a lithium lubricating grease after thermal ageing. J Chem Eng Japan 49:579–587. https://doi.org/10.1252/jcej.15we200

21. Zakeri H (2017) Study of oxidative stability of lubricants blended with p-substituted phenolic antioxidants. Asian J Chem 29:1757–1760

22. Cousseau T, Graça B, Campos A, Seabra J (2015) Grease aging effects on film formation under fully-flooded and starved lubrication. Lubricants 3:197–221. https://doi.org/10.3390/lubricant s3020197

23. Gan Z, Yao T, Zhang M, Hu J, Liao X, Shen Y (2020) Effect of temperature on the composition of a synthetic hydrocarbon aviation lubricating oil. Materials (Basel) 13. https://doi.org/10.3390/ma13071606

24. Jiabao P, Yanhai C, Jinyong Y (2015) Effect of heat treatment on the lubricating properties of lithium lubricating grease. RSC Adv 5:58686–58693. https://doi.org/10.1039/c5ra08917d
25. Cucos A, Budrugeac P, Lingvay I, Bors AM, Voina A (2018) Comparative TG/DTG/DTA+FTIR studies concerning the stability of some mineral and vegetable electro-insulating fluids. Rev Chim 69:2366–2371. https://doi.org/10.37358/rc.18.9.6535
26. Wan Nik WB, Ani FN, Masjuki HH (2005) Thermal stability evaluation of palm oil as energy transport media. Energy Convers Manag 46:2198–2215. https://doi.org/10.1016/j.enconman.2004.10.008
27. Sharma UC, Sachan S (2019) Experimental investigation on thermal stability of karanja biolubricant base oil. Biofuels and Biolubricant 7:203–211
28. Dombrowski E (2007) Lubricant and lubrication. Wiley-VCH Verlag GmbH & Co

Effect of MHD and Casson Free Convection Boundary Layer Flow Over a Stretching Sheet in Hybrid Nanofluid

Sulaiman M. Ibrahim and Mohammed Z. Swalmeh

Abstract This paper examines the heat transfer characteristics of free convection boundary layer flow over a stretching Sheet with a hybrid nanofluid in the Casson field subject to constant heat flux boundary condition. The dimensional governing equations and boundary layer equations are transformed into partial differential equations (PDEs) using some suitable similarity transformation and physical properties. The Keller box method which is an implicit finite difference technique was applied to obtain the numerical solution of the corresponding PDEs. Numerical computations are done using the MATLAB subroutine programming and the results are presented in tables and figures. The impacts of hybrid nanofluids Casson parameters on the local skin friction coefficient and local Nusselt number, beside the velocity and temperature is studied. Hybrid nanofluid has a lower velocity and temperature in addition to possessing the highest local Nusselt number when compared with nanofluid. The outcomes of the local Nusselt number and the wall temperature for the Newtonian fluid are detected to be in perfect accuracy with the literature.

Keywords Magnetohydrodynamic · Hybrid nanofluid · Casson fluid · Stretching sheet

Nomenclature

B_0	Magnetic field
k_f	Thermal conductivity of the based fluid
k_{nf}	Thermal conductivity of the nanofluid
k_{hnf}	Thermal conductivity of the hybrid nanofluid

S. M. Ibrahim
Institute of Strategic Industrial Decision Modelling (ISIDM), School of Quantitative Sciences, Universiti Utara Malaysia, 06010 Sintok, Kedah, Malaysia

M. Z. Swalmeh (✉)
Faculty of Arts and Sciences, Aqaba University of Technology, Aqaba 77110, Jordan
e-mail: msawalmeh@aut.edu.jo

c_p	Specific heat
$(\rho c_p)_f$	Heat capacity
$(\rho c_p)_{nf}$	Heat capacity of the nanfluid
$(\rho c_p)_{hnf}$	Heat capacity of the hybrid nanofluid
M	Magnetic parameter
q_w	Heat flux coefficient
Re	Local Reynold's number
u_s	Stream velocity
u_w	Stretching velocity
T_w	Wall temperature
T_∞	Temperature of the ambient fluids
x, y	Coordinates (m)
Pr	Prandtl number

Greek symbols

χ	Nanoparticle volume fraction parameter
η	Dimensionless similarity variable
ψ	Stream function
ρ	Density
μ_{nf}	Dynamic viscosity of the nanofluid
μ_{hnf}	Dynamic viscosity of the hybrid nanofluid

Subscripts

θ	Temperature
nf	Nanofluid
hnf	Hybrid nanofluid
∞	Ambient environment

1 Introduction

The momentous evolution of various technology for the application and manufacturing of numerous industrial and engineering components and devices has recently received a lot of attention. Many of these devices found in the industries often intensify their thermal characteristics thereby reducing their capacity of heat bearing with the passage of time [1]. Some of the known fluids used for maintaining the temperature around any given design limits includes water, lubricants, air, and many more.

However, the above-mentioned liquids are insufficient to justify the industrial needs. These drawbacks lead to numerous studies on enhanced heat transfer around various geometries [2].

Heat transfer enhancement plays an important role in various industrial and engineering applications due to its improving rate of heat removal and deposition on several geometrical surface [3]. However, because of the poor thermophysical properties of the working fluid, the heat transfer are likely to demonstrates certain deficiencies [4]. Some of these deficiencies can be improved by the use of various kinds of swirl generators. In addition, various geometries also have important role to play in enhancing heat transfer. Recently, some studies on Nusselt number and friction factors of inclined limb in cylindrical dust and the axial rib with screw tape were presented by [5–7]. More literatures also considered other problems such as the free convection flow of Casson nanofluid in the presence of magnetic field [8] and [9] investigated the unsteady radiative flow of Nano and Casson fluids over a vertical plate. For more reference on this topic (see [9–13]). Currently, the research direction in this subject focus on hybrid nanofluid. For instance [14], investigated the unsteady flow and heat transfer over a shrinking sheet in a hybrid nanofluid. Also, researchers such as [15–18] studied the heat transfer over different surfaces in a hybrid nanofluid.

Motivated by the above literature, the study aims to investigate the heat transfer of free convection boundary layer flow over a stretching surface with a hybrid nanofluid in the Casson field subject to constant heat flux boundary condition. The numeric Keller box method [19]; was employed to investigate the free convection flow of Casson hybrid nanofluid and influenced by a magnetic field on a stretching sheet. To the best of our knowledge, the result obtained in this article is new and has neither been considered or studied by other researchers. The computational results from this experiment are plotted in tables to figures and discussed.

2 Mathematical Formulation

In this investigation, the based Casson hybrid nanofluids Sodium Alginate, that include (Cu, Ag)–Al_2O_3 nanoparticles, were considered. In addition, the magnetic (MHD) field with natural convection boundary flow, as well as the constant heat flux boundary condition is studied. The fluid flow has flowed on a stretching sheet, where the flow has initiated at $y = 0$, and is being stabilized in $y > 0$. The boundary condition, Constant heat flux (q_w), was ditto considered, as presented in Fig. 1. The flow is offered to be in the x-direction, consequently, expands along with the stretching sheet surface in the up orientation (y-axis), which is orthogonal to the surface. The influences of Casson Hybrid nanofluid, magnetic and electrical conductivity mediums, have affected the momentum equation.

The gained rheological features of Casson fluid are obtained via the equation (see [10]).

Fig. 1 A physical model of the problem
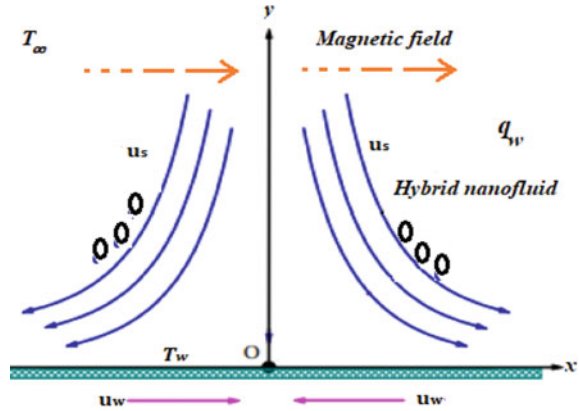
$$
\tau_{ij} =
\begin{cases}
2\left(\mu_B + p_y\big/\sqrt{2\pi}\right)e_{ij} & \pi > \pi_c, \\
2\left(\mu_B + p_Y\big/\sqrt{2\pi_C}\right)e_{ij} & \pi < \pi_c,
\end{cases}
\tag{1}
$$

Hence, depending on the all previous suggestions, the governing equations of above model, Fig. 1, the continuity, momentum and thermal equations, for MHD Hybrid nanofluid on a stretching sheet, Casson field, can be obtained as follows [15, 20]:

$$
\frac{\partial \tilde{u}}{\partial \tilde{x}} + \frac{\partial \tilde{v}}{\partial \tilde{y}} = 0,
\tag{2}
$$

$$
\tilde{u}\frac{\partial \tilde{u}}{\partial \tilde{x}} + \tilde{v}\frac{\partial \tilde{u}}{\partial \tilde{y}} = \nu_{hnf}\left(1 + \frac{1}{\beta}\right)\frac{\partial^2 \tilde{u}}{\partial \tilde{y}^2} - \frac{\sigma_{hnf}}{\rho_{hnf}}B_0^2 \tilde{u},
\tag{3}
$$

$$
\tilde{u}\frac{\partial T}{\partial \tilde{x}} + \tilde{v}\frac{\partial T}{\partial \tilde{y}} = \frac{\kappa_{hnf}}{(\rho C_p)_{hnf}}\frac{\partial^2 T}{\partial \tilde{y}^2}
\tag{4}
$$

with the studied constant heat flux boundary condition:

$$
\tilde{u} = u_w(\tilde{x}) = a\tilde{x}, \ \tilde{v} = 0, \ \frac{\partial T}{\partial \tilde{y}} = \frac{-q_w}{k_f} \text{ at } \tilde{y} = 0,
$$
$$
\tilde{u} \to 0, \ T \to T_\infty \text{ as } \tilde{y} \to \infty,
\tag{5}
$$

where, β is called the Casson parameter, and B_0^2 is the magnetic field strength, for acquainting all other studied and used symbols and quantities, they are defined in nomenclature list. The nanofluid quantities, α_{nf}, ρ_{nf}, $(\rho c_p)_{nf}$, μ_{nf}, k_{nf} and σ_{nf}, and hybrid nanofluid quantities, α_{hnf}, ρ_{hnf}, $(\rho c_p)_{hnf}$, μ_{hnf}, k_{nf} and σ_{hnf}, can be presented in Table 1.

Table 1 Thermo-physical properties [21]

Properties of nanofluid
$\rho_{nf} = (1 - \chi)\rho_f + \chi\rho_s,$
$(\rho c_p)_{nf} = (1 - \chi)(\rho c_p)_f + \chi(\rho c_p)_s,$
$\mu_{nf} = \frac{\mu_f}{(1-\chi)^{2.5}},$
$\frac{k_{nf}}{k_f} = \frac{(k_s + 2k_f) - 2\chi(k_f - k_s)}{(k_s + 2k_f) + \chi(k_f - k_s)},$
$\frac{\sigma_{nf}}{\sigma_f} = 1 + \frac{3(\sigma - 1)\chi}{(\sigma + 2) - (\sigma - 1)\chi}, \quad \sigma = \frac{\sigma_s}{\sigma_f}$
Properties of hybrid nanofluid
$\rho_{hnf} = (1 - \chi_2)[(1 - \chi_1)\rho_f + \chi_1\rho_{s1}] + \chi_2\rho_{s2},$
$(\rho c_p)_{hnf} = (1 - \chi_2)[(1 - \chi_1)(\rho Cp)_f + \chi_1(\rho Cp)_{s1}] + \chi_2(\rho Cp)_{s2},$
$\mu_{hnf} = \frac{\mu_f}{(1-\chi_1)^{2.5}(1-\chi_2)^{2.5}},$
$\frac{k_{hnf}}{k_{bf}} = \frac{k_{s2} + 2k_{bf} - 2\chi_2(k_{bf} - k_{s2})}{k_{s2} + 2k_{bf} + \chi_2(k_{bf} - k_{s2})},$
$\frac{k_{bf}}{k_f} = \frac{k_{s1} + 2k_f - 2\chi_1(k_f - k_{s1})}{k_{s1} + 2k_f + \chi_1(k_f - k_2)},$
$\frac{\sigma_{hnf}}{\sigma_{bf}} = [\frac{\sigma_{s2} + 2\sigma_{bf} - 2\chi_2(\sigma_{bf} - \sigma_{s2})}{\sigma_{s2} + 2\sigma_{bf} + \chi_2(\sigma_{bf} - \sigma_{s2})}],$
$\frac{\sigma_{bf}}{\sigma_f} = [\frac{\sigma_{s1} + 2\sigma_f - 2\chi_1(\sigma_f - \sigma_{s1})}{\sigma_{s1} + 2\sigma_f + \chi_1(\sigma_f - \sigma_{s1})}]$

Consequently, to transform the above dimensional governing Eqs. (2)–(4), and boundary condition (5), to partial differential equations, we utilize the following similarity transformations, as well the physical properties in Table 1 (see [10, 20]).

$$\tilde{u} = \frac{\partial \psi}{\partial \tilde{y}}, \tilde{v} = -\frac{\partial \psi}{\partial \tilde{x}},$$

$$\psi = (a\tilde{v})^{1/2}\tilde{x}f(\eta),$$

$$\eta = (a\tilde{v})^{1/2}\tilde{y}, \theta(\eta) = \frac{T - T_\infty}{T_w - T_\infty}. \tag{6}$$

such that, ψ is called the stream function.

Here, by substituting the Eq. (6) and the hybrid nanofluid properties, Table 1, in Eqs. (2)–(5), we get the equations as below:

$$\frac{\rho_f}{\rho_{hnf}}\left(\frac{1}{(1-\chi_1)^{2.5}(1-\chi_2)^{2.5}}\right)\left(1 + \frac{1}{\beta}\right)f'''$$
$$+ ff'' - (f')^2 - \frac{\rho_f}{\rho_{nf}}\frac{\sigma_{nf}}{\sigma_f}Mf' = 0 \tag{7}$$

$$\frac{1}{\text{Pr}}\left[\frac{k_{hnf}/k_f}{(1-\chi_2)[(1-\chi_1)+\chi_1(\rho Cp)_{s1}/(\rho Cp)_f]+\chi_2(\rho Cp)_{s2}/(\rho Cp)_f}\right]\theta''$$
$$+ f\theta' = 0, \tag{8}$$

and the considering boundary condition, in this study, will be expressed as

$$f' = 1, \ f = 0, \ \theta' = -1 \text{ as } \eta = 0,$$
$$f' \to 0, \ \theta \to 0, \text{ as } \eta = \infty. \tag{9}$$

The parameters χ_1 and χ_2, nanoparticle volume fraction, refers to Al_2O_3 and (Cu or Ag), respectively. Besides, $\text{Pr} = \frac{v_f}{\alpha_f}$ is the Prandtl number and $\text{M} = \left(\frac{\sigma_f B_o^2}{\rho_f a}\right)$ is magnetic parameter.

On the other hand, the important engineering physical quantities are localized, which are the local skin friction coefficient C_f and the local Nusselt number Nu, which are displayed

$$C_f = \left(\frac{\tau_w}{\rho U_w^2}\right), \text{ and } Nu = \left(\frac{aq_w}{k_f(T_w - T_\infty)}\right), \tag{12}$$

τ_w, and q_w are shear stress, heat flux coefficient on the plane of the stretching sheet wall, and are expressed as below.

$$\tau_w = \mu_{hnf}\left(\frac{\partial^2 u}{\partial \tilde{y}^2}\right)_{\tilde{y}=0}, \ q_w = -k_{hnf}\left(\frac{\partial T}{\partial \tilde{y}}\right)_{\tilde{y}=0}. \tag{13}$$

substituting the Eqs. (7) and (11), C_f and Nu will be in the next form

$$\text{Re}^{1/2}C_f = \frac{1}{(1-\chi)^{2.5}}\left(1+\frac{1}{\beta}\right)f''(0), \ \text{Re}^{-1\backslash 2}Nu = -\frac{k_{hnf}}{k_f}\frac{1}{\theta(0)}, \tag{14}$$

such that, $\text{Re}^{1/2} = (a\,\tilde{x}^2/v_f)$ is indicated as the local Reynolds number.

3   Results and Discussion

This section present the numerical performance of MHD effects and magnetic impacts of hybrid nanofluids based on Sodium Alginate/ Ethylene Glycol around a stretching sheet. This was carried out in the presence of free convection and the results are reported in tables and figures below. In addition to the above problem, the study also considered the constant heat flux boundary condition as shown the results presented. The thermo-physical characteristics of used nanoparticles and Sodium Alginate/ Ethylene Glycol is presented in Table 1.

Table 2 Thermophysical properties of nanoparticles of two base Casson Hybrid nanofluids with different mathematical values [2, 8, 22, 23]

Physical properties	Based fluids		Used nanoparticles		
	Sodium Alginate	Ethylene Glycol	Cu	Al_2O_3	Ag
k (W/mK)	0.6376	0.253	401	40	429
ρ(kg/m^3)	989	1115	8933	3970	10,500
c_p (J/kgK)	4175	2430	385	765	235
σ s(Sm^{-1})	2.6×10^{-4}	10.7×10^{-5}	5.96×10^7	3.5×10^7	6.3×10^7
Pr	6.45	195			

Table 3 Comparison of $Re^{-1/2}Nu$ and $\theta(0)$ with several Newtonian fluid (M $= 0$, $\beta = \infty$, and $\chi_1 = \chi_2 = 0$), with different values of Prandlt number Pr

Pr	Elbashbeshy [24]		Salleh et al. [20]		Present	
	Nu	$\theta(0)$	Nu	$\theta(0)$	Nu	$\theta(0)$
0.72	0.46780	2.13767	0.46317	2.15902	0.46324	2.1595
1	0.58210	1.71792	0.58210	1.71828	0.58221	1.71831
3	1.16525		1.16522	0.85817	1.16533	0.85819
5	…	…	…	0.63770	1.5684	0.63777
7	…	…	…	0.52755	1.8959	0.52755
10	2.30730	0.43341	2.30728	0.43322	2.3087	0.43330
100	…	…	…	0.12851	7.7812	0.12857

Also, Tables 2 and 3 present the numerical results comparing the local skin friction and local Nusselt number for different values of Pr, using different Newtonian fluid. The comparison was done using recent published results. It is obvious that the results from this study are in excellent agreement with those considered from recent studies.

In Table 4, we present the variations in the local skin friction and local Nusselt number with respect to the hybrid nanofluid and mono nanofluid. This was carried out in the presence of the nanoparticles suspended in based fluid, with effects various parameters including the Casson, nanoparticle volume fraction, and magnetic parameter. The results presented in the table show that some observed physical properties changes between the mono nanofluids and the hybrid nanofluids, which include Al_2O_3\Sodium Alginate, referring to nanofluids ($\chi_2 = 0$), possess a higher local skin friction from (Cu or Ag)–Al_2O_3, as hybrid nanofluid. In addition, Al_2O_3 possess a lower local Nusselt number from (Cu or Ag)–Al_2O_3\Sodium Alginate compare to the hybrid nanofluid. Consequently, Cu–Al_2O_3 hybrid nanofluid has a lower local skin friction and local Nusselt number when compared to Ag–Al_2O_3 hybrid nanofluid, with the influence of different parameters values for χ_2, β, and M. Further, an increase in the parameter χ_2 will decrease the local skin friction and increase the local nusselt

Table 4 Outcomes of C_f and Nu, for various values of Casson hybrid nanofluid parameters, χ_2, β, and M, with $\chi_1 = 0.1$

			Hybrid nanofluid		Nanofluid	Hybrid nanofluid		Nanofluid
			Cu Al$_2$O$_3$ Sodium Alginate	Ag Al$_2$O$_3$ Sodium Alginate	Al$_2$O$_3$ Sodium Alginate	Cu Al$_2$O$_3$ Sodium Alginate	Ag Al$_2$O$_3$ Sodium Alginate	Al$_2$O$_3$ Sodium Alginate
β	χ_2	M	C_f	C_f	C_f	Nu	Nu	Nu
4	0	0.1	− 6.1958	− 6.1958	− 6.1958	2.9242	2.9242	2.9242
	0.05		− 7.5931	− 7.7692		3.7302	3.7268	
	0.1		− 9.0974	− 9.4384		4.7365	4.7333	
1	0	0.1			− 1.9593			2.9811
1	0.1		− 2.8767	− 2.9846		4.8028	4.822	
3	0				− 4.7993			2.9326
3	0.1		− 7.0465	− 7.3106		4.7495	4.7465	
5	0				− 7.5883			2.9183
5	0.1		− 11.142	− 11.559		4.7280	4.7242	
4	0	0.1			− 6.1958			2.9242
	0.1	0.1	− 9.0974	− 9.4383		4.7365	4.7333	
	0	0.3			− 6.8863			2.8911
	0.1	0.3	− 10.382	− 10.769		4.6768	4.6709	
	0	0.8			− 8.3667			2.7635
	0.1	0.8	− 13.046	− 13.535		4.4972	4.4807	

number, in presence of based fluid suspended nanoparticles. Also, an increase in the parameter β and M will decrease the physical quantities Nu and C_f.

Figures 2, 3, 4, 5, 6 and 7 demonstrate the mutual correlation between the results of (Ag and GO)–Al$_2$O$_3$ nanoparticles based in Sodium Alginate for temperature and velocity profiles, with different values of the Casson β, and magnetic M parameters, as well as nanoparticle volume fraction parameter χ, with several values of η. We observe that the temperature profile $\theta(\eta)$, in Figs. 2, 4, and 6, increases as increase the Casson and magnetic parameters, but it decreases with an increase in the nanoparticle volume fraction parameter. On the other hand, when all studied parameter values are rise, the velocity profile values are reduced. It is also noticed that from these figures, the temperature and the velocity profiles for Al$_2$O$_3$/sodium alginate-based nanofluid is higher than the (Ag or Cu) Al$_2$O$_3$/sodium alginate-based hybrid nanofluid, this is because of the different density between used hybrid nanofluid, and nanofluid. Besides, it is gained that Ag–Al$_2$O$_3$ has a high temperature as compared to Cu–Al$_2$O$_3$/sodium alginate-based hybrid nanofluid, with different values of parameters β, M, and χ. Also, Cu–Al$_2$O$_3$ has a lower velocity profile compared with
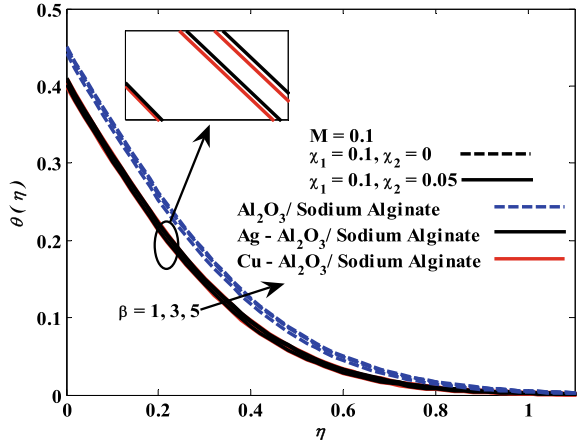
Fig. 2 Temperature against β

Fig. 3 Velocity against β
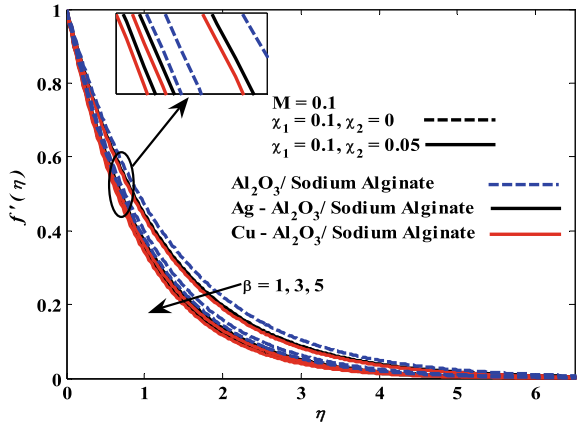

Fig. 4 Temperature against M
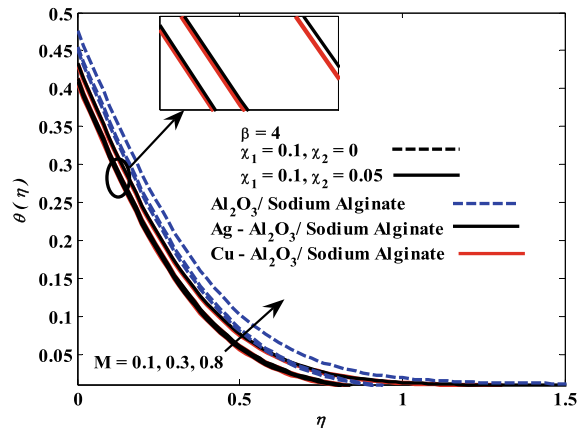
Fig. 5 Velocity against M
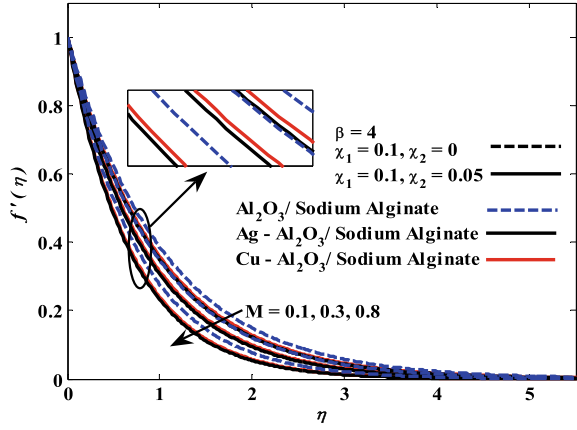
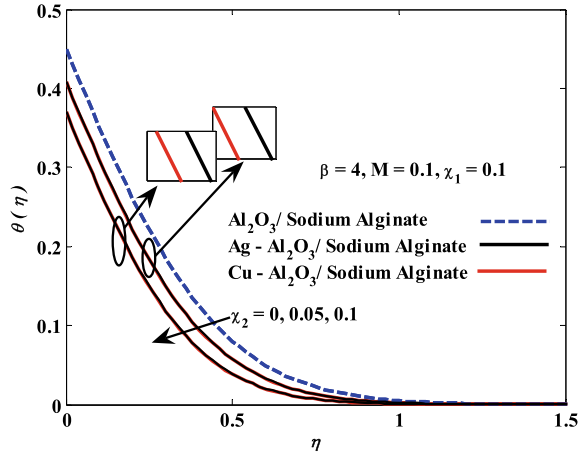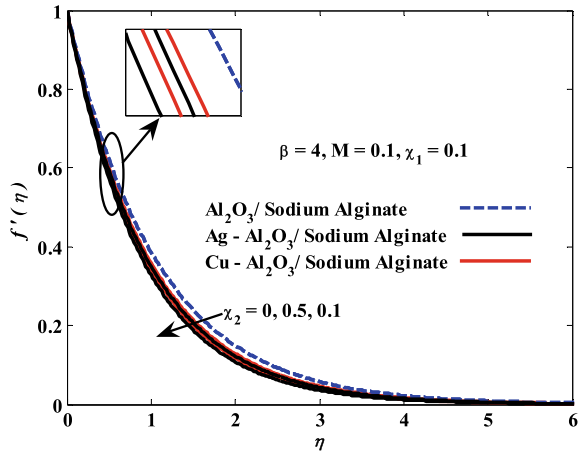**Fig. 6** Temperature against χ_2

Fig. 7 Velocity against χ_2

Ag–Al$_2$O$_3$/sodium alginate, with an increase in the values of β. However, the opposite case happens, when values of the parameters χ and M increase, Cu–Al$_2$O$_3$ has a higher velocity profile compared with Ag–Al$_2$O$_3$/sodium alginate.

4 Conclusion

In this paper, we investigated the heat transfer properties of based Casson hybrid nanofluid containing (Cu, Ag)–Al$_2$O$_3$ nanoparticles which was suspended in sodium alginate based hybrid nanofluid towards stretching sheet. The governing equations of the problem is solved by the Keller box numerical method to obtain numeric results, and in turn analyzes the problem and the result of given parameters. The obtained results are further plotted and discussed for local skin friction and local Nusselt number in addition to velocity and temperature. The findings from this investigation are stated as follows:

I. The hybrid nanofluid possess the highest Nusselt number, in addition to the lowest C_f, temperature and velocity profiles compared to the nanofluid, irrespective the parameter value affecting them.

II. The combination of magnetic field strength and Casson parameter led to the limitation of velocity, and *Nu*, as well as raising the temperature. Also, the parameter of the nanoparticle volume fraction got in restricting the physical quantities, including velocity, temperature, and C_f but, at the same time boosting the Nusselt number.

III. Irrespective of the number of values influencing the parameters, it is obvious that the based hybrid nanofluid holds the highest temperature and velocity profiles compared to mono nanofluid.

IV. Lastly, the MHD hybrid nanofluid flow is clearly influenced by the volume fraction of the nanoparticle, magnetic, in addition to Casson parameters. Therefore, the results from this study present an important and useful knowledge to the field of fluid mechanics.

References

1. Khan A et al (2021) Chemically reactive nanofluid flow past a thin moving needle with viscous dissipation, magnetic effects and hall current. PLoS ONE 16(4):e0249264. https://doi.org/10.1371/journal.pone.0249264
2. Swalmeh M, Alkasasbeh H, Hussanan A, Mamat M (2019) Influence of micro-rotation and micro-inertia on nanofluid flow over a heated horizontal circular cylinder with free convection. Theor Appl Mech 46(2):125–145. https://doi.org/10.2298/TAM181120008S
3. Faqih FMA, Swalmeh MZ, Ibrahim SM, Saeed HGB, Alkasasbeh HT, Sarairah EA (2021) Study of the MHD flow of Casson nanofluid in the presence of oxides nanoparticles based C2H6O2/H2O under constant heat flux boundary condition. Int Rev Mech Eng IREME 15(3) (Art no 3). https://doi.org/10.15866/ireme.v15i3.20428

4. Saqib M, Khan I, Shafie S, Mohamad AQ (2021) Shape effect on MHD flow of time fractional Ferro-Brinkman type nanofluid with ramped heating. Sci Rep 11(1):3725. https://doi.org/10.1038/s41598-020-78421-z

5. Hosain SA, Alim MA, Saha SK (2017) MHD natural convection in open inclined square cavity with a heated circular cylinder 1851:020051. https://doi.org/10.1063/1.4984680

6. Bhattacharyya S, Dey K, Hore R, Banerjee A, Paul AR (2019) Computational study on thermal energy around diamond shaped cylinder at varying inlet turbulent intensity. Energy Procedia 160:285–292. https://doi.org/10.1016/j.egypro.2019.02.155

7. Bhattacharyya S, Vishwakarma DK, Roy S, Biswas R, Ardekani MM (2020) Applications of heat transfer enhancement techniques: a state-of-the-art review. IntechOpen. https://doi.org/10.5772/intechopen.92873

8. Alwawi FA, Alkasasbeh HT, Rashad AM, Idris R (2020) MHD natural convection of sodium alginate Casson nanofluid over a solid sphere. Results Phys 16:102818. https://doi.org/10.1016/j.rinp.2019.102818

9. Mackolil J, Mahanthesh B (2019) Exact and statistical computations of radiated flow of nano and Casson fluids under heat and mass flux conditions. J Comput Des Eng 6(4):593–605. https://doi.org/10.1016/j.jcde.2019.03.003

10. Alkasasbeh H, Swalmeh M, Bani Saeed H, Al Faqih F, Talafha A (2021) Investigation on CNTS-water and human blood based Casson nanofluid flow over a stretching sheet under impact of magnetic field. Front. Heat Mass Transf. FHMT 14(0). Accessed: 26 July 2021 [Online]. Available: http://www.thermalfluidscentral.org/journals/index.php/Heat_Mass_Transfer/article/view/1098

11. Effects of radiation on MHD free convection of a Casson fluid from a horizontal circular cylinder with partial slip in non-Darcy porous medium with viscous dissipation. SpringerLink. https://link.springer.com/article/10.1186/s13661-015-0333-5 (accessed 06 July 2021)

12. Anwar MI, Rafique K, Misiran M, Khan I (2019) Numerical solution of Casson nanofluid flow over a non-linear inclined surface with Soret and Dufour effects by Keller-box method. Front Phys 7. https://doi.org/10.3389/fphy.2019.00139

13. Swalmeh MZ, Alkasasbeh HT, Hussanan A, Mamat M (2019) Numerical investigation of heat transfer enhancement with Ag–GO water and kerosene oil based micropolar nanofluid over a solid sphere. J Adv Res Fluid Mech Therm Sci 59(2) (Art no 2)

14. Waini I, Ishak A, Pop I (2019) Unsteady flow and heat transfer past a stretching/shrinking sheet in a hybrid nanofluid. Int J Heat Mass Transf 136:288–297. https://doi.org/10.1016/j.ijheatmasstransfer.2019.02.101

15. Manjunatha S, Ammani Kuttan B, Jayanthi S, Chamkha A, Gireesha BJ (2019) Heat transfer enhancement in the boundary layer flow of hybrid nanofluids due to variable viscosity and natural convection. Heliyon 5(4):e01469. https://doi.org/10.1016/j.heliyon.2019.e01469

16. Alghamdi W et al (2021) Boundary layer stagnation point flow of the Casson hybrid nanofluid over an unsteady stretching surface. AIP Adv 11(1):015016. https://doi.org/10.1063/5.0036232

17. Krishna MV, Ahammad NA, Chamkha AJ (2021) Radiative MHD flow of Casson hybrid nanofluid over an infinite exponentially accelerated vertical porous surface. Case Stud Therm Eng 27:101229. https://doi.org/10.1016/j.csite.2021.101229

18. Mousavi SM, Rostami MN, Yousefi M, Dinarvand S, Pop I, Sheremet MA (2021) Dual solutions for Casson hybrid nanofluid flow due to a stretching/shrinking sheet: a new combination of theoretical and experimental models. Chin J Phys 71:574–588. https://doi.org/10.1016/j.cjph.2021.04.004

19. Keller HB (2021) A new difference scheme for parabolic problems. In: Hubbard B (ed) (1971) Academic Press, New York, NY, pp 327–350. Accessed: 28 July 2021 [Online]. Available: https://resolver.caltech.edu/CaltechAUTHORS:20170802-111549240

20. Salleh MZ, Nazar R, Pop I (2010) Boundary layer flow and heat transfer over a stretching sheet with Newtonian heating. J Taiwan Inst Chem Eng 41(6):651–655. https://doi.org/10.1016/j.jtice.2010.01.013

21. Alwawi FA, Swalmeh MZ, Qazaq AS, Idris R (2021) Heat transmission reinforcers induced by MHD hybrid nanoparticles for water/water-EG flowing over a cylinder. Coatings 11(6) (Art no 6). https://doi.org/10.3390/coatings11060623

22. Alwawi FA, Alkasasbeh HT, Rashad A, Idris R (2020) Heat transfer analysis of ethylene glycol-based Casson nanofluid around a horizontal circular cylinder with MHD effect. Proc Inst Mech Eng Part C J Mech Eng Sci 234(13):2569–2580. https://doi.org/10.1177/0954406220908624

23. Alwawi FA, Alkasasbeh HT, Rashad AM, Idris R (2019) Natural convection flow of sodium alginate based Casson nanofluid about a solid sphere in the presence of a magnetic field with constant surface heat flux. J Phys Conf Ser 1366:012005. https://doi.org/10.1088/1742-6596/1366/1/012005

24. Elbashbeshy EMA (1998) Heat transfer over a stretching surface with variable surface heat flux. J Phys Appl Phys 31(16):1951–1954. https://doi.org/10.1088/0022-3727/31/16/002

Parametric Study of Average Power from Vibration Energy Harvester

Mohammad Izzat Razali, Abdul Malek Abdul Wahab,
Muhamad Sukri Hadi, and Ahmad Khushairy Makhtar

Abstract Nowadays, renewable energy becomes important due to the increased energy demand and recent limitation of batteries. The technique of vibration energy harvesting has been seen as a promising way to allow self-sufficient wireless sensors and other low-power consumption devices. This is due to the presence of vibration energy in many environments and engineering systems. This research aims to investigate the characteristic of vibration energy harvesting. A single degree of freedom (SDOF) subject to a harmonic base excitation is considered as a harvester. This paper investigates analytically the performance of average power in vibration energy harvester. Results show that higher amplitude will decrease the frequency and increase power density for average power harvested. Furthermore, the amplitude can be higher and give more power density for average power harvesting when the resonance frequency occurs where the applied frequency is equal or closed to the natural frequency. In addition, it is possible to increase the amplitude and power average by tune the parameter of the energy harvester by changing the mass, stiffness, and damping ratio.

Keywords Vibration energy harvesting · Single degree of freedom · Average power

1 Introduction

Over the past two decades, harvesting wasted or underutilized ambient energy has been recognized as a foundation technology for energy-autonomous electronic devices [1]. Energy harvesting is a promising strategy that addressing the global energy crisis without depleting the natural resource [2]. These devices offer a solution by extracting energy from ambient such as sunlight (solar), wind, hydro, vibration (motion), temperature gradient (thermal), and waves of radio frequency (RF) [3].

M. I. Razali · A. M. Abdul Wahab (✉) · M. S. Hadi · A. K. Makhtar
School of Mechanical Engineering, College of Engineering, Universiti Teknologi MARA, 40450
Shah Alam, Selangor, Malaysia
e-mail: abdmalek@uitm.edu.my

577

Vibration energy harvesting (VEH) technologies have attracted a lot of attention since mechanical vibration energy can be found anywhere [4]. However, the absolute level of achievable performance is still an issue in function implementation. This is because most sources of vibration energy consist of a low-frequency broadband range [5].

VEH systems apply piezoelectric, electromagnetic, or electrostatic elements to convert kinetic energy into usable electrical energy [1]. The idea of VEH is to convert vibration into electrical energy through two conversion steps. First, the use of mechanical transducers between the two elements, such as a comparatively moving mass-spring system. Second, electromechanical transducers such as piezoelectric materials or variable capacitors are used to convert the comparative motion into electrical energy [6].

There was a wide scope of studies carried out on the VEH system. Generally, VEH was represented by an equivalent mass spring damper model. The linear damper was a combination of damping provided by electrical and mechanical systems [7]. Stephen analyzed the maximum of average power from the vibration energy harvester by set up the natural frequency and excitation frequency to be equal [8]. While Ashraf analyzed the dependence of the average power of VEH by considering the role of the damping [9]. Guangxhui Xia et al. also investigated the performance of the output power energy harvesting with different parameters such as load resistance and damping [10].

Since the oscillation energy is distributed on different harmonics, the study about the dependence of the average power on the parametric in vibration is important. Thus, this paper evaluates the dependence of average power on mass, stiffness, and damping of the VEH system. A single-degree-of-freedom (SDOF) mechanical oscillator subject to a harmonic base excitation model was introduced in this paper as a VEH system. The response for each condition was compared.

2 Methodology

A single degree of freedom (SDOF) system has been introduced for the harvester of vibration energy as shown in Fig. 1. Where c represents the damping that provides by mechanical and electrical areas, the mass, m represents the equivalent proof mass of the resonator, and the spring with a constant, k represents the elasticity of the resonator beam.

From Fig. 1, the basic equation of the relative motion of the seismic mass towards the base is defined as,

$$m\ddot{x} + (\dot{x} - \dot{y}) + k(x - y) = 0 \tag{1}$$

When the periodic force acts on the base, the mass oscillates with amplitude z. Rearranging Eq. (1) in terms of the relative displacement of the mass $z = x - y$ yields,

Fig. 1 Mass-spring-damper model for VEH system subjected to base
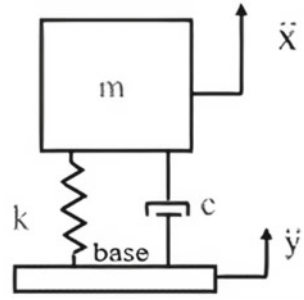
$$m\ddot{z} + c\dot{z} + kz = m\ddot{y} \tag{2}$$

Substitute the base excitation $y = Y\sin(\omega t)$, Eq. (2) becomes,

$$m\ddot{z} + c\dot{z} + kz = -m\omega^2 Y\sin(\omega t) \tag{3}$$

The steady-state solution of Eq. (3) is,

$$Z = \frac{m\omega^2 Y}{\sqrt{\left(k - m\omega^2\right)^2 + c^2\omega^2}} \sin(\omega t - \phi) \tag{4}$$

The phase difference ϕ is given as,

$$\phi = \tan^{-1}\left(\frac{c\omega}{k - m\omega^2}\right) \tag{5}$$

Equation (4) can be simplified by using $\omega_n = \sqrt{\frac{k}{m}}$ and $\zeta = \frac{c}{2\sqrt{km}}$ to get

$$z = \frac{\left(\frac{\omega}{\omega_n}\right)^2 Y}{\sqrt{\left(1 - \frac{\omega}{\omega_n}^2\right)^2 + \left(2\zeta\frac{\omega}{\omega_n}\right)^2}} \sin(\omega t - \phi) \tag{6}$$

Equation (6) is the amplitude of vibration of the mass respected to the base. This equation is used to find the displacement of the spring-mass-damper system in the time domain, where ω/ω_n is the frequency ratio and ζ is the damping ratio.

The electrical and mechanical dampers are considering the same as velocity dampers. The instantaneous energy absorbed by the dampers can be obtained by multiplying the damping constant with the square of instantaneous velocity. The average power is the integration of instantaneous energy absorbed within a complete cycle of vibration divided by time (period). The equation is shown as,

Table 1 Properties of SDOF system

Parameters	Value
Mass m (kg)	1
Stiffness k (N/mm)	107.5
Damping c (Ns/mm)	0.1
Base excitation amplitude y (m)	0.025

$$Pav = \frac{1}{t}\int_0^t c\dot{z}^2 dt = \frac{m\zeta Y^2\left(\frac{\omega}{\omega_n}\right)^3 \omega^3}{\left(1 - \left(\frac{\omega}{\omega_n}\right)^2\right)^2 + \left(2\zeta\frac{\omega}{\omega_n}\right)^2} \qquad (7)$$

Equation (7) determine the average power harvest from the system. Then, the maximum average power can be obtained at the frequency ratio by setting the $\partial Pav/\partial\omega = 0$ as shown,

$$\frac{\omega}{\omega_n} = \sqrt{2 - 4\zeta^2 - \sqrt{(4\zeta^2 - 2)^2 - 3}} \qquad (8)$$

where,

$$\zeta = \frac{c}{2m\omega_n} \qquad (9)$$

Equation (8) shows the frequency ratio only has a valid value when the damping ratio, ζ is less than 0.25 [9]. Equation (9) represents the damping ratio of the system.

MATLAB 2020b software was used to find the response for time-domain and frequency-domain of Eq. (6). Fast Fourier Transform (FFT) was used to compute the frequency response. The power average of the VEH was calculated using Eq. (7). Three different tests were carried out to look at the effect of mass, stiffness, and damper towards power average producing by the VEH system. Table 1 shows the properties of the SDOF system.

The mass, stiffness, damper, and frequency ratio have been varied to compare the performance of power average for the VEH system, as shown in Table 2.

3   Result and Discussion

3.1   The Mass Effect

Figure 2 shows the displacement of the VEH system in the time domain. Three different masses, $m_1 = 1$ kg, $m_2 = 3$ kg, and $m_3 = 5$ kg have been proposed to identify the difference in the responses. The m_3 has a higher amplitude follow by

Table 2 Parameter for the testing

Parameter of mass	
Mass, m (kg)	1
	3
	5
Parameter of stiffness of spring	
Stiffness, k (N/mm)	107.5
	207.5
	307.5
Parameter of damper	
Damper, c (Ns/mm)	0.1
	0.15
	0.25
Frequency ratio	
$\omega < \omega_n$	
$\omega > \omega_n$	
$\omega = \omega_n$	
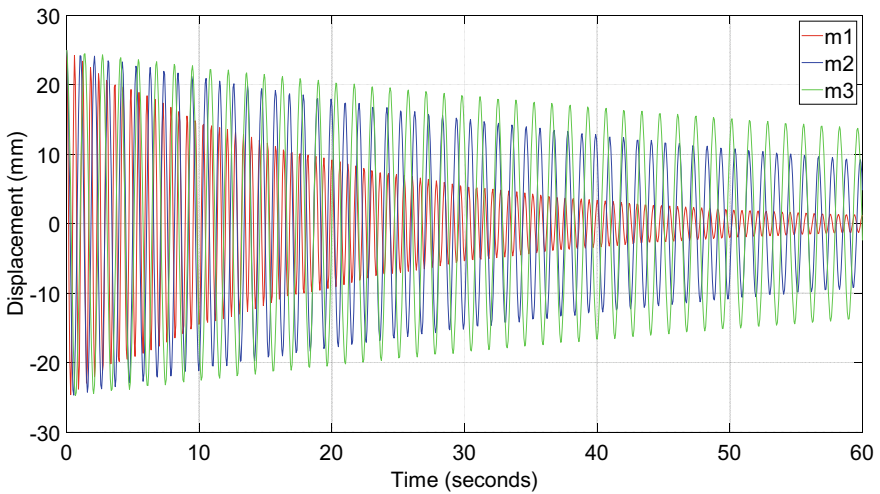
Fig. 2 Time-response for different masses

m_2 and m_1. The higher mass influences the amplitude to enlarge. Heavier mass triggers a larger initial overshoot that causes the system to have a higher amplitude. The displacement for all the masses decreases as time increases. This is due to the damping of the system. However, the displacement of the mass, m_1 decreases drastically compared to other masses. Due to higher energy store in heavier mass, the
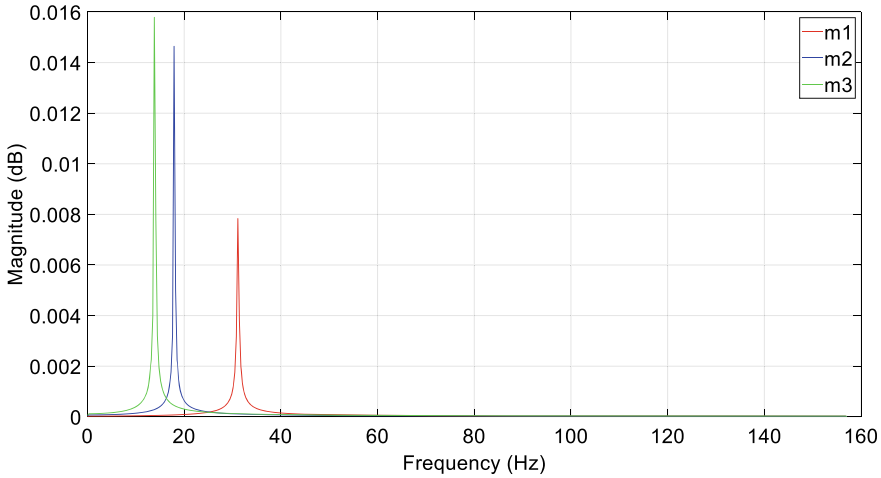
Fig. 3 Frequency–response for different mass

time taken for the energy to dissipate is more compared to lighter mass. This finding is in agreement with the finding of Burchett (2005) who investigated the effect of amplitude in different masses.

The frequency response of the VEH system is shown in Fig. 3. The m_3 shows the lowest value of natural frequency which is $\omega_n = 18$ rad/s but has the highest peak at the magnitude. While m_1 has the highest value of natural frequency, $\omega_n = 36$ rad/s but lowest in amplitude. It can be observed that increasing the mass causing the decrement in the natural frequency of the system. Heavier masses travel more distance to complete one cycle which then causes the system to oscillate slower and have a low natural frequency. This result is in line with the fundamental theory of vibration where the natural frequency is inversely proportional to mass.

To discover the most effective power output measured by the system, the average harvested power has been compared between different masses. Figure 4 shows the variation of average power related to the frequency for different masses. m_3 generates the highest power average, $Pav = 6.5\,mW$. The average power starts to react at 6 Hz by increasing steeply for m_3 and a slight increment for m_2. While m_1 has no power output as the frequency increases. Results show heavier mass produces a large amount of power and increases as frequency going higher. The results are in line with Eq. (7), as the power average is proportional to the square of displacement.

3.2 The Stiffness Effect

Figure 5 shows the time response of the VEH in different stiffness of spring, $k_1 = 107.5$, $k_2 = 207.5$ and $k_3 = 307.5$ N/mm. The system has a similar mass and
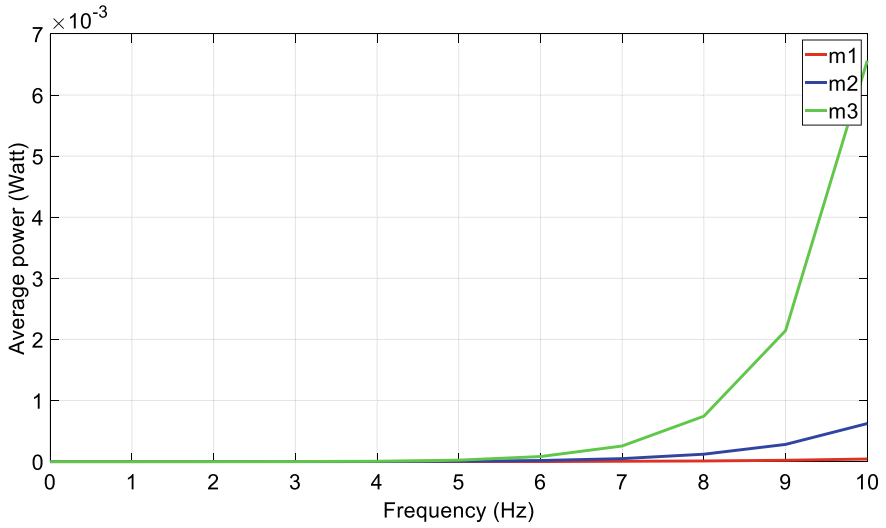
Fig. 4 Average power–frequency for different mass
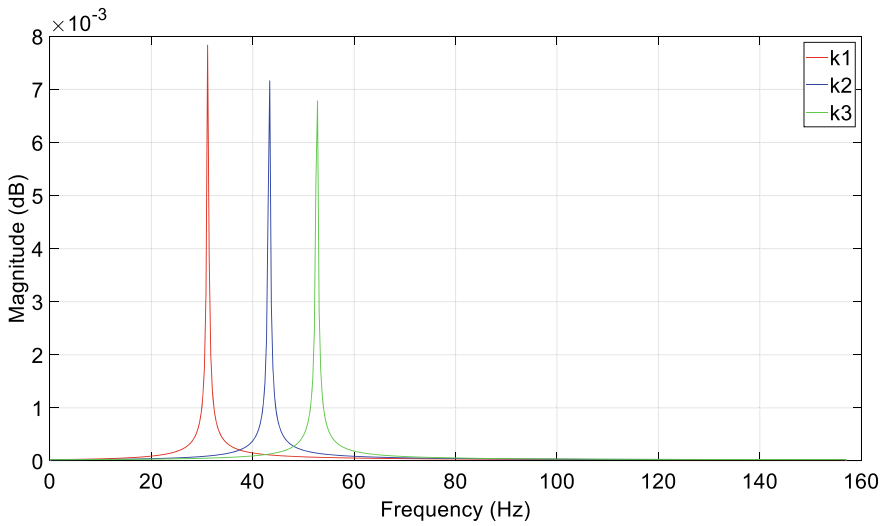
Fig. 5 Time-response for different stiffness

damping. Results show that k_3 has the smallest time cycle and amplitude. While k_1 shows the highest time cycle and amplitude of oscillation. This is because a larger value of stiffness, k, has the larger force constant to resist the system with a similar mass from oscillating at high amplitude and time cycle. These results are in line with the previous work by Casiesz [11].
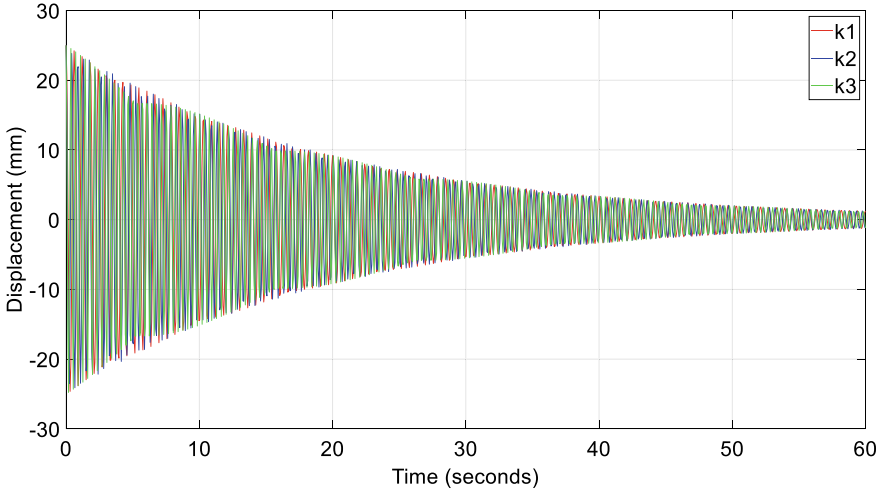
Fig. 6 Frequency–response for different stiffness
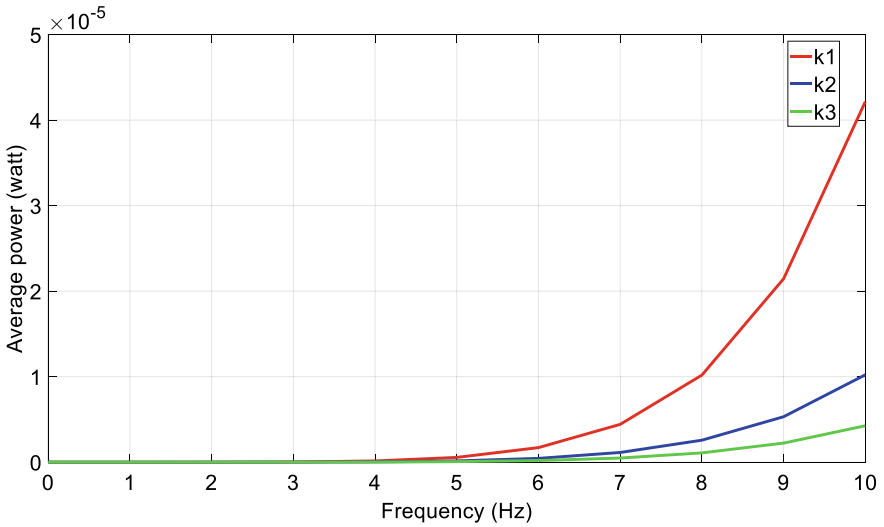
Fig. 7 Average power–frequency for different stiffness

The natural frequency increases with the growth of the stiffness, as revealed in Fig. 6. The stiffness spring constant k_3 has the highest value of natural frequency, compared to k_1 where the value of natural frequency is $= 53$ rad/s and $\omega_n = 31$ rad/s respectively. This result is in line with Ashraf et al. where the stiffness of spring is proportional with the natural frequency of the system [9].
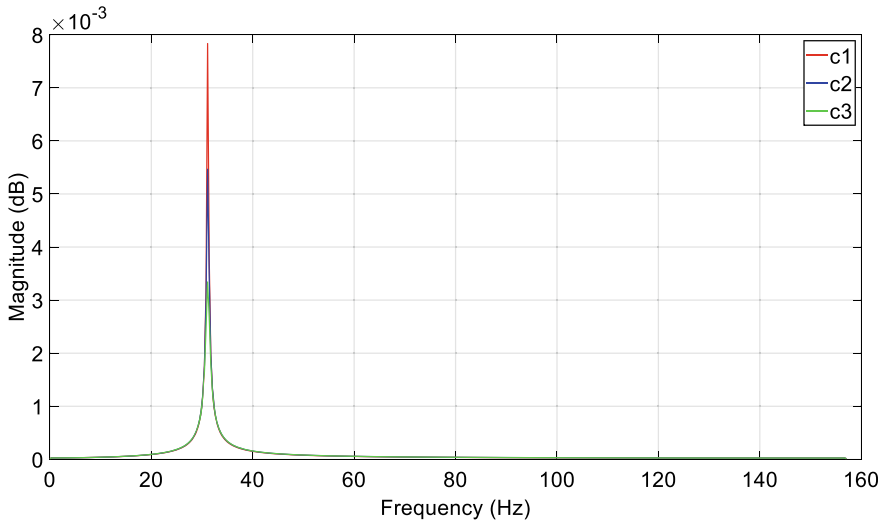
Fig. 8 Time-response different damping

The comparison of average power between the stiffness is shown in Fig. 7. The power average starts to react at 5 Hz for lower stiffness k_1, earlier than higher stiffness k_2 and k_3. The stiffness k_1 produces average power higher than k_2 and k_3 as frequency increases. These results have a good agreement with work by Zhou et al. [4], who stated the increase in stiffness of VEH resulted in decreased bandwidth and significantly reduced the power average.

3.3   The Damping Effect

The VEH system has been tested by varying the damping coefficient value, $c_1 = 0.1$, $c_2 = 0.15$, and $c_3 = 0.25$ Ns/mm. The rest parameters remain unchanging, as indicated in Fig. 8. The lowest damping coefficient value, c_1, shows the highest displacement compared to the highest damping coefficient c_3. Friction or damping condition reduces the mechanical energy of the system. Thus, the damping coefficient gradually reduces the amplitude of the oscillating motion.

The frequency response in Fig. 9 shows the effect of damping towards natural frequency. The graph shows the lowest damping, c_1 has the highest amplitude at 8 $\times$ 10^{-3} dB. While higher damping, c_3 has the lowest amplitude 3×10^{-3} dB at the resonance frequency. These results, agree with the work by Stephen [8] that reported by reducing the damping coefficient, the amplitude of the system can increase to the maximum value. In this condition, changes in damping only affected the peak area of the displacement response.
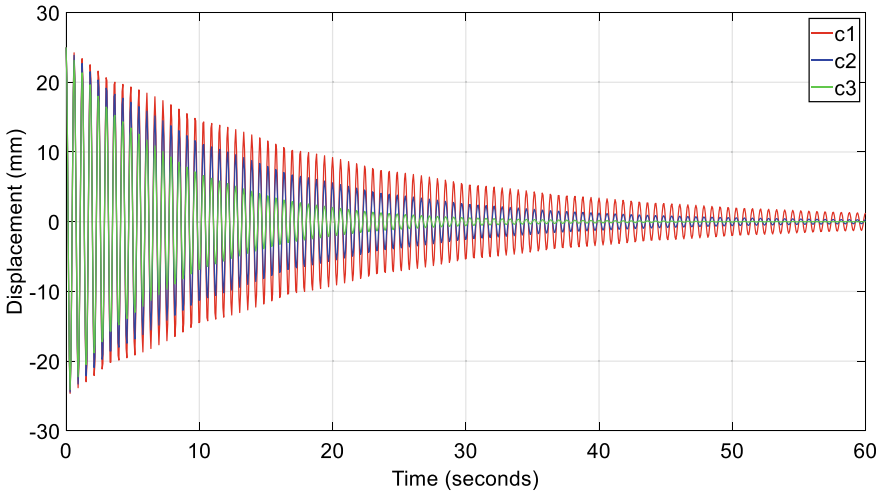
Fig. 9 Frequency–response different damping
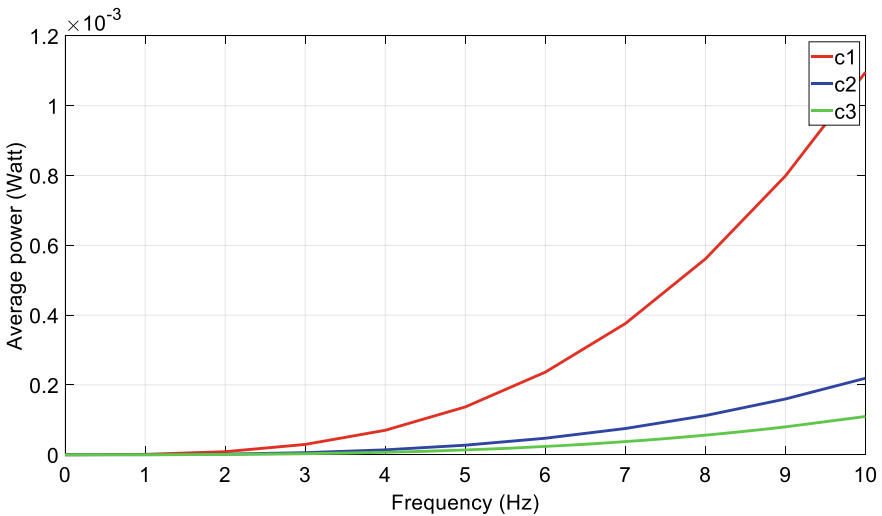
Fig. 10 Average power–frequency for different damping

The average power related to frequency contours is computed and shown in Fig. 10. The average power for damping c_1 shows the highest value of $Pav = 1.1$ mW. While c_2 and c_3 both show the lower value, which is $Pav = 0.21$ mW and $Pav = 0.1$ mW respectively as frequency increases. This finding was in line with the finding of Lei et al. where increasing the mechanical damping reduced the output voltage of the VEH system [12]. Besides being involved with the harvesting and dissipation of
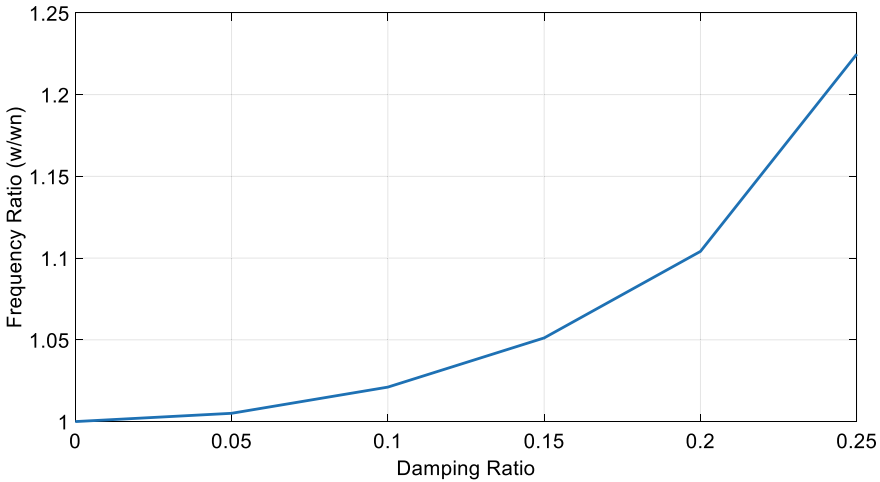
Fig. 11 Variation of optimal frequency ratio with damping ratio

Table 3 Average power with different frequency excitation

$\omega_n = 31$ rad/s	$\omega < \omega_n$ ($\omega = $ **10 rad/s**)	$\omega > \omega_n$($\omega = $ **50 rad/s**)	$\omega = \omega_n$($\omega = $ **31 rad/s**)
Power (μW)	0.000421544	0.2062	288.6

energy, the damping coefficient is important in the VEH system as it transfers the energy from the vibrating base into the system [8].

Figure 11 shows the variation of optimal frequency with damping ratio. The small damping ratio contributes to the frequency ratio close to unity. The production of average power is high at a frequency ratio equal or close to unity due to resonance at a low damping ratio. Table 3 compares the average power harvested for three conditions of excitation frequency based on the properties of VEH in Table 1. Results show the highest power average can be produced once the excitation frequency is equal to or close to the natural frequency of the VEH system that so-called resonance condition. This result is in line with the work by Ashraf [9].

4 Conclusion and Recommendations

The average power performance of the SDOF model as a VEH system was investigated. The performance of average power was compared for different parameters. The output of the power was dependable on the amplitude of the vibration. Thus, the heavier mass, the less stiff, the low damping and resonance produced more power since this condition contributed to high amplitude. However, to scavenge more power

from unused vibration, the implementation of broader bandwidth in the system needs to be considered for the VEH system.

References

1. Kuang Y, Hide R, Zhu M (2019) Broadband energy harvesting by nonlinear magnetic rolling pendulum with subharmonic resonance. Appl Energy 255(August):113822. https://doi.org/10.1016/j.apenergy.2019.113822
2. Wang H, Jasim A (2020) Piezoelectric energy harvesting from pavement. LTD
3. Bhatnagar V, Owende P (2015) Energy harvesting for assistive and mobile applications. Energy Sci Eng 3(3):153–173. https://doi.org/10.1002/ese3.63
4. Zhou K, Dai HL, Abdelkefi A, Ni Q (2020) Theoretical modeling and nonlinear analysis of piezoelectric energy harvesters with different stoppers. Int J Mech Sci 166. https://doi.org/10.1016/j.ijmecsci.2019.105233
5. Search H, Journals C, Contact A, Iopscience M, Address IP (2006) Energy harvesting vibration sources for microsystems applications. 175. https://doi.org/10.1088/0957-0233/17/12/R01
6. Chen N, Jung HJ, Jabbar H, Sung TH, Wei T (2017) A piezoelectric impact-induced vibration cantilever energy harvester from speed bump with a low-power power management circuit. Sens Actuators A Phys 254:134–144. https://doi.org/10.1016/j.sna.2016.12.006
7. Williams CB, Yates RB (1996) Analysis of a micro-electric generator for microsystems. Sens Actuators A Phys 52(1–3):8–11. https://doi.org/10.1016/0924-4247(96)80118-X
8. Stephen NG (2006) On energy harvesting from ambient vibration. J Sound Vib 293(1–2):409–425. https://doi.org/10.1016/j.jsv.2005.10.003
9. Ashraf K, Khir MHM, Dennis JO (2012) Frequency dependence of average power in vibration energy harvesting. In: 2012 4th international conference on intelligent and advanced systems (ICIAS2012). World engineering, science & technology congress (ESTCON), vol 2, no 5, pp 842–845. https://doi.org/10.1109/ICIAS.2012.6306131
10. Xia G, Fang F, Zhang M, Wang Q, Wang J (2019) Performance analysis of parametrically and directly excited nonlinear piezoelectric energy harvester. Arch Appl Mech 89(10):2147–2166. https://doi.org/10.1007/s00419019-01568-3
11. Casiez G, Vogel D (2008) The effect of spring stiffness and control gain with an elastic rate control pointing device. In: CHI '08: Proceedings of the SIGCHI conference on human factors in computing systems, no January, pp 1709–1718. https://doi.org/10.1145/1357054.1357321
12. Lei YM, Wen Z (2015) Study on effects of the damping ratio on output performance of micro electromagnetic vibration energy harvesters. Microsyst Technol 21(1):221–226. https://doi.org/10.1007/s00542-014-2114-y

Investigation on the Effect of Machining Parameters on Mechanical Properties of Friction Stir Processed Mg–Al-Micro Al$_2$O$_3$ Metal Matrix Composites

Zuhairah Zulkfli, M. Faris Zaidi, Nanang Fatchurrohman, and Zamzuri Hamedon

Abstract Low density of magnesium makes it an ideal choice as it is lighter than steel and aluminium alloys. Combination of cast magnesium alloys component can be used widely in the automobile sector and factories but were restricted. Friction stir processing is an infinite machining operation used to enhance the structural workpiece in solid-state strengthening. By using a straight cylindrical tool pin profile which will be used throughout this study, the effects of FSP parameters on magnesium AZ91A can be investigated. Variation of feed rates, (10–58) mm/min with a fixed rotational speed, 1208 RPM were applied for each single FSP pass. Mg alloy will be plated with Al6061 sheets and reinforced with Al$_2$O$_3$ particles before running FSP. Mechanical properties and metallographic requirements are the characterizations in investigating the effects of machining parameters of FSPed workpiece. Both characterizations can be gained via Rockwell hardness test and optical microscopy. Finally, this study discovered that the average hardness of FSPed Mg–Al-Micro Al$_2$O$_3$ was reduced significantly with the increment of feed rates. Next, improved hardness at HAZ points as well as reduced surface roughness at three distances from FSP starting point were detected.

Keywords Friction stir processing (FSP) · Machining parameters · Magnesium AZ91A · Al6061 · Metal matrix composite (MMC) · Hardness · Surface roughness

1 Introduction

Increasing demand for functional properties of production components as well as the need to reduce the mass of a system reflect the functional properties required

Z. Zulkfli (✉) · M. F. Zaidi · Z. Hamedon
Faculty of Manufacturing and Mechatronic Engineering Technology, Universiti Malaysia Pahang, 26600 Pahang, Malaysia
e-mail: zulkflizuhairah@gmail.com

N. Fatchurrohman
Department of Industrial Engineering, Faculty of Engineering, Universitas Putra Indonesia YPTK, Padang 25221, Indonesia

in developing material engineering surface layers. Surface spraying or re-melting using laser beam are the most widely used technique in surface layer processing which reported for years [1]. Matrix composites exhibit higher mechanical properties than unreinforced alloys. It had been used for broad range of applications due to high specific strength, stiffness, wear resistance, good damping capacities, dimensional stability and machinability [2]. Friction stir processing (FSP) of surface layers is a modernized technique nowadays. Friction created between the spinning tool and workpiece helps to heat and soften the material under FSP tool surface [3]. The FSP approach is mainly used for microstructure modification of refined metal components and produce a surface layer of composite to improve the material's mechanical properties [4]. Therefore, better grain construction, surface composite, microstructure change of casting composites, blending with rare components and rise the stability of welded joints can be produced by this process [5].

Due to low strength properties of magnesium (Mg) AZ91A, FSP experiment has been carried out using different machining parameters in order to alter the mechanical properties of the workpiece. Moreover, this study analyses the effects of different machining parameters applied on the Mg AZ91A workpiece mainly on mechanical properties and microstructure as the output characterizations.

The interaction between the FSP machining parameters and comparative results on FSPed magnesium AZ91A concentrating on the mechanical properties of Mg–Al-Micro Al_2O_3 before, during and after the process were considered. FSP parameters involved were the cutting depth [6], rotational speed and traverse speed [7, 8]. These parameters were intended to investigate the relationship between the different processing parameters and hardness. Secondly, to analyse the surface roughness and microstructure of the machined workpiece. The samples will be observed using the LEXT™ OLS5000 Laser Scanning Microscope to examine the surface roughness and microstructure of FSPed workpiece while utilizing the Rockwell hardness tester for hardness testing.

2 Methodology

2.1 Material Preparation

Before starting the FSP process, materials were prepared using the procedures as follows: (1) Starting with a primary machining using horizontal and vertical band saw, the raw magnesium AZ91A block was cut. (2) Then, the blocks undergo squaring process using milling machine. (3) The squared blocks will be slotted 30 mm-width and 1.2 mm-depth. (4) Then, three 6 mm-diameter holes were drilled until 3 mm deep. (5) Al6061 sheets were bent.

Reinforcement Volume Fraction. The volume fraction measurement was done to ensure the FSP reinforcement of aluminum oxide (Al_2O_3) particles efficiency is between 20% and 40%. The reinforced Al_2O_3 particles with ($\leq 10 \ \mu m$ average

Fig. 1 Volume area for
measurement
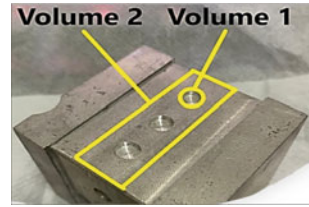
particle size) was used in this study. The area considered for volume fraction
measurement calculation was selected (see Fig. 1).

$$
\begin{aligned}
&= \frac{\textbf{Volume}\,1}{\textbf{Volume}\,2} \times 100\% \\
&= \frac{3(\pi r^2 \textbf{h})}{\textbf{W} \times \textbf{D} \times \textbf{H}} \times 100\% \\
&= \frac{3(3.142 \times 3\,\textbf{mm}^2 \times 3\,\textbf{mm})}{22\,\textbf{mm} \times 18\,\textbf{mm} \times 3\,\textbf{mm}} \times 100\% \\
&= 21.42\%
\end{aligned}
\tag{1}
$$

2.2 Tool Preparation

Tools were prepared using the procedures: (1) H13 steel rod was cut into 100 mm
length using Way Train horizontal band saw machine. (2) Straight cylindrical tools
were fabricated into dimension using ROMI C 420 CNC lathe machine which mainly
consists of a shoulder diameter (D): 18 mm, pin diameter (d): 6 mm and pin length
(L): 3 mm (see Fig. 2).

2.3 Friction Stir Processing Experimental Setup

The experiment setup proceeded with the FSP of Mg–Al-Micro Al_2O_3 metal matrix
composites with the variation of feed rates chosen to boost the strength of base
material (BM) of magnesium. Based on literature review [9], the optimum machining
parameter that enhanced mechanical properties for FSP of magnesium alloy AZ91
were between 10 and 58 (mm/min) at fixed 1208 RPM rotational speed. Six FSP
samples were processed by a single pass with feed rate variations listed in Table 1.

To summarize, subsequential FSP experiment setups were as follows: (1) The
Mg workpiece holes were filled with Al_2O_3 powder. (2) Then, Mg workpiece was
plated with aluminium sheet, Al6061 and clamped together to avoid slipping during
high-speed machining. (3) Start running FSP using manual mode. (4) To proceed, the
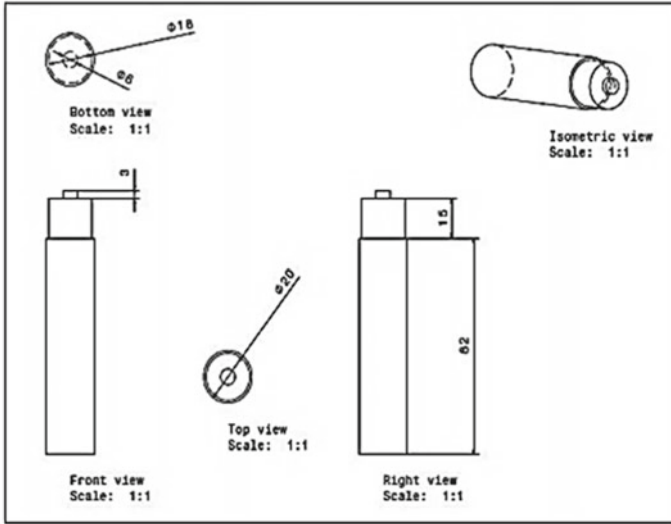
Fig. 2 FSP tool dimension for cylindrical pin profile

Table 1 FSP machining parameters for magnesium alloy AZ91

Feed rate (mm/min)	Rotational speed (RPM)	Depth of tool pin (mm)
10	1208	3.3
17	1208	3.3
25	1208	3.3
34	1208	3.3
46	1208	3.3
58	1208	3.3

samples need to be faced mill again as both materials, Mg–Al were bounded together after FSP to obtain flat surface area. (5) The samples were ready to be used for data collection of hardness test, surface roughness test and microstructure observation.

2.4 Characterization

Hardness Test. Hardness test is one of effective techniques to measure the strength of a structured material. Using Rockwell Hardness Tester, the hardness readings were taken in seven different areas along the traverse FSP line with 3 mm interval difference between each location. The hardness for heat affected zone (HAZ) were taken from point 1–4 with 1 mm interval difference between points from FSP zone.

The hardness measurement procedures were repeated for all the samples. The average hardness values will be calculated after testing completed.

Surface Roughness Test and Microstructure Observation. The surface roughness testing and microstructure of FSPed samples were measured and observed, respectively using the LEXT™ OLS5000 3D Laser Scanning Microscope. The surface roughness test was fixed at three different FSP traverse location on each sample which distanced 10 mm, 20 mm and 30 mm from the starting point. This step was performed to observe the different characteristics on surface after FSP.

3 Results and Discussion

Present analysis focusing on hardness test, surface roughness test and microstructure observation after processing Mg–Al-Micro Al_2O_3 with different feed rates which were (10, 17, 25, 34, 46 and 58) mm/min.

3.1 Hardness Test

The effect of feed rate on the resulting average hardness was illustrated (see Fig. 3). The average hardness decreased from 49.71 HRB to 29.71 HRB. The increment of feed rates will limit the processed area's exposure time to the temperature generated from the rotating tool, hence can rise the temperature attained during the operation. Further refinement can be achieved as the feed rate increases which leads to decrement of the average hardness. However, the average hardness values are higher than as-received Mg AZ91A hardness value which is 29.14 HRB. Hence, this experiment was acceptable since the hardness of FSPed workpiece increased than the hardness of as-received Mg AZ91A.
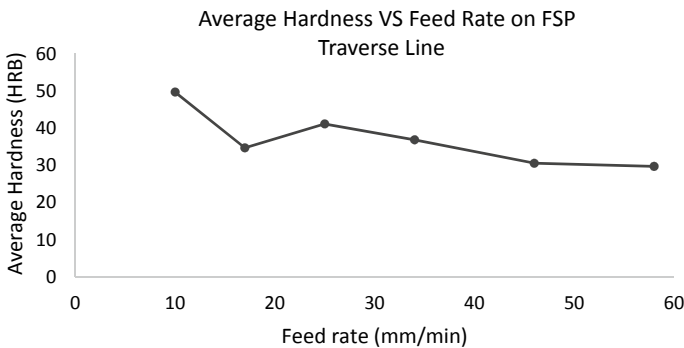
Fig. 3 Average hardness of FSPed Mg–Al-Micro Al_2O_3 against feed rate on FSP traverse line

By increasing the feed rate also reduce the hardness of heat affected zone (HAZ) which distanced 1 mm interval from FSP traverse area. The HAZ hardness values were always lower than FSP traverse area. The hardness values of HAZ points were lower than the average hardness on FSP traverse line for each feed rate. For example, HAZ 1, HAZ 2, HAZ 3, HAZ 4 has hardness values of (8, 20, 38, 46) HRB, respectively which lower than 49.71 HRB average hardness on FSP traverse line at 10 mm/min (see Fig. 4). This was caused by failure of mechanical deformation (stirring) in HAZ although the maximum temperature reached, it is adequate for the material to be softened and weaken the hardness around the nugget zone.

Nevertheless, increasing feed rates have an equal effect as increasing rotational speed on hardness FSPed Mg–Al-Micro Al_2O_3 which greater strength can be achieved with hardness value of (up to 49.71 HRB) compared to FSPed Mg AZ91A with hardness value of 30.33 HRB at 10 mm/min feed rate. As the FSP experiment carried out without measuring the temperature, the workpiece assumed to be over-heated during the machining resulting from rising axial load during feed rate increment between (10 and 58) mm/min. The workpiece was refined hence, hardness was increased.

On the contrary, past study on AZ31 Mg alloy conducted by Darras et al. [9] discovered that the refinement of average grain size was observed from 6 µm to an average size of 3–4 µm. Generally, the established Hall–Petch relationship proved that the hardness is inversely proportional to grain size. Grain refinement increased the hardness from 62 to 72 HV when using increasing feed rate of (20–30) in/min at 1200 rpm.
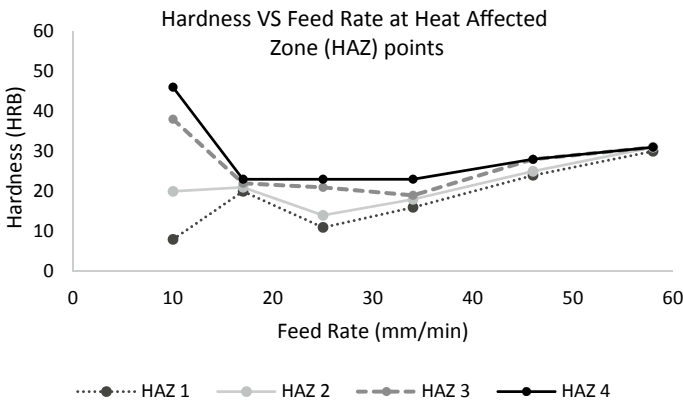
Fig. 4 Hardness of FSPed Mg–Al-Micro Al_2O_3 against feed rate at four HAZ points

3.2 Surface Roughness Test and Wear Characteristics

The correlation between feed rate and surface roughness were investigated by Ramezani et al. [10]. The study critically examined the surface quality and product life via surface roughness. Components with a high surface roughness tends to break easily and have a shorter lifetime due to smaller stress concentration and larger surface roughness. The relationship between feed rate and surface roughness was found (see Fig. 5). As the feed rate increases, the average surface roughness calculated declined from 31.948 to 5.603 μm. This shows that the FSPed Mg–Al-Micro Al$_2$O$_3$ have lower tendency to break which leads to longer lifetime as the feed rate increases.

An increase in sliding distances in the traverse motion led to lower surface roughness related from increasing feed rate (see Fig. 6). The graph shows the same trend of surface roughness values for each distance except the surface roughness at 34 mm/min. Furthermore, it shows that lowest surface roughness values (14.044, 6.838, 13.853, 8.613, 4.575 and 3.118) HRB for (10, 17, 20, 34, 46 and 58) mm/min feed rates, respectively at distance 10 mm where the surface mapping at the same position was the roughest, whereas the highest surface roughness values (52.616, 16.699, 22.621, 35.009, 8.698 and 8.584) HRB for (10, 17, 20, 34, 46 and 58) mm/min feed rates, respectively at distance 30 mm where the surface mapping was the smoothest.

Table 2 consists the surface mapping of FSPed samples at different feed rates. From the surface mapping results, there were several significant adhesive wears approaching to the end of traverse line FSP. Severe adhesive wears were validated by the surface damage with crates or ploughs of rough area [11]. It was shown that the surface mapping at 30 mm from starting point for each feed rate variations contain the biggest size of harsh debris. Debris formed on the surface shows that adhesive mechanism dominates from high feed rate at a longer sliding distance.
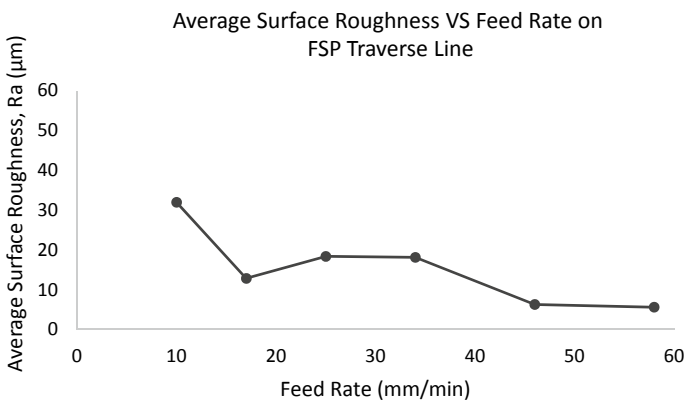

Fig. 5 Average surface roughness of FSPed Mg–Al-Micro Al$_2$O$_3$ against feed rate on FSP traverse line
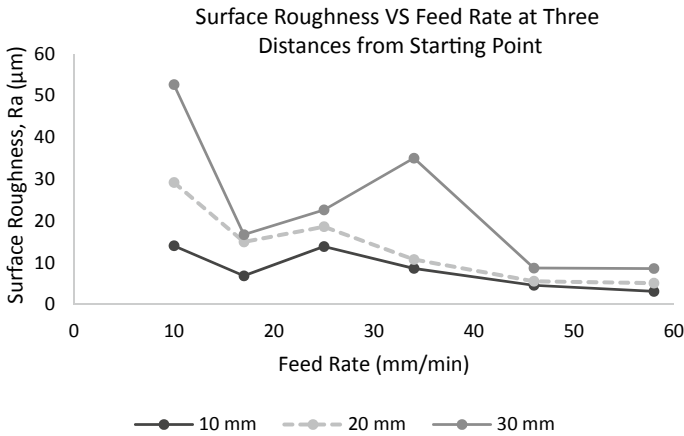
Fig. 6 Surface roughness of FSPed Mg–Al-Micro Al$_2$O$_3$ against feed rate at three distances from starting point
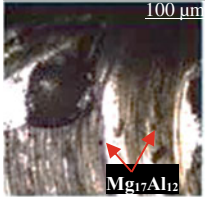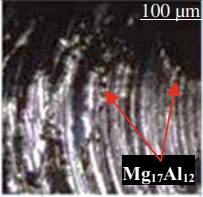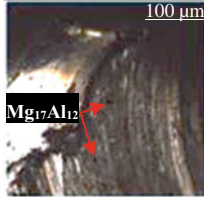
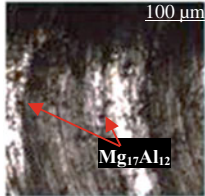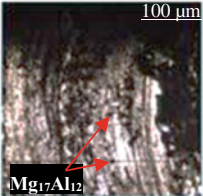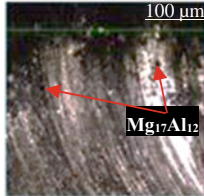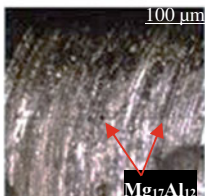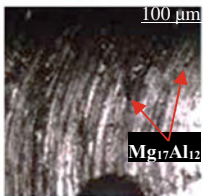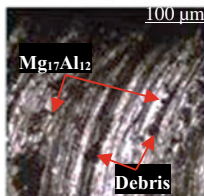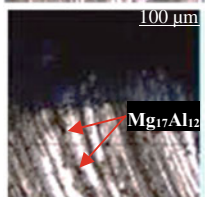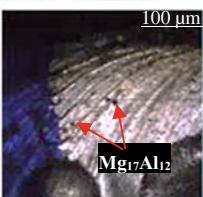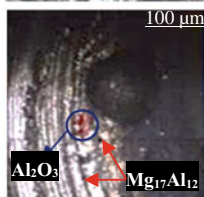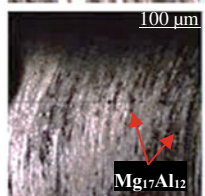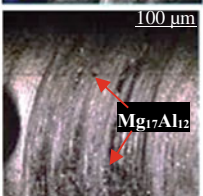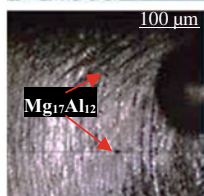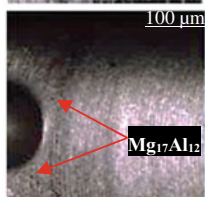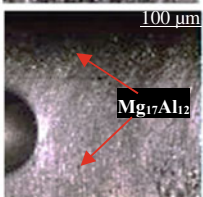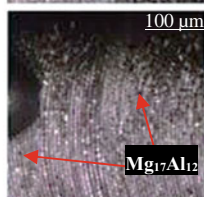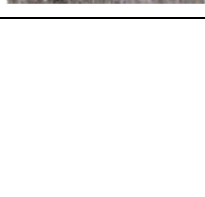The accumulation and elimination of wear debris occurred when there was feed rate increment with sliding distance. As the distance towards the end point increases, the grooves become deeper which means the abrasive wear increases due to large amount of plastic deformation leading to lower hardness when compared to hardness at starting point for each feed rate.

In addition, abrasive wear is a mechanism of sliding abrasive that ploughs and removes the surface of softened materials outside the groove [12]. The longer the sliding distances, the longer contact time between the surfaces of workpiece and tool. Higher rate of adhesive wear can be produced. Formation in situ of particles from contact with the surface of workpiece emerged as abrasive wear when hardened particles bound together with the moving tool along the traverse motion thus increase the tool's roughness. However, rough tool shoulder gradually softened the workpiece when there is constant contact [11].

4 Conclusion

To conclude, different feed rates (10–58) mm/min were applied. The results clearly show that processing parameters influence the hardness of the processed workpiece. The size of the grain was significantly reduced due to high temperature and improved hardness at HAZ points, thus reduced the surface roughness at three distances from FSP starting point. However, the average hardness of FSPed Mg–Al-Micro Al$_2$O$_3$ was reduced significantly with the increment of feed rates. In addition, surface roughness of each FSP tool pin needs to be strictly adjust and control during fabrication as the tool's surface roughness also affect FSP for prospect advancement.

Table 2 Mapping of samples taken by LEXT™ OLS5000 laser scanning microscope

Feed rate (mm/min)	Distance from starting point (mm)		
	10	20	30
10			
17			
25			
34			
46			
58			

References

1. Duan G, Yang L, Liao S, Zhang C, Lu X, Yang Y, Zhang B, Wei Y, Zhang T, Yu B, Zhang X, Wang F (2018) Designing for the chemical conversion coating with high corrosion resistance and low electrical contact resistance on AZ91D magnesium alloy. Corros Sci 35:197–206
2. Marini CD, Fatchurrohman N (2015) A review on the fabrication techniques of aluminium matrix nanocomposites. Jurnal Teknologi 74(10):103–109
3. Fatchurrohman N, Farhana N, Marini CD (2018) Investigation on the effect of friction stir processing parameters on micro-structure and micro-hardness of rice husk ash reinforced Al6061 metal matrix composites. In: IOP conference series: materials science and engineering, vol 319, no 1. IOP Publishing, p 012032
4. Marini CD, Fatchurrohman N, Zulkfli Z (2021) Investigation of wear performance of friction stir processed aluminium metal matrix composites. Mater Today Proc 46:1740–1744
5. Padhy GK, Wu CS, Gao S (2018) Friction stir based welding and processing technologies—processes, parameters, microstructures and applications: a review. J Mater Sci Technol 34(1):1–38
6. Węglowski MS (2018) Friction stir processing—state of the art. Arch Civil Mech Eng 18(1):114–129
7. Zulkfli Z, Fatchurrohman N (2021) Advancement in friction stir processing on magnesium alloys. In: IOP conference series: materials science and engineering, vol 1092, no 1. IOP Publishing, p 012006
8. Wahab NA, Fatchurrohman N, Zulkfli Z (2021) Investigation on the effect of different friction stir machining tools shape on the mechanical properties of magnesium alloy work piece. In: IOP conference series: earth and environmental science, vol 700, no 1. IOP Publishing, p 012003
9. Darras BM, Khraisheh MK, Abu-Farha FK, Omar MA (2007) Friction stir processing of commercial AZ31 magnesium alloy. J Mater Process Technol 191(1–3):77–81
10. Ramezani NM, Rasti A, Sadeghi MH, Pour BJ, Hajideh MR (2015) Experimental study of tool wear and surface roughness on high speed helical milling in D2 steel. In Modares Mech Eng 15(13):198–202
11. Azizieh M, Larki AN, Tahmasebi M, Bavi M, Alizadeh E, Kim HS (2018) Wear behavior of AZ31/Al$_2$O$_3$ magnesium matrix surface nanocomposite fabricated via friction stir processing. J Mater Eng Perform 27(4):2010–2017
12. Zhang MJ, Cao ZY, Yang XH, Liu YB (2010) Microstructures and wear properties of graphite and Al$_2$O$_3$ reinforced AZ91D-Cex composites. Trans Nonferrous Met Soc China 20:s471–s475

Simulation of Craniectomy Size in Decompressive Craniectomy for Ischaemic Stroke

Aina Najwa Nadzri, Mohd Jamil Mohamed Mokhtarudin, Wan Naimah Wan Ab Naim, and Stephen Payne

Abstract Decompressive Craniectomy (DC) surgery is recommended to treat patients who suffered from large ischaemic cerebral infarction. Although DC surgery has been proven to reduce intracranial pressure (ICP) within the skull, too large of DC opening may contribute to risk of tissue injury. Computational studies nowadays are very useful in predicting and decision making, especially in clinical studies. Therefore, a simulation was performed using mathematical modeling on an idealized 3D brain model to evaluate the outcome of different skull opening sizes in DC towards treating the brain tissue swelling in ischaemic stroke. The model is simulated based on poroelastic theory and capillary filtration. Our results show that larger craniectomy size may reduce the midline shift of the ventricle due to swelling tissue. Nevertheless, the bulging of swollen tissue out from the skull opening causes a little amount of stress applied at the edges of the opening. This modelling work may be used for further research in further research in evaluating the suitable craniectomy size for DC.

Keywords Decompressive craniectomy · Stroke · Poroelastic theory · Craniectomy size

A. N. Nadzri (✉) · M. J. Mohamed Mokhtarudin
Department of Mechanical Engineering, College of Engineering, Universiti Malaysia Pahang, 26300 Gambang, Pahang, Malaysia

M. J. Mohamed Mokhtarudin
e-mail: mohdjamil@ump.edu.my

W. N. Wan Ab Naim
Faculty of Mechanical and Automotive Technology Engineering, Universiti Malaysia Pahang, 26600 Pekan, Pahang, Malaysia

S. Payne
Institute of Applied Mechanics, National Taiwan University, Taipei, Taiwan

1 Introduction

Large hemispheric infarction may contribute to the elevation of intracranial pressure (ICP) which can result in brain herniation. The failure of medical treatment to relieve the increasing of ICP in brain has led to the seeking of alternative treatments. Therefore, decompressive craniectomy (DC) surgery may be an effective treatments in treating patients with large brain infarction after ischaemic stroke by creating an additional space to allow for the swelling tissue to extend outward from the skull by removing a portion of bone flap of the skull [1].

In this surgery, the skull opening size is one of the important parameters before the removal process. Large skull opening has always been recommended to reduce the brain swelling. However, too large bone flap removed causes higher risk for complications to occur after the surgery such as infection and hydrocephalus [2]. The minimum diameter of 12 cm for skull opening has been extensively used to minimize ICP level in the brain [3]. The results shown in this article is that 57% of patients who undergo the surgery with skull opening less than 12 cm are found dead after the treatment due to haematoma evacuation and decompression [4].

Computational studies nowadays have been proven to be useful in predicting the clinical outcome and decision making for clinical practice [5]. Hence, in this article, we will evaluate the effect of different sizes of skull opening in minimizing the outcome for swelling of brain tissue due to prolonged ischaemic period by developing the dealized model of 3D brain and application of mathematical modeling based on theory of poroelastic and filtration of capillary previously developed in [6]. Four different of skull opening sizes are used to evaluate their outcome in DC surgery for brain tissue swelling in ischaemic stroke and its complications. This mathematical modeling concept hopefully can be used as prediction strategy into the application of DC for the treatment of ischaemic stroke.

2 Methodology

2.1 Mathematical Model

The swelling of brain tissue formed due to prolonged ischaemic period has been developed by applying filtration of capillary model and equation of poroelastic [6]. The tissue of brain is assumed as an isotropic poroelastic material, which contains of a solid tissue matrix permeated by interstitial fluid and the process of swelling takes place with little amount of strain. The poroelastic model has following equation:

$$\nabla.\sigma_{ij} - \alpha_w \nabla P_w = 0 \tag{1}$$

where the term σ_{ij} is the tissue stress total, P_w is the pressure of interstitial water, α_w is the Biot parameter of water. This equation defined relationship between the stress

of brain tissue and ICP. The equation of interstitial fluid pressure distribution of is as follow:

$$\frac{1}{Q_w}\frac{\partial P_w}{\partial t} - k_w \nabla^2 P_w - S_{b\to w} = 0 \tag{2}$$

where Q_w known as the relative compressibility of water, t is the time while k_w is water permeability in porous tissue. Meanwhile, net flow of water into the tissue of brain from space of capillary due to capillary filtration is defined as term of $S_{b\to w}$. the filtration of capillary is assumed to take place after ischaemic stroke, in which cause by break down of a specialized layer called blood brain barrier (BBB). As a result, particles such as tiny proteins and ions to travel across this layer and accumulate in the extracellular space of brain tissue. The accumulations may cause the water to enter the extracellular space of brain tissue from reperfused blood, which cause swelling of tissue.

σ_{ij}, total stress is linearly correlated to the strain, ε_{ij}, as given by:

$$\sigma_{ij} = 2G\varepsilon_{ij} + \frac{2G\upsilon}{1 - 2\upsilon}\varepsilon_{ii} \tag{3}$$

G is the shear modulus, meanwhile υ is the Poisson's ratio of brain tissue and it has been shown that they play significant roles in the progression of brain swelling [7]. The strain and the displacement of tissue, u_i, are then related, in which associated to the following relationship:

$$\varepsilon_{ij} = \frac{1}{2}\left(\nabla u_i + \nabla u_j\right) \tag{4}$$

Meanwhile, $S_{b\to w}$ term is given below:

$$S_{b\to w} = 2\bar{n}_b \frac{L_p}{R_c} f[(P_b - P_w) - \sigma \Pi_b] \tag{5}$$

where $\bar{n}_b$ is blood fraction baseline volume, L_p is capillary hydraulic permeability, R_c is capillary radius baseline value, σ is the coefficient of reflection, Π_b known as pressure of osmotic in the capillary meanwhile P_b is presumed as a constant, which known to be pressure of blood. Finally, f term indicates as capillaries ratio that maintain open after process of swelling and ischaemia–reperfusion at exact point in space and time.

2.2 Idealized 3D Brain Model

The idealized of brain geometry model, shown in Fig. 1, is developed based on spherical shape suggested by [8]. The brain model is developed by a half sphere

Fig. 1 The idealized 3D
brain model
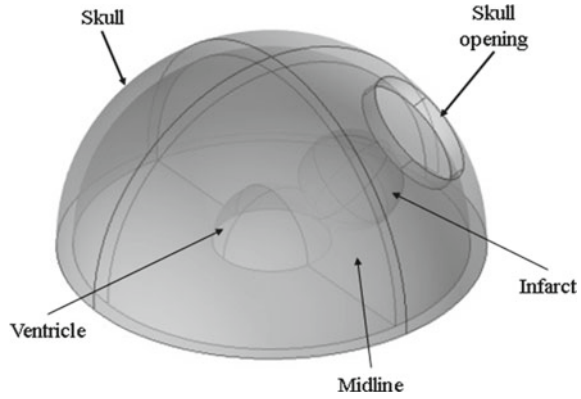
with a hole of half spherical at the center, which indicating the lateral ventricles. Another sphere is constructed within the geometry of half spherical to indicate the infarct of ischaemic. Then, 3D brain model is layered by another half spherical with an opening to represent the skull geometry with DC surgery.

The radius of brain, ventricle and infarct are set to be 80 mm, 24 mm and 14 mm respectively. Meanwhile, to evaluate the opening skull size outcome on DC surgery, the opening skull sizes are varied of 10, 15, 25 and 30 mm.

2.3 Numerical Procedure

The idealized 3D brain model is simulated using finite element software named COMSOL Multiphysic 5.3a. In this simulation, the skull has Young's modulus and Poisson's ratio, described based on Table 1. Meanwhile, the tissue of brain has separate material properties, in which also listed in Table 1 [6].

Boundary Condition. To allow for the outcome of brain tissue swelling on the ventricle movement, the ventricle, R_v, has been set to be moved freely by setting the total stress on the tissue, σ_{ij} on ventricle as follows:

$$\sigma_{ij}(R_v, t) \cdot \text{n} = -P_w(R_v, 0)\text{n} \tag{6}$$

Initial Conditions. Initially, the pressure of interstitial fluid, P_w and the displacement of tissue u are set at baseline $\overline{P}$ and zero, as follow:

$$u(x, 0) = 0 \tag{7}$$

$$P_w(x, 0) = \overline{P} \tag{8}$$

Table 1 Parameter's list

Parameter	Name	Value
Poisson's ratio	ν	0.35
Young's modulus	E_T	2010 Pa
Permeability of brain	K_w	1.4×10^{-14} m^2
Water viscosity	μ_w	1×10^{-5} Pa s
Water Biot parameter	α_w	1
Water relative compressibility	Q_w	3244 Pa
Hydraulic permeability	L_p	3×10^{-11} m/s Pa
Reflection coefficient	σ	0.93
Pressure of osmotic in capillary	Π_b	2445 Pa
Pressure of blood	$\overline{P}_b$	4389 Pa
Pressure baseline value	$\overline{P}$	1330 Pa
Radius of typical capillary	R_c	5×10^{-6} m
Stiffness of capillary wall	E	864.5 Pa
Blood volume fraction baseline value	$\overline{n}_b$	0.03
Fraction of volume water	n_b	0.8
Young's modulus (Skull)	E_s	3.15×10^6 Pa
Poisson's ratio (Skull)	ν_s	0.45

Mesh Element Size. 10-node tetrahedral elements are used to mesh all geometries. Meanwhile, number of elements are varied in within 16,000–19,000. The ischaemic infarct has finer meshes than rest of geometry.

3 Results and Discussion

A simulation of an idealized 3D brain model was performed to evaluate the outcome of DC surgery using different size of skull opening in reducing the midline shift after 5 h of ischaemia–reperfusion. For a simple visualization, the simulation results displayed below based on part of brain that been sliced half through infarcts and skull opening, in which take part at the brain geometry centre.

Figure 2 shows the displacement of tissue of brain for infarct radius of 14 mm with different skull opening sizes. Midline shift that takes place in the middle of ventricle is also known as the brain herniation. In clinical study, brain herniation is used as indicator to predict the severity of brain tissue swelling in stroke [9, 10]. Based on Fig. 2, skull opening size of 30 mm experiences the least herniation compared to the skull opening of 10, 15 and 25 mm of skull opening size. This is because the skull opening causes the reduction of ventricle compression by allowing the brain tissue to swell towards the opening. Even though DC surgery has been proven to reduce
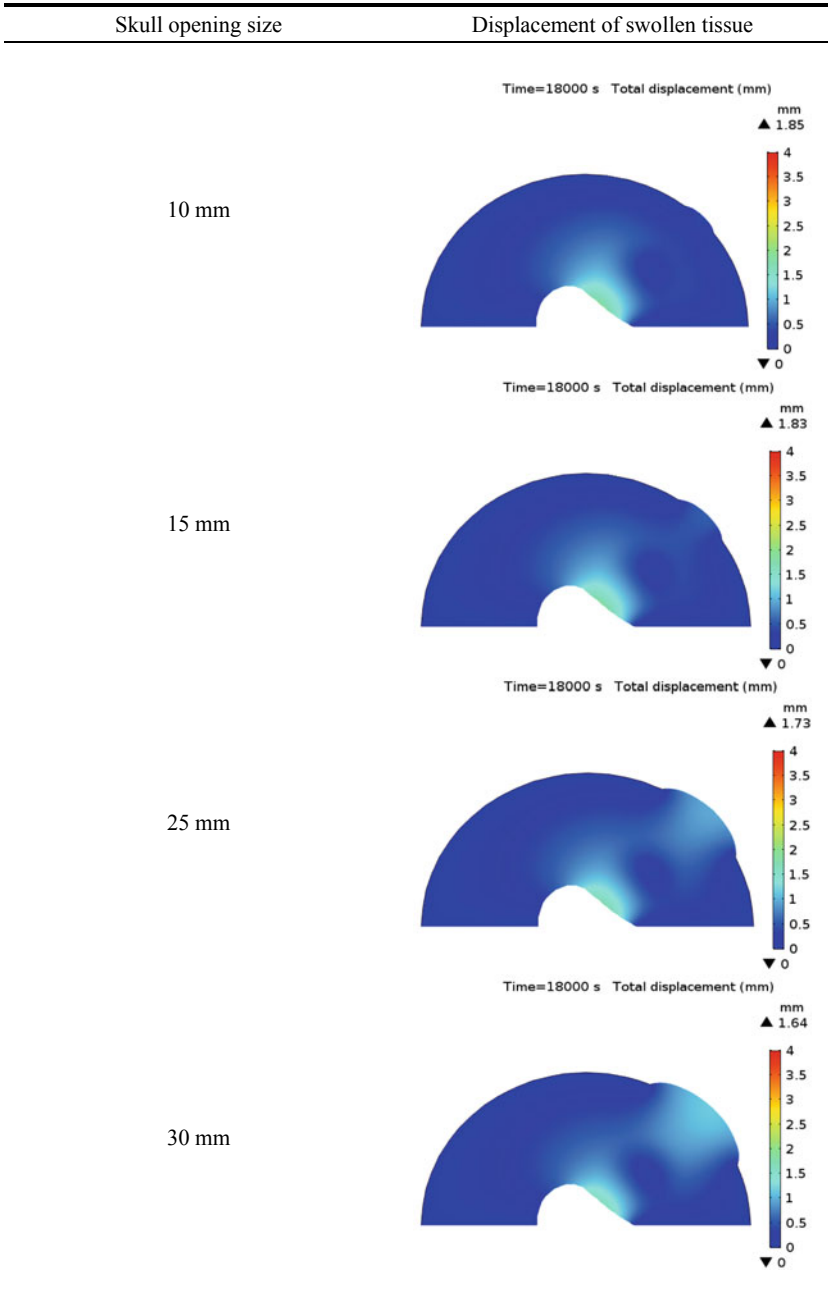
Skull opening size	Displacement of swollen tissue
10 mm	
15 mm	
25 mm	
30 mm	

Fig. 2 The displacement of midline shifted with varies size of opening skull

the elevation of ICP [11] in brain as well as to reduce herniation, this surgery may also contribute some complications that still need to be considered.

Further, Fig. 3 shows that the skull opening size of 10 mm experience major stress in between the opening edges and brain tissue. This is because, small skull opening size increases the compression at the opening edges and also due to high brain tissue strain to bulge out from the skull. This may increase the risk of brain tissue damaged and infections [12].

Meanwhile, the largest skull opening size of 30 mm shows a much higher stress in between the edges of DC opening. Although the larger size of opening reduce the herniation, it may increase the risk of hydrocephalus development [1]. The more the swollen tissue bulged out from the skull, the higher the stress at the area of contact in between the edges of the opening and brain tissue [11]. Too large portion of skull being removed may result in an increase of rate of infections. The DC treatment for brain tissue swelling is still incomplete understood in reducing the severity of the swelling. Based on the findings obtained through this simulation, the larger craniectomy size may improve outcome, however it may also contribute to other complications such as risk of tissue damage, which is observed by the high tissue stress at the opening.

4 Conclusion

In conclusion, the mathematical model developed in this paper can assist the clinicians to obtain related surgical decision before performing the DC surgery on patients with brain tissue swelling due to ischaemic stroke. In our simulation the craniectomy model is developed to show how craniectomy size in DC may affect the brain herniation and complications that may occur after surgery as the treatment for swelling of brain tissue after ischaemia–reperfusion injury in stroke. Further investigation on the effect of ICP during DC surgery can be done to further understanding the efficacy of this treatment.
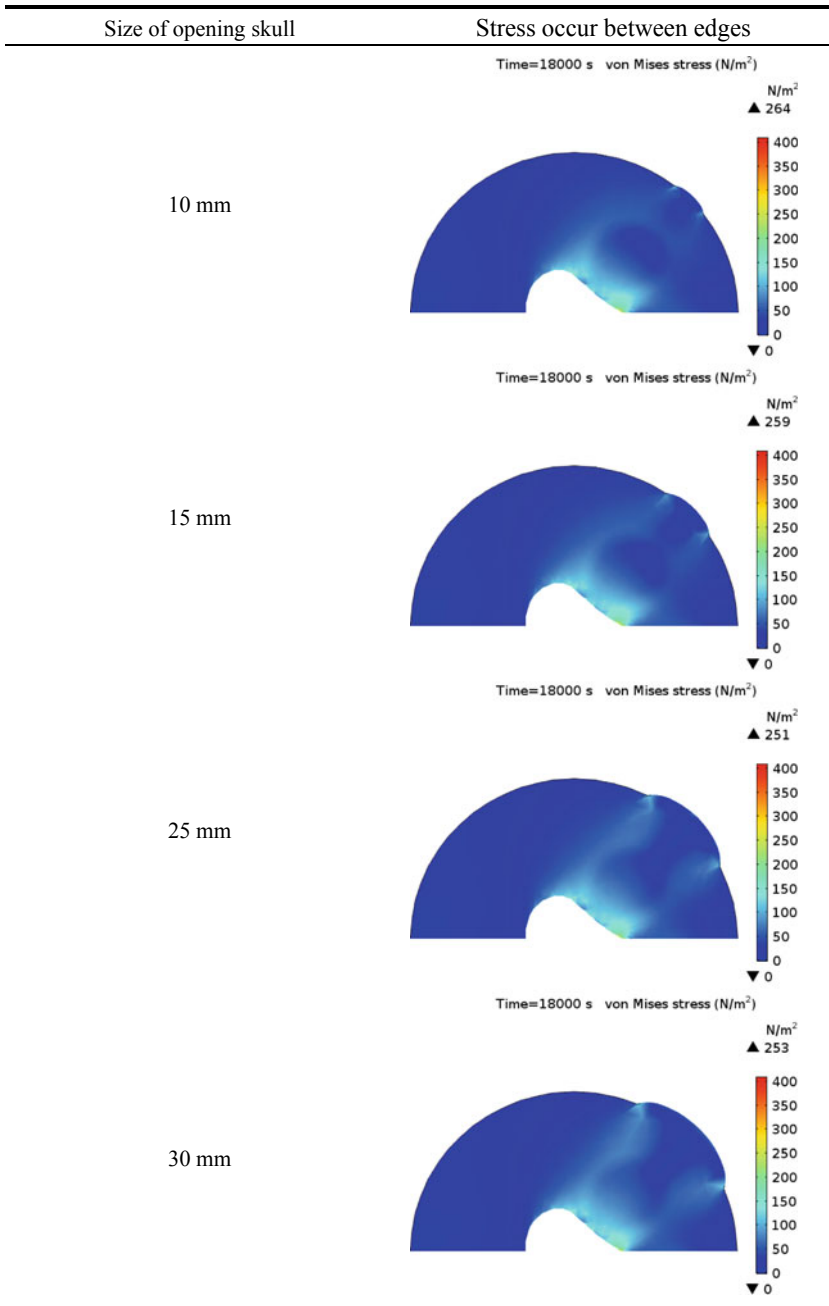
Size of opening skull	Stress occur between edges
10 mm	
15 mm	
25 mm	
30 mm	

Fig. 3 The stress occur between the edges of opening skull

References

1. Kolias AG, Kirkpatrick PJ, Hutchinson PJ (2013) Decompressive craniectomy: past, present and future. Nat Publ Gr., no. Dc, pp 1–11
2. Weickenmeier J, Butler CAM, Young PG, Goriely A, Kuhl E (2017) The mechanics of decompressive craniectomy: personalized simulations. Comput Methods Appl Mech Eng 314:180–195
3. Wagner S, Schnippering H, Aschoff A, Koziol JA, Schwab S, Steiner T (2001) Suboptimum hemicraniectomy as a cause of additional cerebral lesions in patients with malignant infarction of the middle cerebral artery. J Neurosurg 94(5):693–696
4. Tagliaferri F et al (2012) Decompressive craniectomies, facts and fiction: a retrospective analysis of 526 cases. Acta Neurochir (Wien) 154(5):919–926
5. Fletcher TL, Wirthl B, Kolias AG, Adams H, Hutchinson PJ, Sutcliffe MP (2016) Modelling of brain deformation after decompressive craniectomy. Ann Bioemdical Eng 44(12):3495–3509
6. Mohamed Mokhtarudin MJ, Payne SJ (2015) Mathematical model of the effect of ischemia-reperfusion on brain capillary collapse and tissue swelling. Math Biosci 263:111–120
7. Mohamed Mokhtarudin MJ, Shabudin A, Payne SJ (2019) Effects of brain tissue mechanical and fluid transport properties during ischaemic brain oedema: a poroelastic finite element analysis. In: *2018 IEEE-EMBS Conference on Biomedical Engineering and Sciences (IECBES)*, pp 1–6
8. Hakim S, Venegas JG, Burton JD (1976) The physics of the cranial cavity, hydrocephalus and normal pressure hydrocephalus: mechanical interpretation and mathematical model. Surg Neurol 5(3):187–210
9. Steiner T, Ringleb P, Hacke W (2001) Treatment options for large hemispheric stroke. Neurology 57(5 SUPPL. 2):61–68
10. Ryu JH et al (2013) Induced and sustained hypernatremia for the prevention and treatment of cerebral Edema following brain injury. Neurocrit Care 19(2):222–231
11. Nadzri AN, Mokhtarudin MJ, Naim WN, Payne SJ. Simulation of decompressive craniectomy for ischaemic stroke treament: a conceptual modeling study. In: 2020 IEEE-EMBS Conference on Biomedical Engineering and Sciences (IECBES), pp 303–308
12. Von Holst H, Li X, Kleiven S (2012) Increased strain levels and water content in brain tissue after decompressive craniotomy. Acta Neurochir (Wien) 154(9):1583–1593

Understanding the Ergonomics Issues in Sawmill Industries: Why It Becomes a Concern?

**Balqis Syahirah Jamaludin, Ezrin Hani Sukadarin , Mirta Widia ,
and Nazlin Hanie Abdullah**

Abstract This study aims to highlight the ergonomic issues in sawmill industries. Thus, the importance of ergonomics risk factors is sought to be dug out. Sawmill workers are exposed to many occupational safety and health hazards, including ergonomics. Previous studies showed that, with ergonomic principles, the workplace could become safer and indirectly will help in increasing workers' productivity, improve physical and mental wellbeing and job satisfaction among workers. To achieve the study objective, a field observation was conducted, and reviews of published literature were collated to support the findings. In the beginning, a total of 213 articles was identified. However, after undergoing the screening process, only 28 articles are included in this study. Many ergonomics risks are scientifically proven to exist in the sawmill industries. Therefore, the knowledge and understanding of ergonomic risk will help the researchers to plan the next step to improve workers' wellbeing.

Keywords Ergonomic · Sawmill · WMSD

1 Introduction

Successful implementation of ergonomics in the work environment design may balance worker preferences and job requirements. Doing so will increase productivity for the worker and provide workplace health, mental and physical health, and job satisfaction. Previous studies have shown beneficial effects by applying the concepts of ergonomics in workplaces, occupational safety, and health, environment,

B. S. Jamaludin · E. H. Sukadarin (✉) · M. Widia · N. H. Abdullah
Faculty of Industrial Sciences and Technology, Universiti Malaysia Pahang, 26300 Gambang,
Pahang, Malaysia
e-mail: ezrin@ump.edu.my

E. H. Sukadarin · M. Widia · N. H. Abdullah
Advanced Materials and Manufacturing Research Group (AMMRGP), Faculty of Engineering
and Life Sciences, Universiti Selangor, 45600 Bestari Jaya, Selangor, Malaysia

job, machine, and facilities design [1]. In a study conducted by Ali et al. [2] small-scale and unorganised sawmills that provide wide-ranging services with thousands of employees are inadequate in ergonomic procedures, planning, and procedures.

Wood product manufacturing is often labour-intensive and production-oriented, with employees typically work at a rapid pace [3]. Musculoskeletal Disorders (MSDs) among sawmill workers can be devastating and significantly influence daily production, depending on the sort of work they conduct. Heavyweights, uncomfortable postures, and repetitive actions are all substantial risk factors for developing musculoskeletal disorders in these industries. In general, the heavy workload is more vulnerable to load-carrying than the body limit of the workers [4]. The dimensions of the wood, the load, the distance of loading the wood, the number of tasks, and the overall length of tasks are the vital occupational dangers in the sawmill sector. Qutubuddin [5] analysed that most sawmill workers are exposed to several occupational hazards, especially ergonomic problems during sorting, cutting, and processing raw logs.

The previous study showed that sawmill workers are exposed to many occupational safety and health hazards, including ergonomics. Potential problems are the fingers or limbs of the operator's contact with the saw blade or band [6]. Moreover, Queenslan [7] reviewed the hazards of crushing, trapping, bullets, noise, and vibration due to the log debarking process. In sawmill, work activity of manual handling is common. Starting from intake and rough sorting of the woods, debarking, sorting and stacking, adjusting and sorting, wrapping and packaging, and finally loading cleaned wood or logs for delivery, fully mechanising machinery is difficult to be implemented [8].

Potential issues such as inappropriate procedures or repetitive injury associated with bending, gripping, cutting, and awkwardly elevating limbs become the norm when involving human strength and contact. The operation of manually moving and locating logs, such as sorting and stacking where parameters of size and species sort the logs, can lead to overexertion, muscle strain, uncomfortable. Static posture and repetitive work are also common contributing factors to MSDs [9].

According to Poisson et al. [10] most sawmill workers are exposed to hazardous machines like chain conveyors, circular saws, and vertical saws while interacting on equipment at all stages of their life cycle such as in maintenance, adjustment, set-up, troubleshooting, repairs and cleaning, and dismantling. Adjustment and sorting involve cutting off small sections from the log's edges by the band saw. Thus, potential problems are material from the saw blade or band flying towards the operator.

Ergonomic risks have been the subject of numerous studies. However, occupational disease issues continue to rise and have become a matter of concern in the workplace [11]. Therefore, this review needs to be conducted to explore the occupational ergonomics risk factors based on the published articles. The goals of this research are to (1) identified concerns in the sawmill sector, (2) highlight activities and issues from a site visit and (3) based on the issues, suggest workplace control measures that should be implemented. Authors believe that knowledge of the arising issue in the sawmill industry will ease planning to improve workers' wellbeing in the sawmill industry.

2　Methodology

A site visit was conducted to identify the issues in sawmill, particularly in terms of ergonomics. The importance of site visits is to observe the facilities, communicate with workers, and verify the accuracy of previous statements. This phase is crucial in identifying the ergonomic issues in this industry. The sawmill workers that comprised of mill workers and machine operators were observed. The authors also reviewed the published articles regarding ergonomics issues from 1992 to 2019 to further understand the consequences of the exposure. For the reviewing process, the inclusion criteria for the paper selection include; English articles, exposure to any ergonomic risk factor, and ergonomic issues in the sawmill industry. The exclusion criteria were, for example, non-SME Multinational corporations, sectors of government, or sectors that have over 200 employees and ergonomic concerns at other sectors apart from the timber sector. Besides that, duplicate articles in the database are removed.

3　Result and Discussion

3.1　Sawmill Activities

The sawmill runs four areas of operations, namely, kiln-drying, moulding, regrading and surfacing, and transport. The activities of sawmill are depicted in Table 1. Kiln-drying is the process to ensure the wood dry in a chamber with controlled air circulation, humidity, and temperature so that the wood is in moisture content. Moulding is the process of concealing or decorating transitions between surfaces by using four methods: finger-jointed, surfaced four sides, edge-joint laminated board, and surfaced two sides. Besides, regrading and surfacing are required on any defects that may have occurred during the drying. Finally, the wood products will be transported to customers following safe lifting and stacking processes. In Table 1, the safety and health issues that may exist during each operation are also explained.

3.2　Article Searching and Selection

Table 2 shows the results of each phase of retrieving published articles as mentioned in the methodology. Based on the designed search criteria, at the beginning total of 213 articles were identified. However, after undergoing the screening process, only 28 articles are included in this study.

Table 1 The sawmill activities

Operations	Description	Issues
Kiln-Drying	Kiln-drying is one of the most common commercial processes for seasoning wood. External energy is used to drive moisture out of the seasoning process, which speeds up the process [12]	The wood is placed horizontally with wide spaces between each piece and horizontally with strips of wood between each layer to ensure vertical separation and then placed within a chamber where the conditions can be changed to provide the optimum seasoning results. The charge (stacked lumber) is surrounded by air, and the temperature and humidity can be adjusted for optimal drying. Before entering, the kilns must be adequately ventilated and must remain open while working inside. Thus, it is important to direct-fired kilns with fan decks The timbers were left in the kiln for two days to one week. Wood chips and dust should be removed from floors, especially around the heating units, since ignition sources on timber stocks can burn. Then, all wood composites outside kilns must be sealed or stored in containers to keep the passageway clear from obstruction Gaskets around the kiln doors are frequently degraded, allowing gas to escape uncontrollably. When poorly maintained, these same gaskets might become tripping hazards. Thus, safety signage and emergency rescue plan are required in this place
Wood Moulding	**Finger jointed** The purpose of structural finger joints is to keep a piece of wood strong throughout its whole length	A finger joint is a woodworking joint made by gluing shorter pieces of timber end-to-end that have several tapered "fingers" into long pieces. Ergonomics problems occurred, such as poor posture, repetitive motion, reaching out, and bending while arranging the wood piece Personal protective equipment (PPE) that is compulsory to use is safety glasses or safety goggles. This is because the dust from cutting wood and primed wood may irritate eyes, causing discomfort and pain Long sleeves shirts and gloves are also required as the dust from cutting wood, and primed wood may irritate the skin, causing itching and rash Workers should wear suitable respirators while cutting and machining the wood. The dust from cutting wood and primed wood may irritate the nose, throat, and lungs, particularly in respiratory and chest illness sufferers or asthma

(continued)

Table 1 (continued)

Operations	Description	Issues
	 Surfaced four sides (S4S) Surfacing lumber, or dressing lumber, is the act of planning the boards so that each board is smooth and uniformed in thickness	S4S is a finishing process that gives a board planer-finished faces and edges. Bending body and hands while pushing and pulling the timber into and from the machine leads to awkward posture and repetition risk factors. This action can lead to MSDs at the lower back and wrist Emergency instructions and safety signage are required in this area
	 Edge-joint laminated board Laminated timber is a structural wood product made from strips of wood glued	The workers gathered the laminated timber for final checking. Proper lifting technique is a must to avoid muscle injuries due to awkward posture while carrying the wooden boards. Furthermore, safety gloves should be used while lifting the laminated board to minimise workers' exposure to pricks or contact with glues or any other hazardous product Laminated boards are glued to at least four strips or sheets of sawn good. A face mask is needed because workers might be exposed to noxious substances of different nature, such as varnishes, glues, paints, or other hazardous substances like acids or solvents. Volatile Organic Compounds (VOCs) created from the use of varnishes and solvents can induce intoxication, so the company needs to make sure the ventilation is adequate

(continued)

Table 1 (continued)

Operations	Description	Issues
	Surfaced two sides (S2S) S2S is a finish that allows some sections to be slightly rough or "skipped" after dressing	The use of wood planer during S2S involves pushing and pulling acts. Repetitive manual handling might contribute to musculoskeletal system disorders such as tendons, bones, joints, blood vessels, and nerves. Thus, handle height should be between the shoulder and waist to provide a good, neutral stance when pushing or pulling Most of the workers use sanding machines and panel planers in this section. Earmuff must be worn in the workplace to protect the workers from excessive noise at the workplace Workers must be provided with an appropriate face mask to protect them from infections caused by inhaling wood dust and sawdust
Regrading and surfacing	Trimming woods on faults such as split ends, loose knots, and other flaws are managed in this section	Before stacking sawn timber for storage, it is usually inspected for any faults that may have developed during the drying process. When using the vibrating tools, the workers might be exposed to excessive hand-arm vibration. Thus, workers should be reminded to keep their hands warm and dry and not clutch a tight vibrating instrument. Moreover, safety signages are required to be displayed near the machine as a safety precaution The workers must wear earmuffs when using the machine to protect them from excessive noise Floors should be free and clear from wood chips and dust to avoid slips, trips, and falls. Airborne chips and dust generated during machining and sanding processes might cause vision impairment

(continued)

Table 1 (continued)

Operations	Description	Issues
Transport	Sawn timber exported upon request	Manual placement of dunnage entails a lot of bending and reaching, twisting, and other awkward postures. This action may result in cuts and bruises from sharp dunnage and harm to the musculoskeletal systems from repetitive manual handling Direct exposure to ultraviolet (UV) light from the sun, as well as severe heat, is a severe risk when working outdoors. Long periods of exposure to direct sunlight can cause weariness, disorientation, and thirst. So, workers need to be informed on the symptoms of heat-related diseases, such as heat exhaustion or heat stroke, and the indicators of dehydration and allow them to take rest breaks to cool down

Table 2 The result of retrieving published related articles

	Published studies identified through Universiti Malaysia Pahang database—science direct (n = 110)	Studies identified through web of science (n = 11)	Studies identified through ResearchGate (n = 5)	Additional studies identified through google scholar (n = 92)
Identification				
Screening	Studies after duplicates removed (n = 213)			
	Studies screened based on titles (n = 148)	Studies excluded based on titles (n = 65) Reasons: ergonomic not the outcome (63), overlap (2)		
Eligibility	Full-text studies assessed (n = 28)	Full-text studies excluded, with reasons (n = 120) Reasons: unrelated with risk assessment (76), no association (44)		
Included	Studies included in the review (n = 28 articles)			

3.3　Review of Ergonomic Issues in Sawmill Industry

Table 3 depicts the ergonomic issue from the previous studies. The sawmill industry's hazards comprised noise, machinery-related hazards, and ergonomic hazards from lifting heavy loads, reaching for objects, repetitive work, and poor work posture. Heavy work and repetitive motions have mostly been researched for musculoskeletal problems or overexertion, as studied by Holcroft et al. [13]. Manual materials handling such as lifting, pushing, pulling, and carrying timber and logs, was found to be responsible for forty percent of all sawmill injuries [14]. Meanwhile, Bjoring [15] found that repetitive hand movements, especially when combined with force, may cause MSDs in the arm or wrist when severe postures, high external force, high speed, and high static load are present.

　Ng et al. [16] revealed that musculoskeletal disorders MSDs and the global economy. MSDs result from poor work posture, frequent and repetitive movement, force exertion, stress vibrations of psychological and physiological, and physical disability in human beings, such as lower back pain (LBP) and spinal abnormalities. Furthermore, Joshi et al. [17] found that MSDs are a regular occurrence, especially low back pain. The risk identified in work activities, postural loading, vibration effect, tool use, coupling, awkward postures, frequency and duration of movements, and ergonomic workstation design to address the MSDs issues. The

Table 3 Previous studies on the ergonomics issues

Author	1	2	3	4	5	6	7	8
Ng et al. [16]	✓				✓	✓		
Joshi et al. [17]	✓							
Awosan et al. [19]	✓	✓	✓					
Oranye et al. [18]	✓					✓		
Queenslan [7]	✓	✓						✓
Poisson et al. [10]		✓	✓			✓	✓	✓
Griffith [21]	✓							✓
Hermawati et al. [14]	✓						✓	✓
Qutubuddin [5]	✓			✓			✓	
Saldanha et al. [23]	✓	✓	✓	✓			✓	✓
Nunes et al. [25]	✓				✓	✓		
Bello et al. [24]		✓		✓		✓	✓	
Holcroft et al. [13]	✓		✓		✓	✓	✓	✓
Jones et al. [14]	✓			✓	✓			
Bjoring et al. [15]	✓					✓	✓	✓

1 = WMSD; 2 = Noise; 3 = Temperature; 4 = Lifting heavy load; 5 = Forceful Exertion; 6 = Repetitive work; 7 = Poor work posture; 8 = Manual handling

muscles, tendons, tendon sheaths, peripheral nerves, joints, bones, and ligaments are all prevalent WMSDs.

According to Oranye [18] and Awosan et al. [19] the risk of recurrent work injuries is believed to be higher in workers who are experiencing MSDs, resulting in repetitive injuries, job disability, and enormous compensation claims. In the sawmill industries, manual handling is the norm when processing timber, especially when using machinery. Manual handling is defined as the activity that requires a person to raise, lower, move, pulls, carry, throw, restrain or hold an object. Dangers involved with sawmilling, such as machine-related injuries especially when handled incorrectly or without sufficient protections, and excessive noise, can cause irreversible noise-induced hearing damage (NIHL). Other risks include irritation and other negative health effects caused by wood dust and chemicals used in finishing processes, such as allergic skin reactions, asthma, cough, and other respiratory illnesses.

On the other hand, local exhaust ventilation (LEV), which eliminates dust at or near its source, is the most common way of managing wood dust. Exhaust hoods should be placed close to the emission source, either on the woodworking machines or near it. Aside from that, the management of the organisation should take care of indoor air quality. A case reported using the band saw blades might increase silicon concentrations in interior buildings, resulting in harmful indoor air [20]. Queenslan [7] reported that almost all of the job done by sawmill workers involves manual labour. Common issues highlighted are housekeeping, noise, vibration, dust, working at height, hazardous chemicals, manual work lead to MSDs such as repetitive movements, sustained or awkward postures, repetitive or sustained forces, and lastly, psychosocial hazards. Workers are exposed to dangers because they interact with machinery at all stages of its life cycle, including installation, operation, maintenance, troubleshooting, repairs, adjustments, set-up, production disruptions, cleaning, and disassembly.

Gopalakrishnan et al. [8] mentioned that electricity use is significant to operate engines in equipment such as debarker, head saw, re-saw, edger, trimmer, chipper, planer, fans, and pumps, as well as in material handling equipment such as conveyors and belts. Machines can provide various hazards, and exposure to these risks can lead to harm or death. The hazards can be physical such as sharp edges, projections, mechanical such as entanglement, crushing, and cutting. Electrical hazards also can exist. Apart from that, noise and vibration, hot or cold temperatures, physical ergonomics hazards such as awkward working positions, manual handling, repetitive movements also can be found while performing the job in the sawmill industries [10].

Besides, Griffith [21] stated that sawmill processes including timber raising, turning or dragging, adjusting knives of the tool, removing blockages, and cleaning are handled by human strength. Thus, it is essential to walk through the work area, including the access way, and identify all hazards to avoid slips, trips and falls, and MSDS injuries. Surveys such as that conducted by Hermawati et al. [22] have shown that the most often addressed ergonomics issues were working posture and workstation or tool design, followed by material handling and MSDS. Thus, redesigning and evaluating workstations or tools to accommodate worker anthropometry and promote better working postures is crucial.

Activities that are conducted primarily by manual handling often lead to overexertion and long-term risks to health [5]. It has been shown that sawmill workers experience MSDS risks, harsh environmental conditions, strenuous tasks such as manual load handling, awkward postures, and dangerous equipment and machinery [23]. Workplace risks, poor workers' health, mechanical equipment injuries, disabilities, and MSDs caused by poor workplace design, which reduces worker productivity.

Forty percent of sawmill injuries were related to manual material handling, mainly of wood and logs. With the high degree of manual handling in sawmilling processes, employees are exposed to higher risk rates associated with handling logs and operation of machines, environmental hazards, body injury associated with work, and death, in severe cases [24]. The finding showed twenty-seven percent of all industrial back injuries are linked to some form of lifting or manual handling of material. These injuries are usually repeatable and result after months or years of work [25]. An injury is more likely to occur if the employees work in a physically demanding job and are prolonged. MSDS such as repetitive strain injuries (RSI), repetitive motion injuries (RMI), and cumulative trauma disorders (CTDs) are because of soft tissue injuries.

3.4 Review of MSDs Risk

As conjunction from the Table 3, WMSD is the most commonly reported concern in the sawmill business. Workers who are exposed to certain workplace risk factors are at a higher risk of MSDs. High job repetition exhausts a worker's body beyond its capacity to recover, resulting in MSDs. MSDs have the most frequent effect on hands, elbows, ears, eyes, and back. In these areas, they directly affect the nerves, tendons, and muscles. MSDS can also affect particular fingers, elbows, and knees, although they are less common. Table 4 illustrates the previous studies related to the risk of MSDs among sawmill workers.

Prolonged standing during sawmill activities was responsible for 65% of the number and incidence of joint discomfort at back, waist, and foot region. Also, the issue of vascular illnesses, which has grown as an occupational discomfort as a result of sawmill workers standing for long periods [26]. Meanwhile, in a study conducted by Awosan et al. [14] frequent injury reported was due to fatigue, sprains and joint discomfort, back pain, eye infuriation, stress, and exhaustion. Eighty percent of the workers do not undergo occupational health and safety training. So, if workers are uninformed of their working hazards, they are less inclined to defend themselves.

On the other hand, Queenslan [7] reviewed the cause of MSDs where contact with vibrating surfaces such as the heavy seat of machinery or vehicles caused whole-body vibration and lead to low back pain. Heavy lifting, repetitive movements, and improper posture throughout work hours were the main sources of ergonomic risks in the wood processing sectors [27]. Crushed hands, severed fingers, amputations, and blindness are common woodworking accidents, including rotating devices, cutting or shearing blades, in-running nip points, and meshing gears as examples of industrial

Table 4 Causes of musculoskeletal disorders (MSDs)

Author	Causes of musculoskeletal disorders
Sutcu et al. [26]	Loading and unloading of loggers, transportation of huge and heavy goods between machines, and machine loading factors
Awosan et al. [19]	Poor training in occupational health and safety, as well as a lack of understanding of workplace hazards such as back pain, sprains, and joint pains
Queenslan [7]	Grip, manipulate, strike, toss, carry, move (raise, lower, push, pull), hold, or constrain an object or load are all dangerous manual tasks
Mong'are et al. [27]	Hazardous woodworking, high noise levels from operating machines, dust conditions, and work-related musculoskeletal diseases caused by repetitive movements are all factors that are likely to have an impact on employees' health
Saldanha et al. [23]	The inappropriate use of equipment, systems, and tasks creates musculoskeletal system illnesses, particularly back discomfort
Ali et al. [2]	Workers are at risk of MSDs because of hard environmental conditions such as cold temperatures, slick and uneven ground; heavy work likes manual handling of loads, back flexed and twisted, and risky tools and machinery such as chainsaws
Bello et al. [24]	The high occurrence of musculoskeletal and respiratory diseases in the industry was partly due to a disregard for the usage of individual protection devices and other safety equipment
Bjoring et al. [15]	Gripping the spray gun trigger was identified as a high risk for WMSD in the wrist for some of the wood painters

injuries. Previous epidemiological research has shown that assessing the lower arms is critical to avoiding MSDs [28].

In a previous study by Saldanha et al. [23] accidents related to occupational diseases such as RSI and MSDs occur each year in the wood industry, which includes the manufacturing of lumber, veneer, plywood, crowded and pressed wood, products for construction, packaging, industrial, commercial, and domestic use. Moreover, as Ali et al. [2] stated, many employees work in poor postures; nearly 80% of the workers suffered pains in the thighs, legs, and back. As a result of the heavy manual workload, environmental conditions, and dangerous instruments, the loggers may develop MSDs.

Bello et al. [24] reported that fifty-eight percent of sawmill workers were affected with back and lower back injuries. The prevalence of joint discomfort such as back, waist, foot caused by standing in prolonged periods reached sixty-five percent. The worker disregards the use of individual protection such as hand gloves when moving and stacking logs or sawn lumbers and not wearing overalls while carrying logs that primarily serve as lumbar back support.

Bjoring et al. [15] believe that manual spray painting is still widely used in the woodworking sector despite rationalisations. When painting the horizontal surface of the workpiece, the majority of these painters abduct the right upper arm so much that they risk supraspinatus tendinitis. According to recent reports, manual spray

painting is a likable labour task. As a result, spray painters with musculoskeletal issues probably work longer than other employees with similar symptoms.

4 Conclusion

The issue of the sawmilling sector in Malaysia is revealed. Occupational safety and ergonomic issues occur among workers, especially in PPE usage and WMSDs while performing lifting, adjusting machine knives, releasing blockages, and cleaning activities. Furthermore, this industry was susceptible to a wide range of risks, including noise, environmental factors, and ergonomic issues such as awkward work posture, hand-arm, and whole-body vibration. Lifting these problems caused a hazardous workplace environment, affects the worker's health, disabilities such as body injuries while using mechanical equipment, WMSDs and thus result in low efficiency among workers if the ergonomics field is not adequately considered. So, an ergonomic risk assessment should be carried out to determine the workplace risk factors that lead to musculoskeletal disorders.

References

1. Lin RT, Chan CC (2007) Effectiveness of workstation design on reducing musculoskeletal risk factors and symptoms among semiconductor fabrication room workers. Int J Ind Ergon. https://doi.org/10.1016/j.ergon.2006.09.015
2. Ali A, Qutubuddin SM, Hebbal SS, Kumar ACS (2012) An ergonomic study of work-related musculoskeletal disorders among the workers working in typical Indian sawmills. Int J Eng Res 3(9):38–42
3. Top Y, Adanur H, Öz M (2016) Comparison of practices related to occupational health and safety in microscale wood-product enterprises. Saf Sci 82:374–381. https://doi.org/10.1016/j.ssci.2015.10.014
4. Carstairs GL, Ham DJ, Savage RJ, Best SA, Beck B, Billing DC (2018) A method for developing organisation-wide manual handling based physical employment standards in a military context. J Sci Med Sport 21(11):1162–1167. https://doi.org/10.1016/j.jsams.2018.02.008
5. Qutubuddin SM (2013) An ergonomic study of work-related musculoskeletal disorder risks in Indian Saw Mills. IOSR J Mech Civil Eng 7(5):07–13. https://doi.org/10.9790/1684-0750713
6. Bostrand L, Frykman M, Strehlke B, Apud SF, Herstela P (1992) Introduction to ergonomics in forestry in developing countries
7. Queensland Work Health and Safety (2017) Sawmilling Industry Health and Safety Guide 2017. Retrieved from https://www.worksafe.qld.gov.au/laws-and-compliance/work-health-and-safety-laws
8. Gopalakrishnan B, Mardikar Y, Gupta D, Jalali SM, Chaudhari S (2012) Establishing baseline electrical energy consumption in wood processing sawmills for lean energy initiatives: a model based on energy analysis and diagnostics. Energy Eng J Assoc Energy Eng 109(5):40–80. https://doi.org/10.1080/01998595.2012.10531822

9. Chandra AM, Ghosh S, Barman S, Dev S, Gangopadhyay S (2011) An ergonomic study on musculoskeletal health hazards among sawmill workers of West Bengal, India. J Hum Ergol 40(1–2):1–10. https://doi.org/10.11183/jhe.40.1

10. Poisson P, Chinniah Y (2016) Managing risks linked to machinery in sawmills by controlling hazardous energies: theory and practice in eight sawmills. Saf Sci 84:117–130. https://doi.org/10.1016/j.ssci.2015.12.010

11. DOSH (2019) Occupational diseases statistics. Department of occupational safety and health, 10. https://www.dosh.gov.my/index.php/publication-ul/statistik-tahunan/3664-statistik-kemalangan-pekerjaan-2019-1/file

12. Knezevic O, Eng P (1996) Health and safety issues in wood drying operations

13. Holcroft CA, Punnett L (2009) Work environment risk factors for injuries in wood processing. J Safety Res 40(4):247–255. https://doi.org/10.1016/j.jsr.2009.05.001

14. Jones T, Kumar S (2007) Comparison of ergonomic risk assessments in a repetitive high-risk sawmill occupation: saw-filer. Int J Ind Ergon 37(9–10):744–753. https://doi.org/10.1016/j.ergon.2007.05.005

15. Björing G, Hägg GM (2000) Musculoskeletal exposure of manual spray painting in the woodworking industry—an ergonomic study on painters. Int J Ind Ergon 26(6):603–614. https://doi.org/10.1016/S0169-8141(00)00026-3

16. Ng CL, Reaz MBI (2019) Evolution of a capacitive electromyography contactless biosensor: design and modeling techniques. Measur J Int Measur Confederation 145:460–471. https://doi.org/10.1016/j.measurement.2019.05.031

17. Joshi M, Deshpande V (2019) A systematic review of comparative studies on ergonomic assessment techniques. Int J Ind Ergon 74(October):102865. https://doi.org/10.1016/j.ergon.2019.102865

18. Oranye NO, Bennett J (2018) Prevalence of work-related musculoskeletal and non-musculoskeletal injuries in health care workers: the implications for work disability management. Ergonomics. https://doi.org/10.1080/00140139.2017.1361552

19. Awosan KJ, Ibrahim MT, Yunusa E, Isah B, Ango U, Michael A (2018) Section : community medicine knowledge of workplace hazards, safety practices and prevalence of workplace-related health problems among Sawmill workers in Sokoto, Nigeria section : community medicine. Int J Contemp Med Res 5(10):5–12. ISSN (Online): 2393-915X; (Print): 2454-7379|ICV: 77.83

20. Norhidayah A, Ean TJ, Sukadarin EH, Jalil MEA (2016) Physicochemical characteristics of PM10 and PM2.5 in an indoor building. ARPN J Eng Appl Sci 11(18):10786

21. Griffith R (2014) Health and safety in the NHS. Br J Nurs 23(2):112–113. https://doi.org/10.12968/bjon.2014.23.2.112

22. Hermawati S, Lawson G, Sutarto AP (2014) Mapping ergonomics application to improve SMEs working condition in industrially developing countries: a critical review. Ergonomics 57(12):1771–1794. https://doi.org/10.1080/00140139.2014.953213

23. Saldanha MF, Falcao A, Da Silva AD, dos Santos Franz LA (2012). Ergonomic work analysis: a case study in a sawmill located in the south of Brazil. Int J Adv Oper Manag 4(4):283. https://doi.org/10.1504/ijaom.2012.049917

24. Bello SR, Mijinyawa Y (2010) Assessment of injuries in small-scale sawmill industry of southwestern Nigeria. Agric Eng Int CIGR J XII:1–11. http://www.cigrjournal.org/index.php/Ejounral/article/view/1558/1293

25. Nunes IL, Bush PM (2012) Work-related musculoskeletal disorders assessment and prevention. Ergon A Syst Approach, Apr. https://doi.org/10.5772/37229

26. Sütçü A, Semerci NT (2019) Occupational health problems of sawmill workers processing red pine in Turkey. Appl Ecol Environ Res 17(4):7625–7639 https://doi.org/10.15666/aeer/1704_76257639

27. Mong'are RO, Mburu C, Kiiyukia C (2017) Assessment of occupational safety and health status of sawmilling industries in Nakuru County, Kenya. Int J Health Sci 5(4):2372–5079. https://doi.org/10.15640/ijhs.v5n4a9

28. Sukadarin EH, Deros BM, Ghani JA, Nawi NSM, Ismail AR (2016) Postural assessment in pen-and-paper-based observational methods and their associated health effects: a review Postural assessment in pen-and-paper-based observational methods and their associated health effects: a review. Int J Occup Saf Ergon. https://doi.org/10.1080/10803548.2016.1156924

Pressures on Manufacturing Industry to Practice Green Supply Chain Management in Malaysia

Muhammad Fakhrul Yusuf, Rashidah Ramle, and Norhazirawani Abdullah

Abstract Green Supply Chain Management (GSCM) has received increasing attention, at least in recent decades. During this time, it has become apparent that are significant complexities in its management. From both a practical and research perspective, there is a need to simplify and understand this complexity. To further deepen the understanding of the problem, institutional theory, which consists of three institutional pressures, namely government pressure (coercive pressure), market pressure (normative pressure) and competitive pressure (mimetic pressure), was used to investigate the relationship between institutional pressure and GSCM practices in the manufacturing industry in Malaysia. Data were collected using questionnaires in different Malaysian manufacturing companies. The hypotheses were tested using SmartPLS 3. The results from the 118 respondents showed that the command and control instrument and competitive pressure supported the hypothesis, while the economic incentives instrument and market pressure did not support the hypothesis. Finally, the enactment of stringent environmental regulations by the government was found to be most effective in promoting the adoption of GSCM practices.

Keywords Green supply chain management (GSCM) · Institutional theory · Institutional pressures · Sustainable development · PLS-SEM

1 Introduction

Changes in the industrialization of supply chain management (SCM) are happening very fast, which has a negative impact on the environment and ecology. These issues

M. F. Yusuf · N. Abdullah
Faculty of Industrial Management, Universiti Malaysia Pahang, Lebuhraya Tun Razak, 26300 Gambang, Pahang, Malaysia

R. Ramle (✉)
Faculty of Computer and Mathematical Sciences, Universiti Teknologi Mara, Cawangan Perlis, Kampus Arau, 02600 Arau, Perlis, Malaysia
e-mail: idah12@gmail.com

have led to many climate change agreements between nations to act in a more environmentally friendly manner. In response to the increased pressure to become more environmentally friendly, manufacturing companies are moving away from a traditional profit-driven approach to a more balanced approach where both economic and environmental needs are simultaneously pursued as key business objectives [1]. There is no doubt that implementing environmental objectives in the supply chain requires a holistic approach [2]. Green supply chain management (GSCM) is one of the innovations that should be practiced in the industry to overcome the problem. GSCM is a combination of environmental thinking and SCM that includes product design, material sourcing and selection, manufacturing processes, delivery of the final product to the consumer, and end-of-life management of the product [2, 3]. The goal of green supply chain management is to minimize waste and pollution by integrating environmental thinking into product design [4].

In many countries, green innovation has already taken hold. But how many individual companies are addressing this issue? Are they willing to incur more costs for environmental certification such as ISO 14001? Although GSCM research has come a long way, there are still gaps, including but not limited to the identification of GSCM antecedents, their impact on supply chain performance, and barriers from stakeholders, suppliers, and consumers [5]. Abdullah et al. [6] stated that despite the given value and benefits, manufacturers' contribution to green practices falls short of expectations. Due to the difficulties involved, many manufacturers are discouraged from engaging in innovation and remain stuck in familiar routines.

External pressure is the main driving force in getting companies to adopt GSCM practices. Based on several previous findings, [7–12], GSCM has become more important due to pressure from various stakeholders, such as government regulations, government support, consumers, and competitors. These stakeholders exert pressure and motivate companies to minimize the risk of pollution in the supply chain to become an environmentally responsible company [13].

The findings of [11] show that this pressure encourages the adoption of environmentally friendly practices in China. In Malaysia, the awareness of environmental issues is still at moderate level [6, 14]. Therefore, this study aims to determine the relationship between institutional theory and GSCM practices in the manufacturing industry in Malaysia. This theory consists of three institutional factors, namely coercive pressure which consists of two instruments: first, command and control instrument and second, economic incentive instrument. The second pressure is the normative pressure with market pressure as the variable in this study and finally the mimetic pressure with competitive pressure as the variable [15].

2 Literature Review

2.1 Green Supply Chain Management (GSCM)

Since the early 1980s, when the first concept was introduced, the term SCM has been used to describe the planning and control of raw materials, the flow of information and logistics activities within a company and also externally between companies. Over time, the focus of SCM study has broadened. Originally, SCM focused more on material flows. More recent studies emphasize other aspects of SCM such as performance, risk, and integration. In addition, there is an increasing focus on information flows, internal and external relationship networks, and supply network management [4, 16].

Due to environmental issues, many countries are striving for green innovations, and GSCM is one of the green innovations. In today's world, GSCM has become an increasingly complex challenge for companies. Suppliers, customers, regulators, stakeholders, and organizations are increasingly demanding solutions and responses from companies that cause significant environmental impacts in their production cycle [17].

There are 22 different definitions of GSCM by Ahi and Searcy [4], but the most commonly used definition in the literature is by Srivastava [18], who defines GSCM as the integration of environmental thinking into SCM, including product design, material sourcing and selection processes, delivery of the finished product to consumers, and end-of-life management of the product after its useful life [17]. Srivastava [18] added that the scope of GSCM ranges from reactive monitoring of general environmental management programs to more proactive practices implemented through various Rs which are reduce, reuse, rework, reclaim, recycle, reprocess, remanufacture, reverse logistics and more.

2.2 Institutional Theory

Institutional theory is concerned with the deeper and more efficient aspects of institutional structure. It looks at the processes by which systems, including schemes, rules, norms and routines, are developed as authoritative social guidelines for behaviour [15]. Organisations are part of a social system with their own unique culture and values, apart from having a production system. Organisational decisions are based on cultural values, norms and behaviours under the influence of the external environment. When all organisations in the same industry adopt the same institutionalised practises and decision-making approaches, it shows that they are trying to become verified. Institutional theory is used to understand the types of external factors that compel an organisation to adopt or apply a new practise [1]. Based on institutional theory, this study assumes that organisational decisions depend on the social structure in which the organisation operates both externally and internally [19].

The pressures for GSCM practises in this study use an institutional theoretical framework of DiMaggio and Powell [15], which consists of three isomorphic pressure factors, namely coercive pressure, normative pressure, and mimetic pressure. Each of these three pressure factors offers testable hypotheses relevant to the study of green supply chain management antecedents. Many researchers have recognised the importance of institutional theory in explaining corporate behaviour. Institutional theory proposes that organisations can improve their ability to grow and survive in a competitive environment by satisfying their stakeholders [5].

Government Pressures as Coercive Pressure

DiMaggio and Powell [15] stated that coercive isomorphism arises from the pressures exerted on a dependent firm by other organisations, as well as the cultural expectations of the society in which it operates [19]. In this research, government legislation is defined as coercive pressure that drives Malaysian GSCM production practises to improve their performance. Coercive pressure is usually an important factor driving the environmental management practises of producers in developing countries like Malaysia. The government is the overarching organisation that can influence the actions of an organisation [20]. Although government legislation can be an encouragement for GSCM practises, managers usually assume that the government exerts the strongest external pressure on the organisation's environmental initiatives. Organisations must comply with these environmental legislation, otherwise they face legal action, penalties or, in the worst case, exclusion from the market [11]. Following Li [5], other researchers show that innovation-friendly rules provide ample incentives to encourage organisational environmental innovation practises. While there is some empirical evidence, the results are mixed [5, 21].

There are two types of instruments that influence government regulation, namely command and control instruments and economic incentives for GSCM practises. In the command and control instrument, the authorities or governments give instructions to the public or organisations through the enactment of laws, the development of behaviours and the use of enforcement machinery to make people comply with the laws. The command and control instrument in environmental policy essentially involves setting standards to protect or improve the quality of the environment [22]. Economic incentive instruments rely on market prices and relative price changes to change the behaviour of public and private polluters in ways that support environmental protection or improvement [23]. Some researchers believe that economic incentive instruments are more effective than command-and-control instruments because they provide more benefits to the organisation. In this case, the basic message is more important than the choice of basic instruments. Other researchers argue that there is no single rule that is suitable for all cases, but that a combination of policy instruments should be made depending on the different circumstances of each instrument. For example, with the implementation of command-and-control policies such as environmental regulations, emission standards, product restrictions and

economic incentive instruments such as better taxes, trade permits and subsidies for environmental innovation [5, 21].

Market Pressure as Normative Pressure

According to DiMaggio and Powell [15], normative pressure comes from professional pressure. Normative pressure arises from certain norms and standards that are formalised by the approach based on the expectations of the environmental culture. Various groups can be a source of normative pressure, including educational institutions that teach cognitive behaviour, professionals from industry groups and associations, non-governmental organisations (NGOs) with a special interest in particular industries, and also the general public. In addition, suppliers and customers are also one of the main components of this pressure [1].

Li [5] added, market demand can exert strong pressure on companies' environmental initiatives and can be an important normative pressure. Customer demand analysis focuses on identifying, understanding and responding to customers' needs and developing products that meet their expectations [24]. Li [5] also noted that previous studies identified two reasons for companies to produce green products. First, there is an increasing demand for green products from end consumers. According to this, retailers who want to green their supply chain take into account customer pressure, and if customer pressure does not affect companies, they may not be willing to practise GSCM. The other reason is the initiatives within the company to protect the environment [11].

Market pressure can come from two types of consumers. First, from the pressure from overseas customers. With the increasing economic globalisation from seller's to buyer's markets, companies need to adopt environmental practises to meet the demand for exports and sales to overseas customers and partners. This in turn leads to a green multiplier effect, where the requirements for green products and materials must also be adopted by suppliers [25]. Second, domestic customers. Awareness of environmental issues leads domestic customers to want to buy more and more green products, so companies need to take measures to implement GSCM [5].

Competitive Pressure as Mimetic Pressure

Mimetic pressure is a company's default response to uncertainty [15]. Environmental practises have become an area where companies can gain a competitive advantage over their rivals as more and more companies nowadays have high quality goods, good customer service and other competitive advantages. Other studies have also examined the need for companies to pay more attention to changes in their competitors' environmental strategies. In order to gain a competitive advantage, more and more environmentally friendly products are being offered in the market nowadays. Many companies are starting to use environmental innovation as an important differentiation tool to improve their efficiency, product quality and green image. However, there are some problems in understanding competitors' strengths, weaknesses, capabilities and strategies and identifying their technologies to meet the demand of target customers [5].

According to Ye et al. [19], competitive pressure puts pressure on companies to adopt reverse logistics. As reverse logistics management becomes a standard practise and thus an appropriate capability, companies will support and sustain these competitive practises. Moreover, as more companies establish environmentally friendly production facilities, they will put pressure on their upstream suppliers to improve their environmental performance. The growing competition and expectations triggered by the widespread use of reverse logistics and recovery measures will put pressure on top managers to address reverse logistics practises. As reverse logistics is part of the GSCM, this pressure may encourage Malaysian manufacturers to adopt environmentally friendly practises.

From the above arguments, the framework in Fig. 1 was derived and the following hypotheses were developed to be tested in this study.

H1a   Government command and control environmental regulations are positively related to green supply chain management practises.
H1b   Economic incentive instruments are positively related to green supply chain management practises.
H2   Market pressure is positively related to green supply chain management practises.
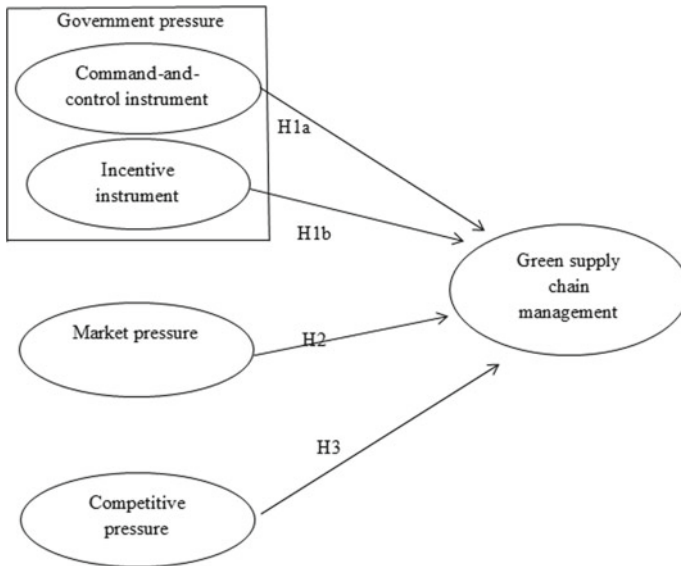H3   Competitive pressure is positively related to green supply chain management practises.

Fig. 1 Research framework

3 Methodology

In this quantitative study, stratified random sampling was used to collect data. Data was collected through email from various manufacturing companies in Malaysia. The 118 respondents who answered the questionnaire were from 21 different manufacturing industries with green certifications such as ISO 9001, ISO 14001, MyHijau, etc.

The questionnaire consists of three parts, namely demographic information, GSCM practises and institutional pressure. GSCM practises were measured using an already established instrument that has been shown to be reliable and valid in previous research [26]. The instrument consists of fourteen items. Each question was scored on a five-point scale, with 1 representing 'not considered', 2 representing 'considering', 3 representing 'currently considering', 4 representing 'beginning implementation' and 5 representing 'successful implementation'. Three-part questions on government pressure, market pressure and competitive pressure were used to measure the construct "institutional pressure". All questions were in the form of a 5-point numerical Likert scale ranging from 1 (strongly disagree) to 5 (strongly agree) [5, 19]. The hypotheses were analysed using the PLS-SEM method. The decision to accept or reject the hypothesis was made and supported by the researcher based on the t-value.

4 Results

Convergent validity means that a measurement should be positively correlated with alternative measurements of the same construct. The average variance extracted (AVE) and the outer loadings of the indicators were determined to establish the convergent validity of the model [27]. The average variance extracted (AVE) is a leading measure of convergent validity. It measures the unidimensionality of a construct to avoid systematic measurement error [28]. Table 1 shows that all constructs yield a AVE of more than 0.5 and can thus be considered acceptable [28].

A look at Table 2 shows that the moderate and strong relationships with GSCM practises are the command and control instrument CCI (0.434) and competitive pressure CP (0.328). And, the economic incentives instrument, EII (-0.163) and market pressure, MP (-0.131) respectively.

To run the PLS-SEM algorithm in SmartPLS, a few parameters need to be set. Figure 2 shows the results after the estimation is complete. The impacts on green supply chain management practises are command and control instrument (CCI) (0.431), economic incentive instrument (EII) (-0.194), market pressure (MP) (-0.134) and competitive pressure (0.327). Path coefficients above 0.2 are significant according to the rule of thumb and path coefficients below 0.1 are usually not significant (Hair et al. 2014). The finding that the economic incentive instrument and market pressure provide a direct path to green supply chain management practises

Table 1 Convergent validity

Construct	Item	Outer loading	CR	AVE
CCI	CC127	0.952	0.951	0.907
	CCI26	0.953		
CP	CP35	0.908	0.936	0.829
	CP36	0.904		
	CP37	0.92		
EII	EII28	0.904	0.922	0.798
	EII29	0.868		
	EII30	0.908		
GSCM	GS12	0.834	0.953	0.594
	GS13	0.835		
	GS14	0.816		
	GS15	0.795		
	GS16	0.768		
	GS17	0.812		
	GS18	0.838		
	GS19	0.796		
	GS20	0.814		
	GS21	0.616		
	GS22	0.786		
	GS23	0.689		
	GS24	0.677		
	GS25	0.664		
MP	MP31	0.759	0.913	0.724
	MP32	0.879		
	MP33	0.881		
	MP34	0.879		

Note *CCI* Command and control instrument; *EII* Economic incentive instrument; *CP* Competitive pressure; *GSCM* Green supply chain management; *MP* Market Pressure

that is below 0.1 was of concern, so further analysis such as a multi-group analysis was planned at a later stage to understand the real-life phenomena compared to the theory.

Bootstrapping is used to identify the supported relationships of the structural model. To support the decision, the T-value must be greater than 1.6457. Table 2 shows that two factors support the decision and the relationship with GSCM practises, namely the command and control instrument and competitive pressure. On the other hand, the economic incentive instrument and market pressure do not support the relationships.

Table 2 Summary of hypotheses testing of initial PLS path model

Hypotheses	Relationship	Std.Beta	Standard error	*t*-value	Confidence interval		Decision
					5.00%	95.00%	
H1a	CCI— > GSCM	0.434	0.119	3.625	0.226	0.614	Supported
H1b	EII— > GSCM	− 0.163	0.121	1.596	− 0.443	− 0.051	Not supported
H2	MP— > GSCM	− 0.131	0.127	1.051	− 0.366	0.057	Not supported
H3	CP— > GSCM	0.328	0.133	2.459	0.11	0.55	Support

*Note * p < 0.05*
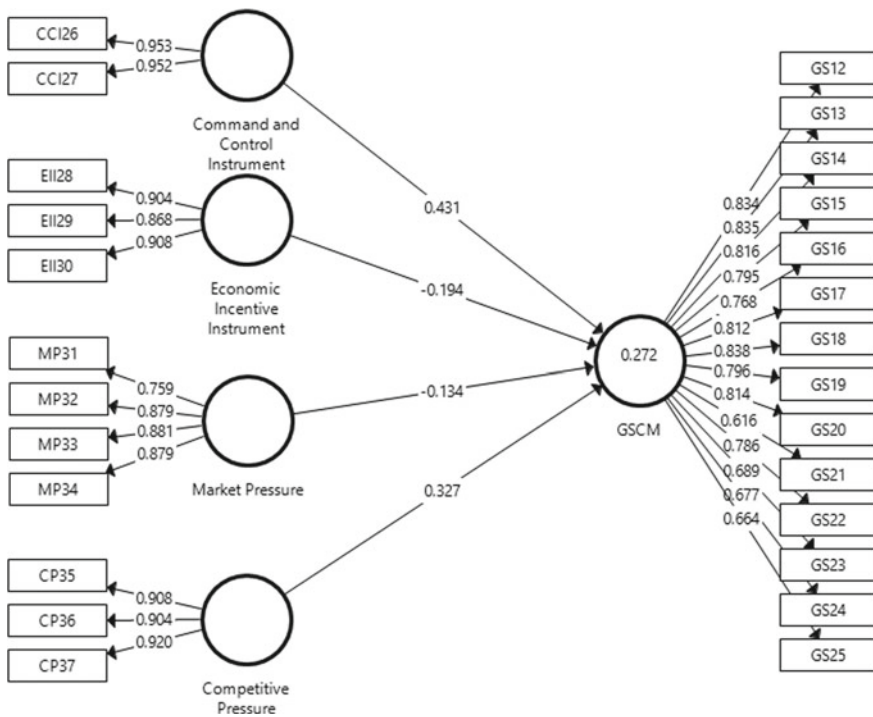
Fig. 2 Hypothesized PLS path model

5 Discussion

The first research objective was to determine the relationship between government pressure and GSCM practices in the manufacturing industry in Malaysia. As shown in Table 2, H1a (command and control instrument) supports the hypothesis that there

is a positive relationship with GSCM practices. This is in line with the findings of Ye et al. [19] who found that command and control instrument is an effective driver of GSCM practices. Esfahbodi et al. [29] found that under institutional pressure, coercion related to compliance due to the influence of those in power is the most important driver of manufacturing firms' environmental initiatives. However, hypothesis H1b (economic incentive instrument) showed that the hypothesis was not supported. The results are consistent with Li [5] who observed that the economic incentive instrument is not well established in China and remains weak, so it does not provide sufficient incentives for manufacturers to adopt GSCM practices. Abdullah et al. [6] also noted that although the government in Malaysia supports manufacturers through loans, subsidies and grants to encourage firms to adopt environmentally friendly practices, the control and pressure of regulations and incentives are rather inconsistent. This is demotivating for manufacturers.

The second research objective was to determine the relationship between market pressure and GSCM practices in the Malaysian manufacturing industry. As shown in Table 2, hypothesis H2 (market pressure) indicating that there is an insignificant relationship with GSCM practices. The results are also consistent with Vanalle et al. [13], who found no positive relationship between normative pressure (market pressure) and GSCM. Yusuf et al. [24] found that the purchase of an eco-friendly product in Malaysia is not primarily because of the environmental benefits, but consumers purchase the product because it fulfils the desired functions and requirements.

The third research objective was to determine the competitive pressure from GSCM practices in the manufacturing industry in Malaysia. As shown in Table 2, hypothesis H3 (competitive pressure) is supported and shows a positive relationship with GSCM practices. The results are consistent with Hsu et al. [30] who found that competitive pressure also has a positive influence on green product practices. Several other studies have also found that competitive pressure has a direct impact on the adoption of green product practices [5, 11]. Companies' improvements in the international market are indirectly reflected in the domestic market, as green products are also marketed in Malaysia. This puts pressure on upstream suppliers and their domestic competitors to improve their environmental practices as well [19].

6   Conclusion

The purpose of this study is to determine the relationship between institutional pressure and GSCM practices in the manufacturing industry in Malaysia. The study found that only two factors positively influence the practices, namely command and control pressure as coercive pressure and competitive pressure as mimetic pressure. Malaysian manufacturers seem to adopt green practices when there are strict environmental regulations to avoid being penalized by the government. They will also adopt green practices for competitive reasons to gain a competitive advantage. However, the economic incentives instrument in the form of coercive measures has little influence on the decision to adopt GSCM practices. This could be due to the

fact that government regulation and support is rather inconsistent. The same is true for market pressure as normative pressure coming from consumers. Low consumer environmental awareness means that manufacturers do not need to set higher standards for environmentally friendly products. In general, this result will help policy makers to enact strict regulations, researchers to conduct further studies on the causes and drivers of GSCM, and manufacturers in Malaysia to incorporate green features in their traditional products. This will also have an impact on raising awareness of green products among consumers in Malaysia.

References

1. Saeed A, Jun Y, Nubuor SA, RasikaPriyankara HP, Jayasuriya MPF (2018) Institutional pressures, green supply chain management practices on environmental and economic performance: a two theory view. Sustain 10(5):1–24
2. Tundys B (2018) Green supply chain—barriers and benefits of implementing the new management strategy—analysis of the empirical research. Eur J Serv Manag
3. Tronnebati I, Jawab F (2020) The similarities and differences between the green and sustainable supply chain management definitions and factors: a literature review. In: 2020 13th International colloquium of logistics and supply chain management, LOGISTIQUA 2020
4. Ahi P, Searcy C (2013) A comparative literature analysis of definitions for green and sustainable supply chain management. J Clean Prod
5. Li Y (2014) Environmental innovation practices and performance: moderating effect of resource commitment. J Clean Prod 66:450–458
6. Abdullah M, Zailani S, Iranmanesh M, Jayaraman K (2016) Barriers to green innovation initiatives among manufacturers: the Malaysian case. Rev Manag Sci 10(4):683–709
7. Hajikhani M, Wahiza Binti Abdul Wahat N, Bin Idris K (2012) Considering on green supply chain management drivers, as a strategic organizational development approach, Malaysian perspective. Aust J Basic Appl Sci
8. Abdullah R, Mat Daud MS, Ahmad F, Shukti AA, Shah MZ (2016) Green logistics adoption among 3PL companies. Int J Supply Chain Manag
9. Shahlan MZ, Sidek AA, Suffian SA, Hazza MHFA, Daud MRC (2018) An examination on the influence of small and medium enterprise (SME) stakeholder on green supply chain management practices. In: IOP conference series: materials science and engineering
10. Puspani NS, Hutomo A, Sinaga O (2019) Role of market: How knowledge acquisition impact on investment recovery and reverse logistics towards sustainability performance. J Adv Res Dyn Control Syst
11. Zhu Q, Sarkis J, Lai K (2013) Institutional-based antecedents and performance outcomes of internal and external green supply chain management practices. J Purch Supply Manag 19(2):106–117
12. Sarkis J, Gonzalez-Torre P, Adenso-Diaz B (2010) Stakeholder pressure and the adoption of environmental practices: the mediating effect of training. J Oper Manag 28(2):163–176
13. Vanalle RM, Ganga GMD, Godinho Filho M, Lucato WC (2017) Green supply chain management: an investigation of pressures, practices, and performance within the Brazilian automotive supply chain. J Clean Prod 151(2):250–259

14. Aldeehani A, Sulaiman S, Aziz FA, Mustapha F (2018) Development of green supply chain management in food industry. In: Proceedings of the International Conference on Industrial Engineering and Operations Management
15. DiMaggio PJ, Powell WW (1983) The iron cage revisited: institutional isomorphism and collective rationality in organizational fields. Am Sociol Rev 48(2):147–160
16. Mukhamedjanova KA (2020) Concept of supply chain management. J Crit Rev
17. de Oliveira UR, Espindola LS, da Silva IR, da Silva IN, Rocha HM (2018) A systematic literature review on green supply chain management: research implications and future perspectives. J Clean Prod
18. Srivastava SK (2007) Green supply-chain management: a state-of-the-art literature review. Int J Manag Rev
19. Ye F, Zhao X, Prahinski C, Li Y (2013) The impact of institutional pressures, top managers' posture and reverse logistics on performance—evidence from China. Int J Prod Econ 143(1):132–143
20. Zhu Q, Sarkis J, Lai K (2007) Initiatives and outcomes of green supply chain management implementation by Chinese manufacturers. J Environ Manage 85(1):179–189
21. Jaffe AB, Newell RG, Stavins RN (2004) Technology policy for energy and the environment. In: Jaffe AB, Lerner J, Stern S (eds) Innovation policy and the economy. Volume 4. Cambridge and London, Brandeis U, pp 35–68
22. Elazegui DD (2002) A law of nature: the command-and-control
23. Bernstein JD (1993) Alternative approaches to pollution control and waste management: regulatory and economic instruments. In: Alternative approaches to pollution control and waste management. Regulatory and economic instruments
24. Yusuf MF, Ashari H, Razalli MR, Ramle R (2016) Environmental technological innovation and market demand: is market orientation a missing link? Int J Bus Manag Study 3(2):1–5
25. Henriques J, Catarino J (2014) Sustainable value and cleaner production—research and application in 19 Portuguese SME. J Clean Prod 1–8
26. Zhu Q, Sarkis J, Geng Y (2005) Green supply chain management in China: pressures, practices and performance. Int J Oper Prod Manag 25(5):449–468
27. Hair JF, Hult GTM, Ringle CM, Sarstedt M (2014) A primer on partial least squares structural equation modeling (PLS-SEM). SAGE Publications Inc.
28. Henseler J, Ringle CM, Sarstedt M (2016) Testing measurement invariance of composites using partial least squares. Int Mark Rev 33(3):405–431
29. Esfahbodi A, Zhang Y, Watson G, Zhang T (2017) Governance pressures and performance outcomes of sustainable supply chain management—an empirical analysis of UK manufacturing industry. J Clean Prod
30. Hsu C-C, Tan KC, Zailani SHM, Jayaraman V (2013) Supply chain drivers that foster the development of green initiatives in an emerging economy. Int J Oper Prod Manag 33(6):656–688

The Crashworthiness Performance of the Energy-Absorbing Composite Structure—A Review

Irshad Ahamad Khilji (ID)**, Siti Nadiah Mohd Saffe** (ID)**,
Chaitanya Reddy Chilakamarry** (ID)**, and Siti Aishah Rusdan**

Abstract The improved energy absorption capacity of composite materials will upgrade people's safety in accidents. Several parameters affect energy absorption such as fibre type, matrix type, fibre architecture, specimen geometry, processing conditions, fibre volume fraction, and test speed. These parameters influence the composite material-specific energy absorption. The distinct characteristic properties of composites play an essential role in a variety of industries. Automotive applications have attracted worldwide attention due to their rapid use and are expected to increase. This review focuses on understanding the effect of a particular parameter on the energy absorption capability of composites, an analysis of the energy absorption properties of polymer composites. The data from the various researchers are collected and categorised in the field of energy absorption of composites. Many testing methods and refraction types for composites are described.

Keywords Crash assessment · Composite material · Energy absorption · Polymer · Testing

1 Introduction

The energy absorbed by metallic materials during an impact or crash of moving vehicles is converted into plastic deformation energy. However, composite structures also absorb energy to convert impact or kinetic energy into deformation-absorbed energy [1]. The energy absorption capacity (EAC) of composite structures is higher than metallic equivalents. Recently, composite materials gained popularity due to their ability to absorb energy from crushing objects. The daily usage of composite

I. A. Khilji · S. N. Mohd Saffe (✉) · S. A. Rusdan
Faculty of Manufacturing and Mechatronics Engineering Technology, Universiti Malaysia Pahang, Pekan, Malaysia
e-mail: sitinadiah@ump.edu.my

C. Reddy Chilakamarry
Faculty of Chemical and Process Engineering Technology, Universiti Malaysia Pahang, Gambang, Kuantan, Malaysia

materials intended for crushing objects by energy absorption attracted human. Prominent investigators specialising in crash resistance have carried out of highly unique research undertakings. The word crashworthiness means the ability to secure stuff from accidents or damage or death of passengers, cargo, or valuables. The factor that impacts the adequate energy absorbed is determined by the material used to produce energy absorption equipment. Energy-absorbing metallic structures (EAMS) have increased in popularity for more than twenty years [2].

Further, researchers have increasingly embraced the utility of energy-absorbing composite structures (EACS) in crashworthiness applications [3]. The desire to apply EACS to aviation, automobiles, vessels, wind turbines and space exploration arises from their significant benefits over metals and alloys. One of the benefits of EACS over EAMS is its lightweight that results in low consumption of fuel, and making it environmentally friendly. Additional benefits include improved mechanical qualities like greater strength, greater specific rigidity, promising vibration regulators, lesser density, and lower noise potential [4].

The significant key role is to provide safety and protection during crash incidents. Thus, choosing the right combination of composite material and the best manufacturing process must be confirmed. A variety of composite materials are used with various syntheses approaches to construct and design composite energy absorbers. The ultimate strength and crash resilience performance of EACS life cycles depend on the material composition, process of production, and sustainability maintenance. As a result of the crash, composite crushed tubes or structures break through a complex microstructural mechanism. Their performance is determined through many parameters that include specific energy absorption (SEA), the ability for energy absorption (EA), crush strength efficiency (CSE), mean crushing force (MCF), and loss of sound transmission (STL) [5–7]. Additional performing indices comprise initial peak force (Fi), peak/critical crushing force (Fp), initial failure indicator (IFI), and energy absorption efficiency (EAE) [8]. Figure 1 depicts the formula with absorption indicators of major crashworthiness. Various research on composite structure claimed that SEA and EA parameters are most important for industry 4.0.

The energy absorber exhibits an improved SEA, CFE, and EA and reduces the initial peak force through crushing or impacts. Increased early peak load and force lead to a decreased crashworthiness efficiency of the crushed tube. Once exposed to quasi-static or lower velocity the dynamic stress conditions, composite tubes, sections, and lattices were examined. Almost many surveys found failure mechanisms following crushing impact circumstances [9]. In technology, many investigators have focused on fracture processes while analysing the crashworthiness of the composite structure. Fibre breaking, delamination, cracking matrix, and debonding matrix are responsible for fracture processes. Figure 2a, b show a ply model schematic from different fracture mechanisms. Matrix cracking and fibre breakage are called an intralaminar breakdown mechanism caused by damage in the layer because of low resin and laminated structure tensile properties [10]. In this case, the stress-energy created on the surface during the fracture is more than the vital energy. Warrior et al. have thoroughly conveyed the influence of inter-luminary methods on the crushing implementation of EACS [11]. Many researchers reported the crushing failure due
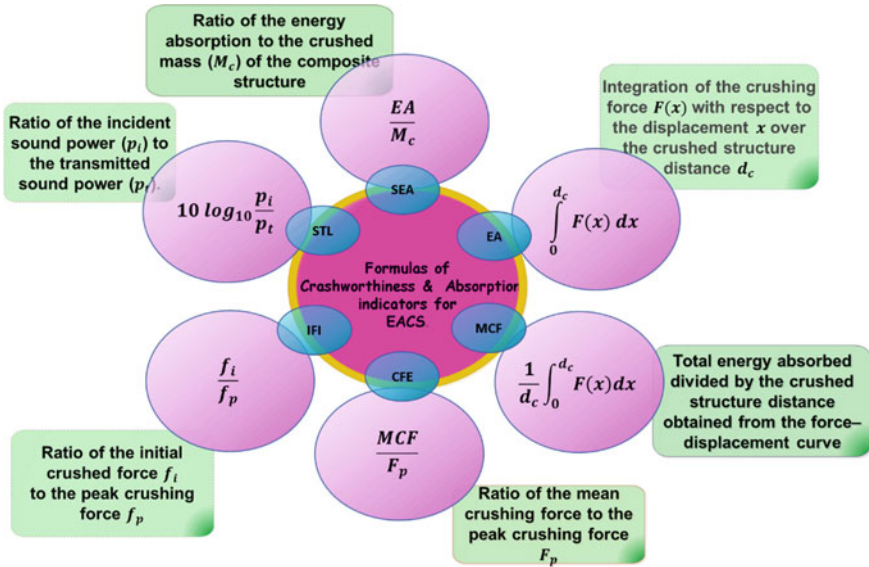
Fig. 1 Formulas for EACS

to lamina bending, brittle fracturing, splaying, and transverse disintegration [12]. Another purpose of this assessment is to investigate the various composite materials that researchers have utilised to create energy absorbers. These can be obtained in either a natural or artificial manner. Polymer composites can be formed using different fabrication procedures to make varied energy absorption composite structures due to fibre reinforcements and matrix resins [13].

Composites are materials created by combining existing materials that are made up of at least two materials. The first continuous component, the matrix, acts as a binder, while the secondary discontinuous component (particle, fibre, or layer distribution) is enforced [14]. Because of their excellent mechanical properties, they are used in a variety of industries. However, high prices and labour-intensive production primarily hamper composites. The automotive industry was the first to use composites in motorsport. Composite materials are now used in mass-produced cars as well as sports and luxury vehicles. Car manufacturers are working to reduce vehicle weight and emissions by improving vehicle safety and durability for long life. The composite materials manufacturers noticed the use of composites to develop an appropriate technology that will make composite parts easier, cheaper, and faster [15]. Composite structures are the most advanced in the automotive industry, and their use in the production of automotive components has a promising future. Automobile manufacturers make an attempt to lower the vehicles weight by enhancing their durability and safety. The number of cars driven and the amount of pollution emitted are consistently regulated [16]. Composite materials provide various advantages with a wide range of qualities that satisfy the needs of today's automobiles.
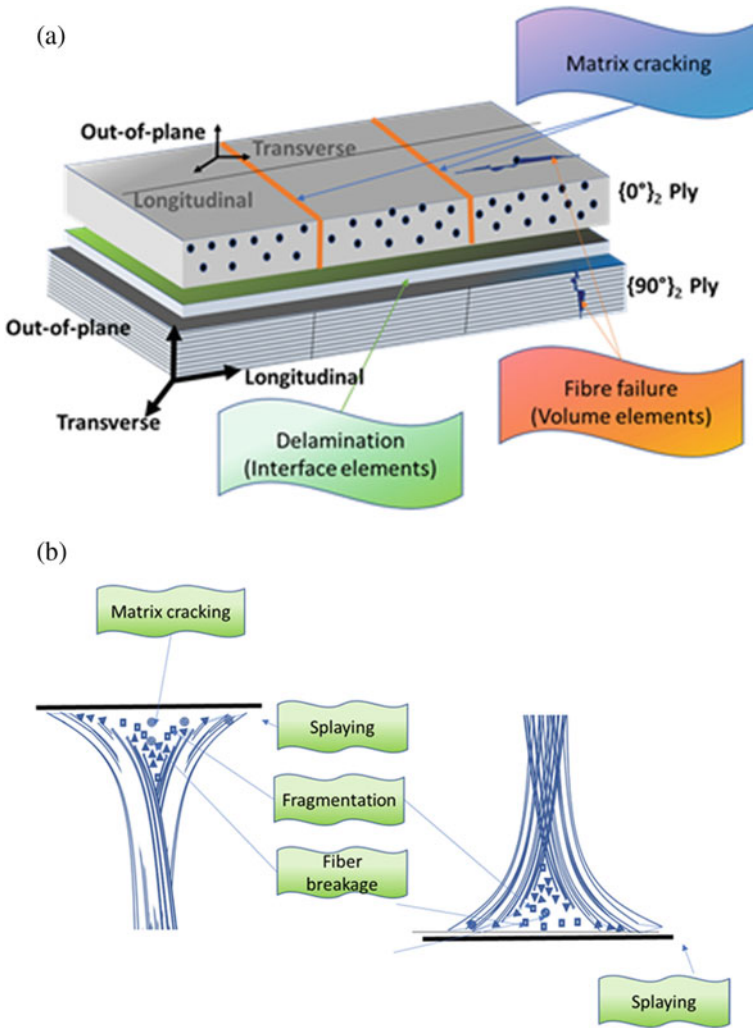
Fig. 2 a Ply model schematic different fracture mechanisms. **b** Schematic of fibre fracture mechanisms

Composites are primarily used in automobile manufacturing alternative to steel and other metal materials, to decrease weight, enhance strength and durability. The adoption of contemporary composite materials triggered a revolution in automobile technology worldwide at the beginning of the 1990s. In 1984, McLaren made carbon fibre from the monocoque of F1 vehicle [17]. The use of composites is currently more or less standard, particularly in sports vehicles. There are many advantages of composite material over conventional material, as shown in Fig. 3.
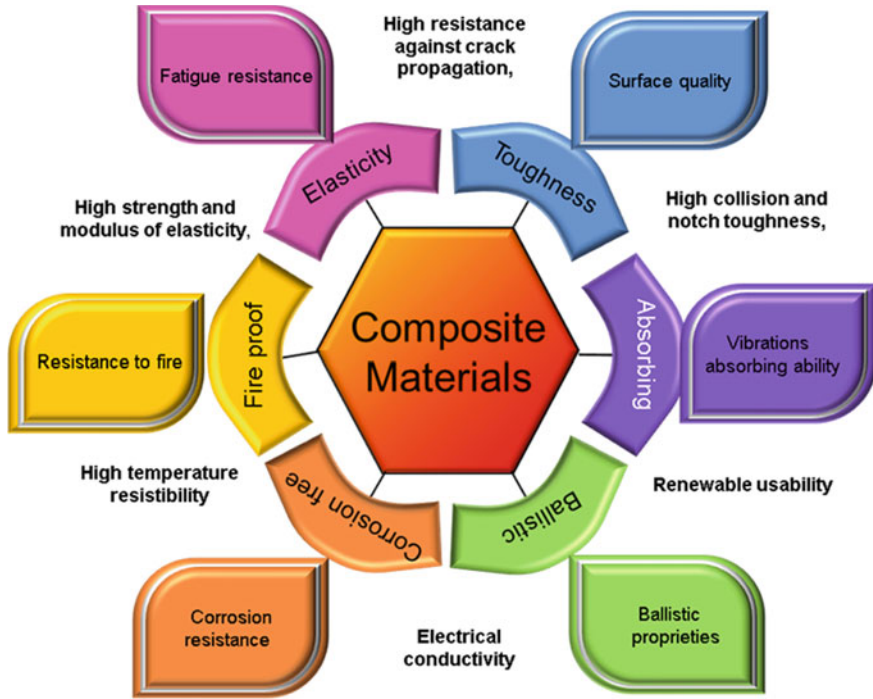
Fig. 3 Advantages of composite material

Using composite material, manufacturers can reduce vehicle weight by more than 30% by carbon fibre or other composite material [18]. Reducing vehicle weight lowers fuel consumption as fuel is an emerging issue for automobile engineers and vehicle manufacturers. The most substantial reason for using composite material is its high impact strength, making it more safe and secure against accident impact and saving human life [19]. However, we still need to improve the strength of this material. The fundamental reason for using composite material is shown and described in Fig. 4. Composite material is reusable, like steel and plastic. However, the composite material require unique manufacturing process and a high-skilled engineer for developing new material with high cost and time. This review focuses on types of composite material, energy absorption characteristics.

2 Material for Energy Absorber

Energy absorbers constructed using composite materials exhibit mechanical qualities that are not found in their metallic equivalents. These features include increased strength, decreased weight, increased specific stiffness, increased vibration and noise
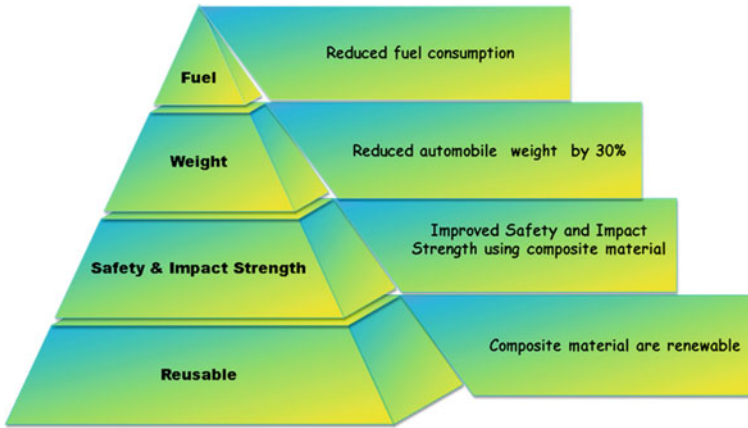
Fig. 4 Composite material strength

control capability. Composite materials are employed to construct the structures thatcombine fibre reinforcement with a polymer matrix. Fibre/matrix composites combined with suitable amounts of hardener/curing materials for faster curing and strengthening of polymer materials depending on developing processes [20]. The two types of polymer matrices are thermosetting and thermoplastic, while fibre reinforcement can be natural or synthetic origin [21]. Sandwich and nanostructure as advanced materials used in the automobiles sector. However, hybrid structures used for the front bumper and windshield. Synthetic compound structures like carbon GRP and glass GRP are used for high speed and armed class vehicles.

3   Polymeric Matrices and Foams

Usually, thermoplastics or thermosets are used as polymeric matrices in crashworthiness applications. All thermoplastics have a rigid molecular structure that reform on heating. Polyamide [22], polypropylene, polystyrene [23], polyvinyl chloride, polyether ether ketone are thermoplastics. Whereas, thermosets have a low molecular weight and are incapable of reforming. The standard type of thermosets is epoxy resin, vinyl ester resins [24].

3.1   Synthetics Composite

EACS has been formed by combining a variety of synthetic materials with their polymers. Carbon, glass, and aramid fibres are synthetic fibres used in EACS are listed in Fig. 5, the caron/graphite and glass two fibre types are often used due
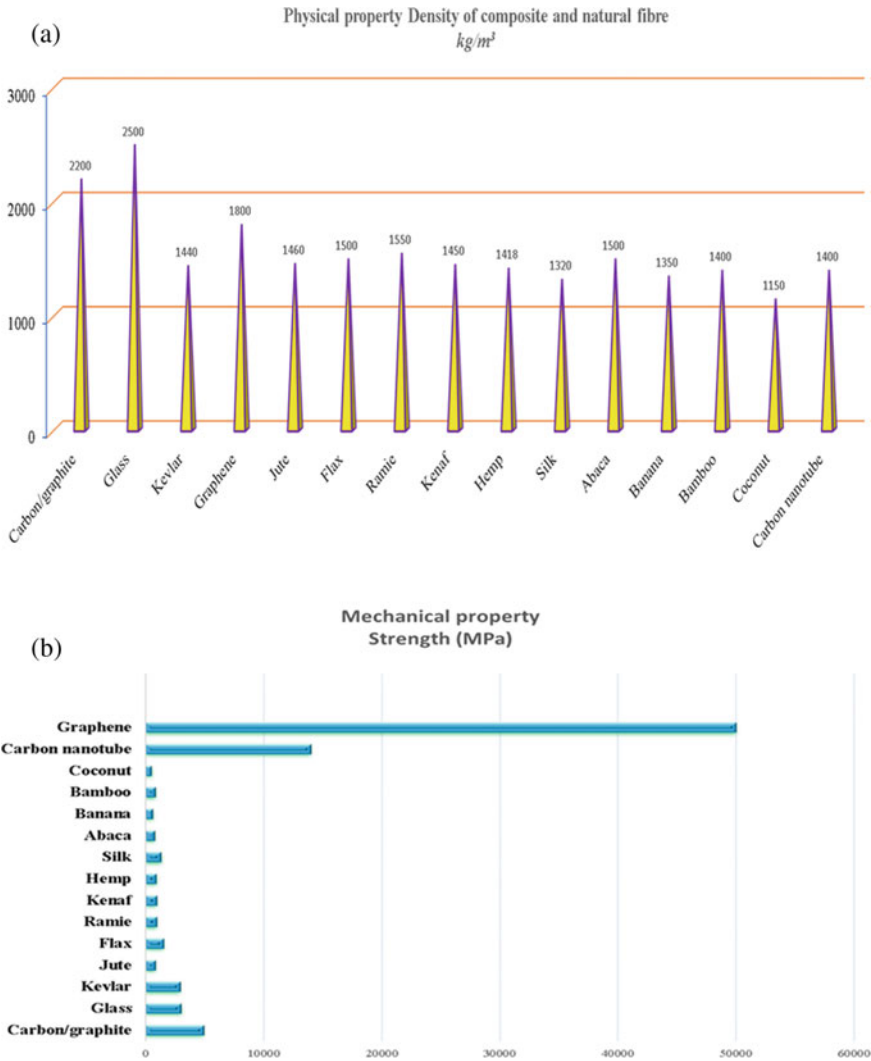
Fig. 5 **a** Physical property of energy-absorbing composite and natural fibre. **b** Mechanical property of energy-absorbing composite and natural fibre

to greater mechanical strength than the Kevlar fibre. Many aspects of the energy absorption capability of reinforced polymer of glass fibre and carbon were reported by Ochelski and Gotowicki [25]. They observed 20% greater specific energy absorption for the epoxy composite of carbon than glass. To enhance the mechanical strength of synthetic fibres, graphene nanoparticles blended with EACS structure as shown in Fig. 5a, b (Graph). Glass fibre has the most robust physical property than natural and synthetic composite. The combination of synthetic composites with nanoparticles

functions as good reinforcing elements to improve the energy absorbers of crushing characteristics. The model for the crash box's mechanical behaviour was developed by Elmarakba et al. [26]. The composite comprised of three materials like glass fibres, with graphene nanoparticles (round shape) placed in a polymer matrix. The mass of more than 1673 Pond is used for crushing the box to calculate values by finite element and mean field homogenization (MFH). The finding determines graphene composite has better compactibility then glass fibre reinforces composite in terms of SEA value.

3.2   Carbon Fibre Based Reinforced Polymer (CFRP)

Many researchers worked on the crash resilience of CFRP nano-composite structures. Zhu et al. recently developed single-cell with multi-cell CFRP forms to evaluate the overall absorbance of energy throughout the distinct dual configurations and concluded that the multi-cell structure generated a greater EAC than the single-cell design [27]. The CFRP presented by Xin et al. shows the effect of the cut angle on the crushed tubes of SEA. The investigator also examined the energy absorbing of the crushed structure enhanced by adjustment of the cuts [28]. For instance, Boria et al. examined the CFRP wall thickness, conical structures angle, and internal diameter of minor conical structure as a significant EA parameter. Based on the results, the inclination angle greatly influences the failure of a structural model [29].

Though, the EAC was improved by increasing the CFRP laminate thickness and the average diameter and by lowering the wall thickness. Energy absorbers created by combining graphite, a carbon fibre, with matrix resin. EAC of circular graphite/epoxy tubes impact was examined experimentally by Siromani et al. [30]. According to their findings, the effect of the trigger mechanism results in a substantial drop in peak load and simultaneous increase in SEA.

3.3   Glass Fibre Reinforced Polymer (GFRP)

Glass Fibre Reinforced Polymer has received considerable attention, similar to carbon fibre reinforced nano-composite tubes the glass fibres with their matrices is used as energy absorbers. Glass Fibre Reinforced Polymer is available in various forms A-GFRP, C-GFRP, D-GFRP, E-GFRP, and S-GFRP. The E-GFRP and S-GFRP are primar energy absorption forms. The amount of fibre and staking series affect the implementation of the composite. Solaimurugan et al. investigated the effect of fibre orientation and stacking sequence with GFRP tube shown SEA enhancement upon axial impact by the increasing axial fibre content [31].

3.4 Composite Sandwich Structures

Sandwich structure form is designed by composite energy absorbers. The inspiration for this design style is to create a lightweight and strong structure. Use of such design in automobiles and other commercial vehicles reduce vehicle weight by improving fuel efficiency. Sandwich composite structures are constructed from two adjacent lightweight plates of any size that joined by a core. To further enhance the energy absorption sandwich device's crushing ability, the core is also structurally aided by polymer or metallic foams. For instance, Sun et al. used closed-cell Al foam substrate and different panels to support metallic foams to examine their dynamic impact resistance [32]. In collaboration with other scientists, a few researchers have previously investigated the absorption and impact architecture of aluminium-based graded core sandwich structures for low-speed impact; their findings indicate the deformation and failure characteristics of the impact panel are significantly affected by the density gradients of the graded foam core. Metallic foams were recently structured as honeycombs for providing better safety in addition to superior structural strength [33].

4 Functionally Graded Crash-Resistant Composites

Functionally graded crash-resistant composites emerge with great potential to provide more excellent, effective energy absorption patterns. Crushing tubes are also manufactured via integrating various composites' features in one energy-absorbing graded component. The graduated design has lightweight qualities, strong bonding, and reduced stress due to smooth interface changes [34]. The progressive change in the Unit Cell increases the connecting force, guarantees that the mechanism of failure is progressive during a crash and improves the energy absorber's crash resistance. Therefore, functionally graded crash-resistant composites are an excellent technique to reduce fracture in composite constructions [35]. It is also highly efficient for isolating noise and vibration and can be an alternative material for the equipment's casing to reduce vibration and noise in the crash. But the use of graded materials for energy absorbents is not studied well. One of the probable reasons for this may be the task to form a single material type by combining a composite material with two or more incompatible features. Therefore, most research has recommended metallic materials with functionally graded thickness (FGT) and functionally graded foams (FGF). FGT metal alloys are a unique type of composite materials produced by infiltration of molten metals, resulting in graded preforms of varied shapes. FGT metal alloys are categorized as a unique composite material produced when molten metals are melted infiltration to generate preforms of varied forms [36].

5 Solutions to the Problems, for the Sustainable Development of Energy Absorber Crash Assessment

This review has demonstrated that EACS performs better in a crash than metallic counterpart if crushed under axial or oblique stress conditions. However, several problems in the synthetic structure and its manufacturing methods remain challenging. Practical solutions to some of these difficulties have been provided with probable progress in manufacturing highly efficient energy absorbers. EACS damage evaluations are also revealed with potential composite fixes. Figure 6 pie chart demonstrates the future need for crash assessment regarding the material used for future-ready vehicles, advanced manufacturing process with better adhesive material that last longer, and low cost for repair and sustainability.

5.1 Material Comparison

The comparison of different metallic and composite materials is shown in Fig. 7. Among the various materials, IM carbon is excellent for composite material in specific strength, tensile strength, and elasticity, followed by HM carbon and fiberglass.

Weight reduction and vehicle usage decrease

Automobile makers are employing new, ultra-light polymers to reduce carbon dioxide emissions. The composite material is the main advantage of making vehicles lightweight and more secure against accidental impact and fuel efficiency. Still,
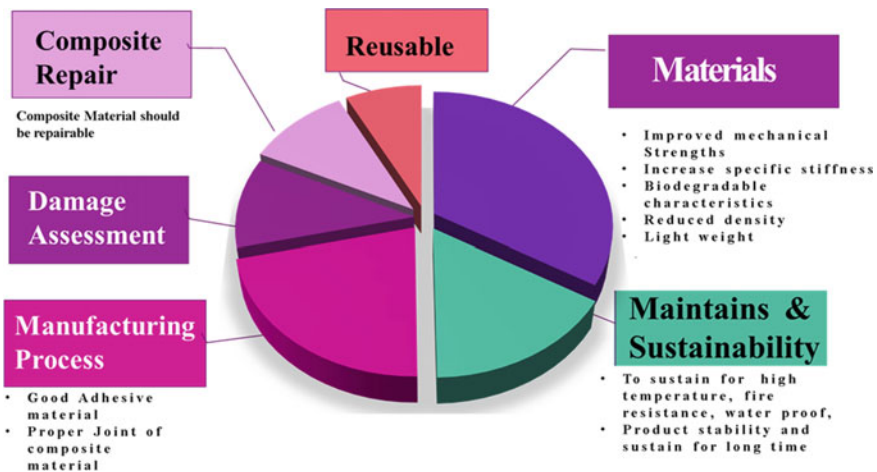

Fig. 6 Crashworthiness assessment for industry 4.0 ready vehicles
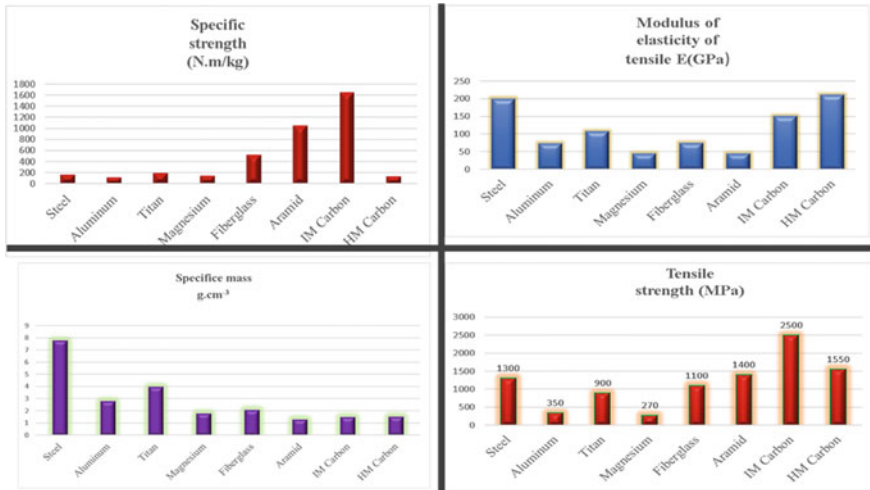
Fig. 7 Comparative chart for different metal and composite material

the only obstacle to use such materials is their high price and complex production process. Figure 8 show the comparison of carbon composite with other essential material used for vehicle body manufacturing. The lower vehicle weight by 30%, resulted in fuel efficiency of 7% and is helpful for reducing CO_2 to build eco-friendly and EURO 7 standard vehicles [37]. Also, a comparison with an engine that provides higher efficiency than a diesel engine.

The tensile strengths are the material structure's capacity to absorb energy via a controllable approach. The requirements for the durability of automobiles are:

- Reconfigurable vehicle end part that protects the integrity of the rear passenger area and protects the gas tank [38].
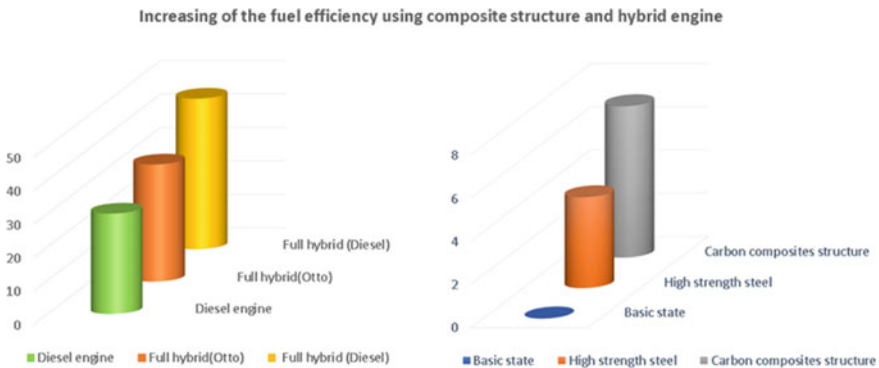

Fig. 8 Fuel efficiency comparison with composite material and primary material

- The side framework and doors of vehicle were design in ergonomics standerds [39].
- Rooftop structure should protects passenger when vehicle turnover [40].
- Proper utilisation of available space using the latest ergonomics [41].

5.2 Manufacturing Technique

In producing energy-absorbing materials, the hybrid components are generally inadequately connected, resulting in increased structure weight and less energy absorption during impact. A good adhesion material can provide an actual answer to increasing hybrid structure's stability. More studies focused on the testing and production of materials can increase hybrid structure adhesion quality [42].

5.3 Assessment of Damage

Residual pre-impact crashworthiness could arise through production, maintenance, and handling of the energy absorber. These numerous tiny impacts may result in the formation of early cracks. The energy absorber suffers from metal fatigue and pre-damage, lowering its entire crashworthiness [43].

5.4 Composite Material Repairing

The most challenging issue of composite repair is composite constructions includes detecting fractures, riveting, and bolting. Because they enhance tensile stress and increase structure weight, other repair techniques like scarfing and injection repair techniques need depth research, or apart from repair, composite structures need to develop to replace a particular part. It is a common practice called scarf patches; it provides the best stress transfer and effectiveness.

6 Conclusion

This review summarises investigations on the crash behaviour of EACS. The increasing amount of fatalities, injuries, and damage to precious objects in the previous decades during the disaster crash has raised academics' interest in finding more effective means of detaining the situation. Structures or gadgets built of composite materials absorb energy exhibit more integrity and crash resilience than metallic equivalents. They are unmatched to other materials because of their

low weight, environmental friendliness, low densities, more incredible strengths, higher specific rigidity, and excellent possibilities for noise reduction. However, this research has demonstrated that choosing composite materials and manufacturing processes may significantly impact their more effective energy absorption capacity. Finally, there have been several ideas and plans for future progress.

References

1. Tan H, He Z, Li E, Cheng A, Chen T, Tan X, Li Q, Xu B (2021) Struct Multidiscip Optim
2. Smith D, Graciano C, Martínez G (2021) Thin-Walled Struct. 160:107371
3. Hongyong J, Yiru R, Reinf J (2019) Plast Compos 39
4. Isaac CW, Ezekwem C (2021) Compos Struct 257:113081
5. Isaac CW, Pawelczyk M, Wrona S (2020) Appl Sci 10:1543
6. Alkateb M, Sapuan S, Leman Z, Ishak M, Jawaid M (2018) Def Technol 14:327
7. San Ha N, Lu G (2020) Compos Part B Eng 181:107496
8. Xie J, Waas AM (2015) J Appl Mech 82
9. Tariq F, Uzair M, Shifa M (2021) J Sandw Struct Mater 10996362211036988
10. Jefferson AJ, Arumugam V, Dhakal H (2018) Repair of polymer composites: methodology, techniques, and challenges. Woodhead Publishing
11. Warrior N, Turner T, Robitaille F, Rudd C (2004) Compos Part Appl Sci Manuf 35:431
12. Reyes G, Cantwell W (2000) Mater Struct Energy Absorpt London UK 33
13. Ilami M, Bagheri H, Ahmed R, Skowronek EO, Marvi H (2021) Adv Mater 33:2003139
14. Baillie C, Southam C, Buxton A, Pavan P (2000) Adv Compos Lett 9
15. Baars J, Domenech T, Bleischwitz R, Melin HE, Heidrich O (2021) Nat Sustain 4:71
16. Ismail I, Abdelrazek E, Ismail M, Emara A (2021) Int J Automot Mech Eng 18:8728
17. Kender Š, Brezinová J, Sailer H (2020) Trans Motauto World 5:3
18. Ahmad H, Markina AA, Porotnikov MV, Ahmad F, Conf IOP (2020) Ser Mater Sci Eng 971:032011
19. Hussain NN, Regalla SP, Rao YVD, Dirgantara T, Gunawan L, Jusuf A (2021) Proc Inst Mech Eng Part J Mater Des Appl 235:114
20. Summerscales J (2018) Mar Compos Des Perform. Elsevier/Woodhead imprint
21. Liu H, Liu J, Ding Y, Zheng J, Kong X, Zhou J, Harper L, Blackman BR, Kinloch AJ, Dear JP (2020) J Mater Sci 55:15741
22. Costas M, Morin D, Langseth M, Romera L, Díaz J (2016) Thin-Walled Struct 99:45
23. Aktay L, Toksoy AK, Güden M (2006) Mater Des 27:556
24. Niknejad A, Assaee H, Elahi SA, Golriz A (2013) Compos Struct 100:479
25. Ochelski S, Gotowicki P (2009) Compos Struct 87:215
26. Elmarakbi A, Azoti W, Serry M (2017) Appl Mater Today 6:1
27. Zhu G, Yu Q, Zhao X, Wei L, Chen H (2020) Compos Struct 233:111631
28. Xin Z, Duan Y, Zhou J, Xiao H (2019) Compos Struct 209:150
29. Boria S, Scattina A, Belingardi G (2015) Compos Struct 130:18
30. Siromani D, Henderson G, Mikita D, Mirarchi K, Park R, Smolko J, Awerbuch J, Tan T-M (2014) Compos Part Appl Sci Manuf 64:25
31. Solaimurugan S, Velmurugan R (2015) Int J Veh Struct Syst IJVSS 7

32. Sun G, Zhang H, Lu G, Guo J, Cui J, Li Q (2017) Mater Des 118:175
33. Sun G, Li G, Hou S, Zhou S, Li W, Li Q (2010) Mater Sci Eng A 527:1911
34. Yang X, Ma J, Wen D, Yang J (2020) Prog Aerosp Sci 114:100618
35. Nian Y, Wan S, Zhou P, Wang X, Santiago R, Li M (2021) Mater Des 209:110011
36. Movahedi N, Murch GE, Belova IV, Fiedler T (2019) Mater Des 168:107652
37. Zhang D, Gao J, Tang D, Wu X, Shi J, Chen J, Peng Y, Zhang S, Wu Y (2021) One Earth 4:135
38. Murali PK, Kaboli M, Dahiya R, Kaboli IM (2021) Adv Intell Syst
39. Reyes JEA, Barbosa CJM, Nonato MEB, Olayres TN, Tamba ER. Springer, pp 317–324
40. Chai Z, Nie T, Becker J (2021) Auton. Driv. Chang. Future (Springer), pp 137–178
41. Porter JM, Case K, Freer M, Bonney MC (1993)
42. Sinmazçelik T, Avcu E, Bora MÖ, Çoban O (2011) Mater Des 32:3671
43. Pawar PM, Ganguli R (2011) Structural health monitoring using genetic fuzzy systems. Springer Science & Business Media

Evaluation of Cooling Channels Design for Plastic Injection Mold

Muhammad Harris Hisham and Alias Mohd Saman

Abstract Injection molding is the most common type of plastic production process. As the time goes, the production needs to develop and explore advance techniques to keep up to with the demand from the market for a faster and greater product. The quality and time of production for plastic injection molding can be improved by better cooling channel design. Faster cooling of the molding part means a shorter process cycle time. This study aims to evaluate the different cooling channel design for the mold. A case study of automotive cup holder was used in this study. Cooling channels were designed and verified by the used of Moldflow Insight simulation to achieve the best injection molding performance and effective design. Three cooling channels were proposed and analyzed the molding performance in term of time for ejection temperature, average part temperature, volumetric shrinkage, and deformation. The results shown that conformal cooling channel design give the best result compares to others. This type of cooling channel provides faster cooling, lowest part temperature as well as product quality.

Keywords Plastic injection molding · Cooling channels · Moldflow insight

1 Introduction

Injection molding is a significant process in the plastic industry. The process consumes around 32% of the world's plastic [1]. The capability of injection molding to produce a complicated shape when compared to other processes is one of the reasons for its appeal. Injection molding process begins with a grain of plastic being fed into the barrel through a hopper, heated, then compressed and injects into the cavity of the mold [2]. The plastic material must be heated to liquid condition before being injected into the mold and then cooled to return to solid state. The process

M. H. Hisham · A. Mohd Saman (✉)
School of Mechanical Engineering, College of Engineering, Universiti Teknologi MARA (UiTM), 40450 Shah Alam, Selangor, Malaysia
e-mail: aliasms@uitm.edu.my

might also have an impact on the product's quality. A well-designed cooling channel can reduce cooling time while maintaining consistent temperature distribution.

Injection molding has several cycle phases including mold close, injection stroke, holding period, cooling period, mold opening and lastly ejection period [3]. Cooling is the important step; it took about 50–80% of the cycle time [4]. The cycle time can be controlled by cooling process, therefore determine the cost-effective of an injection molding process. An efficient cooling channel design can reduce the cooling time and provide a uniform temperature distribution, thus improve the quality of the final product. A cooling channel usually done by drilling a straight hole inside the core and cavity, called conventional cooling channel. The conventional cooling channel however does not able to give a uniform thermal cooling compared to the conformal cooling channel because its capability to conforms to the shape of the cavity in the mold.

Studies were done on the cycle time reduction in injection molding process by providing varies cooling channel design shows different in results of time to reach ejection temperature, freezing time, shrinkage, and temperature variance [2–6]. Another study shows the used of 3D printing to improve cooling efficiency of a conformal cooling channel [7]. The channel's cross section was adjusted to ensure that the temperature difference is kept to the lowest.

The use of analytical formulas and programming in injection molding was also introduced. Researchers used Boundary Element Method (BEM) and sequential Quadratic Programming to optimize the cooling channel [8]. The correlation between cooling channel's location, solidification, and temperature distribution was also performed [9]. Variable mold cavity thicknesses and cooling channels were simulated with a finite volume model and confirmed with a numerical computation. Various cooling channel designs were made to optimize the cooling effect and minimize the cooling defects in injection molding process by using Taguchi method [10]. Finite element analysis is used to analyses thermal stresses in the mold surface geometry generated around the mold.

Plastic injection parts produce to meet the quality set by the customers. Product quality can be defined into dimensional properties, surface properties and mechanical properties [11]. These can be achieved by controlling the parameters during plastic molten injection and solidification such as injection pressure and speed, mold and processing temperature and cooling time. The experiment has been conducted to investigate the interaction between process parameters to minimize the shrinkage and warpage defects of thin-wall section [12].

Previous case study utilizes the inputs from flow analysis for designing a plastic Injection Molded Component [13]. Other researchers use multiple design parameters of cooling channel such as cross section shape and diameter, pitch diameter together with design of experiment to identify best combination of parameters give the best performance [14].

This study emphases on the optimization of the cooling channels for plastic injection molding using Moldflow simulation. The effect of cooling channel on product quality and process can be significant. The cooling channel is normally design by the mold maker based on practical knowledge and expertise. The project's goal is

to improve the cooling channels of the mold. A good cooling channel design helps ensure product quality and prevent defects like shrinkage, mold release problem, and internal tension. A case study is made to see the design performance of the cooling channel based on the parameters of the process. Several parameters are chosen for the process and the results from the cooling analysis are then compared between them.

2 Methodology

2.1 Product Specification

The case study used was a cup holder in a car that can be seen in Fig. 1. This part is used to hold the canned drinks for the car passengers. Cooling control is important in order to improve the product cycle time as well as to eliminate the defect occurrences. 3D model was developed by using CATIA software then convert to the STL format file which compatible with Moldflow software. Overall dimension of the cup holder is 170 mm × 100 mm × 70 mm with overall thickness of 2.5 mm. Figure 2 shows the 3D model of the part. Table 1 shows the specifications of the product material which is Acrylonitrile butadiene styrene (ABS). ABS possess good characteristics such as high rigidity, strong strain resistance and good impact resistance which suitable for its function. Table 1 shows thermal and mechanical properties of ABS.

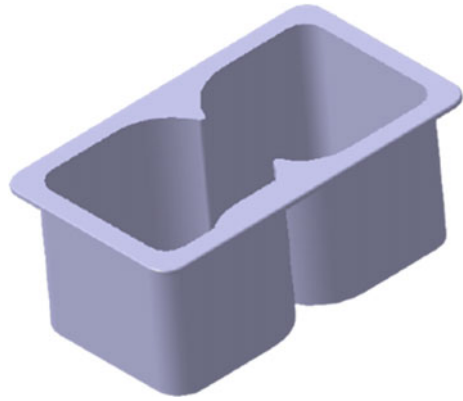**Fig. 1** Actual cup holder product

Fig. 2 3D model of cup
holder

Table 1 Thermal and
mechanical properties

Number	Property	Value
1	Density (g/cm^3)	1.1
2	Melt temperature (°C)	260
3	Thermal conductivity (10^{-4} cal/s cm °C)	4.1
4	Heat capacity (cal/g °C)	1.86

2.2 Cooling Channels Design

Cooling channels system is the main focus of this study. Cooling channels functions
to absorb the heat from the mold cavity effectively. They must be able to keep the
temperature and heat transfer rate uniform across the mold cavity. In this study,
three cooling system designs were proposed which are straight drill cooling channel
(DCC), conventional series cooling channel (SCC) and conformal cooling channel
(CCC).

As shown in Fig. 3, 3 cooling channel designs were proposed. The elements
proposed included cooling tubes (dark blue), gating system (green) and 2 product
cavities (light blue). DCC consist of 4 cooling tubes at the top and 4 at the bottom of
the part cavity. SCC has similar design as the DCC but come with 2 inlet and 2 outlet
which connected to flow all over the part. The CCC conforms to the shape of the
product, with some area of the cooling tube entering the internal shape of the product
as shown in Fig. 3c. The diameter for all the cooling channels was keep constant at
8 mm, with circular shape in cross-section. Distance between of the channels and
to the cavity wall was fixed at 50 and 25 mm. However, the channels at the bottom
side (core-side) for the DCC and SCC were straight and not maintained the channel-
cavity wall distance. The best flow for all the cooling channels is turbulent flow and
Reynold number above 10,000 [5]. Because of its strong cooling effect, water was
chosen as the cooling medium. Inlet water temperature was set at 25 °C. Unlike oil,
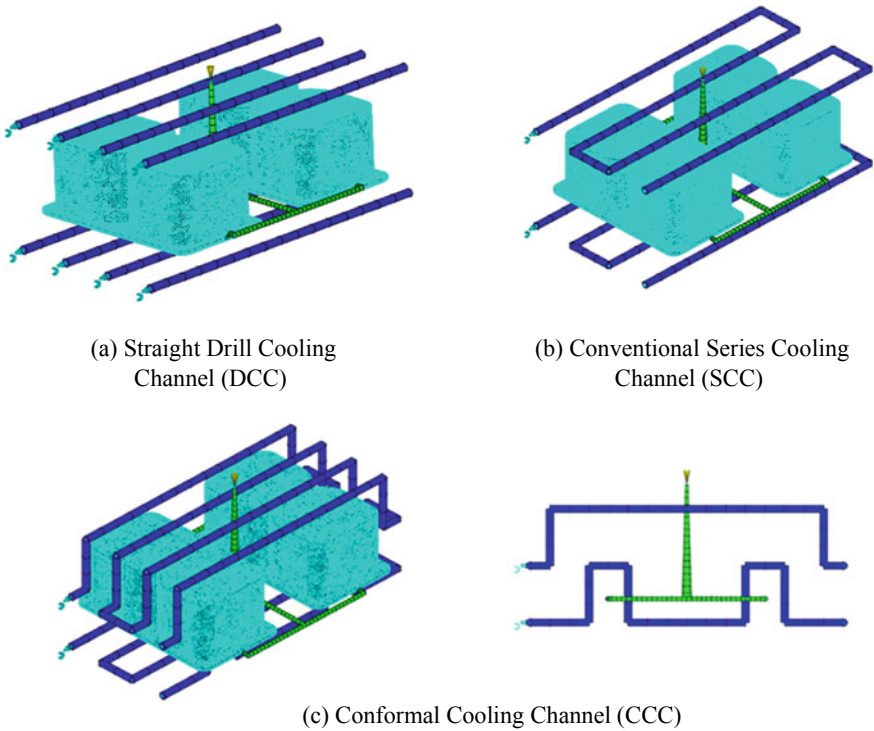water is inexpensive and ecologically beneficial.

(a) Straight Drill Cooling
Channel (DCC)

(b) Conventional Series Cooling
Channel (SCC)

(c) Conformal Cooling Channel (CCC)

Fig. 3 Cooling channel designs with gating system and product cavities

2.3 Moldflow Analysis

Step for cooling channels analysis or cool FEM + fill + pack + warp analysis starts with the creation of the mold component, which produced around the product. The size of the mold is adjusted such the cooling system and gating system is inside the mold. A small part of the inlet, outlet and runner system being allowed to be outside of the mold. This can be seen in Fig. 4.

Before running the analysis, 3D mold mesh is created to represents the mold by filling the volume of the mold with four-node, tetrahedral elements. The element only covers the mold area, not including the cooling channels and gating system. The total number of elements for each design are 3,184,613, 3,005,454 and 2,877,454 for DCC, SCC and CCC respectively.
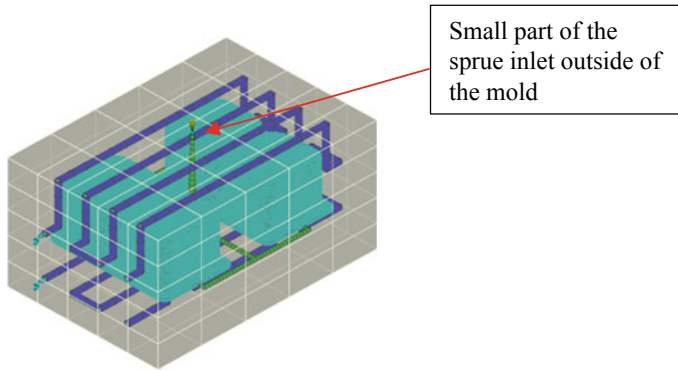
Small part of the
sprue inlet outside of
the mold

Fig. 4 Mould area around the part

3   Results and Discussion

In this section, simulation results in terms of time to reach ejection temperature
(time required to reach the ejection temperature, which is measured from the start
of fill), volumetric shrinkage at ejection, and the average temperature of the part are
discussed.

3.1   *Time to Reach Ejection Temperature*

Time to reach ejection temperature is important because it display the time required
before reach the ejection temperature. This is recorded from the start of the cycle.
Molded plastic part is considered ready to be removed from its mold once it is near
or below the heat deflection temperature (HDT). At this time, part deformation will
be resulted within the acceptable limits.

Figure 5 shows the comparison of time to reach ejection temperature for different
cooling channel. The time to reach ejection temperature for DCC and SCC cooling
channels recorded similar results of 30 s. While CCC cooling channel needs about
19.9 s to reach the ejection temperature. Design of DCC and SCC is almost identical,
therefore similar result is understandable. The CCC was designed that the channel is
conformed to the cavity walls at both cavity and core sides. Therefore, highly effective
cooling was achieved, and earlier ejection temperature was reached. In overall, CCC
provided the fastest time to reach ejection temperature for the part, where 37% of
time reduction compared to the other 2 cooling channels. This is preferable because it
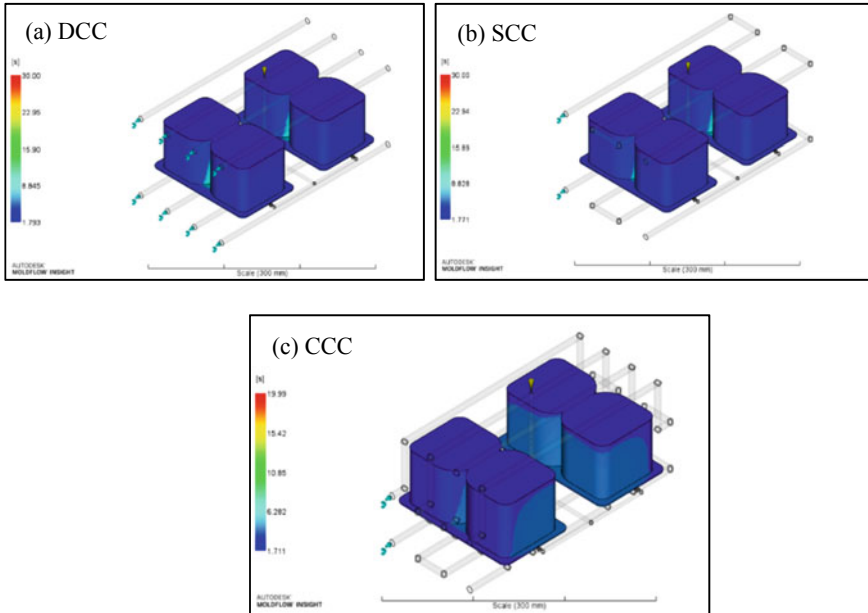will reduce the overall process cycle time and subsequently increase the productivity.

Fig. 5 Time to reach ejection temperature for different cooling channels

3.2 Volumetric Shrinkage at Ejection

The volumetric shrinkage at ejection is the compression of the polymer due to the change in temperature from melt temperature to reference temperature. This parameter gives information about the percentage reduction in the volume of the part at the time of ejection. The lower the percentage of the volumetric shrinkage the better the part accuracy.

Figure 6 shows the volumetric shrinkage results for different cooling channels. The simulation result show that DCC resulted 6.88%, contrasted to SCC 6.86%, and CCC 6.62% of volumetric shrinkage. The conformal cooling channel has the lowest percentage of volumetric shrinkage between them all. With the reduction of 0.2%. Additionally, Fig. 6c shows that better tabulation of shrinkage percentage (uniform green color) compares to the other two. This indicates that the cooling effect was more effective for CCC, which provided identical cooling rate for overall part cavities.

3.3 Average Temperature

The average temperature for the part is the overall temperature profile across the part thickness. The average temperature for the part shows the effectiveness of the cooling channels in transferring the heat. The value is halfway between the target
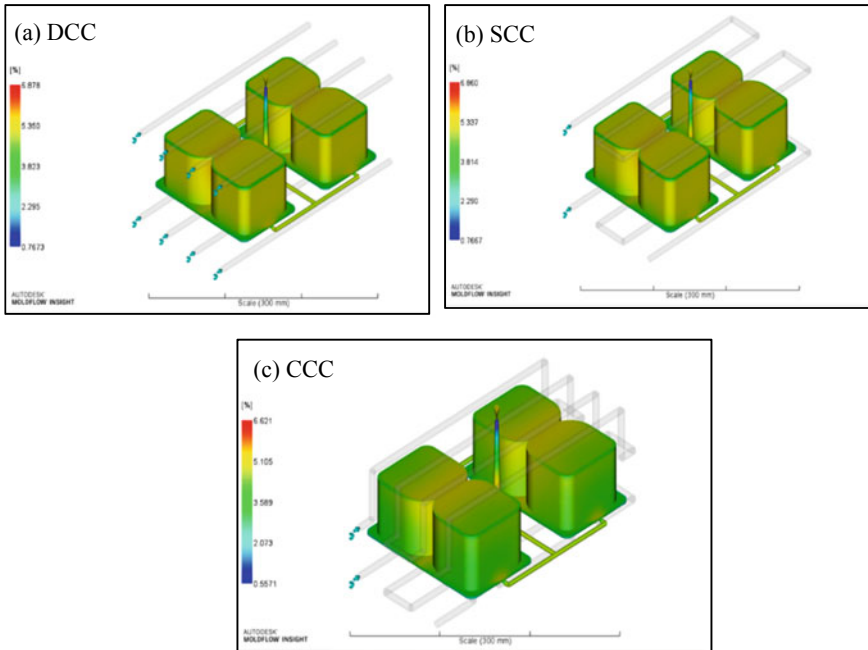
Fig. 6 Volumetric Shrinkage at ejection for different cooling channels

mold temperature and the ejection temperature. The initial temperature of the part is 260 °C during the injection of the material. For the comparison, the temperatures were calculated at t = 30 s.

Figure 7 shows the result of the temperature part average from Moldflow simulation. While Fig. 8 shows a comparison of temperature part average of the different cooling channel configurations. The DCC part average temperature is 76.9 °C, SCC 75.71 °C, and CCC is 52.34 °C. The lowest temperature part average is CCC with the overall temperature reduction almost 25 °C of temperature. The CCC preferable because it provides the lowest average temperature, subsequently speed up part ejection process which reduce the overall cycle time.

3.4 Deformation

The total deformation of the part is affected by shrinkage, orientation, and cooling system. Figure 9 shows the most deflection on the part is red and the lowest deflection in blue color. The part mostly deforms on the edge side of the cup holder. The deformation is very similar between the parts for each cooling channels, because of similar cavity design. The color variation shows that CCC provided better proportion of deflection color which indicated uniform cooling rate was attained.
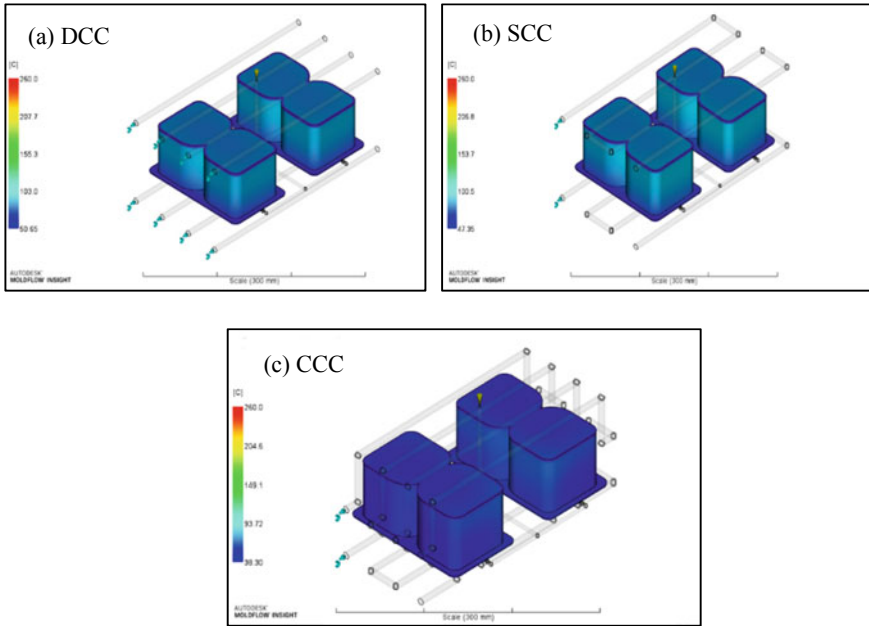
Fig. 7 Temperature part average for different cooling channels

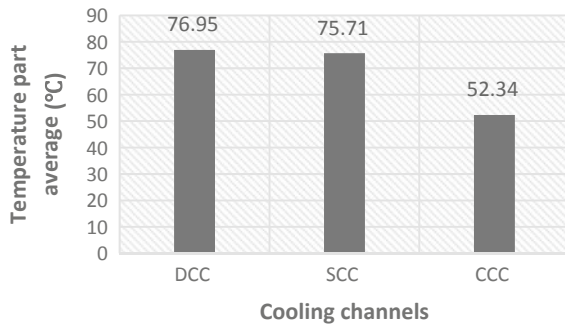**Fig. 8** Comparison of temperature part average for different cooling channels

Figure 10 shows that the DCC and SCC parts has the utmost deformation compares to the CCC. In general, maximum deformation occur at DCC and SCC parts with a deformation of 0.722 mm the CCC part with 0.656 mm. Even though the value is small, but the occurrences show CCC has the most optimal cooling temperature distribution and gave lowest product deformation.
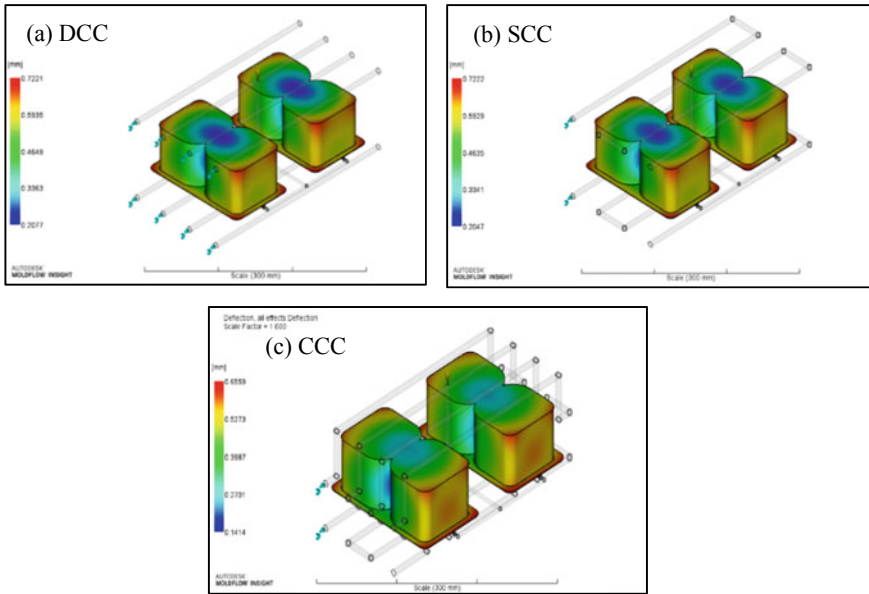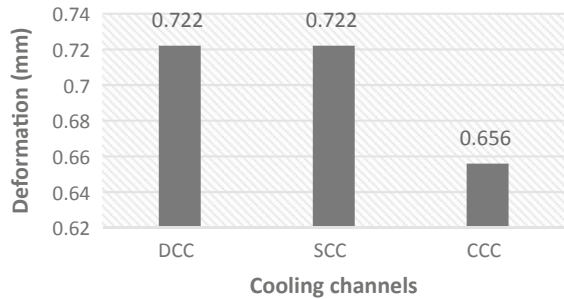
Fig. 9 Deflection for different cooling channels

Fig. 10 Comparison of deformation for different cooling channels

4 Conclusion

This study evaluates the cooling channel for plastic injection mold by using Moldlfow simulation. Three variations of cooling channels design were created names as straight drill cooling channel (DCC), conventional series cooling channel (SCC) and conformal cooling channel (CCC) with the constant process parameters have been analyses. The result from the simulation analysis is then compare between each other. The analysis result shows that the conformal cooling channel has advantage over other type of cooling channels, with smaller deformation, lowest average temperature of part, smallest volumetric shrinkage, and shortest time for part to reach ejection temperature.

Uniform cooling system of molded part in the plastic injection mold is very important to be prepared by appropriate cooling system design. This is to ensure that the cooling cycle is optimized, and part defects can be eliminated. In this paper, the evaluation of different cooling channel has been done by using of computer simulation. This can be an advantage to the manufacturer in deciding the best cooling options for the mold.

References

1. Mukras SMS (2020) Experimental-based optimization of injection molding process parameters for short product cycle time. Adv Polym. Technol
2. Yadegari M, Masoumi H, Gheisari M (2016) Optimization of cooling channels in plastic injection molding. Int J Appl Eng Res 11(8):5777–5780
3. Powell JA (2000) Part and mold design thermoplastic. Bayer Mater Sci 2(2):137–145
4. Khan M, Afaq SK, Khan NU, Ahmad S (2014) Cycle time reduction in injection molding process by selection of robust cooling channel design. ISRN Mech Eng 2014
5. Senkerik V, Stanek M, Manas M, Manas D, Skrobak A, Navratil J (2012) Gate location and cooling system optimization. Int J Math Comput Simul 6(6):558–565
6. Prasetiyo AB, Fauzun F (2018) Numerical study of effect of cooling channel configuration and size on the product cooling effectiveness in the plastic injection molding. MATEC Web Conf 197:8–11
7. Park HS, Dang XP (2010) Optimization of conformal cooling channels with array of baffles for plastic injection mold. Int J Precis Eng Manuf 11(6):879–890
8. Schmidt F et al (2011) Efficient mold cooling optimization by using model reduction. Int J Mater Form 4(1):73–82 Springer Verlag
9. Hassan H, Regnier N, Le Bot C, Defaye G (2010) 3D study of cooling system effect on the heat transfer during polymer injection molding. Int J Therm Sci 49(1):161–169
10. Venkatesh G, Ravi Kumar Y (2017) Thermal analysis for conformal cooling channel. Mater Today Proc 4(2):2592–2598
11. Panneerselvam V, Turan FM (2019) Optimization of process parameters of injection moldings for plastic pallets manufacturing industry. J Mod Manuf Syst Technol 02:75–83
12. Erzurumlu T, Ozcelik B (2006) Minimization of warpage and sink index in injection-molded thermoplastic parts using Taguchi optimization method. Mater Des 27(10):853–861
13. Kharche AP (2018) Design enrichment for plastic injection mold using flow analysis. Int J Eng Res Technol 7(05):604–608
14. Jahan SA, El-Mounayri H (2016) Optimal conformal cooling channels in 3D printed dies for plastic injection molding. Procedia Manuf 5:888–900